

Modern NMR Spectroscopy for Exploring New Intermediates and Reaction Pathways in Organo- and Photocatalysis, Organometallic and Inorganic Chemistry

Dissertation

zur Erlangung des Doktorgrades der Naturwissenschaften

(Dr. rer. nat.)

der Fakultät für Chemie und Pharmazie

der Universität Regensburg



vorgelegt von

Verena Streitferdt

aus Ingolstadt

im Jahr 2020

Die vorliegende Dissertation beruht auf Arbeiten, die zwischen Januar 2017 und November 2020 am Arbeitskreis von Frau Professor Dr. Ruth M. Gschwind am Institut für Organische Chemie der Universität Regensburg durchgeführt wurden.

Promotionsgesuch eingereicht am: 30. November 2020

Die Arbeit wurde angeleitet von: Prof. Dr. Ruth M. Gschwind

Promotionsausschuss:

Vorsitzender: Apl. Prof. Dr. Rainer Müller

1. Gutachterin: Prof. Dr. Ruth M. Gschwind

2. Gutachter: Prof. Dr. Werner Kremer

3. Prüfer: Prof. Dr. Nikolaus Korber

Meinen Eltern

*Die Phantasie kommt hier nicht zu kurz,
und abweichende Resultate lassen auch der nächsten
Generation noch die Hoffnung auf Neues.*

Hans-Georg von Schnering

**Modern NMR Spectroscopy for Exploring
New Intermediates and Reaction
Pathways in Organo- and Photocatalysis,
Organometallic and Inorganic Chemistry**

Verena Streitferdt

TABLE OF CONTENTS

1 INTRODUCTION AND OUTLINE	1
1.1 Nuclear Magnetic Resonance Spectroscopy as Powerful Analytical Method	1
1.2 References	6
2 ADVANTAGES OF BROADBAND EXCITATION IN NMR	11
2.1 Introduction.....	12
2.2 Incorporation of the xyBEBOP in 1D Pulse Programs with ¹ H-Decoupling.....	15
2.3 Incorporation of the xyBEBOP in HMQC Experiments.....	18
2.4 Conclusion.....	25
2.5 Pulse Programs.....	26
2.5.1 bulu_zg_shape.....	26
2.5.2 bulu_zgpg.....	26
2.5.3 hmqcgpqfbulusp2.....	27
2.5.4 hmbcgpndqf_bulusp2.....	29
2.6 References.....	30
3 UNPRECEDENTED MECHANISM OF AN ORGANOCATALYTIC ROUTE TO CONJUGATED ENYNES WITH A JUNCTION TO CYCLIC NITRONATES	33
3.1 Abstract.....	34
3.2 Introduction.....	34
3.3 Results and Discussion.....	36
3.3.1 Compound Pool for Mechanistic Studies.....	36
3.3.2 Identification of Cyclic Nitronate as Second Product.....	37
3.3.3 Common Pathway of Nitronates and Enynes to a Central Linking Intermediate.....	37
3.3.4 Mechanism of the Conjugated Enyne Formation.....	41
3.3.5 Mechanism of the Cyclic Nitronate Formation.....	43

TABLE OF CONTENTS

3.3.6	Selectivity: Conjugated Enyne versus Cyclic Nitronate.....	45
3.3.7	Yield and scope of the combined route to conjugated enynes and cyclic nitronates.....	46
3.3.8	Summary of Mechanistic Proposal and Conclusion.....	47
3.4	Experimental Section.....	48
3.4.1	General Procedure for the Synthesis of Homo-Dimers.....	48
3.4.2	General Procedure for the Synthesis of Hetero-Dimers.....	49
3.4.3	Computational Details.....	50
3.5	Acknowledgements.....	50
3.6	References.....	50
3.7	Supporting Information.....	53
3.7.1	Experimental Details.....	53
3.7.2	Mechanistic study.....	54
3.7.2.1	Detection and characterization of the central intermediate in the conjugated enyne and cyclic nitronate formation.....	54
3.7.3	Identification of Intermediate 4 as a Linking Intermediate of the Enyne and Nitronate Pathway.....	56
3.7.4	Proposed Mechanisms to Intermediate 4.....	56
3.7.5	Conjugated Enyne Formation.....	57
3.7.5.1	Literature Known Reactions Supporting the Mechanism towards Enynes.....	57
3.7.5.2	Detection of Side Products in the Conjugated Enyne and Cyclic Nitronate Formation.....	58
3.7.6	Variation of the Starting Material Structure.....	61
3.7.6.1	Electronic Variation.....	61
3.7.6.2	Structural Variation.....	63
3.7.7	Temperature Variation.....	65
3.7.7.1	Temperature Decrease.....	65

TABLE OF CONTENTS

3.7.7.2	Temperature Increase.....	66
3.7.8	Catalyst and Solvent Screening.....	67
3.7.8.1	Catalyst Screening by GC-FID.....	67
3.7.8.2	Solvent Screening.....	71
3.7.9	Polymerization Problematic.....	74
3.7.10	Scope.....	75
3.7.10.1	Nitroalkene Dimers.....	75
3.7.10.2	Conjugated Enynes.....	76
3.7.10.3	Cyclic Nitronates.....	77
3.7.11	General Procedures.....	78
3.7.11.1	General procedure for the synthesis of nitroalkenes 1 and 2.....	78
3.7.11.2	Dimers.....	79
3.7.12	Enynes.....	79
3.7.13	Nitronates.....	80
3.7.13.1	General procedure for cyclic nitronates 6.....	80
3.7.13.2	Reduction of Cyclic Nitronate 6a to 3-(but-1-en-1-yl)-4-propyl-4,5-dihydroisoxazole...80	80
3.7.14	Chemical Assignments.....	81
3.7.14.1	Nitroalkenes.....	81
3.7.14.2	Dimers.....	84
3.7.14.3	Cyclic Nitronate.....	92
3.7.14.4	Intermediate 4a.....	96
3.7.14.5	Conjugated Enynes.....	97
3.7.15	Computational Details.....	108
3.7.16	Additional Analytical Data.....	122
3.7.17	References.....	124

TABLE OF CONTENTS

4 DIRECT CATALYTIC TRANSFORMATION OF WHITE PHOSPHORUS INTO ARYLPHOSPHINES AND PHOSPHONIUM SALTS	127
4.1 Abstract.....	128
4.2 Introduction.....	128
4.3 Results and Discussion.....	130
4.3.1 Reaction development.....	130
4.3.2 Reaction scope.....	132
4.3.3 Mechanistic studies.....	134
4.4 Conclusion.....	136
4.5 Acknowledgements.....	136
4.6 References.....	137
4.7 Supporting Information.....	139
4.7.1 General information.....	139
4.7.2 General procedure for photocatalytic functionalization of P ₄ (0.1 mmol scale).....	141
4.7.3 Optimization of reaction conditions.....	142
4.7.4 Characterization of optimized 0.1 mmol scale reactions.....	143
4.7.4.1 Tetraphenyl phosphonium iodide.....	144
4.7.4.2 Tri(<i>o</i> -tolyl)phosphine.....	144
4.7.4.3 Tetra(<i>m</i> -tolyl)phosphonium iodide.....	145
4.7.4.4 Tetra(<i>p</i> -tolyl)phosphonium iodide.....	145
4.7.4.5 Tris(2-methoxyphenyl)phosphine.....	146
4.7.4.6 Tetrakis(3-methoxyphenyl)phosphonium iodide.....	147
4.7.4.7 Tetrakis(4-methoxyphenyl)phosphonium iodide.....	147
4.7.4.8 Tris(2-(methylthio)phenyl)phosphine.....	148
4.7.4.9 Tris(2-(methyl benzoate))phosphine.....	149

TABLE OF CONTENTS

4.7.4.10 Tetrakis(3-(methyl benzoate))phosphonium iodide	149
4.7.4.11 Tris(4-(methyl benzoate))phosphine.....	150
4.7.4.12 Tetrakis(3-(trifluoromethyl)phenyl)phosphonium iodide	150
4.7.4.13 Tris(4-(trifluoromethyl)phenyl)phosphonium iodide	151
4.7.4.14 Mesityl- and Dimesityl-phosphine.....	151
4.7.4.15 2,6-Dimesitylphenylphosphine.....	152
4.7.4.16 Tris(triphenylstannyl)phosphine.....	153
4.7.5 Reaction on a 1 mmol scale.....	154
4.7.5.1 Photocatalytic preparation of tetraphenylphosphonium iodide from P ₄	154
4.7.5.2 Photocatalytic preparation of tetra(<i>p</i> -tolyl)phosphonium iodide from P ₄	156
4.7.5.3 Photocatalytic preparation of tetrakis(3-methoxyphenyl)phosphonium iodide from P ₄	158
4.7.5.4 Photocatalytic preparation of tri(<i>o</i> -tolyl)phosphine from P ₄	160
4.7.5.5 Photocatalytic preparation of tris(2-methoxyphenyl)phosphine from P ₄	162
4.7.5.6 Photocatalytic preparation of tris(2-(methylthio)phenyl)-phosphine from P ₄	164
4.7.5.7 Photocatalytic preparation of tris(triphenylstannyl)phosphine from P ₄	166
4.7.6 Cyclic voltammetry studies	169
4.7.7 Emission quenching experiments.....	171
4.7.8 UV/VIS spectroscopic studies.....	175
4.7.9 In situ NMR experiments.....	177
4.7.9.1 Procedure for ³¹ P and ¹ H monitoring of the model reaction	177
4.7.9.2 ³¹ P and ¹ H monitoring of photocatalytic PhPH ₂ and Ph ₂ PH arylation reactions	178
4.7.9.3 ³¹ P and ¹ H monitoring of solutions of P ₄ and PhI	179
4.7.9.4 Photo-CIDNP effect.....	181
4.7.10 Photocatalytic phenylation of Ph ₃ P, Ph ₂ PH and PhPH ₂	182

TABLE OF CONTENTS

4.7.11 References.....	183
4.8 Additional Findings by NMR.....	185
4.8.1 Exchanging the metal catalyst by an organocatalyst.....	185
4.8.2 NMR approaches to unveil further intermediates of the productive pathway.....	192
4.8.2.1 Cooling of the reaction mixture & increase of catalyst loading.....	193
4.8.2.2 Radical Trapping with TEMPO.....	201
4.8.2.3 Spin trapping.....	204
4.8.3 Investigation of the origin of the intermediate-bound protons by isotopic labeling of TEA.....	210
4.8.4 Verification of PH ₃ as sequential precursor.....	212
4.8.5 Varying the Concentration of Starting Material.....	215
4.8.6 Identification of Phosphorus Side Products by In Situ NMR.....	217
4.8.7 Conclusion of the Additional Findings.....	220
4.8.8 References.....	221
5 A PHOSPHININE-DERIVED 1-PHOSPHA-7-BORA-NORBORNADIENE: FRUSTRATED LEWIS PAIR TYPE	
ACTIVATION OF TRIPLE BONDS.....	225
5.1 Abstract.....	226
5.2 Introduction.....	226
5.3 Results and Discussion.....	227
5.3.1 Synthesis, characterisation and mechanism of formation of 1-phospha-7-boranorborna- diene 2.....	227
5.3.2 Variable temperature NMR characterisation of isomers 2 and Iso-2a.....	231
5.3.3 Reactivity of 2 toward nitriles.....	232
5.3.4 Reactivity of 2 toward alkynes.....	235
5.4 Conclusion.....	239
5.5 Experimental Section.....	240

5.6 Acknowledgements.....	245
5.7 References.....	246
5.8 Supporting Information.....	249
5.8.1 Variable temperature NMR monitoring – formation of 2.....	249
5.8.2 Variable temperature NMR monitoring of 2.....	253
5.8.3 Variable temperature NMR monitoring – formation of 5c.....	257
5.8.4 Reaction of 6 with 4-(trifluoromethyl)phenylacetylene.....	259
6 FACILE C=O BOND SPLITTING OF CARBON DIOXIDE INDUCED BY METAL LIGAND COOPERATIVITY IN A PHOSPHININE IRON(0) COMPLEX.....	261
6.1 Abstract.....	262
6.2 Introduction.....	262
6.3 Results and Discussion.....	263
6.4 Conclusion.....	268
6.5 Acknowledgements.....	268
6.6 References.....	268
6.7 Supporting Information.....	271
6.7.1 Variable Temperature NMR.....	271
6.7.1.1 Variable temperature $^{31}\text{P}\{^1\text{H}\}$ NMR spectra of compounds 1- σ and 1- π	271
6.7.1.2 $^{31}\text{P}\{^1\text{H}\}$ NMR monitoring of the formation of 1- σ and 1- π at 273 K.....	273
7 ON THE REACTIVITY OF $\text{NHC}^{\text{TBU}}\text{AuCl}$ TOWARDS $\text{Rb}_6\text{Cs}_6\text{Si}_{17}$: THE FIRST GOLD - SILICON CLUSTER $[(\text{NHC}^{\text{TBU}}\text{Au})_6(\text{H}_2\text{-Si}_4)]\text{Cl}_2 \cdot 7 \text{NH}_3$ AND AN IMIDE CAPPED GOLD TRIANGLE $(\text{NHC}^{\text{TBU}}\text{Au})_3\text{NHCl}$.....	277
7.1 Abstract.....	278
7.2 Introduction.....	278
7.3 Results and Discussion.....	279
7.3.1 Crystallographic Investigations.....	279

TABLE OF CONTENTS

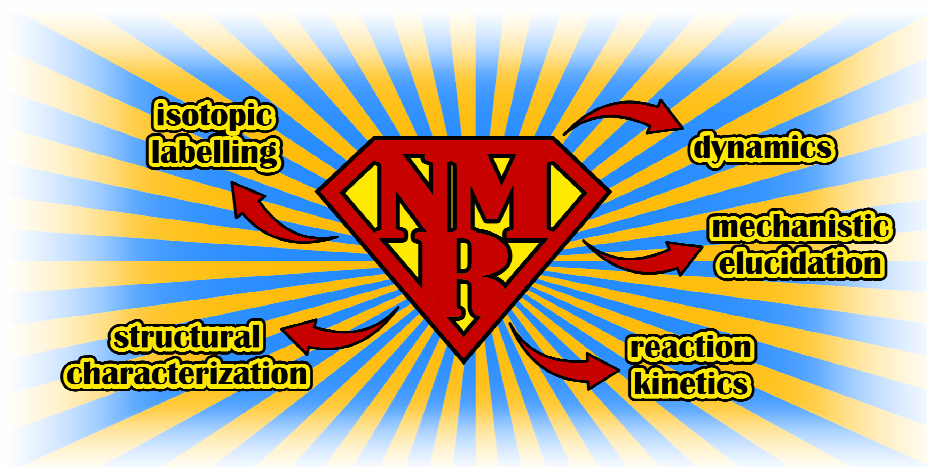
7.3.2	Theoretical calculations.....	281
7.3.3	NMR Studies.....	283
7.3.4	Structural Assignment.....	284
7.3.5	Proposed Mechanism towards the Formation of 1.....	285
7.3.6	Chemical Exchange and ²⁹ Si Studies.....	286
7.4	Conclusion.....	287
7.5	Experimental Section.....	287
7.6	Acknowledgements.....	289
7.7	References.....	289
7.8	Supporting Information.....	293
7.8.1	X-ray analysis.....	293
7.8.1.1	(NHC ^t BuAu) ₃ NHCl.....	293
7.8.1.2	[(NHC ^t BuAu) ₆ (η ² -Si ₄)]Cl ₂ · 7 NH ₃	294
7.8.1.3	[(NHC ^t Bu) ₂ Au]Cl · 7 NH ₃	296
7.8.2	Theoretical calculations.....	298
7.8.2.1	ELF.....	298
7.8.2.2	NBO.....	298
7.8.3	NMR-Spectroscopy.....	301
7.8.3.1	Diffusion ordered spectroscopy (DOSY).....	301
7.8.3.2	Characterizations/Assignment.....	303
7.8.3.3	Proton Trapping.....	315
7.8.3.4	Silicon Species.....	318
7.8.4	References.....	319
8	NMR-DETECTION OF AN ELUSIVE PROTONATED AND COINAGE METALIZED SILICIDE [NHC^{DIPP}Cu(H⁴-Si₉)H]²⁻ IN SOLUTION.....	321

TABLE OF CONTENTS

8.1 Abstract.....	322
8.2 Introduction.....	322
8.3 Results and Discussion.....	323
8.4 Conclusion.....	328
8.5 Acknowledgements.....	328
8.6 References.....	328
8.7 Supporting Information.....	331
8.7.1 Experimental Details.....	331
8.7.2 NMR Spectroscopy.....	332
8.7.2.1 General Information.....	332
8.7.2.2 Structural Investigations.....	332
8.7.2.3 Long-Range H-Si Cross Peak Investigations and Signal-to-Noise Analysis.....	336
8.7.3 X-ray Crystallography.....	340
8.7.4 Computational Details.....	342
8.7.5 References.....	345
9 CONCLUSION.....	347
10 GLOSSARY.....	353

1 INTRODUCTION AND OUTLINE

1.1 Nuclear Magnetic Resonance Spectroscopy as Powerful Analytical Method



It was not least due to the early key milestones such as the discovery of proton magnetic resonance in water^[1] and paraffin^[2] in the 1940s and the observation that the resonant frequency of a nucleus correlates with its chemical and structural environment in the 1950s^[3] that nuclear magnetic resonance (NMR) developed as one of the most powerful analytical methods in chemistry, medicine, biology, pharmacy and numerous other fields.^[4] The possibility of obtaining direct information about the atomic connectivity, a property that can otherwise only be accessed by X-ray crystallographic techniques, makes NMR stand out from the crowd of spectroscopic methods.^[5] Consequently, next to mass spectrometry NMR is nowadays the main method for structural investigations^[4] and thus indispensable for an everyday business of research chemists.^[4] Because of the continuous improvements of hard- and software, processing and acquisition methods, there now exists an uncountable number of NMR experiments tackling most diverse tasks and problems. The advantages of NMR are manifold. To mention but a few: NMR is a non-destructive and quantitative analyzation technique, which does not require major preparation procedures prior to sample analysis. This provides an otherwise often rare opportunity to study compounds in their natural environment or under real reaction conditions. NMR also enables to monitor chemical reactions *in situ* and thereby provides information about reaction kinetics, intermediate, product, by-product and side-product formation.^[6] In that way, NMR helps to understand the underlying mechanism which is essential for optimizing reaction conditions, controlling product distributions and their yields, for exploring the substrate scope and for framing novel synthetic concepts. In some cases, NMR can even provide information about radical species,^[6] a competence that is mainly ascribed to the techniques of EPR (Electron paramagnetic resonance) or UV/Vis spectroscopy.

1 INTRODUCTION AND OUTLINE

This thesis presents novel and groundbreaking results that were obtained in the course of investigating new chemical reactions and processes in solution in the various fields of organo- and photocatalysis, organometallic and inorganic chemistry. These results were obtained by applying modern and innovative NMR techniques alongside methods such as developing and optimizing synthetic strategies, UV/Vis spectroscopy or X-ray crystallography. Special 1D and 2D multinuclear NMR experiments were used and even modified to ensure optimal adaptation to the different reagents and thus go far beyond routine experiments. This *inter alia* included the implementation of a broadband pulse in 1D and 2D NMR experiments in order to meet the challenges encountered with widely distributed NMR signals of mixtures of heteronuclear compounds. The studies performed in the different research fields and presented herein all have in common that elusive intermediate species and chemical processes in solution and their underlying mechanisms were elucidated by using cutting-edge NMR techniques showcasing the versatility of NMR as powerful analytical tool.

Chapter two describes the implementation of a 90° broadband pulse (xyBEBOP) into 1D and 2D pulse sequences, which laid the groundwork for numerous reaction monitorings and signal screenings. This chapter first gives an overview of the development of broadband excitation and discusses both advantages and drawbacks of common broadband pulses and the xyBEBOP pulse. Implemented in a 1D sequence, uniform broadband excitation can entail considerable time savings, since only a single spectrum has to be recorded to cover signals distributed over a large frequency range,^[7] in contrast to a standard hard pulse whose maximum excitation window is technically restricted. Broadband excitation is especially valuable for monitoring chemical reactions engendering widely distributed signals since it allows their simultaneous and uniform excitation and detection. For the photocatalytic functionalization of white phosphorus (P₄), which will be addressed separately in chapter 4, broadband 1D ³¹P-NMR experiments with ¹H-decoupling were desired to simultaneously detect all signals of starting material, intermediates and products spread over an approximate frequency range of over 600 ppm and to increase the signal-to-noise ratio for ³¹P nuclei coupled to protons. Therefore, the xyBEBOP pulse was incorporated in pulse programs with decoupling sequences and the performance of the new sequences was compared to sequences containing standard 90° hard pulses. Furthermore, for the topic of *Zintl* ions in solution that will be presented in chapters seven and eight, it was desired to implement the broadband pulse xyBEBOP in the indirect dimension of inverse detected 2D ¹H-²⁹Si-HMQC and HMBC experiments in order to facilitate screening for protonated silicide clusters. The motivation behind this was that during screening of the indirect ²⁹Si frequency dimension (F1) for ¹H-²⁹Si-cross peaks by standard 2D HMQCs of confined spectral windows, aliasing artifacts^[4,8] were observed caused by cross peaks located outside the spectral window. While this phenomenon is commonly exploited in Biomolecular NMR^[9,10] to reduce the spectral window in F1 and consequently measurement time, for the investigation of samples containing unknown signals, however, these artifacts can be confusing. Against this background, the xyBEBOP was also implemented in a 2D HMQC pulse sequence and the performance of the new experiment was tested and compared to standard HMQC experiments containing simple 90° hard pulses. The NMR experiments developed in this chapter not only laid the

foundation for ^{31}P - and ^{29}Si - investigations in this thesis, but clearly also for investigations on other NMR active heteronuclei.

Chapter three delves into the field of organocatalysis and demonstrates that combining *in situ* NMR, isotopic labeling and theoretical calculations helped to elucidate the mechanism of an unusual triple bond formation of a one-pot reaction towards conjugated enynes and cyclic nitronates. Both conjugated enynes and cyclic nitronates are important building blocks in the field of natural products and drug design.^[11–20] These compounds are usually generated by fundamentally different procedures. While there already exist numerous metal-free approaches towards cyclic nitronates^[21] conjugated enynes are commonly accessed by metal-catalyzed cross-couplings.^[22–26] Some time back, an innovative, combined and organocatalytic route towards conjugated enynes and cyclic nitronates starting from nitroalkenes was discovered in our working group.^[27] However, a profound mechanistic understanding was missing. The study provided in this work aimed to fill this gap. By ^1H -NMR reaction monitoring and ^{13}C and ^{15}N labelling studies and theoretical calculations a comprehensive mechanism could be proposed, which was found to proceed similarly for both enyne and nitronate until the formation of a cyclic intermediate. Thereafter, the routes were found to separate yielding conjugated enynes *via* a retro-1,3-dipolar cycloaddition and cyclic nitronates through complex intramolecular rearrangements. The proposed mechanism was corroborated by *in situ* NMR reaction monitoring, the detection and identification of by-products, screening various reaction conditions and by theoretical calculations. Furthermore, determinants affecting the product distribution could be identified. In addition, the substrate scope was explored and it was found that conjugated enynes can be obtained in moderate to good yields whereas high yields can be achieved for cyclic nitronates.

The next chapter deals with another field of catalysis, that of photocatalysis. Over the last decades, photochemistry and photocatalysis have become one of the forefront research areas. Despite their increasing importance, indispensable mechanistic investigations to understand the often elusive reactions are still rare. The application of NMR as additional spectroscopic tool besides UV/Vis and EPR gained importance especially due to landmark inventions such as *in situ* illumination setups allowing for *in situ* monitoring of photochemical processes inside the NMR spectrometer.^[28] Thus, NMR is now more than ever able to promote photochemical research by contributing with *in situ* reaction profiling, identification of intermediates, elucidation of downstream and dark pathways etc.^[28] Chapter four presents the first photocatalytic functionalization of P_4 towards precious triarylphosphines and tetraarylphosphonium salts. This groundbreaking new approach outranges state-of-the-art methodologies^[29–37] of organofunctionalization of P_4 by offering a more environmentally friendly and direct one-step procedure instead of inefficient, stepwise processes involving hazardous chemicals. The application of UV/Vis together with various 1D and 2D NMR techniques helped to elucidate key mechanistic steps and intermediates of this complex functionalization of P_4 . These NMR techniques include: *in situ* ^1H - and $^{31}\text{P}\{^1\text{H}\}$ -NMR reaction monitoring by broadband excitation allowing the simultaneous detection of the widely distributed ^{31}P -signals of starting material, intermediates and product, low temperature NMR and radical trapping studies to check for short lived intermediates, *in situ* recorded 2D ^1H - ^{31}P -HMQC experiments to elucidate structural motifs of

1 INTRODUCTION AND OUTLINE

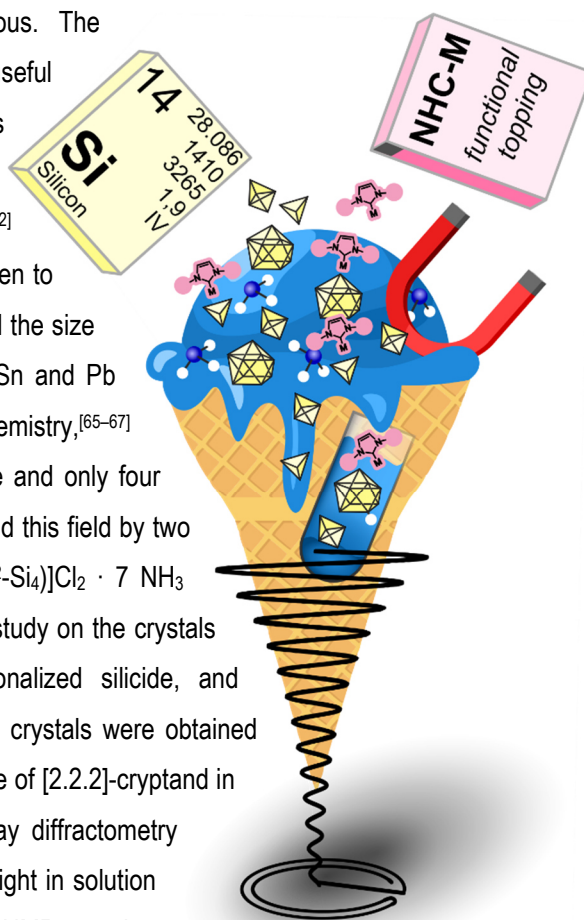
intermediates and side products and ^2H isotopic labeling studies to clarify the origin of intermediate bound protons. As a whole, this study presents the identification of the productive pathway of the photocatalytic functionalization of P_4 , the elucidation of its underlying mechanism and the detection of potential side reactions, which may lay the groundwork for future reaction optimizations.

In chapter five and six NMR could prove its potential in the field of organometallics. Chapter five presents the organometallic synthesis and detailed characterization of an unprecedented 1-phospha-7-norbornadiene exhibiting a direct and polar P-B-bond and discusses its reactivity towards triple bonds. Although 1-phospha-7-norbornadiene formally constitutes a classical Lewis adduct, results obtained by NMR as well as theoretical calculations suggested that structural isomers can be accessed exhibiting significantly different characteristics, in particular those of a frustrated Lewis pair (FLP). FLPs contain unquenched Lewis acidic and Lewis basic sites and are often able to activate small molecules such as H_2 , CO_2 , nitriles, alkynes, etc.^[38–40] Encouraged by the potential FLP-type behavior, 1-phospha-7-norbornadiene was undertaken reactivity studies and found to readily activate the strong polar $\text{C}\equiv\text{N}$ and apolar $\text{C}\equiv\text{C}$ triple bonds of nitriles and acetylenes generating exceptional insertion and addition products. The application of reactants exhibiting several different nuclei (^1H , ^{13}C , ^{11}B , ^{19}F , ^{31}P) called for investigations by multinuclear NMR. By means of *in situ* $^{31}\text{P}\{^1\text{H}\}$ -NMR and $^{11}\text{B}\{^1\text{H}\}$ -NMR reaction monitoring at variable temperatures in combination with DFT calculations reaction intermediates and structural isomers were uncovered. Thereupon, comprehensive mechanisms for both formation of 1-phospha-7-norbornadiene and its reaction with nitriles and acetylenes could be postulated. In addition, exceptional multinuclear 1D and inverse 2D NMR experiments were performed to unveil the labile nature the P-B bond of 1-phospha-7-norbornadiene. For this purpose, pulse programs had to be adapted ($^{31}\text{P}\{^{19}\text{F}, ^1\text{H}\}$ -NMR and $^1\text{H}\text{-}^{31}\text{P}\{^{11}\text{B}, ^1\text{H}\}$ -HSQCs) whereby the potential of two different triple resonance probes (TBI-P: ^1H , ^{31}P and tunable BB channel; TBI-F: ^1H , ^{19}F and tunable BB channel) could be fully exploited. This study paves the way towards a new class of organic phosphorus species and highlights their potential to engage in FLP-type reactivity.

Chapter six tackles the omnipresent research task of activating CO_2 for further transformations. Along with increasing environmental awareness, demands to reduce the CO_2 footprint are now more than ever ubiquitous. Therefore not only strategies for the initial reduction of CO_2 production are required, but also for the conversion of existing CO_2 into useful chemicals. One such desirable strategy aims at designing molecules capable of directly cleaving the $\text{C}=\text{O}$ bond in CO_2 . However, due to the strong $\text{C}=\text{O}$ bond,^[40] these strategies are challenging. Yet, there already exist established routes applying highly reducing, low-valent 3d metals^[41–44] or precious^[45–49] and f-block metals^[50,51]. In contrast, approaches using earth-abundant late 3d metals are still unknown, despite their importance on CO_2 reduction in biological processes.^[52,53] Inspired by the successful cleavage of small molecules as a result of metal-ligand cooperativity in late 3d metal complexes,^[54–60] an iron complex $[\text{Cp}^*\text{FeL}]^-$ was developed coordinating chelating phosphinine ligands, which earlier were found to exhibit non-innocent, reactive behavior towards external reagents. Indeed, this complex was found to be reactive towards CO_2 . Moreover, it could be demonstrated, that the

kind of reaction (either addition or C=O bond splitting) depends on the coordination mode of the attached phosphinine ligand. Besides the main application of X-ray crystallography and NMR to identify the structures of intermediates and products, with *in situ* $^{31}\text{P}\{^1\text{H}\}$ NMR monitoring and theoretical calculations insights into the formation of the iron complex could be provided. It was mainly due to the application of liquid NMR, that it was discovered that $[\text{Cp}^*\text{FeL}]^-$ exists as two equilibrating isomers in solution, which consequently lead to the different modes of reactivity towards CO_2 . This study reports on the first example of C=O bond cleavage of CO_2 mediated by a single Fe center.

In chapter seven and eight, the application of liquid NMR as valuable analysis tool moves on from the field of organometallics towards the field of inorganics, in particular, towards silicon *Zintl* ions. *Zintl* ions are polyanionic clusters incorporated in intermetallic compounds of alkali or alkaline earth metals and group 11 – 16 elements. These intermetallic compounds were named *Zintl* phases, in honor of the German chemist Eduard Zintl, who achieved to prove the existence of polyanions of Pb, Sn, Sb and Bi.^[61] *Zintl* ions gained increasing attention when it was discovered that these polyanions can be extracted in solution from their solid phases which allowed for solution chemistry such as functionalizations or their application as reactants or as preshaped building blocks in the development of nanomaterials.^[62] However, soluble *Zintl* ions can only be obtained from phases of group 14 and 15 elements.^[63] Among them, *Zintl* ions of silicon (silicides) are of particular interest, since silicon holds an important role in our daily lives, as the use of Si-based technology is now, more than ever, ubiquitous. The semiconducting property of silicides renders them as useful material for nanoelectronics.^[62] Besides, silicides constitute precursors for mesostructured extended solids, new crystalline modifications and nanoparticles.^[62] For latter, functionalized silicon-building blocks have proven to be successful, as their functionalization enabled to control the size of nanoparticles.^[64] While the heavier homologues Ge, Sn and Pb were found to have an extensive complexation chemistry,^[65-67] transition metal (TM) functionalized silicides are still rare and only four examples^[68-71] are known. Chapter seven and eight extend this field by two new examples of functionalized silicides $[(\text{NHC}^{\text{tBu}}\text{Au})_6(\eta^2\text{-Si}_4)]\text{Cl}_2 \cdot 7 \text{NH}_3$ and $[\text{NHC}^{\text{Dipp}}\text{Cu}(\eta^4\text{-Si}_9)\text{H}]^{2-}$. Chapter seven presents the study on the crystals $[(\text{NHC}^{\text{tBu}}\text{Au})_6(\eta^2\text{-Si}_4)]\text{Cl}_2 \cdot 7 \text{NH}_3$, the first gold-functionalized silicide, and $(\text{NHC}^{\text{tBu}}\text{Au})_3\text{NHCl}$, an imide capped gold triangle. These crystals were obtained from a reaction of $\text{Rb}_6\text{Cs}_6\text{Si}_{17}$ with $\text{NHC}^{\text{tBu}}\text{AuCl}$ in presence of [2.2.2]-cryptand in liquid ammonia and characterized by single crystal X-ray diffractometry and theoretical calculations. In this study, exceptional insight in solution processes in liquid ammonia could be provided by ^1H -NMR reaction monitoring together with various 2D NMR experiments. ^1H - ^1H -DOSY and



1 INTRODUCTION AND OUTLINE

elaborate ^1H - ^{13}C - and ^1H - ^{15}N 2D NMR experiments helped to identify the majority of dissolved NHC-species. This shed light on the mechanism of crystal formation in solution through the detection and characterization of two potential precursors. Furthermore, 2D ^1H - ^1H -NOESY experiments unveiled Brønsted acid-base equilibria that significantly affect the product outcome. Chapter eight presents a detailed solution NMR study on the first two-fold hetero-functionalized silicon cluster $[\text{NHC}^{\text{Dipp}}\text{Cu}(\eta^4\text{-Si}_9)\text{H}]^{2-}$. The preparation of a sample of fully ^{29}Si -enriched Zintl phase $\text{K}_6\text{Rb}_6\text{Si}_{17}$, transition metal complex $\text{NHC}^{\text{Dipp}}\text{CuCl}$ and cryptand in liquid ammonia built the groundwork for these NMR studies. The characterization of this cluster was achieved by ^1H -NMR signal monitoring, integration, 2D ^1H - ^{29}Si -HMQC spectra and 1D $^1\text{H}\{^{29}\text{Si}\}$ -NMR spectra with selective silicon decoupling. The NMR data were corroborated by theoretical calculations. In addition, by ^1H -NMR investigations at different temperatures, the rigidity of the metallized and protonated cluster $[\text{NHC}^{\text{Dipp}}\text{Cu}(\eta^4\text{-Si}_9)\text{H}]^{2-}$ could be classified. To our knowledge the detection of $[\text{NHC}^{\text{Dipp}}\text{Cu}(\eta^4\text{-Si}_9)\text{H}]^{2-}$ represents the first case of a protonated coinage metallized group 14 Zintl cluster in solution so far.

1.2 References

- [1] F. Bloch, W. W. Hansen, M. Packard, *Phys. Rev.* **1946**, 69, 127.
- [2] E. M. Purcell, H. C. Torrey, R. V. Pound, *Phys. Rev.* **1946**, 69, 37–38.
- [3] J. T. Arnold, S. S. Dharmatti, M. E. Packard, *J. Chem. Phys.* **1951**, 19, 507.
- [4] T. D. W. Claridge, *High-Resolution NMR Techniques in Organic Chemistry*, Elsevier, Oxford, **2009**.
- [5] R. T. Williamson, B. L. Marquez, *Magn. Reson. Chem.* **2017**, 55, 252.
- [6] J. Bargon, L. T. Kuhn, Eds., *In Situ NMR Methods in Catalysis*, Springer Berlin Heidelberg, **2007**.
- [7] C. Koch, *NMR Spectroscopic Investigations on Copper-Catalyzed Reactions and Zintl Anions*, University of Regensburg, **2015**.
- [8] A. M. Torres, W. S. Price, *Common Problems and Artifacts Encountered in Solution-State NMR Experiments. Concepts Magn Reson Part A*, **2017**.
- [9] M. R. Gryk, J. Vyas, M. W. Maciejewski, *Prog. Nucl. Magn. Reson. Spectrosc.* **2010**, 56, 329–345.
- [10] J. Cavanagh, W. J. Fairbrother, A. G. Palmer, N. J. Skelton, M. Rance, *Protein NMR Spectroscopy*, Elsevier Inc., **2007**.
- [11] M. Konishi, H. Ohkuma, K. Matsumoto, T. Tsuno, H. Kamei, T. Miyaki, T. Oki, H. Kawaguchi, G. D. Vanduyne, J. Clardy, *J. Antibiot.* **1989**, 42, 1449–1452.

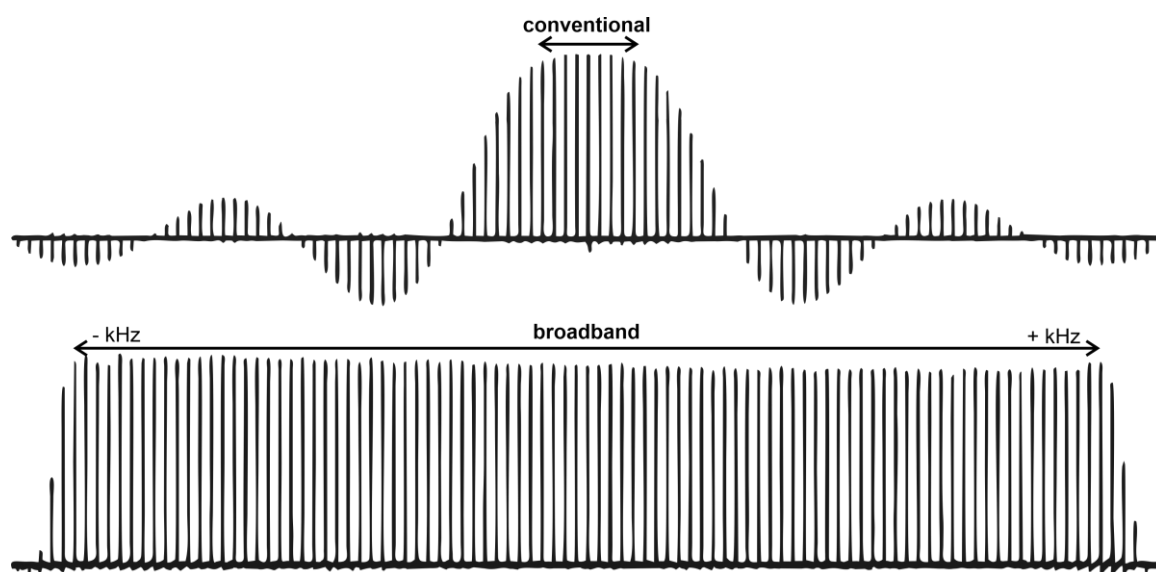
- [12] A. Stuetz, G. Petranyi, *J. Med. Chem.* **1984**, 27, 1539–1543.
- [13] D. E. Rudisill, L. A. Castonguay, J. K. Stille, *Tetrahedron Lett.* **1988**, 29, 1509–1512.
- [14] J. R. Frost, C. M. Pearson, T. N. Snaddon, R. A. Booth, R. M. Turner, J. Gold, D. M. Shaw, M. J. Gaunt, S. V. Ley, *Chem. - A Eur. J.* **2015**, 21, 13261–13277.
- [15] T. Masaoka, Y. Hasegawa, T. Ueda, T. Takubo, H. Shibata, H. Nakamura, N. Tatsumi, J. Yoshitake, N. Senda, *Eur. J. Cancer* **1976**, 12, 143–149.
- [16] B. M. Trost, L. Li, S. D. Guile, *J. Am. Chem. Soc.* **1992**, 114, 8745–8747.
- [17] B. M. Trost, L. S. Chupak, T. Lübbers, *J. Am. Chem. Soc.* **1998**, 120, 1732–1740.
- [18] K. Karthikeyan, T. Veenus Seelan, K. G. Lalitha, P. T. Perumal, *Bioorg. Med. Chem. Lett.* **2009**, 19, 3370–3373.
- [19] M. C. Pirrung, L. N. Tumey, C. R. H. Raetz, J. E. Jackman, K. Snehalatha, A. L. McClerren, C. A. Fierke, S. L. Gantt, K. M. Rusche, *J. Med. Chem.* **2002**, 45, 4359–4370.
- [20] R. Maurya, P. Gupta, G. Ahmad, D. K. Yadav, K. Chand, A. B. Singh, A. K. Tamrakar, A. K. Srivastava, *Med. Chem. Res.* **2008**, 17, 123–136.
- [21] H. Feuer, *Nitrile Oxides, Nitrones, and Nitronates in Organic Synthesis: Novel Strategies in Synthesis, 2nd Ed.*, John Wiley & Sons, New Jersey, **2008**.
- [22] Y. Hatanaka, T. Hiyama, *J. Org. Chem.* **1988**, 53, 918–920.
- [23] Y. Hatanaka, K. Matsui, T. Hiyama, *Tetrahedron Lett.* **1989**, 30, 2403–2406.
- [24] L.-X. Shao, M. Shi, *J. Org. Chem.* **2005**, 70, 8635–8637.
- [25] D. Saha, T. Chatterjee, M. Mukherjee, B. C. Ranu, *J. Org. Chem.* **2012**, 77, 9379–9383.
- [26] N. Miyaura, K. Yamada, A. Suzuki, *Tetrahedron Lett.* **1979**, 20, 3437–3440.
- [27] M. B. Schmid, *NMR Spectroscopic Investigations on Aminocatalysis: Catalysts and Intermediates, Conformations and Mechanisms Dissertation*, **2011**.
- [28] P. Nitschke, N. Lokesh, R. M. Gschwind, *Prog. Nucl. Magn. Reson. Spectrosc.* **2019**, 114–115, 86–134.
- [29] D. E. C. Corbridge, *Phosphorus 2000. Chemistry, Biochemistry and Technology*, Elsevier, **2000**.
- [30] W. Schipper, *Eur. J. Inorg. Chem.* **2014**, 2014, 1567–1571.
- [31] M. Caporali, L. Gonsalvi, A. Rossin, M. Peruzzini, *Chem. Rev.* **2010**, 110, 4178–4235.

1 INTRODUCTION AND OUTLINE

- [32] M. Scheer, G. Balázs, A. Seitz, *Chem. Rev.* **2010**, *110*, 4236–4256.
- [33] S. Khan, S. S. Sen, H. W. Roesky, *Chem. Commun.* **2012**, *48*, 2169–2179.
- [34] D. H. R. Barton, J. Zhu, *J. Am. Chem. Soc.* **1993**, *115*, 2071–2072.
- [35] D. H. R. Barton, R. A. Vonder Embse, *Tetrahedron* **1998**, *54*, 12475–12496.
- [36] B. M. Cossairt, C. C. Cummins, *New J. Chem.* **2010**, *34*, 1533–1536.
- [37] S. K. Ghosh, C. C. Cummins, J. A. Gladysz, *Org. Chem. Front.* **2018**, *5*, 3421–3429.
- [38] D. W. Stephan, *J. Am. Chem. Soc.* **2015**, *137*, 10018–10032.
- [39] G. C. Welch, R. R. San Juan, J. D. Masuda, D. W. Stephan, *Science (80-.)*. **2006**, *314*, 1124–1126.
- [40] C. M. Mömming, E. Otten, G. Kehr, R. Fröhlich, S. Grimme, D. W. Stephan, G. Erker, *Angew. Chemie - Int. Ed.* **2009**, *48*, 6643–6646.
- [41] C. T. Saouma, M. W. Day, J. C. Peters, *Chem. Sci.* **2013**, *4*, 4042–4051.
- [42] L. J. Procopio, P. J. Carroll, D. H. Berry, *Organometallics* **1993**, *12*, 3087–3093.
- [43] J. C. Bryan, S. J. Geib, A. L. Rheingold, J. M. Mayer, *J. Am. Chem. Soc.* **1987**, *109*, 2826–2828.
- [44] G. Fachinetti, C. Floriani, A. Chiesi-Villa, C. Guastini, *J. Am. Chem. Soc.* **1979**, *101*, 1767–1775.
- [45] J. Langer, A. Hamza, I. Pápai, *Angew. Chemie Int. Ed.* **2018**, *57*, 2455–2458.
- [46] W. C. Kaska, S. Nemeš, A. Shirazi, S. Potuznik, *Organometallics* **1988**, *7*, 13–15.
- [47] M. A. McLoughlin, *Inorg. Chem.* **1999**, *38*, 3223–3227.
- [48] M. Feller, U. Gellrich, A. Anaby, Y. Diskin-Posner, D. Milstein, *J. Am. Chem. Soc.* **2016**, *138*, 6445–6454.
- [49] S. I. Kalläne, T. Braun, M. Teltewskoi, B. Braun, R. Herrmann, R. Laubenstein, *Chem. Commun.* **2015**, *51*, 14613–14616.
- [50] I. Castro-Rodriguez, K. Meyer, *J. Am. Chem. Soc.* **2005**, *127*, 11242–11243.
- [51] N. Tsoureas, L. Castro, A. F. R. Kilpatrick, F. G. N. Cloke, L. Maron, *Chem. Sci.* **2014**, *5*, 3777–3788.
- [52] D. J. Evans, *Coord. Chem. Rev.* **2005**, *249*, 1582–1595.
- [53] S. W. Ragsdale, M. Kumar, *Chem. Rev.* **1996**, *96*, 2515–2540.

- [54] D. Oren, Y. Diskin-Posner, L. Avram, M. Feller, D. Milstein, *Organometallics* **2018**, *37*, 2217–2221.
- [55] A. R. Sadique, W. W. Brennessel, P. L. Holland, *Inorg. Chem.* **2008**, *47*, 784–786.
- [56] C. C. Lu, C. T. Saouma, M. W. Day, J. C. Peters, *J. Am. Chem. Soc.* **2007**, *129*, 4–5.
- [57] D. S. Laitar, P. Müller, J. P. Sadighi, *J. Am. Chem. Soc.* **2005**, *127*, 17196–17197.
- [58] C. Yoo, Y. E. Kim, Y. Lee, *Acc. Chem. Res.* **2018**, *51*, 1144–1152.
- [59] D. Sahoo, C. Yoo, Y. Lee, *J. Am. Chem. Soc.* **2018**, *140*, 2179–2185.
- [60] C. Bianchini, A. Meli, *J. Am. Chem. Soc.* **1984**, *106*, 2698–2699.
- [61] F. Laves, in *Naturwissenschaften*, Springer Berlin Heidelberg, **1941**, pp. 244–256.
- [62] M. Beekman, S. M. Kauzlarich, L. Doherty, G. S. Nolas, *Materials (Basel)*. **2019**, *12*, 1139.
- [63] S. Scharfe, F. Kraus, S. Stegmaier, A. Schier, T. F. Fässler, *Angew. Chemie* **2011**, *123*, 3712–3754.
- [64] M. H. Nayfeh, L. Mitas, in *Nanosilicon*, **2008**, pp. 1–78.
- [65] J. Campbell, H. P. A. Mercier, H. Franke, D. P. Santry, D. A. Dixon, G. J. Schrobilgen, *Inorg. Chem.* **2002**, *41*, 86–107.
- [66] B. Kesanli, J. Fettinger, D. R. Gardner, B. Eichhorn, *J. Am. Chem. Soc.* **2002**, *124*, 4779–4786.
- [67] H. L. Xu, N. V. Tkachenko, Z. C. Wang, W. X. Chen, L. Qiao, A. Muñoz-Castro, A. I. Boldyrev, Z. M. Sun, *Nat. Commun.* **2020**, *11*, 1–8.
- [68] J. M. Goicoechea, S. C. Sevov, *Organometallics* **2006**, *25*, 4530–4536.
- [69] M. Waibel, F. Kraus, S. Scharfe, B. Wahl, T. F. Fässler, *Angew. Chemie* **2010**, *122*, 6761–6765.
- [70] F. S. Geitner, T. F. Fässler, *Chem. Commun.* **2017**, *53*, 12974–12977.
- [71] S. Joseph, M. Hamberger, F. Mutzbauer, O. Härtl, M. Meier, N. Korber, *Angew. Chemie Int. Ed.* **2009**, *48*, 8770–8772.

2 ADVANTAGES OF BROADBAND EXCITATION IN NMR



This chapter was written by Verena Streitferdt. All Figures were designed by Verena Streitferdt. The pulse programs `bulu_zpgg`, `bulu_zggd` and `hmbcgpndqf_bulusp2` were written and tested by Verena Streitferdt. The pulse program `hmqcgpqfbulusp2` was written and tested on the ABC-transporter by Philipp Nitschke. The pulse program `hmqcgpqfbulusp2` was further tested on samples of Zintl phases in liquid ammonia by Verena Streitferdt. The pulse shapes of the xyBEBOP pulses were kindly provided by Prof. Dr. Burkhard Luy.

2 ADVANTAGES OF BROADBAND EXCITATION IN NMR

2.1 Introduction

Heteronuclear NMR spectroscopy is an indispensable technique for structural characterizations and reaction monitoring in all fields of chemistry. While the resonant frequencies of protons usually appear in a very narrow frequency range, those of heteronuclei are often spread over a large shift range, e.g. 4000 ppm^[1] for ³¹P or 1000 ppm for ²⁹Si (to our knowledge, the highest shift was reported for a dialkylsilylene at 567.4 ppm^[2] and the lowest shift for $[\mu\text{-HSi}_4]^{4-}$ at -404.5 ppm^[3]). Uniform excitation over a similarly large frequency range by a standard 90° hard pulse is impossible since the excitation profile is defined by a sinc function (see Figure 2.1) and by the pulse duration which cannot be adjusted arbitrarily short.^[4] According to Heisenberg's Uncertainty Principle, a radio frequency pulse spreads around its center by $1/\Delta t$ Hz with Δt being the pulse duration (= pulse width) and can therefore excite a window of $2 \times 1/\Delta t$ Hz (excitation windows for ¹H, ³¹P and ²⁹Si are given for a 90° pulse of 12.4 μs in Figure 2.1).^[4] This relationship demonstrates that shorter pulses excite a greater range of spins than long (soft) pulses. Shorter pulses require a higher power output for an optimal excitation of the spins.^[4] The maximum output power is restricted by the spectrometer hardware which limits the decrease in pulse duration and accordingly the maximum excitation window.

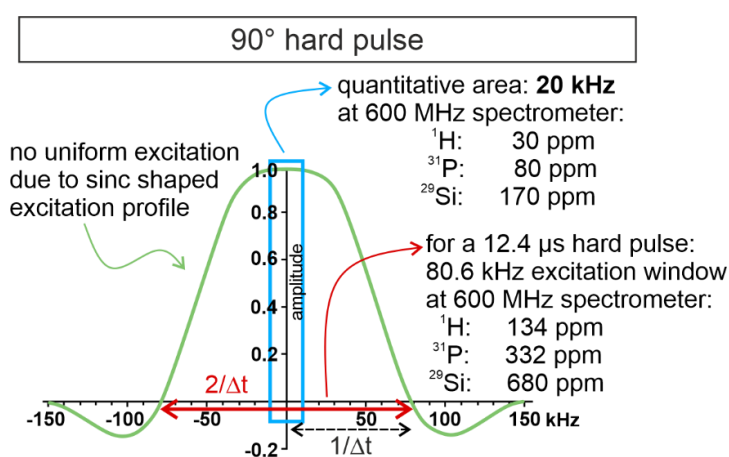


Figure 2.1 | Excitation profile of a 90° hard pulse with a duration of 12.4 ms.^[5] This curve was reproduced from a ¹⁹F excitation profile reported in literature.^[5]

Thus, in order to cover a wide frequency range when applying a standard 90° hard pulse for excitation, several spectra of a confined spectral width have to be recorded with altering transmitter frequency. Consequently, the spectra are recorded with a time offset wherefore this procedure is only appropriate for investigating stable compounds or chemical mixtures, but not for unstable compounds, low concentrations or reaction monitorings. Besides, the frequency range in which quantitative studies with a 90° pulse can be performed is limited to a quite small range of about 20 kHz^[5] (see blue frame in Figure 2.1) which, on a 600 MHz spectrometer, corresponds to around 30 ppm for ¹H, 80 ppm for ³¹P and 170 ppm for ²⁹Si. Hence, a broadband pulse with uniform and quantitative excitation over a wide chemical shift range would be desirable.^[5]

2 ADVANTAGES OF BROADBAND EXCITATION IN NMR

In the last decades, much attention has been paid to improving broadband excitation, resulting in the development of a wide variety of pulses starting with composite pulses^[6] in 1979. Composite pulses consist of a sequence of pulses with different duration and phase that altogether lead to a certain net rotation.^[4] These straightforward pulse sequences entailed greater excitation bandwidths and higher tolerance to B_1 inhomogeneity and resonance offset^[4] compared to normal hard pulses. Just five years later the first adiabatic pulses were presented.^[7] The transmitter frequency in adiabatic pulses is swept over the excitation area whereby much wider frequency ranges can uniformly be excited. Moreover, adiabatic pulses exhibit great tolerance towards B_1 inhomogeneities and miscalibrated RF power.^[4] In the pulse family of adiabatic pulses, further improvements were achieved with regard to expanding the excitation bandwidth and increasing the tolerance towards RF miscalibrations and inhomogeneities.^[8-13] One such improvement was the design of the ABSTRUSE^[8] (**A**djustable, **B**roadband, **S**ech/Tanh-Rotation **U**niform **S**elective **E**xcitation) sequence in 2002 which relies on multiple adiabatic hyperbolic secant (HS) pulses with a total duration of 12 ms. While this pulse sequence can uniformly excite a window of around 40 kHz and is moderately tolerant towards RF inhomogeneity, it is prone to effects of J -modulation and problems associated with fast spin relaxation due to the very long pulse duration.^[14] However, the usage of hyperbolic secant pulses for excitation is not applicable to quantitatively excite very wide frequency ranges, because of its intense peak pulse amplitude.^[4] In 2016, a variant of the ABSTRUSE sequence was reported relying on CHIRP pulses instead of HS pulses.^[5] The 6 ms long sequence called CHORUS (**chirped, ordered pulses for ultra-broadband spectroscopy**) is able to uniformly and quantitatively excite over 250 kHz (see Figure 2.2 blue frame), a more than 12-fold larger excitation window than for a standard 90° hard pulse, and is tolerant to B_1 inhomogeneity (see Figure 2.2).^[5] Again, the long pulse duration (even though half as short as the ABSTRUSE sequence) is prone to effects of J -modulation (this was demonstrated by the authors) and intensity loss as a result of spin relaxation.^[5] Only last year in 2019, a compressed CHORUS pulse sequence was published (see Figure 2.2c).^[15] The new version was found to have a better performance when the 180° CHIRP pulses differ in their durations by half the length of the 90° CHIRP pulse (see Figure 2.2c equation (1)). Thereby, shorter pulse lengths can be applied while allowing for uniform excitation of larger frequency ranges. Pulse lengths that satisfy equation (2) in Figure 2.2 can be used allowing an individual adjustment of the CHORUS sequence. The authors showed that for example a compressed sequence of a total duration of 4 ms is able to excite an exceptional frequency range of over 500 kHz.^[15]

2 ADVANTAGES OF BROADBAND EXCITATION IN NMR

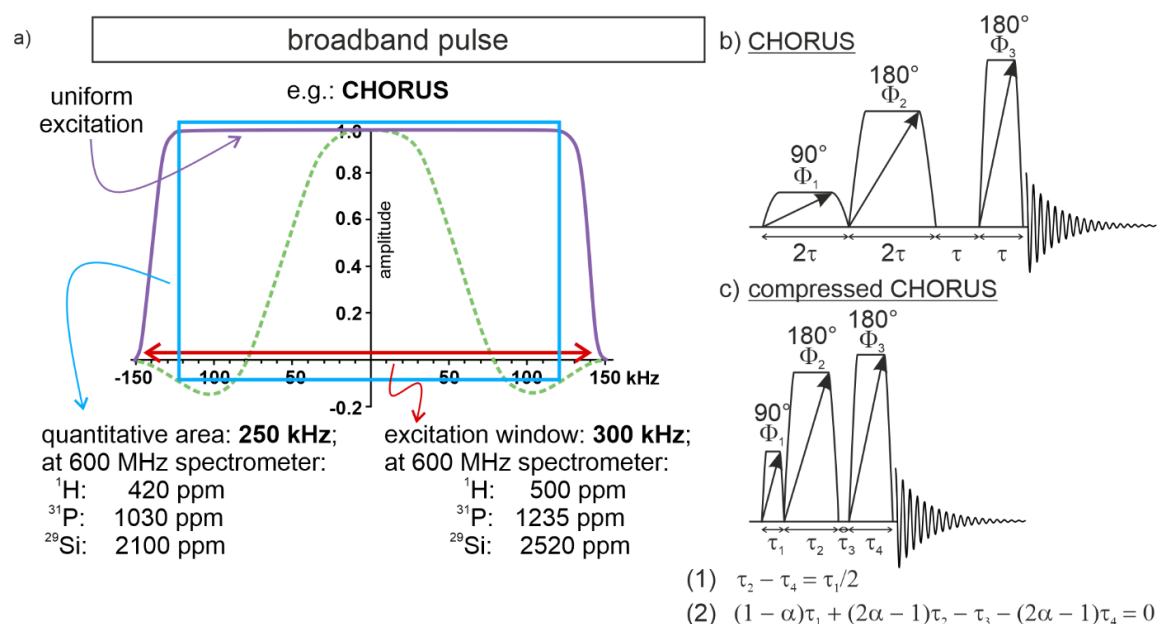


Figure 2.2 | Broadband excitation by the CHORUS pulse sequence. a) Excitation profile of the CHORUS pulse sequence with a total duration of 6 ms (purple) in comparison with that of a 90° hard pulse of 12.4 μs (green dotted).^[5] The profiles were reproduced from literature.^[5] b) Pulse sequence of CHORUS with τ being the unit pulse duration (τ = 1 ms for a total 6 ms CHORUS pulse).^[5] c) Pulse sequence of compressed CHORUS with τ₁, τ₂, τ₄ being the pulse durations and τ₃ a fixed delay. The compressed CHORUS was found to have a better performance compared to the original CHORUS sequence (a) when the 180° CHIRP pulses differ in their durations by half the length of the 90° CHIRP pulse (equation (1)). Pulse lengths that satisfy equation (2) can be used which allows an individual adjustment of the CHORUS sequence.^[15] α denotes the ratio of a chirp pulse length that is required to hit any frequency of interest during the frequency sweep.^[15]

Several years ago, Prof. Dr. Burkhard Luy provided to our working group yet unpublished pulses (xyBEBOP) that can either uniformly excite 500 kHz associated with a pulse length of 0.5 ms or even 1000 kHz that requires a duration of 1 ms.^[16] Hence, these pulses can excite very large chemical shift ranges while exhibiting relatively short durations compared to other pulse sequences (see above). The design of the xyBEBOP pulses relies on the method of optimal control theory.^[17–20] In 2003, a pioneering BEBOP (broadband excitation by optimized pulses) pulse was reported which uniformly excites a range of 40 kHz while tolerating RF miscalibrations up to around 45%.^[14] Due to the shorter pulse duration of 2 ms, it is considerably less vulnerable to relaxation and J-modulation effects.^[14] The performance of the xyBEBOP pulse covering 1000 kHz was extensively tested in our working group on real samples containing low soluble tin *Zintl* ions appearing in a wide chemical shift range in the ¹¹⁹Sn NMR spectrum and exhibiting large scalar couplings of up to $J(^{119}\text{Sn}^{117}\text{Sn}) = 1600 \text{ Hz}$.^[16] The results were reported in 2015 and demonstrated that indeed, all resonances could be obtained within a single spectrum which was clear from artifacts. However, the xyBEBOP pulse causes phasing problems, so that it is not possible to manually phase all signals at once.^[16] Yet, this can be circumvented by processing the data with magnitude calculation (mc) whereby for each point *i* in the spectrum the absolute intensity is calculated according to

$$ABS(i) = \sqrt{(R(i)^2 + I(i)^2)} \quad (1)$$

with *R* being the real part and *I* being the imaginary part of the spectrum.^[21] It was demonstrated, that the integration errors of spectra recorded with the xyBEBOP and processed with mc were within the

2 ADVANTAGES OF BROADBAND EXCITATION IN NMR

experimental errors of spectra recorded with a 90° hard pulse.^[16] This indicates that excitation by xyBEBOP and processing with mc satisfies quantitative requirements. However, mc processing of spectra obtained by xyBEBOP excitation lead to larger errors in line widths and coupling constants.^[16] These errors could be significantly reduced by individual manual phasing of the signals of interest whereby good agreements with the values obtained by 90° hard pulse excitation were achieved.^[16] Hence, apart from the few limitations, the application of the xyBEBOP pulse instead of a 90° hard pulse entails considerable time savings, since only a single spectrum has to be recorded to cover a large frequency range.

Since the xyBEBOP pulse enables the simultaneous acquisition of widely distributed resonant frequencies, it is therefore especially valuable for reaction monitoring or signal screening by heteronuclear NMR.

2.2 Incorporation of the xyBEBOP in 1D Pulse Programs with ¹H-Decoupling

In this work, the xyBEBOP pulse was *inter alia* applied for the reaction monitoring by ³¹P-NMR of the photocatalytic functionalization of white phosphorus (P₄). Thereby, ³¹P-NMR signals of starting material, intermediates, product and side-products spread over an approximate frequency range of over 600 ppm could be detected simultaneously (P₄: $\delta(^{31}\text{P}) = -522$ ppm; side-products/-intermediates: $\delta(^{31}\text{P})$ up to +100 ppm). In order to increase the signal-to-noise ratio (S/N) for ³¹P nuclei which exhibit coupling to protons (almost every signal except that of P₄), the xyBEBOP pulse was incorporated in pulse programs with gated and power-gated decoupling sequences (see Figure 2.3).

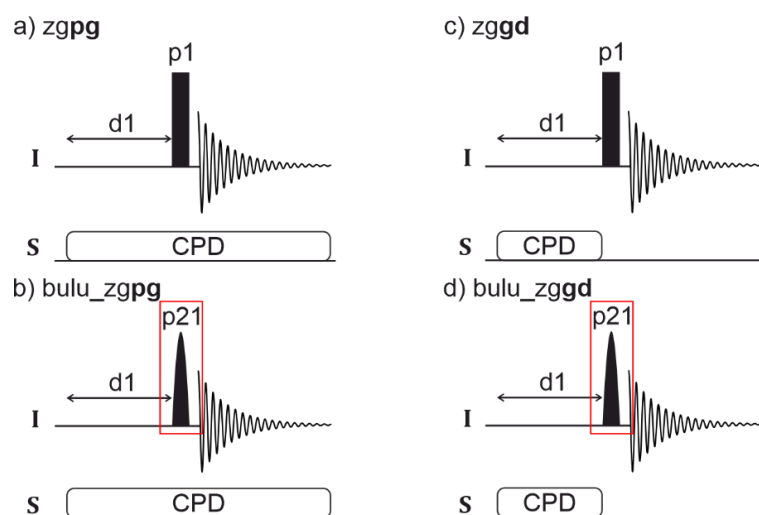


Figure 2.3 | Implementation of the broadband pulse xyBEBOP in standard Bruker experiments with heteronuclear spin decoupling. Pulse sequences are displayed for the standard Bruker pulse program *zgpg* (a), the modified version *bulu_zgpg* with the shaped pulse xyBEBOP (b), the standard Bruker pulse program *zggd* (c) and its modified version *bulu_zggd* with the shaped pulse xyBEBOP (d). The pulse sequence in b) is similar to that of the Bruker standard pulse program *selzgpg*, but the pulse programs slightly differ.

Gated decoupling (*gd*) makes use of signal enhancement due to NOE transfer from the constantly saturated ¹H spins during the recovery delay (*d1*) prior to 90° excitation and acquisition.^[4] This allows an increase in signal intensity while maintaining the splitting pattern which can give valuable information about the

2 ADVANTAGES OF BROADBAND EXCITATION IN NMR

structural nature of products or intermediates. In the power-gated (*pg*) case, decoupling is applied during *d1* and acquisition which achieves signal enhancement due to NOE transfer and collapse of the splitting pattern.^[4] Hence, next to signal enhancement, *pg* decoupling enables to simplify the spectrum which is especially beneficial when there are many signals or overlapping signals due to large $^1J_{\text{HP}}$ coupling such as for phosphine oxides ($\text{O}=\text{P}(\text{H})\text{R}^1\text{R}^2$; $^1J_{\text{HP}} \approx 600$ Hz) detected in the ^{31}P NMR monitoring of spin trapping experiments of the photocatalytic functionalization of P_4 (see chapter 4).

In order to implement the xyBEBOP pulse into NMR experiments with ^1H -decoupling, the 90° hard pulse *p1* simply had to be replaced by a shaped pulse *p21* (= xyBEBOP) in the *Bruker* standard pulse programs *zgpg* (power-gated decoupling) and *zggd* (gated decoupling)(see Figure 2.3).

The additional decoupling of the *pg* sequence during acquisition compared to the *gd* sequence led to further considerable signal enhancement by the collapse of the ^{31}P signals which are “broadened” due to $^3J_{\text{HP}}$, $^4J_{\text{HP}}$ and $^5J_{\text{HP}}$ couplings (compare S/N ratios in Figure 2.4). Therefore, in this thesis power-gated decoupling was ubiquitously applied for $^{31}\text{P}\{^1\text{H}\}$ -NMR reaction monitoring.

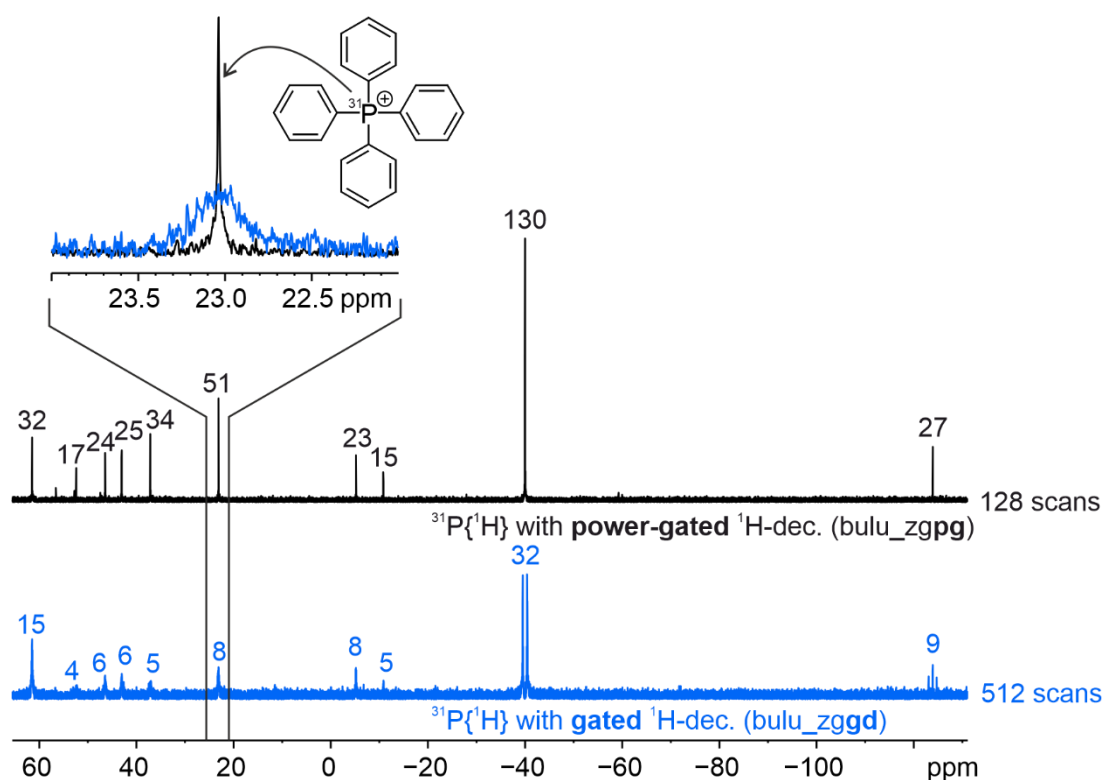


Figure 2.4 | Comparison of $^{31}\text{P}\{^1\text{H}\}$ -NMR spectra recorded during the reaction monitoring of P_4 (50 mM) with TEA (57.6 eq.), PhI (44 eq.) and an organocatalyst (8.8 mol%, see chapter 4). The black spectrum was obtained by the *bulu_zgpg* experiment and the blue spectrum by the *bulu_zggd* experiment. Numbers above signals signify corresponding S/N ratios. This comparison demonstrates that power-gated decoupling leads to considerably better signal enhancement than gated decoupling. Key acquisition parameters: AQ = 0.6 s; SW = 625 kHz; TD = 750k; pulse shape used: xyBEBOP for 1000 kHz excitation with $\Delta t = 1$ ms.

The decoupling performance of the pulse program incorporating the xyBEBOP pulse (500 kHz with $\Delta t = 0.5$ ms) was tested on a sample containing H_2PPh with $^1J_{\text{HP}} = 200$ Hz (0.05 mmol) in the reaction mixture with triethylamine, iodobenzene and an Ir-catalyst in deuterated acetonitrile (see Figure 2.5; for

2 ADVANTAGES OF BROADBAND EXCITATION IN NMR

further information on the reaction see chapter 4). Spectra with a spectral width (SW) of 500 kHz were acquired by either 90° hard pulse or xyBEBOP excitation both without ¹H-decoupling (pulse programs *zg* and *bulu_zg_shape*^[16]) and with power-gated ¹H-decoupling (pulse programs *zgpg* and *bulu_zgpg*). The acquisition parameters of all spectra were held constant and the spectra were manually phased after processing. First, ³¹P signal excitation by xyBEBOP was compared with excitation by a hard pulse (see Figure 2.5a). Both pulses lead to identical signal intensities, patterns and line widths. This was already observed by Carina Koch when investigating the performance of the xyBEBOP (1000 kHz with Δt = 1ms) pulse on ¹¹⁹Sn-NRMR signals.^[16] Next, the performance of the xyBEBOP was tested in presence of power-gated ¹H-decoupling (see Figure 2.5b). The ³¹P{¹H}-signal obtained by xyBEBOP excitation showed similar multiplet collapse, signal intensity and line width compared to the signal obtained by hard pulse excitation. This demonstrates, that the xyBEBOP pulse can be used in presence of ¹H-decoupling without any drawback.

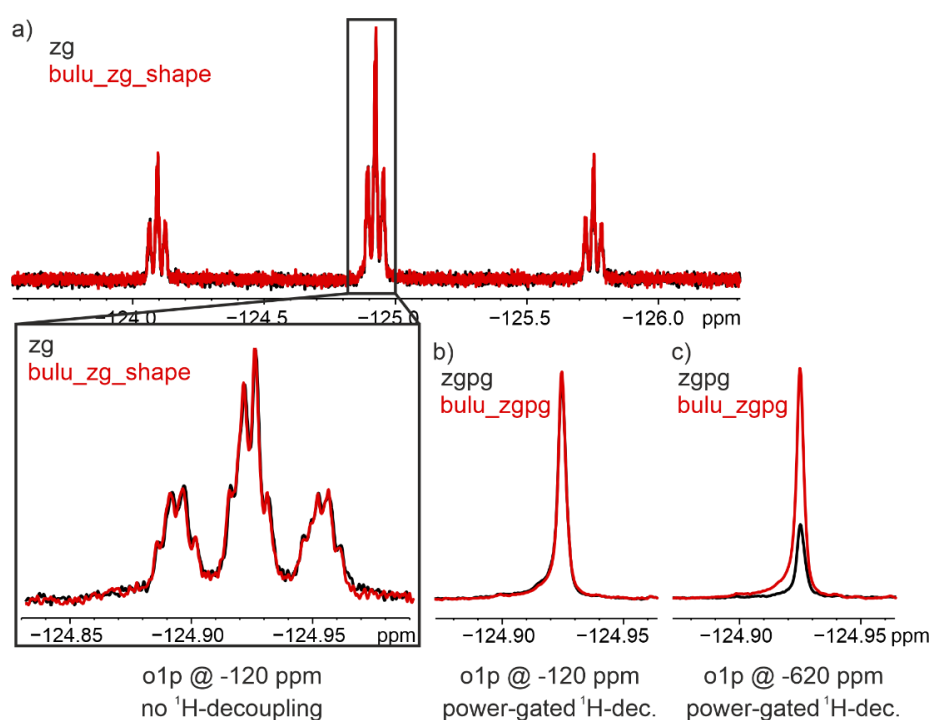


Figure 2.5 | Performance test of the xyBEBOP pulse (500 kHz with Δt = 0.5 ms) on ³¹P without and with power-gated ¹H-decoupling compared to the 90° hard pulse. The test was performed prior to illumination on a sample containing H₂PPh (0.05 mmol) in the reaction mixture with triethylamine, iodobenzene and an Ir-catalyst (for further information on the sample see chapter 4). a) Comparison of ³¹P signals of H₂PPh obtained by 90° hard pulse excitation (black, Bruker standard pulse program: *zg*) and by xyBEBOP excitation (red, user defined pulse program: *bulu_zg_shape*^[16]). The magnified region demonstrates that both pulses lead to identical signal intensities, patterns and line widths. b) Comparison of ³¹P signals of H₂PPh obtained by 90° hard pulse (black Bruker standard pulse program: *zgpg*) and xyBEBOP (red, user defined pulse program: *bulu_zgpg*) excitation with power-gated ¹H-decoupling. This shows again no difference in signal intensities, patterns and line widths. c) Comparison of ³¹P signals of H₂PPh obtained similar to b) but with different transmitter frequencies (o1p) of the respective pulses. Applying xyBEBOP together with ¹H-decoupling leads to unaltered signal intensity and line width also for an o1p set far off the resonant frequency of interest, in contrast to the 90° hard pulse which causes a decrease in signal intensity when applied “off resonance”. Key acquisition parameters: TD = 3000k; NS = 8; SW = 500 kHz; AQ = 3 s; D1 = 2 s.

Then, the transmitter frequencies (o1p) of the xyBEBOP and hard pulse were set far off resonance ($\delta(^{31}\text{P}(\text{H}_2\text{PPh}) - \text{o1p} = 495 \text{ ppm})$) and their performances were compared under power-gated ¹H-decoupling.

2 ADVANTAGES OF BROADBAND EXCITATION IN NMR

While the change in σ_{1p} for xyBEBOP had no influence on the $^{31}\text{P}\{^1\text{H}\}$ signal intensity, shape and line width, the change in σ_{1p} of the hard pulse resulted in a considerable decrease in signal intensity. This shows that also far off resonance, the xyBEBOP performs well in presence of ^1H -decoupling in contrast to the 90° hard pulse. The pulse programs are supplied in chapter 2.5.

2.3 Incorporation of the xyBEBOP in HMQC Experiments

For the topic of silicon *Zintl* ions (see chapter 7 and chapter 8), the xyBEBOP pulse was applied for the acquisition of ^{29}Si -NMR spectra of samples containing low soluble *Zintl* phases ($\text{K}_6\text{Rb}_6\text{Si}_{17}$) with 100% ^{29}Si enrichment in liquid ammonia. ^{29}Si -NMR signals of silicon *Zintl* ions can appear in a large chemical shift range of around 750 ppm with $[\text{Si}_5]^{2-}$ exhibiting a lowfield shift of +348.7 ppm^[3] for two of its five silicon atoms and with $[\mu\text{-HSi}_4]^{3-}$ exhibiting a highfield shift of -404.5 ppm^[3] for the silicon atoms without H-Si bond. Therefore, using the xyBEBOP pulse which can uniformly excite large frequency ranges offers the benefit of acquiring a single spectrum covering the whole shift range and therefore considerably reduces measurement time.^[16] For ^{29}Si nuclei, the intramolecular presence of protons can also be exploited for signal enhancement as was mentioned above for ^{31}P nuclei. For ^{31}P nuclei, signal amplification was accomplished by ^1H -decoupling especially during the d1-period which relies on the transfer of magnetization by NOE (nuclear Overhauser effect) and is influenced by the sign of the magnetogyric ratios (γ).^[4] For nuclei exhibiting negative magnetogyric ratios such as ^{15}N and ^{29}Si the NOE resulting from decoupling causes a decrease or even inversion of the signals.^[4] Still, the sensitivity for ^{15}N or ^{29}Si can be enhanced by means of polarization transfer such as through INEPT sequences where the signal enhancement depends on the absolute value of the magnetogyric ratio in contrast to NOE. The factors for signal intensity enhancement of selected ^1H -X groups upon polarization transfer (f_{INEPT}) or NOE (f_{NOE}) are given in Table 2.1 based on equations (2) and (3).^[4]

Table 2.1 | Factors for signal intensity enhancement of the X-signal in ^1H -X groups resulting out of polarization transfer (f_{INEPT}) and largest achievable NOE (f_{NOE}).^[4]

X:	^{13}C	^{15}N	^{29}Si	^{31}P
f_{INEPT}	3.98	9.87	5.03	2.47
f_{NOE}	2.99	-3.94	-1.52	2.24

$$f_{\text{INEPT}} = \frac{I_{\text{INEPT}}}{I_0} = \left| \frac{\gamma_{\text{H}}}{\gamma_{\text{X}}} \right| \quad (2)$$

$$f_{\text{NOE}} = \frac{I_{\text{NOE}}}{I_0} = 1 + \frac{\gamma_{\text{H}}}{2\gamma_{\text{X}}} \quad (3)$$

With I_{INEPT} , I_{NOE} and I_0 being the signal intensities with enhancement by polarization transfer, NOE and without enhancement respectively. In general, the S/N ratios of a 1D experiment with nuclei of half-integer spin can be expressed by:

2 ADVANTAGES OF BROADBAND EXCITATION IN NMR

$$\frac{S}{N} \propto NAT^{-1}B_0^3\gamma_{exc}\gamma_{obs}^3T_2^*(NS)^{1/2} \quad (4)$$

where N denotes the number of molecules within the NMR active volume, term A expresses the abundance of the NMR-active spins, T is the temperature and B_0 the static magnetic field, γ_{exc} and γ_{obs} signifies the magnetogyric ratios of the initially excited and the observed nucleus, T_2^* represents the effective spin-spin relaxation time and NS is the number of acquired scans.^[4] Equation 4 makes clear, that for every ^1H -X combination, highest S/N ratio will be obtained by initially exciting and detecting the proton spins since they exhibit the largest magnetogyric ratio (except for ^3H ; $\gamma(^3\text{H}) = 28.5 \times 10^7 \text{ rad} \times \text{T}^{-1} \times \text{s}^{-1}$; $\gamma(^1\text{H}) = 26.8 \times 10^7 \text{ rad} \times \text{T}^{-1} \times \text{s}^{-1}$).^[22] A comprehensive overview over the increase in relative sensitivity depending on the nucleus initially excited and that detected is given in Figure 2.6.

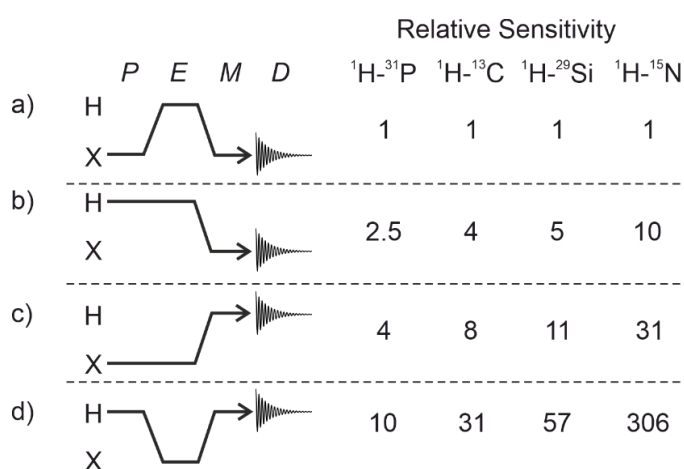


Figure 2.6 | Common illustrations of heteronuclear shift correlation differing in excited and detected nucleus.^[4] P, E, M and D indicate preparation, evolution, mixing and detection period, respectively. The sensitivity of the different methods a) – d) of ^1H -correlation experiments with ^{31}P , ^{13}C , ^{29}Si , and ^{15}N are given referenced to the least sensitive method X-H-X (a). b) Traditional H-H-X approach such as INEPT. c) X-X-H approach and d) the inverse and most sensitive method H-X-H.^[4]

Hence, as long as protons are present within a molecule containing the heteronucleus of interest, especially for ^{29}Si and ^{15}N the inverse approach (see Figure 2.6d) exploiting the high-sensitivity nucleus ^1H such as in 1D and 2D HSQC, HMQC or HMBC experiments should be the method of choice, particularly for low concentrated systems.

In recent years, highly interesting protonated silicon *Zintl* ions were detected in solution by NMR^[3,23,24] which allowed exceptional insights into cluster dynamics and protonation equilibria in solution. Encouraged by those findings, in this thesis, ^1H - ^{29}Si -HMQC experiments were used to screen for protonated silicides in solution. Therefore, the 2D versions were selected, since they can provide information about both ^1H and ^{29}Si chemical shift. As first step, the screening was performed by recording several 2D ^1H - ^{29}Si -HMQC spectra differing in transmitter frequency of the pulses in the ^{29}Si -dimension (indirect dimension, F1) in order to cover a large frequency area. The spectra are displayed in Figure 2.7a and highlighted in different colors for different transmitter frequencies (tf). During that screening, however, a common phenomenon was observed, which is that resonant frequencies lying outside the selected spectral width appear at incorrect positions, hence as artifacts, within the 2D spectrum (see Figure 2.7a).^[4,25] Depending on the acquisition

2 ADVANTAGES OF BROADBAND EXCITATION IN NMR

mode, such artifacts appear either due to aliasing (for QF, States, States-TPPI or Echo-Antiecho as acquisition mode)^[26] or folding (for TPPI as acquisition mode).^[4,25] Aliased peaks appear in the spectrum at a distance of one (or a multiple of)^[27] spectral width from the real frequencies whereas folded peaks appear mirrored around the spectral margin (see Figure 2.7b).^[4,25] While for the direct dimension (F2) and for 1D spectra these artifacts can be avoided by oversampling and digital filtering, this is not possible for the indirect dimension (F1).^[4,25] In Biomolecular NMR, the phenomena of folding and especially aliasing are intentionally exploited in 2D and 3D experiments to reduce the spectral width in the indirect dimension and consequently to significantly decrease the acquisition time.^[28,29] However, this is only applicable if the nature of the folded or aliased cross peaks is known. In contrast, when these cross peaks are unknown, such as the peaks **A** and **B** in the screening displayed in Figure 2.7a, aliasing and folding artifacts can be confusing. In order to verify if a cross peak is an aliasing or folding artifact, the SW can be increased or the transmitter frequency slightly altered which results in a change of the detected frequency of an artifact but not of a real peak. This is however time consuming, especially for low concentrated samples, as such of *Zintl* phases or low abundant nuclei, and may not easily clarify how often^[27] aliasing or folding occurred (see Figure 2.7a).

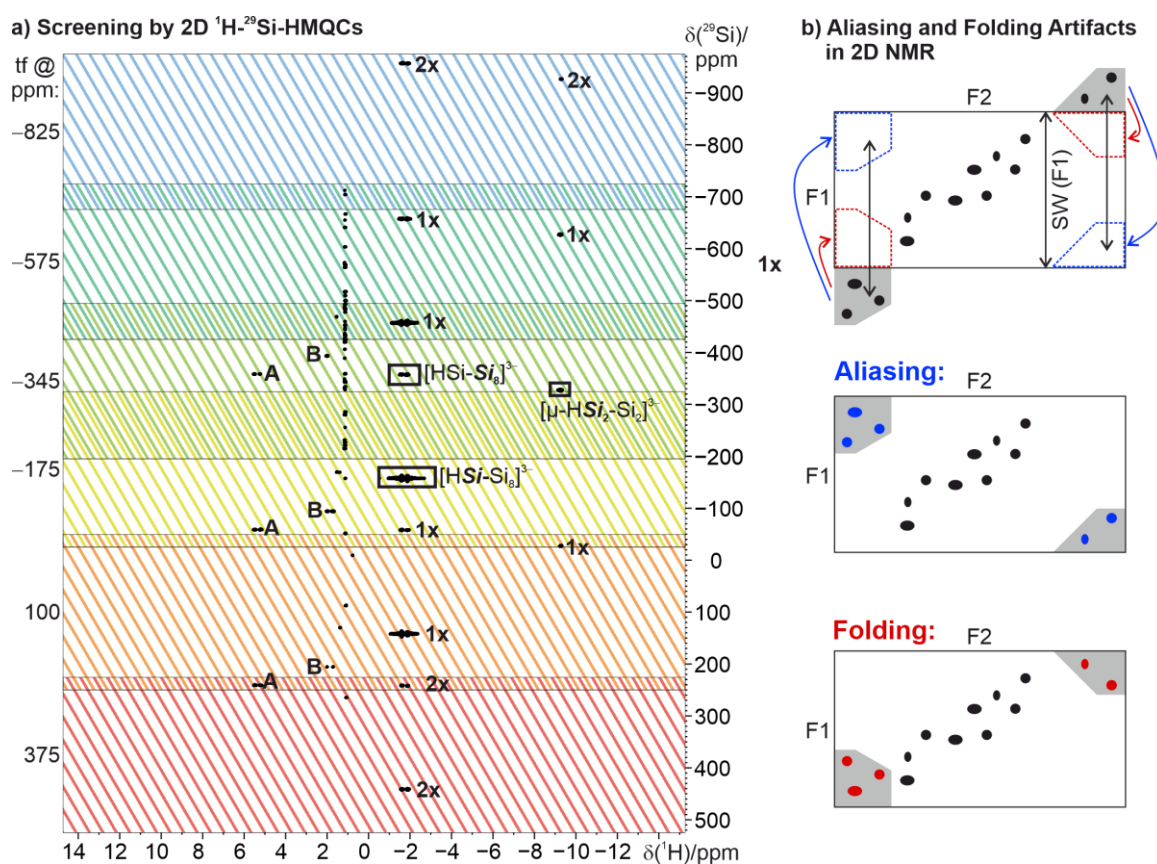


Figure 2.7 | a) Screening of a sample containing K₆Rb₆Si₁₇ (1 eq.) and [2.2.2]-cryptand (2 eq.) in liquid ammonia by standard 2D ¹H-²⁹Si-HMQC experiments at 203 K. The spectra were recorded with varying transmitter frequencies (tf) in the indirect dimension (F1) and with spectral overlap. Besides the literature known peaks^[3,24] of [HSi₉]³⁻ and [μ-HSi₄]³⁻ several other peaks appeared. The majority of the other peaks appeared due to one-fold or two-fold aliasing of the cross peaks of [HSi₉]³⁻ and [μ-HSi₄]³⁻ (indicated by 1× or 2×). For unknown cross peaks **A** and **B**, aliasing can be challenging. Key acquisition parameters for every spectrum: TD(F2) = 2k; TD(F1) = 256; SW(F2) = 60 ppm; SW(F1) = 300 ppm; AQ(F2) = 28 ms; AQ(F1) = 7 ms; d1 = 1.5 s; CNST2 = 30 Hz; NS = 16. b) Schematic representation of how aliasing and folding occurs for cross peaks lying outside the spectral width.^[4,25]

2 ADVANTAGES OF BROADBAND EXCITATION IN NMR

It would therefore be desirable to increase the spectral width as much as to cover the entire possible shift range in the indirect dimension within a single 2D experiment, which however is not possible with standard hard pulses. Therefore, we intended to implement the broadband pulse xyBEBOP in the indirect dimension of a 2D HMQC experiment to enable uniform excitation over a large frequency range (500 kHz).

For the implementation of the xyBEBOP pulse in a 2D HMQC experiment, the gradient enhanced pulse sequence containing only 90° pulses was chosen (*hmqcgpqf*), since the shape of xyBEBOP is designed for exciting spins by 90°. In the *Bruker* standard pulse sequence *hmqcgpqf* the two 90° hard pulses on the X-channel simply had to be replaced by shaped pulses. The first pulse has to be defined by the shape of the xyBEBOP (500 kHz, 0.5 ms) while the second pulse by the shape of the time-reversed^[14] xyBEBOP (500 kHz, 0.5 ms) (see Figure 2.8).^[30]

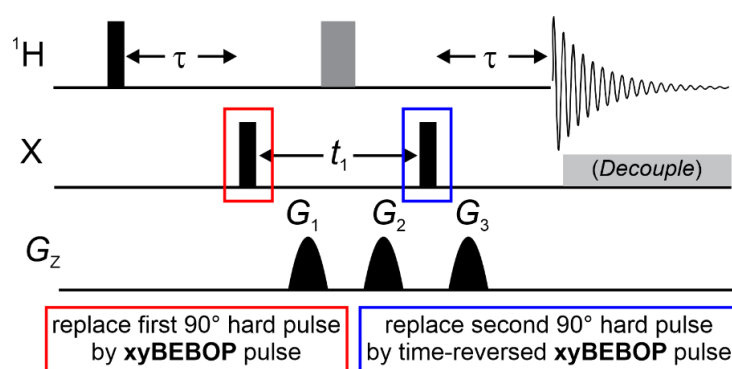


Figure 2.8 | Implementation of the broadband xyBEBOP pulse in the *Bruker* standard pulse sequence *hmqcgpqf*. Therefore, the two 90° hard pulses on the X-channel simply had to be replaced by shaped pulses. The first pulse has to be defined by the shape of the xyBEBOP (500 kHz, 0.5 ms) while the second pulse by the shape of the time-reversed^[14] xyBEBOP (500 kHz, 0.5 ms).^[30]

Then, the performance of the modified HMQC sequence incorporating broadband pulses in the indirect dimension (*hmqcgpqfbulusp2*) was compared with the standard HMQC sequence. A first testing was performed by ¹H-¹³C-HMQCs on a solution of an ABC-transporter^[31] (4 mM) in DMSO-d₆ (for structure see Figure 2.9 and literature^[31]). For the testing, three *hmqcgpqf* and three *hmqcgpqfbulusp2* experiments were recorded with (i) a narrow SW in F1 of around 23 kHz and a transmitter frequency at 69 ppm, (ii) a large SW in F1 of 500 kHz and a transmitter frequency at 69 ppm and (iii) a large SW in F1 of 500 kHz and a transmitter frequency far off resonance at -1000 ppm. The respective spectra are displayed in Figure 2.9a. The corresponding ¹³C-projections are displayed in Figure 2.9b and colored in black when extracted from an *hmqcgpqf* experiment and in red when extracted from an *hmqcgpqfbulusp2* experiment. The comparison of the ¹³C-projections within cases (i) and (ii) shows that the peaks obtained from *hmqcgpqfbulusp2* are reduced in intensity by an average of 9% compared to the peaks obtained from *hmqcgpqf*. This reduction in intensity may arise from increased relaxation losses as a consequence of extending the delay between ¹H-excitation and detection ($\approx 2 \times \Delta + t_1$) by ~ 1 ms ($= 2 \times \Delta t$ of 500 kHz xyBEBOP) when applying the xyBEBOP pulses instead of the 90° hard pulses. Case (iii) demonstrates the benefit of applying broadband excitation in the indirect dimension: when the transmitter frequency on the ¹³C channel is set far off resonance, cross peaks can still be detected with the xyBEBOP pulses in contrast to the 90° hard pulses.

2 ADVANTAGES OF BROADBAND EXCITATION IN NMR

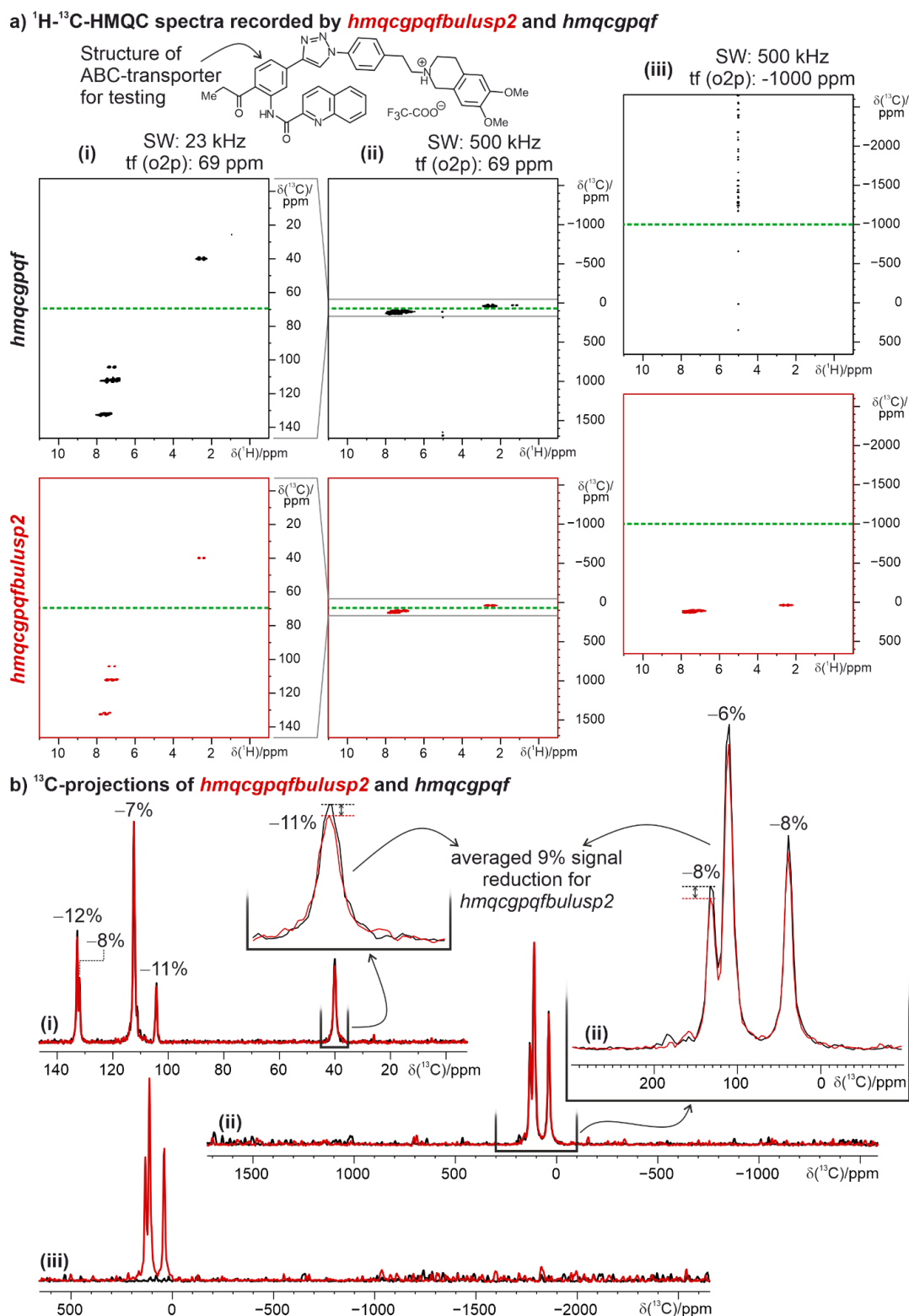


Figure 2.9 | Performance testing of the modified HMQC sequence incorporating xyBEBOP broadband pulses in the indirect dimension (*hmqcgpqfbulusp2*) in comparison to the standard HMQC sequence.
a) Comparison of ^1H - ^{13}C -HMQC spectra (obtained by *hmqcgpqf* and *hmqcgpqfbulusp2*) recorded of a solution of an ABC-transporter³¹¹ (4 mM) in DMSO at 298 K with (i) a narrow SW in F1 of around 23 kHz and a transmitter frequency at 69 ppm, (ii) a large SW in F1 of 500 kHz and a transmitter frequency at 69 ppm and (iii) a large SW in F1 of 500 kHz and a transmitter frequency far off resonance at -1000 ppm. Key acquisition parameters for both *hmqcgpqfbulusp2* and *hmqcgpqf*: TD(F2) = 512; TD(F1) = see a); SW(F2) = 12 ppm; SW(F1) = see a); AQ(F2) = 35 ms; AQ(F1) = 22 ms for (i), 1 ms for (ii) and (iii); d1 = 1.5 s; CNST2 = 145 Hz; NS = 4. Further key acquisition parameters for *hmqcgpqfbulusp2*: P12 = 500 μs ; P13 = 500 μs ; SPNAM21 = shape of xyBEBOP; SPNAM22 = shape of time-reversed xyBEBOP; SPOAL21 = 1; SPOAL22 = 0.5.

2 ADVANTAGES OF BROADBAND EXCITATION IN NMR

While the application of broadband pulses in 1D heteronuclear experiments can lead to considerable measurement time savings since a large frequency range can be covered within a single spectrum, this is not true for 2D experiments, since here the experimental time is mostly determined by the number of increments recorded in the indirect dimension. The number of increments recorded (= TD) for a certain spectral width (SW) determines the spectral resolution (FID resolution, FIDRES) by

$$FIDRES[Hz] = \frac{SW[Hz]}{TD} \quad [32] \quad (5)$$

This implies that upon increasing the spectral width in the indirect dimension, TD has to be increased accordingly in order to maintain a certain resolution, and therefore the experimental time increases for 2D experiments in contrast to 1D experiments. In other words, at constant spectral resolution, recording one 2D spectrum with a SW in F1 of 500 kHz takes as long as, for example, two or four 2D spectra with a SW in F1 of 250 kHz or 125 kHz respectively. However, when recording 2D HMQC spectra by *hmqcgpqfbulusp2*, the spectral width in the indirect dimension can be increased (up to 500 kHz) and so aliasing and folding artifacts can be avoided while still being able to uniformly excite the full frequency range. This is especially valuable when investigating unknown reaction mixtures or compounds producing unknown cross peaks in the 2D spectra. Therefore, as next step, the *hmqcgpqfbulusp2* experiment was used to record 2D ^1H - ^{29}Si HMQC spectra of the same sample in which the aliasing and folding artifacts were observed not only for known cross peaks but also for unknown ones (see Figure 2.7a). Combining this with the intention of cross peak screening several 2D ^1H - ^{29}Si HMQC spectra (*hmqcgpqfbulusp2*) with varying evolution delays optimized for different J_{HSi} coupling constants were recorded (see Figure 2.10). This allowed revealing the real resonance frequencies of the unknown cross peaks **A** and **B**. In addition, many other, previously unknown cross peaks were observed (peaks **C** – **L**). These cross peaks show that compounds containing an H-Si spin system were generated in solution (see Figure 2.10c, different spin systems are indicated by different colors of the lines in between related cross peaks). Only little is known about solution processes of silicon *Zintl* phases. Therefore, in order to gain a deeper understanding of the processes in solutions of *Zintl* ions, these cross peaks and spin systems are worth further investigation to clarify their structural nature. Besides, these spectra demonstrate that the *hmqcgpqfbulusp2* experiment using xyBEBOP pulses succeeded in recording cross peaks appearing within a large frequency range (here around 600 ppm \approx 71.5 kHz in the indirect dimension) under real experimental conditions. Yet, instead of aliasing or folding artifacts, another artifact at -558 ppm was observed which is exactly the same distance (200 ppm) away from the cross peak $[\text{HSi-Si}_8]^{3-}$ (-358 ppm) as is the cross peak $[\text{HSi-Si}_8]^{3-}$ (-158 ppm). These artifacts were also observed in 2D ^1H - ^{29}Si HMQC spectra recorded with the standard pulse program *hmqcgpqf* and can consequently be excluded as a result of xyBEBOP implementation. This artifact is more prominent at longer evolution delays and might be a multiple-quantum artifact as a consequence of 100% ^{29}Si enrichment. The artifact was not observed in 2D ^1H - ^{29}Si HMBC spectra recorded with the standard pulse program *hmbcgpndqf*. Besides the elimination of multiple quantum artifacts, the HMBC sequence has the additional advantage that it lacks the second evolution delay whereby less intensity is lost due to relaxation and

2 ADVANTAGES OF BROADBAND EXCITATION IN NMR

consequently cross peaks in higher intensity can be obtained. Therefore, the xyBEBOP pulse was additionally incorporated in an HMBC sequence (new pulse program: *hmqcgpqf_bulusp2*) similar to the incorporation in an HMQC sequence (see Figure 2.8) and the new sequence could also be effectively used for investigating samples of *Zintl* phases in liquid ammonia (the program is given in chapter 2.5.4).

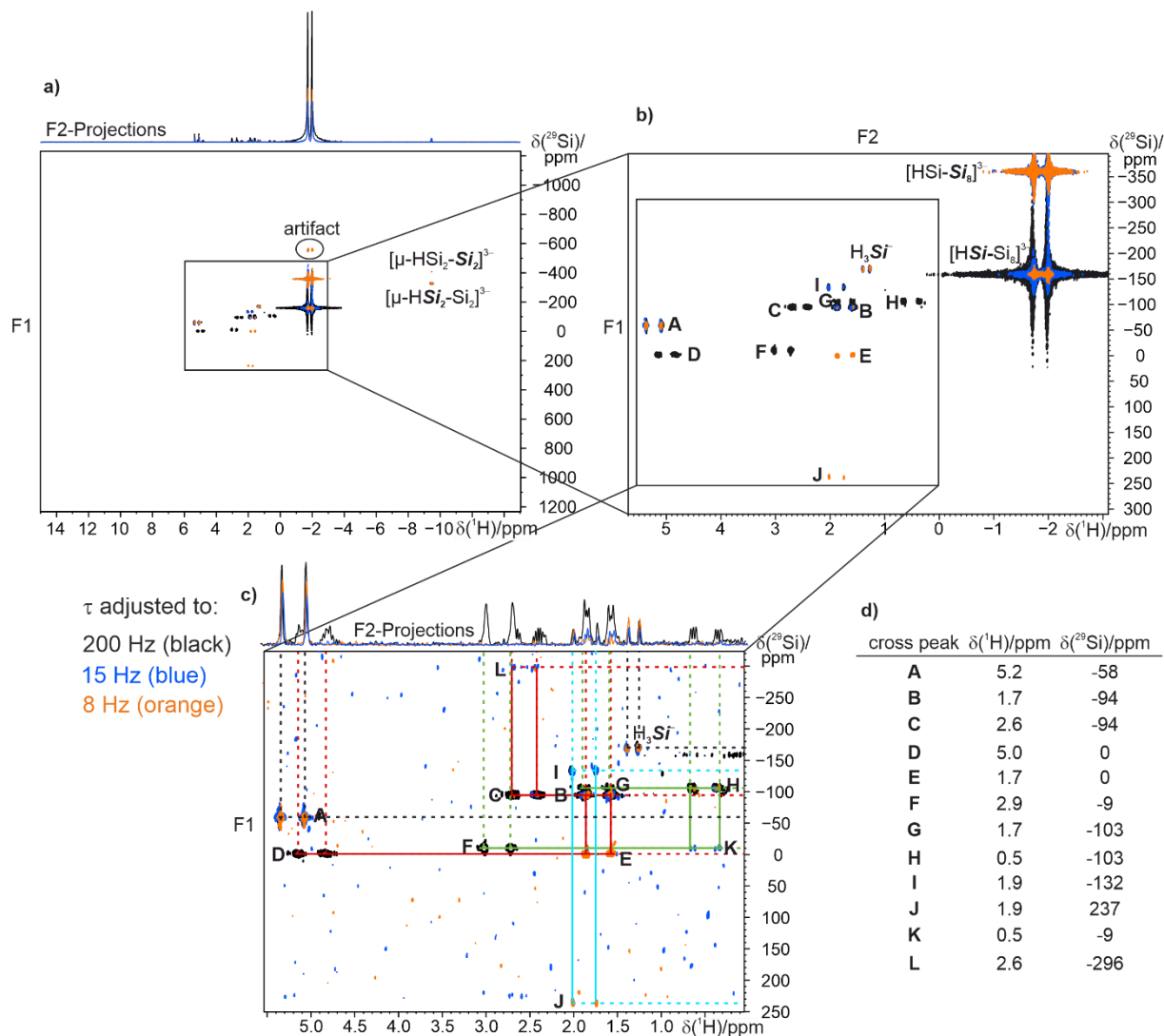


Figure 2.10 | Testing of the *hmqcgpqf_bulusp2* experiment under real reaction conditions in combination with J_{HSi} coupling constant screening. 2D ^1H - ^{29}Si HMQC spectra (*hmqcgpqf_bulusp2*) recorded of a sample containing $\text{K}_6\text{Rb}_6\text{Si}_{17}$ (1 eq.) and [2.2.2]-cryptand (2 eq.) in liquid ammonia at 203 K. The evolution delays of the spectra were adjusted to 200 Hz (black cross peaks), 15 Hz (blue cross peaks) and 8 Hz (orange cross peaks). a) Stacking of the 2D ^1H - ^{29}Si HMQC spectra without zoom demonstrates that all ^1H - ^{29}Si cross peaks can be covered within a single spectrum. b) Magnified region of the spectrum of a) displays the plethora of hitherto unknown cross peaks A – L. c) The 2D ^1H - ^{29}Si HMQC (*hmqcgpqf_bulusp2*) screening by adjusting different evolution delays allowed to detect H-Si spin system among the unknown cross peaks. Different spin systems are indicated by different colors of the lines in between related cross peaks. d) Assignment of ^1H - and ^{29}Si -NMR shift to the corresponding cross peaks. The displayed F2-projections were calculated for all rows of the spectra. Key acquisition parameters for all HMQCs: TD(F2) = 4k; TD(F1) = 256; SW(F2) = 30 ppm; SW(F1) = 300 kHz; AQ(F2) = 114 ms; AQ(F1) = 0.8 ms; d1 = 1.5 s; CNST2 = see Figure 2.10; NS = 32; P12 = 500 μs ; P13 = 500 μs ; SPNAM21 = shape of xyBEBOP; SPNAM22 = shape of time-reversed xyBEBOP; SPOAL21 = 1; SPOAL22 = 0.5.

2.4 Conclusion

In summary, the broadband pulse xyBEBOP (500 kHz, $\Delta t = 0.5$ ms) was successfully implemented in heteronuclear 1D experiments with ^1H -decoupling and in the F1 dimension of 2D HMQC and HMBC experiments.

Against the background of increasing the S/N-ratio for ^{31}P nuclei distributed among a large frequency range and exhibiting couplings to protons, xyBEBOP was implemented in standard *zgpg* and *zggd* pulse sequences. The performance of the new sequence (*bulu_zgpg*) was compared to the standard sequences applying a hard pulse. When both pulses were applied close to the resonant frequency of the test signal (H_2PPh), they lead to identical signal intensities, multiplet collapse and line widths of the $^{31}\text{P}\{^1\text{H}\}$ -NMR. When the pulses were applied considerably off resonance, the $^{31}\text{P}\{^1\text{H}\}$ signal obtained by hard pulse excitation was decreased in intensity in contrast to that obtained by xyBEBOP excitation, which remained unaltered. This demonstrates, that the xyBEBOP pulses can be used in presence of ^1H -decoupling for exciting large frequency ranges (either 500 kHz with $\Delta t = 0.5$ ms or 1000 kHz with $\Delta t = 1$ ms). The new pulse program *bulu_zgpg* was used in the majority of the $^{31}\text{P}\{^1\text{H}\}$ -NMR reaction monitorings of the photocatalytic functionalization of white phosphorus (P_4) and phenylphosphines (see chapter 4) and enabled the simultaneous detection of the signals of starting material, intermediates and products spread over an approximate frequency range of over 600 ppm.

In addition, the xyBEBOP was also implemented in the HMQC and HMBC sequences *hmqcgpqf* and *hmbcgpndqf* with the intention of facilitating the screening for protonated silicon cages in solution (see chapter 8) by 2D ^1H - ^{29}Si -experiments. During a screening of a sample of silicon *Zintl* phases in liquid ammonia (by standard 2D ^1H - ^{29}Si -HMQC spectra with varying transmitter frequency of the excitation pulses in the ^{29}Si -dimension) aliasing artifacts were obtained caused by peaks lying outside the spectral width of the indirect dimension (F1). These artifacts, however, are undesirable when investigating unknown reaction mixtures or compounds. Hence, the broadband pulse xyBEBOP was implemented in the 2D HMQC sequence *hmqcgpqf* with the intention of increasing the spectral width in F1 to an extent that covers the entire possible shift range while concomitantly allowing a uniform excitation over the complete range. The testing of the new sequence *hmqcgpqf_bulusp2* demonstrated that cross peaks are decreased in intensity of about 9% compared to the standard sequence containing hard pulses, which is probably owed to stronger relaxation losses as a consequence of extending the delay between ^1H -excitation and detection. Yet, the testing also demonstrated the strengths of the *hmqcgpqf_bulusp2* experiment, which lie in uniform excitation in F1, also when the transmitter frequency is set far off resonance, and in avoiding aliasing artifacts because the whole shift area can be covered within a single spectrum. The 2D HMQC experiment incorporating the xyBEBOP pulse (*hmqcgpqf_bulusp2*) and a corresponding 2D HMBC experiment (*hmbcgpndqf_bulusp2*) were extensively and successfully applied for screening for protonated silicon cluster in samples of *Zintl* phases in liquid ammonia.

2 ADVANTAGES OF BROADBAND EXCITATION IN NMR

These broadband experiments are of course not restricted to the sole application for ^{31}P or ^{29}Si NMR, but should in principle also be applicable and beneficial for other NMR active heteronuclei exhibiting large chemical shift ranges such as ^{117}Sn , ^{119}Sn or ^{207}Pb ^[16].

2.5 Pulse Programs

2.5.1 bulu_zg_shape

```
;zg
;avance-version (06/11/09)
;1D sequence
;
;$CLASS=HighRes
;$DIM=1D
;$TYPE=
;$SUBTYPE=
;$COMMENT=

#include <Avance.incl>

"acqt0=0"

1 ze
2 30m
  d1
  (p21:sp21 ph2):f1
  ;p1 ph1
  go=2 ph31
  30m mc #0 to 2 F0(zd)
exit

ph1=1
ph2=0
ph31=0

;p11 : f1 channel - power level for pulse (default)
;p1 : f1 channel - high power pulse
;d1 : relaxation delay; 1-5 * T1
;NS: 1 * n, total number of scans: NS * TD0

;$Id: zg,v 1.10 2009/07/02 16:40:47 ber Exp $
```

2.5.2 bulu_zgpg

```
;zgpg
;avance-version (12/01/11)
;1D sequence with power-gated decoupling
;
;$CLASS=HighRes
;$DIM=1D
;$TYPE=
;$SUBTYPE=
;$COMMENT=

#include <Avance.incl>
#include <Delay.incl>
```

2 ADVANTAGES OF BROADBAND EXCITATION IN NMR

```
"d11=30m"

"DELTA=d1-100m"

"acqt0=-p1*2/3.1416"

1 ze
  d11 p112:f2
2 30m do:f2
  10u p113:f2
  d11 cpd2:f2
  DELTA
  4u do:f2
  10u p112:f2
  100m cpd2:f2
  3u p10:f1
  (p21:sp21 ph2):f1
  go=2 ph31
  30m do:f2 p113:f2 mc #0 to 2 F0(zd)
exit

ph2=0 2 2 0 1 3 3 1
;ph2=0
ph31=0 2 2 0 1 3 3 1
;ph31=0

;p11 : f1 channel - power level for pulse (default)
;p112: f2 channel - power level for CPD/BB decoupling
;p113: f2 channel - power level for second CPD/BB decoupling
;p1 : f1 channel - high power pulse
;d1 : relaxation delay; 1-5 * T1
;d11: delay for disk I/O [30 msec]
;ns: 1 * n, total number of scans: NS * TD0
;cpd2: decoupling according to sequence defined by cpdprg2
;pcpd2: f2 channel - 90 degree pulse for decoupling sequence

;$Id: zgpg,v 1.11.8.1 2012/01/31 17:56:42 ber Exp $
```

2.5.3 hmqcgpqfbulusp2

```
;hmqcgpqf
;avance-version (12/01/11)
;HMQC
;2D H-1/X correlation via heteronuclear zero and double quantum
; coherence
;with decoupling during acquisition
;using gradient pulses for selection
;use pulseprogram 'hmqcgpndld' for setup
;
;$CLASS=HighRes
;$DIM=2D
;$TYPE=
;$SUBTYPE=
;$COMMENT=

#include <Avance.incl>
#include <Grad.incl>
#include <Delay.incl>

"p2=p1*2"
"d2=1s/(cnst2*2)"
"d12=20u"
"d13=4u"

"d0=3u"
```

2 ADVANTAGES OF BROADBAND EXCITATION IN NMR

```
"in0=inf1/2"
```

```
"DELTA1=d2-p16-d16-d13-d12"
```

```
1 ze
2 d1 do:f2
3 p1 ph1
  d2 p10:f2 UNBLKGRAD
  p12:sp21:f2 ph3
  d0
  p16:gp1
  d16
  p2 ph2
  d13
  p16:gp2
  d16
  d0
  p13:sp22:f2 ph4
  d13
  p16:gp3
  d16
  DELTA1
  d12 p112:f2 BLKGRAD
  go=2 ph31 cpd2:f2
  d1 do:f2 mc #0 to 2 F1QF(caldel(d0, +in0))
exit
```

```
ph1=0
ph2=0
ph3=0 2
ph4=0 0 2 2
ph31=0 2 2 0
```

```
;p10 : 0 W
;p11 : f1 channel - power level for pulse (default)
;p12 : f2 channel - power level for pulse (default)
;p112: f2 channel - power level for CPD/BB decoupling
;p1 : f1 channel - 90 degree high power pulse
;p2 : f1 channel - 180 degree high power pulse
;p3 : f2 channel - 90 degree high power pulse
;p12: f2 channel -x duration of y-bebop shape pulse 1000 u
;p13: f2 channel -x duration of y-bebop shape pulse 1000 u
;sp21: f2 channel - xy-bebop shape pulse
;sp22: f2 channel - xy-bebop shape pulse 2
;p16: homospoil/gradient pulse
;d0 : incremented delay (2D) [3 usec]
;d1 : relaxation delay; 1-5 * T1
;d2 : 1/(2J)XH
;d12: delay for power switching [20 usec]
;d13: short delay [4 usec]
;ns: 1 * n
;ds: 16
```

```
;d16: delay for homospoil/gradient recovery
;cnst2: = J(XH)
;inf1: 1/SW(X) = 2 * DW(X)
;in0: 1/(2 * SW(X)) = DW(X)
;nd0: 2
;td1: number of experiments
;FnMODE: QF
;cpd2: decoupling according to sequence defined by cpdprg2
;pcpd2: f2 channel - 90 degree pulse for decoupling sequence
```

```
;use gradient ratio: gp 1 : gp 2 : gp 3
; 50 : 30 : 40.1 for C-13
; 70 : 30 : 50.1 for N-15
```

```
;for z-only gradients:
;gpz1: 50% for C-13, 70% for N-15
;gpz2: 30%
;gpz3: 40.1% for C-13, 50.1% for N-15
```

```
;use gradient files:
;gpnaml: SMSQ10.100
```

2 ADVANTAGES OF BROADBAND EXCITATION IN NMR

```
;gpnam2: SMSQ10.100  
;gpnam3: SMSQ10.100
```

```
;$Id: hmqcgpqf,v 1.6 2012/01/31 17:49:23 ber Exp $
```

2.5.4 hmbcgpndqf_bulusp2

```
;hmbcgpndqf  
;avance-version (12/01/11)  
;HMBC  
;2D H-1/X correlation via heteronuclear zero and double quantum  
; coherence  
;optimized on long range couplings  
;no decoupling during acquisition  
;using gradient pulses for selection  
;  
;$CLASS=HighRes  
;$DIM=2D  
;$TYPE=  
;$SUBTYPE=  
;$COMMENT=  
  
#include <Avance.incl>  
#include <Grad.incl>  
  
"p2=p1*2"  
"d6=1s/(cnst13*2)"  
  
"d0=3u"  
  
"in0=infl/2"  
  
1 ze  
2 d1 do:f2  
3 p1 ph1  
d6 p10:f2  
p12:sp21:f2 ph3  
d0  
50u UNBLKGRAD  
p16:gp1  
d16  
p2 ph2  
50u  
p16:gp2  
d16  
d0  
p13:sp22:f2 ph4  
4u  
p16:gp3  
d16  
d12 p112:f2 BLKGRAD  
go=2 ph31 cpd2:f2  
d1 do:f2 mc #0 to 2 F1QF(caldel(d0, +in0))  
exit  
  
ph1=0  
ph2=0 0 2 2  
ph3=0 2  
ph4=0 0 0 0 2 2 2 2  
ph31=0 2 0 2 2 0 2 0  
  
;p11 : f1 channel - power level for pulse (default)  
;p12 : f2 channel - power level for pulse (default)  
;p112: f2 channel - power level for CPD/BB decoupling  
;p1 : f1 channel - 90 degree high power pulse  
;p2 : f1 channel - 180 degree high power pulse  
;p3 : f2 channel - 90 degree high power pulse  
;p12: f2 channel -x duration of y-bebop shape pulse 500 u or 1000 u  
;p13: f2 channel -x duration of y-bebop shape pulse 500 u or 1000 u
```

2 ADVANTAGES OF BROADBAND EXCITATION IN NMR

```
;p16: homospoil/gradient pulse
;d0 : incremented delay (2D) [3 usec]
;d1 : relaxation delay; 1-5 * T1
;d6 : delay for evolution of long range couplings
;d16: delay for homospoil/gradient recovery
;cnst13: = J(XH) long range
;inf1: 1/SW(X) = 2 * DW(X)
;in0: 1/(2 * SW(X)) = DW(X)
;nd0: 2
;ns: 2 * n
;ds: 16
;td1: number of experiments
;FnMODE: QF
;cpd2: decoupling according to sequence defined by cpdprg2
;pcpd2: f2 channel - 90 degree pulse for decoupling sequence

;use gradient ratio: gp 1 : gp 2 : gp 3
; 50 : 30 : 40.1 for C-13
; 70 : 30 : 50.1 for N-15

;for z-only gradients:
;gpz1: 50% for C-13, 70% for N-15
;gpz2: 30%
;gpz3: 40.1% for C-13, 50.1% for N-15

;use gradient files:
;gpnam1: SMSQ10.100
;gpnam2: SMSQ10.100
;gpnam3: SMSQ10.100

;$Id: hmbcgpndqf,v 1.5.8.1 2012/01/31 17:56:25 ber Exp $
```

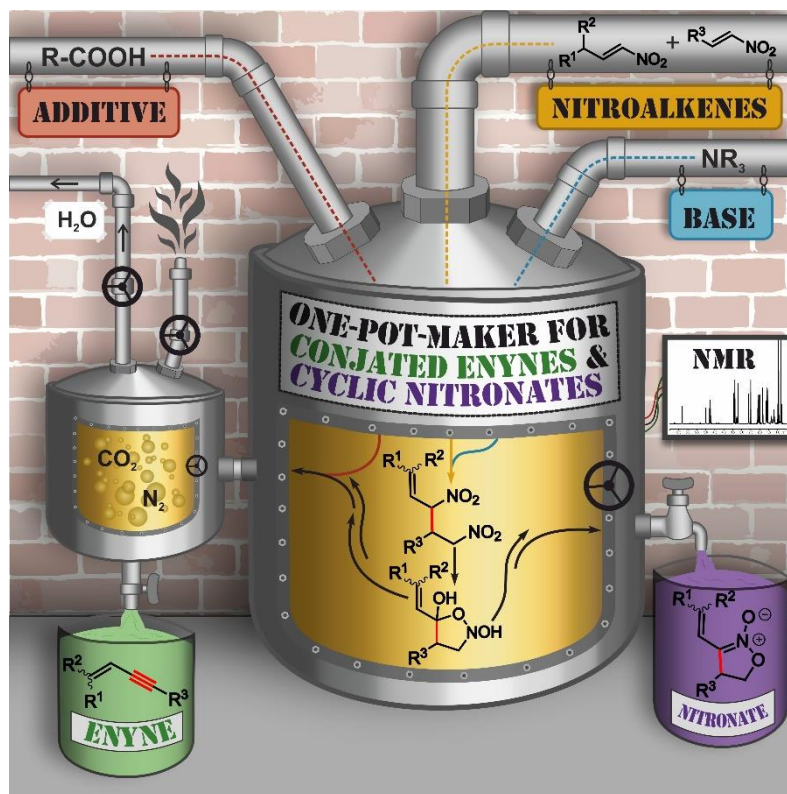
2.6 References

- [1] S. Berger, S. Braun, H.-O. Kalinowski, *NMR-Spektroskopie von Nichtmetallen: 31P-NMR-Spektroskopie*, Georg Thieme Verlag, **1993**.
- [2] M. Kira, S. Ishida, T. Iwamoto, C. Kabuto, *J. Am. Chem. Soc.* **1999**, *121*, 9722–9723.
- [3] F. Hastreiter, C. Lorenz, J. Hioe, S. Gärtner, N. Lokesh, N. Korber, R. M. Gschwind, *Angew. Chemie Int. Ed.* **2019**, *58*, 3133–3137.
- [4] T. D. W. Claridge, *High-Resolution NMR Techniques in Organic Chemistry*, Elsevier, Oxford, **2009**.
- [5] J. E. Power, M. Foroozandeh, R. W. Adams, M. Nilsson, S. R. Coombes, A. R. Phillips, G. A. Morris, *Chem. Commun.* **2016**, *52*, 2916–2919.
- [6] M. H. Leviti, R. Freeman, *J. Magn. Reson.* **1979**, *33*, 473–476.
- [7] M. S. Silver, R. I. Joseph, D. I. Hoult, *J. Magn. Reson.* **1984**, *59*, 347–351.
- [8] K. E. Cano, M. A. Smith, A. J. Shaka, *J. Magn. Reson.* **2002**, *155*, 131–139.
- [9] V. L. Ermakov, G. Bodenhausen, *Chem. Phys. Lett.* **1993**, *204*, 375–380.
- [10] J. M. Böhlen, G. Bodenhausen, *J. Magn. Reson. - Ser. A* **1993**, *102*, 293–301.
- [11] J. M. Böhlen, M. Rey, G. Bodenhausen, *J. Magn. Reson.* **1989**, *84*, 191–197.
- [12] M. Garwood, L. DelaBarre, *J. Magn. Reson.* **2001**, *153*, 155–177.
- [13] A. Tannús, M. Garwood, in *NMR Biomed.*, John Wiley & Sons, Ltd, **1997**, pp. 423–434.

2 ADVANTAGES OF BROADBAND EXCITATION IN NMR

- [14] T. E. Skinner, T. O. Reiss, B. Luy, N. Khaneja, S. J. Glaser, *J. Magn. Reson.* **2003**, *163*, 8–15.
- [15] M. Foroozandeh, M. Nilsson, G. A. Morris, *J. Magn. Reson.* **2019**, *302*, 28–33.
- [16] C. Koch, *NMR Spectroscopic Investigations on Copper-Catalyzed Reactions and Zintl Anions*, University of Regensburg, **2015**.
- [17] N. C. Nielsen, C. Kehlet, S. J. Glaser, N. Khaneja, in *Encycl. Magn. Reson.*, John Wiley & Sons, Ltd, Chichester, UK, **2010**.
- [18] A. Bryson Jr., Y.-C. Ho, *Applied Optimal Control*, Hemisphere, Washington, DC, **1975**.
- [19] A. P. Sage, *Optimum Systems Control*, Prentice-Hall, Inc., Englewood Cliffs, NJ, **1968**.
- [20] L. Pontryagin, B. Boltyanskii, R. Gamkrelidze, E. Mishchenko, *The Mathematical Theory of Optimal Processes*, Wiley-Interscience, New York, **1962**.
- [21] Bruker Corporation, *TopSpin User Manual, Processing Commands and Parameters*, **2019**.
- [22] R. K. Harris, in *Chem. Soc. Rev.*, The Royal Society Of Chemistry, **1976**, pp. 1–22.
- [23] L. J. Schiegerl, A. J. Karttunen, J. Tillmann, S. Geier, G. Raudaschl-Sieber, M. Waibel, T. F. Fässler, *Angew. Chemie Int. Ed.* **2018**, *57*, 12950–12955.
- [24] C. Lorenz, F. Hastreiter, J. Hioe, N. Lokesh, S. Gärtner, N. Korber, R. M. Gschwind, *Angew. Chemie Int. Ed.* **2018**, *57*, 12956–12960.
- [25] A. M. Torres, W. S. Price, *Common Problems and Artifacts Encountered in Solution-State NMR Experiments. Concepts Magn Reson Part A*, **2017**.
- [26] D. Jeannerat, *Magn. Reson. Chem.* **2003**, *41*, 3–17.
- [27] D. Jeannerat, *Magn. Reson. Chem.* **2000**, *38*, 415–422.
- [28] M. R. Gryk, J. Vyas, M. W. Maciejewski, *Prog. Nucl. Magn. Reson. Spectrosc.* **2010**, *56*, 329–345.
- [29] J. Cavanagh, W. J. Fairbrother, A. G. Palmer, N. J. Skelton, M. Rance, *Protein NMR Spectroscopy*, Elsevier Inc., **2007**.
- [30] *This was kindly suggested by Prof Dr. Burkhard Luy.*
- [31] F. Antoni, M. Bause, M. Scholler, S. Bauer, S. A. Stark, S. M. Jackson, I. Manolaridis, K. P. Locher, B. König, A. Buschauer, G. Bernhardt, *Eur. J. Med. Chem.* **2020**, *191*, 112133.
- [32] Bruker Corporation, *TopSpin, Acquisition Commands and Parameters*, **2019**.

3 UNPRECEDENTED MECHANISM OF AN ORGANO-CATALYTIC ROUTE TO CONJUGATED ENYNES WITH A JUNCTION TO CYCLIC NITRONATES



Verena Streitferdt, Michael H. Haindl, Johnny Hioe, Fabio Morana, Polyssena Renzi, Felicitas von Rekowski, Alexander Zimmermann, Martina Nardi, Kirsten Zeitler, and Ruth M. Gschwind*

European Journal of Organic Chemistry

Eur. J. Org. Chem. **2019**, 2019, 328-337.

DOI: 10.1002/ejoc.201801153

This chapter was written by Verena Streitferdt based on a draft from Michael H. Haindl with input from all authors. All Figures of the manuscript were designed by Verena Streitferdt. The Figures of the Supporting Information were designed by Verena Streitferdt and Michael H. Haindl. Verena Streitferdt, Michael H. Haindl, Fabio Morana, Polyssena Renzi, Felicitas von Rekowski, Alexander Zimmermann and Martina Nardi investigated the substrate scope and performed *in situ* NMR studies. Kirsten Zeitler and Ruth M. Gschwind assisted in evaluating data and writing the manuscript and contributed with fruitful discussions.

Reprinted (adapted) with permission from *Eur. J. Org. Chem.* (via RightsLink). Text and Figures may differ from the original publication. Source of this chapter: <https://doi.org/10.1002/ejoc.201801153>

3.1 Abstract

Conjugated enynes as well as cyclic nitronates are crucial building blocks for numerous natural products and pharmaceuticals. However, so far, no common and metal-free synthetic route to both conjugated enynes and cyclic nitronates has been reported. Here, *in situ* NMR, labelling studies and theoretical calculations were combined to investigate the mechanism of the unusual triple bond formation towards conjugated enynes. Starting from nitroalkene dimers, first an isoxazolidine-2,5-diol derivative is formed as central intermediate. From this, enynes were generated *via* a combination of oxidation, dehydration and retro 1,3-dipolar cycloaddition, whereas for nitronates a base induced intramolecular reorganization is proposed. While the product distribution could be controlled and high yields of nitronate were achieved, only medium to good yields for enynes were obtained due to polymerization losses. Nevertheless, we hope that these mechanistic investigations may provide a basis for further developments of organocatalytic or metal-free preparations of conjugated enynes and nitronates.

3.2 Introduction

In the fields of natural products and drug design, nitronates and conjugated enynes are valuable building blocks. While the structural motif of a conjugated enyne occurs in many pharmaceuticals and natural compounds (e.g. Dynemicin A^[1], Terbinafine^[2,3] (Lamisil®), callipeltosides^[4] or Neocarzinostatin^[5]), nitronates, especially cyclic nitronates, find application in the synthesis of biologically active compounds,^[6,7] drug candidates^[8-10] and natural products.^[11] Due to the fundamental structural dissimilarities between cyclic nitronates and conjugated enynes, these compounds are generally accessed by disparate strategies. The most established methods for the formation of conjugated enynes are metal catalyzed cross-couplings exploiting the presence of double and triple bonds in the starting materials.^[3,12-17] Although metal-free procedures, especially organocatalytic ones, to conjugated enynes would be very valuable, they are rarely found in literature.^[18] On the other hand, numerous metal-free procedures for the synthesis of cyclic nitronates already exist among which intramolecular cyclization *via* substitution and cycloadditions are commonly employed.^[19] Despite their structural divergences, conjugated enynes and nitronates exhibit common reactivities. The zwitterionic structure of nitronates allows them to react as α -C-electrophiles, but also as ambident nucleophiles due to their O- and α -C-nucleophilicity.^[19] Moreover, nitronates are 1,3-dipoles and thus can *inter alia* participate in [3+2]-cycloadditions generating highly functionalized heterocycles.^[19] Similar to nitronates, also conjugated enynes can partake in cycloadditions.^[20] Furthermore, they can be subjected to other ring-closing^[21,22] and coupling reactions,^[23,24] or they can serve as transition metal ligands.^[25]

A few years ago, in our working group Markus Schmid discovered the first organocatalytic route to conjugated enynes, in which the C-C triple bond is constituted out of a C-C single bond in a one-pot reaction.^[26] Starting from α,β -unsaturated nitroalkenes **1** and **2** with proline-based catalysts, first nitroalkene dimers **3** were generated *via* a *Rauhut-Currier*-like reaction^[27-29] (see Figure 3.1 top) followed by the fragmentation to conjugated enynes.^[26] Furthermore, the pronounced formation of another product was

3 CONJUGATED ENYNES AND CYCLIC NITRONATES

observed, which could be suppressed upon addition of benzoic acid and was tentatively assigned to a nitronic acid derivative.^[26]

However, the mechanism of this unprecedented fragmentation as well as the nature of the other product remained unclear. The postulated mechanism *via* fragmentation to enyne and nitromethane was regarded to be improbable, because nitromethane did not accumulate during the reaction in the expected amount.^[26]

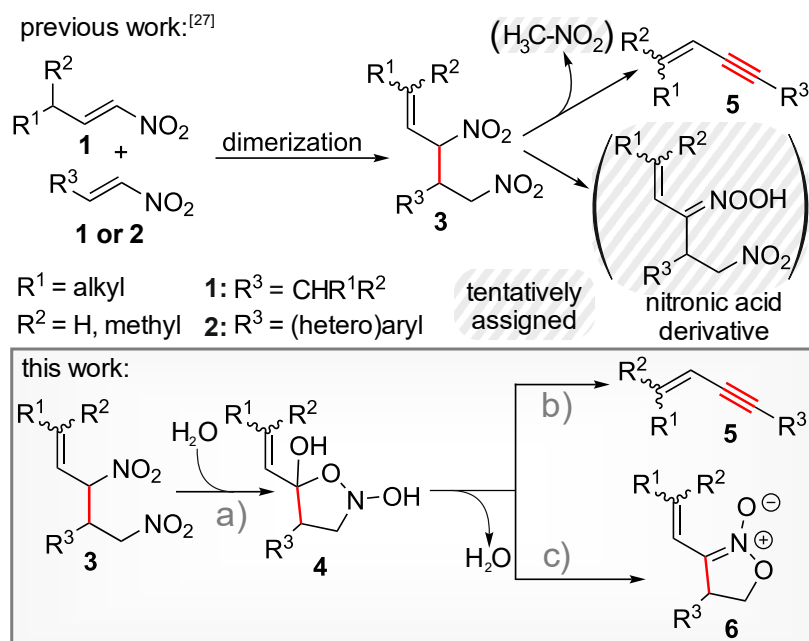


Figure 3.1 | General reaction scheme to conjugated enyne **5** and cyclic nitronate **6** from nitroalkenes **1** and **2** or dimer **3** *via* linking intermediate **4**. The mechanism starting from dimer **3**, highlighted by a gray frame, is elucidated in this work: a) Cyclization of dimer **3** to intermediate **4**; b) fragmentation of **4** to conjugated enyne **5**; c) rearrangement of **4** to cyclic nitronates **6**.

Herein, we present our profound mechanistic study on the unusual organocatalytic formation of conjugated enynes by means of NMR in combination with theoretical calculations. The product generated alongside the enyne could be identified as a cyclic nitronate. In addition, an unprecedented cyclic intermediate **4** was discovered, which was found to be common to the mechanistic pathways of both conjugated enyne **5** and cyclic nitronate **6** (see Figure 3.1 bottom). Furthermore, ¹³C and ¹⁵N labelling studies allowed for the identification of N₂ and CO₂ as fragmentation byproducts in the enyne formation. Hence, a comprehensive mechanism for the first combined metal-free synthesis of conjugated enynes and cyclic nitronates is proposed. A retro-1,3-dipolar cycloaddition as a fragmentation towards the enyne as well as complex intramolecular rearrangements towards the nitronate are postulated. In addition, factors influencing the product outcome are identified and approaches to modify this outcome are presented.

3.3 Results and Discussion

3.3.1 Compound Pool for Mechanistic Studies

While the dimerization of nitroalkenes follows the expected *Rauhut-Currier*-type mechanism,^[26,27] the mechanistic pathway to conjugated enynes was still unsettled. Therefore, we focused our NMR study on the mechanism and intermediates downstream to nitroalkene dimers. As starting material for our studies dimer **3a**, synthesized from the unsubstituted nitropentene **1a**, was selected to allow investigations on double bond isomerization, while dimers **3b-c** were chosen to examine electronic effects (see Figure 3.2a; for syntheses see SI).

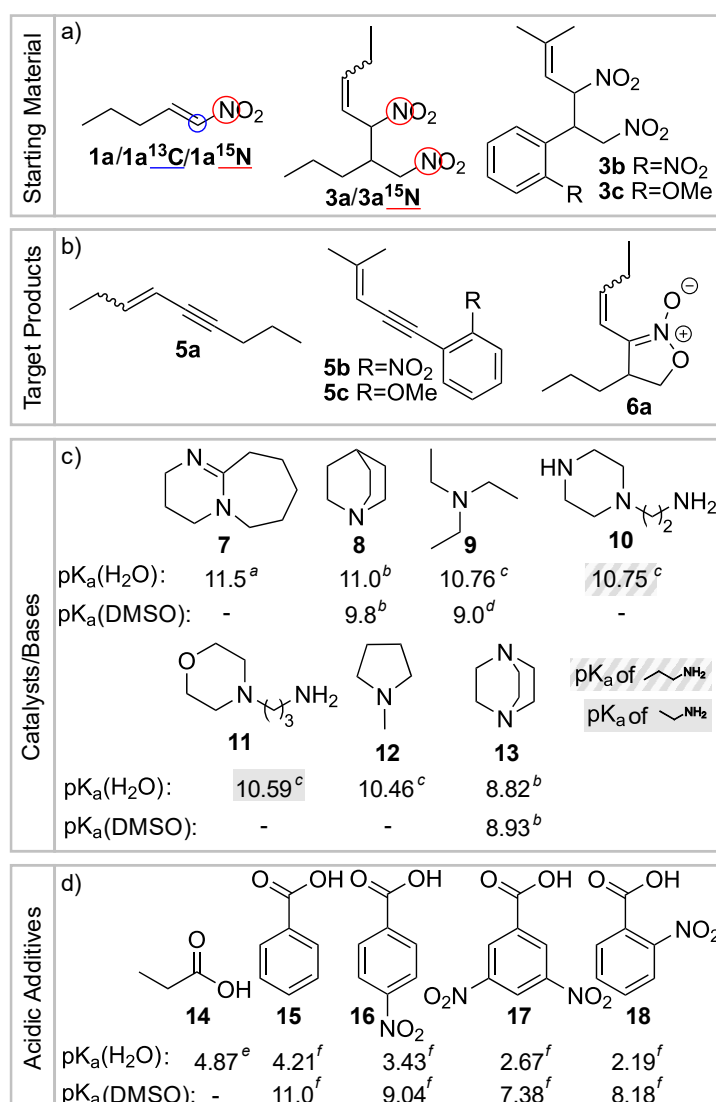


Figure 3.2 | Model substrates for the mechanistic investigation of the reaction to conjugated enynes **5a-c** and cyclic nitronate **6a**; atoms marked in blue and red were labelled with ¹³C and ¹⁵N, respectively; pK_a values are given at 25 °C: ^a[30], ^b[31], ^c[32], ^d[33], ^e[34], ^f[35]; for syntheses see SI.

¹⁵N labeled dimer **3a¹⁵N** was used for structural investigations on intermediate **4** during *in situ* NMR reaction monitoring. For the investigation of the fragmentation byproducts by ¹⁵N and ¹³C labeling, one-pot reactions were applied to avoid compound loss by further conversion to the dimer (see Figure 3.2a, **1a¹⁵N** and **1a¹³C**).

3 CONJUGATED ENYNES AND CYCLIC NITRONATES

Various bases, acids or their combinations were examined (see Figure 3.2c-d, for further catalyst screening see SI), since the initial studies revealed that the reaction to both enyne and nitronate requires a base.^[26] Acids as additional additives potentially suppress the formation of nitronates.^[26] An NMR solvent screening including DMSO, DMF, methanol, benzene, dioxane, nitromethane, dichloromethane and acetonitrile revealed that highest yields were obtained in DMSO (for more information see SI). Therefore, hereafter exclusively the studies in DMSO- d_6 are discussed. Consequently, in Figure 3.2c-d the pK_a values are given in DMSO as far as available. Otherwise, pK_a values in water are provided.

Overall, no significant mechanistic deviations were found for one-pot reactions and those starting from dimers regarding intermediate species (outcome and product distribution was dependent on solvent and reaction conditions). Therefore, the information of both reaction types could be combined.

3.3.2 Identification of Cyclic Nitronate as Second Product

Parallel to the formation of **5**, the generation of a side product was observed.^[26] Characterization of this side product by 2D NMR spectroscopy and mass spectrometry revealed this compound not as the originally suspected nitronic acid derivative,^[26] but as the cyclic nitronate **6a**. The structure of **6a** could be further confirmed by removal of the exocyclic oxygen by $P(OCH_3)_3$ ^[36] and thereby reducing **6a** to the corresponding cyclic *O*-alkyl-oxime (see SI). The highest yield of **6a** (84%) was obtained with the base triazabicyclodecene (for synthesis and chemical assignment of **6a** see SI).

3.3.3 Common Pathway of Nitronates and Enynes to a Central Linking Intermediate

Applying nitroalkene dimers as starting material, NMR reaction monitoring revealed the formation of a new intermediate **4** (see Figure 3.1 bottom) in the initial phase of the reaction. The detectable concentration of intermediate **4** highly depends on the base strength (see Figure 3.3). This is shown on the reaction profiles of **3a** with DBU **7** and quinuclidine **8** (Figure 3.3b). Applying DBU as base, dimer **3a** was instantly and nearly completely converted to intermediate **4a** (10% *E*-isomer and 83% *Z*-isomer, see Figure 3.3a). Employing quinuclidine **8** as base generated significantly smaller amounts of **4a** (initial 30%). The application of further bases corroborated the trend, that stronger bases generate higher amounts of **4** (see Figure SI 3.5). In addition, the type and strength of base affect significantly the product distribution between enynes and nitronates. With DBU about 60% nitronate **6a** and 9% of enyne **5a** was formed, while in presence of the less basic quinuclidine, enyne **5a** was the major product with 29% yield and only 10% of nitronate **6a** was generated. Furthermore, mechanistic investigations of the nitronate formation showed a clear correlation between the basicity, yield and formation rate of nitronate (see section "Selectivity" and Figure 3.11).

3 CONJUGATED ENYNES AND CYCLIC NITRONATES

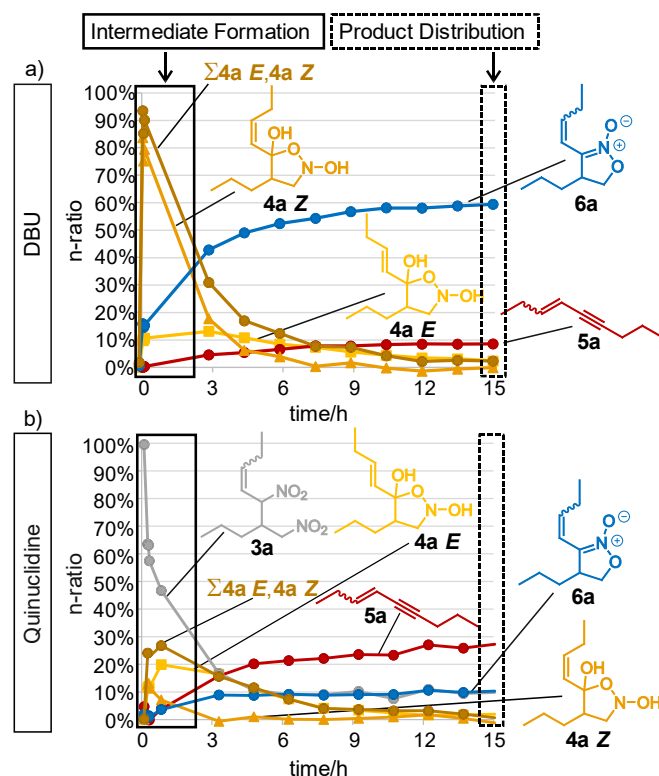


Figure 3.3 | Base dependent formation of the central linking intermediate **4a** as precursor for both enyne and nitronate. Strong bases caused high amounts of **4a** and nitronate (a), while enynes were the main product with weaker bases (b); a) **3a** (55 mM) with DBU (82 mM) in DMSO- d_6 at 298K; b) **3a** (55 mM) with quinuclidine (82 mM) in DMSO- d_6 at 298K.

Next, the question arose, whether intermediate **4a** is part of the mechanistic pathway of both main products, enyne and nitronate. Figure 3.3 reveals that **4a** was present in high concentrations independent of the main product indicating that **4a** is a linking element for the formation of both enynes and nitronates. This was further corroborated by a modified experiment with DBU: Using a starting point with mainly **4a** detectable and only traces of dimer **3a** left, benzoic acid **15** was added leading to an increased amount of enyne (for data see SI). The structure of intermediate **4a** was investigated during *in situ* NMR reaction monitoring, since it was too unstable for other methods. Various 2D NMR experiments were used to assign the proton and carbon spin systems of this quite unusual intermediate (see Figure 3.4 and SI for spectra). To identify heteroatoms and their connectivity in **4a** theoretical calculations and ^{15}N -isotope labelling were applied. 1D proton decoupled ^{13}C spectra of *in situ* generated **4a** ^{15}N revealed a single ^{13}C - ^{15}N coupling constant of 6.3 Hz between carbon **B** and the nitrogen, which excluded a nitrogen directly bound to the quaternary carbon **A** (see Figure 3.4).

Theoretical calculations of ^1H , and ^{13}C chemical shifts enabled to differentiate between potential arrangements of oxygen moieties in **4a** (for details see SI). The structure of **4a** fitting best to both experimental and theoretical data is displayed in Figure 3.4 revealing as basic structure an isoxazolidine-2,5-diol.

3 CONJUGATED ENYNES AND CYCLIC NITRONATES

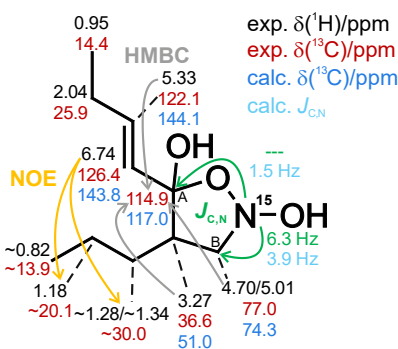


Figure 3.4 | Structural assignment of the central linking intermediate **4** shown on **4a E**. Combined NMR and theoretical data reveal as central feature an isoxazolidine-2,5-diol (for details see text and SI).

Next, the mechanistic pathway towards linking intermediate **4** was investigated (see Figure 3.5). The correlation between formation of **4** and the base strength (see Figure 3.3 and text above) indicates a deprotonation as the rate determining step. Two different deprotonations of **3a** would be conceivable: in α -position to the secondary nitro group (A) and in α -position to the primary nitro group (B). Both routes were investigated with quantum chemical calculations. The energy profiles of route A with and without DBU or water reveal, after the deprotonation towards **19a**, a concerted cyclization and protonation mechanism towards **20a** (see Figure 3.5). Calculations showed that free **20a** is 42.8 kJ/mol less stable than **3a**. However, coordination of DBU results in massive stabilization of **20a** by 35.3 kJ/mol compared to the base free case. Thus, the base does not serve only as de- and reprotonating agent, but also acts as stabilizer of intermediate **20a** via a hydrogen bond.

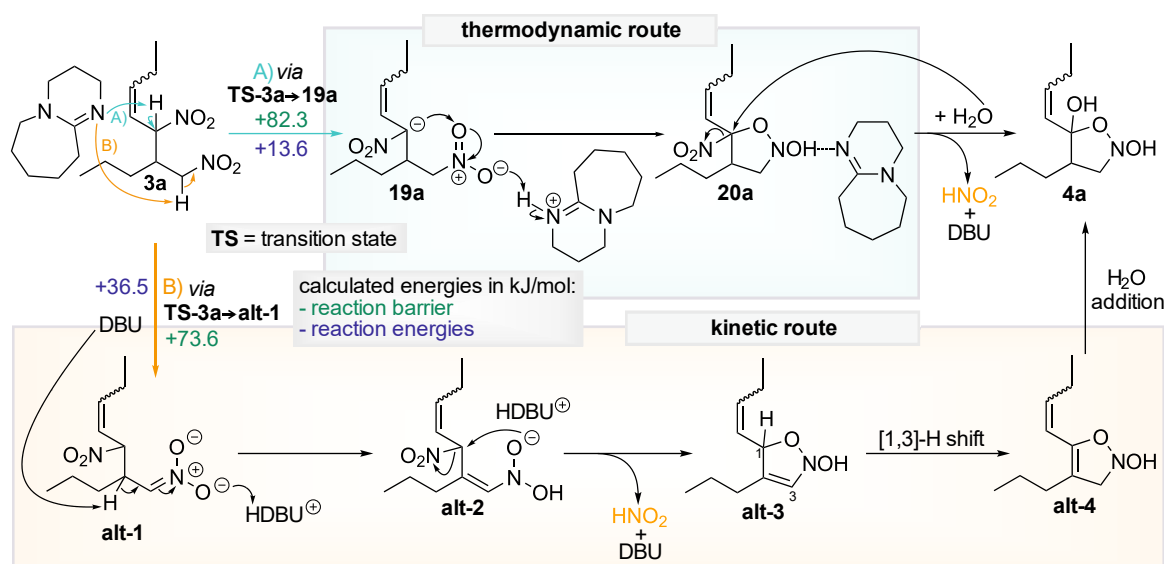


Figure 3.5 | Proposed mechanism from dimer **3a** to linking intermediate **4a**. Theoretical calculations predicted that two pathways may lead towards **4a**: A) Deprotonation in α -position to the secondary nitro group is the thermodynamically favored route over **19a** via subsequent concerted ring closure to **20a**. Substitution of the nitro group in **20a** by water generates intermediate **4a**. Our calculations revealed that DBU can stabilize **20a** and thus enables the formation of **4a**. B) Deprotonation in α -position to the primary nitro group is the kinetically favored route via nitronate **alt-1** followed by an interconversion to **alt-2** and subsequent ring closure by intramolecular substitution of the secondary nitro group to **alt-3**. Via an ensuing [1,3]-H-shift to **alt-4** and addition of water addition, intermediate **4a** may be generated.

3 CONJUGATED ENYNES AND CYCLIC NITRONATES

Such stabilization strategy have been also utilized and observed in enamine catalysis.^[37] Furthermore, calculations showed that coordination of the conjugated acid to the primary nitro group in **19a** enables a concerted process: the attack of the carbanion on the other nitroxylic oxygen of this nitro group and the proton transfer. This indicates that in the formation of intermediate **4a** protonation of **19a** is essential for the reaction to occur. Altogether, the base facilitates the pathway towards **20a** and subsequently **4a**. Since DMSO-*d*₆ always contains some amount of water, intermediate **20a** is expected to be transformed *via* an S_N reaction into **4a** upon release of HNO₂.

A second alternative towards **4a** may be the abstraction of the proton in the α-position next to the primary nitro group (path B in Figure 3.5). This leads to the formation of an unstable intermediate **alt-1**. Quantum chemical calculations predicted that the deprotonation of **3a** to **alt-1** is by 22.9 kJ/mol more demanding than the deprotonation leading to **19a**. On the other hand, the abstraction of the α-proton of the primary nitro group is kinetically slightly favored by 8.7 kJ/mol. Hence, the second pathway might be feasible in case **alt-1** is stabilized by the formation of hydrogen bonds to the conjugated acid (H-DBU⁺) as for **20a** to the base. Subsequently, the reactive **alt-1** probably rapidly interconverts to **alt-2** through an [1,4]-H shift, which is followed by an intramolecular ring closure to **alt-3** *via* the attack of the oxygen of the *N*-hydroxyhydroxylamine releasing HNO₂. Finally, the formation of **4a** is suggested to be concluded *via* an [1,3]-H shift generating **alt-4** and the subsequent addition of water (for other potential mechanisms to intermediate **4** and their exclusion see SI).

Our calculations of the first reaction barriers (TS-**3a**→**19a** and TS-**3a**→**alt-1**) and reaction energies (**3a** towards **19a** and **alt-1**) revealed, that the formation of intermediate **4** may proceed *via* both pathways A and B. While pathway A is thermodynamically favored, pathway B is kinetically favored.

Base dependent shifts of the protons attached to the double bond in **4a** were observed (see Figure SI 3.4). Thus, a stabilization of **4a** by hydrogen bonding to bases is highly probable similar to the situation of **20a**.

Furthermore, the NMR profiles displayed in Figure 3.3 indicate that partial isomerization of the double bond proceeds within the formation pathway of **4**. While the starting material **3a** consisted of 95% *Z*-isomer and 5% *E*-isomer, the amount of the *E*-isomer in **4a** was found to be significantly higher (10% with DBU; 20% with quinuclidine; see Figure 3.3). This isomerization towards the energetically lower *E*-isomer may take place at the stage of the allylic anion **19a** or **alt-3** in case of deprotonation at position 1. In accordance with that, the NMR reaction profiles revealed a faster conversion of **4a Z** than **4a E** for both bases (see Figure 3.3).

3.3.4 Mechanism of the Conjugated Enyne Formation

Next, we investigated the fragmentation mechanism from intermediate **4** towards conjugated enyne **5** (see Figure 3.1 bottom). Since no further intermediates could be detected, the identification of fragmentation byproducts was of most importance to get experimental evidence for discriminating other potential mechanistic pathways. The most obvious byproduct would be CH_3NO_2 *via* an elimination.^[26] However, accumulation of nitromethane in parallel to the product formation was never observed. Instead, *in situ* ^{13}C NMR monitoring of the one-pot reaction of $1\text{a}^{13}\text{C}$ revealed the generation of $^{13}\text{CO}_2$ correlating directly to the formation of $5\text{a}^{13}\text{C}$ (see Figure 3.6; for further experimental confirmation of CO_2 as byproduct see SI).

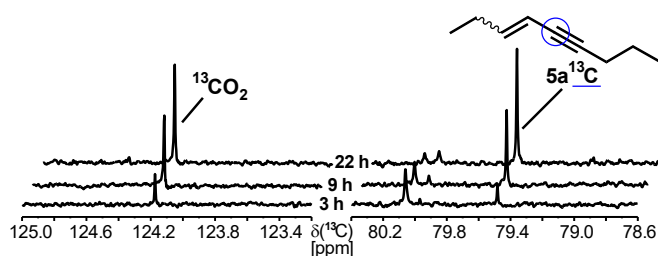


Figure 3.6 | Correlated formation of $^{13}\text{CO}_2$ and enyne $5\text{a}^{13}\text{C}$ indicating CO_2 as fragmentation byproduct of the enyne pathway (^{13}C NMR reaction monitoring of $1\text{a}^{13}\text{C}$ (40 mM) with diphenylprolinol (20 mM) in DMSO-d_6 at 300 K).

To elucidate the fate of the nitrogen we applied ^{15}N NMR *in situ* reaction monitoring to a one-pot reaction of $1\text{a}^{15}\text{N}$. *Inter alia* pronounced signals at 310.8 ppm and 617.7 ppm appeared. The chemical shift of 310.8 ppm matches well a literature value of molecular nitrogen (310.1 ppm).^[38] In the initial stage of the reaction, the N_2 signal increases together with the enyne formation. After about 4 h, the signal intensities deviate most probably due to degassing effects of N_2 (for data see SI). This is, however, not the case for CO_2 probably due to its significantly higher solubility in DMSO than N_2 .^[39] The ^{15}N signal at 617.7 ppm is close to the literature value of sodium nitrite in water (608 ppm)^[40]. Considering the differences of our system in terms of solvents (DMSO versus H_2O), counterions (Na^+ versus H-base^+) and the potential presence of free HNO_2 , the signal at 617.7 ppm can readily be assigned to $\text{X}^+\text{-NO}_2^-$ generated in the formation of intermediate **4a** (for kinetic profile and the assignment of the other ^{15}N -signals see SI). Additionally to CO_2 and N_2 , H_2O was observed as third byproduct of the fragmentation of **4a** into enyne. During ^1H NMR monitoring of reactions from **3a** to enyne **5a**, a significant increase of the water signal could be observed. Similar to CO_2 and N_2 , the water build-up correlates qualitatively with the enyne formation (for data see SI). Thus, CO_2 , N_2 and water represent byproducts in the conjugated enyne **5** formation.

Based on the experimental detection of CO_2 , N_2 and H_2O as byproducts and supported by quantum chemical calculations we propose the transformation of intermediate **4** into conjugated enyne **5** *via* a combination of oxidation, dehydration and retro 1,3-dipolar cycloaddition as depicted in Figure 3.7.

3 CONJUGATED ENYNES AND CYCLIC NITRONATES

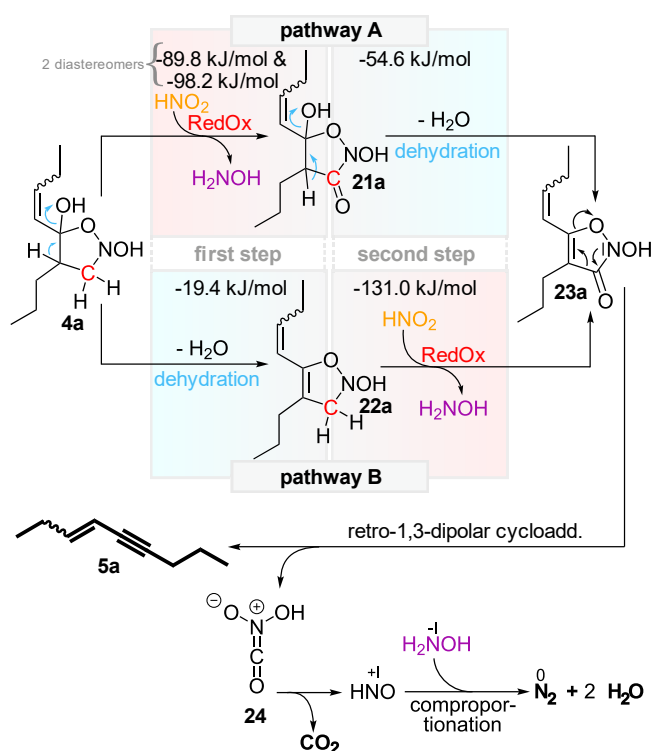


Figure 3.7 | Proposed mechanism from intermediate **4a** to conjugated enyne **5a** (NMR detected compounds are bold). The oxidation step is in both pathways strongly exergonic/exothermic, while the dehydration is entropically driven and enthalpically demanding for pathway B ($\Delta H = +32.4$ kJ/mol; $\Delta G = -19.4$ kJ/mol), respectively weakly exothermic for pathway A ($\Delta H = -1.1$ kJ/mol; $\Delta G = -54.6$). Depending on the experimental conditions different combinations of oxidation and dehydration lead to intermediate **23a**. Next a retro-1,3-dipolar cycloaddition fragments **23a** to **5a** and **24**. Then **24** decomposes further to CO_2 and HNO with HNO comproporionating with H_2NOH to N_2 and water.

The order of oxidation (by HNO_2) and dehydration depends most likely on the experimental condition. Our theoretical calculations show that both pathways **A** and **B** depicted in Figure 3.7 between **4a** and **23a** are strongly exergonic. In case **A** the oxidation occurs first and **21a** together with hydroxylamine H_2NOH are generated in an exergonic fashion (-89.8 to -98.2 kJ/mol depending on the diastereomeric starting intermediate). This is followed by the dehydration step to **23a**, which is also exergonic ($\Delta G = -54.6$ kJ/mol; dehydration of **21a**(*R,R*)) but mainly driven by the entropy ($T^*\Delta S = +53.5$ kJ/mol). In case **B**, the order is reversed. The dehydration step is significantly less exergonic compared to the first step in case **A** ($\Delta G = -19.4$ kJ/mol; dehydration of **4a**(*R,R*)). However the substrate **22a** possesses higher oxidation potential, and therefore the subsequent step to **23a** is even more facilitated ($\Delta G = -131.0$ kJ/mol). Subsequently, we propose a fragmentation of **23a** via a retro 1,3-dipolar cycloaddition to the conjugated enyne **5a** and compound **24**, which could be described as an “oxidized nitron” (see Figure 3.7). Further, we propose a Nef-type decomposition^[41,42] of the unstable side product **24** to CO_2 and HNO . HNO in turn comproporionates with the oxidation byproduct H_2NOH to N_2 and H_2O (see Figure 3.7). The proposed mechanism in Figure 3.7 is in accordance with all three experimentally detected byproducts CO_2 , N_2 and H_2O . Furthermore, we observed the formation of DMS in the reaction to conjugated enyne **5a** implying a reduction of the solvent DMSO (for more information see SI). This hints at the presence of redox active species corroborating the proposed redox reaction in the mechanism from **3a** to **5a** (see Figure 3.7).

3 CONJUGATED ENYNES AND CYCLIC NITRONATES

In agreement with our proposed mechanism, conventional nitrones are well known for forward 1,3-dipolar cycloadditions with terminal alkynes (see Figure SI 3.6)^[43] via postulated cyclic five-membered rings resembling **23a**.^[44] Next, Nef-type reactions can be assumed for the decomposition of **24**, which are feasible in a wide pH range (see Figure SI 3.6).^[41,42]

While the buildup of N₂ was detected (see above) as comproportionation product of HNO and H₂NOH, a degradation of HNO to N₂O^[45,46] (see Figure SI 3.6) was not observed in the NMR kinetic measurements of **1a**^{15N} (¹⁵N₂O signals should appear at around 155 ppm and 240 ppm)^[47].

Next, the effects of different acids, substituents and bases were investigated to get further insights into the mechanism of the conjugated enyne formation. A carboxylic acid as additive accelerated significantly the formation of enyne and suppressed the formation of nitronate almost completely (compare Figure 3.8a with Figure 3.8b). Acid as additive is considered to have two effects in the enyne mechanism. The dehydration should be facilitated and the oxidizing power of HNO₂ increased due to a lower pH. Furthermore, with electron poor compound **3b** (see Figure 3.1), we also observed a faster enyne **5b** formation than with the electron rich **3c** into **5c** in the presence of benzoic acid **15** as additive. This corroborates the theoretical calculations revealing the dehydration as an enthalpically demanding step (for kinetic profiles see Figure SI 3.9). Without acidic additives, the enyne formation is in general by far slower (see Figure 3.8a).

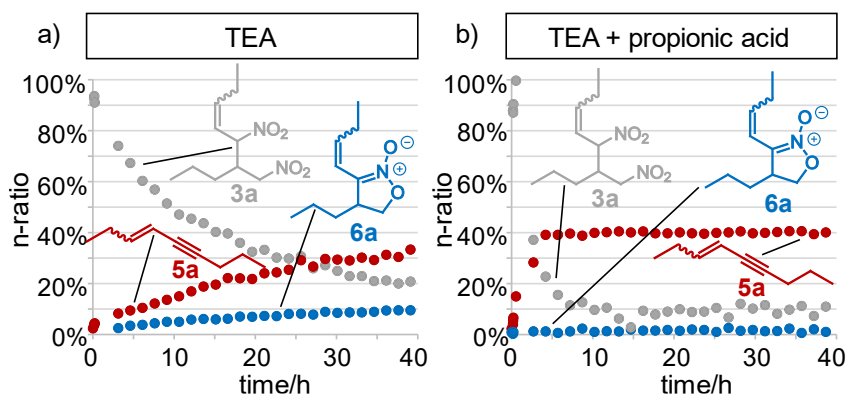


Figure 3.8 | Acids accelerated the enyne formation and suppress nitronates. a) slow formation of **5a** and **6a** in presence of TEA **9** without acid (not completed after 40 h; **3a** (55 mM) with TEA (72 mM) in DMSO-d₆ at 298K); b) 10-fold faster formation of **5a** and suppression of **6a** in presence of TEA with acid **14** (**3a** (55 mM) with TEA (77 mM) and propionic acid (115 mM) in DMSO-d₆ at 298K).

3.3.5 Mechanism of the Cyclic Nitronate Formation

Next, by applying various acidic additives as well as bases the mechanistic pathway towards nitronates **6** was examined and corroborated by theoretical calculation. Addition of carboxylic acids suppressed the nitronate formation significantly (see Figure 3.8 and chapter above). In accordance with that, the formation rate and yield of nitronate **6a** increased with higher pK_a values (see Figure 3.11; for pK_a see Figure 3.1). These experimental data suggest a deprotonation of intermediate **4a** as key step towards nitronates (see Figure 3.9a).

3 CONJUGATED ENYNES AND CYCLIC NITRONATES

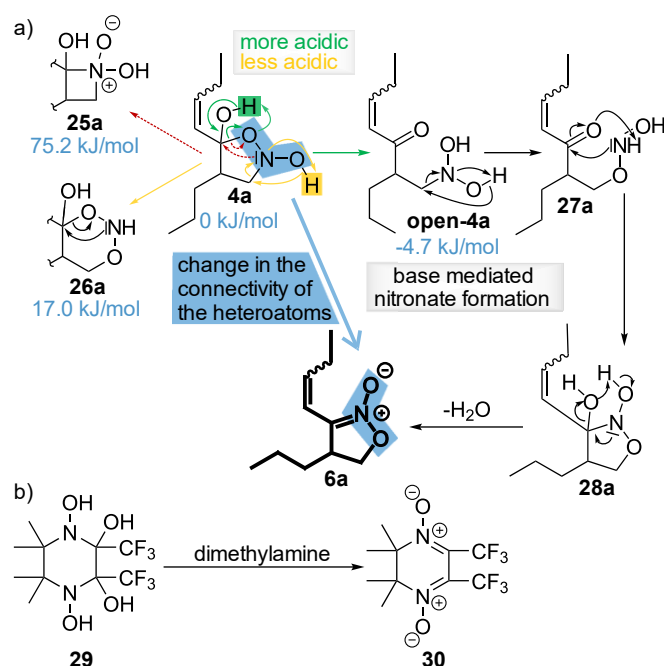


Figure 3.9 | a) Proposed mechanism from intermediate **4a** to cyclic nitronate **6a** based on quantum chemical calculations. Relative intermediate energies of cyclic intermediates **25a** and **26a** and open chain intermediate **open-4a** indicate that the reaction most likely proceeds via **open-4a** after hemiketal opening. Further, a rearrangement of the nitrogen and oxygen atoms towards **27a** is proposed. Intramolecular ringclosure is suggested to generate **28a** which leads to nitronate **6a** after dehydration; b) recently reported dehydration^[48] similar to the postulated step from **28a** to **6a**.

Since no further intermediates between **4a** and nitronate **6a** were detected experimentally, theoretical calculations were used to compare the relative energetics of possible intermediate structures. Several possible pathways leading to **6a** were considered including the formation of cyclic intermediates **25a** and **26a** and open chain intermediate **open-4a**. Both cyclic intermediates are energetically strongly disfavored compared to intermediate **4a**. Since a significant production of nitronate **6a** in mild basic condition was observed (see Figure 3.8a), such uphill energetic profiles to **25a** and **26a** are hence very unlikely. In contrast, the base mediated rearrangement of **4a** to the open chain intermediate **open-4a** is thermodynamically slightly favored over **4a** by 4.7 kJ/mol. Moreover, our calculations revealed that the hemiketalic proton is more acidic than the N-hydroxylic one. Therefore, we propose the formation of nitronate **6a** to proceed via the open chain intermediate **open-4a**. Further, we suggest a first change in heteroatom connectivity by a rearrangement of **open-4a** to **27a**. Next, we propose a reformation of the 5-membered ring together with a second change of heteroatom connectivity towards intermediate **28a**. Finally, a dehydration of **28a** to cyclic nitronate **6a** is suggested. Recently, a similar dehydration step *inter alia* under basic conditions was reported (see Figure 3.9b).^[48]

3.3.6 Selectivity: Conjugated Enyne versus Cyclic Nitronate

As discussed above both products share a common mechanistic pathway to the central linking intermediate **4**, which subsequently splits towards conjugated enynes **5** and cyclic nitronates **6**. Hence, we examined factors influencing the product distribution, more precisely acidic additives, temperature and basicity.

The use of sufficient amounts of acids in addition to the base suppressed the formation of nitronate **6** down to a few percent and accelerated the generation of conjugated enyne **5** (see preceding discussion and Figure 3.8). In a small screening of acids benzoic acid **15** led to the fastest formation of **5a** (see Figure 3.10). However, stronger acids were found to be detrimental, because they in turn decelerated the enyne formation considerably (see Figure 3.10). This essential balance between basic and acidic experimental conditions corroborated the proposed mechanism (see Figure 3.8, Figure 3.7a and Figure 3.9a).

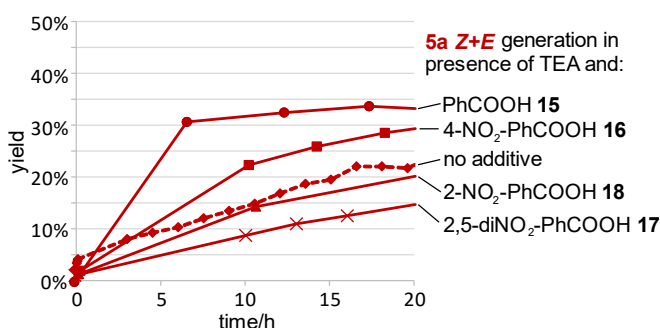


Figure 3.10 | The stronger the acid, the slower is the enyne formation. With too strong acids **17** and **18** the reaction velocity towards enyne even falls below that in absence of acidic additive (**3a** (55 mM) with TEA (1.3 eq.) and acid (1.3 eq.) in DMSO-d₆ at 298K).

For the generation of the linking intermediate **4** a certain basicity is indispensable (see Figure 3.8), while acids accelerate the enyne and suppress nitronate formation. Surprisingly, elevated temperatures altered this product distribution in an experiment of **3a** with TEA and benzoic acid. There, at 298 K nitronate **6a** was suppressed below 3% yield in the presence of benzoic acid. However, applying 320 K, 13% of nitronate was produced even in presence of benzoic acid. This hints at an alternative nitronate pathway potentially involving higher energetic intermediates at elevated temperatures (for more information see SI).

Based on these results, a synthetic route to **6a** (84 %) was developed combining elevated temperature and a strong base (**3a** with triazabicyclododecene at 50 °C; for procedure see SI). Under purely basic conditions, we also observed a rough correlation between the basicity and product distribution. While, with strong bases DBU **7** and 1-(2-aminoethyl)-piperazine **10** nitronate **6a** was clearly the major product with all other bases enyne emerged as major product (except for **11** where no enyne **5a** was generated). For the nitronates **6a**, the rates and yields increased with stronger bases (see Figure 3.11). For the conjugated enyne **5** no clear correlation was observed between basicity, yield and rate most probably due to the complex mechanism.

3 CONJUGATED ENYNES AND CYCLIC NITRONATES

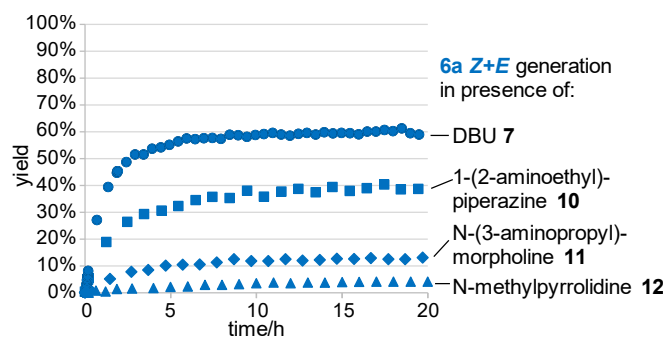


Figure 3.11 | Strong bases lead to higher rates and yields in the formation of nitronate **6a** (**3a** (80 mM) with 1 eq. of base respectively: DBU **7**, 1-(2-aminoethyl)piperazine **10**, N-(3-aminopropyl)morpholine **11** and N-methylpyrrolidine **12**).

3.3.7 Yield and scope of the combined route to conjugated enynes and cyclic nitronates

While for the synthesis of cyclic nitronates, there already exist several metal-free strategies,^[19] for conjugated enynes they are rare.^[18] Hence, we mainly focused on examining the scope of conjugated enynes **5**. We found that conjugated enynes could be generated starting from both homo- and heterodimers (derived from the dimerization of **1** with **1** or **1** with **2**) as well as directly from nitroalkenes **1** and **2** within a one-pot reaction. Besides aliphatic enyne **5a**, which was obtained in good to moderate NMR yields up to 57 %, and the aromatic enynes **5b** and **5c** several other aliphatic, heteroaromatic and functionalized/non-functionalized aromatic conjugated enynes could be generated successfully. This demonstrates a tolerance of the enyne formation towards electronically and sterically different substituted dimers **3** and nitroalkenes **1** and **2** (for scope and procedures see Figure SI 3.20). To the cyclic nitronate formation, only aliphatic precursors were applied. Yet, higher yields were achieved up to 84 % (for scope and procedures see Figure SI 3.21).

While, selectivity issues could be solved successfully (see above), the yields of both enynes **5** and nitronates **6** have remained limited so far due to the well-known polymerization problems connected with nitroalkenes.^[49] This polymerization was evident from mass spectrometry (electrospray ionisation) throughout a one-pot reaction of **1a** with DBU revealing molecular ion peaks with m/z ratios higher than 800 (see Table SI 3.3). Furthermore, in the NMR spectra, the sum over all ¹H- signals belonging to the combined enyne and nitronate mechanism decreased in the ongoing reaction. Despite, several efforts including various bases, acidic additives, concentrations and temperatures, so far we have not been able to suppress effectively this detrimental polymerisation process. Nevertheless, in other reactions involving nitroalkenes such polymerisation processes could be successfully controlled.^[49] Thus, we are confident that the broad community of synthetic chemists working in the field of catalysis will find a way to raise the yields of this promising organocatalytic method to build up triple bonds in conjugated enynes.

3.3.8 Summary of Mechanistic Proposal and Conclusion

The first comprehensive mechanistic proposal of the combined metal-free route to conjugated enynes **5** and cyclic nitronates **6** is depicted in Figure 3.12.

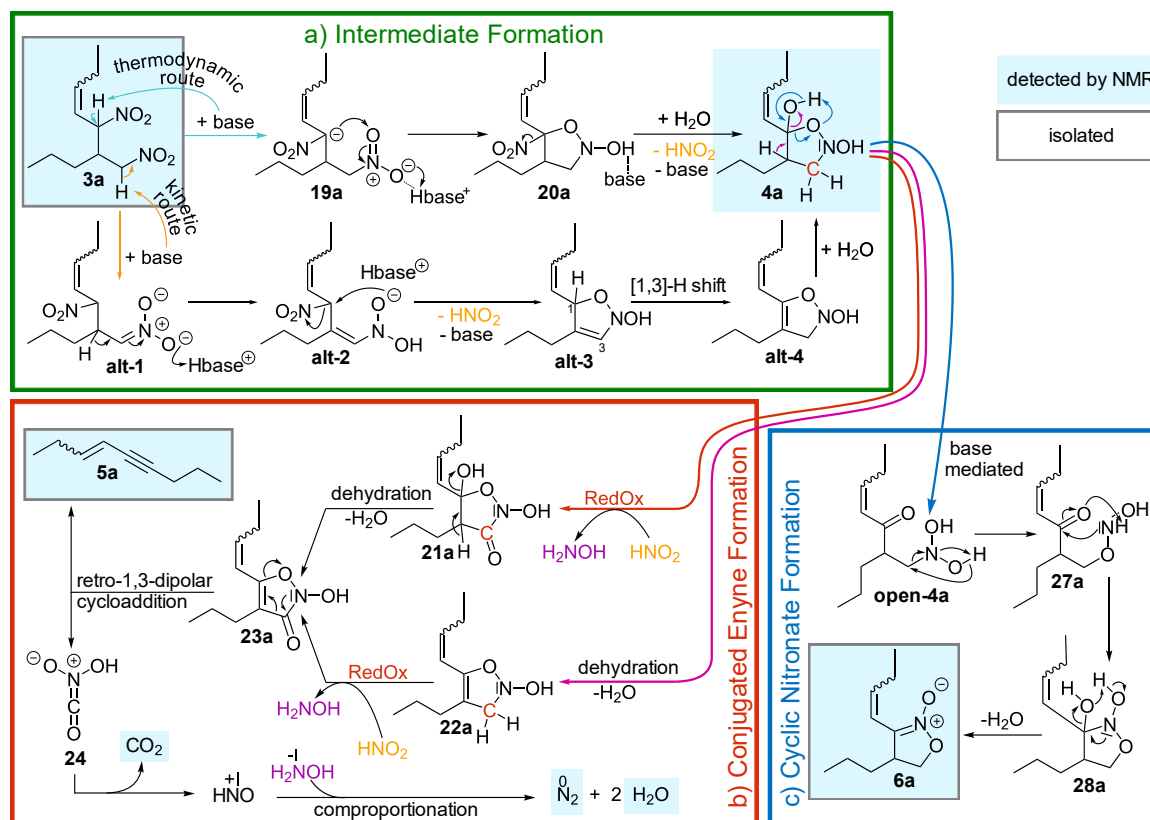


Figure 3.12 | Overview of the proposed mechanism to conjugated enynes **5** and cyclic nitronates **6** shown for the nitropentene-derived dimer **3a**: a) formation of the central linking intermediate **4a** via two possible routes of base induced cyclizations; b) enyne pathway via a combination of oxidation, dehydration and retro-1,3-dipolar cycloaddition; c) nitronate formation via base mediated intramolecular reorganization of nitrogen and oxygen atoms. Blue boxes highlight the NMR-detected, gray frames the isolated compounds.

Starting from nitroalkene dimers **3** NMR reaction profiles reveal a base initiated reaction to an isoxazolidine-2,5-diol derivative as intermediate **4** (see Figure 3.12a). The unusual structure of this intermediate was corroborated by various NMR experiments including ^{15}N labelling and theoretical calculations. Furthermore, NMR reaction profiles revealed **4** as central linking intermediate followed by separated pathways to enynes **5** (see Figure 3.12b) and nitronates **6** (see Figure 3.12c). While the enyne formation can proceed at both medium and high pH values, effective nitronate formation required basic conditions opening up an effective control of the product distribution. The unusual buildup of the triple bond out of a single bond in the enyne pathway is proposed to proceed via a combination of oxidation, dehydration and retro-1,3-dipolar cycloaddition. Theoretical calculations suggested the oxidation of intermediate **4a** as first step in the formation of **23a** under basic conditions. With acidic additives, both oxidation to **21a** and dehydration to **22a** may compete as first steps. The thereby generated unsaturated isoxazolidinone ring in **23a** is proposed to fragment via a retro-1,3-dipolar cycloaddition into conjugated enyne **5** and an oxidized nitrene **24**. This mechanistic proposal is corroborated by the experimentally detected byproducts N_2 , CO_2 and H_2O . CO_2 and

3 CONJUGATED ENYNES AND CYCLIC NITRONATES

HNO may originate from the decomposition of **24**. HNO further comproportionates with H₂NOH to the detected N₂ and H₂O. In the pathway towards cyclic nitronate **6** (Figure 3.12c), theoretical calculations propose intramolecular rearrangements over open chain intermediates **open-4a** and **27a** to achieve the required change in heteroatom connectivity from **4** to **6**. The results of various reaction conditions corroborated the mechanism presented in Figure 3.12. For example the addition of acids accelerated the formation of enynes **5** and suppressed nitronates nearly completely. In contrast, strong bases clearly facilitated the formation of nitronates **6**.

While mechanistic and selectivity issues were solved and high yields up to 84% could be achieved for nitronates, only medium to good yields (< 57%) were obtained for enynes, due to polymerization pathways well known for nitroalkenes. Nevertheless, we are confident that our mechanistic investigations have laid a groundwork for further improvements of this highly valuable, combined metal-free route to conjugated enynes and cyclic nitronates. Further, we hope that our results pave the way for further developments of organocatalytic or metal-free formations of conjugated enynes.

3.4 Experimental Section

NMR-spectroscopic experiments were performed on a Bruker Avance III HD 400 MHz spectrometer, equipped with 5 mm BBO BB-¹H/D probe head with Z-Gradients, a Bruker Avance III HD 600 MHz spectrometer, equipped with a 5 mm TBI ¹H/¹⁹F and a Bruker Avance III 600 MHz equipped with a CryoProbe™ Prodigy. Chemical shifts δ in ppm are referenced on residual solvent signals or on internal standards. For NMR measurements employing standard NMR solvents 5 mm NMR tubes were used. NMR-reaction kinetics were performed using tetramethylsilane (TMS) or octamethylcyclotetrasiloxane (OMS) as internal standard. The samples for NMR-reaction monitoring were prepared from stock solutions of the respective reagents and reactants. For starting points (t = 0) spectra of the samples lacking the base were recorded. Afterwards, the base was added, and the reaction was monitored by NMR. High-resolution mass spectra (HRMS) were obtained on a Jeol AccuTOF GCX instrument with an EI and a LIFDI source and on an Agilent Q-TOF 6540 UHD with an ESI source.

Nitroalkenes **1a**, **1a^{13C}** and **1a^{15N}** were synthesized following a literature procedure.^[50]

3.4.1 General Procedure for the Synthesis of Homo-Dimers

Nitroalkene **1** (1 mmol) and L-proline (1 mmol) were mixed in DMSO (10 mL). The reaction was left under stirring at room temperature overnight. The mixture was dissolved in water and extracted with dichloromethane. The combined organic phase was washed three times with a saturated solution of lithium chloride, dried over MgSO₄ and the solvent was evaporated. The product was purified by column chromatography (PE/DEE 100/0 – 6/1).

5-nitro-6-(nitromethyl)non-3-ene D1 (D2) (3a): 78% yield. **3a Z:** ¹H NMR (600 MHz, DMSO-d₆): δ = 5.91 (5.94) (m, 1H), 5.56 (5.59) (m, 1H), 5.55 (5.59) (m, 1H), 4.63 (4.60/4.66) (m, 2H), 2.91 (2.95) (m, 1H), 2.16

(2.14) (m, 2H), 1.31 (1.35/1.26) (m, 2H), 1.30 (1.39) (m, 2H), 0.95 (0.95) (t, $J = 7.6$ Hz (7.6 Hz), 3H), 0.85 (0.85) (t, $J = 7.1$ Hz (7.1 Hz), 3H) ppm. ^{13}C NMR (600 MHz, DMSO- d_6): $\delta = 141.7$ (141.4), 120.0 (120.1), 85.0 (84.3), 74.9 (75.2), 39.2 (39.2), 29.4 (30.2), 20.4 (20.4), 18.6 (18.6), 13.5 (13.5), 13.2 (13.2) ppm. **3a E**: ^1H NMR (600 MHz, DMSO- d_6): $\delta = 6.08$ (6.03) (dt (dt), $J = 15.3$ Hz (15.3 Hz), 6.2 Hz (6.2 Hz) 1H), 5.55 (5.69) (m (ddt) ($J = 15.3$ Hz, 9.7 Hz, 1.5 Hz), 1H), 5.22 (5.25) (dd, $J = 9.3$ Hz, 8.6 Hz (9.3 Hz, 6.9 Hz), 1H), ~ 4.62 (~ 4.62) (m, 2H), 2.92 (2.92) (m, 1H), 2.04 (2.10) (m, 2H), 1.60 (~ 1.35) (m, 2H), ~ 1.24 (~ 1.28) (m, 2H), 0.94 (1.05) (t, $J = 7.6$ Hz (7.4 Hz, 3H), 0.85 (0.85) (t, $J = 7.1$ Hz, 3H) ppm. ^{13}C NMR (600 MHz, DMSO- d_6): $\delta = 142.4$ (142.2), 119.9 (119.8), 90.7 (89.5), 75.0 (75.6), ~ 39.2 (~ 39.2), 30.8 (29.8), 24.4 (24.5), ~ 18.5 (~ 18.5), ~ 13.5 (~ 13.5), ~ 13.3 (~ 13.3) ppm. HRMS (ESI): calcd. for $\text{C}_{10}\text{H}_{18}\text{N}_2\text{O}_4$ [$\text{M} + \text{H}$] $^+$ 231.1339; found 231.1341.

3.4.2 General Procedure for the Synthesis of Hetero-Dimers

L-proline (0.2 mmol) and benzoic acid (0.2 mmol) were dissolved in DMSO (7 mL) at room temperature. Subsequently, the corresponding nitroalkenes (0.3 mmol each) were added. The solution was stirred for 24 hours under atmospheric conditions. After the reaction was quenched by adding brine (10 mL) the reaction mixture was extracted 4 times with diethyl ether (10 mL each). The combined organic layers were washed 4 times with distilled water (10 mL each) and dried over magnesium sulfate. After evaporation of the solvent the raw product was purified by flash column chromatography (PE:EA = 9:1).

1-(5-methyl-1,3-dinitrohex-4-en-2-yl)-2-nitrobenzene (3b): Nitroalkenes (*E*)-3-methyl-1-nitrobut-1-ene and (*E*)-1-nitro-2-(2-nitrovinyl)benzene were applied as starting material. 24% yield. ^1H NMR (400 MHz, DMSO- d_6): $\delta = 8.09$ (7.89) (d (d), $J = 7.9$ Hz (7.9 Hz)), 7.94 (7.94) (dd, $J = 8.1$ Hz, 1.2 Hz), 7.78 (7.78) (ddd, $J = 7.8$ Hz, 7.8 Hz, 1.1 Hz), 7.59 (7.59) (ddd, $J = 7.8$ Hz, 7.8 Hz, 1.2 Hz), 5.90 (6.03) (dd (dd), $J = 9.9$ Hz, 9.9 Hz (10.1 Hz, 10.1 Hz)), 5.44 (5.29) (dq (dq), $J = 9.7$ Hz, 1.3 Hz, 1.3 Hz (10. Hz, 1.3 Hz, 1.3 Hz)), 5.08 (5.22) (dd (dd), $J = 13.8$ Hz, 8.6 Hz (14.4 Hz, 10.3 Hz)), 4.96 (5.08) (dd (m), $J = 13.8$ Hz, 5.5 Hz), 4.79 (4.88) [ddd (ddd), $J = 9.8$ Hz, 8.7 Hz, 5.4 Hz (9.9 Hz, 9.9 Hz, 4.4 Hz)], 1.82 (1.59) (d (d), $J = 1.1$ Hz (1.2 Hz)), 1.79 (1.53) (d (d), $J = 1.0$ Hz (1.1 Hz)) ppm. ^{13}C NMR (400 MHz, DMSO- d_6): $\delta = 149.9$ (150.3), 146.3 (146.4), 133.3 (133.3), 129.6 (129.6), 129.4 (129.1), 129.1 (129.0), 124.8 (124.8), 118.5 (116.6), 86.8 (85.3), 75.9 (76.7), 40.5 (39.7), 25.4 (25.1), 18.4 (18.1) ppm. HRMS (ESI): calcd. for $\text{C}_{13}\text{H}_{15}\text{N}_3\text{O}_6$ [$\text{M} + \text{Na}$] $^+$ 332.0853; found 332.0855.

1-methoxy-2-(5-methyl-1,3-dinitrohex-4-en-2-yl)benzene (3c): Nitroalkenes (*E*)-3-methyl-1-nitrobut-1-ene and 1-methoxy-2-[(*E*)-2-nitrovinyl]benzene were applied as starting material. 24% yield. ^1H NMR (400 MHz, DMSO- d_6): $\delta = 7.31$ (7.31) (dd, $J = 7.5$ Hz, 1.7 Hz, 1H), 7.29 (7.29) (ddd, $J = 7.9$ Hz, 7.9 Hz, 1.6 Hz, 1H), 7.03 (7.00) (dd (dd), $J = 8.3$ Hz, 0.7 Hz (8.2 Hz, 0.7 Hz), 1H), 6.91 (6.91) (ddd, $J = 7.4$ Hz, 7.4 Hz, 1.0 Hz, 1H), 5.87 (5.82) (dd (dd), $J = 10.2$ Hz, 10.2 Hz (9.9 Hz, 9.9 Hz), 1H), 5.46 (5.19) (dq (dq), $J = 9.9$ Hz, 1.4 Hz, 1.4 Hz (9.9 Hz, 1.4 Hz, 1.4 Hz), 1H), 4.89/4.80 (5.11/4.91) (dd/dd (dd), $J = 13.4$ Hz, 8.8 Hz/13.4 Hz, 5.6 Hz (13.3 Hz, 10.1 Hz), 2H), 4.40 (4.50) (ddd (ddd), $J = 10.2$ Hz, 8.8 Hz, 5.7 Hz (9.9 Hz, 9.9 Hz, 4.7 Hz), 1H), 3.83 (3.81) (s (s), 3H) 1.79 (1.55) (d (d), $J = 1.4$ Hz (1.4 Hz), 3H), 1.79 (1.53) (d (d), $J = 1.4$ Hz (1.3 Hz), 3H)

3 CONJUGATED ENYNES AND CYCLIC NITRONATES

ppm. ^{13}C NMR (400 MHz, DMSO-d_6): δ = 149.9 (150.3), 145.0 (142.7), 129.6 (129.6), 129.4 (129.4), 122.7 (122.4), 120.6 (120.6), 117.1 (117.3), 111.7 (111.4), 86.0 (85.5), 75.5 (75.8), 55.7 (55.6), 42.2 (41.3), 25.4 (25.1), 18.3 (17.8) ppm. HRMS (ESI): calcd. for $\text{C}_{14}\text{H}_{18}\text{N}_2\text{O}_5$ $[\text{M} + \text{Na}]^+$ 317.1108; found 317.1112.

For scope and syntheses of conjugated enynes and cyclic nitronates see Supporting Information.

3.4.3 Computational Details

For the calculation, a smaller model of dimer **3a** was employed. The *n*-propyl group and the terminal ethyl group connected with the double bond were substituted by a methyl group. All structures were optimized at M06-2X/def2-SVP level of theory using empirical dispersion D3 in continuum of DMF (CPCM).^[51–53] Thermochemical correction was performed at the same level of theory as the geometry optimization. Single point calculations were carried out at PWPB95-D3/def2TZVPP level of theory.^[54] The software used for the geometry optimization and frequency analysis was Gaussian09 version D.01.^[55] For the single points, ORCA 4.0.1 was employed.^[56] For further details see Supporting Information.

3.5 Acknowledgements

We would like to thank the German Science Foundation (DFG, GS 13/3-1 and GS 13/4-14) for financial support.

3.6 References

- [1] M. Konishi, H. Ohkuma, K. Matsumoto, T. Tsuno, H. Kamei, T. Miyaki, T. Oki, H. Kawaguchi, G. D. Vanduyne, J. Clardy, *J. Antibiot.* **1989**, *42*, 1449–1452.
- [2] A. Stuetz, G. Petranyi, *J. Med. Chem.* **1984**, *27*, 1539–1543.
- [3] D. E. Rudisill, L. A. Castonguay, J. K. Stille, *Tetrahedron Lett.* **1988**, *29*, 1509–1512.
- [4] J. R. Frost, C. M. Pearson, T. N. Snaddon, R. A. Booth, R. M. Turner, J. Gold, D. M. Shaw, M. J. Gaunt, S. V. Ley, *Chem. - A Eur. J.* **2015**, *21*, 13261–13277.
- [5] T. Masaoka, Y. Hasegawa, T. Ueda, T. Takubo, H. Shibata, H. Nakamura, N. Tatsumi, J. Yoshitake, N. Senda, *Eur. J. Cancer* **1976**, *12*, 143–149.
- [6] B. M. Trost, L. Li, S. D. Guile, *J. Am. Chem. Soc.* **1992**, *114*, 8745–8747.
- [7] B. M. Trost, L. S. Chupak, T. Lübbers, *J. Am. Chem. Soc.* **1998**, *120*, 1732–1740.
- [8] K. Karthikeyan, T. Veenus Seelan, K. G. Lalitha, P. T. Perumal, *Bioorg. Med. Chem. Lett.* **2009**, *19*, 3370–3373.
- [9] M. C. Pirrung, L. N. Tumey, C. R. H. Raetz, J. E. Jackman, K. Snehalatha, A. L. McClerren, C. A. Fierke, S. L. Gantt, K. M. Rusche, *J. Med. Chem.* **2002**, *45*, 4359–4370.
- [10] R. Maurya, P. Gupta, G. Ahmad, D. K. Yadav, K. Chand, A. B. Singh, A. K. Tamrakar, A. K. Srivastava, *Med. Chem. Res.* **2008**, *17*, 123–136.
- [11] H. Jiang, P. Elsner, K. Jensen, A. Falcicchio, V. Marcos, K. A. Jørgensen, *Angew. Chemie Int. Ed.* **2009**, *48*, 6844–6848.
- [12] Y. Hatanaka, T. Hiyama, *J. Org. Chem.* **1988**, *53*, 918–920.

3 CONJUGATED ENYNES AND CYCLIC NITRONATES

- [13] Y. Hatanaka, K. Matsui, T. Hiyama, *Tetrahedron Lett.* **1989**, 30, 2403–2406.
- [14] B. P. Andreini, A. Carpita, R. Rossi, B. Scamuzzi, *Tetrahedron* **1989**, 45, 5621–5640.
- [15] L.-X. Shao, M. Shi, *J. Org. Chem.* **2005**, 70, 8635–8637.
- [16] D. Saha, T. Chatterjee, M. Mukherjee, B. C. Ranu, *J. Org. Chem.* **2012**, 77, 9379–9383.
- [17] N. Miyaoura, K. Yamada, A. Suzuki, *Tetrahedron Lett.* **1979**, 20, 3437–3440.
- [18] P.-F. Li, H.-L. Wang, J. Qu, *J. Org. Chem.* **2014**, 79, 3955–3962.
- [19] H. Feuer, *Nitrile Oxides, Nitrones, and Nitronates in Organic Synthesis*, John Wiley & Sons, **2008**.
- [20] J. M. Robinson, S. F. Tlais, J. Fong, R. L. Danheiser, *Tetrahedron* **2011**, 67, 9890–9898.
- [21] M. Uchiyama, H. Ozawa, K. Takuma, Y. Matsumoto, M. Yonehara, K. Hiroya, T. Sakamoto, *Org. Lett.* **2006**, 8, 5517–5520.
- [22] L. Anastasia, C. Xu, E. Negishi, *Tetrahedron Lett.* **2002**, 43, 5673–5676.
- [23] V. Komanduri, M. J. Krische, *J. Am. Chem. Soc.* **2006**, 128, 16448–16449.
- [24] Y.-T. Hong, C.-W. Cho, E. Skucas, M. J. Krische, *Org. Lett.* **2007**, 9, 3745–3748.
- [25] G. Gervasio, P. J. King, D. Marabello, E. Sappa, *Inorg. Chim. Acta* **2003**, 350, 215–244.
- [26] M. B. Schmid, *NMR Spectroscopic Investigations on Aminocatalysis: Catalysts and Intermediates, Conformations and Mechanisms Dissertation*, **2011**.
- [27] P. Shanbhag, P. R. Nareddy, M. Dadwal, S. M. Mobin, I. N. N. Namboothiri, *Org. Biomol. Chem.* **2010**, 8, 4867–4873.
- [28] K. Kaur, I. N. N. Namboothiri, *Chimia (Aarau)*. **2012**, 66, 913–920.
- [29] D. Nair, T. Kumar, I. Namboothiri, *Synlett* **2016**, 27, 2425–2442.
- [30] F. Ravalico, S. L. James, J. S. Vyle, *Green Chem.* **2011**, 13, 1778–1783.
- [31] R. L. Benoit, D. Lefebvre, M. Fréchette, *Can. J. Chem.* **1987**, 65, 996–1001.
- [32] P. Roose, K. Eller, E. Henkes, R. Roszbacher, H. Höke, in *Ullmann's Encycl. Ind. Chem.*, Wiley-VCH Verlag GmbH & Co. KGaA, Weinheim, Germany, **2015**, pp. 1–55.
- [33] I. M. Kolthoff, M. K. Chantooni, S. Bhowmik, *J. Am. Chem. Soc.* **1968**, 90, 23–28.
- [34] W. M. Haynes, *CRC Handbook of Chemistry and Physics, 97th Edition*, CRC Press, Boca Raton, **2016**.
- [35] J. Jover, R. Bosque, J. Sales, *QSAR Comb. Sci.* **2008**, 27, 563–581.
- [36] Z. Shi, B. Tan, W. W. Y. Leong, X. Zeng, M. Lu, G. Zhong, *Org. Lett.* **2010**, 12, 5402–5405.
- [37] M. B. Schmid, K. Zeitler, R. M. Gschwind, *Chem. - A Eur. J.* **2012**, 18, 3362–3370.
- [38] C. H. Bradley, G. E. Hawkes, E. W. Randall, J. D. Roberts, *J. Am. Chem. Soc.* **1975**, 97, 1958–1959.
- [39] J. H. Dymond, *J. Phys. Chem.* **1967**, 71, 1829–1831.
- [40] J. B. Lambert, G. Binsch, J. D. Roberts, *Proc. Natl. Acad. Sci. U. S. A.* **1964**, 51, 735–737.
- [41] L. Kurti, B. Czako, *Strategic Applications of Named Reactions in Organic Synthesis*, Elsevier, **2005**.

3 CONJUGATED ENYNES AND CYCLIC NITRONATES

- [42] R. Ballini, G. Bosica, D. Fiorini, M. Petrini, *Tetrahedron Lett.* **2002**, *43*, 5233–5235.
- [43] M. Kinugasa, S. Hashimoto, *J. Chem. Soc. Chem. Commun.* **1972**, *4*, 466–467.
- [44] M. Miura, M. Enna, K. Okuro, M. Nomura, *J. Org. Chem.* **1995**, *60*, 4999–5004.
- [45] F. T. Bonner, M. N. Hughes, *Comments Inorg. Chem.* **1988**, *7*, 215–234.
- [46] F. Doctorovich, P. J. Farmer, M. Marti, *The Chemistry and Biology of Nitroxyl (HNO)*, Elsevier, **2016**.
- [47] S. Berger, S. Braun, H.-O. Kalinowski, *NMR-Spektroskopie von Nichtmetallen*, Georg Thieme Verlag, Stuttgart, **1993**.
- [48] L. V. Saloutina, E. V. Tretyakov, P. A. Slepukhin, V. I. Saloutin, O. N. Chupakhin, *J. Heterocycl. Chem.* **2017**, *54*, 1887–1890.
- [49] V. Barbier, F. Couty, O. R. P. David, *European J. Org. Chem.* **2015**, *2015*, 3679–3688.
- [50] B. M. Trost, C. Müller, *J. Am. Chem. Soc.* **2008**, *130*, 2438–2439.
- [51] Y. Zhao, D. G. Truhlar, *Theor. Chem. Acc.* **2008**, *120*, 215–241.
- [52] S. Grimme, J. Antony, S. Ehrlich, H. Krieg, *J. Chem. Phys.* **2010**, *132*, 154104.
- [53] J. Tomasi, B. Mennucci, R. Cammi, *Chem. Rev.* **2005**, *105*, 2999–3093.
- [54] L. Goerigk, S. Grimme, *J. Chem. Theory Comput.* **2011**, *7*, 291–309.
- [55] M. J. Frisch, G. W. Trucks, H. B. Schlegel, G. E. Scuseria, M. A. Robb, J. R. Cheeseman, G. Scalmani, V. Baone, G. A. Petersson, H. Nakatsuji, X. Ki, M. Caricato, A. Marenich, J. Bloino, B. G. Janesko, R. Gomperts, B. Mennucci, H. P. Hratchian, J. V. Ortiz, A. F. Izmaylov, J. L. Sonnenberg, D. Williams-Young, F. Ding, F. Lipparini, F. Egidi, J. Goings, B. Peng, A. Petrone, T. Henderson, D. Ranasinghe, V. G. Zakrzewski, J. Gao, N. Rega, G. Zheng, W. Liang, M. Hada, M. Ehara, K. Toyota, R. Fukuda, J. Hasegawa, M. Ishida, T. Nakajima, Y. Honda, O. Kitao, H. Nakai, T. Vreven, K. Throssell, J. A. Montgomery, J. E. Peralta, Jr., F. Ogliaro, M. Bearpark, J. J. Heyd, E. Brothers, K. N. Kudin, V. N. Staroverov, T. Keith, R. Kobayashi, J. Normand, K. Raghavachari, A. Rendell, J. C. Burant, S. S. Iyengar, J. Tomasi, M. Cossi, J. M. Millam, M. Klene, C. Adamo, R. Cammi, J. W. Ochterski, R. L. Martin, K. Morokuma, O. Farkas, J. B. Foresman, D. J. Fox, *Gaussian 09, Revision D.01*, Gaussian, Inc., Wallingford CT, **2016**.
- [56] F. Neese, *Wiley Interdiscip. Rev. Comput. Mol. Sci.* **2012**, *2*, 73–78.

3.7 Supporting Information

3.7.1 Experimental Details

NMR-spectroscopic experiments were performed on a Bruker Avance III HD 400 MHz spectrometer, equipped with 5 mm BBO BB-¹H/D probe head with Z-Gradients, a Bruker Avance III HD 600 MHz spectrometer, equipped with a 5 mm TBI ¹H/¹⁹F and a Bruker Avance III 600 MHz equipped with a CryoProbe™ Prodigy. For NMR measurements employing standard NMR solvents 5 mm NMR tubes were used. NMR data were processed, evaluated and plotted with TopSpin 3.2 software. Further plotting of the spectra was performed with Corel Draw X19 software. ¹H, ¹³C chemical shifts were referenced to TMS or the respective solvent signals. ¹⁵N chemical shifts were referenced to NH₃. Reaction kinetics were performed using tetramethylsilane (TMS) or octamethylcyclotetrasiloxane (OMS) as internal standard. High-resolution mass spectra (HRMS) were obtained on a Jeol AccuTOF GCX instrument with an EI and a LIFDI source and on an Agilent Q-TOF 6540 UHD with an ESI source.

All pulse programs used are standard Bruker NMR pulse programs:

¹H NMR: Pulse program: zg; Relaxation delay = 2 - 15 s, Acquisition time = 2.1 – 2.7 s, SW = 22.0 ppm, TD = 64k, NS = 8 – 64; zg30; Relaxation delay = 2 - 15 s, Acquisition time = 2.1 – 2.7 s, SW = 22.0 ppm, TD = 64k, NS = 8 – 64;

2D-¹H,¹H NOESY: Pulse program: noesygpph; Relaxation delay = 5 - 8 s, NS = 8-32, mixing time (D8) = 300.00 ms; TD = 4096; increments = 512 - 1k;

2D-¹H,¹H COSY: Pulse program: cosygpqf; Relaxation delay = 5 - 8 s, NS = 8-32, TD = 4096; increments = 512 - 1k;

¹³C NMR: Pulse program: zgpg30; Relaxation delay = 2.00 s, Acquisition time = 1 s, SW = 200 ppm, TD = 64k, NS = 32;

2D-¹H,¹³C HSQC: Pulse program: hsqcedetgpsisp2.3; Relaxation delay = 4 - 8 s, NS = 8-32, 1 JXH = 145 Hz; TD = 4096; increments = 512 - 1k;

2D-¹H,¹³C HMBC: Pulse program: hmbcgpplpndqf; Relaxation delay = 3 - 8 s, NS = 8-32, 1 JXH = 145 Hz, JXH(long range) = 10 Hz; TD = 4096; increments = 512 - 1k;

¹⁵N NMR: Pulse program: zg; Relaxation delay = 40.00 s, Acquisition time = 4.14 s, SW = 130 ppm, TD = 64k, NS = 16;

3.7.2 Mechanistic study

3.7.2.1 Detection and characterization of the central intermediate in the conjugated enyne and cyclic nitronate formation

The species we identified as the central intermediate **4a** in the enyne **5a** and cyclic nitronate **6a** formation was detected in high amounts applying a reaction mixture of 80 mM dimer **3a** (for synthetic procedures see chapter 3.7.10) and 100mol% of DBU **7** in DMSO- d_6 at 300K.

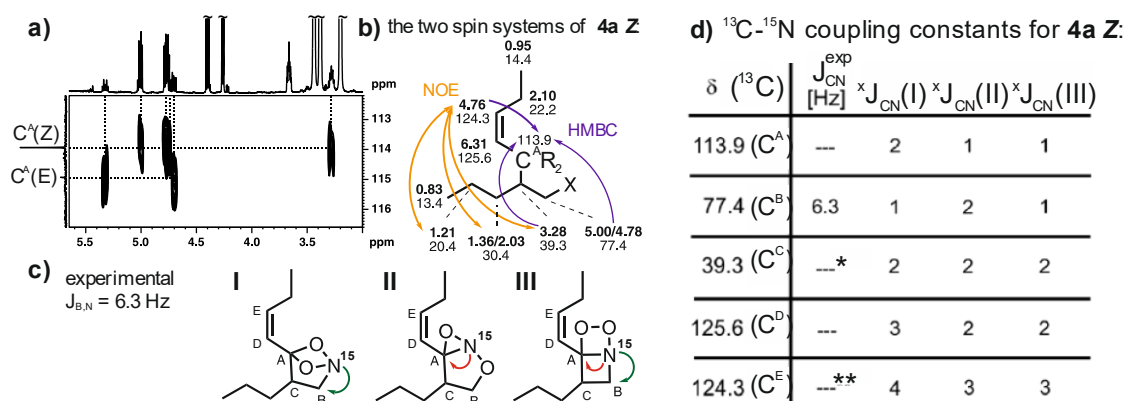


Figure SI 3.1 | a) A slice of the ^1H - ^{13}C HMBC spectrum of the central intermediate **4a** showing the corresponding cross peaks for **4a Z** as well as for **4a E**. b) The two separated spin systems of **4a Z** including its ^1H (bold) and ^{13}C (normal) chemical shifts (in ppm) and the proof of their connectivity via the common quaternary carbon atom C^{A} through ^1H - ^1H NOE contacts (orange arrows) and ^1H - ^{13}C HMBC cross peaks (purple arrows). c) Arrows in green indicate coupling constants which would fit the experimentally detected one. Arrows in red indicate that these coupling constants could lie in the range of the experimentally detected one, though didn't appear in the spectrum. d) experimental determined ^{13}C - ^{15}N scalar coupling constants ($J_{\text{CN}}^{\text{exp}}$) for carbon atoms C^{A} to C^{E} of the corresponding ^{15}N labeled compound **4a Z** ^{15}N . In addition the number of bonds (X) of the theoretical scalar coupling in the candidate structures is listed. * (signal overlap) / ** (a very broad ^{13}C signal) prevent reliable coupling constant extraction.

2D ^1H - ^1H COSY, ^1H - ^{13}C HSQC, ^1H - ^1H NOESY and ^1H - ^{13}C HMBC NMR experiments and the thereof generated ^1H and ^{13}C chemical shifts, coupling patterns and connectivities of spin systems, together with NOE data lead initially to three different candidates for **4a** with differently arranged nitrogen and oxygen moieties (see Figure SI 3.1c I-III). A slice of a HMBC spectrum is depicted in Figure SI 3.1a (for complete spectrum see Figure SI 3.25) which shows signals of a pair of two separated spin systems each of which were assigned to **4a Z** and **4a E**, respectively. In the first spin system, the proton resonance at 4.76 ppm shows an allylic $^3J_{\text{HC}}$ coupling to $\text{C}^{\text{A}}(\text{Z})$ whereas in the second spin system three proton resonances (at 3.28 ppm, 5.00 ppm and 4.78 ppm) show J couplings to the same carbon atom which positively proofs spin system connectivity. This is further confirmed by NOE contacts of the proton at 4.76 ppm of the first spin system with protons at 1.36 ppm, 3.28 ppm and 1.21 ppm of the second spin system (see Figure SI 3.1b). In order to distinguish between the three candidate structures I-III, additionally, experimental ^{13}C - ^{15}N coupling constants were necessary. Therefore, **3a** ^{15}N , the double ^{15}N -labeled analogue of **3a** was synthesized starting with ^{15}N -labeled nitroalkene **1a** ^{15}N and applied in the reaction with DBU in DMSO- d_6 . ^{13}C - ^{15}N coupling constants were extracted from 1D proton decoupled ^{13}C spectra (for spectra see chapter 3.7.14). A summary of the extracted coupling constant and the number of bonds (X) of the theoretical scalar coupling in the candidate structures I-III for **4a Z**/**4a Z** ^{15}N is shown in Figure SI 3.1d. Depending on the compound,

3 CONJUGATED ENYNES AND CYCLIC NITRONATES

typically the magnitude of $^1J_{\text{CN}}$ coupling constants is lying in the range of 2 – 36 Hz.^[1] Medium range $^2J_{\text{CN}}$ and $^3J_{\text{CN}}$ coupling constants are smaller (1 – 11 Hz and 0.7 – 6 Hz) and especially in saturated systems sometimes are undetectable.^[1] Examples for ^{13}C - ^{15}N couplings over more than 3 bonds are very rare, these coupling constants typically are very low (0.3 – 3.9 Hz) and can only be extracted from unsaturated compounds.^[1] In the actual experiment only the ^{13}C signal at 77.4 ppm (C^{B}) shows a distinct coupling (6.3 Hz) to a ^{15}N atom which would correspond to a 1J coupling in molecules **I** and **III** and a 2J coupling in molecule **II** (for spectra see chapter 3.7.14). Most importantly, for carbon C^{A} , no coupling constant could be extracted. This excludes molecules **II** and **III**, because in both structures C^{A} is directly connected to a nitrogen atom and should therefore show a strong 1J coupling. Only in molecule **I** the coupling would be a 2J coupling which may not be detectable. Among the three candidate structures only molecule **I** remained plausible. Furthermore, we wanted to validate candidate **I** as intermediate structure by quantum chemical calculations. Our calculations revealed that next to the coupling of ^{15}N to carbon **B**, also a coupling to carbon **A** should be detectable (see Figure SI 3.2). Since this was not the case, we suggested a fourth candidate **IV** (see Figure SI 3.2) presumably also less ring strained than candidate **I**. Quantum chemical calculations revealed a small coupling constant of 1.5 Hz between the nitrogen and carbon **A**. Our spectra corroborated these calculations since in our spectra, a coupling of 1.5 Hz is too small to be resolved (see Figure SI 3.2). Thus, candidate **IV** fits best to both experimental and theoretical data and was assigned as central intermediate **4a** in the formation of conjugated enyne **5a** and cyclic nitronate **6a**.

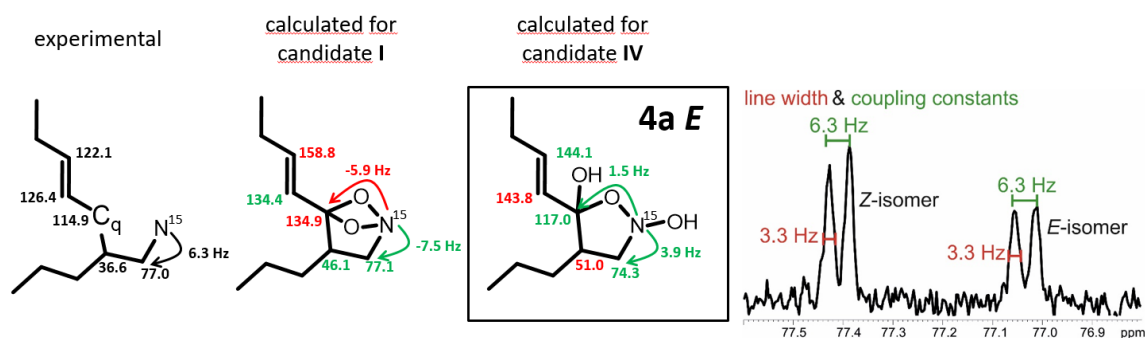


Figure SI 3.2 | Left: Experimental ^{13}C -NMR shifts of intermediate **4a** and calculated ^{13}C -NMR shifts of possible structures for **4a**. Right: Experimental line width and coupling constant of carbon atom B in a 1D proton decoupled ^{13}C NMR spectrum.

Both OH-protons of **4a** could not be observed in the NMR-spectra due to either fast chemical exchange or signal overlap with the extremely broad water peak (non-dried DMSO-d_6 always contains a considerable amount of water; we observed an extreme peak broadening of the water signal in the NMR spectra during all of our reaction kinetics).

The configuration of the double bond was derived from the proton coupling constants of D and E attached protons (**4a Z**: $^3J_{\text{DE}} = 12$ Hz; **4a E**: $^3J_{\text{DE}} = 16$ Hz). For the complete chemical shift assignment of **4a** please refer to chapter 3.7.11.

3.7.3 Identification of Intermediate 4 as a Linking Intermediate of the Enyne and Nitronate Pathway

In addition to the reaction kinetics with DBU and quinuclidine described in the manuscript, the role of **4a** as a common intermediate to both enyne and nitronate pathway was identified by the following experiment. To a 77 mM solution of dimer **3a** and OMS as internal standard (1.3 mM) in DMSO- d_6 was added DBU (1.3 eq) and an NMR spectrum was recorded, revealing nearly full conversion of **3a** to intermediate **4a** (ratios in first recorded spectrum: 85% **4a**, 7% **3a**, 3% **6a**). To this solution, 0.5 eq of benzoic acid were added. After the reaction was finished, The NMR-spectra revealed 13% enyne **5a** and 26% nitronate **6a**. Hence, higher amounts of enyne in the last spectrum than the amount of dimer in the first spectrum indicate **4a** as intermediate also in the enyne formation.

3.7.4 Proposed Mechanisms to Intermediate 4

Since we did not detect any further intermediates from dimer **3a** to central intermediate **4a**, we postulated next to the two pathways discussed in the manuscript two further mechanistic pathways for the reaction to **4a**. Both of them are suggested to start by deprotonation of **3** on the tertiary carbon atom next to the nitro group (see Figure SI 3.3). Afterwards these pathways differentiate: a) the carbanion attacks the nitrogen forming a 4-membered ring in compound **31a** which subsequently rearranges to **20a**; b) after a second deprotonation and generation of compound **32a**, a 3-membered ring in compound **33a** is formed followed by a rearrangement to **20a**. Quantum chemical calculations showed that pathway a and b are energetically not feasible.

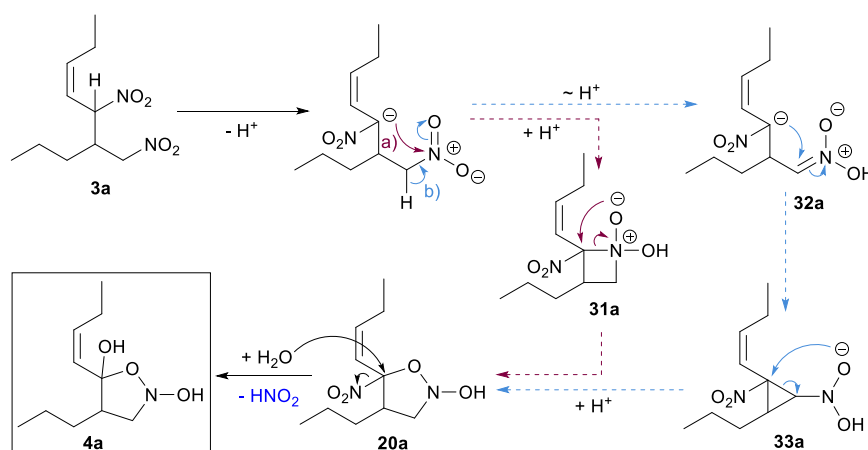


Figure SI 3.3 | Proposed mechanisms for the formation of intermediate **4** in the conjugated enyne **5** and cyclic nitronate **6** formation. Mechanism a and b could be excluded according to quantum chemical calculations.

Base dependent shifts of the protons attached to the double bond in **4a** were observed (see Figure SI 3.4). Thus, a stabilization of **4a** by hydrogen bonding to bases is highly probable similar to the situation of **20a** (see manuscript).

3 CONJUGATED ENYNES AND CYCLIC NITRONATES

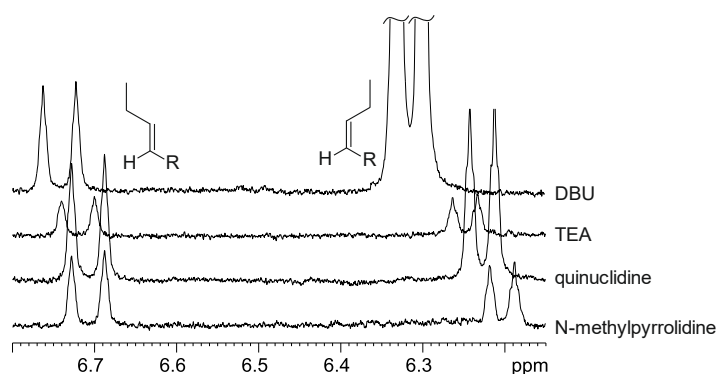


Figure SI 3.4 | Stacked regions of the shift of the double bond protons in intermediate **4a**. The shifts depend on the applied base.

Furthermore, with stronger bases, higher initial amounts of intermediate **4a** were obtained in the $^1\text{H-NMR}$ reaction monitoring (see Figure SI 3.5).

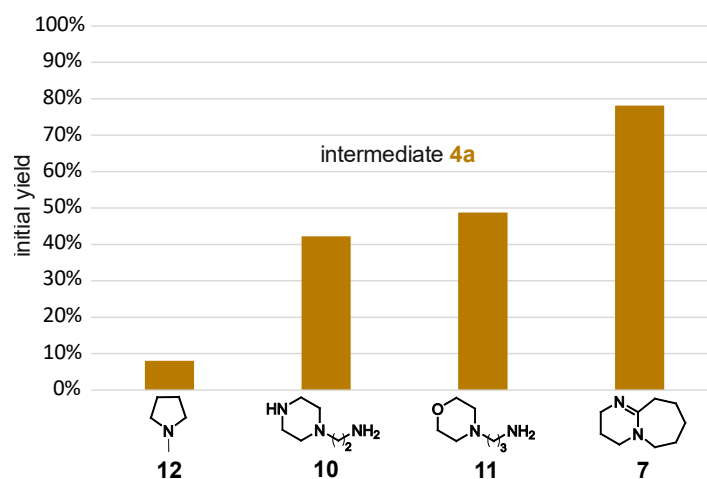


Figure SI 3.5 | Stronger bases generate higher amounts of intermediate **4a**. The yields of **4a** around 12 minutes after starting the reactions are displayed in this figure. Reaction conditions: dimer **3a** (80 mM) with corresponding base (1 eq.) in DMSO-d_6 at RT.

3.7.5 Conjugated Enyne Formation

For the mechanistic proposal and a detailed discussion see manuscript Figure 3.7.

3.7.5.1 Literature Known Reactions Supporting the Mechanism towards Enynes

For the mechanistic pathway towards conjugated enyne we propose the formation of an “oxidized” nitron **24** (see manuscript Figure 3.7). Conventional nitrones **34** are well known for forward 1,3-dipolar cycloadditions with terminal alkynes in a Kinugasa reaction (see Figure SI 3.6a),^[2] via postulated cyclic five-membered intermediates **35**, which exhibits a structural similarity to **23a** (see manuscript Figure 3.7).^[3]

For the decomposition of **24**, Nef-type reactions are proposed which are feasible in a wide pH range.^[4,5] At $\text{pH} < 7$ the decomposition of **24** may proceed via the proton catalyzed generation of compound **37** followed by its decomposition to water, HNO and CO_2 (see Figure SI 3.6b).^[4] On the other hand, at $\text{pH} > 7$ compound

3 CONJUGATED ENYNES AND CYCLIC NITRONATES

24 could decompose *via* the formation of an acyl nitroso compound **39** by an intramolecular oxygen atom transfer over cyclic compound **38** (see Figure SI 3.6c).^[5] A few years ago a similar fragmentation of the acyl nitroso compound **40** to HNO and CO₂ was reported (see Figure SI 3.6d).^[6]

The buildup of N₂ was detected as comproportionation product of HNO and H₂NOH (see manuscript Figure 3.7). A degradation of HNO to N₂O^[7,8] (Figure SI 3.6e) could not be observed in the NMR kinetic measurements of 1a¹⁵N and was therefore excluded (¹⁵N₂O signals should appear at around 155 ppm and 240 ppm)^[9].

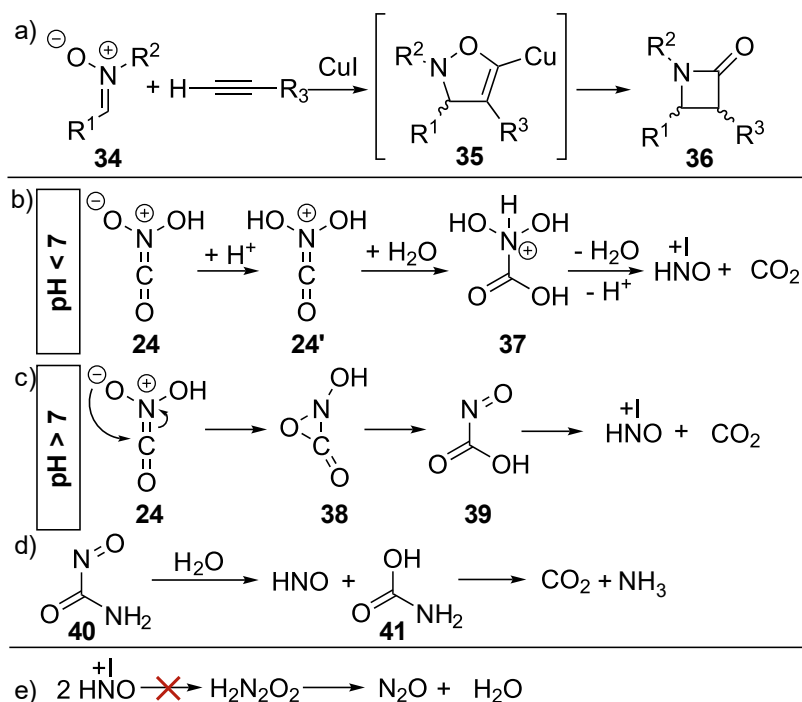


Figure SI 3.6 | a) Forward 1,3-dipolar cycloadditions with terminal alkynes.^[2,3] b) and c) Proposed decomposition of **24** via Nef-reactions.^[4,5] d) Fragmentation of the acyl nitroso compound **40** to HNO and CO₂ similar to our proposal.^[6] e) A degradation of HNO to N₂O^[7,8] could be excluded for our mechanism.

3.7.5.2 Detection of Side Products in the Conjugated Enyne and Cyclic Nitronate Formation

Experimental Confirmation of Carbon Dioxide as Byproduct

The extrusion of CO₂ as a side product in the enyne **5** formation was further confirmed by a chemical test. The reaction to **5a** is always accompanied by ascending gas bubbles. By passing the evolving gas of a non-labelled, larger scale reaction of nitropentene **1a** (1 eq.) with DPP (0.5 eq.) to **5a** under inert conditions through a saturated Ba(OH)₂ solution, a white precipitate (BaCO₃) was observed confirming the presence of CO₂.

Nitrogen Species

Both, the secondary and the primary nitro group in molecule **3** are cleaved the reaction to conjugated enyne **5**. Possible fates of this nitro group are e.g. nitromethane (or [CH₂NO₂]⁻)^[10] and nitrous acid (HNO₂). In terms of NMR discrimination and verification of both molecules and/or other nitrogen species, in principal the NMR

3 CONJUGATED ENYNES AND CYCLIC NITRONATES

active nitrogen isotope ^{15}N , especially its chemical shift can be used. Since, ^{15}N natural abundance is very low (about 0.4%) ^{15}N enriched compounds have to be used in order to get acceptable signal to noise ratios with a reasonable number of scans. Therefore, ^{15}N labeled nitroalkene $1\text{a}^{15}\text{N}$ was synthesized following a literature procedure^[11] and applied in the enyne formation catalyzed by diphenylprolinol (DPP) and benzoic acid **15** as additive in DMSO-d_6 at 300 K. ^{15}N NMR *in situ* reaction monitoring (Figure SI 3.7c) revealed the formation of many ^{15}N species during the reaction, especially in the chemical shift region of 300 to 600 ppm which includes the typical chemical shift range of nitro compounds (350 to 400 ppm)^[11].

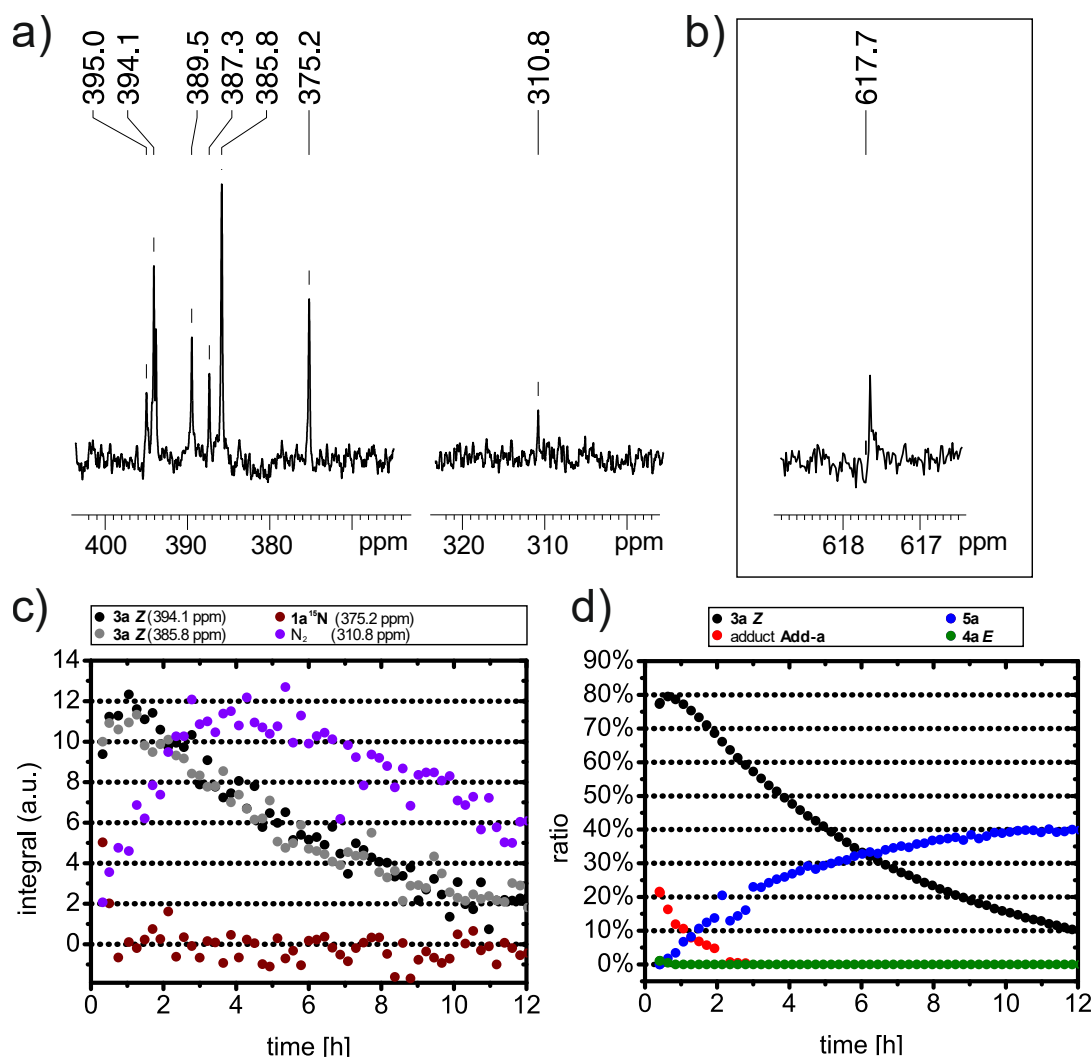


Figure SI 3.7 | a) 1D ^{15}N spectrum and b) 1D ^{15}N inverse gated decoupled spectrum both after about 20 min reaction time. ^{15}N and ^1H kinetic data is presented in c) and d) respectively. The *in situ* reaction mixture of the presented data was: ^{15}N labelled nitropentene $1\text{a}^{15}\text{N}$ (80 mM), DPP (20 mM), benzoic acid **15** (20 mM) in DMSO-d_6 at room temperature.

In parallel ^1H reaction monitoring (Figure SI 3.7d) was applied in order to enable the comparison of both ^{15}N and ^1H kinetic profiles. Figure SI 3.7a,b shows slices of ^{15}N spectra, measured after about 20 min reaction time. The signals of the nitro groups of the starting material $1\text{a}^{15}\text{N}$ (375.2 ppm) and the dimer intermediate **3a Z** (diastereomer1, diastereomer2) (394.1 ppm, 385.8 ppm) could be identified and both species show the expected performance in the plotted ^{15}N reaction kinetics (Figure SI 3.7c). In addition, five ^{15}N singlets at 395.0 ppm, 389.5 ppm, 387.3 ppm, 310.8 ppm and 617.7 ppm were detected. The three signals at 395 ppm,

3 CONJUGATED ENYNES AND CYCLIC NITRONATES

389.5 ppm and 387.3 ppm lie in the chemical shift range of nitro compounds and occur only in the very beginning of the ^{15}N reaction monitoring and disappear completely after a reaction time of 2 hours. Since in a similar time frame in the ^1H reaction monitoring (Figure SI 3.7d) the catalyst-nitroalkene adduct^[10] **Add-a** disappears, two of these three signals correspond most likely to the nitro groups of the two possible diastereoisomers of this species. The third signal probably is also a nitro group but its precise identity remains unclear so far.

More relevant are the signals at 310.8 ppm and 617.7 ppm (see Figure SI 3.7), because they are not in the chemical shift region of nitro groups. The ^{15}N reaction monitoring of the signal at 310.8 ppm reveals at first glance intermediate characteristics, building up at the beginning of the reaction, reaching its maximum concentration after about 4 hours reaction time and subsequently degrading. The maximal buildup coincides with the maximal concentration of the dimer intermediate **3a Z** (diastereomer1, diastereomer2) which indicates that **3a** is the precursor of this species. Its chemical shift of 310.8 ppm matches different literature known organic compounds^[1] e.g. imines (305-380 ppm), pyridines or pyridine like nitrogen atoms (250-520 ppm) and diazo compounds (255-445 ppm) as well as bimolecular nitrogen N_2 (310.1 ppm).^[12] Since only one intermediate ^{15}N signal was detected and pyridine or pyridine like nitrogen atoms as well as diazocompounds must show two different ^{15}N signals, these compounds are excluded. Imines or oximes show characteristic proton chemical shifts (6.9-8.4 ppm)^[13] which were never detected and can therefore also be excluded. Initially, dissolved bimolecular nitrogen was also considered unlikely, because it is not obvious why and how it should act as an intermediate and not as a product. However, there is the possibility that the generated carbon dioxide (see manuscript) is displacing dissolved N_2 from the solution. The detected intermediate is not intermediate **4a** which occurs in between the dimer **3a** and enyne **5a**, because in the proton spectra only traces of **4a** were detected at the very beginning of the reaction (Figure SI 3.7d). The most probable candidate for the ^{15}N signal at 310.8 ppm therefore is molecular nitrogen (N_2) as proposed in the manuscript. The occurring ^{15}N signal at 617.7 ppm (see Figure SI 3.7b) does roughly match a literature value of sodium nitrite (608 ppm in water).^[14] No kinetics have been measured for this signal and consequently it remains unclear if the signal builds up during the enyne formation reaction. However, the mechanism proposed in the manuscript can explain the accumulation of that compound since dimer **3a** is not completely converted to enyne **5a** or nitronate **6a**.

Water

Comparing stacked plots of the ^1H water region for the samples **3a** + DPP **7** with and without addition of benzoic acid **15** are shown in Figure SI 3.8. Without addition of **15**, the ^1H water signal slightly broadens and the water amount increases during the reaction (it approximately doubles compared to the water integral in the starting spectrum). Addition of benzoic acid **15** leads to a strong broadening of the ^1H water signal (not integrable due to strong signal overlap). Since in presence and absence of benzoic acid a water increase is observed and since in both cases enyne **5a** is formed but only in absence of benzoic acid nitronate **6a** is

3 CONJUGATED ENYNES AND CYCLIC NITRONATES

generated, one can conclude that the water buildup correlates with the enyne formation and thus represents a side product in the enyne **5a** formation.

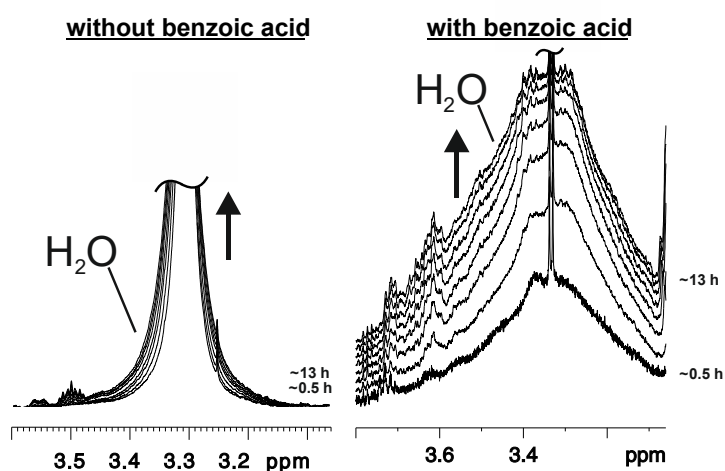


Figure SI 3.8 | Stacked plots are presented of the ^1H water signals of the samples DPP (20 mM) and dimer **3a** (40 mM) in DMSO-d_6 @ 300 K without (left) and with (right) benzoic acid **15** (20 mM) as additive. In both cases, a water build-up was observed. In presence of benzoic acid **15** the water signal broadened considerably.

3.7.6 Variation of the Starting Material Structure

3.7.6.1 Electronic Variation

In order to investigate the influence of the electronic structure of the starting material dimer **3** on its reactivity in the enyne **5** formation the two sterically very similar but electronically different dimers, 1-(5-methyl-1,3-dinitrohex-4-en-2-yl)-2-nitrobenzene **3b** and 1-methoxy-2-(5-methyl-1,3-dinitrohex-4-en-2-yl)benzene **3c** were synthesized (for procedures refer to chapter 3.7.10). The compounds only differ in the ortho-substituent of the phenyl moiety which is an electron deficient nitro group for **3b** and an electron rich methoxy group for **3c** (see Figure SI 3.9a).

3 CONJUGATED ENYNES AND CYCLIC NITRONATES

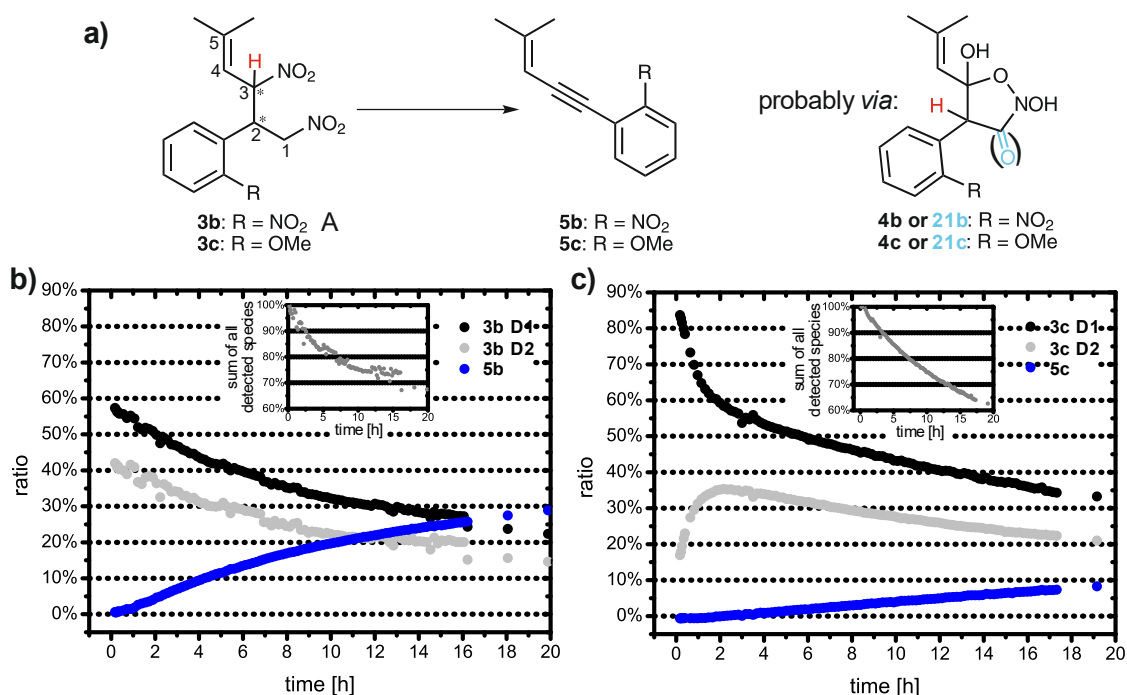


Figure SI 3.9 | a) Investigated reaction of dimers **3b/3c** (40mM) with DPP (50 mol%) and benzoic acid **15** (50 mol%). The proton marked in red gets deprotonated resulting in a negative charge on the tertiary sp³-carbon which can either be destabilized (**4b** or **21b**) or stabilized (**4c** or **21c**) by the aromatic residue. b) ¹H NMR kinetic of enyne **5b** formation. c) ¹H NMR kinetic of enyne **5c** formation.

In the proposed reaction mechanisms from dimers **3** to enynes **5** a deprotonation at the tertiary carbon (see Figure SI 3.9a) is proposed probably resulting in a carbanion as transition state. We observed a faster enyne formation with electron poor dimer **3b** than with the electron rich dimer **3c** in the presence of benzoic acid **15** as additive. This corroborates the theoretical calculations revealing the dehydration as an enthalpically demanding step and hints at a deprotonation on the tertiary carbon in **4** or **21**. Both dimers **3b** (nitro substituted) and **3c** (methoxy substituted) were applied in ¹H NMR *in situ* reaction monitoring in DMSO-d₆ at 300K, together with 50 mol% of DPP as base and 50 mol% benzoic acid, respectively. The results (Figure SI 3.9b,c) show that in both cases the dimers **3b/3c** are consumed and enyne formation **5b/5c** occurs (for ¹H and ¹³C chemical shift assignment refer to chapter 3.7.11). The loss in sum of the detected species (see plots in plots), is most probably due to an active polymerization process, and is similar in both cases (30%-40%).

Also noticeable is the isomerization process of the two diastereoisomers of the methoxy substituted dimer **3c** (see Figure SI 3.9c). Isomer **3c** (diastereomer1) was consumed throughout the reaction time of 20 hours. In contrast, in the beginning of the reaction, **3c** (diastereomer2) built up from about 15% to 35% after two hours and in the following started to decrease, reaching an equilibrium with its isomer **3c** (diastereomer1) in the end of the monitoring period. This indicates that the dimer **3** or intermediate **4** formation is a reversible process.

3.7.6.2 Structural Variation

In order to further shed light into the enyne **5** formation mechanism, the two differently branched nitroalkenes 2-nitrohex-2-ene **1b** and 2-methyl-1-nitrobut-1-ene **1c** were tested for their reaction performance (catalyst: DPP, additive: benzoic acid **15** in DMSO- d_6) monitored by *in situ* NMR. These substrates were chosen, because their structure prevents two possible reaction steps in an alternative mechanism after formation of the dimer **3** (see Figure SI 3.10). Starting from nitroalkene **1b**, after dimerization to **42**, 1,2-elimination of nitrous acid is possible and would lead to 5-methyl-6-(1-nitroethyl)nona-3,5-diene **43** (see Figure SI 3.10, top) with the nitro group not being part of the conjugated π -system. Since now, compared to linear nitroalkenes, a methyl substituent replaces the proton in position 4, subsequent deprotonation at this position, is blocked. There is the theoretical possibility of nitroethane elimination *via* deprotonation of the CH_2 group in position 4'. But the result of such an unlikely elimination step would be an allene instead of an enyne. By identification of either the nitrous acid elimination product **43** or the corresponding allene formed *via* nitroethane elimination starting from the α -branched nitroalkene **1b**, an alternative mechanistic proposal can be validated.

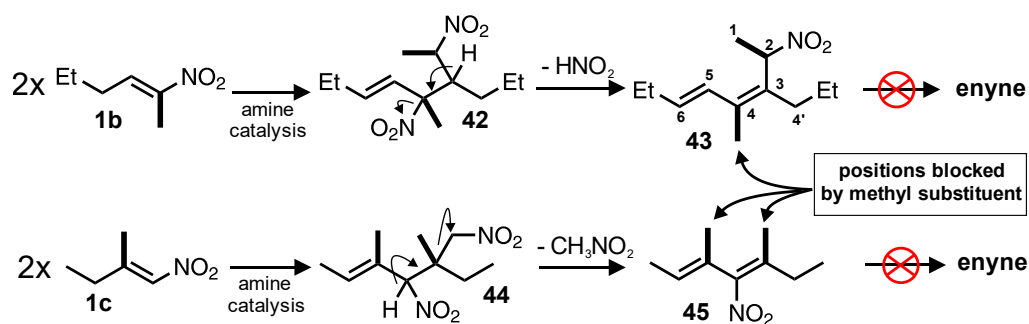


Figure SI 3.10 | Reaction path of the branched nitroalkene **1b** and **1c** in the enyne formation reaction according to an alternative reaction mechanism. In both cases enyne formation should not be possible. The introduced methyl groups that block elimination of nitrous acid or nitromethane are marked with arrows.

Starting from nitroalkene **1c**, after secondary amine catalyzed dimerization to **44**, deprotonation at the carbon with the secondary nitro group attached is possible and could initiate a nitromethane elimination leading to 3,5-dimethyl-4-nitrohepta-2,4-diene **45** (see Figure SI 3.10, bottom) with the nitro group being attached to a sp_2 carbon, which is part of the conjugated dien π -system. From here on 1,2-elimination of the remaining nitro group as nitrous acid is not possible, because both β -positions (relative to the nitro group) are blocked by the introduced methyl substituents. Identification of **45** as a product would validate an active nitro methane elimination.

1b was synthesized previously in our working group and after purification its reactivity with DPP and benzoic acid **15** in DMSO- d_6 was monitored (see Figure SI 3.11). **1d** was rapidly consumed and remained stable at a ratio of about 20% after 5 hours. In this reaction mixture, neither the dimer intermediate **3d** nor the expected products **43** or allene derivative could be identified. Instead the main product was identified as (*E*)-2-nitrohex-3-ene **46** building up fastest in the beginning of the reaction, simultaneously with the strongest decline of **1b**. The reaction mechanism that leads to **46** is assumed to start with a reversible nucleophilic

3 CONJUGATED ENYNES AND CYCLIC NITRONATES

attack of the secondary nitrogen of DPP to the β -position of the nitroalkene **1b**, forming a catalyst-adduct (see Figure SI 3.11). Apparently, 1,2-elimination initialized by deprotonation of the CH₂ proton in position 4, leading to the less crowded double bond in **46** is favored (Hofmann product). This reaction step is irreversible, because the resulting double bond is no longer activated for a nucleophilic attack *via* conjugation with the nitro group. The active base that initializes the elimination process has to be considerably sterically demanding, otherwise the higher substituted and more stable Zaitsev product **1b** would be formed. Most probably, the active base in this case is again the secondary amine DPP.

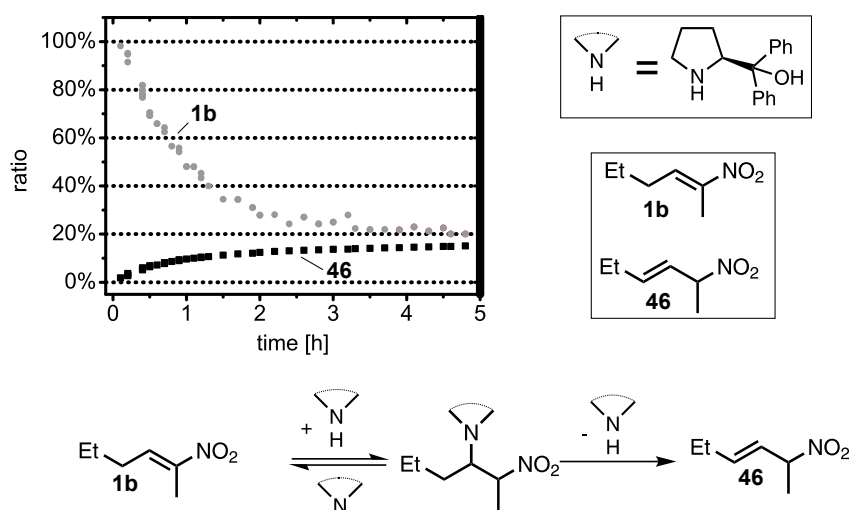


Figure SI 3.11 | ¹H NMR reaction monitoring of a mixture of **1d** (100 mM), DPP (38 mM) and **15** (50 mM) in DMSO-d₆ @ 298 K shows the consumption of **1b** and the formation of **46** as the main product. The secondary amine DPP is abbreviated as shown in the top right corner.

No other reaction products could be identified. The disproportionate loss of starting material compared to the amount of product formed is assigned to an active polymerization process of **1b**. Since, not even the dimerization to **42** takes places, this shows that α -branched nitroalkenes like **1b** cannot be applied in the enyne formation reaction.

A mixture of *E/Z* isomers of **1c** was synthesized according to a literature procedure and its reactivity with DPP and benzoic acid **15** in DMSO-d₆ was monitored by *in situ* by NMR (see Figure SI 3.12, top). The isomeric mixture of starting material is consumed fast and an *E/Z* mixture of 2-methyl-1-nitrobut-2-ene **47** is formed. The mechanism of this reaction is assumed to start with a nucleophilic addition (see Figure SI 3.12, bottom) of the secondary amine functionality of the catalyst on the β -position of **1c** to form a catalyst-nitroalkene adduct. From here on, three different E2 eliminations are occurring parallel, first *via* deprotonation of a α -CH₂ proton back to the stabilized nitroalkene **1c**, second and third, *via* deprotonation of a γ -CH₂ proton to the product **47 E** and **47 Z**. After the starting material vanished completely (after about 3 hours) **47 Z** is still building-up slowly while **47 E** starts to degrade. Therefore, either isomer **47 Z** is thermodynamically more stable than isomer **47 E**, or, more likely, the formation of **47 E** is reversible whereas the formation of **47 Z** is irreversible (see Figure SI 3.12, bottom).

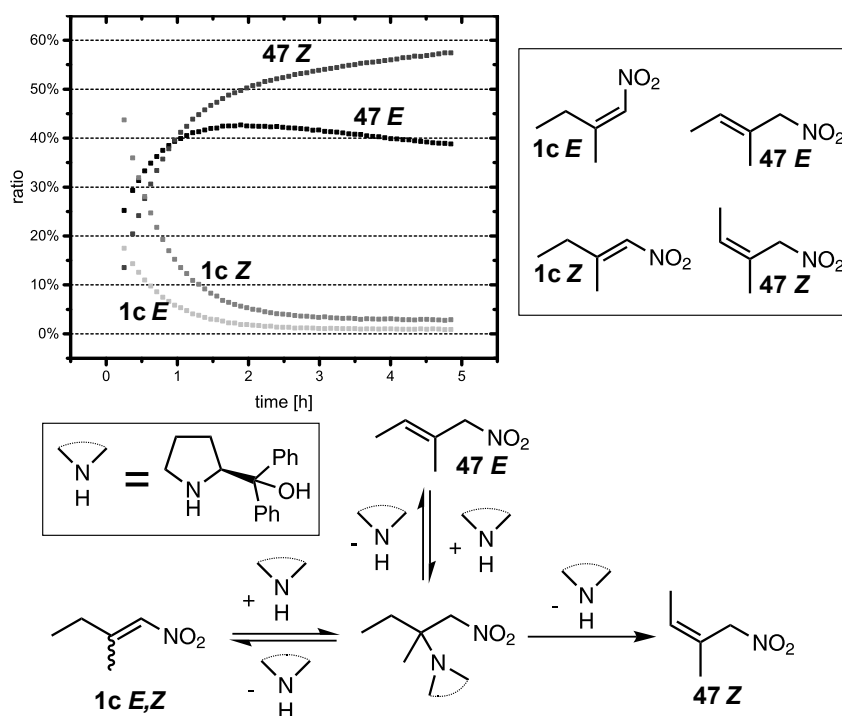


Figure SI 3.12 | ^1H NMR reaction monitoring of a mixture of **1c** (mixture of *E* and *Z* isomer) (in sum ≈ 50 mM), DPP (≈ 50 mM) and benzoic acid **15** (≈ 50 mM) in DMSO- d_6 @ 300 K shows the consumption of **1c** and the formation of **47** (mixture of *Z* and *E*) as the main product. A possible reaction mechanism is depicted.

Again, the desired reactivity *i.e.* the dimerization of **1c** and subsequent reaction steps were not detected. Therefore again, these results show that also β -branched nitroalkenes are not applicable in the enamine formation reaction, because they show a complete different reactivity.

It is noted here, that in contrast to the α -branched nitroalkene **1b**, β -branched **1c** is not consumed by a polymerization process. Presumably, alkyl substituents in β -position of nitroalkenes hamper their polymerization tendency.

3.7.7 Temperature Variation

3.7.7.1 Temperature Decrease

In order to slow down the reaction rate and possibly enable the detection of further short lived intermediates and/or to improve the outcome of the reaction in terms of the yield, low temperature measurements were envisaged. Because of the high melting point of DMSO (292 K), these measurements were conducted in DMF which stays liquid down to 212 K. Figure SI 3.13 shows NMR reaction kinetics of **1a** (40 mM), DPP (50 mol%) and benzoic acid **15** (50 mol%) in DMF- d_7 at 270 K. As expected the reaction rate is strongly decelerated compared to the reaction at 300 K in DMSO- d_6 . The build-up and decrease of two intermediates in the enyne formation reaction, *e.g.* the catalyst-nitroalkene adduct **Add-a** and the dimer **3a** (total) (*Z*, both diastereoisomers) was monitored. **Add-a** reaches a maximum concentration after about 0.5 days, dimer **3a** after about 2.25 days. Surprisingly, the maximum concentration of **Add-a** and the maximum slope of **3a** (total) do not occur simultaneously. This should be the case if the former is the direct precursor of the latter in the reaction mechanism. In fact the maximum slope of **3a** (total) already occurs earlier in the reaction

3 CONJUGATED ENYNES AND CYCLIC NITRONATES

profile which indicates that in DMF there must be an alternative active reaction pathway from the nitroalkene **1** to the dimer **3**.

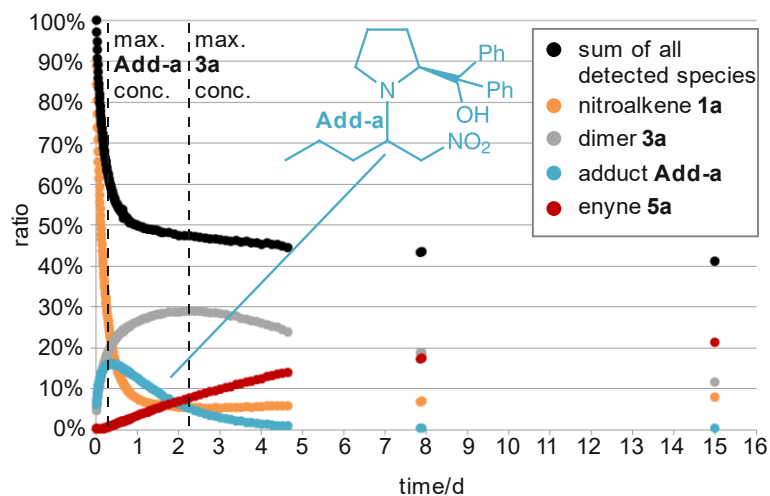


Figure SI 3.13 | NMR reaction kinetics of **1a** (40 mM), DPP (50 mol%) and benzoic acid **15** (50 mol%) in DMF- d_7 at 270 K. The sum was set to 100% in the first spectrum.

After an initialization phase, the total enyne amount **5a** shows a linear increase up to about 5 days reaction time and reaches a ratio of about 14% (28% yield) after 8 days (42% yield after 15 days, data not shown). Noticeable is the decrease of the sum of all detected species derived from **1a** (see Figure SI 3.13, black data points) most severe in the beginning of the reaction (about 50% after 1 day reaching 40% after 15 days). This effect also occurs in DMSO at 300K and is most probably connected with an active polymerization process, consuming either/and nitroalkene **1a**, dimer **3a**.

Although the reaction rate was drastically decelerated by monitoring enyne **5a** formation from nitropentene **1a** at low temperatures (270 K), no additional short-lived reaction intermediates could be detected and the yield of the reaction was not improved.

3.7.7.2 Temperature Increase

Initially, we aimed at preventing the omnipresent polymerization process by increasing the temperature. Thus, the temperature in the reaction from dimer **3a** (23 mM) to enyne **5a** in presence of TEA (30 mM) and benzoic acid (30 mM) at elevated temperature (320 K) was examined. Smaller concentrations as usual (50 - 80 mM) were applied to slow down the reaction at elevated temperatures and the reaction kinetic is displayed in Figure SI 3.14. Regarding the diagram, it can be noticed that by elevating the temperature, not only the enyne **5a** is formed (19%), but also the corresponding nitronate **6a** (13%). Usually, in presence of benzoic acid, nitronate **6a** is suppressed to less than 3% yield. Additionally, an unidentified by-product (9%) was detected at 320 K (data not shown). Furthermore, an intermediate could be detected during the reaction. Its signals forms and vanishes again at 6.83 ppm and 6.17 ppm (data not shown).

3 CONJUGATED ENYNES AND CYCLIC NITRONATES

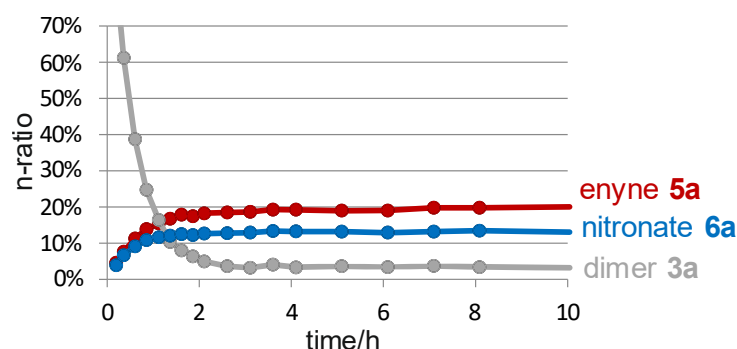


Figure SI 3.14 | Reaction kinetic of a solution of dimer **3a** (23 mM), TEA (30 mM) and benzoic acid (30 mM) in DMSO- d_6 measured at 320 K. Integrals were normalized to an integral of benzoic acid.

This experiment showed that an increase in temperature does not hamper polymerization and allows the formation of nitronate **6a** and an unknown by-product (which is not connected to the nitronate formation). Hence, this hints at an alternative nitronate pathway potentially involving higher energetic intermediates at elevated temperatures and other unproductive reactions.

3.7.8 Catalyst and Solvent Screening

3.7.8.1 Catalyst Screening by GC-FID

In order to test many catalysts for their performance in the direct enyne formation from nitroalkenes, in a shorter time than possible by NMR, a GC-FID procedure has been developed.

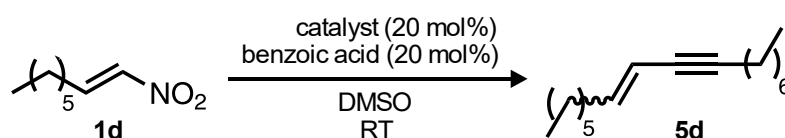


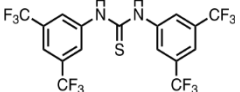
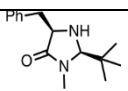
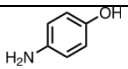
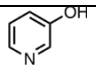
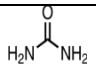
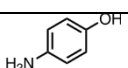
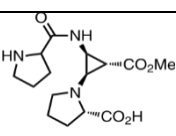
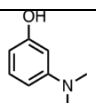
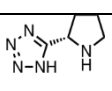
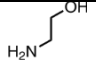
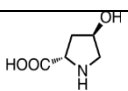
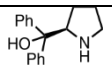
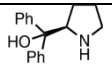
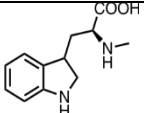
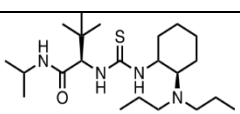
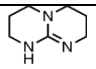
Figure SI 3.15 | Reaction conditions applied in the GC-FID screening of the catalyzed direct enyne **5d** formation from nitroalkene **1d**. Concentrations: **1d** (62.5 mM), catalyst (12.5 mM) benzoic acid (12.5 mM). Reaction time: 24-48 h. GC standard compound: pentadecan.

Since, the retention time of non-3-en-5-yne **5a** was in the region of the retention time of the solvent DMSO, nitroocten **1d** (for synthesis procedure refer to chapter 3.7.10), a nitroalkene with a longer alkyl chain, was used which yields pentadec-6-en-8-yne **5d** in the enyne formation reaction (see Figure SI 3.15).

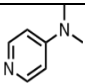
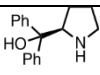
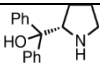
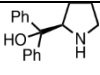
Table SI 3.1 | Results of the GC-FID screening of potential catalysts for the direct enyne **5d** formation from **1d**. Standard conditions: **1d** (63 mM), catalyst (20 mol%), benzoic acid **15** (20mol%), in DMSO at room temperature, open system, reaction time 21 to 48 hours. Total conversion was not determined. *no benzoic acid **reaction @ 343 K ***inert conditions. For calibration lines, retention times and raw GC data see below.

No.	Catalyst	Reaction Time [h]	E / Z Ratio	Yield
1		24	1.0	2%

3 CONJUGATED ENYNES AND CYCLIC NITRONATES

No.	Catalyst	Reaction Time [h]	E / Z Ratio	Yield
2		24	9.1	2%
3		24	6.3	3%
4		24	4.5	3%
5		24	6.6	4%
6		24	7.0	4%
7		24	6.3	5%
8		24	8.0	5%
9		24	4.3	6%
10		24	7.7	7%
11		24	1.6	7%
12		36	5.6	9%
13*		21	4.3	11%
13**		21	2.7	15%
14		24	5.1	16%
15		24	5.7	16%
16		24	2.2	21%

3 CONJUGATED ENYNES AND CYCLIC NITRONATES

No.	Catalyst	Reaction Time [h]	E / Z Ratio	Yield
17		24	4.4	21%
13***		24	5.8	26%
18		48	3.8	30%
13		48	3.93	33%

In Table SI 3.1 the results of the GC-FID screening are summarized sorted by the determined enyne **5d** yield. Benzoic acid **15** (20 mol%) together with potential organocatalysts (20 mol%) like MacMillan Imidazolidinones (no. 1 and 3), the Ley catalyst (no. 10), a hydroxyl-substituted L-proline (no. 12), urea (no. 6), thioureas (no. 2 and 15), as well as DPP (no. 13, 18; both stereoisomers) were applied. Since the functional groups in DPP are a secondary amine as well as a primary alcohol, also simple compounds, containing alcohol groups (no. 5) or amine groups (no. 8, 14, 16, 17) or both (no. 7, 9, 11, 12) were tested. All catalysts which show a significant yield (> 10%, no. 13 - 18) contain at least one secondary or tertiary amine. On the other hand, a secondary amine alone is not sufficient for a significant catalytic activity because molecules no. 1, 3, 8, 10 and 12 are not very effective (all <10%). The best catalyst in this screening was DPP (~30%, no. 13, 18; both stereoisomers) which contains a secondary amine as well as a tertiary alcohol. Molecule no. 12 containing a secondary amine and a carboxylic acid shows a significantly lower yield of 9%. The common property of all catalysts with moderate to high activity is a secondary or tertiary amine and a decent basic¹ character (e.g. contain at least one tertiary amine or alcohol). This result fits the mechanistic proposal (see manuscript).

An elevated temperature does not improve yield and selectivity (13**, DPP @ 343 K).

GC-Screening – Technical Details. The GC-FID system 7820A was used for the catalyst screening with the column HP 5 19091J 413 (30 mm x 0.32 mm x 0.25 μ m), both from Agilent. For calibration, a stock solution of 33.33 mg of analytical pure **5d** (74.7% *E*, 25.3% *Z*) in 10 mL DMSO was prepared. Three calibration samples were prepared, with 1.496 mL (1.84×10^{-5} mol *E*-isomer, 6.21×10^{-6} mol *Z*-isomer), 0.6 mL (7.37×10^{-6} mol *E*-isomer, 2.49×10^{-6} mol *Z*-isomer) and 0.2 mL (2.46×10^{-6} mol *E*-isomer, 8.30×10^{-7} mol *Z*-isomer) of stock solution, 3.9 μ L pentadecan each and DMSO (to a total volume of 1.5 mL). After GC-FID measurements of each sample, calibration lines for **5d E** and **5d Z** were generated (see Figure SI

¹ Molecule no. 14 (16%) is an exception. It contains two secondary amines but also a carboxylic group and therefore has only a low basicity compared to the other active compounds.

3 CONJUGATED ENYNES AND CYCLIC NITRONATES

3.16). The retention times were 6.51 min for **5d Z**, 6.90 min for **5d E** and 6.42 min for the standard substance pentadecan. The equations derived from the calibration lines are as follows.

$$I = \left(1.34 \times 10^8 \frac{1}{\text{mol}} \pm 5 \times 10^6 \frac{1}{\text{mol}}\right) \times n - (92 \pm 63) \quad \text{for } \mathbf{5d E}$$

$$I = \left(1.30 \times 10^8 \frac{1}{\text{mol}} \pm 3 \times 10^6 \frac{1}{\text{mol}}\right) \times n - (7 \pm 11) \quad \text{for } \mathbf{5d Z}$$

(I: normed integral (a.u.); n: amount of substance [mol])

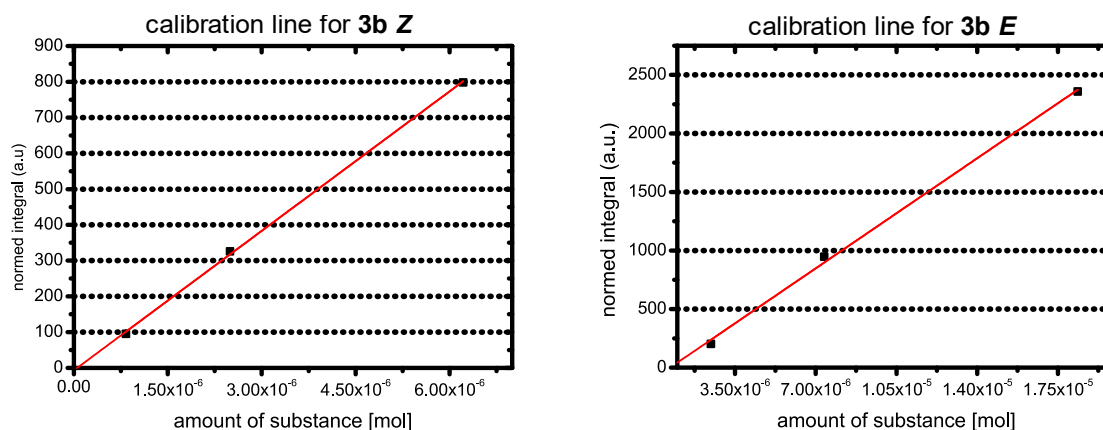


Figure SI 3.16 | Reaction scheme and calibration lines of the GC screening for the enyne **5d** formation from nitroalkene **1d**. R2 values of the calibration lines are 0.99667 (**5d E**) and 0.99908 (**5d Z**). Concentrations are **1d** (62.5 mM), catalyst (12.5 mM) benzoic acid (12.5 mM). Reaction time was 21–48 h. GC standard compound was pentadecan.

The reaction conditions of the catalyst screening were as follows. Catalyst (0.2 equiv, 0.1 mmol, 12.5 mM) and 12.2 mg benzoic acid **15** (0.2 equiv, 0.1 mmol, 12.5 mM) were dissolved in 8 mL DMSO and 78.6 mg **1d** (1.0 equiv, 0.5 mmol, 62.5 mmol) was added. After the reaction time has elapsed, 1.46 mL of the reaction mixture was transferred in a GC vial, 3.9 μL pentadecan was added and a GC-FID measurement was performed. In the following, the raw results of the GC-Screening are shown in Table SI 3.2.

Table SI 3.2 Raw data of the GC-FID screening of different catalysts for the enyne **5d** formation reaction from nitroalkene **1d**. Catalyst structures and calculated yields are depicted in the manuscript.

Catalyst No.	Raw Integral (5d E)	Normed Integral (5d E)	Raw Integral (5d Z)	Normed Integral (5d Z)	Integral (Pentadec.)
1	39.2	21.9	7.4	4.1	1788.7
2	35.5	17.8	10.0	5.0	1991.5
3	104.8	61.1	29.0	16.9	1714.6
4	115.0	64.0	48.5	27.0	1797.2
5	273.8	129.7	54.3	25.7	2111.4

3 CONJUGATED ENYNES AND CYCLIC NITRONATES

Catalyst No.	Raw Integral (5d E)	Normed Integral (5d E)	Raw Integral (5d Z)	Normed Integral (5d Z)	Integral (Pentadec.)
6	152.5	104.4	30.1	20.6	1460.6
7	175.3	145.9	35.6	29.6	1201.3
8	220.8	165.0	32.7	24.4	1337.8
9	242.9	204.7	71.2	60.0	1186.5
10	432.0	259.8	62.0	37.3	1663.0
11	284.2	158.5	252.6	140.9	1792.5
12	499.0	379.1	122.1	92.8	1316.2
13*	651.7	457.1	166.2	116.6	1425.7
13**	665.9	569.9	273.3	233.9	1168.5
14	1193.1	740.7	244.0	151.5	1610.7
15	1076.1	719.5	195.3	130.6	1495.7
16	1252.3	801.0	600.2	383.9	1563.5
17	962.1	961.8	225.0	224.9	1000.3
13***	1831.6	1249.4	318.8	217.5	1466.0
18	2723.0	1360.9	726.9	363.3	2000.9
13	1955.0	1489.4	502.6	382.9	1312.6

3.7.8.2 Solvent Screening

Fully deuterated DMSO, DMF, methanol, benzene, dioxane, nitromethane, acetone, dichloromethane, and acetonitrile were chosen as NMR solvents for the optimization of the enyne formation reaction. We applied nitropentene **1a** (80 mM), as well as 25 mol% of the original catalyst DPP and the additive benzoic acid **15**. After a reaction time of 15–20 min ¹H spectra showed that productive enyne formation only takes place in the highly polar, aprotic solvents DMSO and DMF (ϵ_r of approximately 37)^[15]. In the unpolar aprotic solvents benzene, dioxane and dichloromethane and in the less polar aprotic solvents nitromethane, acetonitrile and acetone no reactivity was monitored at all, whereas in the polar protic solvent methanol only unproductive reactions took place. The *in situ* yield of **5a** for the reaction in DMF reached about 29% (14.5% ratio) after a

3 CONJUGATED ENYNES AND CYCLIC NITRONATES

reaction time of 19.5 hours and full conversion of the starting material (see Figure SI 3.17, bottom). Therefore, we revealed that a simple change of solvent from DMSO to DMF does not improve the yield (yield in DMSO: 35%).

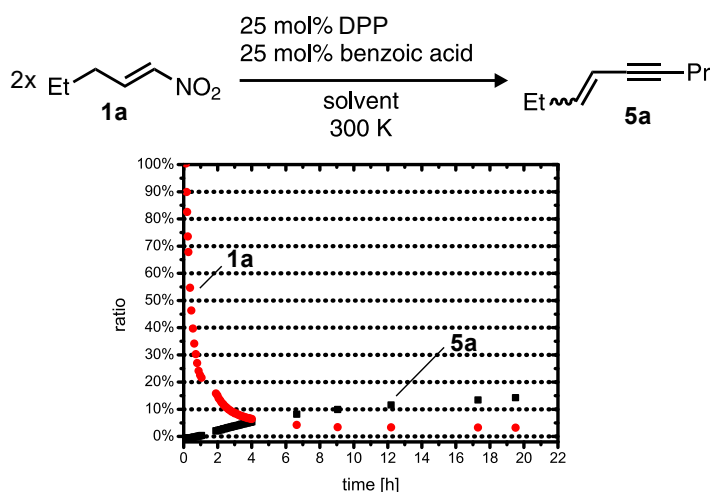


Figure SI 3.17 | Top shows Reaction conditions for the solvent screening of the reaction of **1a** to **5a** (*E* and *Z*). Bottom shows ¹H *in situ* NMR reaction kinetics of the formation of **5a** in DMF-d₇ at 300 K (the sum was set to 100% for the first spectrum).

While in the polar aprotic solvents DMSO and DMF, the reaction of **1a** with 1eq. of DBU resulted in **6a** as main product with only small detectable amounts of unknown side products, in the non-polar solvent dichloromethane many unidentified signals appeared during the course of the reaction. Considering that we propose charge separated and polar compounds as reaction intermediates and transition states (see manuscript) for both nitronate and enyne formation, we suggest that DMSO and DMF can stabilize these compounds better than DCM due to their higher dielectric constants and dipole moments.^[16] Thereby, DMSO and DMF presumably prevent unproductive pathways apparently occurring in DCM.

Potential Participation of Solvent Molecules

Variation of reaction conditions showed that the enyne **5** formation from nitroalkenes **1** is strongly solvent dependent (see chapter 3.7.8.2). Only in the polar aprotic solvents DMSO and DMF the desired enyne formation was detected. Therefore, the possibility that solvent molecules are directly involved in the reaction was considered likely. Through variation of the ratio of fully deuterated DMSO to non-deuterated DMSO and acquisition of proton and deuterium spectra, such a direct involvement of solvent molecules was investigated.

Deuterium spectra of a mixture of the nitroalkene **1a**, DPP and the additive benzoic acid **15** showed, in addition to the expected solvent signal (DMSO at 2.5 ppm), the occurrence of two new signals, *i.e.* a doublet at 2.01 ppm (coupling constant: 1.8 Hz) as well as a singlet at 2.00 ppm with the relative integrals of 2.00 to 2.92 (see Figure SI 3.18b). In total, around 0.2 equivalents (main product enyne **5a** as 1 equivalent) of DMS arise during the reaction. The coupling constant of the doublet is similar to the ²J_{HD} coupling constant of DMSO-d₅ (1.9 Hz).^[17] Together with the relative integrals and its chemical shift it would fit to a DMS-d₅

3 CONJUGATED ENYNES AND CYCLIC NITRONATES

derivative. The corresponding proton spectra of a reaction mixture of **1a**, DPP and **15** showed two signals (quintet at 2.00 ppm and singlet at 2.05 ppm) in the chemical shift region of DMS which also appeared in a reaction mixture of **3a**, DPP and **15**. The addition DMS to the reaction mixture of **1a** lead to an increase of the signal at 2.00 ppm (see Figure SI 3.18a) revealing that DMS is generated during the reaction.

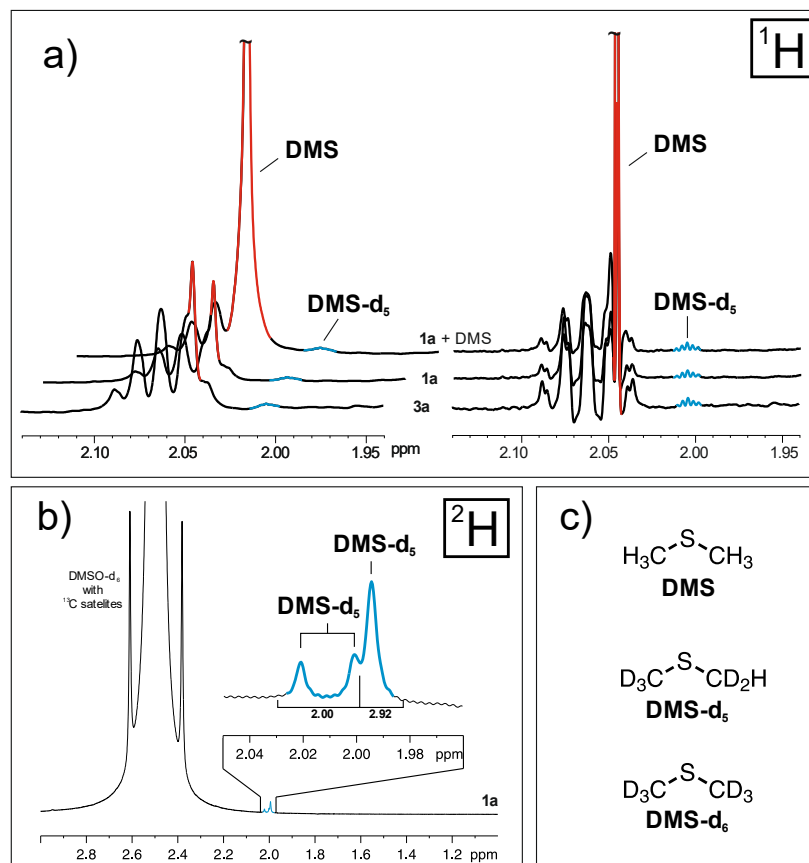


Figure SI 3.18 | a) DMS and DMS- d_5 signals of stacked ^1H -NMR spectra (measured with solvent suppression) of a reaction mixture of **3a** (40 mM), DPP (20 mM) and PhCOOH **15** (20 mM) in DMSO- d_6 /DMSO (1/1) at RT (bottom), a reaction mixture of **1a** (40 mM), DPP (20 mM) and **15** (20 mM) in DMSO- d_6 /DMSO (1/1) at RT (middle) and a reaction mixture of **1a** (40 mM), DPP (20 mM) and **15** (20 mM) in DMSO- d_6 /DMSO (1/1) with addition of DMS at RT (top). Left: processing of spectra with exponential function. Right: processing of spectra with Gaussian function. b) shows a section of ^2H spectrum with signals of detected DMSO-derivatives formed during the reaction of nitropentene **1a**, DPP (50 mol%) and **15** (50 mol%) in DMSO- d_6 (plus one droplet of DMSO) at RT. c) shows the identified compounds DMS and DMS- d_5 and the not detected compound DMS- d_6 .

No deuterium signal which would fit to the fully deuterated species DMS- d_6 (see Figure SI 3.18c) was detected which is very surprising at first glance because the corresponding fully deuterated DMSO- d_6 is present in a very large excess compared to the DMSO- d_5 molecule. This could be explained if the mechanism leading to DMS and DMS- d_5 contains both, a deprotonation-/dedeuteration step of DMSO as well as a reprotonation step. Since the water amount in these samples is pretty high and water molecules are very acidic in comparison to DMSO molecules, the probability that reprotonation instead of redeuteration occurs is very high. Therefore, the product molecule would usually contain at least one proton, which would explain that the amount of fully deuterated derivative DMSO- d_6 is below the NMR detection limit. In addition the formation of a doubly protonated species is unlikely because the isotope effect makes α -deprotonation about three to seven times more likely than α -dedeuteration.^[18]

3 CONJUGATED ENYNES AND CYCLIC NITRONATES

Overall, we revealed that during the reaction to conjugated enynes (not nitronates since acid is present) DMSO is reduced to DMS. A possible corresponding reducing agent can be found in the mechanistic pathway towards conjugated enynes **5**. There, a redox reaction is suggested to occur implying the potential presence of reducing agents. We considered the reduction of DMSO by HNO to DMS as likely. The redox potential for the reduction of DMSO to DMS at pH = 7 is +160 mV ($\text{DMSO} + 2\text{H}^+ + 2\text{e}^- \rightarrow \text{DMS} + \text{H}_2\text{O}$).^[19] The redox potential for the reduction of NO^\bullet to ${}^1\text{NO}^-$ at pH \geq pK_a is around -1.7 V (singlet state; $\text{NO}^\bullet + \text{e}^- \rightarrow {}^1\text{NO}^-$) while at lower pH the redox potential is around -0.15 ($\text{NO}^\bullet + \text{e}^- + \text{H}^+ \rightarrow {}^1\text{HNO}$).^[7] Hence, in both pH cases, the redox potential of the reduction to HNO is lower than the reduction to DMS at pH = 7. Thus, the reduction of DMSO by HNO was considered likely.

3.7.9 Polymerization Problematic

During NMR reaction monitoring, the sum over all ${}^1\text{H}$ - signals belonging to the combined enyne and nitronate mechanism decreased in the ongoing reaction. Despite, several efforts including various bases, acidic additives, concentrations and temperatures, so far we have not been able to suppress effectively this detrimental polymerization process. The presence of polymerization could further be confirmed by analyzing a reaction mixture of nitropentene **1a** (80 mM) with DBU (1 eq.) in dichloromethane (DCM). Therefore, the reaction was started by the addition of DBU and directly after the reaction mixture turned yellow, 100 μL of this mixture were dissolved with DCM to 1 mL. This was then injected on a reversed phase system of a HPLC (Agilent 1290 Infinity) and analyzed by electrospray ionization (ESI-MS) in a Q-TOF 6540 UHD. Several molecular ions could be detected, *inter alia* the nitropentene-dimer **3a** and nitronate **6a**. Besides, many molecular ions with a higher m/z ratio than nitropentene **1a**, dimer **3a**, enyne **5a** or nitronate **6a** could be detected. Some of these ions, which have a high m/z ratio and a good match of their m/z -ratio with the theoretical m/z ratio of the proposed formula (named as score), are listed in Table SI 3.3.

Table SI 3.3 | List of Molecular ions that were detected by ESI-MS in a reaction mixture of **1a** with DBU and have a higher m/z ratio than **1a**, **3a**, **5a** and **6a**.

entry	formula	Score/%	retention time/min	mass/(g/mol)	m/z /(kg/C)
1	C40 H60 N11 O11	97.99	3.5	870.447	871.4539
2	C42 H69 N6 O13	99.1	3.492	865.4917	866.499
3	C51 H64 N5 O	96.76	5.003	762.5113	763.5184
4	C36 H48 N4 O12	95.49	1.642	728.327	729.3345
5	C36 H48 N4 O12	96.44	1.56	728.3266	729.3339
6	C32 H52 N15 O	97.38	5.003	662.4475	663.4548
7	C29 H48 N6 O6	98.89	3.485	576.3629	577.3703
8	C32 H57 N5 O2	97.18	4.659	543.4505	544.4575
9	C20 H37 N5 O10	99.81	1.647	507.2541	508.2613
10	C20 H37 N5 O10	99.34	1.566	507.2538	508.2609

3 CONJUGATED ENYNES AND CYCLIC NITRONATES

Unfortunately, the intermediate **4a** could not be detected by this experiment because the use of aqueous ammonium acetate as buffer for the reversed phased system transformed **4a** towards dimer **3a**. This could be also observed by $^1\text{H-NMR}$ by adding a crystal of ammonium acetate to the reaction of nitropentene **1a** with DBU.

3.7.10 Scope

3.7.10.1 Nitroalkene Dimers

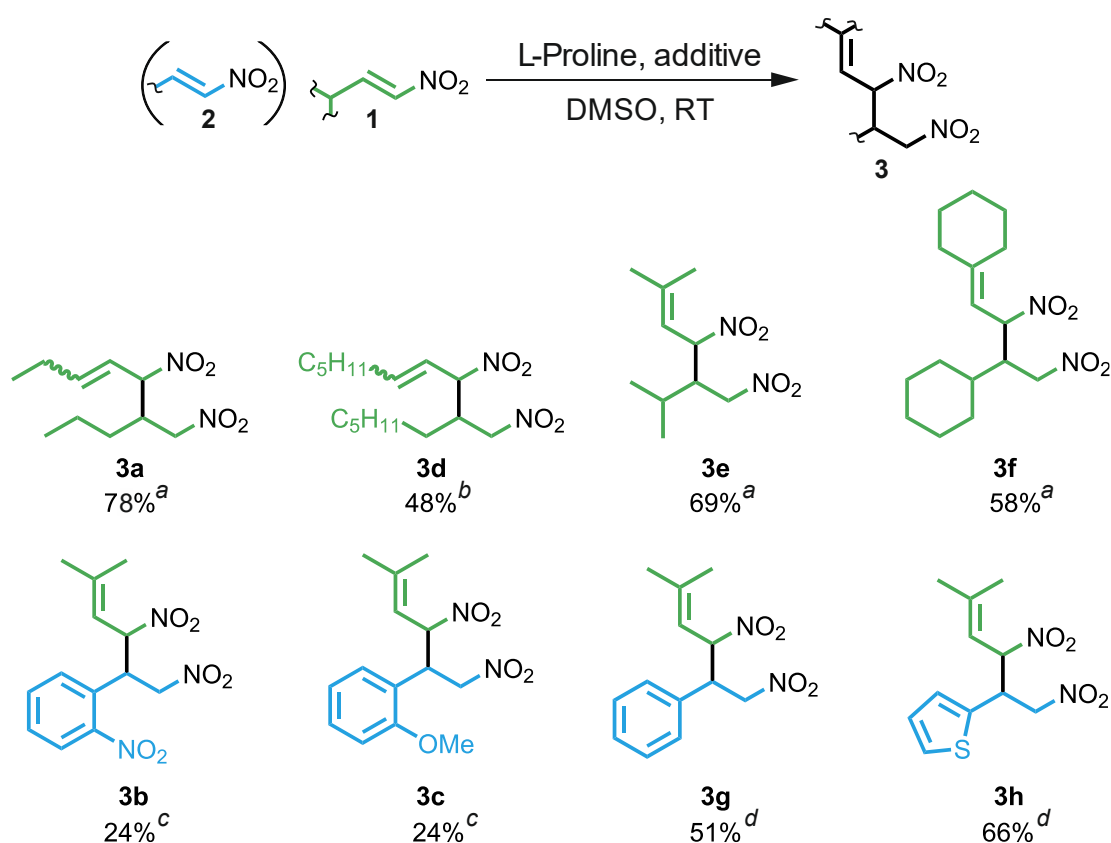


Figure SI 3.19 | Scope of the nitroalkene dimers; all yields are isolated ones; **a** **1a/1e/1f** (100 mM), L-proline (1 eq.), no additive, 24h; **b** **1d** (80 mM), L-proline (0.5 eq.), PhCOOH (0.5 eq.), 24h; **c** **1e** and **2a/2b** (40 mM), L-proline (0.8 eq.), PhCOOH (0.8 eq.), 24h; **d** **1e** and **2c/2d** (40 mM), L-proline (0.8 eq.), PhCOOH (0.8 eq.), 45h.

3 CONJUGATED ENYNES AND CYCLIC NITRONATES

3.7.10.2 Conjugated Enynes

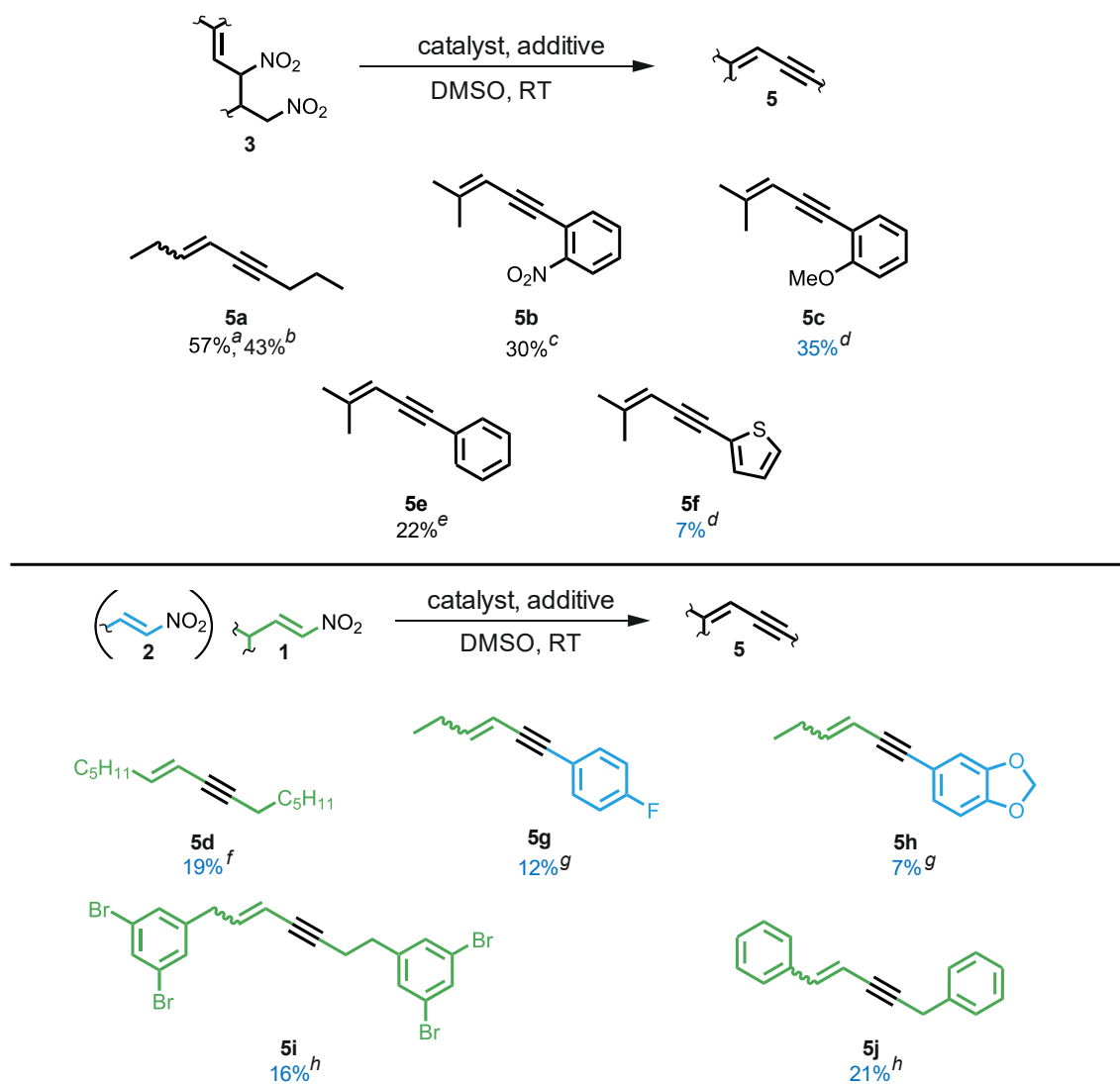


Figure SI 3.20 | Scope of the conjugated enynes. Black yields were observed in the NMR, blue yields were isolated. For NMR monitoring, DMSO- d_6 was used instead of DMSO. **a** **3a** (80 mM), Diethylaniline (80 mM), no additive, 37 days; **b** **3a** (55 mM), TEA (1.4 eq.), propionic acid (2.1 eq.), 5 h; **c** **3b** (40mM), DPP (50 mol%), benzoic acid (50 mol%); **d** **3c/3h** (70 mM after dropwise addition) dropwise over 20 h to TEA (1 eq.) and PhCOOH (1 eq.); **e** **3g** (46 mM), TEA (1 eq.), PhCOOH (1 eq.), 3 days; **f** **1d** (100 mM), DPP (0.2 eq.), PhCOOH (0.2 eq.), 21 h; **g** **1a** (1.2 eq.) dropwise added over 4.5 h to **2e/2f** (100 mM) and L-proline (1 eq.), no additive, 60 h. **h** **1g**/(3-nitroallyl)benzene (100 mM), L-proline (0.1 eq.), no additive, overnight.

3 CONJUGATED ENYNES AND CYCLIC NITRONATES

3.7.10.3 Cyclic Nitronates

Since for the synthesis of conjugated nitronates there already exist many metal-free procedures, we mainly focused on the investigation of the enyne scope.

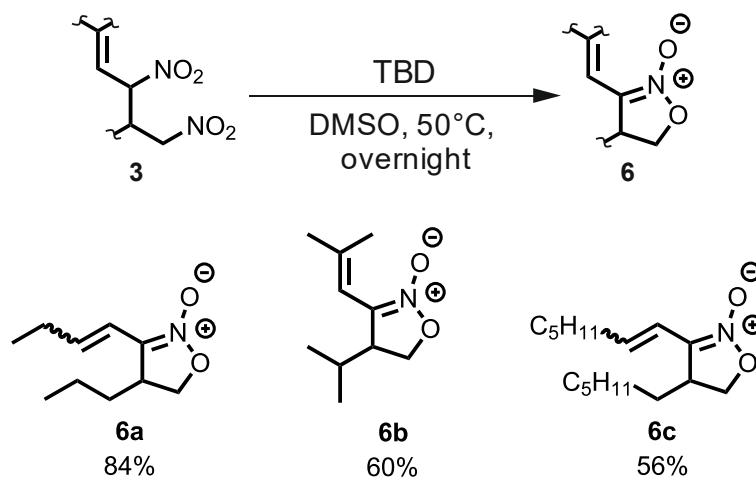


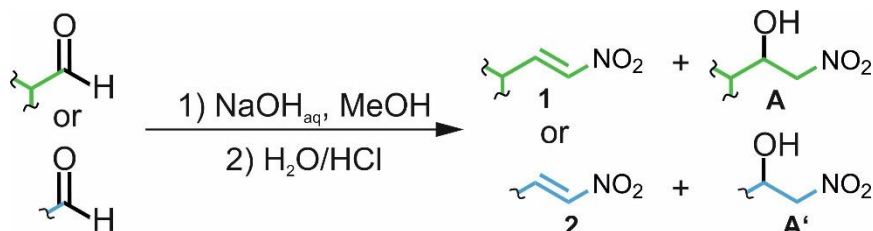
Figure SI 3.21 | Scope of the conjugated nitronates; all yields are isolated ones. **6a**: 0.7 mmol of TBD and **3a**. **6b**: 0.22 mmol of TBD and **3e**. **6c**: 0.16 mmol of TBD and **3d**.

3 CONJUGATED ENYNES AND CYCLIC NITRONATES

3.7.11 General Procedures

3.7.11.1 General procedure for the synthesis of nitroalkenes **1** and **2**

The nitroalkenes **1a-e**, **1g**, **1a^{13C}**, **1a^{15N}** and **2b** were synthesized following a literature procedure.^[11]



In a round bottom flask equipped with a stirring bar, corresponding aldehyde (10 mmol) and nitromethane (10 mmol) were dissolved in methanol (3.2 mL) at a temperature below 0°C (ice, sodium chloride mixture). After the dropwise addition of a solution of sodium hydroxide (11.8 mmol, 7.6 mM) in water, a white precipitate was formed. Further MeOH (3.2 mL) was added and the resulting slurry was stirred at 0°C for 1 hour. Water was added until the precipitate was completely dissolved. After addition of 3.2 mL of 8.7 M HCl the reaction mixture was stirred for 15 minutes, extracted three times with dichloromethane, and dried over MgSO₄. The solvent was evaporated and nitroalkene **1-2** was purified by column chromatography (gradient elution with petroleum ether/Et₂O).

The corresponding nitro alcohol **A/A'** can be converted, when necessary, to the corresponding nitroalkene by elimination in the presence of TFAA and Et₃N according to the following procedure:

To a solution of compound **A/A'** (0.57 mmols in 2 ml of DCM), TFAA was added dropwise at 0°C. Then Et₃N was added dropwise at 0°C. The mixture was allowed to stir at the same temperature for 15 min. At 0°C, the mixture was quenched with sat NH₄Cl. The aqueous layer was extracted with DCM twice. The combined organic layers were washed with sat. NH₄Cl, dried over Na₂SO₄ and filtered. The product obtained was used without any further purification in the next step.

Yields:

1a: 67%

1a^{13C}: 28%

1a^{15N}: 56%

1b: was synthesized after another procedure^[20]

1c: was synthesized after another procedure^[21]

1d: 13%

1e: 40%

1g: 89%

2b: 72%

3.7.11.2 Dimers

General procedure for homo-dimer

Nitroalkene **1** (1 mmol) and L-proline (1 mmol) were mixed in DMSO (10 mL). The reaction was left under stirring at room temperature overnight. The mixture was dissolved in water and extracted with dichloromethane. The combined organic phase was washed three times with a saturated solution of lithium chloride, dried over MgSO₄ and the solvent was evaporated. The product was purified by column chromatography (PE/DEE 100/0 – 6/1).

General procedure for hetero-dimer

L-proline (0.8 equiv, 0.2 mmol) and benzoic acid (0.8 equiv, 0.2 mmol) were dissolved in 7 mL DMSO at room temperature. Subsequently, nitroalkene **2** (1.0 equiv, 0.3 mmol) and nitroalkene **1** (1.0 equiv, 0.3 mmol) were added. The solution was stirred for 24 hours under atmospheric conditions. After the reaction was quenched by adding 10 mL brine the reaction mixture was extracted 4 times with 10 mL diethyl ether each. The combined organic layers were washed 4 times with 10 mL distilled water each and dried over magnesium sulfate. After evaporation of the solvent the raw product was purified by flash column chromatography (PE:EA = 9:1) yielding **3**.

Yields: (for diverging procedures see caption of Figure SI 3.19)

3a: 78%

3b: 24%

3c: 24%

3d: 51%

3e: 69%

3f: 58%

3g: 66%

3h: 51%

3.7.12 Enynes

For individual procedures and yields see Figure SI 3.20.

3 CONJUGATED ENYNES AND CYCLIC NITRONATES

3.7.13 Nitronates

3.7.13.1 General procedure for cyclic nitronates **6**

To a 100 mM solution of triazabicyclodecene (TBD) (1 eq.) in DMSO was added dimer **3** (1 eq.) and the reaction was stirred at 50°C overnight. Then the product was purified by column chromatography (TLC eluent: Pentane/Et₂O: 1/1) yielding **6**.

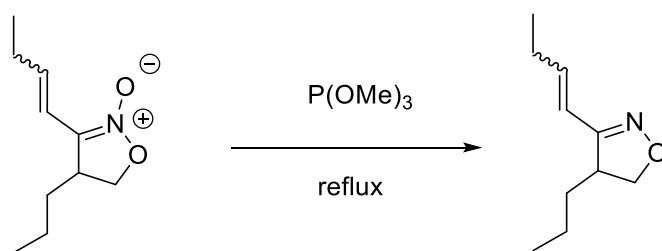
Yields: (for diverging procedures see caption of Figure SI 3.21)

6a: 84%

6b: 60%

6c: 56%

3.7.13.2 Reduction of Cyclic Nitronate **6a** to 3-(but-1-en-1-yl)-4-propyl-4,5-dihydroisoxazole



6a (133 mg, 0.72 mmol, 1 eq.) was dissolved in 5.8 ml P(OMe)₃ (68 eq.) in a flask equipped with a condenser. The solution was well degassed and heated to reflux under argon. After 12 h, when the starting material was totally consumed (TLC petroleum ether/ Et₂O 1/1) the reaction was cooled to 0°C and Et₂O was added. The solution was washed with 1N HCl. The organic layers were dried and concentrated *in vacuo*. The crude product was purified by column chromatography (petroleum ether/ Et₂O) (yield 23% 3-(but-1-en-1-yl)-4-propyl-4,5-dihydroisoxazole; mixture of isomers which can be separated by column chromatography).

MH⁺ = 168.1649 m/z

(Z)-3-(but-1-en-1-yl)-4-propyl-4,5-dihydroisoxazole: ¹H NMR (600 MHz, CD₂Cl₂): δ [ppm] = 5.90 (dt, J = 11.6 Hz, 7.3 Hz, 1H), 5.82 (dt, J = 11.6 Hz, 1.7 Hz, 1H), 4.26 (dd, J = 9.9 Hz, 8.1 Hz, 1H), 4.04 (dd, J = 8.1 Hz, 6.2 Hz, 1H), 3.22-3.28 (m, 1H), 2.35-2.44 (m, 2H), 1.54-1.62 (m, 2H), 1.25-1.42 (m, 2H), 1.04 (t, J = 7.5 Hz, 3H), 0.93 (t, J = 7.2 Hz, 3H).

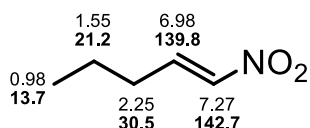
(E)-3-(but-1-en-1-yl)-4-propyl-4,5-dihydroisoxazole: ¹H NMR (600 MHz, CD₂Cl₂): δ [ppm] = 6.25 (dt, J = 16.1 Hz, 1.7 Hz, 1H), 6.15 (dt, J = 16.1 Hz, 6.3 Hz, 1H), 4.15-4.21 (m, 2H), 3.30-3.36 (m, 1H), 2.20-2.25 (m, 2H), 1.57-1.64 (m, 2H), 1.29-1.48 (m, 2H), 1.07 (t, J = 7.4 Hz, 3H), 0.93 (t, J = 7.3 Hz, 3H).

3.7.14 Chemical Assignments

Diastereomers are indicated as **D1** and **D2**. Chemical shifts of **D2** are given in brackets.

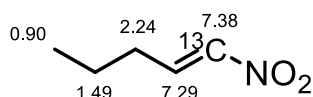
^1H -NMR shifts are given in normal font, ^{13}C -NMR shifts in bold font.

3.7.14.1 Nitroalkenes

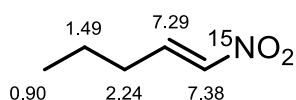
(E)-1-nitropent-1-ene (1a)

^1H NMR (400 MHz, CDCl_3): δ [ppm] = 7.27 (dt, J = 13.4 Hz, 7.5 Hz, 1H), 6.98 (dt, J = 13.6 Hz, 1.7 Hz, 1H), 2.25 (qd, 7.4 Hz, 1.5 Hz, 2H), 1.55 (sex, J = 7.4 Hz, 2H), 0.98 (t, 7.4 Hz, 3H).

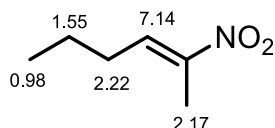
A chemical assignment can also be found in literature. [11]

 ^{13}C -labelled (E)-1-nitropent-1-ene (1a ^{13}C)

^1H NMR (600 MHz, DMSO-d_6): δ [ppm] = 7.38 (ddt, J = 97.5 Hz, 13.2 Hz, 1.4 Hz, 1H), 7.29 (m, 1H), 2.24 (dtd, J = 14.5 Hz, 7.2 Hz, 1.4 Hz, 2H), 1.49 (tq, J = 14.6 Hz, 7.3 Hz, 2H), 0.90 (t, J = 7.4 Hz, 3H).

 ^{15}N -labelled (E)-1-nitropent-1-ene (1a ^{15}N)

^1H NMR (600 MHz, DMSO-d_6): δ [ppm] = 7.38 (ddt, 1 H), 7.29 (dtd, 1 H), 2.24 (qd, 2 H), 1.49 (m, 2 H), 0.90 (t, 3 H).

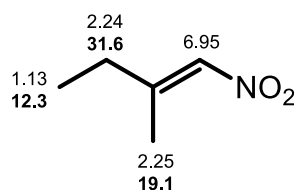
(E)-2-nitrohex-2-ene (1b)

^1H NMR (300 MHz, CDCl_3): δ [ppm] = 7.14 (t, J = 7.2 Hz, 1 H), 2.22 (q, J = 7.2 Hz, 2 H), 2.17 (s, 3 H), 1.55 (m, 2 H), 0.98 (t, 3 H).

A chemical assignment can also be found in literature. [22]

3 CONJUGATED ENYNES AND CYCLIC NITRONATES

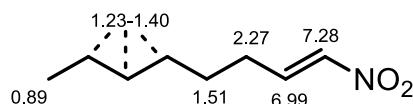
2-methyl-1-nitrobut-1-ene (1c)



^1H NMR (400 MHz, CDCl_3): δ [ppm] = 6.97 – 6.93 (m, J = 1.3 Hz, 1H), 2.25 (d, J = 1.4 Hz, 3H), 2.28 – 2.20 (m, 5H), 1.11 (t, 3H).

A chemical assignment can also be found in literature.^[21]

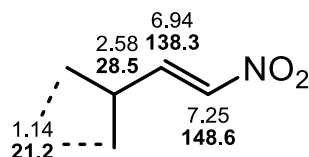
(E)-1-nitrooct-1-ene (1d)



^1H NMR (400 MHz, CD_2Cl_2): δ [ppm] = 7.28 (dt, J = 13.3 Hz, 7.4 Hz, 1H), 6.99 (dt, J = 13.3 Hz, 1.6 Hz, 1H), 2.27 (qd, J = 7.4 Hz, 1.6 Hz, 2H), 1.51 (m, 2H), 1.23-1.40 (m, 6H), 0.89 (t, J = 7.0 Hz, 3H).

An elemental analysis can be found in literature.^[23]

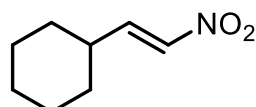
(E)-3-methyl-1-nitrobut-1-ene (1e)



^1H NMR (400 MHz, CDCl_3): δ [ppm] = 7.25 (dd, J = 13.4 Hz, 7.1 Hz, 1H), 6.94 (dd, J = 13.5 Hz, 1.3 Hz, 1H), 2.58 (octd, J = 12.7 Hz, 1.4 Hz, 1H), 1.14 (d, J = 6.8 Hz, 6H).

A chemical assignment can also be found in literature. ^[11]

(E)-(2-nitrovinyl)cyclohexane (1f)

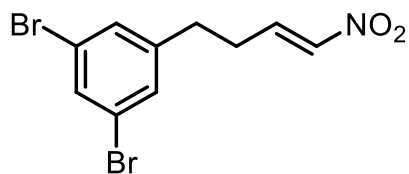


^1H NMR (400 MHz, CDCl_3): δ [ppm] = 7.22 (dd, J = 13.5 Hz, 7.2 Hz, 1H), 6.93 (dd, J = 13.5 Hz, 1.3 Hz, 1H), 2.20-2.31 (m, 1H), 1.75-1.86 (m, 4H), 1.67-1.75 (m, 1H), 1.09-1.40 (m, 5H).

A chemical assignment can also be found in literature. ^[11]

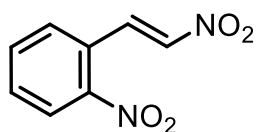
3 CONJUGATED ENYNES AND CYCLIC NITRONATES

(E)-1,3-dibromo-5-(4-nitrobut-3-en-1-yl)benzene (1g)



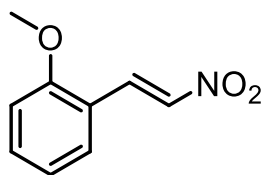
$^1\text{H NMR}$ (400 MHz, CD_2Cl_2): δ [ppm] = 7.57 (1H), 7.31 (2H), 7.23 (dt, J = 13.4 Hz, 7.3 Hz, 1H), 6.99 (dt, J = 13.4 Hz, 1.6 Hz, 1H), 2.80 (d, J = 7.3 Hz, 2H), 2.57 (qd, J = 7.4 Hz, 1.6 Hz, 2H).

(E)-1-nitro-2-(2-nitrovinyl)benzene (2a)



$^1\text{H NMR}$ (400 MHz, DMSO-d_6): δ [ppm] = 8.43 (d, J = 13.5 Hz, 1 H), 8.20 (dd, 1 H), 8.12 (d, J = 13.5 Hz, 1 H), 7.97 (dd, 1 H), 7.86 (td, 1 H), 7.78 (td, 1 H).

1-methoxy-2-[(E)-2-nitrovinyl]benzene (2b)



$^1\text{H NMR}$ (400 MHz, CDCl_3): δ [ppm] = 8.15 (d, 13.6, 1H), 7.88 (d, 13.6, 1H), 7.46 (m, 2H), 7.00 (m, 2H), 3.96 (s, 3H).

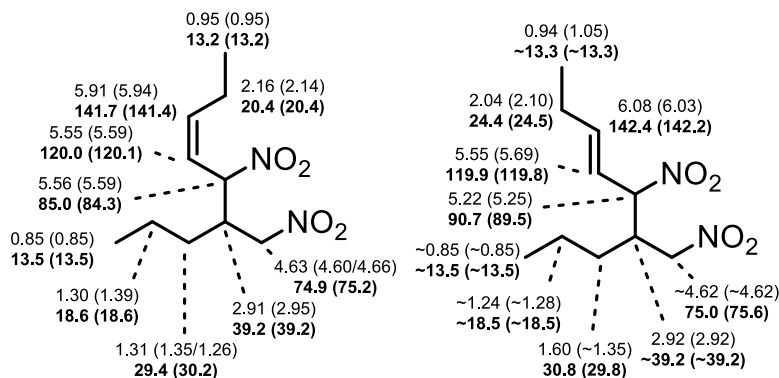
A chemical assignment can also be found in literature. ^[11]

3 CONJUGATED ENYNES AND CYCLIC NITRONATES

3.7.14.2 Dimers

5-nitro-6-(nitromethyl)non-3-ene D1 (D2) (3a)

600 MHz, in DMSO-d₆



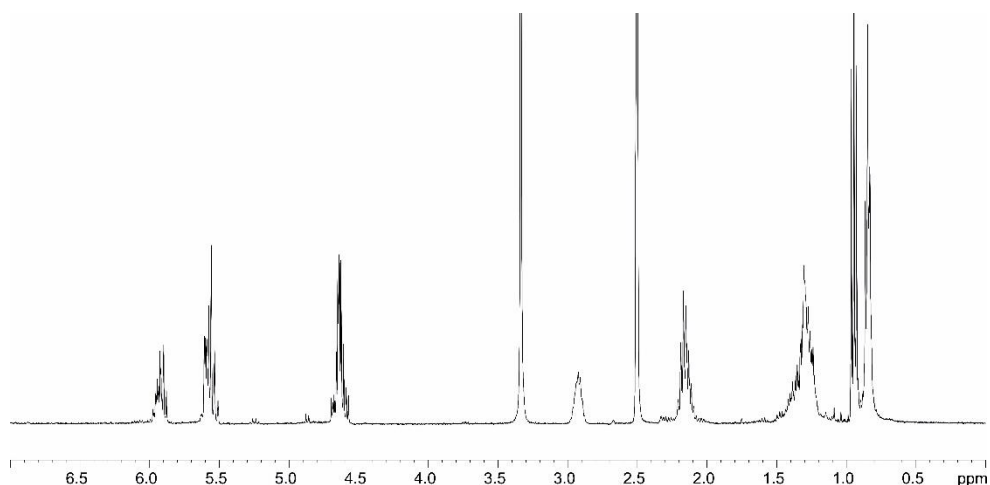
3a Z: ¹H NMR (600 MHz, DMSO-d₆): δ [ppm] = 5.91 (5.94) (m, 1H), 5.56 (5.59) (m, 1H), 5.55 (5.59) (m, 1H), 4.63 (4.60/4.66) (m, 2H), 2.91 (2.95) (m, 1H), 2.16 (2.14) (m, 2H), 1.31 (1.35/1.26) (m, 2H), 1.30 (1.39) (m, 2H), 0.95 (0.95) (t, J = 7.6 Hz (7.6 Hz), 3H), 0.85 (0.85) (t, J = 7.1 Hz (7.1 Hz), 3H).

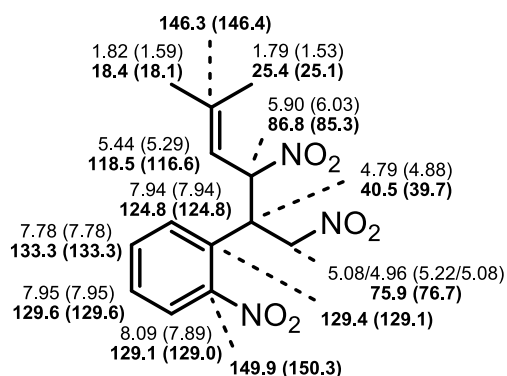
3a Z: ¹³C NMR (600 MHz, DMSO-d₆): δ [ppm] = 141.7 (141.4), 120.0 (120.1), 85.0 (84.3), 74.9 (75.2), 39.2 (39.2), 29.4 (30.2), 20.4 (20.4), 18.6 (18.6), 13.5 (13.5), 13.2 (13.2).

3a E: ¹H NMR (600 MHz, DMSO-d₆): δ [ppm] = 6.08 (6.03) (dt (dt), J = 15.3 Hz (15.3 Hz), 6.2 Hz (6.2 Hz) 1H), 5.55 (5.69) (m (ddt) (J = 15.3 Hz, 9.7 Hz, 1.5 Hz), 1H), 5.22 (5.25) (dd, J = 9.3 Hz, 8.6 Hz (9.3 Hz, 6.9 Hz), 1H), ~4.62 (~4.62) (m, 2H), 2.92 (2.92) (m, 1H), 2.04 (2.10) (m, 2H), 1.60 (~1.35) (m, 2H), ~1.24 (~1.28) (m, 2H), 0.94 (1.05) (t, J = 7.6 Hz (7.4 Hz, 3H), 0.85 (0.85) (t, J = 7.1 Hz, 3H).

3a E: ¹³C NMR (600 MHz, DMSO-d₆): δ [ppm] = 142.4 (142.2), 119.9 (119.8), 90.7 (89.5), 75.0 (75.6), ~39.2 (~39.2), 30.8 (29.8), 24.4 (24.5), ~18.5 (~18.5), ~13.5 (~13.5), ~13.3 (~13.3).

HRMS (ESI): calcd. for C₁₀H₁₈N₂O₄ [M + H]⁺ 231.1339; found 231.1341.

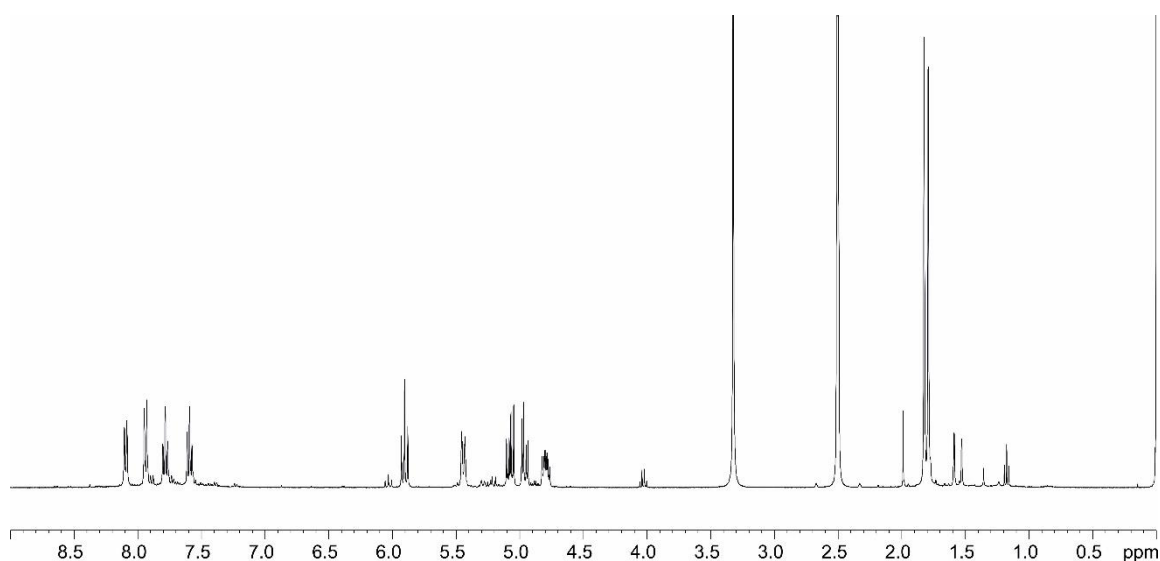


1-(5-methyl-1,3-dinitrohex-4-en-2-yl)-2-nitrobenzene (3b)600 MHz, in DMSO-d₆

¹H NMR (400 MHz, DMSO-d₆): δ [ppm] = 8.09 (7.89) (d (d), J = 7.9 Hz (7.9 Hz)), 7.94 (7.94) (dd, 8.1 Hz, 1.2 Hz), 7.78 (7.78) (ddd, J = 7.8 Hz, 7.8 Hz, 1.1 Hz), 7.59 (7.59) (ddd, J = 7.8 Hz, 7.8 Hz, 1.2 Hz), 5.90 (6.03) (dd (dd), J = 9.9 Hz, 9.9 Hz (10.1 Hz, 10.1 Hz)), 5.44 (5.29) (dq (dq), J = 9.7 Hz, 1.3 Hz, 1.3 Hz (10. Hz, 1.3 Hz, 1.3 Hz)), 5.08 (5.22) (dd (dd), J = 13.8 Hz, 8.6 Hz (14.4 Hz, 10.3 Hz)), 4.96 (5.08) (dd (m), J = 13.8 Hz, 5.5 Hz), 4.79 (4.88) (ddd (ddd), J = 9.8 Hz, 8.7 Hz, 5.4 Hz (9.9 Hz, 9.9 Hz, 4.4 Hz)), 1.82 (1.59) (d (d), J = 1.1 Hz (1.2 Hz)), 1.79 (1.53) (d (d), J = 1.0 Hz (1.1 Hz)).

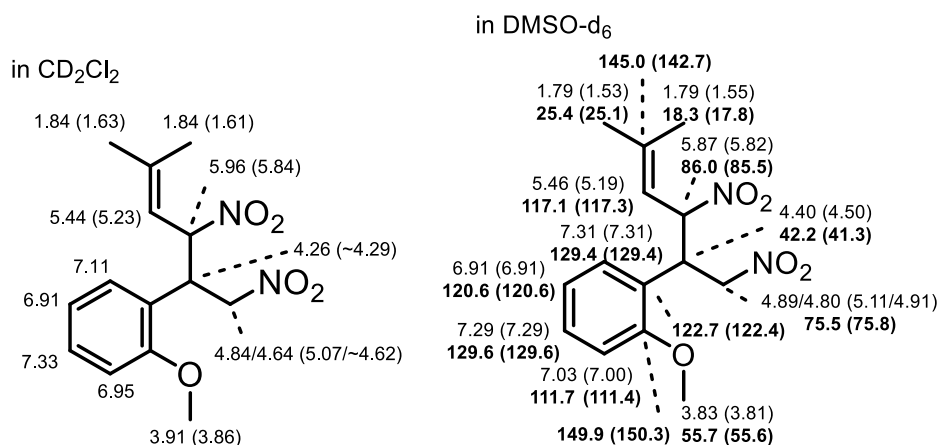
¹³C NMR (400 MHz, DMSO-d₆): δ [ppm] = 149.9 (150.3), 146.3 (146.4), 133.3 (133.3), 129.6 (129.6), 129.4 (129.1), 129.1 (129.0), 124.8 (124.8), 118.5 (116.6), 86.8 (85.3), 75.9 (76.7), 40.5 (39.7), 25.4 (25.1), 18.4 (18.1).

HRMS (ESI): calcd. for C₁₃H₁₅N₃O₆ [M + Na]⁺ 332.0853; found 332.0855.



3 CONJUGATED ENYNES AND CYCLIC NITRONATES

1-methoxy-2-(5-methyl-1,3-dinitrohex-4-en-2-yl)benzene (3c)



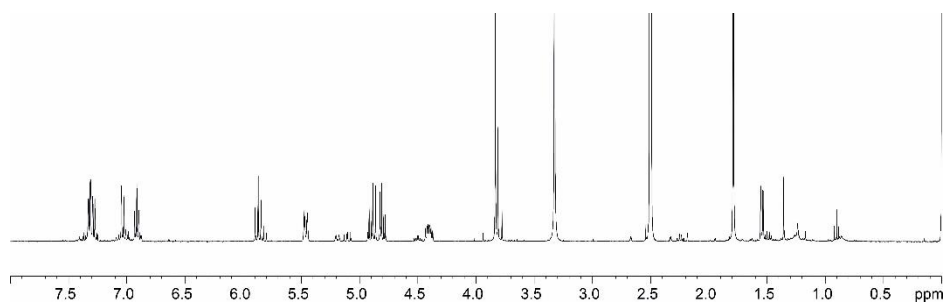
¹H NMR (400 MHz, CD₂Cl₂): δ [ppm] = 7.33 (ddd, J = 8.3 Hz, 7.5 Hz, 1.7 Hz, 1H), 7.11 (dd, J = 7.5, 1.7), 6.95 (dd, J = 8.4 Hz, 1.3 Hz, 1H), 6.91 (td, J = 7.5 Hz, 1.2 Hz, 1H), 5.96 (5.84) (t (t), J = 10.4 Hz (9.8 Hz), 1H), 5.44 (5.23) (dq (dq), J = 10.2 Hz, 1.5 Hz (9.9 Hz, 1.4 Hz), 1H), 4.84/4.64 (5.07/~4.62) (dd/dd (dd/dd), J = 13.2 Hz, 8.4 Hz /13.2 Hz, 5.1 Hz, (13.1 Hz, 9.8 Hz /13.0 Hz, 4.4 Hz), 2H), 4.26 (~4.29) (dq, J = 8.5 Hz, 5.3 Hz, 1H), 3.91 (3.86) (s (s), 3H), 1.84 (d, J = 1.5 Hz, 6H), (1.63) (d, J = 1.5 Hz, 3H), (1.61) (d, J = 1.5 Hz, 3H).

¹H NMR (400 MHz, DMSO-d₆): δ [ppm] = 7.31 (7.31) (dd, J = 7.5 Hz 1.7 Hz), 1H), 7.29 (7.29) (ddd, J = 7.9 Hz, 7.9 Hz, 1.6 Hz, 1H), 7.03 (7.00) (dd (dd), J = 8.3 Hz, 0.7 Hz (8.2 Hz, 0.7 Hz), 1H), 6.91 (6.91) (ddd, J = 7.4 Hz, 7.4 Hz, 1.0 Hz, 1H), 5.87 (5.82) (dd (dd), J = 10.2 Hz, 10.2 Hz (9.9 Hz, 9.9 Hz), 1H), 5.46 (5.19) (dq (dq), J = 9.9 Hz, 1.4 Hz, 1.4 Hz (9.9 Hz, 1.4 Hz, 1.4 Hz), 1H), 4.89/4.80 (5.11/4.91) (dd/dd (dd), J = 13.4 Hz, 8.8 Hz/13.4 Hz, 5.6 Hz (13.3 Hz, 10.1 Hz), 2H), 4.40 (4.50) (ddd (ddd), J = 10.2 Hz, 8.8 Hz, 5.7 Hz (9.9 Hz, 9.9 Hz, 4.7 Hz), 1H), 3.83 (3.81) (s (s), 3H) 1.79 (1.55) (d (d), J = 1.4 Hz (1.4 Hz), 3H), 1.79 (1.53) (d (d), J = 1.4 Hz (1.3 Hz), 3H).

¹³C NMR (400 MHz, DMSO-d₆): δ [ppm] = 149.9 (150.3), 145.0 (142.7), 129.6 (129.6), 129.4 (129.4), 122.7 (122.4), 120.6 (120.6), 117.1 (117.3), 111.7 (111.4), 86.0 (85.5), 75.5 (75.8), 55.7 (55.6), 42.2 (41.3), 25.4 (25.1), 18.3 (17.8).

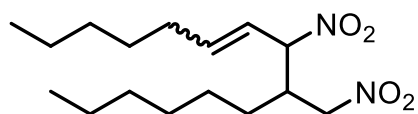
HRMS (ESI): calcd. for C₁₄H₁₈N₂O₅ [M + Na]⁺ 317.1108; found 317.1112.

Spectrum in DMSO-d₆



3 CONJUGATED ENYNES AND CYCLIC NITRONATES

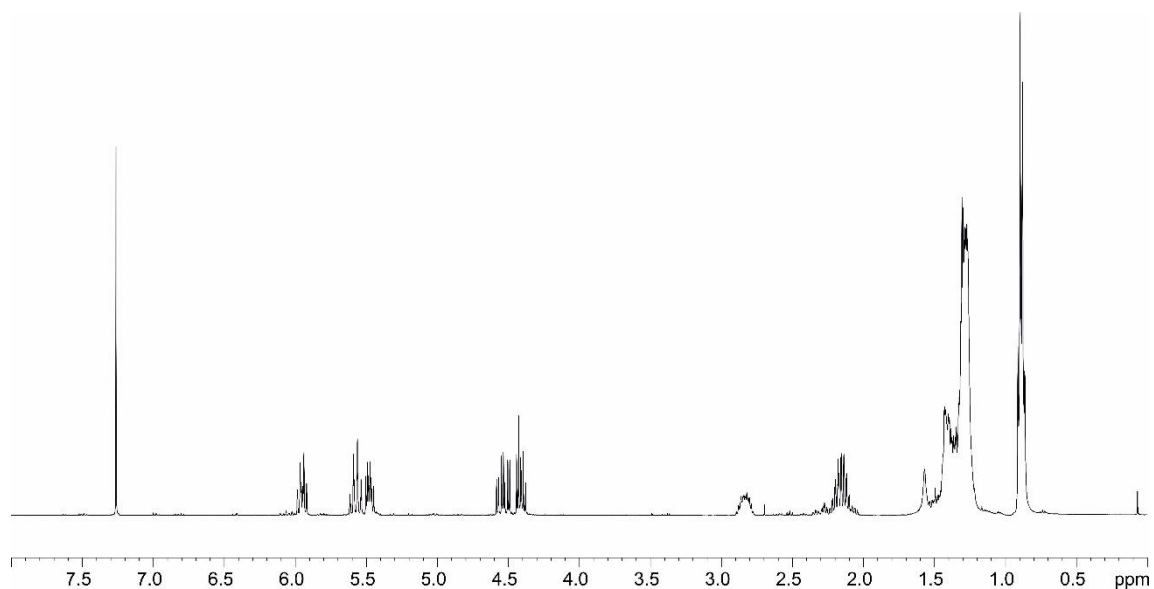
8-nitro-9-(nitromethyl)pentadec-6-ene **D1** and **D2** (**3d**)



^1H NMR of **D1** and **D2** of **3d-Z** (400 MHz, CDCl_3): δ [ppm] = 5.95 (dt, J = 10.5 Hz, 7.7 Hz, 1H), 5.52-5.62 (m, 1H), 5.43-5.1 (m, 1H), 4.55/4.42/4.50/4.40 (m, 2H), 1.2-1.43 (m, 16H), 0.84-0.92 (m, 6H).

^{13}C NMR of **D1** and **D2** of **3d-Z** (400 MHz, CDCl_3): δ [ppm] = 141.6, 141.0, 120.7, 120.3, 85.5, 84.4, 75.0, 74.4, 40.9, 40.8, 31.42, 31.40, 31.34, 31.32, 28.96, 28.92, 28.65, 28.62, 28.0, 27.92, 27.91, 27.6, 26.3, 26.2, 22.48, 22.47, 22.41, 14.0, 13.9.

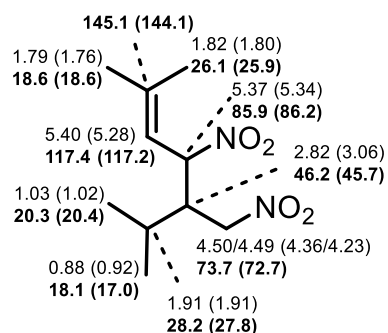
HRMS (ESI): calcd. for $\text{C}_{16}\text{H}_{30}\text{N}_2\text{O}_4$ $[\text{M} + \text{H}]^+$ 315.2278; found 315.2282.



3 CONJUGATED ENYNES AND CYCLIC NITRONATES

2,6-dimethyl-4-nitro-5-(nitromethyl)hept-2-ene D1 (D2) (3e)

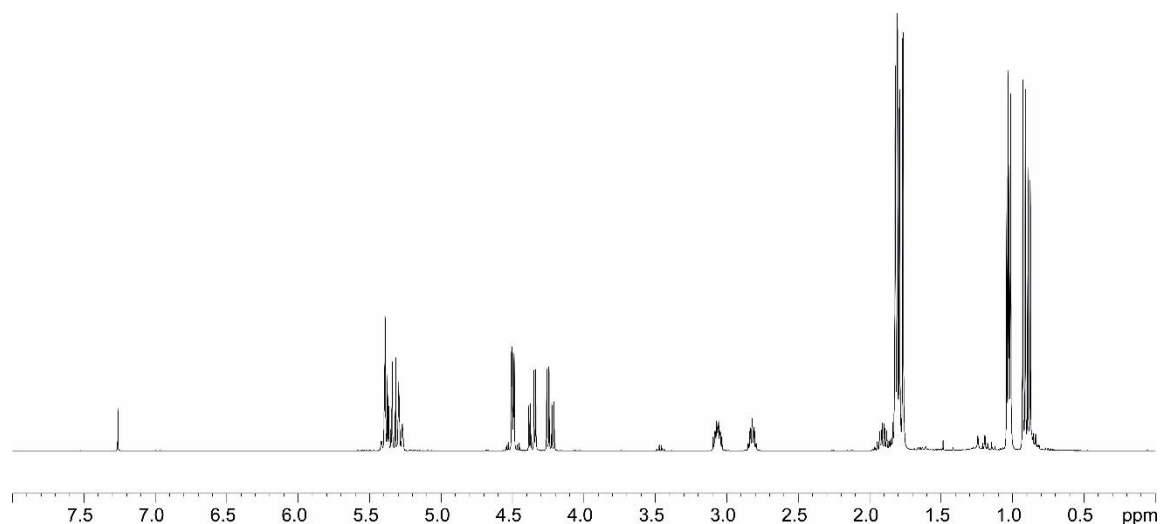
400 MHz, in CDCl₃



¹H NMR (400 MHz, CDCl₃): δ [ppm] = 5.40 (5.28) (m, 1H), 5.37 (5.34) (m, 1H), 4.50/4.49 (4.36/4.23) (m, (dd/dd, J = 14.2 Hz, 4.9 Hz/14.2, 6.5 Hz), 2H), 2.82 (3.06) (m, 1H), 1.91 (1.91) (m, 1H), 1.82 (1.80) (d (d), J = 1.3 Hz (1.3 Hz), 3H), 1.79 (1.76) (d (d), J = 1.2 Hz (1.3 Hz), 3H), 1.03 (1.02) (d (d), J = 6.9 Hz (6.9 Hz), 3H), 0.88 (0.92) (d (d), J = 6.9 Hz (7.0 Hz), 3H).

¹³C NMR (400 MHz, CDCl₃): δ [ppm] = 145.1 (144.1), 117.4 (117.2), 85.9 (86.2), 73.7 (72.7), 46.2 (45.7), 28.2 (27.8), 26.1 (25.9), 20.3 (20.4), 18.6 (18.6), 18.1 (17.0).

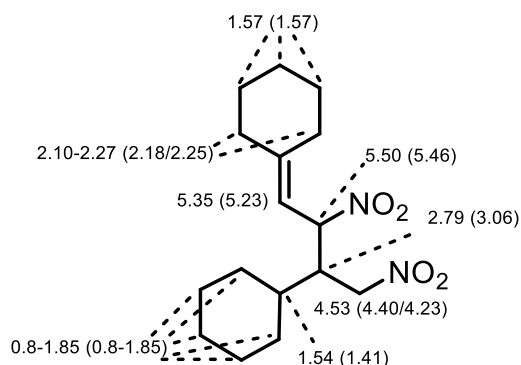
HRMS (ESI): calcd. for C₁₀H₁₈N₂O₄ [M + Na]⁺ 253.1159; found 253.1161



3 CONJUGATED ENYNES AND CYCLIC NITRONATES

(3-cyclohexyl-2,4-dinitrobutylidene)cyclohexane **D1** (**D2**)(3f)

400 MHz, in CDCl₃

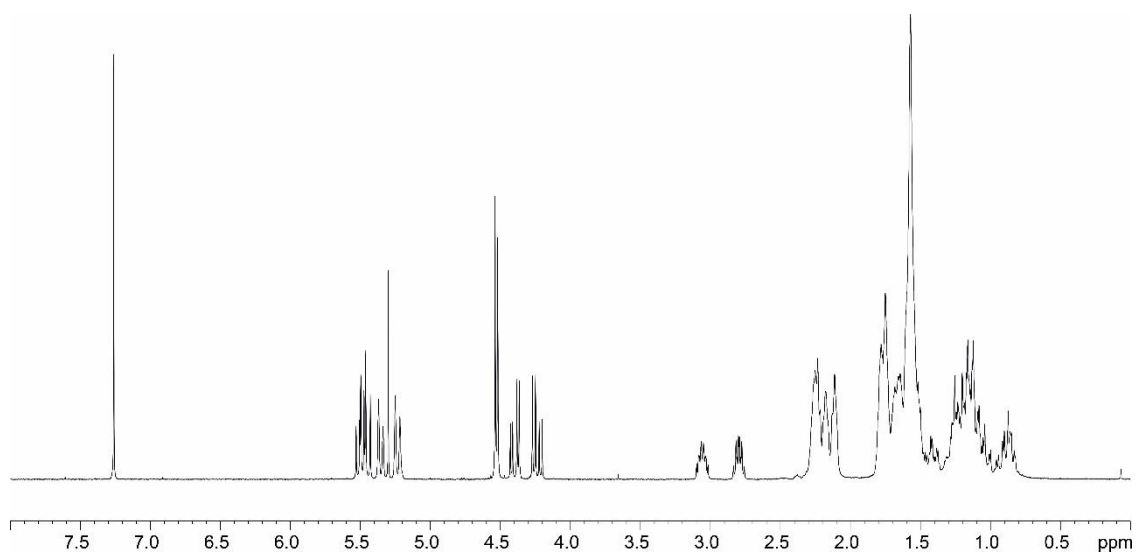


¹H NMR of **D1** (**D2**) (400 MHz, CDCl₃): δ [ppm] = 5.50 (5.46) (dd (t), J = 9.6 Hz, 7.4 Hz (10.0 Hz), 1H), 5.35 (5.23) (dt (dt), J = 9.5 Hz, 1.2 Hz (10.1 Hz, 1.2 Hz), 1H), 4.53 (4.40/4.23) (d (dd/dd), J = 5.4 Hz (14.2 Hz, 4.9 Hz/14.2 Hz, 6.4 Hz), 2H), 2.79 (3.06) (m (m), 1H), 2.10-2.27 (2.18/2.25) (m (m), 4H), 0.8-1.85 (0.8-1.85) (m (m), 17H).

¹³C NMR of **D1** and **D2** (400 MHz, CDCl₃): δ [ppm] = 152.4, 151.3, 114.0, 113.8, 84.9, 84.7, 74.0, 73.4, 46.2, 45.4, 38.5, 38.3, 37.3, 37.2, 30.9, 30.7, 29.8, 29.7, 28.8, 28.3, 28.0, 27.9, 27.7, 27.6, 26.44, 26.39, 26.38, 26.36, 26.35, 26.2, 26.1.

HRMS (ESI): calcd. for C₁₆H₂₆N₂O₄ [M + Na]⁺ 333.1785; found 333.1785.

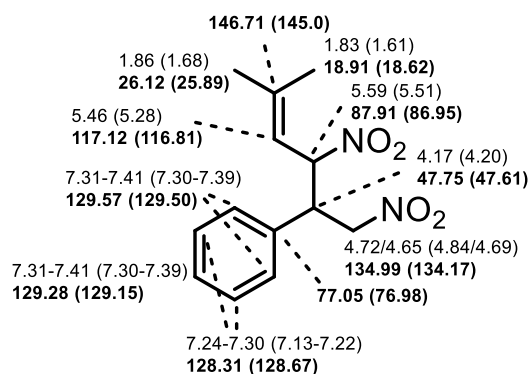
Spectrum in CDCl₃



3 CONJUGATED ENYNES AND CYCLIC NITRONATES

(5-methyl-1,3-dinitrohex-4-en-2-yl)benzene D1 (D2) (3g)

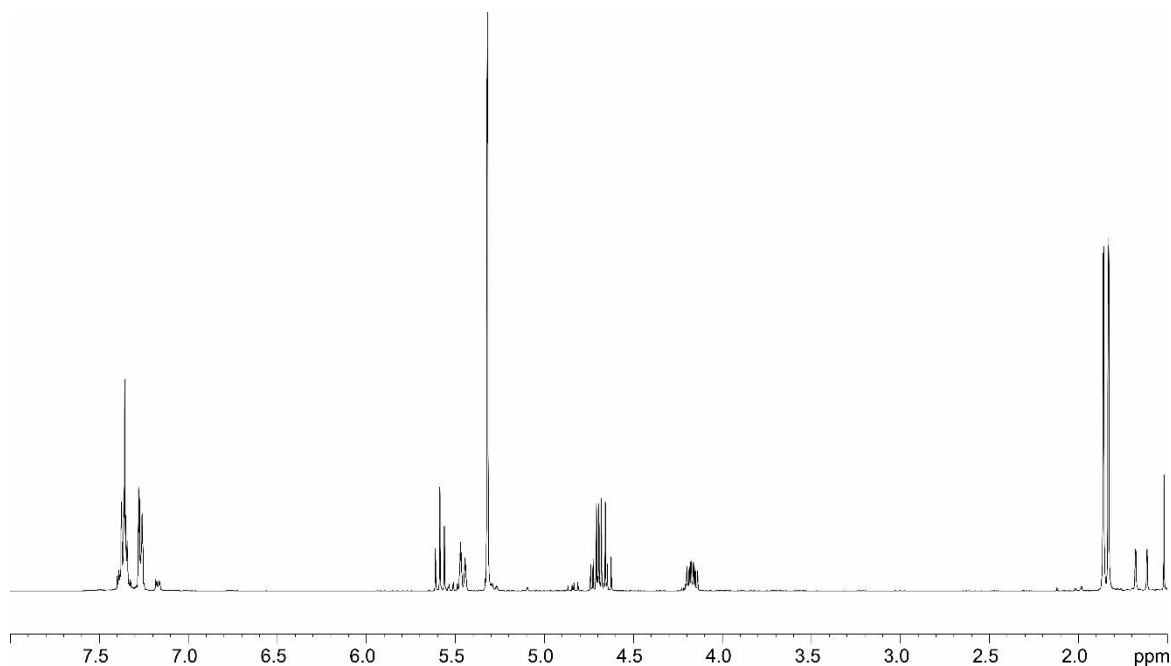
400 MHz, in CD₂Cl₂



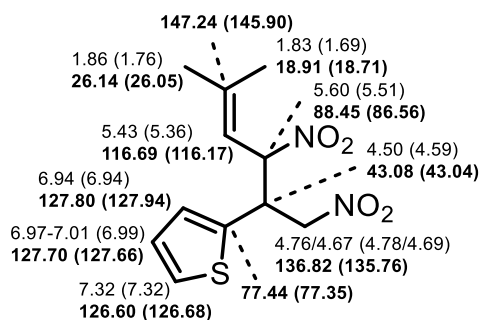
¹H NMR (400 MHz, CD₂Cl₂): δ [ppm] = 7.31-7.41 (7.30-7.39) (m, 3H), 7.24-7.30 (7.13-7.22) (m, 2H), 5.59 (5.51) (t (dd), J = 9.8 Hz (9.9 Hz, 7.9 Hz), 1H), 5.46 (5.28) (dspet (dsept), J = 10.0 Hz, 1.5 Hz (9.8 Hz, 1.5 Hz), 1H), 4.72/4.65 (4.84/4.69) (dd/dd (dd/dd), J = 13.2 Hz, 5.5 Hz/13.2 Hz, 8.8 Hz (13.3 Hz, 9.4 Hz/13.3 Hz, 5.2 Hz), 2H), 4.17 (4.20) (m, 1H), 1.86 (d (d), J = 1.5 Hz (1.5 Hz), 1.68) (3H), 1.83 (1.61) (d (d), J = 1.5 Hz (1.5 Hz), 3H).

¹³C NMR (400 MHz, CD₂Cl₂): δ [ppm] = 146.71 (145.0), 134.99 (134.17), 129.57 (129.50), 129.28 (129.15), 128.31 (128.67), 117.12 (116.81), 87.91 (86.95), 77.05 (76.98), 47.75 (47.61), 26.12 (25.89), 18.91 (18.62).

HRMS (ESI): calcd. for C₁₃H₁₆N₂O₄ [M + Na]⁺ 287.1002; found 287.1003.



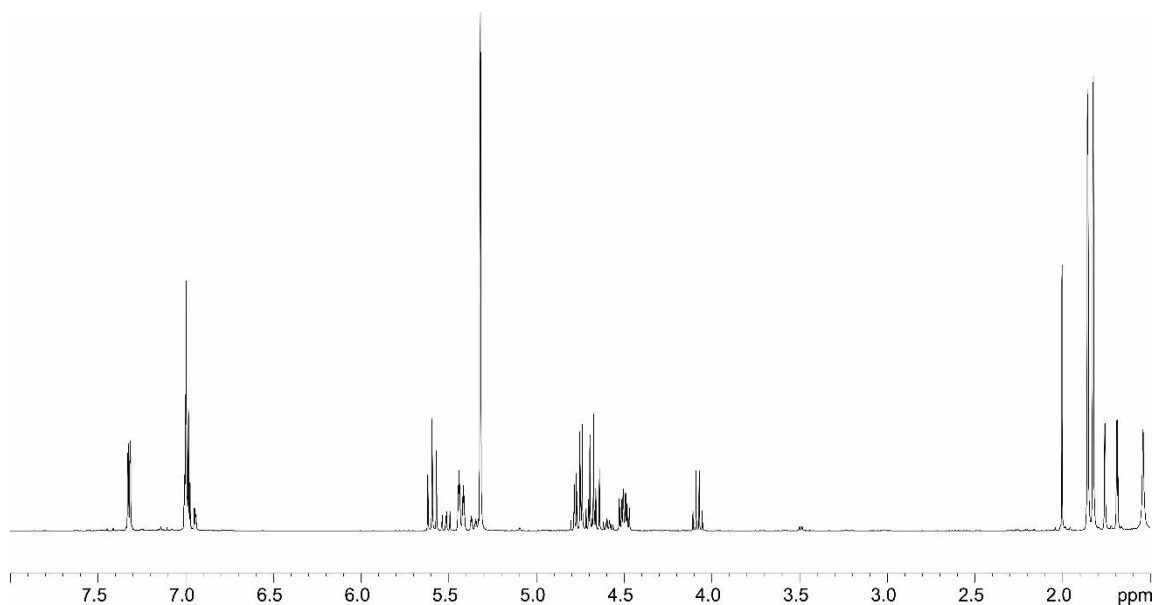
2-(5-methyl-1,3-dinitrohex-4-en-2-yl)thiophene D1 (D2) (3h)

400 MHz, in CD₂Cl₂

¹H NMR (400 MHz, CD₂Cl₂): δ [ppm] = 7.32 (7.32) (m, 1H), 6.97-7.01 (6.99) (m, 1H), 6.94 (6.94) (m, 1H), 5.60 (5.51) (t (dd), J = 9.8 Hz (9.9 Hz, 7.9 Hz), 1H), 5.43 (5.36) (dsept (dsept), J = 10.0 Hz, 1.5 Hz (9.9 Hz, 1.5 Hz), 1H), 4.76/4.67 (4.78/4.69) (dd/dd (dd/dd), J = 13.4 Hz, 5.5Hz/13.4 Hz, 8.3 Hz (13.4 Hz, 8.8 Hz/13.4 Hz, 5.4 Hz), 2H), 4.50 (4.59) (m, 1H), 1.86 (1.76) (d (d), J = 1.5 Hz (1.5 Hz), 3H), 1.83 (1.69) (d (d), J = 1.5 Hz (1.5 Hz), 3H).

¹³C NMR (400 MHz, CD₂Cl₂): δ [ppm] = 147.24 (145.90), 136.82 (135.76), 127.80 (127.94), 127.70 (127.66), 126.60 (126.68), 116.69 (116.17), 88.45 (86.56), 77.44 (77.35), 43.08 (43.04), 26.14 (26.05), 18.91 (18.71).

HRMS (ESI): calcd. for C₁₁H₁₄N₂O₄S [M + H]⁺ 271.0747; found 271.0746.

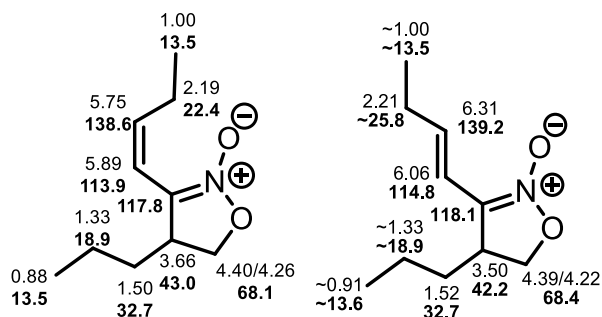


3 CONJUGATED ENYNES AND CYCLIC NITRONATES

3.7.14.3 Cyclic Nitronate

(but-1-enyl)-4-propyl-4,5-dihydroisoxazole 2-oxide (6a)

600 MHz, in DMSO-d₆



HRMS (ESI): calcd. for C₁₀H₁₇NO₂ [M + H]⁺ 184.1332; found 184.1332.

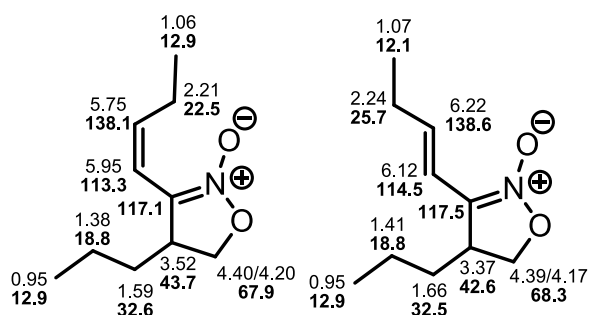
6a Z: ¹H NMR (600 MHz, DMSO-d₆): δ [ppm] = 5.89 (ddd, J = 11.9 Hz, 1.7 Hz, 1.0 Hz, 1H), 5.75 (dt, J = 11.9 Hz, 7.7 Hz, 1H), 4.40/4.26 (dd/dd, J = 8.0 Hz, 8.0 Hz / 7.7 Hz, 3.1 Hz, 2H), 3.66 (m, 1H), 2.19 (m, 2H), 1.50 (m, 2H), 1.33 (m, 2H), 1.00 (3H), 0.88 (3H).

6a Z: ¹³C NMR (600 MHz, DMSO-d₆): δ [ppm] = 138.6, 117.8, 113.9, 68.1, 43.0, 32.7, 22.4, 18.9, 13.5.

6a E: ¹H NMR (600 MHz, DMSO-d₆): δ [ppm] = 6.31 (dt, J = 16.0 Hz, 6.7 Hz, 1H), 6.06 (dt, J = 16.0 Hz, 1.4 Hz, 1H), 4.39/4.22 (dd/dd, J = 8.2 Hz, 8.2 Hz / 7.8 Hz, 3.3 Hz, 2H), 3.50 (m, 1H), 2.21 (m, 2H), 1.52 (m, 2H), ~1.33 (m, 2H), ~1.00 (3H), ~0.91 (3H).

6a E: ¹³C NMR (600 MHz, DMSO-d₆): δ [ppm] = 139.2, 118.1, 114.8, 68.4, 42.2, 32.7, ~25.8, ~18.9, ~13.6, ~13.5.

600 MHz, in CD₂Cl₂



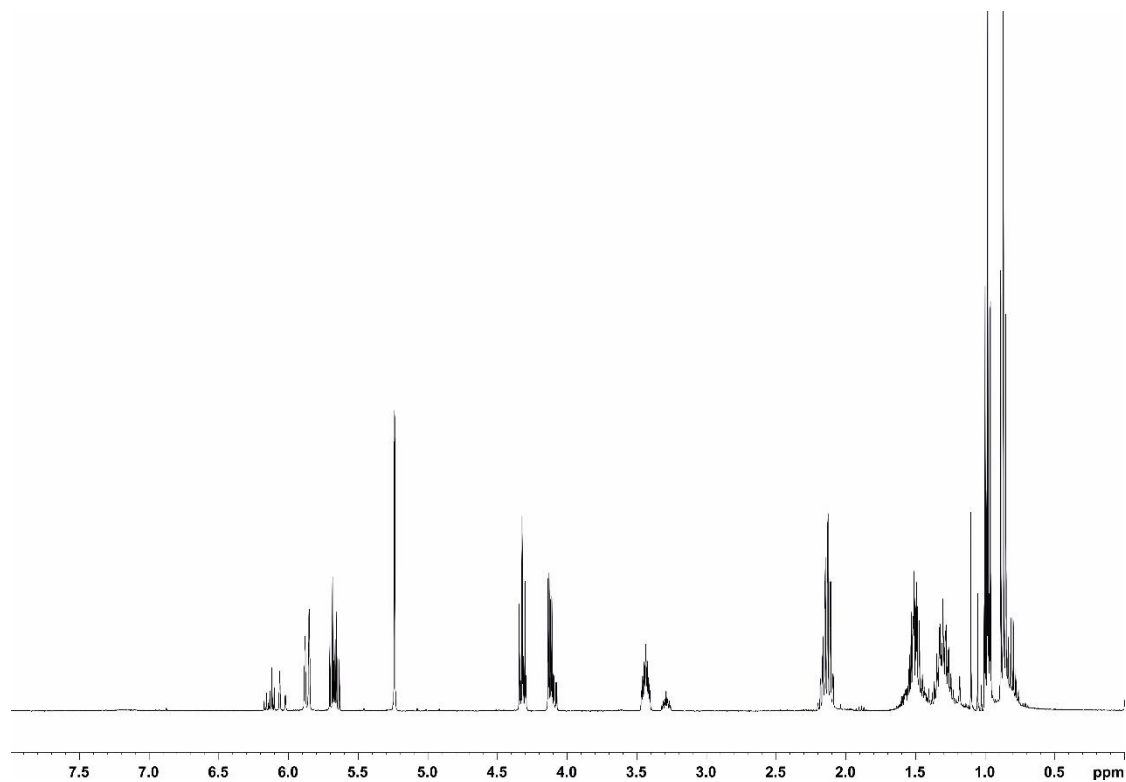
6a Z: ¹H NMR (600 MHz, CD₂Cl₂): δ [ppm] = 5.95 (ddd, J = 11.9 Hz, 2.7 Hz, 1.8 Hz, 1H), 5.75 (dt, 11.9 Hz, 7.6 Hz, 1H), 4.40/4.20 (t/dd, J = 8 Hz/7.8 Hz, 3.2 Hz, 2H), 3.52 (m, 1H), 2.21 (m, 2H), 1.59 (m, 2H), 1.38 (m, 2H), 1.06 (t, J = 7.4 Hz, 3H), 0.95 (t, J = 7.3 Hz, 3H).

6a Z: ¹³C NMR (600 MHz, CD₂Cl₂): δ [ppm] = 138.1, 117.1, 113.3, 67.9, 43.7, 32.6, 22.5, 18.8, 12.9.

3 CONJUGATED ENYNES AND CYCLIC NITRONATES

6a E: ^1H NMR (600 MHz, CD_2Cl_2): δ [ppm] = 6.22 (dt, $J = 16.1$ Hz, 6.3 Hz, 1H), 6.12 (d, $J = 16.2$ Hz, 1H), 4.39/4.17 (t/dd, $J = 8.2$ Hz/7.8 Hz, 3.3 Hz, 2H), 3.37 (m, 1H), 2.24 (m, 2H), 1.66 (m, 2H), 1.41 (m, 2H), 1.07 (t, $J = 7.4$ Hz, 3H), 0.95 (3H).

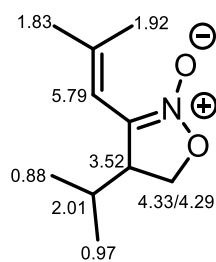
6a E: ^{13}C NMR (600 MHz, CD_2Cl_2): δ [ppm] = 138.6, 117.5, 114.5, 68.3, 42.6, 32.5, 25.7, 18.8, 12.9, 12.1.



3 CONJUGATED ENYNES AND CYCLIC NITRONATES

4-isopropyl-5-(2-methylprop-1-en-1-yl)-3,4-dihydro-2H-pyrrole 1-oxide (6b)

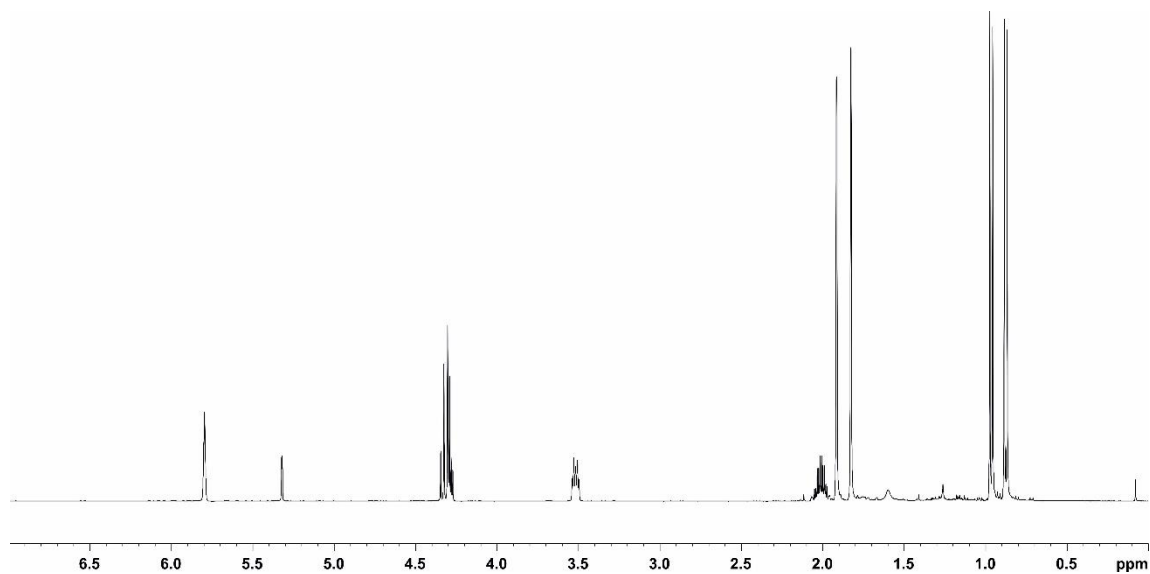
400 MHz, in CD₂Cl₂



6b ¹H NMR (600 MHz, CD₂Cl₂): δ [ppm] = 5.79 (m, 1H), 4.33/4.29 (d, J = 8.0 Hz, 1H/dd, J = 8.0 Hz, 3.8 Hz, 1H), 3.52 (dtd, 8.8 Hz, 3.8 Hz, 1.2 Hz, 1H), 2.01 (m, 1H), 1.92 (d, J = 1.7 Hz, 3H), 1.83 (d, J = 1.4 Hz, 1H), 0.97 (d, J = 7.0 Hz, 3H), 0.88 (d, J = 6.9 Hz, 3H).

¹³C NMR (400 MHz, CD₂Cl₂): δ [ppm] = 142.9, 117.5, 112.0, 64.9, 50.6, 29.5, 27.3, 20.8, 19.9, 16.5.

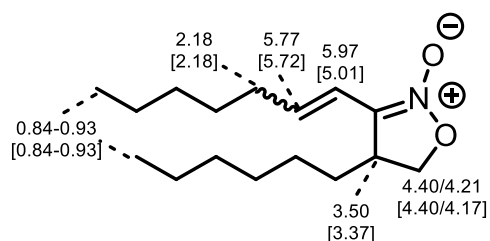
HRMS (ESI): calcd. for C₁₀H₁₇NO₂ [M + H]⁺ 184.1332; found 184.1335.



3 CONJUGATED ENYNES AND CYCLIC NITRONATES

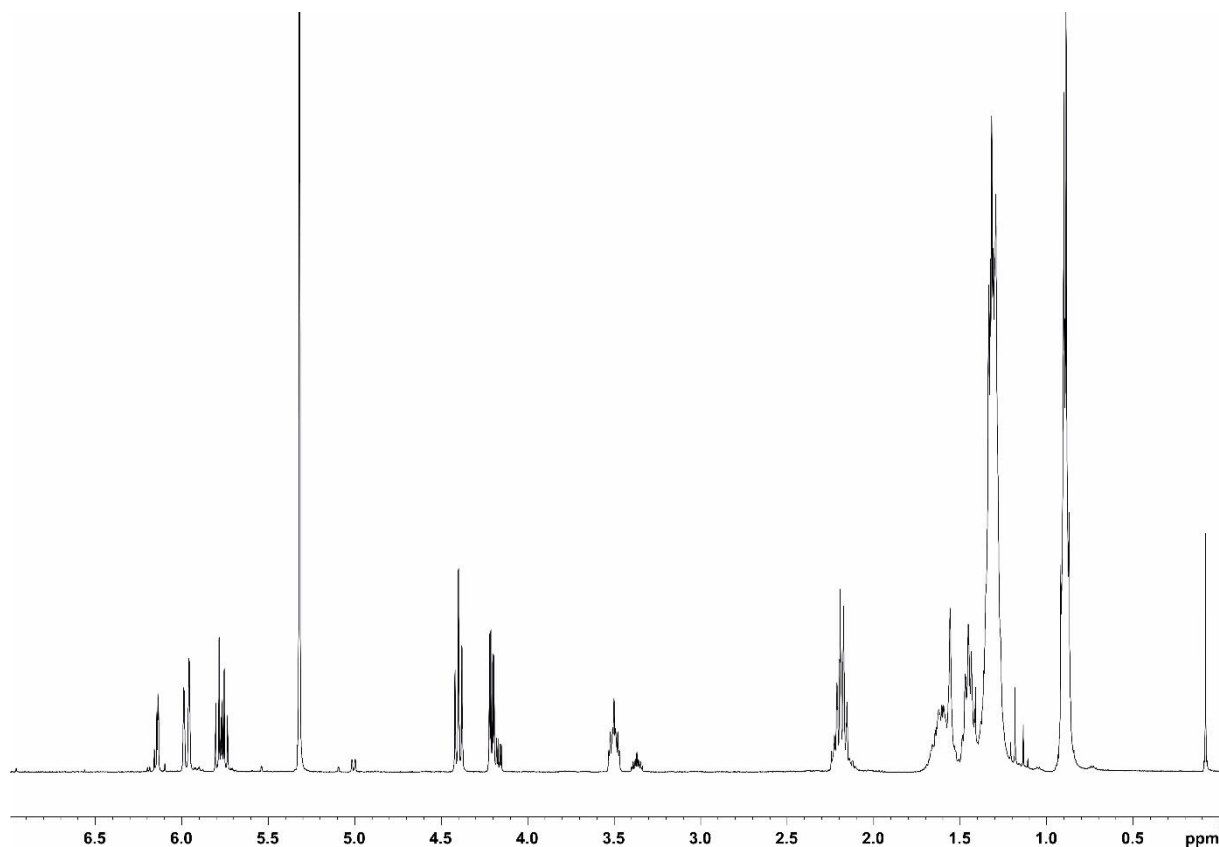
3-(hept-1-en-1-yl)-4-hexyl-4,5-dihydroisoxazole 2-oxide (6c *E* and [6c *Z*])

400 MHz, in CD₂Cl₂



6c *E* and [6c *Z*] ¹H NMR (600 MHz, CD₂Cl₂): δ [ppm] = 5.97 [5.01] (ddd [dd], J = 12.0 Hz, 1.8 Hz, 0.8 Hz [7.4 Hz, 1.2 Hz], 1H), 5.77 [5.72] (dt, J = 12.0 Hz, 7.7 Hz, 1H), 4.40/4.21 [4.40/4.17] (t/dd [t/dd], J = 8 Hz/7.7 Hz, 3.2 Hz [8 Hz/7.7 Hz, 3.3 Hz], 2H), 3.50 [3.37] (m [m], 2H), 2.18 [2.18] (m [m], 2H), 1.2-1.76 [1.2-1.76] (16H), 0.84-0.93 [0.84-0.93] (6H).

HRMS (ESI): calcd. for C₁₆H₂₉NO₂ [M + H]⁺ 268.2271; found 268.2279.

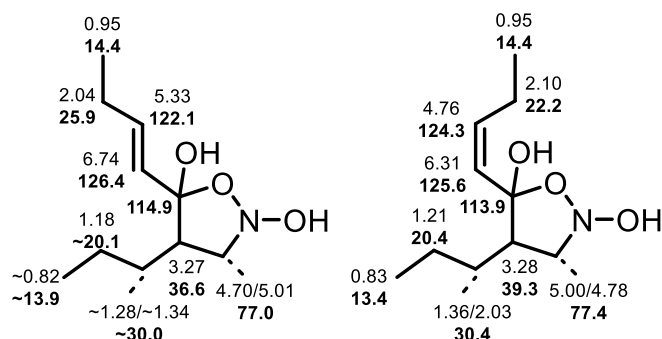


3 CONJUGATED ENYNES AND CYCLIC NITRONATES

3.7.14.4 Intermediate 4a

5-(but-1-en-1-yl)-4-propylisoxazolidine-2,5-diol (4a)

600 MHz, during *in situ* NMR reaction monitoring in DMSO-d₆

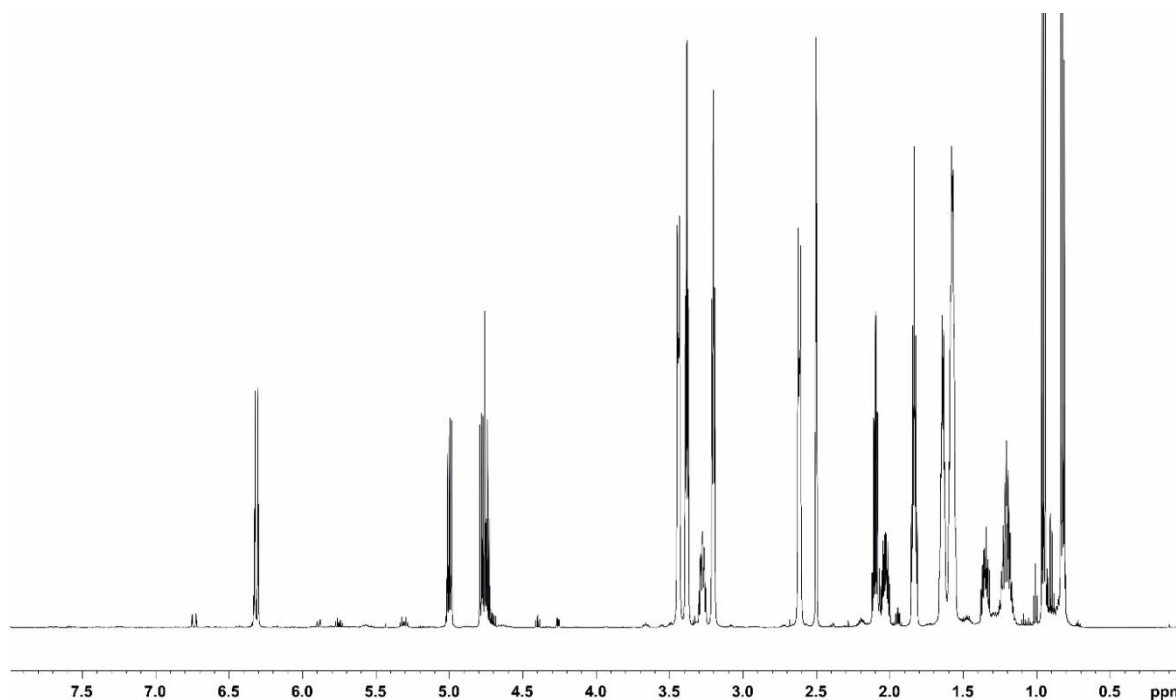


4a E: ¹H NMR (600 MHz, DMSO-d₆): δ [ppm] = 6.74 (dt, J = 16.0 Hz, 1.6 Hz, 1H), 5.33 (dt, J = 16.0 Hz, 6.7 Hz, 1H), 4.70/5.01 (dd/dd, J = 12.0 Hz, 6.8 Hz/12.0 Hz, 7.5 Hz, 2H), 3.27 (m, 1H), 2.04 (m, 2H), ~1.28/~1.34 (m/m, 2H), 1.18 (m, 2H), 0.95 (t, J = 7.5 Hz, 3H), ~0.82 (t, J = 7.3 Hz, 3H).

4a E: ¹³C NMR (600 MHz, DMSO-d₆): δ [ppm] = 126.4, 122.1, 114.9, 77.0, 36.6, ~30.0, 25.9, ~20.1, 14.4, ~13.9.

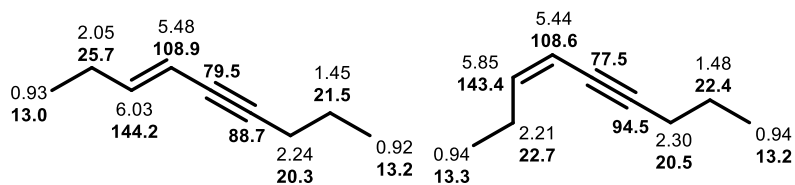
4a Z: ¹H NMR (600 MHz, DMSO-d₆): δ [ppm] = 6.31 (dt, J = 12.1 Hz, 1.9 Hz, 1H), 5.00/4.78 (dd/dd, J = 11.9 Hz, 6.3 Hz/11.9 Hz, 7.5 Hz, 2H), 4.76 (dt, J = 12.1 Hz, 7.3 Hz, 1H), 3.28 (m, 1H), 2.10 (quind, J = 7.4 Hz, 1.9 Hz, 2H), 1.36/2.03 (m/m, 2H), 1.21 (m, 2H), 0.95 (t, J = 7.5 Hz, 3H), 0.83 (t, J = 7.3 Hz, 3H).

4a Z: ¹³C NMR (600 MHz, DMSO-d₆): δ [ppm] = 125.6, 124.3, 113.9, 77.4, 39.3, 30.4, 22.2, 20.4, 14.4, 13.4.



3.7.14.5 Conjugated Enynes

non-3-en-5-yne (5a)

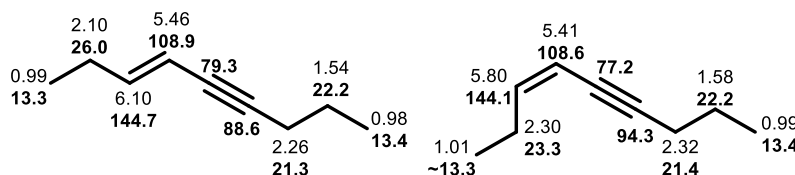
600 MHz, in DMSO-d₆

5a E: ¹H NMR (600 MHz, DMSO-d₆): δ [ppm] = 6.03 (dt, J = 15.9 Hz, 6.5 Hz, 1H), 5.48 (dqin, J = 15.9 Hz, 1.9 Hz, 1H), 2.24 (td, J = 7.1 Hz, 2.0 Hz, 2H), 2.05 (m, 2H), 1.45 (sext, J = 7.2 Hz, 2H), 0.93 (3H), 0.92 (3H).

5a E: ¹³C NMR (600 MHz, DMSO-d₆): δ [ppm] = 144.2, 108.9, 88.7, 79.5, 25.7, 21.5, 20.3, 13.2, 13.0.

5a Z: ¹H NMR (600 MHz, DMSO-d₆): δ [ppm] = 5.85 (dt, J = 10.4 Hz, 7.3 Hz, 1H), 5.44 (dqin, J = 10.4 Hz, 1.6 Hz, 1H), 2.30 (td, J = 7.0 Hz, 2.2 Hz, 2H), 2.21 (m, 2H), 1.48 (m, 2H), 0.94 (6H).

5a Z: ¹³C NMR (600 MHz, DMSO-d₆): δ [ppm] = 143.4, 108.6, 94.5, 77.5, 22.7, 22.4, 20.5, 13.3, 13.2.

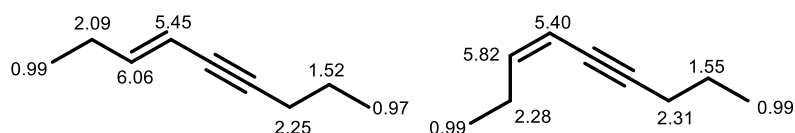
600 MHz, in CDCl₃

5a E: ¹H NMR (600 MHz, CDCl₃): δ [ppm] = 6.10 (dt, J = 15.9 Hz, 6.6 Hz, 1H), 5.46 (dqin, J = 15.8 Hz, 2.0 Hz, 1H), 2.26 (td, J = 7.0 Hz, 2.1 Hz, 2H), 2.10 (2H), 1.54 (m, 2H), 0.99 (t, J = 7.3 Hz, 3H), 0.98 (t, J = 7.3 Hz, 3H).

5a E: ¹³C NMR (600 MHz, CDCl₃): δ [ppm] = 144.7, 108.9, 88.6, 79.3, 26.0, 22.2, 21.3, 13.4, 13.3.

5a Z: ¹H NMR (600 MHz, CDCl₃): δ [ppm] = 5.80 (dt, J = 10.7 Hz, 7.4 Hz, 1H), 5.41 (dqin, J = 10.6 Hz, 1.6 Hz, 1H), 2.32 (m, 2H), 2.30 (m, 2H), 1.58 (m, 2H), ~1.01 (3H), ~0.99 (3H).

5a Z: ¹³C NMR (600 MHz, CDCl₃): δ [ppm] = 144.1, 108.6, 94.3, 77.2, 23.3, 22.2, 21.4, 13.4, ~13.3.

400 MHz, in CD₂Cl₂

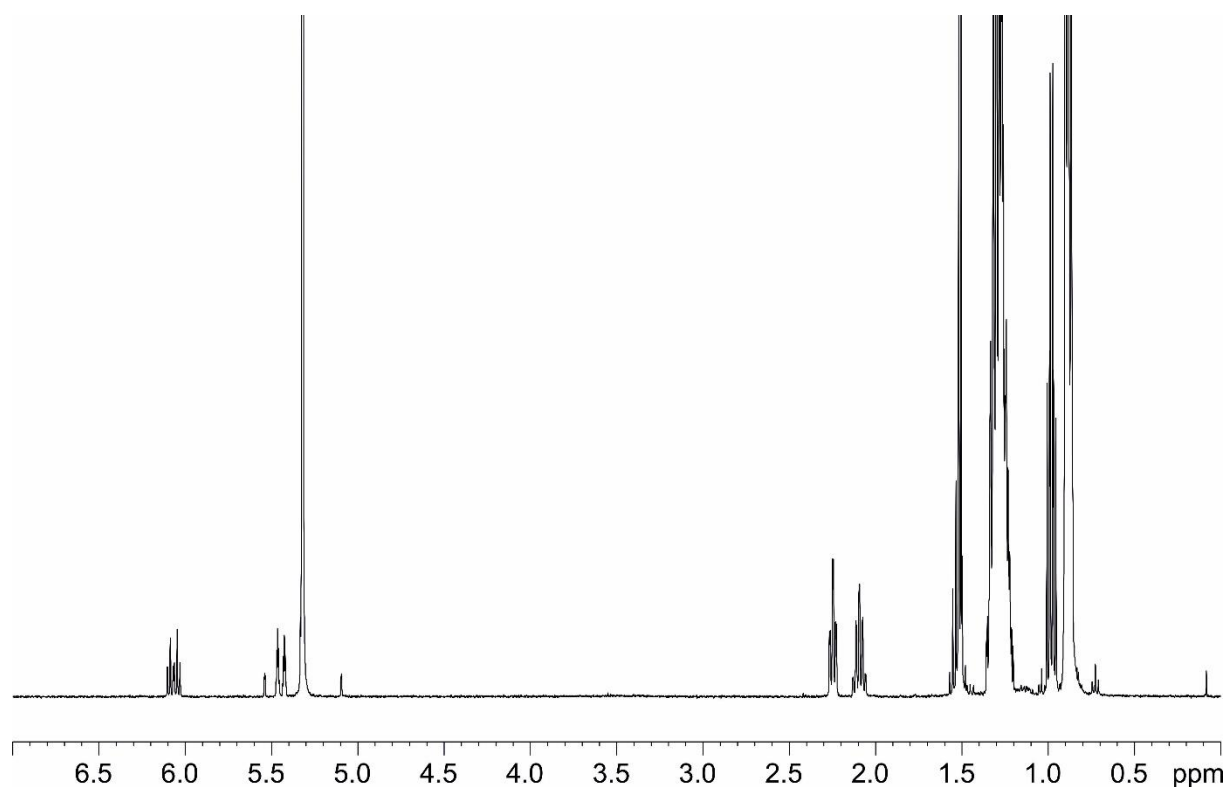
3 CONJUGATED ENYNES AND CYCLIC NITRONATES

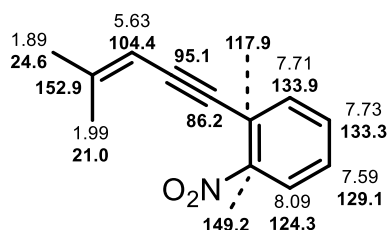
5a E: ^1H NMR (600 MHz, CDCl_3): δ [ppm] = 6.06 (dt, J = 15.9 Hz, 6.6 Hz, 1H), 5.45 (dq, J = 15.9 Hz, 2.0 Hz, 1H), 2.25 (td, J = 7.1 Hz, 2.2 Hz, 2H), 2.09 (m, 2H), 1.52 (sext, J = 7.2 Hz, 2H), 0.99 (t, J = 7.4 Hz, 3H), 0.97 (t, J = 7.3 Hz, 3H).

5a Z: ^1H NMR (600 MHz, CDCl_3): δ [ppm] = 5.82 (dt, J = 10.7 Hz, 7.3 Hz, 1H), 5.40 (dq, J = 10.7 Hz, 1.8 Hz, 1H), 2.31 (m, 2H), 2.28 (m, 2H), 1.55 (sext, J = 7.3 Hz, 2H), 0.99 (t, 7.4 Hz, 6H).

A chemical assignment can also be found in literature.^[24]

Spectrum in CD_2Cl_2

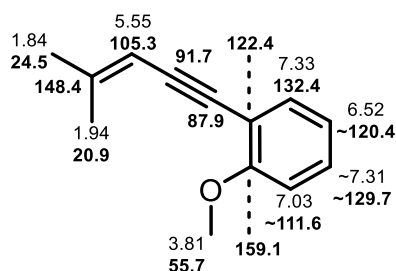


1-(4-methylpent-3-en-1-ynyl)-2-nitrobenzene (5b)600 MHz, in DMSO- d_6 (assignment during *in situ* NMR reaction monitoring)

^1H NMR (600 MHz, DMSO- d_6): δ [ppm] = 8.09 (1H), 7.73 (1H), 7.71 (1H), 7.59 (1H), 5.63 (1H), 1.99 (3H), 1.89 (3H).

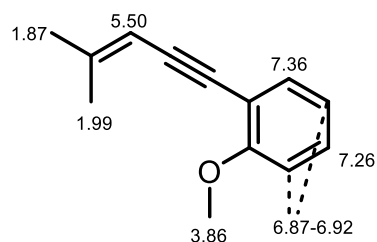
^{13}C NMR (600 MHz, DMSO- d_6): δ [ppm] = 152.9, 149.2, 133.9, 133.3, 129.1, 124.3, 117.9, 104.4, 95.1, 86.2, 24.6, 21.0.

HRMS (EI): calcd. for $\text{C}_{12}\text{H}_{11}\text{NO}_2$ $[\text{M}]^+$ 201.07843; found 201.07861.

1-methoxy-2-(4-methylpent-3-en-1-ynyl)benzene (5c)600 MHz, in DMSO- d_6 (assignment during *in situ* NMR reaction monitoring)

^1H NMR (600 MHz, DMSO- d_6): δ [ppm] = 7.33 (1H), ~7.31 (1H), 7.03 (1H), 6.52 (1H), 5.55 (1H), 3.81 (3H), 1.94 (3H), 1.84 (3H).

^{13}C NMR (600 MHz, DMSO- d_6): δ [ppm] = 159.1, 148.4, 132.4, ~129.7, 122.4, ~120.4, ~111.6, 105.3, 91.7, 87.9, 55.7, 24.5, 20.9.

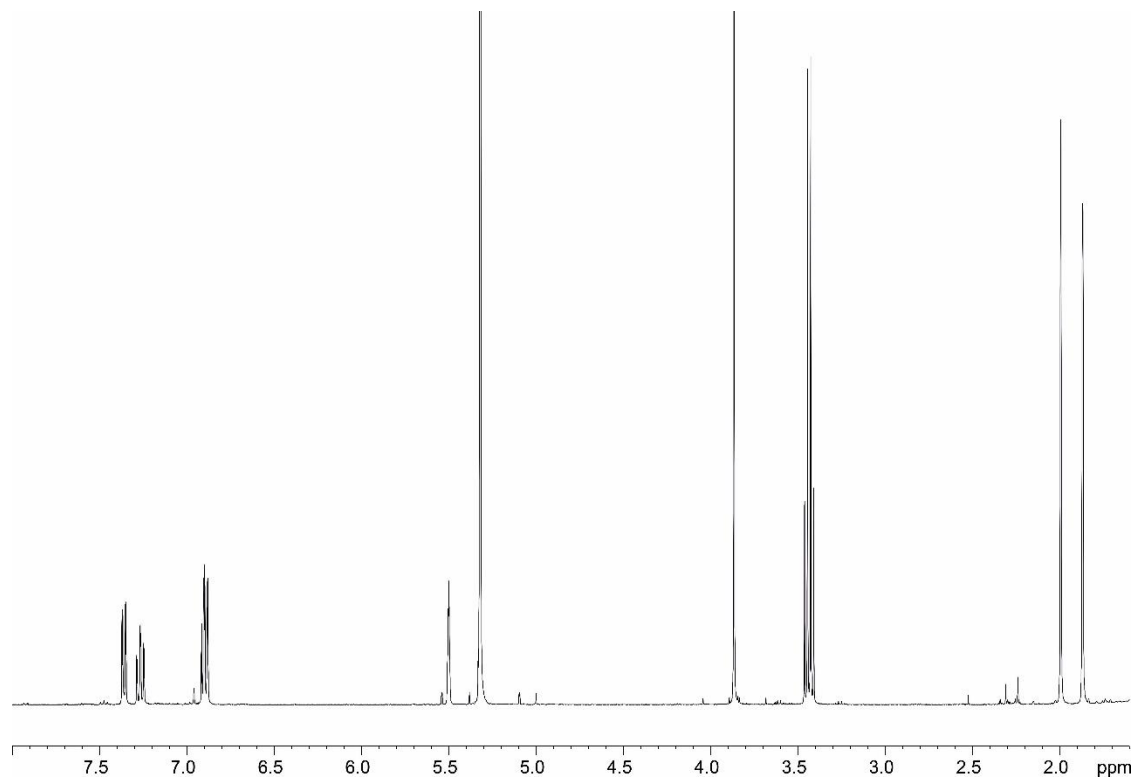
400 MHz, in CD_2Cl_2 

3 CONJUGATED ENYNES AND CYCLIC NITRONATES

^1H NMR (400 MHz, CD_2Cl_2): δ [ppm] = 7.36 (dd, J = 7.7 Hz, 1.8 Hz, 1H), 7.26 (m, 1H), 6.87-6.92 (m, 2H), 5.50 (sept, J = 1.4 Hz, 1H), 3.86 (s, 3H), 1.99 (d, J = 1.4 Hz, 3H), 1.87 (d, J = 1.5 Hz, 3H).

A chemical assignment can also be found in literature.^[25]

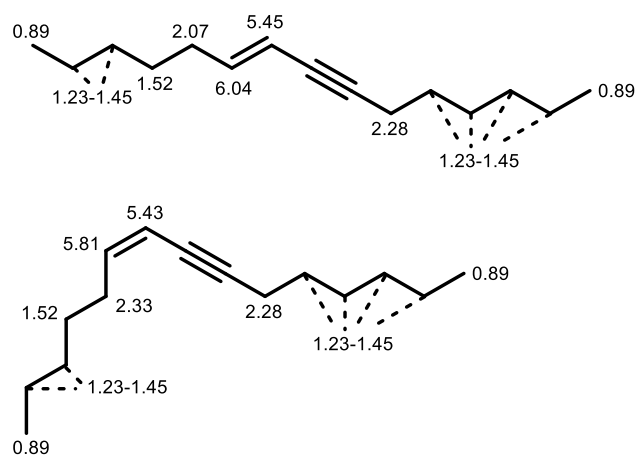
Spectrum in CD_2Cl_2



3 CONJUGATED ENYNES AND CYCLIC NITRONATES

Pentadec-6-en-8-yne (5d)

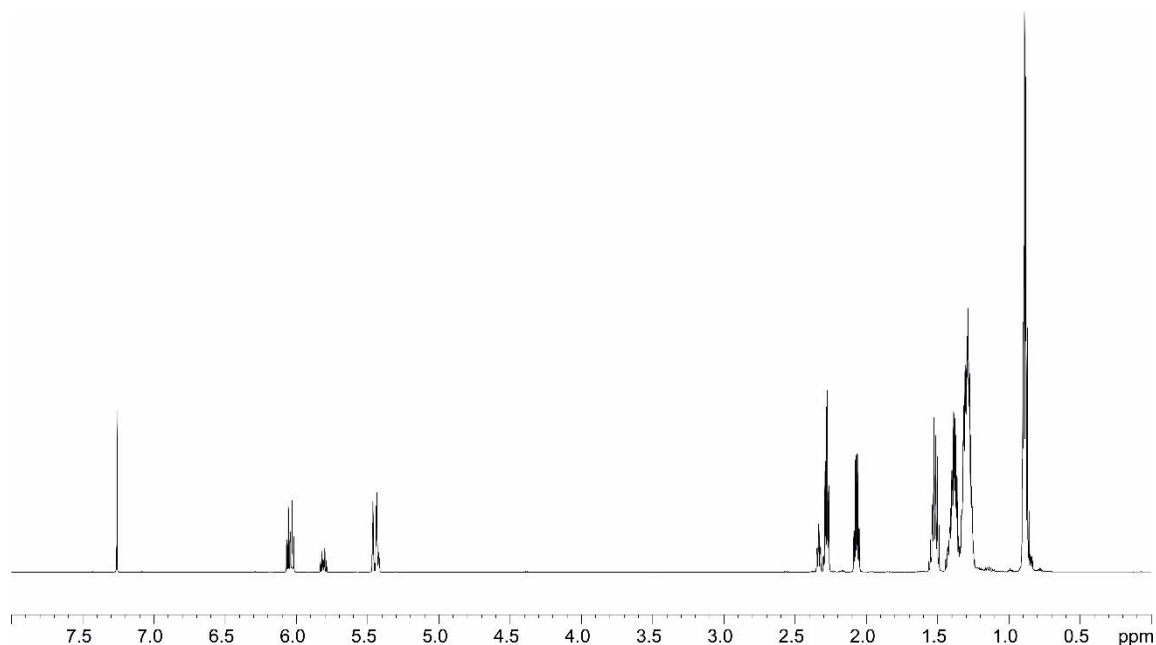
400 MHz, in CDCl₃



5d E ¹H NMR (400 MHz, CDCl₃): δ [ppm] = 6.04 (dt, J = 15.9 Hz, 7.0 Hz, 1H), 5.45 (dqin, J = 15.9 Hz, 1.9 Hz, 1H), 2.28 (m, 2H), 2.07 (ddd, J = 7.4 Hz, 7.2 Hz, 1.7 Hz, 2H), 1.52 (m, 2H), 1.23-1.45 (m, 12H), 0.89 (m, 6H).

5d Z ¹H NMR (400 MHz, CDCl₃): δ [ppm] = 5.81 (dt, J = 10.7 Hz, 7.3 Hz, 1H), 5.43 (m, 1H), 2.33 (td, J = 7.1 Hz, 2.2 Hz, 2H), 2.28 (m, 2H), 1.52 (m, 2H), 1.23-1.45 (m, 12H), 0.89 (m, 6H).

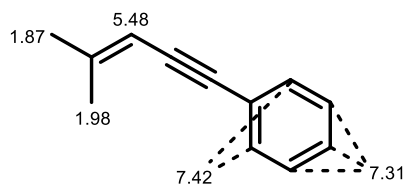
LRMS (FID): calcd. for C₁₅H₂₆ [M]⁺ 206.2; found 206.1.



3 CONJUGATED ENYNES AND CYCLIC NITRONATES

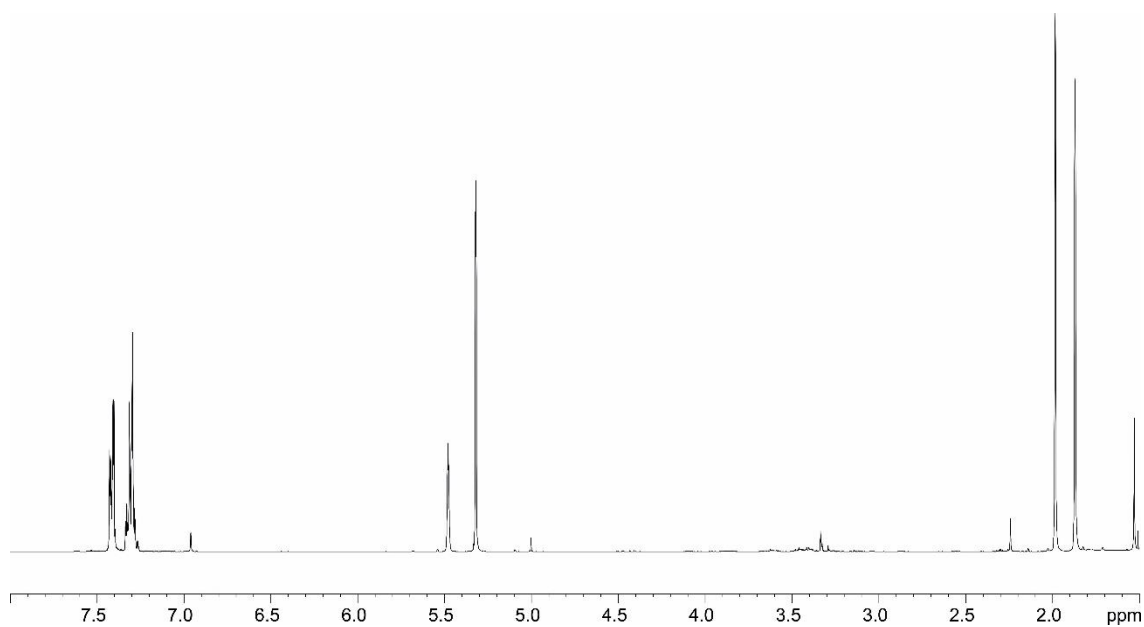
(4-methylpent-3-en-1-yn-1-yl)benzene (5e)

400 MHz, in CD₂Cl₂



¹H NMR (400 MHz, CD₂Cl₂): δ [ppm] = 7.42 (m, 2H), 7.31 (m, 3H), 5.48 (sept, J = 1.5 Hz, 1H), 1.98 (d, J = 1.5 Hz, 3H), 1.87 (d, J = 1.6 Hz, 3H).

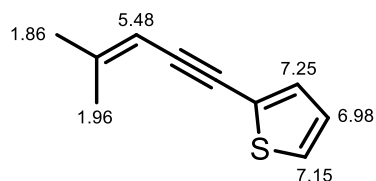
A chemical assignment can also be found in literature.^[22]



3 CONJUGATED ENYNES AND CYCLIC NITRONATES

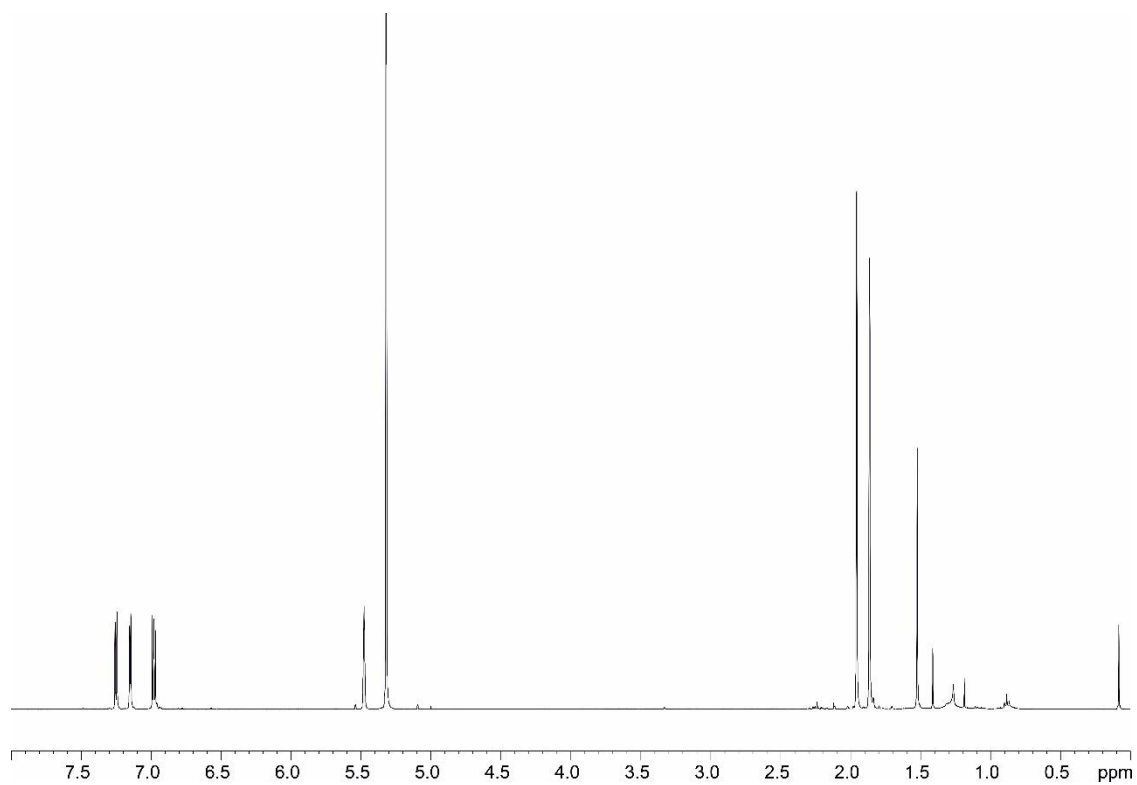
2-(4-methylpent-3-en-1-yn-1-yl)thiophene (5f)

400 MHz, in CD₂Cl₂



¹H NMR (400 MHz, CD₂Cl₂): δ [ppm] = 7.25 (dd, J = 5.2 Hz, 1.3 Hz, 1H), 7.15 (dd, J = 3.6 Hz, 1.3 Hz, 1H), 6.98 (dd, J = 5.2 Hz, 3.6 Hz, 1H), 5.48 (sept, J = 1.4 Hz, 1H), 1.96 (d, J = 1.3 Hz, 3H), 1.86 (d, J = 1.7 Hz, 3H).

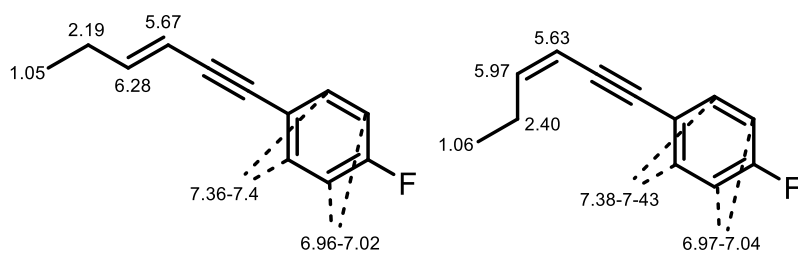
HRMS (EI): calcd. for C₁₀H₁₀S [M]⁺ 162.04977; found 162.04981.



3 CONJUGATED ENYNES AND CYCLIC NITRONATES

1-fluoro-4-(hex-3-en-1-yn-1-yl)benzene (**5g**)

400 MHz, in CDCl₃



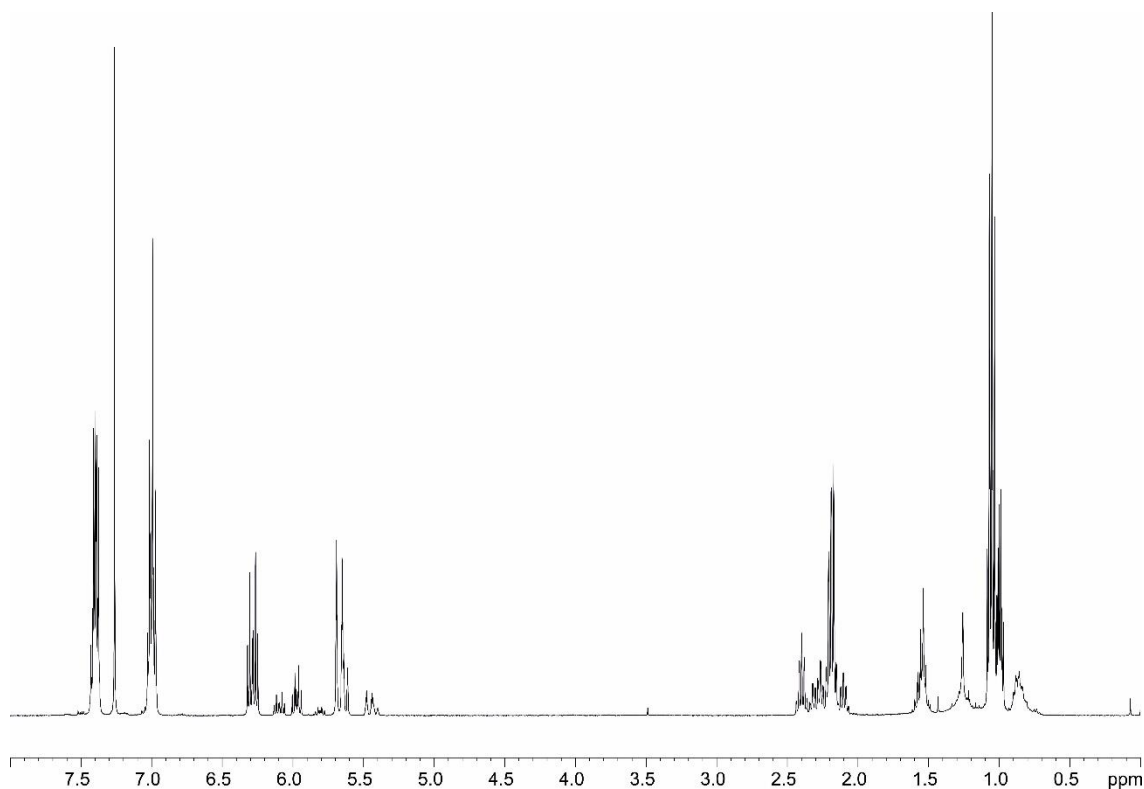
5g E ¹H NMR (400 MHz, CDCl₃): δ [ppm] = 7.36-7.4 (m, 2H), 6.96-7.02 (m, 2H), 6.28 (dt, J = 15.9 Hz, 1.8 Hz, 1H), 5.67 (dt, J = 15.8 Hz, 1.8 Hz, 1H), 2.19 (m, 2H), 1.05 (t, J = 7.5 Hz, 3H).

5g E: ¹³C NMR (400 MHz, CDCl₃): δ [ppm] = 161.2, 146.8, 133.3, 119.9, 115.6, 108.7, 88.0, 87.0, 26.4, 13.1.

5g Z ¹H NMR (400 MHz, CDCl₃): δ [ppm] = 7.38-7.43 (m, 2H), 6.97-7.04 (m, 2H), 5.97 (dt, J = 10.8 Hz, 7.4 Hz, 1H), 5.63 (dt, J = 10.8 Hz, 1.5 Hz, 1H), 2.40 (quind, J = 7.5 Hz, 1.5 Hz, 2H), 1.06 (t, J = 7.6 Hz, 3H).

5g Z: ¹³C NMR (400 MHz, CDCl₃): δ [ppm] = 163.7, 146.0, 133.4, 119.9, 115.8, 108.3, 92.5, 86.1, 24.0, 13.6.

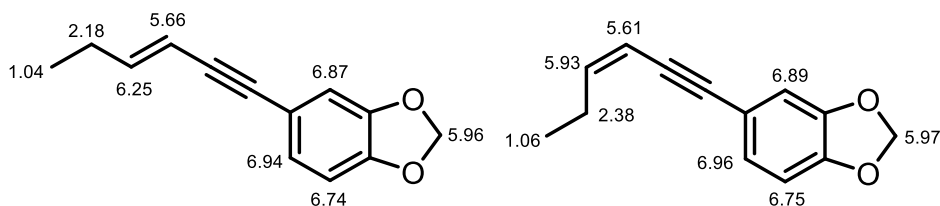
HRMS (EI): calcd. for C₁₂H₁₁F [M]⁺ 174.08393; found 174.08432.



3 CONJUGATED ENYNES AND CYCLIC NITRONATES

5-(hex-3-en-1-yn-1-yl)benzo[d][1,3]dioxole (5h)

400 MHz, in CDCl₃



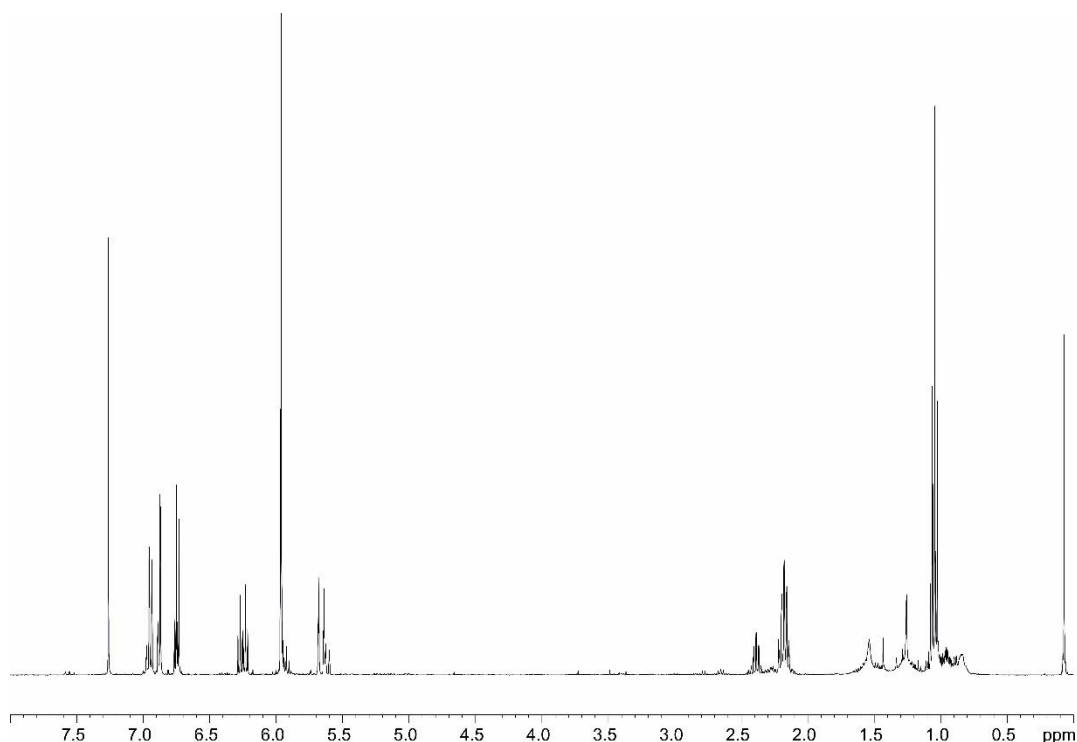
5h E ¹H NMR (400 MHz, CDCl₃): δ [ppm] = 6.94 (dd, J = 8.1 Hz, 1.7 Hz, 1H), 6.87 (d, J = 1.6 Hz, 1H), 6.74 (d, J = 8.0 Hz, 1H), 6.25 (dt, J = 15.9 Hz, 6.6 Hz, 1H), 5.96 (s, 2H), 5.66 (dt, J = 15.9 Hz, 6.6 Hz, 1H), 2.18 (quind, J = 7.4 Hz, 1.8 Hz, 2H), 1.04 (t, J = 7.5 Hz, 3H).

5h E: ¹³C NMR (400 MHz, CDCl₃): δ [ppm] = 146.2, 126.1, 117.1, 111.6, 108.8, 108.5, 101.4, 87.9, 86.8, 26.4, 13.2.

5h Z ¹H NMR (400 MHz, CDCl₃): δ [ppm] = 6.96 (dd, J = 8.0 Hz, 1.6 Hz, 1H), 6.89 (d, J = 1.6 Hz, 1H), 6.75 (d, J = 8.0 Hz, 1H), 5.97 (s, 2H), 5.93 (dt, J = 10.7 Hz, 7.3 Hz, 1H), 5.61 (dt, J = 10.7 Hz, 1.5 Hz, 1H), 2.38 (quind, J = 7.5 Hz, 1.5 Hz, 2H), 1.06 (t, J = 7.6 Hz, 3H).

5g Z: ¹³C NMR (400 MHz, CDCl₃): δ [ppm] = 145.5, 126.1, 117.1, 111.5, 108.6, 108.5, 101.4, 93.5, 84.9, 23.9, 13.6.

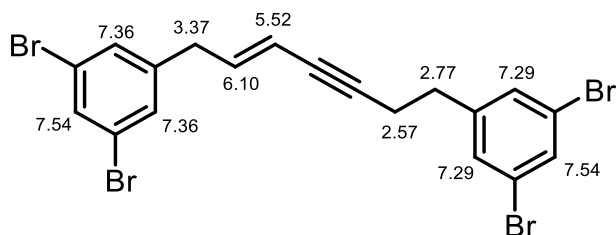
HRMS (EI): calcd. for C₁₃H₁₂O₂ [M]⁺ 200.08318; found 200.08354.



3 CONJUGATED ENYNES AND CYCLIC NITRONATES

5,5'-(hept-2-en-4-yne-1,7-diyl)bis(1,3-dibromobenzene) (5i)

400 MHz, in CD₂Cl₂

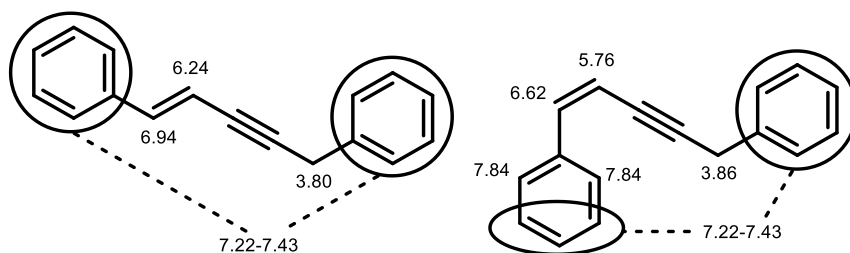


¹H NMR (400 MHz, CD₂Cl₂): δ [ppm] = 7.54 (d, J = 1.8 Hz, 2H), 7.36 (d, J = 1.8 Hz, 2H), 7.29 (d, J = 1.8 Hz, 2H), 6.10 (dt, J = 15.8 Hz, 7.0 Hz, 1H), 5.52 (dt, J = 15.8 Hz, 1.9 Hz, 1H), 3.37 (dd, J = 7.0 Hz, 1.6 Hz, 2H), 2.77 (t, J = 7.1 Hz, 2H), 2.57 (td, J = 7.1 Hz, 2.1 Hz, 2H).

HRMS (LIFDI): calcd. for C₁₉H₁₄Br₄ M⁺ 561.7783; found 561.7610.

pent-1-en-3-yne-1,5-diyl dibenzene (5j)

400 MHz, in CD₂Cl₂



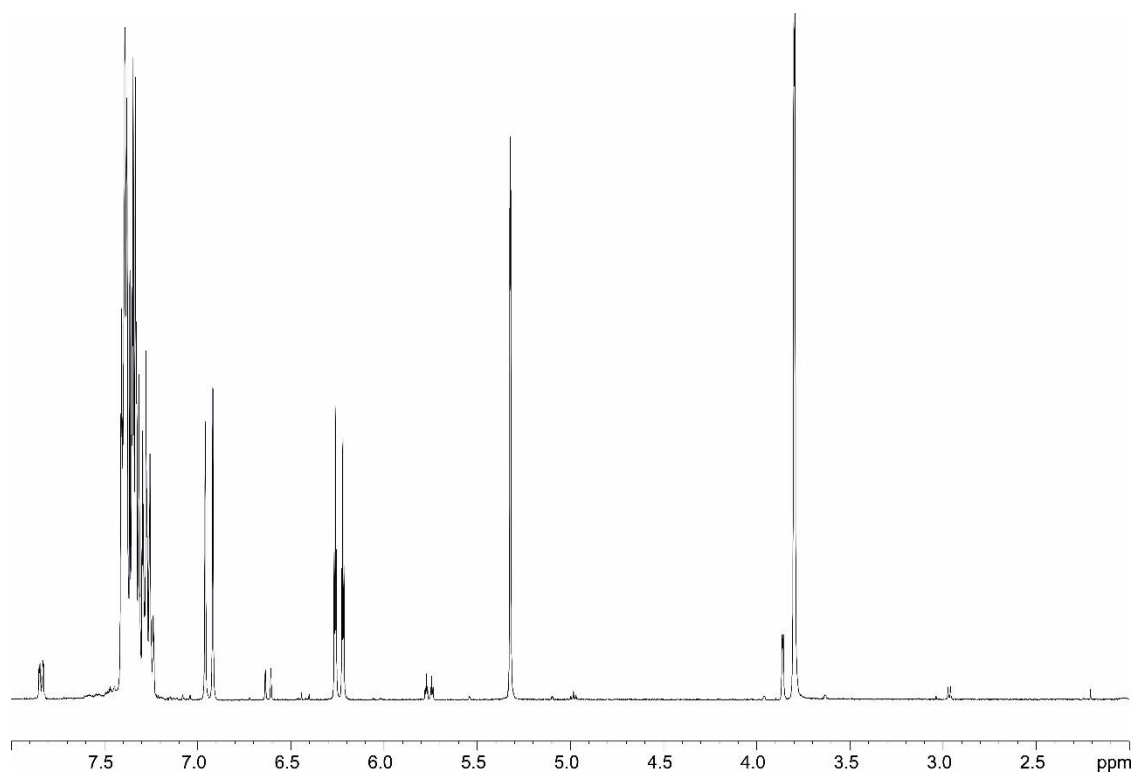
5j E ¹H NMR (400 MHz, CD₂Cl₂): δ [ppm] = 7.22-7.43 (m, 10H), 6.94 (d, J = 16.3 Hz, 1H), 6.24 (dt, J = 16.3 Hz, 2.3 Hz, 1H), 3.80 (d, J = 2.3 Hz, 2H).

5j E ¹³C NMR (400 MHz, CD₂Cl₂): δ [ppm] = 141.0, 137.4, 136.9, 129.1, 129.0, 128.9, 128.4, 127.1, 126.5, 108.9, 90.5, 82.1, 26.3.

5j Z ¹H NMR (400 MHz, CD₂Cl₂): δ [ppm] = 7.84 (m, 2H), 7.22-7.43 (m, 8H), 6.62 (d, J = 11.8 Hz, 1H), 5.76 (dt, J = 11.9 Hz, 2.5 Hz, 1H), 3.86 (d, J = 2.6 Hz, 3H).

HRMS (EI): calcd. for C₁₇H₁₄ [M]⁺ 218.10900; found 218.10935.

3 CONJUGATED ENYNES AND CYCLIC NITRONATES

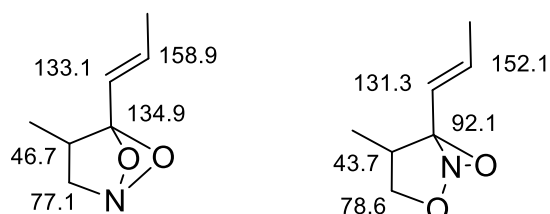


3 CONJUGATED ENYNES AND CYCLIC NITRONATES

3.7.15 Computational Details

For the calculation, a smaller model of dimer **3a** was employed. The *n*-propyl group and the terminal ethyl group connected with the double bond were substituted by a methyl group. All structures were optimized at M06-2X/def2-SVP level of theory using empirical dispersion D3 in continuum of DMF (CPCM).^[26–28] Thermochemical correction was performed at the same level of theory as the geometry optimization. Single point calculations were carried out at PWPB95-D3/def2TZVPP level of theory.^[29] The software used for the geometry optimization and frequency analysis was Gaussian09 version D.01.^[30] For the single points, ORCA 4.0.1 was employed.^[31]

Calculated chemical shifts for other possible structures of linking intermediates



The most stable conformations of calculated compounds

Dimer 3a

E (R,S)-Diastereomer

```
1\1\GINC-WORKER0\FOpt\RM062X\def2SVP\C7H12N2O4\JHIOE\16-Oct-2017\0\#p
m062x/def2svp empiricaldispersion=gd3 opt freq int=ultrafine scrf=(cp
cm,solvent=N,N-dimethylformamide)\title\0,1\C,-0.0894044213,-1.34779
99561,0.2488884312\H,-0.6517084133,-1.7382565033,1.1018726148\C,0.9632
913931,-2.0161503762,-0.230137396\H,1.5000997442,-1.5994725319,-1.0911
474126\C,1.479543972,-3.3049975072,0.3231579279\H,2.5242675512,-3.1936
48309,0.6498607588\H,0.8781312632,-3.6463943911,1.1755916337\H,1.47251
34411,-4.0863822345,-0.451370487\C,-0.5205008742,-0.0339203864,-0.3157
531035\C,-0.4764082585,1.1579111489,0.6630568052\C,0.9704400214,1.3581
689881,1.0841856719\H,1.3503493137,0.5622752327,1.7340337275\H,1.64204
30569,1.464881942,0.2197275165\N,-1.9541052086,-0.1009836234,-0.819789
5013\O,-2.6395199087,-1.0352200567,-0.4873506956\O,-2.3274795095,0.823
1819395,-1.5001604856\N,1.1490379224,2.6314831654,1.8599038308\O,0.453
9328453,3.5763159716,1.5727101376\O,2.0101168131,2.6400546637,2.703523
1977\H,-0.7816855422,2.044609305,0.0907454736\C,-1.4049725582,0.979881
3874,1.8617072433\H,-1.1066758987,0.1190545618,2.4770989565\H,-1.38132
71595,1.8786313426,2.4925641626\H,-2.4460755874,0.8346403328,1.5407798
815\H,0.0592129425,0.2172838342,-1.2143222895\Version=ES64L-G09RevD.0
1\State=1-A\HF=-683.3649302\RMSE=8.941e-09\RMSE=3.164e-06\Dipole=1.513
4839,-1.608399,-0.2354761\Quadrupole=-1.0350104,-1.0692965,2.1043069,-
7.3281953,-10.6059498,-4.4320211\PG=C01 [X(C7H12N2O4)]\@
```

E (R,R) == (S,S) Diastereomer

```
1\1\GINC-LOGIN\FOpt\RM062X\def2SVP\C7H12N2O4\JHIOE\13-Oct-2017\0\#p m
062x/def2svp empiricaldispersion=gd3 opt freq int=ultrafine scrf=(cpcm
,solvent=N,N-dimethylformamide)\title\0,1\C,-0.3496806211,-1.3032778
71,0.6399008982\H,-0.7132102334,-1.5880952641,1.6332479208\C,0.6583735
```

905,-1.9577151441,0.0572846986\H,0.9949747743,-1.6208421741,-0.9314644
 14\C,1.3948199049,-3.108303739,0.6621951596\H,2.4552291601,-2.84686990
 04,0.798957721\H,0.9730123078,-3.3899201838,1.6355885467\H,1.366160969
 ,-3.9814976663,-0.0059310752\C,-0.9751461394,-0.0921196294,0.018244804
 \C,-0.7487015103,1.2058001969,0.8202991561\C,0.7011382045,1.323099979,
 1.2795578303\H,0.9227829291,2.3399760831,1.632520656\H,0.9555306134,0.
 6127965543,2.0717106398\N,-2.473382727,-0.2892114474,-0.0739389381\O,-
 3.0658287983,-0.5200498151,0.95275466\O,-2.9853965564,-0.1897396907,-1
 .1612549858\N,1.7165031242,1.0595539323,0.204006037\O,2.7920395169,0.6
 502119183,0.5609089219\O,1.4148494972,1.2865859053,-0.9452013302\H,-0.
 6535146549,0.0341919248,-1.0206677844\H,-1.3168127597,1.0930896947,1.7
 576619851\C,-1.2680542706,2.4317589895,0.0719949646\H,-1.1460884681,3.
 332971343,0.6876569549\H,-0.7228920933,2.572319159,-0.8699298237\H,-2.
 3382989498,2.3259747854,-0.1547575932\\Version=ES64L-G09RevD.01\State=
 1-A\HF=-683.3664094\RMSD=8.709e-09\RMSF=1.109e-05\Dipole=0.8016702,0.3
 557975,1.3142225\Quadrupole=-13.4794172,11.0915475,2.3878697,-4.699434
 8,0.3149495,3.3792224\PG=C01 [X(C7H12N2O4)]\@

Z (R,S)-Diastereomer

1\1\GINC-WORKER0\FOpt\RM062X\def2SVP\C7H12N2O4\JHIOE\13-Oct-2017\0\#p
 m062x/def2svp empiricaldispersion=gd3 opt freq int=ultrafine scrf=(cp
 cm,solvent=N,N-dimethylformamide)\title\0,1\C,-0.0899140007,-1.30158
 9702,0.2218509072\H,-0.5141578129,-1.6506964167,1.1659169639\C,0.94718
 57345,-1.9618416816,-0.308296519\H,1.3090171537,-2.8302361961,0.251925
 8709\C,1.6891148843,-1.6713291582,-1.5762410963\H,1.6208991362,-2.5335
 917451,-2.2562013881\H,1.3285263109,-0.781487351,-2.1075598385\H,2.756
 6324717,-1.521917208,-1.3564536282\C,-0.6919028216,-0.0636159385,-0.35
 9213012\C,-0.5067114342,1.2142804051,0.4979718389\C,0.9550519101,1.386
 3703773,0.88025087\H,1.1263271843,2.3792256331,1.318661776\H,1.3139125
 572,0.6178017044,1.5729853721\N,-2.1856525183,-0.216335623,-0.55499829
 26\O,-2.7563150185,-1.1190612448,0.003419928\O,-2.7225427452,0.6271995
 195,-1.2320950962\N,1.8779731864,1.3227036619,-0.2999853517\O,2.973294
 1548,0.8526483149,-0.121411893\O,1.4808622467,1.7678499102,-1.35254563
 93\H,-0.8059671183,2.0639236668,-0.1308386124\C,-1.3501374227,1.204661
 4619,1.7728332165\H,-1.1173670736,0.3359466248,2.4053659312\H,-1.15811
 74633,2.1133170502,2.358993423\H,-2.4219896229,1.1877157881,1.53365150
 08\H,-0.3238579984,0.1401724568,-1.3703452713\\Version=ES64L-G09RevD.0
 1\State=1-A\HF=-683.3663356\RMSD=5.990e-09\RMSF=3.431e-06\Dipole=0.846
 2194,0.1445291,1.5073549\Quadrupole=-11.9999584,6.4280252,5.5719332,-4
 .4844224,-0.5670949,6.1799176\PG=C01 [X(C7H12N2O4)]\@

Z (R,R) == (S,S) -Diastereomer

1\1\GINC-WORKER1\FOpt\RM062X\def2SVP\C7H12N2O4\JHIOE\17-Oct-2017\0\#p
 m062x/def2svp empiricaldispersion=gd3 opt freq int=ultrafine scrf=(cp
 cm,solvent=N,N-dimethylformamide)\title\0,1\C,-0.4038199022,1.368336
 9916,-0.8414627969\H,-1.010347109,1.4940334416,-1.7422277991\C,0.65701
 56507,2.1561080121,-0.6360551527\H,0.8565833695,2.9137483709,-1.400846
 4829\C,1.6378090891,2.1080290912,0.4936808043\H,1.7740543823,3.1104777
 59,0.9236869672\H,1.3444129819,1.423028271,1.2990475109\H,2.6190516347
 ,1.7851480013,0.1125194331\C,-0.8103118514,0.2298855306,0.0473936102\C
 ,-0.5148163277,-1.1662309449,-0.5350096987\C,0.9821519352,-1.329565087
 4,-0.7600741918\H,1.5965815113,-0.983101232,0.0791563829\H,1.223183637
 9,-2.3812333191,-0.9675612552\N,-2.3047064778,0.3026672988,0.269069556
 4\O,-3.0100076506,0.2467463068,-0.7094898119\O,-2.700515479,0.38427237
 01,1.4049548484\N,1.4860321714,-0.5950730249,-1.9701297208\O,2.5760673
 16,-0.0839274022,-1.8912409215\O,0.7964206408,-0.6000455559,-2.9599538

3 CONJUGATED ENYNES AND CYCLIC NITRONATES

946\H,-0.3889709614,0.315943223,1.0553093334\H,-1.0125289743,-1.241401
0084,-1.5125815169\C,-1.0217205768,-2.2741567129,0.3879095387\H,-0.815
0283508,-3.2596500861,-0.0495129092\H,-0.5355707001,-2.2222299434,1.37
32711649\H,-2.1076561496,-2.1985052511,0.5345426819\Version=ES64L-G09
RevD.01\State=1-A\HF=-683.3660139\RMSD=9.614e-09\RMSF=6.969e-06\Dipole
=1.3177791,-0.8512759,1.0808813\Quadrupole=-8.8855893,12.4527428,-3.56
71535,1.0303702,7.0703289,-1.1905759\PG=C01 [X(C7H12N2O4)]\@

Intermediate 19a

E

1\1\GINC-WORKER1\FOpt\RM062X\def2SVP\C7H11N2O4(1-)\JHIOE\16-Oct-2017\O
\#p m062x/def2svp empiricdispersion=gd3 opt freq int=ultrafine scrf
=(cpcm,solvent=N,N-dimethylformamide)\title\1,1\C,-2.0525311054,-0.
1423092615,0.0478822352\H,-1.8701073817,-1.1958404066,0.2878966443\C,-
3.3235309823,0.1549839707,-0.3086220025\H,-3.5803355238,1.1829619372,-
0.5572183679\C,-4.4079295568,-0.8809685138,-0.3772254246\H,-5.24525623
26,-0.6412366296,0.2995203245\H,-4.0315598303,-1.8784468648,-0.1055777
553\H,-4.8432678591,-0.949479312,-1.3883324991\C,-0.8628094342,0.67111
31641,0.1773156212\C,0.4756324723,0.0919058616,0.5696320024\C,1.363513
0935,0.0195177197,-0.6833743953\H,1.4744672762,1.0303545374,-1.0934241
966\H,0.9857063031,-0.6955598755,-1.4211183127\N,-0.8569894238,1.99472
8644,-0.101048036\O,-1.909649495,2.5953361684,-0.4300641276\O,0.226342
413,2.6481303352,-0.0280573158\N,2.7299263139,-0.4446616092,-0.3132882
607\O,3.1060294685,-1.5173891727,-0.7274609879\O,3.3743521549,0.263691
3595,0.4273658747\H,0.9646653905,0.8199171318,1.233509367\C,0.41371429
02,-1.2617622787,1.271652275\H,1.4062947567,-1.5362095046,1.6586204682
\H,0.0865270601,-2.0639947739,0.5936504176\H,-0.2791002679,-1.22781805
68,2.1237369621\Version=ES64L-G09RevD.01\State=1-A\HF=-682.8842161\RM
SD=4.724e-09\RMSF=5.232e-06\Dipole=-0.1949893,-3.0780467,0.0789488\Qua
drupole=-9.3420001,-5.0769699,14.41897,8.8303765,-2.3851672,-0.4534749
\PG=C01 [X(C7H11N2O4)]\@

Z

1\1\GINC-WORKER1\FOpt\RM062X\def2SVP\C7H11N2O4(1-)\JHIOE\16-Oct-2017\O
\#p m062x/def2svp empiricdispersion=gd3 opt freq int=ultrafine scrf
=(cpcm,solvent=N,N-dimethylformamide)\title\1,1\C,-1.8951262344,-0.
4935003384,0.7425679551\H,-1.7756133773,-1.354358656,1.4108484598\C,-3
.0548061827,-0.4192528585,0.0576929546\H,-3.8181320956,-1.1728021258,0
.2780837172\C,-3.370682916,0.5885141759,-1.0001832945\H,-2.4482479845,
0.9059139759,-1.512004166\H,-3.8013701717,1.5057608317,-0.5684591377\H
,-4.0699450034,0.177864593,-1.7427679275\C,-0.7508636081,0.4047393696,
0.6681148479\C,0.6651597066,-0.1105221502,0.6352170866\C,1.1711959943,
0.0009578685,-0.8126961838\H,1.138759815,1.0559664024,-1.1096349788\H,
0.6149183523,-0.6482388086,-1.4967603088\N,-0.8898838786,1.7473010778,
0.6074841051\O,-2.0038498347,2.3104696823,0.7564285708\O,0.1421062952,
2.4682419976,0.442062775\N,2.5955561998,-0.4274409159,-0.8927565576\O,
2.8603210179,-1.4379313632,-1.5035124829\O,3.4093520426,0.2378923678,-
0.292064745\H,1.2943322909,0.5728577296,1.2246782889\C,0.8195568625,-1
.5338121943,1.1627572723\H,1.8793819971,-1.8287098405,1.1765500854\H,0
.2719932601,-2.2582209231,0.5413245199\H,0.4409780724,-1.6099365876,2.
1914720139\Version=ES64L-G09RevD.01\State=1-A\HF=-682.8791301\RMSD=4.
732e-09\RMSF=1.490e-05\Dipole=-0.0511656,-2.7926353,-0.6610733\Quadrup
ole=-9.1093127,-3.4346321,12.5439448,8.9649215,5.7478331,-7.2726526\PG
=C01 [X(C7H11N2O4)]\@

Dimer 3a + Base

```

1\1\GINC-LOGIN\FOpt\RM062X\def2SVP\C13H24N4O4\JHIOE\18-Oct-2017\0\#p
m062x/def2svp empiricdispersion=gd3 opt freq int=ultrafine scrf=(cpc
m,solvent=N,N-dimethylformamide)\title\0,1\C,-0.7235474878,-1.257328
209,-0.2646601178\H,-1.3494602274,-1.7274413094,0.4991572389\C,0.14944
98174,-1.9787332769,-0.9742745046\H,0.752817107,-1.4598085323,-1.72729
85461\C,0.3807636667,-3.4468311382,-0.8234084224\H,1.4255183319,-3.645
7043561,-0.5404894154\H,-0.2803767025,-3.8862433627,-0.0651163992\H,0.
2116706722,-3.9578610903,-1.7835623832\C,-0.8420949581,0.2206954313,-0
.4531735772\C,-0.3185962772,1.0781039342,0.7192313919\C,1.1682964289,0
.8208502455,0.9163465588\H,1.5822394073,1.5056977886,1.6676900704\H,1.
3954885132,-0.217000207,1.1799897902\N,-2.2835276115,0.6317695853,-0.6
750672899\O,-3.1536269907,-0.1912825511,-0.5361003077\O,-2.4738742499,
1.7876768026,-0.9732234561\N,1.9281561091,1.1040082873,-0.3454661917\O
,2.666033541,0.2451913838,-0.7646389804\O,1.7557928673,2.1816417029,-0
.8629865872\H,-0.4408985647,2.1293760387,0.4242847546\C,-1.0652077514,
0.8200178822,2.0251571086\H,-0.9391231966,-0.2186522417,2.362302763\H,
-0.6906887758,1.4837662788,2.815689402\H,-2.1399078587,1.01775329,1.90
59765907\H,-0.3451440784,0.5402396231,-1.3874750293\C,-0.2579546204,-0
.436164462,-3.9211548252\C,1.8560296282,0.6273666098,-3.8788934467\C,2
.4854699128,-0.7564550318,-3.9704041041\C,1.6426894087,-1.631737583,-4
.882531746\H,2.0118468941,1.1679627287,-4.8303679435\H,2.3537249635,1.
2193917048,-3.0981992264\H,3.5141769668,-0.6967405191,-4.3522569204\H,
2.5368384294,-1.2049486487,-2.9659121026\H,1.7431548748,-1.2986501171,
-5.9328653774\H,1.9804899356,-2.6779002631,-4.8422958569\N,0.430991379
9,0.5997768295,-3.5886680021\N,0.247284819,-1.5918219766,-4.4690598964
\C,-1.7421736889,-0.4069707146,-3.6495229803\H,-1.9990389969,0.5938665
256,-3.2855893875\H,-2.3210504126,-0.6086207932,-4.5619351166\C,-0.607
8466503,-2.6281595505,-5.0109734357\H,-0.9522496688,-2.4019415648,-6.0
3587614\H,-0.0416055961,-3.5685269392,-5.0437814854\H,-1.4851655458,-2
.7926733006,-4.3753168996\H,-2.0269378544,-1.1591973637,-2.897624578\
Version=ES64L-G09RevD.01\State=1-A\HF=-1028.3274893\RMSD=6.499e-09\RMS
F=3.331e-06\Dipole=1.0360978,-2.4444884,0.8107617\Quadrupole=-13.96725
97,-4.1852017,18.1524613,1.6497486,2.6965946,10.2395171\PG=C01 [X(C13H
24N4O4)]\@

```

TS 19a->20a

```

1\1\GINC-WORKER0\SP\RM062X\def2SVP\C13H24N4O4\JHIOE\29-Jun-2018\0\#p
m062x/def2svp empiricdispersion=gd3 int=ultrafine scrf=(cpcm,solvent
=N,N-dimethylformamide,externaliteration,dovacuum)\title\0,1\C,0,2,3
59022,1.175137,-0.918484\H,0,2.096967,1.559261,-1.909007\C,0,3,140159,
1.90651,-0.112757\H,0,3.351323,1.536058,0.896405\C,0,3,750237,3.219916
,-0.490316\H,0,4.849674,3.171552,-0.450021\H,0,3.454752,3.519343,-1.50
51\H,0,3.445585,4.012296,0.21061\C,0,1,799916,-0.134277,-0.553788\C,0,
2,616736,-1.260774,-0.001504\C,0,2,455033,-1.228303,1.575495\H,0,2,623
283,-2.210668,2.028558\H,0,3,134658,-0.478958,2.002467\N,0,0,696768,-0
.51247,-1.401843\O,0,-0.002834,0.389382,-1.851221\O,0,0,472165,-1.6909
68,-1.652106\N,0,1,092702,-0.80747,1.757424\O,0,0,917806,0.251669,1.07
1344\O,0,0,191758,-1.761681,1.662708\H,0,2,135418,-2.189002,-0.32759\C
,0,4,095071,-1.285391,-0.379529\H,0,4,613582,-0.37665,-0.04692\H,0,4,5
84634,-2.149872,0.090976\H,0,4,221324,-1.374541,-1.467204\C,0,-2,36169
,0.281828,0.800401\C,0,-2,440719,-1.501737,-0.853401\C,0,-3,877476,-1.
062861,-1.068778\C,0,-3,936748,0.453967,-1.050558\H,0,-1,813798,-1.228
656,-1.71316\H,0,-2,365723,-2.588457,-0.717827\H,0,-4,251828,-1.437627
,-2.029405\H,0,-4,521586,-1.465864,-0.272668\H,0,-3,431894,0.880634,-1

```

3 CONJUGATED ENYNES AND CYCLIC NITRONATES

.932659\H,0,-4.976972,0.805986,-1.056982\N,0,-1.91399,-0.864967,0.3464
75\N,0,-3.305227,0.976522,0.163619\H,0,-1.061205,-1.277873,0.85624\C,0
,-1.802916,0.785535,2.09784\H,0,-1.199113,-0.009504,2.545452\H,0,-1.16
313,1.660882,1.926441\C,0,-3.79174,2.267604,0.623418\H,0,-3.924424,2.9
19877,-0.249632\H,0,-4.759832,2.163818,1.136443\H,0,-3.073295,2.743588
,1.295858\H,0,-2.620634,1.062934,2.774976\Version=ES64L-G09RevD.01\St
ate=1-AHF=-1028.2834845\RMSD=2.864e-09\Dipole=-2.3848402,1.9484589,0.
4934017\Quadrupole=23.5030152,-9.4951808,-14.0078345,-5.5476509,2.0097
368,3.8276577\PG=C01 [X(C13H24N4O4)]\@

Intermediate 20a

E (R,S)-Diastereomer

1\1\GINC-WORKER1\FOpt\RM062X\def2SVP\C7H12N2O4\JHIOE\18-Oct-2017\0\#p
m062x\def2svp empiricaldispersion=gd3 opt freq int=ultrafine scrf=(cp
cm,solvent=N,N-dimethylformamide)\title\0,1\C,0.6193152334,0.5371748
978,1.2863396301\C,1.8674607531,-0.3280122557,1.1190628838\C,-0.124476
4366,0.1793715687,-0.0254945972\H,0.0019882366,0.1131973675,2.09041750
27\H,2.3408247935,-0.6223590212,2.0608334174\H,2.601154489,0.151296296
7,0.4581669906\C,0.8687296662,2.0129070158,1.5486296293\H,-0.072514712
2,2.5787128661,1.568629489\H,1.5270364071,2.4511383914,0.7837501233\C,
-1.6207400986,0.1688937252,0.0570770194\H,-2.1004710106,1.1389754755,0
.2031687576\C,-2.3248932574,-0.9630277179,0.0195997412\H,-1.7801318902
,-1.9024402974,-0.1158457013\C,-3.8110583095,-1.0393225702,0.162835304
2\H,-4.0828749151,-1.6655587364,1.0258685843\H,-4.2574297857,-0.045198
2901,0.2948569273\N,1.3764940557,-1.5315206776,0.4429018497\O,0.411874
6941,-1.0269903985,-0.466029049\H,-4.2596043146,-1.5130788566,-0.72318
96958\H,1.3588235293,2.1334464151,2.5233805065\N,0.3184937677,1.244513
8768,-1.0709106939\O,1.3829570576,1.0801788479,-1.6076669286\O,-0.3951
588619,2.2045283768,-1.2196755427\O,0.6623553512,-2.2467621853,1.40108
56093\H,0.7262289779,-3.1665181944,1.1098022926\Version=ES64L-G09RevD
.01\State=1-AHF=-683.363979\RMSD=3.960e-09\RMSF=8.341e-06\Dipole=-0.4
826958,-0.8946575,1.8818799\Quadrupole=3.0754753,1.4513915,-4.5268668,
1.8190273,4.4632154,3.5971555\PG=C01 [X(C7H12N2O4)]\@

E (R,R) == (S,S) -Diastereomer

1\1\GINC-WORKER1\FOpt\RM062X\def2SVP\C7H12N2O4\JHIOE\18-Oct-2017\0\#p
m062x\def2svp empiricaldispersion=gd3 opt freq int=ultrafine scrf=(cp
cm,solvent=N,N-dimethylformamide)\title\0,1\C,0.8057240515,-0.373263
1591,1.0912193159\C,1.6582205387,-1.3653407917,0.2920915254\C,-0.04955
95732,0.1905156398,-0.0712074786\H,2.0271797874,-2.217283327,0.8717557
35\H,2.4992333096,-0.8597197462,-0.1987654797\C,-1.4237932079,0.691864
0452,0.2584758977\H,-1.4656323621,1.6121447246,0.8453489201\C,-2.52624
05586,0.033728554,-0.1018540452\H,-2.4075085978,-0.8892299232,-0.67843
49569\C,-3.9168416205,0.4648774747,0.2372337556\H,-4.4280250853,-0.313
0496247,0.8239973855\H,-3.9224327706,1.400193109,0.8117158929\N,0.7803
093082,-1.8705059749,-0.7716728043\O,-0.0605858785,-0.7654585666,-1.07
19910422\H,-4.5093478631,0.6085453199,-0.6786890664\N,0.7709346442,1.4
037137716,-0.6277727641\O,1.4362939672,1.2329955037,-1.6132182579\O,0.
7084440681,2.4279526487,0.0074392603\O,-0.0462087126,-2.8341258947,-0.
2048598649\H,-0.243644852,-3.4365620562,-0.9351390699\C,-0.0262248396,
-0.9941212708,2.2086265017\H,0.6440523865,-1.4797331484,2.9310691674\H
,-0.6016275967,-0.2230451273,2.7376901808\H,-0.7207568264,-1.745593933
5,1.8151859437\H,1.4267594232,0.4313203632,1.5054862781\Version=ES64L
-G09RevD.01\State=1-AHF=-683.3612766\RMSD=6.608e-09\RMSF=8.404e-06\Di
pole=-0.7873018,-1.5266173,1.2661587\Quadrupole=4.8713148,-2.0960246,-

2.7752902,-3.8394413,4.5674555,3.31071\PG=C01 [X(C7H12N2O4)]\@

Z (R,S)-Diastereomer

1\1\GINC-LOGIN\FOpt\RM062X\def2SVP\C7H12N2O4\JHIOE\13-Oct-2017\0\#p m062x\def2svp empiricaldispersion=gd3 opt freq int=ultrafine scrf=(cpcm,solvent=N,N-dimethylformamide)\title\0,1\C,-0.7099102371,1.02552779 69,-1.0018643003\C,-2.0553849107,0.3609971714,-0.7545114089\C,0.211037 1893,0.1003556747,-0.1889418689\H,-0.4073808507,0.8498009367,-2.045746 9886\H,-2.76717593,0.5193114826,-1.5727125441\H,-2.5067721518,0.714825 5109,0.1872524882\C,-0.6484386997,2.5112584892,-0.6928293742\H,0.37738 4409,2.8906395341,-0.7960353417\H,-0.9986092452,2.7281547484,0.3264226 098\C,1.6648058346,0.1184303128,-0.5677716634\H,1.9296104969,0.7696598 468,-1.4029860437\C,2.5970787541,-0.6206073391,0.0382382801\H,3.621766 4138,-0.5394132317,-0.3370337505\C,2.3893905172,-1.5317676146,1.206269 0293\H,2.931359908,-1.1459360022,2.0837417508\H,1.3313312959,-1.659498 8754,1.4669117789\N,-1.7495288579,-1.0801718591,-0.6615132392\O,-0.341 9685452,-1.1545400474,-0.3059447914\H,2.8069766728,-2.5257795208,0.989 7195262\H,-1.2881148261,3.0606341096,-1.3954457161\O,-2.4408381843,-1. 6740337996,0.3550213724\H,-2.2165123917,-1.1836265191,1.1704111025\N,0 .0690682736,0.5495772235,1.3133234729\O,-0.8222424959,0.0457248741,1.9 611437093\O,0.806554271,1.4067002372,1.7149325204\Version=ES64L-G09Re vD.01\State=1-A\HF=-683.3583564\RMSD=6.301e-09\RMSF=8.250e-06\Dipole=0 .6240577,1.3424413,-0.954222\Quadrupole=4.2552011,-3.5340144,-0.721186 8,-8.4430977,-0.2891633,-7.0762112\PG=C01 [X(C7H12N2O4)]\@

Z (R,R) == (S,S) -Diastereomer

1\1\GINC-WORKER0\FOpt\RM062X\def2SVP\C7H12N2O4\JHIOE\13-Oct-2017\0\#p m062x\def2svp empiricaldispersion=gd3 opt freq int=ultrafine scrf=(cpcm,solvent=N,N-dimethylformamide)\title\0,1\C,-1.0303922135,1.069430 972,-0.8580798334\C,-2.113366878,0.0987925389,-0.3974644847\C,0.206016 733,0.2745726591,-0.4018867318\H,-3.0504474503,0.201773179,-0.95648889 63\H,-2.3281865809,0.1991616411,0.6788768718\C,1.5448038595,0.67444209 06,-0.9568967953\H,1.5777612619,1.6287134569,-1.4828408041\C,2.6581983 849,-0.0522640154,-0.8224728619\H,3.5640508077,0.3511434961,-1.2858817 716\C,2.816991263,-1.350385187,-0.0957205992\H,3.6668998712,-1.2843190 287,0.5988971806\H,1.9182013703,-1.6419430607,0.459296094\N,-1.5391524 799,-1.2342668117,-0.6785244457\O,-0.0995063426,-1.0414810946,-0.65122 2941\H,3.0553791887,-2.1540640615,-0.8094554784\O,-1.83330201,-2.12827 74694,0.3101269469\H,-1.491643126,-1.7521991216,1.1453918042\N,0.27360 27007,0.4748272726,1.1638451144\O,-0.1059743697,-0.4296782858,1.872494 741\O,0.6701412862,1.5382448661,1.5542869014\C,-1.0356628437,1.2745494 054,-2.3701095431\H,-2.0018851294,1.6975010555,-2.6744664318\H,-0.2489 087213,1.9688306064,-2.6895549899\H,-0.8956456818,0.3179173689,-2.8930 79711\H,-1.0911366299,2.0306021676,-0.3321041851\Version=ES64L-G09Rev D.01\State=1-A\HF=-683.3560332\RMSD=6.162e-09\RMSF=1.194e-05\Dipole=0. 1370397,1.3557054,-0.900364\Quadrupole=7.4813058,-4.5420423,-2.9392635 ,-6.9200429,-2.083023,-5.5277579\PG=C01 [X(C7H12N2O4)]\@

Intermediate 20a + Base

1\1\GINC-WORKER1\FOpt\RM062X\def2SVP\C13H24N4O4\JHIOE\18-Oct-2017\0\#p m062x\def2svp empiricaldispersion=gd3 opt freq int=ultrafine scrf=(cpcm,solvent=N,N-dimethylformamide)\title\0,1\C,0.9442488371,-0.34196 38472,0.8882887292\C,1.645442514,-1.4488182546,0.102074747\C,-0.084411 7505,0.1227992428,-0.1770962641\H,0.3429026728,-0.8069568032,1.6806334 476\H,2.0965985499,-2.2226507532,0.731360833\H,2.3943874208,-1.0338524

3 CONJUGATED ENYNES AND CYCLIC NITRONATES

886,-0.5857752344\C,1.8488548803,0.7264271002,1.4787268092\H,1.2657908
953,1.5271631406,1.9537784007\H,2.497904203,1.1733582743,0.7107352066\
C,-1.4064823055,0.5888750402,0.356973752\H,-1.4100009219,1.5496840939,
0.8756997116\C,-2.5050166653,-0.1620828014,0.2653804915\H,-2.425350162
6,-1.1239663159,-0.2518153431\C,-3.8360520814,0.2105761208,0.836060891
1\H,-4.1675614756,-0.5440405522,1.5652822338\H,-3.8051057167,1.1890751
964,1.3328813019\N,0.5773451698,-2.0555989522,-0.6943347813\O,-0.19344
81445,-0.908244119,-1.0969541511\H,-4.6007622996,0.2405035096,0.045350
2121\H,2.4951306623,0.2769011004,2.2439505273\N,0.5972553203,1.3026669
128,-0.9354645443\O,1.3809264305,1.020524666,-1.8042449002\O,0.3577651
743,2.4221626394,-0.5553384164\O,-0.2171337442,-2.7643139975,0.1793764
984\H,-0.7856058406,-3.3590908133,-0.4520697399\C,-1.439723002,-5.3915
560597,-1.7382300686\C,-2.4068858893,-3.3348829292,-2.4308921268\C,-2.
3883660256,-3.9052685539,-3.8415648479\C,-2.788362919,-5.3694251599,-3
.7843369419\H,-3.4461230379,-3.3004943718,-2.0561671297\H,-2.029199541
8,-2.3013648898,-2.4150265688\H,-3.0697667768,-3.3556982597,-4.5041875
692\H,-1.3715883374,-3.8169356962,-4.2547388344\H,-3.8694970659,-5.470
7941589,-3.5840184477\H,-2.5893782226,-5.8633876581,-4.7474013302\N,-1
.5850000598,-4.1231670603,-1.5300514328\N,-2.0283977752,-6.0729564848,
-2.7558183802\C,-0.555502255,-6.152213016,-0.7840477408\H,-0.070608661
4,-5.4300276943,-0.1189424352\H,-1.1423739401,-6.8574452708,-0.1785760
358\C,-1.9261730348,-7.5068506813,-2.9375861303\H,-2.9198003937,-7.912
8381928,-3.1787425632\H,-1.2426570428,-7.7601063622,-3.7646814848\H,-1
.575706049,-8.0004438056,-2.0269253793\H,0.2124605879,-6.723491584,-1.
3226832807\Version=ES64L-G09RevD.01\State=1-A\HF=-1028.3327621\RMSE=8
.042e-09\RMSE=3.142e-06\Dipole=-1.5168315,-3.4482336,-0.0301343\Quadrupole=-1.1887671,1.6106116,-0.4218445,-0.1096101,9.1975752,15.1126551\PG=C01 [X(C13H24N4O4)]\@

Intermediate 4a

E (R,R) == (S,S) -Diastereomer

1\1\GINC-LOGIN\FOpt\RM062X\def2SVP\C7H13N1O3\JHIOE\06-Oct-2017\0\#p m
062x\def2svp empiricaldispersion=gd3 opt freq int=ultrafine scrf=(cpcm
,solvent=N,N-dimethylformamide)\title\0,1\C,0.799883279,1.2070796871
,0.2144699192\C,1.4939243394,0.7487479142,-1.0691980354\C,0.0173980046
, -0.0784986384,0.6424308037\H,1.5555172587,1.3739973031,0.9954151527\H
,2.4940969076,1.1664053244,-1.2261569644\H,0.8693559663,0.9451441089,-
1.9521788438\C,-0.0241576592,2.4761635601,0.0548778478\H,-0.5527157855
,2.7218450178,0.9858955702\H,-0.7709919701,2.3745197907,-0.7451312177\
C,-1.4788293691,0.0464725752,0.6087181054\H,-1.89720219,0.2790336778,-
0.3755216133\C,-2.2703243053,-0.1083305946,1.6697926355\H,-1.799478807
, -0.343122919,2.6292265772\C,-3.7614880332,0.0171147988,1.6445830821\H
, -4.0973599563,0.8105425936,2.3294694439\H,-4.1299420196,0.2473755829,
0.6359678605\N,1.5944019418,-0.7071586465,-0.9347930395\O,0.3637697206
, -1.0460611313,-0.3730294128\H,-4.2365282978,-0.9147102785,1.987118774
3\H,0.6312924491,3.3211331322,-0.1992061798\O,0.4180277153,-0.53445143
09,1.892931907\H,1.3748994125,-0.6736929028,1.8367279083\O,2.575558514
7,-0.919969817,0.0592859391\H,2.9142049134,-1.8064694279,-0.1272842101
\Version=ES64L-G09RevD.01\State=1-A\HF=-554.2340426\RMSE=5.337e-09\RM
SF=1.264e-05\Dipole=0.4526391,0.8085953,-0.1652756\Quadrupole=4.979942
8,-1.3616989,-3.6182439,-2.6672558,-0.9145167,-2.1458745\PG=C01 [X(C7H
13N1O3)]\@

E (R,S) -Diastereomer

1\1\GINC-WORKER0\FOpt\RM062X\def2SVP\C7H13N1O3\JHIOE\06-Oct-2017\0\#p

m062x/def2svp empiricaldispersion=gd3 opt freq int=ultrafine scrf=(cp
 cm,solvent=N,N-dimethylformamide)\title\0,1\C,-0.5577246587,1.213880
 5235,-0.4096567445\C,-1.8546063249,0.6669460236,-1.0270643364\C,0.1517
 583829,-0.0896785386,0.0908934793\H,0.0628198173,1.6534751354,-1.20172
 8607\H,-1.7712520972,0.5522055758,-2.114666652\H,-2.7515954749,1.24955
 17017,-0.7893653314\C,-0.7657361362,2.251367637,0.6860689902\H,0.18915
 56194,2.5136959366,1.1615519145\H,-1.4490729094,1.8785561505,1.4616551
 076\C,1.5071952741,-0.2861481569,-0.5253025394\H,1.5103230453,-0.29473
 26017,-1.6203988463\C,2.6372485268,-0.4247631134,0.1674525074\H,2.5726
 681085,-0.4065815384,1.2595625985\C,3.9929730504,-0.6000257599,-0.4419
 978163\H,4.4530883893,-1.540799835,-0.1035509624\H,3.9441065981,-0.609
 62683,-1.5390888412\O,0.2525874916,-0.1745937949,1.4724849773\N,-2.007
 5120251,-0.6852051698,-0.4753463795\O,-0.6943112634,-1.1463107415,-0.4
 092304255\H,4.6690075522,0.2102248667,-0.1290874928\H,-1.2032748534,3.
 1650195408,0.2608060469\H,-0.6532373802,-0.1684190563,1.8156162881\O,-
 2.4509795734,-0.5006264229,0.8554995741\H,-2.915848279,-1.3219944122,1
 .0683208209\Version=ES64L-G09RevD.01\State=1-A\HF=-554.2348994\RMSD=9
 .936e-09\RMSF=6.886e-06\Dipole=-0.4340505,0.7353099,-0.1615055\Quadrup
 ole=4.249147,-3.1525358,-1.0966112,0.1393465,-2.9935608,-3.2791902\PG=
 C01 [X(C7H13N1O3)]\@

Z (R,R) == (S,S) -Diastereomer

1\1\GINC-WORKER1\FOpt\RM062X\def2SVP\C7H13N1O3\JHIOE\27-Jun-2018\0\#p
 m062x/def2svp empiricaldispersion=gd3 opt freq int=ultrafine scrf=(cp
 cm,solvent=N,N-dimethylformamide)\title\0,1\C,-0.4220652089,0.726085
 0283,0.75655418\C,-1.814171058,0.2043206388,1.1240323256\C,0.189544289
 6,-0.4908834163,-0.0184378275\H,-1.8091346989,-0.2709314555,2.11507245
 08\H,-2.6116042135,0.9535358728,1.0804356132\C,1.3982493123,-1.1375096
 413,0.6105096491\H,1.1682004613,-2.0252816973,1.2044861735\C,2.6627559
 284,-0.7184598424,0.5158604647\H,3.4171843825,-1.316496164,1.038282594
 8\C,3.1778102906,0.4923493301,-0.201897868\H,3.7624926584,1.1172928749
 ,0.4904753311\H,2.3711225093,1.0906223852,-0.6390512567\O,0.4753646777
 ,-0.1690233186,-1.3450669127\N,-2.0914433879,-0.8517298145,0.147767324
 3\O,-0.855928524,-1.4836589738,0.0239133549\H,3.8640363601,0.19564653,
 -1.0105585332\H,-0.3509644426,0.166440567,-1.725290729\O,-2.3393079925
 ,-0.1763621297,-1.068209926\H,-2.8832328614,-0.7934383911,-1.577032802
 9\C,0.3611853974,1.2308320935,1.9593117967\H,-0.177594447,2.0645740799
 ,2.4320786596\H,1.3574431304,1.5899624463,1.668770673\H,0.490924003,0.
 435953507,2.7075396104\H,-0.5170533164,1.5398493105,0.0231444344\Vers
 ion=ES64L-G09RevD.01\State=1-A\HF=-554.2305196\RMSD=8.013e-09\RMSF=4.6
 74e-06\Dipole=-0.3673781,0.944843,0.4215646\Quadrupole=3.2937185,-3.65
 86061,0.3648876,-0.6365057,3.9162725,0.3847489\PG=C01 [X(C7H13N1O3)]\
 @

Z (R,S)-Diastereomer

1\1\GINC-WORKER1\FOpt\RM062X\def2SVP\C7H13N1O3\JHIOE\06-Oct-2017\0\#p
 m062x/def2svp empiricaldispersion=gd3 opt freq int=ultrafine scrf=(cp
 cm,solvent=N,N-dimethylformamide)\title\0,1\C,-0.7812271702,1.039103
 3123,-0.6302545687\C,-2.0278402591,0.2686928113,-1.09798237\C,0.098106
 6422,-0.0877532889,0.0089717261\H,-0.2447360511,1.4279039062,-1.505401
 8366\H,-2.0122031379,0.0748273857,-2.1779084314\H,-2.978224968,0.74559
 64604,-0.8342968599\C,-1.0782702644,2.1909319483,0.3212800117\H,-0.149
 0224343,2.6319651248,0.7066108623\H,-1.6810529546,1.8531808959,1.17592
 34945\C,1.5209660468,-0.1553735968,-0.4902609964\H,2.2638312866,-0.000
 7811401,0.2954431768\C,1.92415663,-0.3755816507,-1.7441595782\H,3.0051

3 CONJUGATED ENYNES AND CYCLIC NITRONATES

222157,-0.3834739252,-1.9184504012\C,1.0703612742,-0.601430693,-2.9542
680178\H,1.3963310766,-1.5078384812,-3.4857806318\H,0.0104172551,-0.71
6244001,-2.7046761068\O,0.1817153662,-0.0010391462,1.396960331\N,-1.95
99711091,-1.0388635712,-0.4297813799\O,-0.5909230127,-1.2979465185,-0.
365004906\H,1.1827001494,0.2349419904,-3.6621700715\H,-1.6428251567,2.
9749431823,-0.2018549862\H,-0.7214265126,-0.0854884659,1.737209571\O,-
2.4062714803,-0.8054089444,0.8923138932\H,-2.7285295518,-1.6671398243,
1.1920993857\\Version=ES64L-G09RevD.01\State=1-A\HF=-554.2309353\RMSE=
4.551e-09\RMSEF=1.915e-05\Dipole=-0.7428999,0.5770604,-0.5493997\Quadru
pole=1.5828675,-2.5055868,0.9227193,0.9336832,-4.8111434,-2.6207798\PG
=C01 [X(C7H13N1O3)]\@

Intermediate 21a

E (R,R) == (S,S) -Diastereomer

1\1\GINC-WORKER1\FOpt\RM062X\def2SVP\C7H11N1O4\JHIOE\27-Jun-2018\0\#p
m062x\def2svp empiricaldispersion=gd3 opt freq int=ultrafine scrf=(cp
cm,solvent=N,N-dimethylformamide)\title\0,1\C,0.4428629231,1.0321246
876,0.4900127966\C,1.8420804586,0.482538571,0.307113432\C,-0.342866804
9,-0.2373602203,0.1261507493\C,-1.7437820788,-0.0281248221,-0.36380076
72\H,-1.8304825184,0.4428202433,-1.3474607961\C,-2.8230943067,-0.34876
10883,0.3518711541\H,-2.6744544984,-0.801187395,1.338705474\C,-4.23499
39618,-0.1279243573,-0.0880517495\H,-4.7630860369,0.5239185034,0.62389
94073\H,-4.2800254243,0.3297639936,-1.0847618241\N,1.7708722603,-0.485
8841325,-0.7270487294\O,0.4205804371,-0.7326169745,-0.9899899346\H,-4.
7854360041,-1.0803220458,-0.1114620795\O,-0.2342953025,-1.0972822337,1
.2067477557\H,-0.6562114974,-1.9371218753,0.9738556677\O,2.4303976807,
-1.6428187899,-0.4083100602\H,2.9211499008,-1.8802167812,-1.2077631702
\O,2.845443573,0.7366869502,0.9084060242\C,0.1981370202,1.621787364,1.
8625398518\H,0.8652619656,2.4774567835,2.028351501\H,-0.8409124468,1.9
668430264,1.9487466966\H,0.387709259,0.8717396581,2.6401223259\H,0.258
3087626,1.7698027348,-0.3075705455\\Version=ES64L-G09RevD.01\State=1-A
\HF=-628.182391\RMSE=7.332e-09\RMSEF=1.348e-05\Dipole=-1.914207,-0.1720
917,-0.6420219\Quadrupole=-0.4146475,2.477313,-2.0626656,-2.4576854,-6
.1297379,0.334551\PG=C01 [X(C7H11N1O4)]\@

E (R,S)-Diastereomer

1\1\GINC-WORKER0\FOpt\RM062X\def2SVP\C7H11N1O4\JHIOE\24-Jun-2018\0\#p
m062x\def2svp empiricaldispersion=gd3 opt freq int=ultrafine scrf=(cp
cm,solvent=N,N-dimethylformamide)\title\0,1\C,0.5592529549,1.2080501
103,0.6749848904\C,2.0093498129,0.8077280695,0.4872318665\C,-0.0930193
12,-0.0947461528,0.1881087573\H,0.3703296192,1.3604115526,1.7443732174
\C,0.1958355196,2.4440276593,-0.1441013447\H,-0.8575698943,2.709186647
,0.0146880453\H,0.3553411219,2.261193903,-1.2161425731\C,-1.5001946845
, -0.0124380527,-0.3230816808\H,-1.6270664358,0.4914552083,-1.285287043
3\C,-2.546559515,-0.4937174503,0.3503173923\H,-2.3627270185,-0.9775120
474,1.3159159157\C,-3.9665743851,-0.4163397584,-0.1109053989\H,-4.5797
937747,0.1302527675,0.6211660011\H,-4.0484486088,0.0854360621,-1.08377
14673\N,2.0473727685,-0.0722660555,-0.6257036397\O,0.7349654206,-0.431
4623905,-0.9421483222\H,-4.4004781532,-1.4239644116,-0.1950796034\H,0.
8184412859,3.2945080467,0.1620562138\O,0.0940277823,-1.0145122654,1.20
89585238\H,-0.2054142336,-1.8810291431,0.8970224072\O,2.8235373982,-1.
1768531247,-0.4026177849\H,3.3430939745,-1.2874489459,-1.2115283679\O,
2.982850847,1.1272943522,1.1066425555\\Version=ES64L-G09RevD.01\State=
1-A\HF=-628.1791255\RMSE=4.745e-09\RMSEF=2.222e-05\Dipole=-1.8849524,-0

3 CONJUGATED ENYNES AND CYCLIC NITRONATES

.2592799,-0.7960957\Quadrupole=0.2861581,2.5411119,-2.82727,-2.0383643
,-7.1325097,-0.1903833\PG=C01 [X(C7H11N1O4)]\@

Z (R,R) == (S,S) -Diastereomer

1\1\GINC-WORKER1\FOpt\RM062X\def2SVP\C7H11N1O4\JHIOE\28-Jun-2018\0\#p
m062x/def2svp empiricaldispersion=gd3 opt freq int=ultrafine scrf=(cp
cm,solvent=N,N-dimethylformamide)\title\0,1\C,0.4195605301,0.8134559
2,-0.5239795581\C,1.7356529949,0.0637952194,-0.5340755105\C,-0.2815274
009,0.0163892232,0.5870468621\C,-1.7854182677,0.0697049727,0.630495171
5\H,-2.1819540411,0.6292129256,1.4812535838\C,-2.6372348336,-0.4482651
863,-0.2606817619\H,-3.7015343399,-0.2845316646,-0.061131988\C,-2.3335
51949,-1.2153772121,-1.5104523776\H,-2.7247813125,-0.6718945391,-2.384
3222501\H,-1.264288564,-1.4038958562,-1.6492832285\N,1.4452669082,-1.2
801120484,-0.1865180193\O,0.1281915733,-1.3295369139,0.2849133653\H,-2
.8541489778,-2.1847473986,-1.4889616557\O,0.292616547,0.428698554,1.78
29297282\H,-0.0821072209,-0.0963800993,2.5042550455\O,2.3174967572,-1.
7859528247,0.7383958269\H,2.5344329688,-2.6737033523,0.4201329337\O,2.
8421377185,0.4681664549,-0.7461660664\C,0.5762673667,2.3046222545,-0.3
106556677\H,1.1682304111,2.7386701642,-1.1266945912\H,-0.4069996703,2.
7932974166,-0.2951051349\H,1.0867785619,2.5038596726,0.639331664\H,-0.
1071977799,0.5977362977,-1.4672252411\Version=ES64L-G09RevD.01\State=
1-A\HF=-628.1774492\RMSD=7.265e-09\RMSF=9.315e-06\Dipole=-1.8745306,-
.4916708,-0.0314141\Quadrupole=-3.86583,2.1178703,1.7479598,-5.1533396
,0.7830542,-0.2882912\PG=C01 [X(C7H11N1O4)]\@

Z (R,S)-Diastereomer

1\1\GINC-WORKER1\FOpt\RM062X\def2SVP\C7H11N1O4\JHIOE\28-Jun-2018\0\#p
m062x/def2svp empiricaldispersion=gd3 opt freq int=ultrafine scrf=(cp
cm,solvent=N,N-dimethylformamide)\title\0,1\C,0.3753865468,0.8802075
16,0.5243602152\C,1.8259381922,0.4910566054,0.3121533168\C,-0.27298210
17,-0.4220475692,0.0288232301\H,0.2062236689,1.0262550255,1.5980651123
\C,-0.0090989378,2.1186751568,-0.2810542874\H,-1.0598414629,2.37681372
08,-0.0966726265\H,0.1227363202,1.937000837,-1.3569748495\C,-1.6895759
686,-0.3643023755,-0.4735780593\H,-1.7900782485,-0.3465744958,-1.56088
577\C,-2.779736106,-0.3085821766,0.2979785185\H,-3.7439197516,-0.26798
01044,-0.2192845674\C,-2.8452284516,-0.271935616,1.7939437019\H,-3.445
2569626,-1.115742863,2.1673662709\H,-1.8565849471,-0.3158865966,2.2627
913789\N,1.8540596338,-0.3710726804,-0.8139987993\O,0.5414422664,-0.73
10869745,-1.119187681\H,-3.3602842411,0.6443401486,2.1201597988\H,0.61
85187067,2.9702156553,0.012004725\O,-0.0516830287,-1.3569634946,1.0328
11524\H,-0.4454093075,-2.1989004841,0.7625290284\O,2.6417531104,-1.473
3835392,-0.6223365929\H,3.1510150557,-1.5640373329,-1.4402064312\O,2.8
047440347,0.8074320774,0.9246949037\Version=ES64L-G09RevD.01\State=1-
A\HF=-628.17599\RMSD=8.503e-09\RMSF=1.032e-05\Dipole=-1.8635104,-0.164
6825,-0.5797679\Quadrupole=-0.2832683,1.5818325,-1.2985641,-2.3844169,
-7.5502806,0.7662477\PG=C01 [X(C7H11N1O4)]\@

Intermediate 22a

E

1\1\GINC-WORKER1\FOpt\RM062X\def2SVP\C7H11N1O2\JHIOE\29-Jun-2018\0\#p
m062x/def2svp empiricaldispersion=gd3 opt freq int=ultrafine scrf=(cp
cm,solvent=N,N-dimethylformamide)\title\0,1\C,0.5445982778,1.0250511
7,-0.133198758\C,2.0306659362,0.8053604653,-0.2615370781\C,-0.02998266
89,-0.1306028413,-0.4967159183\C,-0.0786128596,2.3161027089,0.27210439
11\H,-1.1742757727,2.2587003812,0.2603920505\H,0.2290101793,3.12801824

3 CONJUGATED ENYNES AND CYCLIC NITRONATES

09,-0.4053335168\C,-1.4262477164,-0.5157347555,-0.6201685905\H,-2.1594
983358,0.271686006,-0.4240076183\C,-1.8304242298,-1.7494551157,-0.9562
803452\H,-1.0655703158,-2.5093475248,-1.1453250902\C,-3.2596017661,-2.
1646770305,-1.0934242067\H,-3.4926379984,-2.9944636671,-0.4084275912\H
,-3.9433106962,-1.3323724535,-0.8795550601\N,2.1684243156,-0.661948372
2,-0.3509381106\O,0.9083754457,-1.0960961876,-0.8310151508\H,-3.463869
0914,-2.5328501171,-2.110728042\H,0.2394519142,2.6058446209,1.28548374
54\O,2.2445645223,-1.1146000539,0.9682016776\H,2.716397516,-1.95501753
51,0.8978165487\H,2.4333482273,1.2574264603,-1.1826839607\H,2.62654485
66,1.1527879108,0.5913839643\Version=ES64L-G09RevD.01\State=1-A\HF=-4
77.8685783\RMSD=4.216e-09\RMSF=2.919e-05\Dipole=-0.2544771,0.4641946,0
.1650314\Quadrupole=2.4007173,3.4772936,-5.8780109,1.0560629,1.9184523
,-0.2464295\PG=C01 [X(C7H11N1O2)]\@

Z

1\1\GINC-WORKER1\FOpt\RM062X\def2SVP\C7H11N1O2\JHIOE\29-Jun-2018\0\#p
m062x\def2svp empiricaldispersion=gd3 opt freq int=ultrafine scrf=(cp
cm,solvent=N,N-dimethylformamide)\title\0,1\C,1.0312886748,1.0349412
226,-0.0601482788\C,2.269895625,0.2601303125,-0.4284225006\C,0.0041202
498,0.1808144456,-0.1961951791\C,1.0394530438,2.4760871787,0.316695474
4\H,0.0274630192,2.8564301575,0.5021584358\H,1.4933993136,3.0841766585
,-0.4813851528\C,-1.4226062713,0.4194043916,-0.026996577\H,-1.66040983
01,1.4644129713,0.1844114903\C,-2.4477352565,-0.4470185015,-0.09914008
38\H,-3.4415508923,-0.0155871057,0.0601349067\C,-2.4318183319,-1.92054
665,-0.3633403324\H,-3.0095289457,-2.1455246428,-1.2737460141\H,-1.419
5958489,-2.317234034,-0.4775031267\N,1.8335470996,-1.1486904424,-0.394
9068429\O,0.4322946347,-1.0782264301,-0.5949948868\H,-2.9359525185,-2.
451339048,0.4590544397\H,1.6393920677,2.6401949619,1.2251448943\O,2.00
37005587,-1.5670680999,0.9262804703\H,2.1130262005,-2.5245756888,0.854
3309056\H,2.615114417,0.502515537,-1.4468517325\H,3.1114811406,0.37417
44061,0.2657482806\Version=ES64L-G09RevD.01\State=1-A\HF=-477.8653878
\RMSD=2.961e-09\RMSF=3.015e-06\Dipole=0.153673,0.4757355,0.138475\Quad
rupole=2.6792794,3.2282793,-5.9075587,0.9394481,-0.2696084,-1.305984\P
G=C01 [X(C7H11N1O2)]\@

Intermediate 23a

E

1\1\GINC-WORKER1\FOpt\RM062X\def2SVP\C7H9N1O3\JHIOE\24-Jun-2018\0\#p
m062x\def2svp empiricaldispersion=gd3 opt freq int=ultrafine scrf=(cpc
m,solvent=N,N-dimethylformamide)\title\0,1\C,-1.0414376718,1.0566451
387,-0.0130529971\C,-2.2059631064,0.2432485763,-0.3101740165\C,0.03423
19918,0.2308146515,-0.1357813198\C,-1.113482014,2.5172545002,0.2746676
894\H,-1.6506175317,3.0368389774,-0.5318495541\H,-0.1157457552,2.96228
27604,0.3674607656\C,1.4524966343,0.4946552313,0.0318120296\H,1.720440
0345,1.5277219232,0.2636359623\C,2.3937270598,-0.4540644112,-0.0842631
133\H,2.0755392739,-1.4763700952,-0.3135752632\C,3.8563619854,-0.21601
79231,0.0812917858\H,4.3961744756,-0.5002353589,-0.8348010776\H,4.0733
498017,0.8350819282,0.3098981844\H,-1.663603338,2.7035552975,1.2083586
502\N,-1.7130122078,-1.0913177639,-0.3651206541\O,-0.3169238026,-1.041
3276218,-0.444305911\O,-2.2251690405,-1.9459591236,-1.2658948769\H,-2.
1782774896,-1.5279849477,-2.1456897277\H,4.2582137899,-0.8468220658,0.
8887047647\O,-3.3712194193,0.5191226467,-0.4804074907\Version=ES64L-G
09RevD.01\State=1-A\HF=-551.8302765\RMSD=4.658e-09\RMSF=1.222e-05\Dipo
le=2.5581876,0.6676036,-0.4315901\Quadrupole=-3.5543571,0.4251919,3.12

3 CONJUGATED ENYNES AND CYCLIC NITRONATES

91652,-0.6310157,2.1983066,2.5982296\PG=C01 [X(C7H9N1O3)]\@

Z

1\1\GINC-WORKER1\FOpt\RM062X\def2SVP\C7H9N1O3\JHIOE\27-Jun-2018\0\#p
m062x\def2svp empiricaldispersion=gd3 opt freq int=ultrafine scrf=(cpc
m,solvent=N,N-dimethylformamide)\title\0,1\C,-0.7222924165,1.0741775
591,0.0284969008\C,-1.9539954766,0.3083156231,0.0746142587\C,0.2922170
601,0.1645598703,0.0767990252\C,-0.6927853289,2.5560767039,-0.12838795
89\H,-1.3564691911,2.8574768885,-0.9513226643\H,0.3164559945,2.9243556
867,-0.3464805621\C,1.7268333358,0.4004947826,0.0496833295\H,1.9868836
284,1.4594539445,0.0157305976\C,2.7267688938,-0.4985193815,0.058538307
6\H,3.7356180904,-0.0739637486,0.0364954363\C,2.6737336316,-1.99085145
26,0.0935186995\H,3.1768766562,-2.3534330695,1.0034762291\H,1.65836893
56,-2.393297308,0.0645550889\H,-1.0538598096,3.0541843286,0.7832577807
\N,-1.5435373334,-1.0173673582,0.3805814602\O,-0.1610219018,-1.1079388
955,0.1905398958\O,-2.1858566355,-2.0582931064,-0.1725070779\H,-2.2065
080563,-1.9277329457,-1.1387854084\H,3.2477754014,-2.3947489218,-0.754
2076435\O,-3.1128572083,0.6177613904,-0.0840311647\Version=ES64L-G09R
evD.01\State=1-A\HF=-551.8268489\RMSD=8.623e-09\RMSF=3.998e-06\Dipole=
2.3728193,0.1818894,-0.8147814\Quadrupole=-3.4798238,2.6497703,0.83005
36,1.1024823,2.5307541,2.6698849\PG=C01 [X(C7H9N1O3)]\@

Intermediate 26a

E (R,R) == (S,S) -Diastereomer

1\1\GINC-WORKER0\FOpt\RM062X\def2SVP\C7H13N1O3\JHIOE\27-Feb-2018\0\#p
m062x\def2svp empiricaldispersion=gd3 opt freq int=ultrafine scrf=(cp
cm,solvent=N,N-dimethylformamide)\title\0,1\C,1.8982387194,0.6327573
846,0.2663626443\C,0.384892222,0.8492906087,0.2761924815\C,-0.36169609
87,-0.4913279361,0.2827041416\H,2.2175611994,0.1797352291,1.2227241747
\H,0.0867594344,1.4419360841,1.1521205729\H,0.1121652514,1.3984683593,
-0.6369213725\N,1.544858415,-1.4795334225,-0.4930539653\O,2.2133490792
, -0.2864278188,-0.7799187254\O,0.1816596151,-1.2796688474,-0.786559815
8\C,-1.8376391363,-0.4080634954,0.0119734824\H,-2.3231102795,-1.389394
3174,-0.0305599517\C,-2.5481711718,0.7094170178,-0.1375573963\H,-2.041
4945091,1.6786440617,-0.0821227408\C,2.6805022197,1.899296699,0.003538
2607\H,2.4721235818,2.637065759,0.7895293415\H,3.7580398854,1.68889652
74,-0.0074010051\H,2.3923528204,2.3278341073,-0.9667533456\C,-4.025008
2546,0.7476563491,-0.3773035924\H,-4.4511468318,-0.2632852662,-0.42030
05481\H,-4.5328569781,1.3099563766,0.4206622322\H,-4.2512967991,1.2660
297849,-1.3211798176\O,-0.1967840089,-1.1728358306,1.4907220701\H,0.71
08374313,-1.5158005356,1.4887181751\H,1.8458358633,-2.1073346984,-1.23
93502203\Version=ES64L-G09RevD.01\State=1-A\HF=-554.2260393\RMSD=6.22
3e-09\RMSF=1.767e-05\Dipole=0.2085612,0.7755004,-0.061643\Quadrupole=2
.8518034,1.8579356,-4.709739,-2.8675897,2.5430795,2.2466586\PG=C01 [X(
C7H13N1O3)]\@

Intermediate 25a

E (R,R) == (S,S) -Diastereomer

1\1\GINC-LOGIN\FOpt\RM062X\def2SVP\C7H13N1O3\JHIOE\02-Jul-2018\0\#p m
062x\def2svp empiricaldispersion=gd3 opt freq int=ultrafine scrf=(cpcm
,solvent=N,N-dimethylformamide)\title\0,1\C,1.4596317565,0.041545156
2,0.3524704106\H,1.6489735517,0.0075478432,1.4304314401\C,2.4668102218
, -0.1069042577,-0.5107691818\H,2.2692179561,-0.0696580376,-1.586812999
5\C,3.8914413192,-0.3274159132,-0.1111481059\H,4.5356844997,0.46508138

3 CONJUGATED ENYNES AND CYCLIC NITRONATES

19,-0.5205360365\H,4.0047813435,-0.3455071367,0.9805873465\H,4.2637601
296,-1.2787548737,-0.5203018752\C,0.0236071586,0.2653311448,0.01876008
79\C,-0.4113870531,0.2167433215,-1.4770031456\H,0.4133604242,0.3717758
822,-2.1810871316\C,-0.8031546205,-1.2600280293,-1.2966151233\H,-1.782
3581419,-1.5911278896,-1.6602196146\H,-0.0076128196,-1.968025985,-1.55
3801586\N,-0.8359514105,-1.0892906519,0.1908229841\O,-1.9976984989,-0.
7987397947,0.7126628965\O,-0.2098645937,-2.1462925925,0.8638379897\C,-
1.5696167892,1.146663521,-1.797995072\H,-1.2648514824,2.1957211122,-1.
6860173652\H,-1.9060884026,0.9898359251,-2.8320073499\H,-2.4142963507,
0.9549835829,-1.1230788396\O,-0.5599682744,1.1736291716,0.8378030242\H
,-1.4418528593,0.7237689023,1.0266685239\H,-0.7026083642,-2.162650553,
1.7025788629\Version=ES64L-G09RevD.01\State=1-A\HF=-554.1988667\RMSD=
6.298e-09\RMSE=1.421e-05\Dipole=1.1716664,-0.5845459,-1.0832855\Quadru
pole=-0.4907073,-3.5559719,4.0466792,0.0319409,1.3910912,-1.8827181\PG
=C01 [X(C7H13N1O3)]\@

Base (model for DBU)

1\1\GINC-WORKER1\FOpt\RM062X\def2SVP\C6H12N2\JHIOE\16-Oct-2017\0\#p m
062x\def2svp empiricdispersion=gd3 opt freq int=ultrafine scrf=(cpcm
,solvent=N,N-dimethylformamide)\title\0,1\C,0.4987301968,-0.72472495
99,0.0023815323\C,-1.8287236023,-0.7461588314,-0.2445232013\C,-1.84582
58505,0.6229215059,0.4243823723\C,-0.6788921197,1.4370192705,-0.105843
9247\H,-2.0202032393,-0.621758217,-1.3275820379\H,-2.6468008257,-1.373
6809767,0.1404676883\H,-2.7898591675,1.1535762958,0.2400013964\H,-1.74
14873757,0.4915951862,1.5130618196\H,-0.8941620322,1.8030393145,-1.126
2474874\H,-0.5111799745,2.3260435307,0.5234649198\N,-0.5698420843,-1.4
390995851,-0.0450518026\N,0.5439143064,0.6447393127,-0.1098636522\C,1.
8156701781,-1.4388612084,0.1872230497\H,1.5997240029,-2.4990822634,0.3
4976537\H,2.452233342,-1.3403513879,-0.7042326884\C,1.7665976948,1.417
6141823,-0.1131872268\H,1.6848381637,2.2236117037,-0.8585323523\H,1.96
29001152,1.8843931523,0.8681564048\H,2.6295103335,0.8029853272,-0.3857
718292\H,2.375555938,-1.0412903519,1.0455456496\Version=ES64L-G09RevD
.01\State=1-A\HF=-344.9410107\RMSE=9.504e-09\RMSE=2.828e-06\Dipole=0.5
967969,1.5325027,-0.0311192\Quadrupole=3.8813857,-3.1915384,-0.6898473
,-1.3806748,0.1023666,-0.1582874\PG=C01 [X(C6H12N2)]\@

Protonated Base-H (model for DBU-H)

1\1\GINC-LOGIN\FOpt\RM062X\def2SVP\C6H13N2(1+)\JHIOE\16-Oct-2017\0\#p
m062x\def2svp empiricdispersion=gd3 opt freq int=ultrafine scrf=(cp
cm,solvent=N,N-dimethylformamide)\title\1,1\C,-2.3370728057,0.266800
2164,0.8442414261\C,-2.3957264633,-1.5270271537,-0.8381876367\C,-3.829
7978373,-1.0849272351,-1.0655949974\C,-3.9080672222,0.4295264779,-1.01
20448137\H,-1.7544355928,-1.2407036204,-1.685367435\H,-2.3248683272,-2
.6125660303,-0.7078704443\H,-4.1849731705,-1.4369587434,-2.041301814\H
,-4.4781467994,-1.5189689137,-0.2907641505\H,-3.418644853,0.8888968143
,-1.8849219903\H,-4.9529412401,0.7651621591,-0.9978774391\N,-1.9036253
427,-0.8942416479,0.3804704627\N,-3.271778252,0.9493040589,0.206354893
9\H,-1.1856254227,-1.3678976246,0.9168967731\C,-1.7309695341,0.7839994
082,2.1113344069\H,-1.0551641428,0.0363028699,2.53761641\H,-1.15989769
32,1.6995810644,1.9077538598\C,-3.7522428479,2.2539016086,0.6454191461
\H,-3.8052376073,2.9145819048,-0.2292857549\H,-4.7557616358,2.15843716
56,1.0830299987\H,-3.0757041438,2.7011019698,1.3770465385\H,-2.5157342
561,1.015174521,2.8418779802\Version=ES64L-G09RevD.01\State=1-A\HF=-3
45.418942\RMSE=5.837e-09\RMSE=6.492e-06\Dipole=0.4696211,-0.0583891,0.
3843384\Quadrupole=-1.5753998,1.867298,-0.2918982,-3.4946696,3.8406772
,2.6846319\PG=C01 [X(C6H13N2)]\@

HNO₂

1\1\GINC-LOGIN\FOpt\RM062X\def2SVP\H1N1O2\JHIOE\24-Jun-2018\0\#p m062x/def2svp empiricaldispersion=gd3 opt freq int=ultrafine scrf=(cpcm,solvent=N,N-dimethylformamide)\title\0,1\N,-2.2003175929,0.3889726727,-0.00620891\O,-2.82750878,1.5881234975,-0.00620891\O,-1.0368904841,0.5146969268,-0.00620891\H,-3.7749205829,1.373566293,-0.00620891\Version=ES64L-G09RevD.01\State=1-A\HF=-205.4619688\RMSD=3.100e-09\RMSF=6.496e-05\Dipole=-1.1455092,0.052597,0.\Quadrupole=1.8851653,-1.8896695,0.0045041,-0.4096392,0.,0.\PG=CS [SG(H1N1O2)]\@

NH₂OH

1\1\GINC-WORKER1\FOpt\RM062X\def2SVP\H3N1O1\JHIOE\24-Jun-2018\0\#p m062x/def2svp empiricaldispersion=gd3 opt freq int=ultrafine scrf=(cpcm,solvent=N,N-dimethylformamide)\title\0,1\N,-1.3877109388,0.8295451992,-0.0048990763\H,-0.9689424112,-0.1024734758,-0.0014368725\H,-0.9684634379,1.2975675866,-0.8106407835\O,-0.8412869719,1.4814085842,1.1235887408\H,-1.6162532103,1.7683369457,1.6197741015\Version=ES64L-G09RevD.01\State=1-A\HF=-131.5550709\RMSD=3.060e-09\RMSF=5.287e-05\Dipole=-0.0552986,-0.1308665,-0.2263914\Quadrupole=-1.7786048,0.5093486,1.2692562,-1.2620783,-2.1853654,0.6602806\PG=C01 [X(H3N1O1)]\@

Nitronate 6a

1\1\GINC-LOGIN\FOpt\RM062X\def2SVP\C7H11N1O2\JHIOE\15-Sep-2017\0\#p m062x/def2svp empiricaldispersion=gd3 opt freq int=ultrafine scrf=(cpcm,solvent=N,N-dimethylformamide)\title\0,1\C,-1.2141847131,0.9267002123,-0.4754610129\C,-2.3227736739,-0.131142986,-0.4837168391\C,-0.0419317412,0.0578718894,-0.1064644298\H,-1.0819105522,1.3528194729,-1.4793313867\H,-2.4484920039,-0.5773429758,-1.4819544152\H,-3.2853056983,0.2398831879,-0.1129745062\C,-1.4347151081,2.0436216853,0.545948097\H,-0.5512446349,2.6936531086,0.6119594214\H,-1.6247897459,1.6149687292,1.5409599024\C,1.3585176798,0.420355311,-0.1983950495\H,1.5326807336,1.388146944,-0.6795001819\C,2.4128418461,-0.2983319325,0.2305733646\H,2.2318876567,-1.2618754824,0.7103008506\C,3.8300075687,0.1526357981,0.0838777304\H,4.4105148259,-0.5745374204,-0.5049587151\H,3.8964880271,1.1328911603,-0.4067458656\H,4.3207154997,0.21785744,1.0674100839\H,-2.297258676,2.6610956815,0.2594066812\O,-1.8728656906,-1.1409631464,0.4213486122\N,-0.4702016491,-1.0588933239,0.4239557942\O,0.1133436396,-2.0073686632,0.9387386841\Version=ES64L-G09RevD.01\State=1-A\HF=-477.8732681\RMSD=4.055e-09\RMSF=7.418e-06\Dipole=-0.2509146,2.0227162,-1.0951367\Quadrupole=6.6356701,-5.2425567,-1.3931134,-2.4821911,2.31631,1.5335662\PG=C01 [X(C7H11N1O2)]\@

3.7.16 Additional Analytical Data

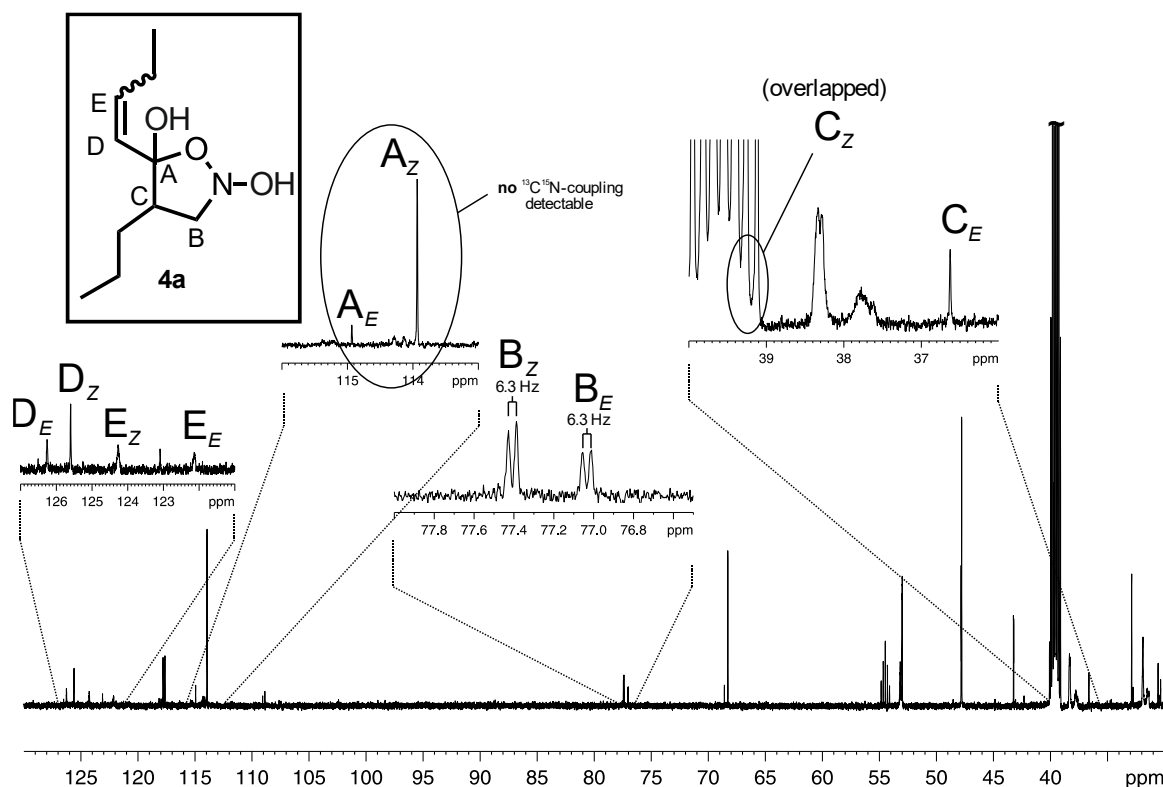


Figure SI 3.22 | Power gated decoupled spectrum of a mixture of $3a^{15}N$ (~250 mM) and DBU (~250 mM) in $DMSO-d_6$ @ 300 K at a proton resonance frequency of 600 MHz. Highlighted are the most relevant chemical shift areas for the intermediate species $4a^{15}N$ together with extracted ^{13}C - ^{15}N coupling constants.

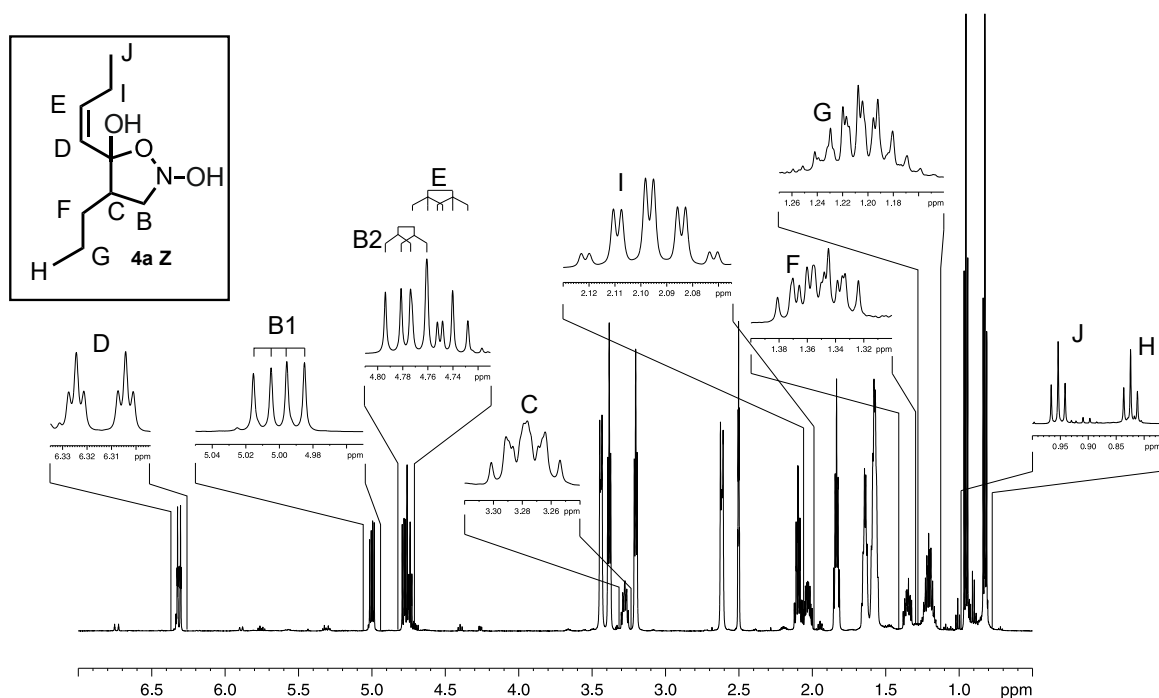


Figure SI 3.23 | Slice of 1H spectrum of a mixture of $3a$ (80 mM) and DBU (80 mM) after 5 min reaction time in $DMSO-d_6$ at 300 K at a proton resonance frequency of 600 MHz. All 1H resonances of the formed intermediate isomer $4a Z$ are magnified.

3 CONJUGATED ENYNES AND CYCLIC NITRONATES

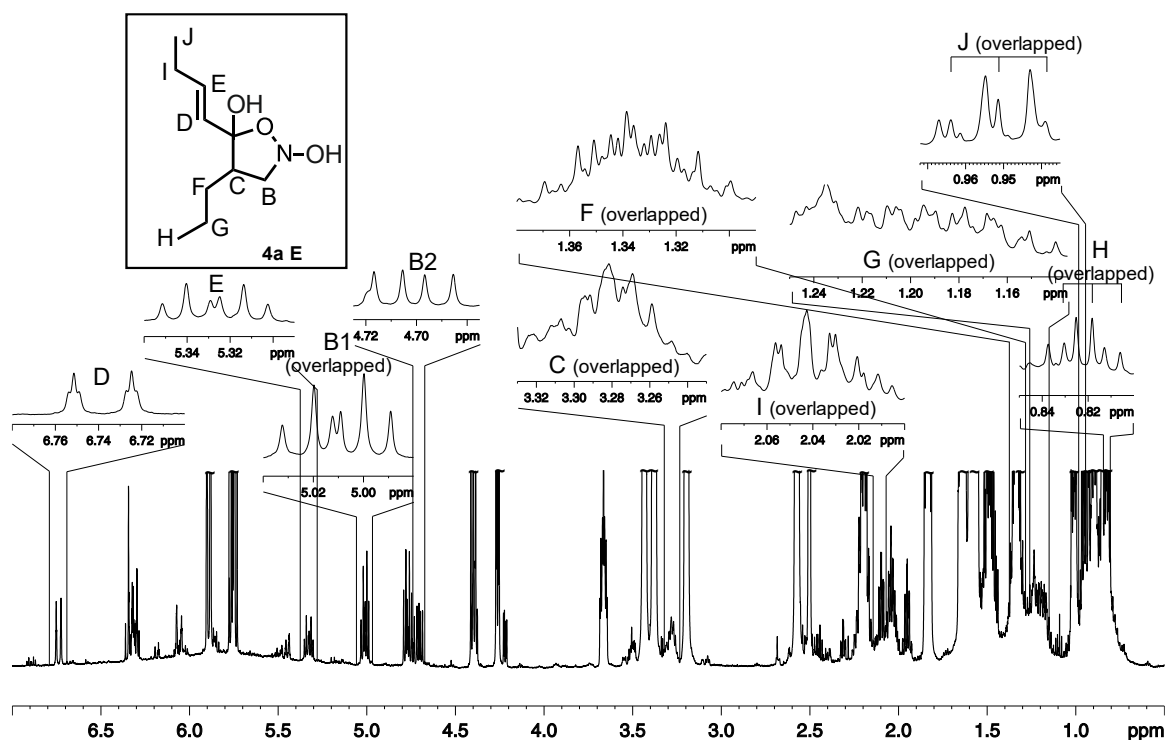


Figure SI 3.24 | Slice of ^1H spectrum of a mixture of **3a** (80 mM) and DBU (80 mM) after 1 h 51 min reaction time in DMSO-d_6 at 300 K at a proton resonance frequency of 600 MHz. All ^1H resonances of the formed intermediate isomer **4a E** are magnified. Resonances marked with (overlapped) are strongly overlapped by other signals.

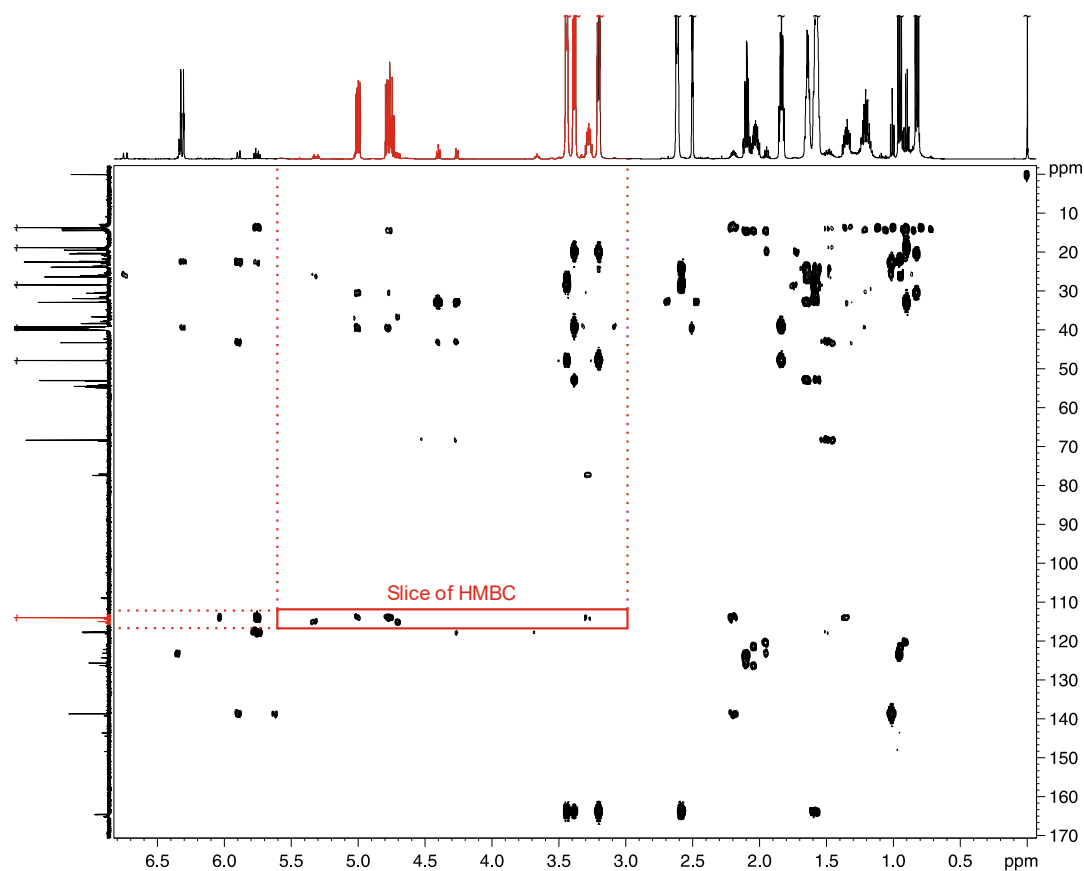


Figure SI 3.25 | Complete ^1H - ^{13}C -HMBC of a reaction mixture of dimer **3a** (80 mM) and DBU (80 mM) in DMSO-d_6 at 300K after a reaction time of 1 h 22 min. The regions marked in red are shown in Figure SI 3.1 as a slice of this HMBC.

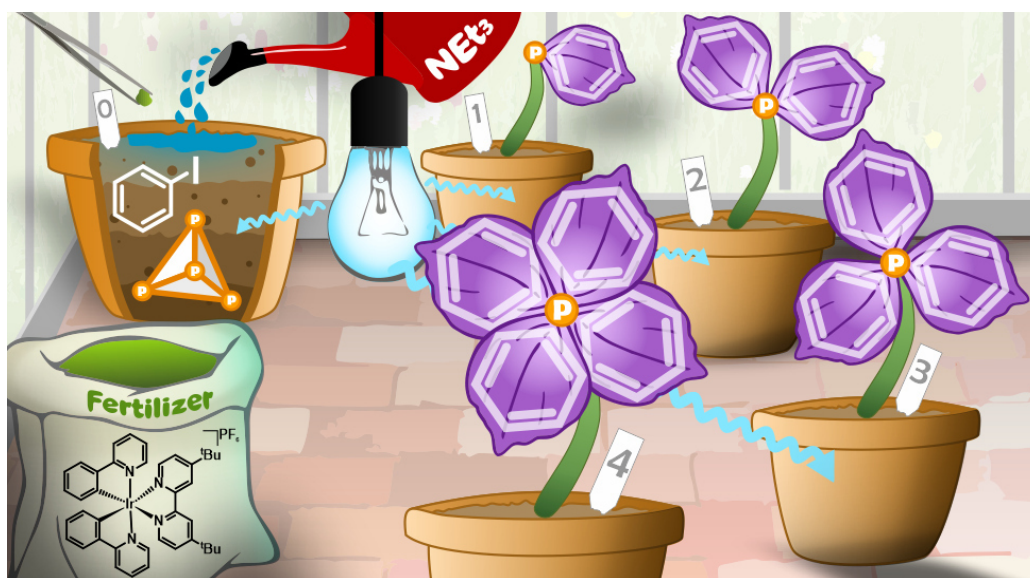
3.7.17 References

- [1] G. C. Levy, R. L. Lichter, *Nitrogen-15 Nuclear Magnetic Resonance Spectroscopy*, John Wiley & Sons Inc, **1979**.
- [2] M. Kinugasa, S. Hashimoto, *J. Chem. Soc. Chem. Commun.* **1972**, 4, 466–467.
- [3] M. Miura, M. Enna, K. Okuro, M. Nomura, *J. Org. Chem.* **1995**, 60, 4999–5004.
- [4] L. Kurti, B. Czako, *Strategic Applications of Named Reactions in Organic Synthesis*, Elsevier, **2005**.
- [5] R. Ballini, G. Bosica, D. Fiorini, M. Petrini, *Tetrahedron Lett.* **2002**, 43, 5233–5235.
- [6] S. King, *Curr. Top. Med. Chem.* **2005**, 5, 665–673.
- [7] F. Doctorovich, P. J. Farmer, M. Marti, *The Chemistry and Biology of Nitroxyl (HNO)*, Elsevier, **2016**.
- [8] F. T. Bonner, M. N. Hughes, *Comments Inorg. Chem.* **1988**, 7, 215–234.
- [9] S. Berger, S. Braun, H.-O. Kalinowski, *NMR-Spektroskopie von Nichtmetallen*, Georg Thieme Verlag, Stuttgart, **1993**.
- [10] M. B. Schmid, *NMR Spectroscopic Investigations on Aminocatalysis: Catalysts and Intermediates, Conformations and Mechanisms Dissertation*, **2011**.
- [11] B. M. Trost, C. Müller, *J. Am. Chem. Soc.* **2008**, 130, 2438–2439.
- [12] C. H. Bradley, G. E. Hawkes, E. W. Randall, J. D. Roberts, *J. Am. Chem. Soc.* **1975**, 97, 1958–1959.
- [13] E. Pretsch, P. Bühlmann, C. Affolter, M. Badertscher, *Spektroskopische Daten Zur Strukturaufklärung Organischer Verbindungen*, Springer, Heidelberg, **2000**.
- [14] J. B. Lambert, G. Binsch, J. D. Roberts, *Proc. Natl. Acad. Sci. U. S. A.* **1964**, 51, 735–737.
- [15] J. W. Essex, W. L. Jorgensen, *J. Phys. Chem.* **1995**, 99, 17956–17962.
- [16] A. S. Sarac, *Nanofibers of Conjugated Polymers*, CRC Press, Singapore, **2017**.
- [17] M. J. O'Neil, P. E. Heckelman, C. B. Koch, K. J. Roman, *The Merck Index, an Encyclopedia of Chemicals, Drugs, and Biologics*, Merck & Co., Inc, New Jersey, **2006**.
- [18] R. P. Bell, *The Proton in Chemistry*, Cornell University Press, Ithaca, **1973**.
- [19] P. M. Wood, *FEBS Lett.* **1981**, 124, 11–14.
- [20] J. Hübner, J. Liebscher, M. Pätzelt, *Tetrahedron* **2002**, 58, 10485–10500.
- [21] W.-W. Lin, Y.-J. Jang, Y. Wang, J.-T. Liu, S.-R. Hu, L.-Y. Wang, C.-F. Yao, *J. Org. Chem.* **2001**, 66, 1984–1991.
- [22] C. P. Burke, Y. Shi, *J. Org. Chem.* **2007**, 72, 4093–4097.
- [23] F. I. Carroll, J. D. White, M. E. Wall, *J. Org. Chem.* **1963**, 28, 1236–1239.
- [24] T. Mitsudo, Y. Nakagawa, K. Watanabe, Y. Hori, H. Misawa, **1985**, 565–571.
- [25] M. Jacubert, A. Tikad, O. Provot, A. Hamze, J. D. Brion, M. Alami, *European J. Org. Chem.* **2010**, 4492–4500.
- [26] Y. Zhao, D. G. Truhlar, *Theor. Chem. Acc.* **2008**, 120, 215–241.

3 CONJUGATED ENYNES AND CYCLIC NITRONATES

- [27] S. Grimme, J. Antony, S. Ehrlich, H. Krieg, *J. Chem. Phys.* **2010**, *132*, 154104.
- [28] J. Tomasi, B. Mennucci, R. Cammi, *Chem. Rev.* **2005**, *105*, 2999–3093.
- [29] L. Goerigk, S. Grimme, *J. Chem. Theory Comput.* **2011**, *7*, 291–309.
- [30] M. J. Frisch, G. W. Trucks, H. B. Schlegel, G. E. Scuseria, M. A. Robb, J. R. Cheeseman, G. Scalmani, V. Baone, G. A. Petersson, H. Nakatsuji, X. Ki, M. Caricato, A. Marenich, J. Bloino, B. G. Janesko, R. Gomperts, B. Mennucci, H. P. Hratchian, J. V. Ortiz, A. F. Izmaylov, J. L. Sonnenberg, D. Williams-Young, F. Ding, F. Lipparini, F. Egidi, J. Goings, B. Peng, A. Petrone, T. Henderson, D. Ranasinghe, V. G. Zakrzewski, J. Gao, N. Rega, G. Zheng, W. Liang, M. Hada, M. Ehara, K. Toyota, R. Fukuda, J. Hasegawa, M. Ishida, T. Nakajima, Y. Honda, O. Kitao, H. Nakai, T. Vreven, K. Throssell, J. A. Montgomery, J. E. Peralta, Jr., F. Ogliaro, M. Bearpark, J. J. Heyd, E. Brothers, K. N. Kudin, V. N. Staroverov, T. Keith, R. Kobayashi, J. Normand, K. Raghavachari, A. Rendell, J. C. Burant, S. S. Iyengar, J. Tomasi, M. Cossi, J. M. Millam, M. Klene, C. Adamo, R. Cammi, J. W. Ochterski, R. L. Martin, K. Morokuma, O. Farkas, J. B. Foresman, D. J. Fox, *Gaussian 09, Revision D.01*, Gaussian, Inc., Wallingford CT, **2016**.
- [31] F. Neese, *Wiley Interdiscip. Rev. Comput. Mol. Sci.* **2012**, *2*, 73–78.

4 DIRECT CATALYTIC TRANSFORMATION OF WHITE PHOSPHORUS INTO ARYLPHOSPHINES AND PHOSPHONIUM SALTS



Ulrich Lennert, Percia Beatrice Arockiam, **Verena Streitferdt**, Daniel J. Scott, Christian Rödl, Ruth M. Gschwind and Robert Wolf*

Nature Catalysis

Nat. Catal. **2019**, 2, 1101–1106.

DOI: 10.1038/s41929-019-0378-4

Verena Streitferdt performed all *in situ* and *ex situ* NMR studies in coordination with Ruth. M. Gschwind and wrote the Additional Findings and corresponding parts of the Supporting Information. Ulrich Lennert developed the initial catalytic procedure. Ulrich Lennert and Percia Beatrice Arockiam performed further optimization and together with Daniel J. Scott investigated the substrate scope. Verena Streitferdt, Ruth M. Gschwind, Ulrich Lennert and Daniel J. Scott performed mechanistic investigations. Christian Rödl performed (spectro)electrochemical experiments. The samples with NaPH_2 were prepared by Robin Rothfelder. The samples with H_2PPh in the SI were prepared from José Ricardo-Cammarata. Robert Wolf oversaw and directed the project. Ulrich Lennert and Daniel J. Scott prepared the manuscript, with input from all authors.

Reprinted (adapted) with permission from *Nat. Catal.* (via RightsLink). Text and Figures may differ from the original publication. Source of this chapter: <https://doi.org/10.1038/s41929-019-0378-4>

4 CATALYTIC TRANSFORMATION OF WHITE PHOSPHORUS

4.1 Abstract

Phosphorus compounds are ubiquitous in the chemical sciences, finding applications throughout industry and academia. Of particular interest to synthetic chemists are organophosphorus compounds, which contain P–C bonds. However, state-of-the-art processes for the synthesis of these important materials rely on an inefficient, stepwise methodology involving an initial oxidation of white phosphorus (P_4) with hazardous chlorine gas and the subsequent displacement of chloride ions. Catalytic P_4 organofunctionalization reactions have remained elusive, as they require multiple P–P bond-breaking and P–C bond-forming events to break down the P_4 core, all of which must occur in a controlled manner. Herein, we describe an efficient transition metal-catalyzed process capable of forming P–C bonds from P_4 . Using blue-light photocatalysis, this method directly affords valuable triarylphosphines and tetraarylphosphonium salts in a single reaction step.

4.2 Introduction

The academic, industrial and societal importance of phosphorus chemistry is difficult to overstate. Phosphorus is one of the six essential ‘biogenic elements’ required in large quantities by every living organism, and synthetic phosphorus compounds find myriad industrial and commercial applications due to their diverse array of useful chemical, physical and biological properties^[1]. This importance is reflected in the fact that white phosphorus (P_4) is currently produced on an estimated scale of >1 million tons per year (ref.^[2]). P_4 is by far the most reactive and industrially relevant form of elemental phosphorus, and acts as the common precursor from which effectively all synthetic phosphorus-containing species are ultimately prepared^[3]. Notable families of industrially relevant organophosphorus species prepared from P_4 include triarylphosphines (Ar_3P) and salts of the related quaternary phosphonium cations (Ar_4P^+). The former are widely used both in organic chemistry (notably in the classic Wittig reaction)^{[4],[5]} and as ligands for metal complexes^[6–11], including the homogeneous catalysts for numerous landmark chemical reactions (for example, industrial-scale hydroformylation)^[12]. The latter meanwhile find uses as ion-pair extractants^[13], phase-transfer catalysts^[14–16], aryl transfer reagents^[17,18] and additives in Heck reactions^[19]. Like most organophosphorus species, these compounds are currently prepared using hazardous and wasteful multi-step procedures involving an initial oxidation of P_4 to give phosphorus chlorides (PCl_3 , PCl_5), followed by the displacement of chloride with suitable organometallic nucleophiles (Figure 4.1a; ref.^[1]).

4 CATALYTIC TRANSFORMATION OF WHITE PHOSPHORUS

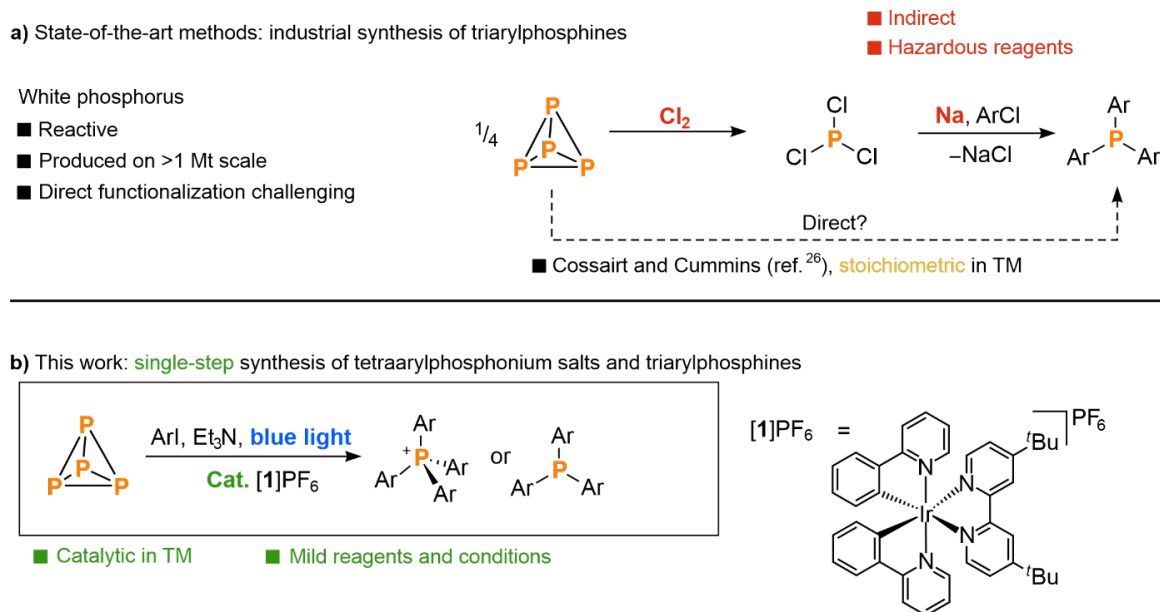


Figure 4.1 | Functionalization of white phosphorus. a) State-of-the-art methods for the industrial synthesis of triarylphosphines. b) Direct catalytic functionalization of P₄ to give triarylphosphines and tetraarylphosphonium salts, as described in this work. TM, transition-metal complex.

Far superior would be efficient catalytic methods to form the desired P–C bonds directly from P₄; however, such reactions are all but unknown^[20]. Notably, P₄ activation through binding to reactive low-valent transition-metal complexes^[21] or unsaturated main-group species^[22] such as carbenes^{[3],[23]} has become well established in recent years (albeit with results that are often challenging to predict). However, selective subsequent functionalization and, in particular, release of the resulting organophosphorus compounds remain highly problematic (the new P_n moieties typically act as strong many-electron donors with correspondingly low lability)^[21,22]. Similarly, although direct reactions of P₄ with organic or organometallic nucleophiles are known, these typically proceed with poor yields and selectivities, or only lead to partial breakup of the P₄ tetrahedron^[3]. As a result, even stoichiometric functionalization reactions that efficiently convert P₄ into valuable monophosphorus species remain rare. In this context, Barton and co-workers have previously shown that P₄ can act as an excellent trap for carbon-centered radicals and have applied this methodology to the synthesis of phosphonic acids^[24,25]; however, this method is inefficient with respect to phosphorus atom economy. Based on this work, Cossairt, Cummins and co-workers were also able to develop a direct, stoichiometric method for P₄ activation: in the presence of an equimolar amount of a titanium(III) complex [or, in more recent work, samarium(II) halides; refs. ^[26,27]], halogenated organic compounds undergo halide atom abstraction to yield reactive organoradicals, and subsequent addition to P₄ yields the corresponding tertiary monophosphines. Herein, we describe a catalytic method for the preparation of valuable triarylphosphines and tetraarylphosphonium salts directly from P₄ using visible light. These useful organophosphorus compounds can be obtained from P₄ and aryl iodides using an iridium photocatalyst and blue-light irradiation in the presence of triethylamine. We present the scope of this catalytic system and we propose an outline mechanism based on NMR monitoring and other spectroscopic observations.

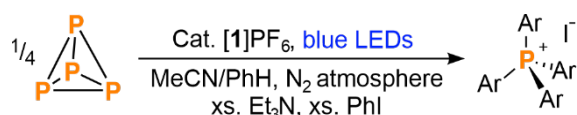
4.3 Results and Discussion

4.3.1 Reaction development

We reasoned that an efficient method for the catalytic transformation of P_4 directly into useful organophosphorus compounds could be developed if carbon-centered radicals were catalytically generated from a suitable precursor in the presence of P_4 ; fortunately, recent years have seen dramatic progress in this area through the use of photoredox methods driven by visible or UV light for the addition of carbon-centered radicals to unsaturated organic substrates^[28–31], and we anticipated that photocatalytic functionalization of white phosphorus could plausibly proceed by similar mechanisms. Notably, these methods do not require the use of powerful stoichiometric reagents that might be vulnerable to unproductive, direct reactions with P_4 . Thus, as a model system, the reduction of halobenzenes was chosen for initial investigation. After screening several established visible-light-driven photoredox catalysts (see Supplementary Table 1 for further details), we were delighted to observe that the catalytic conversion of P_4 into tetraphenylphosphonium iodide is viable using the known photocatalyst $[\text{Ir}(\text{dtbbpy})(\text{ppy})_2]\text{PF}_6$ (**[1]** PF_6 ; dtbbpy = 4,4'-di-*tert*-butyl-2,2'-bipyridine, ppy = 2-(2-pyridyl)phenyl; structure shown in Figure 4.1b). Employing **[1]** PF_6 , blue-light irradiation (455 nm) of a solution of P_4 , PhI (as a simple model substrate) and Et_3N (as a reductive quencher of the excited-state photocatalyst, *vide infra*) in a 3:1 MeCN/PhH (v/v) mixture (chosen to ensure solubility of all components) for 18 hours yielded with excellent selectivity the phosphonium salt $[\text{Ph}_4\text{P}]$: 76% conversion to $[\text{Ph}_4\text{P}]\text{I}$ was observed by quantitative ^{31}P NMR spectroscopy (Table 4.1, entry 1). Following oxidation, the Et_3N reductant is presumed to undergo formal hydrogen atom loss to give the iminium salt $[\text{Et}_2\text{NC}(\text{H})\text{Me}]\text{I}$, the formation of which also accounts for the fate of the PhI-derived iodide, but this has not been confirmed experimentally. On a preparative scale, the clean salt could be isolated from the reaction mixture by simple crystallization from H_2O on the open bench, followed by recrystallization from EtOH (Table 4.2, entry 1, Supplementary Method 2). This represents an effective example both of a catalytic transformation of P_4 directly into an organophosphorus species and of a successful catalytic functionalization of P_4 using a transition-metal complex^[20]. Switching from PhI to the less reactive PhBr or PhCl was found to be severely detrimental (Table 4.1, entries 2 and 3); further variations of solvent, oxidant, catalyst loading and reaction time (Supplementary Tables 2 and 3) indicated that the reaction parameters given in Table 4.1 are optimal. Control experiments confirmed that all the reaction components (PhI, Et_3N , **[1]** PF_6 and blue light) are necessary to observe the formation of the product (Table 4.1, entries 4–7). Interestingly, full consumption of white phosphorus was still observed in the absence of PhI (Table 4.1, entry 4), which suggests the possibility that it can be directly reduced under these reaction conditions (in this case, the formation of small amounts of PH_3 was observed by ^{31}P NMR spectroscopy, suggesting possible hydrogen atom transfer to P_4 from the oxidized sacrificial donor $[\text{Et}_3\text{N}]^+$).

4 CATALYTIC TRANSFORMATION OF WHITE PHOSPHORUS

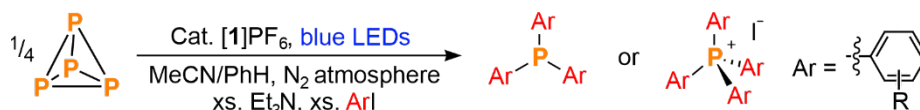
Table 4.1 | Photocatalytic functionalization of P₄ to [Ph₄P]I: screening of radical sources and control experiments



Entry	Conditions ^a	Conversion to [Ph ₄ P]I (%) ^b	Full conversion of P ₄
1	Standard	76	✓
2	PhBr instead of PhI	<1 ^c	✓
3	PhCl instead of PhI	0 ^c	✓
4	No PhI	0	✓
5	No [1]PF ₆	0	✗
6	No light	0	✗
7	No Et ₃ N	0	✗

^aThe standard reaction was performed with 123 μl iodobenzene (11 equiv. based on phosphorus atoms, 44 equiv. based on P₄), 200 μl Et₃N (14.4 equiv. based on phosphorus atoms), 3.1 mg P₄ (0.025 mmol, 1 equiv.) and 2.0 mg [1]PF₆ (2.2 mol% based on phosphorus atoms) in 2 ml MeCN/PhH (3:1, v/v) as solvent. The other reactions were performed with the noted modifications. The samples were prepared under N₂ atmosphere in a sealed tube and placed in a water-cooled block during irradiation (18 h) with blue LED light (455 nm). ^bConversions determined by quantitative ³¹P NMR experiments with Ph₃PO as an internal standard. ^cA complex mixture of phosphorus-containing species was observed by ³¹P NMR spectroscopy. xs, excess.

Table 4.2 | Substrate scope for photocatalytic P₄ functionalization



Entry	R	Time (h)	Product	Yield (%) ^{a,b}
1	H	18		34 (76)
2	<i>para</i> -Me	30		41 (54)
3	<i>meta</i> -OMe	24		60 (63, 3 ^c)
4	<i>ortho</i> -Me	18		71 (79)
5	<i>ortho</i> -OMe	30		37 (54)
6	<i>ortho</i> -SMe	18		19 (21)

^aIsolated yields. Reactions were performed with substrate (11.0 equiv. based on phosphorus atoms, 44 equiv. based on P₄), 2.0 ml Et₃N (14.4 equiv. based on phosphorus atoms), 31 mg P₄ (0.25 mmol, 1 equiv.) and 20 mg [1]PF₆ (2.2 mol% based on phosphorus atoms) in 20 ml MeCN/PhH (3:1, v/v) as solvent

4 CATALYTIC TRANSFORMATION OF WHITE PHOSPHORUS

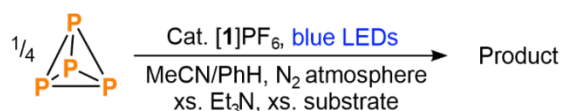
(Supplementary Methods 2–7). The samples were prepared under N₂ atmosphere in a sealed tube and placed in a water-cooled block during irradiation with blue light (455 nm). ^bThe values in parentheses are conversions determined by quantitative ³¹P NMR experiments with subsequently added Ph₃PO as an internal standard for equivalent reactions on 0.1 mmol scale (Supplementary Method 1). ^cConversion to the corresponding triarylphosphine.

4.3.2 Reaction scope

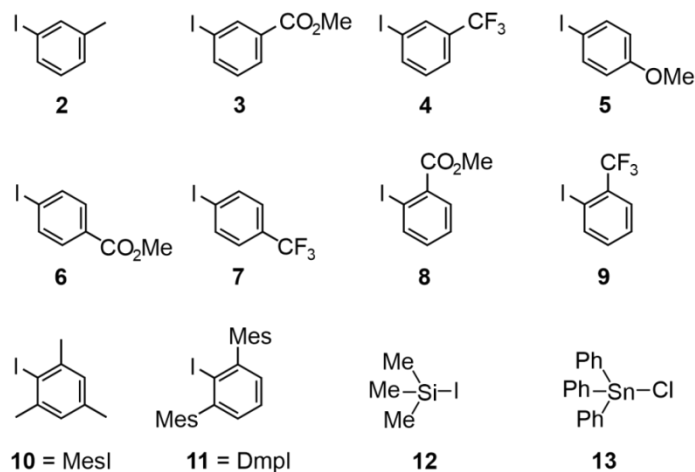
Having established the optimum procedure for the model substrate PhI, attention was shifted to investigating the scope of this new reaction. Gratifyingly, under identical conditions, a variety of substituted iodobenzene coupling partners could successfully be employed (Tables 2 and 3), including substrates bearing both electron-donating (Me, OMe) and electron-withdrawing (COOMe, CF₃) groups. Interestingly, and in contrast to the model substrate PhI, in many cases the expected [PAr₄] salt was accompanied by significant quantities of the tertiary phosphine PAr₃ in the product mixture, often with high selectivity for the latter. In particular, the reaction of (*ortho*-Tol)I (*ortho*-Tol = 2-methylphenyl) was found to give exclusively the tertiary phosphine (*ortho*-Tol)₃P (Table 4.2, entry 4), which has found extensive use as a bulky ligand in transition-metal coordination chemistry and related catalysis^[6–11], and could be cleanly isolated from a scaled-up reaction mixture by simple sublimation (71% isolated yield, 216 mg; Supplementary Method 5). Other substituted derivatives of [Ph₄P]I and Ph₃P could also be isolated using similar procedures (Table 4.2, entries 2, 3, 5, 6, Supplementary Methods 3, 4, 6, 7), although in practice this was limited to examples that proceeded with good conversion and high selectivity. The difference in reaction outcome between PhI and (*ortho*-Tol)I is most likely steric in nature, with the additional bulk of the *ortho*-Me group limiting the maximum coordination number at phosphorus. Indeed, when even bulkier substrates were employed the reaction was observed to stall earlier still: at the secondary (MesI; Mes = mesityl, 2,4,6-trimethylphenyl; Table 3, entry 9) or even primary phosphines (DmpI; Dmp = 2,6-dimesitylphenyl; Table 3, entry 10). In addition, electron-withdrawing groups also seemingly disfavour the quaternary phosphonium salt (for example, compare entry 4 to entries 5 and 6 in Table 3), plausibly due to destabilization of the requisite positive charge. Finally, a pair of heteroatomic substrates were investigated (Table 3, entries 11 and 12). Although the silicon-centered substrate Me₃SiI yielded no P–Si-bonded products, the reaction with Ph₃SnCl was found to selectively yield the potentially useful ‘P^{3–}’ synthon (Ph₃Sn)₃P with excellent conversion. The observed reactivity is qualitatively consistent with the known ready accessibility of tin-based radicals and the much lower stability of silicon-centered analogues^[32].

4 CATALYTIC TRANSFORMATION OF WHITE PHOSPHORUS

Table 4.3 | Further substrate scope for photocatalytic P₄ functionalization



Substrates:



Entry	Time (h)	Substrate	Product	Conv. (%) ^a
1	18	2		63 (5 ^b)
2	24	3		48 (8 ^b)
3	24	4		25 (20 ^b)
4	18	5		37 (5 ^b)
5	18	6		39
6	24	7		30
7	24	8		11
8	24	9		-
9	18	10		24 (3 ^c)
10 ^d	18	11		12
11	18	12	No P-Si bond formation	-
12	18	13		77, 14 ^e

Refer to Table 1 and Supplementary Method 1 for the standard conditions. ^aConversions determined by quantitative ³¹P NMR experiments with subsequently added Ph₃PO as an internal standard. ^bConversion into the corresponding triarylphosphine. ^cConversion into the corresponding monoarylphosphine. ^dThe reaction was performed with 88.1 mg 11 (2.0 equiv. based on phosphorus atom, 8.0 equiv. based on P₄), 200 μl Et₃N (14.4 equiv. based on phosphorus atom), 3.1 mg P₄ (0.025 mmol, 1 equiv.) and 2.0 mg [1]PF₆ (2.2 mol%) in 2 ml MeCN/PhH (1:3, v/v) as solvent. The sample was prepared under N₂ atmosphere in a sealed tube and

4 CATALYTIC TRANSFORMATION OF WHITE PHOSPHORUS

placed in a water-cooled block during irradiation with blue light (455 nm). ^eThe second value is the isolated yield for the equivalent reaction on 1 mmol scale (see Supplementary Method 8).

4.3.3 Mechanistic studies

The results of mechanistic investigations strongly suggest that the functionalization of P₄ proceeds by the mechanism summarized in Figure 4.2. Radical generation proceeds through a reductive quenching cycle in which the catalyst in its excited state first oxidizes Et₃N (steps i and ii) and then (as the reduced complex [1]) reduces PhI to Ph· (step iii). The aryl radicals thus generated then sequentially functionalize P₄ (step iv), producing in sequence PhPH₂, Ph₂PH, Ph₃P and finally Ph₄P⁺ (steps v–viii). Other Ph_xP_yH_z species must presumably be formed en route to PhPH₂; however, attempts to observe these early intermediates have thus far been unsuccessful and we are therefore unable to propose a specific mechanism for the initial break-up of the tetrahedral P₄ core.

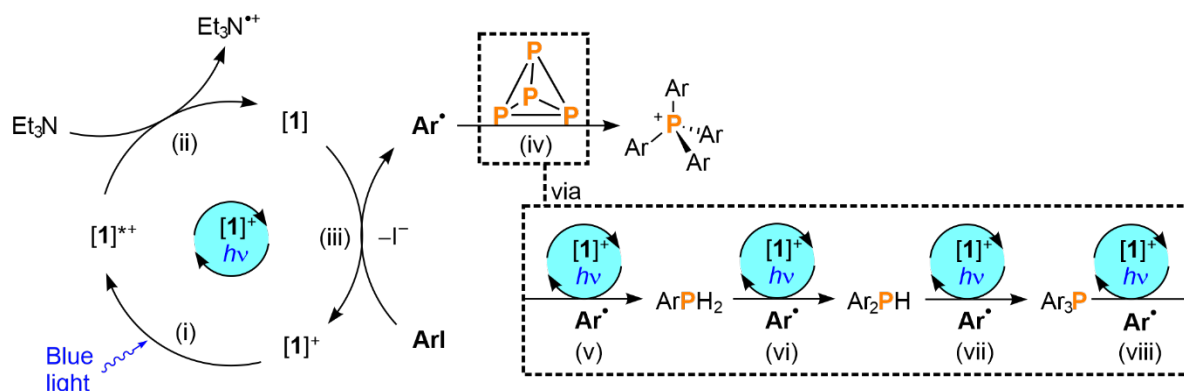


Figure 4.2 | Catalytic cycle. Proposed mechanism for the photocatalytic functionalization of white phosphorus to triarylphosphines and tetraarylphosphonium salts with [1]⁺ in the presence of aryl halides.

Nevertheless, we note that the formation of stable Ar₂P₄, Ar₃P₃ and Ar₄P₄ compounds through the direct reaction of P₄ with carbon-centered radicals has previously been demonstrated (for example, see ref. 26). At this point the complexity of this reaction must be acknowledged, however. For each P₄ molecule functionalized, 6 P–P and at least 16 C–I bonds are broken, 16 C–P bonds are formed and at least 16 Et₃N are oxidized. As such, the possibility that other elementary reaction steps may be mechanistically significant cannot be excluded. For example, UV/Vis observations (*vide infra*) and additional *in situ* NMR experiments (see Supplementary Discussions) both suggest that the direct activation of P₄ by the reduced photocatalyst [1] is a plausible side-reaction (either productive or unproductive). The proposed mechanism is nevertheless in line with both spectroscopic and electrochemical investigations. Measured redox potentials (Supplementary Figs. 42–44) support the plausibility of a reductive quenching mechanism in which the excited state of the photocatalyst is reduced by Et₃N to produce the neutral complex [1] (Figure 4.2, steps i and ii). Further, conclusive evidence for this proposal was provided by emission quenching experiments, which showed that out of all the reaction components (including intermediate phosphines PhPH₂, Ph₂PH and Ph₃P), only Et₃N effectively quenches the excited state of the [1]⁺ catalyst in MeCN/PhH (Supplementary Figs. 45–52). Furthermore, photo-CIDNP (photochemically induced dynamic nuclear

4 CATALYTIC TRANSFORMATION OF WHITE PHOSPHORUS

polarization) effects were detected during *in situ* NMR experiments (*vide infra*), indicative of the direct reaction of Et_3N with the photoexcited state of $[\mathbf{1}]^+$ (Supplementary Fig. 62). An alternative oxidative quenching mechanism, in which the photoexcited state reacts directly with the aryl iodide, is thus highly improbable (Supplementary Fig. 53). Following reduction by Et_3N , complex $[\mathbf{1}]$ can in turn effect reduction of the PhI substrate (Figure 4.2, step iii), thereby forming phenyl radicals $\text{Ph}\cdot$. This was corroborated by UV/Vis spectroscopy (Supplementary Fig. 54). Whereas a solution containing Et_3N and $[\mathbf{1}]\text{PF}_6$ in MeCN/PhH showed only a broad absorption band up to 500 nm, two new bands ($\lambda_{\text{max}} = 501$ and 537 nm) were formed after irradiation with 455 nm blue light (a new orange-red coloration was also noticeable by eye), which was taken to indicate the formation of the reduced neutral catalyst $[\mathbf{1}]$ as discussed above (despite its importance in many reported photocatalytic cycles, to our knowledge neutral $[\mathbf{1}]$ has not previously been characterized in detail; as such, chemical and electrochemical reduction experiments have been performed to support this assignment, as described in detail in the Supplementary Information, see also Supplementary Figs. 55 and 56). The initial spectrum was quickly regenerated upon addition of excess PhI (within seconds), confirming the ability of the substrate to effect the oxidation of $[\mathbf{1}]$ back to the catalyst resting state $[\mathbf{1}]^+$ (a similar recovery was also observed upon addition of P_4 as a solution in PhH). In the absence of PhI and P_4 , the $[\mathbf{1}]\text{PF}_6$ signal recovered far more slowly (over the course of approx. 20 minutes in the absence of blue light irradiation, presumably due to re-oxidation by the previously generated $[\text{Et}_3\text{N}]^+$ cation or decomposition products thereof). Having established a feasible mechanism for aryl radical generation, *in situ* NMR monitoring was used to investigate subsequent P_4 functionalization. A slightly altered 1:1 MeCN/PhH solvent mixture was used to ensure homogeneity throughout. This change was not found to significantly alter the final reaction outcome (see Supplementary Method 9). Time-resolved $^{31}\text{P}\{^1\text{H}\}$ NMR spectroscopy showed rapid consumption of the P_4 starting material (completely consumed within 5 hours under *in situ* NMR conditions) with the primary, secondary and tertiary monophosphines (PhPH_2 , Ph_2PH and Ph_3P) all visible as sequential reaction intermediates (Figure 4.3).

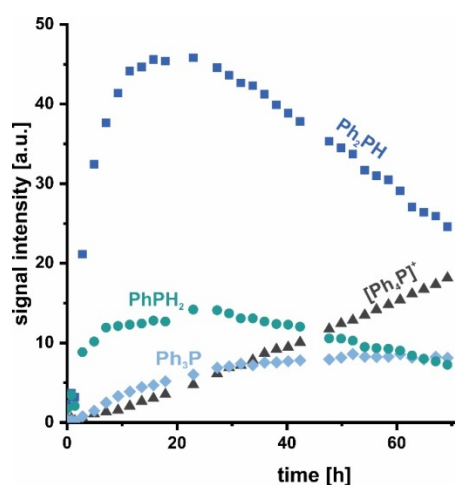


Figure 4.3 | Time-resolved $^{31}\text{P}\{^1\text{H}\}$ NMR study. *In situ* ^{31}P NMR monitoring of the formation of primary, secondary and tertiary phosphines and quaternary phosphonium salts during photocatalytic P_4 functionalization using PhI as substrate (see Supplementary Method 9 for full reaction details). The relatively long reaction time can probably be attributed to the reduced irradiation power of the *in situ* light source and non-stirring conditions in the NMR tube.

4 CATALYTIC TRANSFORMATION OF WHITE PHOSPHORUS

Although practical limitations preclude a quantitative analysis, it is qualitatively clear that the concentrations of these species in the initial stages of the reaction are too low to fully account for the consumption of P_4 . This suggests the presence of other as-yet-unidentified phosphorus-containing intermediates. Traces of the diphosphine Ph_4P_2 were observed by ^{31}P NMR spectroscopy. The hydrogen atoms in the primary and secondary products most likely derive from the Et_3N reductant (experiments using deuterated solvents showed no deuterium incorporation), either by deprotonation or hydrogen atom abstraction from its oxidation products. The subsequent loss of these hydrogen atoms (as required for conversion into Ph_4P^+) presumably involves similar steps; for example, 1H NMR analysis shows the formation of PhH during the course of the reaction, plausibly through hydrogen atom abstraction by a phenyl radical. 1H NMR spectroscopy also suggests the formation of Et_2NH as a minor side-product, which is also observed in many other photochemical reactions that use Et_3N as a reductant^[33]. Given the observation of $PhPH_2$, Ph_2PH and Ph_3P as successive reaction intermediates, control experiments were performed using these phosphines as individual starting materials in place of P_4 . In all cases, conversion into Ph_4P^+ was observed *via* the respective downstream intermediates, with similar or superior conversions to the analogous reaction using P_4 , consistent with the above *in situ* observations. Notably, each individual arylation step appears to be photochemically mediated, with comparable conversions never observed in the absence of light, $[1]PF_6$ or Et_3N . Low, but non-zero conversions were observed for these substrates in the absence of $[1]PF_6$ or Et_3N , suggesting some, much slower, background photochemical reaction (see Supplementary Tables 4–6, Supplementary Figs. 58, 59).

4.4 Conclusion

We have described herein the direct catalytic formation of P–C bonds from P_4 . Synthetically useful triarylphosphines and tetraarylphosphonium salts were formed in yields up to around 80%. This Cl_2 -free process represents an important step towards direct and catalytic approaches for the production of organophosphorus compounds and highlights the ability of modern photoredox techniques to solve pressing challenges in inorganic as well as organic chemistry. Furthermore, the successful catalytic functionalization of P_4 illustrates the promising potential of radical methods for the activation and functionalization of white phosphorus, and their increasing significance in organophosphorus chemistry. Ongoing research efforts in our groups are focused on further clarifying the mechanism of this highly elaborate transformation, as well as expanding the range of viable organic radical precursors.

4.5 Acknowledgements

We thank K. Zeitler (Universität Leipzig), O. Garcia Mancheño (Universität Münster) and J. C. Sloatweg (University of Amsterdam) for valuable comments on the manuscript, P. Nitschke (Gschwind group, University of Regensburg) for assistance with NMR measurements and B. Luy (Karlsruhe Institute of Technology) for providing the broadband pulse xyBEBOP. Support by the DFG graduate program 'Chemical Photocatalysis' (GRK 1626) and the European Research Council (ERC CoG 772299) is also gratefully acknowledged.

4.6 References

- [1] D. E. C. Corbridge, *Phosphorus 2000. Chemistry, Biochemistry and Technology*, Elsevier, **2000**.
- [2] W. Schipper, *Eur. J. Inorg. Chem.* **2014**, 2014, 1567–1571.
- [3] J. E. Borger, A. W. Ehlers, J. C. Slootweg, K. Lammertsma, *Chem. - A Eur. J.* **2017**, 23, 11738–11746.
- [4] G. Wittig, U. Schöllkopf, *Chem. Ber.* **1954**, 87, 1318–1330.
- [5] G. Wittig, W. Haag, *Chem. Ber.* **1955**, 88, 1654–1666.
- [6] Y. Guo, H. Fu, H. Chen, X. Li, *Catal. Commun.* **2008**, 9, 1842–1845.
- [7] Paul C. J. Kamer, A. Piet W. N. M. van Leeuwen, J. N. H. Reek, *Acc. Chem. Res.* **2001**, 34, 895–904.
- [8] R. Martin, S. L. Buchwald, *Acc. Chem. Res.* **2008**, 41, 1461–1473.
- [9] L. H. Pignolet, *Homogeneous Catalysis with Metal Phosphine Complexes*, Springer US, **1983**.
- [10] D. S. Surry, S. L. Buchwald, *Angew. Chemie Int. Ed.* **2008**, 47, 6338–6361.
- [11] T. Fujihara, S. Yoshida, J. Terao, Y. Tsuji, *ChemInform* **2009**, 11, 2121–2124.
- [12] A. Börner, R. Franke, in *Hydroformylation Fundam. Process. Appl. Org. Synth.*, Wiley-VCH Verlag GmbH & Co. KGaA, Weinheim, Germany, **2016**, pp. 73–266.
- [13] M. S. El-Shahawi, S. S. M. Hassan, A. M. Othman, M. A. Zyada, M. A. El-Sonbati, *Anal. Chim. Acta* **2005**, 534, 319–326.
- [14] C. M. Starks, C. L. (Charles L. Liotta, M. E. Halpern, *Phase-Transfer Catalysis: Fundamentals, Applications, and Industrial Perspectives*, Springer Netherlands, **1994**.
- [15] S. Kondo, T. Mori, H. Kunisada, Y. Yuki, *Macromol. Rapid Commun.* **1990**, 11, 309–313.
- [16] K. Manabe, *Tetrahedron Lett.* **1998**, 39, 5807–5810.
- [17] B. T. Ramanjaneyulu, M. Pareek, V. Reddy, R. Vijaya Anand, *Helv. Chim. Acta* **2014**, 97, 431–437.
- [18] Z. Deng, J. H. Lin, J. C. Xiao, *Nat. Commun.* **2016**, 7, 10337.
- [19] M. T. Reetz, G. Lohmer, R. Schwickardi, *Angew. Chemie Int. Ed.* **1998**, 37, 481–483.
- [20] Y. H. Budnikova, T. V. Gryaznova, V. V. Grinenko, Y. B. Dudkina, M. N. Khrizanforov, *Pure Appl. Chem.* **2017**, 89, 311–330.
- [21] M. Caporali, L. Gonsalvi, A. Rossin, M. Peruzzini, *Chem. Rev.* **2010**, 110, 4178–4235.
- [22] M. Scheer, G. Balázs, A. Seitz, *Chem. Rev.* **2010**, 110, 4236–4256.
- [23] S. Khan, S. S. Sen, H. W. Roesky, *Chem. Commun.* **2012**, 48, 2169–2179.
- [24] D. H. R. Barton, J. Zhu, *J. Am. Chem. Soc.* **1993**, 115, 2071–2072.
- [25] D. H. R. Barton, R. A. Vonder Embse, *Tetrahedron* **1998**, 54, 12475–12496.
- [26] B. M. Cossairt, C. C. Cummins, *New J. Chem.* **2010**, 34, 1533–1536.
- [27] S. K. Ghosh, C. C. Cummins, J. A. Gladysz, *Org. Chem. Front.* **2018**, 5, 3421–3429.

4 CATALYTIC TRANSFORMATION OF WHITE PHOSPHORUS

- [28] B. König, *Chemical Photocatalysis*, De Gruyter, Berlin, Boston, **2013**.
- [29] N. A. Romero, D. A. Nicewicz, *Chem. Rev.* **2016**, *116*, 10075–10166.
- [30] L. Marzo, S. K. Pagire, O. Reiser, B. König, *Angew. Chemie Int. Ed.* **2018**, *57*, 10034–10072.
- [31] J. Twilton, C. C. Le, P. Zhang, M. H. Shaw, R. W. Evans, D. W. C. MacMillan, *Nat. Rev. Chem.* **2017**, *1*, 0052.
- [32] A. G. Davies, in *Chem. Tin*, Springer Netherlands, **1998**, pp. 265–289.
- [33] V. S. Vyas, V. W. H. Lau, B. V. Lotsch, *Chem. Mater.* **2016**, *28*, 5191–5204.

4.7 Supporting Information

4.7.1 General information

All reactions and manipulations were performed under an N₂ atmosphere (< 0.1 ppm O₂, H₂O) through use of an MBraun Unilab glovebox. All glassware was oven-dried (160 °C) overnight prior to use. Benzene was dried over Na and stored over molecular sieves (3 Å). Acetonitrile, dimethylsulfoxide and dimethylformamide were distilled from CaH₂ and stored over molecular sieves (3 Å). THF was purified using an MBraun SPS-800 system and stored over molecular sieves (3 Å). C₆D₆ was distilled from K and stored over molecular sieves (3 Å). CD₃CN was stored over molecular sieves (3 Å). KC₈ was prepared in accordance with the literature.^[1] All other chemicals were purchased from major suppliers (Aldrich, ABCR) liquids were purified by Kugelrohr distillation and freeze-pump-thaw degassed three times prior use; P₄, Ph₃P and Ph₃PO were purified by sublimation; all others were used as received.

GC-MS spectra were recorded using a mass detector model Agilent-5977B coupled with a GC oven 7820A and a Restek 5 Sil MS column with H₂ as carrier gas, using a 30 m × 0.25 mm × 0.25 μm column. Injection parameters: temperature of injection = 250 °C, split ratio = 25/1, volume injected = 1 μL, flow rate = 1.2 mL/min. Oven parameters: starting temperature = 50 °C, rate = 15 °C/min, end temperature = 300 °C, held for 5 min. Mass parameters: Temp source = 230 °C, Quad temperature = 150 °C, start mass = 50.00, end mass = 550.00.

With the exception of *in situ* experiments (for details of which, see chapter 4.7.9), qualitative NMR spectra were recorded at room temperature on Bruker Avance 400 (400 MHz) spectrometers and were processed using Topspin 3.2. Chemical shifts, δ, are reported in parts per million (ppm); ¹H NMR and ¹³C NMR shifts are reported relative to SiMe₄ and were referenced internally to residual solvent peaks, while ³¹P NMR shifts were referenced externally to 85 % H₃PO₄ (aq.). NMR samples were prepared in the glovebox using NMR tubes fitted with screw caps. Optimization reactions (see Table SI 4.3) and photocatalytic phenylation reactions of Ph₃P, Ph₂PH and PhPH₂ (see Figure SI 4.10) were analyzed by ³¹P{¹H} spectra using only a single scan (DS = 0, D1 = 2 s). The accuracy of this method was confirmed by preparing solutions of (*o*-tol)₃P or Ph₄PCl and 0.05 mmol Ph₃PO in MeCN/PhH (1.5 mL, 0.5 mL, respectively), and comparing the measured and expected relative integrations (Figure SI 4.1).

4 CATALYTIC TRANSFORMATION OF WHITE PHOSPHORUS

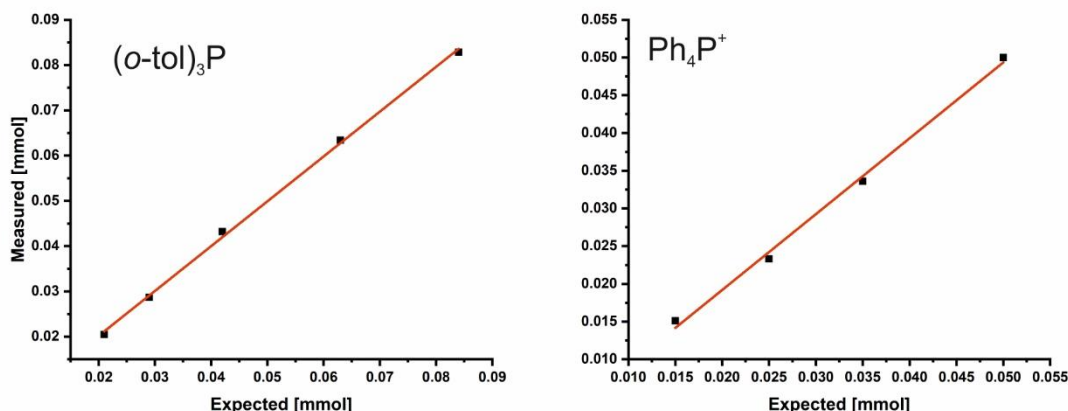


Figure SI 4.1 | Plots showing the consistency between measured (by integration against 0.05 mmol Ph_3PO using a $^{31}\text{P}\{^1\text{H}\}$ experiment (zgpg) with a single scan) and expected (based on mass added) molar quantities of $(o\text{-tol})_3\text{P}$ (left) or Ph_4P^+ (right) in MeCN/PhH (3:1) solutions.

Quantitative measurements for the substrate screening were conducted on a Bruker Avance III HD 600 MHz spectrometer with a fluorine selective TBIF probe and on a Bruker Avance NEO 600 MHz spectrometer with a double resonance broad band probe (BBO H&F). Yields were determined by 1D ^{31}P -NMR spectroscopy. In order to meet quantitative conditions special attention was payed to the following aspects:

- Pulse lengths were calibrated. The O1P of the spectrum was set close to the frequencies of interest to enable maximum excitation. In cases where the distance between signals of interest was greater than 21000 Hz, one spectrum was recorded for each signal of interest, having its O1P close to the respective frequency.
- T_1 relaxation times were determined for all peaks of interest and a D1 of $\geq 5 \times T_1$ was used to ensure full relaxation between scans.
- The NS was adjusted so that the S/N-ratio (signal to noise ratio) was higher than 100/1. In order to reduce measurement time and to increase the S/N-ratio compared to a standard 1D experiment using only a 90° pulse (zg experiment), the zgig pulse program (inverse gated decoupled) was used, applying proton decoupling during the acquisition time. Since the zgig pulse program uses decoupling, it had to be ensured that any signal enhancement due to NOE (nuclear Overhauser effect) is negligible. Therefore, zg and zgig experiments were conducted and the integrals of the signals of interest were compared. For all reaction mixtures investigated (except those for the product DmpPH_2), the integrals corresponding to both the internal standard (Ph_3PO) and the product stayed constant. In the case of DmpPH_2 , in the zgig experiment a higher integral for the signal of the product was obtained compared to the zg experiment (probably due to greater impact of the NOE since two protons are bound to the phosphorus atom). Hence, the zg pulse program was used to determine the yield of DmpPH_2 .
- After acquisition, the spectra were processed and integrated and the yields were determined by referencing the integral of the product to that of the standard Ph_3PO . In cases where two spectra

4 CATALYTIC TRANSFORMATION OF WHITE PHOSPHORUS

with different O1P had to be recorded (see above) these spectra were scaled to each other with the command intser.

- The qualitative spectra of the substrate screening are shown in chapter 4.7.4 for reasons of clarity and comprehensibility.

4.7.2 General procedure for photocatalytic functionalization of P_4 (0.1 mmol scale)

To a 10 mL stoppered tube equipped with a stirring bar were added the appropriate iodobenzene derivative (1.1 mmol, 11 equiv. based on the phosphorus atom), electron donor (1.44 mmol, 14.4 equiv.), catalyst (2.2 μ mol, 2.2 mol%), and P_4 (0.025 mmol, 1 equiv.). The mixture was dissolved in a mixture of MeCN (1.5 mL) and benzene (0.5 mL). The tube was sealed, placed in a water-cooled block (to ensure a near-ambient temperature was maintained, Figure SI 4.2), and irradiated with blue light (455 nm (\pm 15 nm), 3.2 V, 700 mA, Osram OSOLON SSL 80) for 18 h (unless stated otherwise). A solution of Ph_3PO (13.9 mg, 0.05 mmol) in approximately 0.5 mL of PhH was subsequently added to act as an internal standard. The resulting mixture was subjected to GC-MS and NMR analysis.

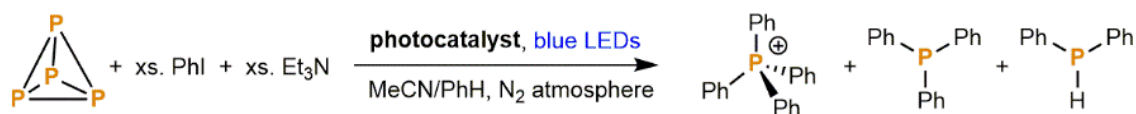


Figure SI 4.2 | Illustration of the equipment setup used for photocatalytic reactions at 0.1 mmol scale.

4 CATALYTIC TRANSFORMATION OF WHITE PHOSPHORUS

4.7.3 Optimization of reaction conditions

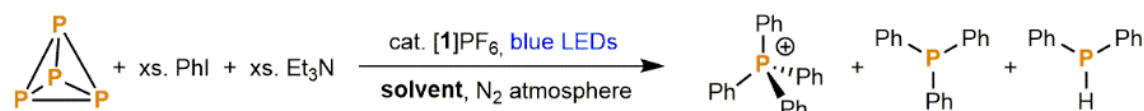
Table SI 4.1 | Photocatalytic functionalization of P₄ to [Ph₄P]⁺: screening of photocatalysts^[a]



Entry	Photocatalyst	Full conv. of P ₄ ?	Conv. to [Ph ₄ P] ⁺ / %	Conv. to Ph ₃ P / %	Conv. to Ph ₂ PH / %
1	[1]PF ₆	✓	76	0	0
2	Ir(ppy) ₃	✓	0	0	0
3	RuCl ₂ (bpy) ₃ · 6H ₂ O	✗	0	0	0
4	EOSIN Y	✗	0	0	0
5 ^[b]	EOSIN Y	✗	0	0	0
6 ^[b]	Rhodamine 6G	✗	0	0	0
7	(Ir[dF{CF ₃ }ppy] ₂ [dtbpy])PF ₆	✓	25	22	8

[a] For the general procedure, see section 4.7.2. [b] Irradiated with green LEDs (528 nm).

Table SI 4.2 | Photocatalytic functionalization of P₄ to [Ph₄P]⁺: screening of solvents^[a]

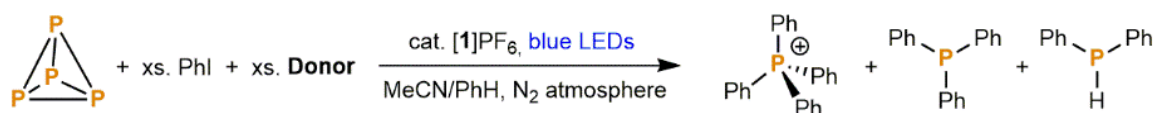


Entry	Solvent	Full conv. of P ₄ ?	Conv. to [Ph ₄ P] ⁺ / %	Conv. to Ph ₃ P / %	Conv. to Ph ₂ PH / %
1	DMF / PhH (3:1)	✓	7	11	5
2	DMF / PhH (3:1)	✓	25	13	1
3	DMSO	✓	28	11	3
4	DMF	✓	5	13	5

[a] The general procedure (section 4.7.2) was modified to use the solvent system indicated (identical solvent volume).

4 CATALYTIC TRANSFORMATION OF WHITE PHOSPHORUS

Table SI 4.3 | Photocatalytic functionalization of P₄ to [Ph₄P]⁺: screening of sacrificial electron donors^[a]



Entry	Solvent	Full conv. of P ₄ ?	Conv. to [Ph ₄ P] ⁺ / %	Conv. to Ph ₃ P / %	Conv. to Ph ₂ PH / %
1	EtN(<i>i</i> Pr) ₂	X	2	7	11
2	EDTA	✓	0	0	0
3	DBU	X	0	0	0
4	DABCO	X	0	0	0
5	2,6-lutidine	✓	0	0	0
6	<i>p</i> -anisidine	✓	0	0	0
7	(HOCH ₂ CH ₂) ₃ N	X	0	0	0
8	Ph ₃ N	✓	0	0	0
9	<i>n</i> Bu ₃ N	X	31	12	0

[a] For the general procedure, see section 4.7.2.

4.7.4 Characterization of optimized 0.1 mmol scale reactions

The substrate screening was performed for each substrate at least twice to ensure reproducibility. The spectra of the qualitative single scan ³¹P{¹H} (zgpg) NMR experiments are shown for every substrate to give an overview of the phosphorus species formed. The conversions were determined by quantitative ³¹P NMR (zg and zgig) experiments as mentioned in the text (see Table SI 4.1 for further information).

4 CATALYTIC TRANSFORMATION OF WHITE PHOSPHORUS

4.7.4.1 Tetraphenyl phosphonium iodide (Table 4.2, Entry 1)

The general procedure was followed using iodobenzene (130 μ L, 1.1 mmol), which resulted in 76% conversion to tetraphenylphosphonium iodide as judged by quantitative $^{31}\text{P}\{^1\text{H}\}$ (zgpg) NMR spectroscopy (ESI-MS: expected = 339 m/z; observed = 339 m/z).

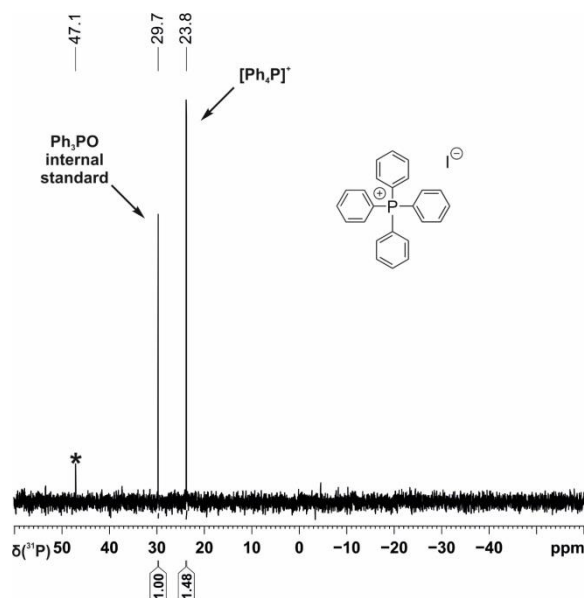


Figure SI 4.3 | Qualitative single scan $^{31}\text{P}\{^1\text{H}\}$ (zgpg) NMR spectrum for the photocatalytic functionalization of P_4 using iodobenzene. * marks the signal of an unknown by-product.

4.7.4.2 Tri(*o*-tolyl)phosphine (Table 4.2, Entry 4)

The general procedure was followed using 2-iodotoluene (140 μ L, 1.1 mmol), which resulted in 79% conversion to tri(*o*-tolyl) phosphine as judged by quantitative $^{31}\text{P}\{^1\text{H}\}$ (zgpg) NMR spectroscopy (GC-MS: expected = 304 m/z; observed = 304 m/z).

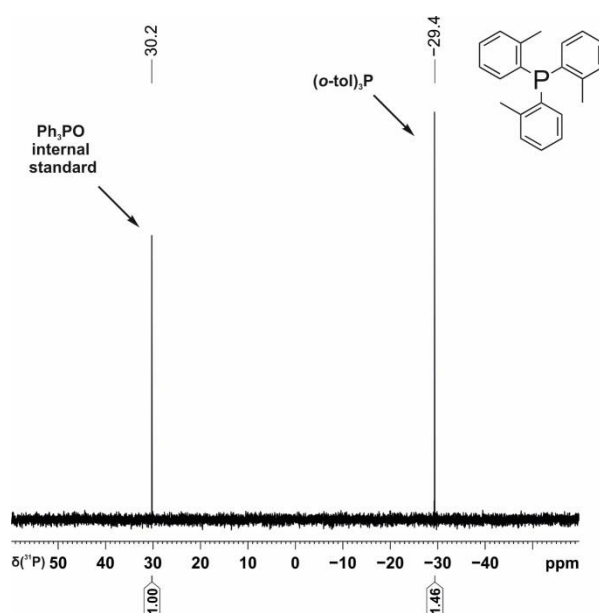


Figure SI 4.4 | Qualitative single scan $^{31}\text{P}\{^1\text{H}\}$ (zgpg) NMR spectrum for the photocatalytic functionalization of P_4 using 2-iodotoluene.

4 CATALYTIC TRANSFORMATION OF WHITE PHOSPHORUS

4.7.4.3 Tetra(*m*-tolyl)phosphonium iodide (Table 4.3, Entry 1)

The general procedure was followed using 3-iodotoluene (140 μL , 1.1 mmol), which resulted in 63% conversion to tetra(*m*-tolyl)phosphonium iodide and 5% conversion to tri(*m*-tolyl) phosphine as judged by quantitative $^{31}\text{P}\{^1\text{H}\}$ (zgig) NMR spectroscopy.

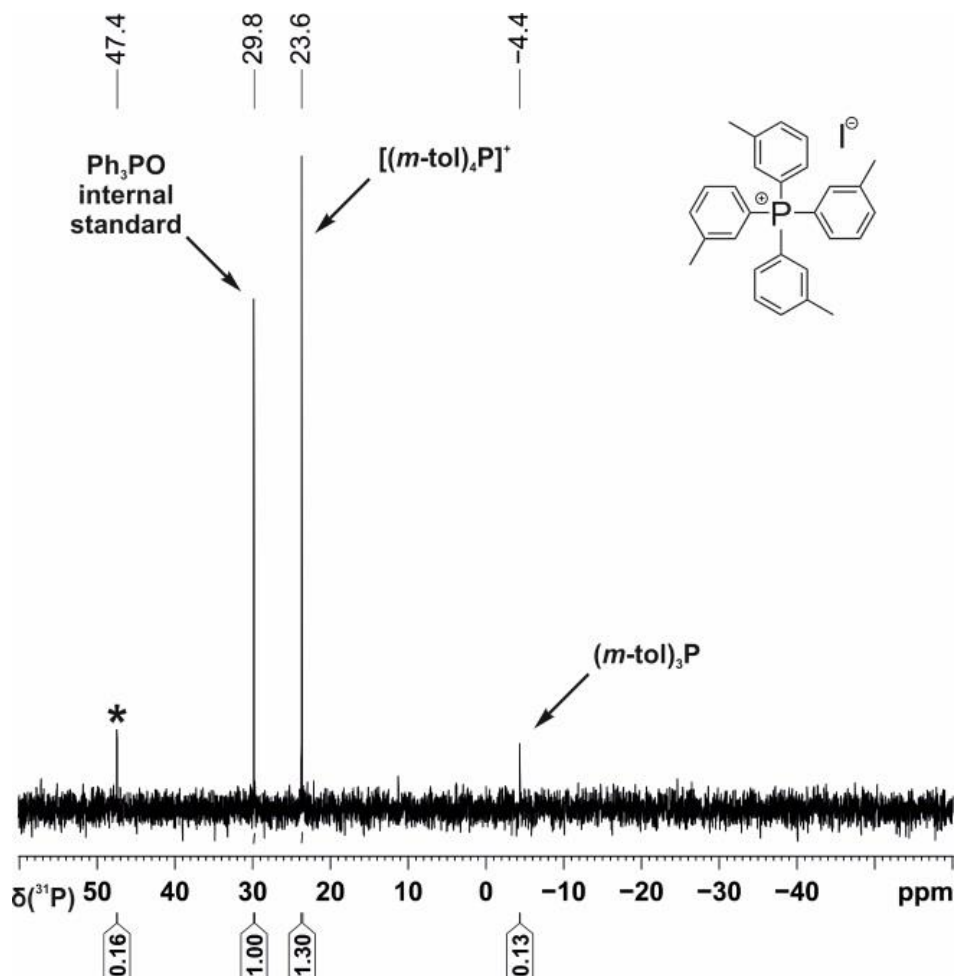


Figure SI 4.5 | Qualitative single scan $^{31}\text{P}\{^1\text{H}\}$ (zgpg) NMR spectrum for the photocatalytic functionalization of P_4 using 3-iodotoluene. * marks the signal of an unknown by-product.

4.7.4.4 Tetra(*p*-tolyl)phosphonium iodide (Table 4.2, Entry 2)

The general procedure was followed using 4-iodotoluene (239.8 mg, 1.1 mmol), which resulted in 54% conversion to tetra(*p*-tolyl)phosphonium iodide as judged by quantitative $^{31}\text{P}\{^1\text{H}\}$ (zgig) NMR spectroscopy.

4 CATALYTIC TRANSFORMATION OF WHITE PHOSPHORUS

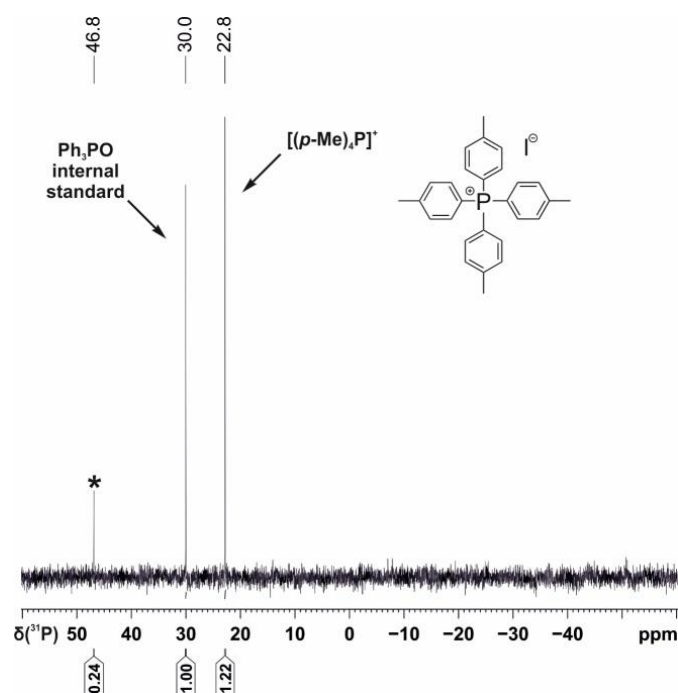


Figure SI 4.6 | Qualitative single scan $^{31}\text{P}\{^1\text{H}\}$ (zgpg) NMR spectrum for the photocatalytic functionalization of P_4 using 4-iodotoluene. * marks the signal of an unknown by-product.

4.7.4.5 *Tris(2-methoxyphenyl)phosphine* (Table 4.2, Entry 5)

The general procedure was followed using 2-iodoanisole (143 μL , 1.1 mmol), which resulted in 54% conversion to tris(2-methoxyphenyl)phosphine as judged by quantitative $^{31}\text{P}\{^1\text{H}\}$ (zfg) NMR spectroscopy (GC-MS: expected = 352 m/z; observed = 352 m/z).

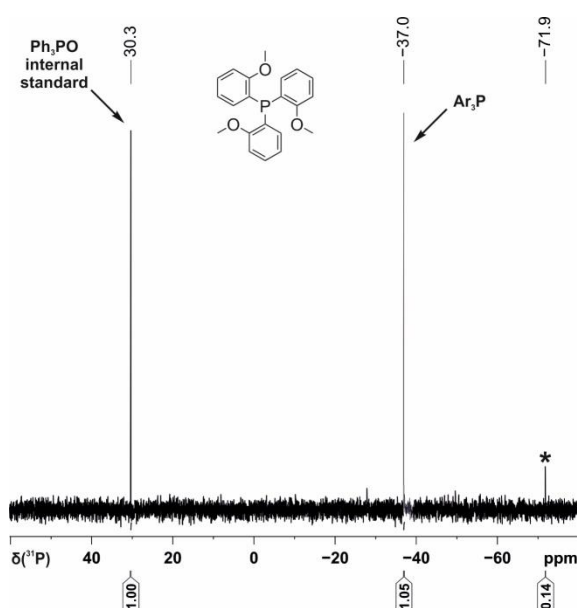


Figure SI 4.7 | Qualitative single scan $^{31}\text{P}\{^1\text{H}\}$ (zfg) NMR spectrum for the photocatalytic functionalization of P_4 using 2-iodoanisole. * marks the signal of an unknown by-product.

4 CATALYTIC TRANSFORMATION OF WHITE PHOSPHORUS

4.7.4.6 *Tetrakis(3-methoxyphenyl)phosphonium iodide* (Table 4.2, Entry 3)

The general procedure was followed using 3-iodoanisole (131 μL , 1.1 mmol), which resulted in 63% conversion to tetrakis(3-methoxyphenyl)phosphonium iodide and 3% conversion to tris(3-methoxyphenyl)phosphine as judged by quantitative $^{31}\text{P}\{^1\text{H}\}$ (zgig) NMR spectroscopy.

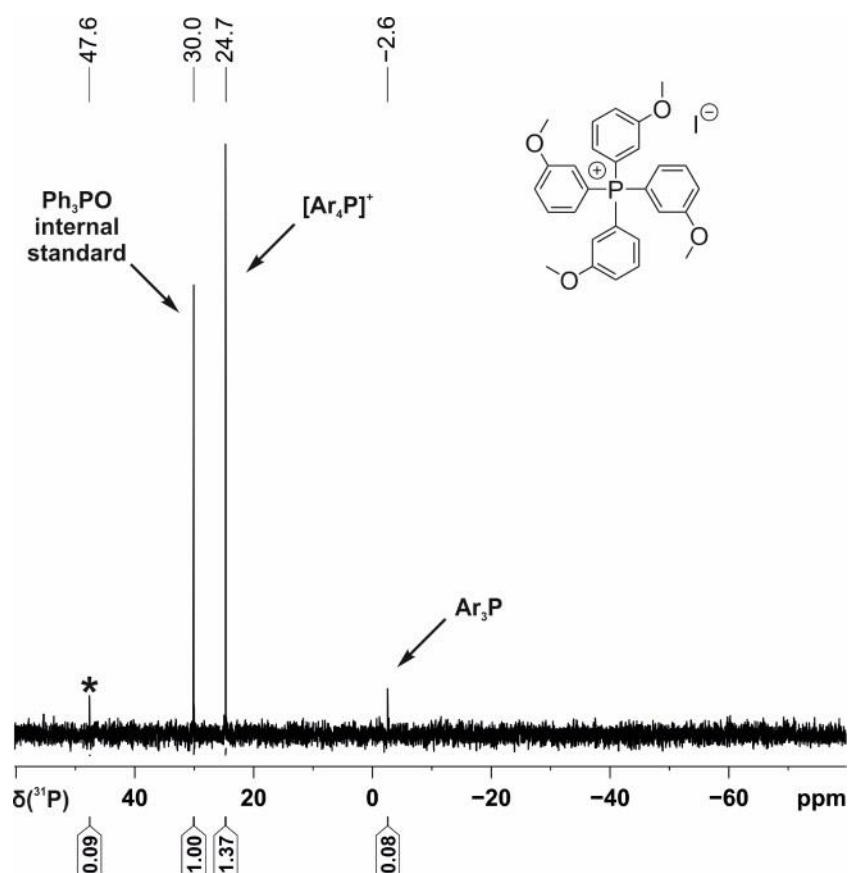


Figure SI 4.8 | Qualitative single scan $^{31}\text{P}\{^1\text{H}\}$ (zgpg) NMR spectrum for the photocatalytic functionalization of P₄ using 3-iodoanisole. * marks the signal of an unknown by-product.

4.7.4.7 *Tetrakis(4-methoxyphenyl)phosphonium iodide* (Table 4.3, Entry 2)

The general procedure was followed using 4-iodoanisole (257 mg, 1.1 mmol), which resulted in 37% conversion to tetrakis(4-methoxyphenyl)phosphonium iodide and 5% conversion to tris(4-methoxyphenyl)phosphine as judged by quantitative $^{31}\text{P}\{^1\text{H}\}$ (zgig) NMR spectroscopy.

4 CATALYTIC TRANSFORMATION OF WHITE PHOSPHORUS

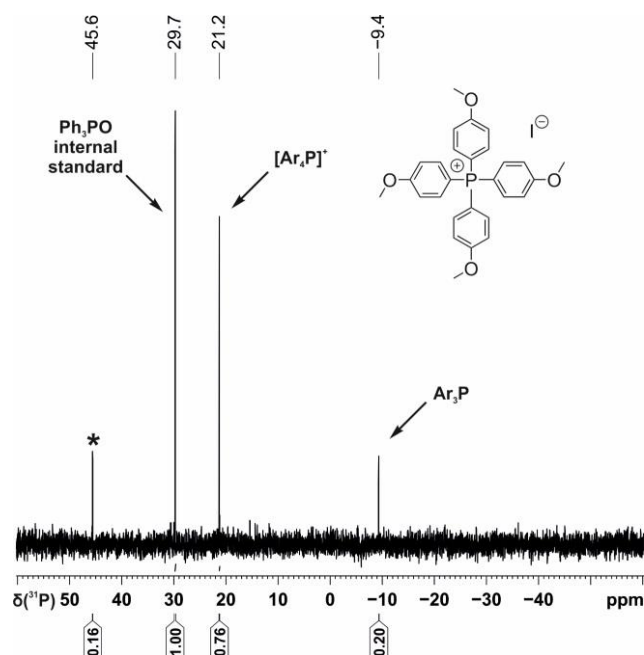


Figure SI 4.9 | Qualitative single scan $^{31}\text{P}\{^1\text{H}\}$ (zgpg) NMR spectrum for the photocatalytic functionalization of P_4 using 4-iodoanisole. * marks the signal of an unknown by-product.

4.7.4.8 *Tris(2-(methylthio)phenyl)phosphine (Table 4.2, Entry 6)*

The general procedure was followed using 2-iodothioanisole (160 μL , 1.1 mmol), which resulted in 21% conversion to tris(2-(methylthio)phenyl)phosphine as judged by quantitative $^{31}\text{P}\{^1\text{H}\}$ (zgif) NMR spectroscopy (GC-MS: expected = 401 m/z; observed = 400 m/z).

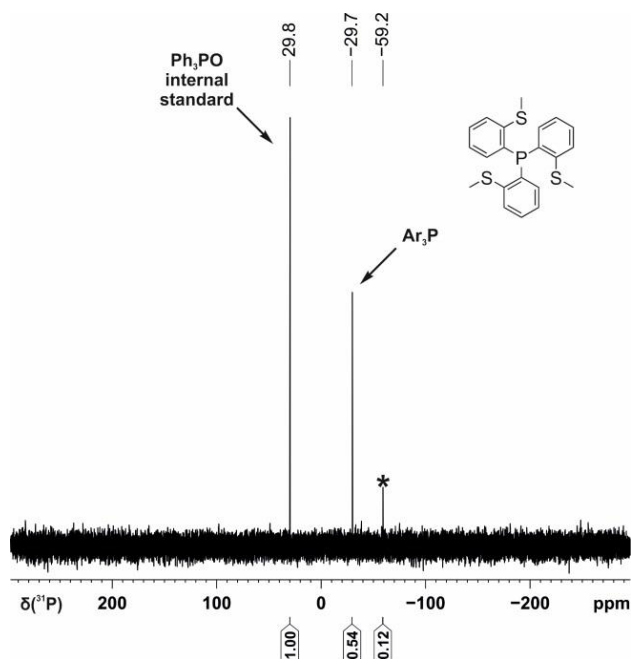


Figure SI 4.10 | Qualitative single scan $^{31}\text{P}\{^1\text{H}\}$ (zgif) NMR spectrum for the photocatalytic functionalization of P_4 using 2-iodothioanisole. * marks the signal of an unknown by-product.

4 CATALYTIC TRANSFORMATION OF WHITE PHOSPHORUS

4.7.4.9 *Tris(2-(methyl benzoate))phosphine (Table 4.3, Entry 5)*

The general procedure was followed using methyl 2-iodobenzoate (161 μ L, 1.1 mmol), which resulted in 11% conversion to tris(2-(methyl benzoate))phosphine as judged by quantitative $^{31}\text{P}\{^1\text{H}\}$ (zgig) NMR spectroscopy (GC-MS: expected = 436 m/z; observed = 436 m/z).

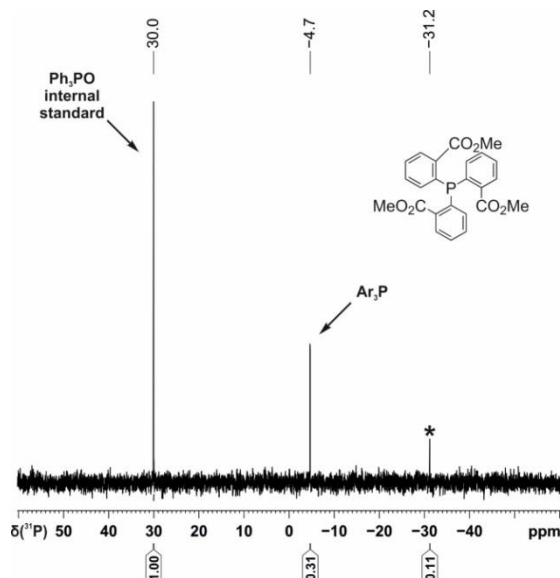


Figure SI 4.11 | Qualitative single scan $^{31}\text{P}\{^1\text{H}\}$ (zgpg) NMR spectrum for the photocatalytic functionalization of P_4 using methyl 2-iodobenzoate. * marks the signal of an unknown by-product.

4.7.4.10 *Tetrakis(3-(methyl benzoate))phosphonium iodide (Table 4.3, Entry 3)*

The general procedure was followed using methyl 3-iodobenzoate (288 mg, 1.1 mmol), which resulted in 48% conversion to tetrakis(3-(methyl benzoate))phosphonium iodide and 8% conversion to tris(3-(methyl benzoate))phosphine as judged by quantitative $^{31}\text{P}\{^1\text{H}\}$ (zgig) NMR spectroscopy.

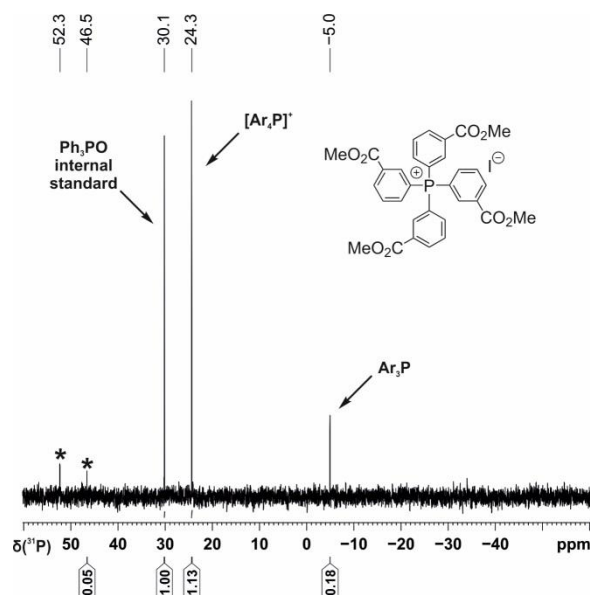


Figure SI 4.12 | Qualitative single scan $^{31}\text{P}\{^1\text{H}\}$ (zgpg) NMR spectrum for the photocatalytic functionalization of P_4 using methyl 3-iodobenzoate. * marks the signals of unknown by-products.

4 CATALYTIC TRANSFORMATION OF WHITE PHOSPHORUS

4.7.4.11 *Tris(4-(methyl benzoate))phosphine (Table 4.3, Entry 6)*

The general procedure was followed using methyl 4-iodobenzoate (156 μL , 1.1 mmol), which resulted in 39% conversion to tris(4-(methyl benzoate))phosphine as judged by quantitative $^{31}\text{P}\{^1\text{H}\}$ (zgpg) NMR spectroscopy (GC-MS: expected = 436 m/z; observed = 436 m/z).

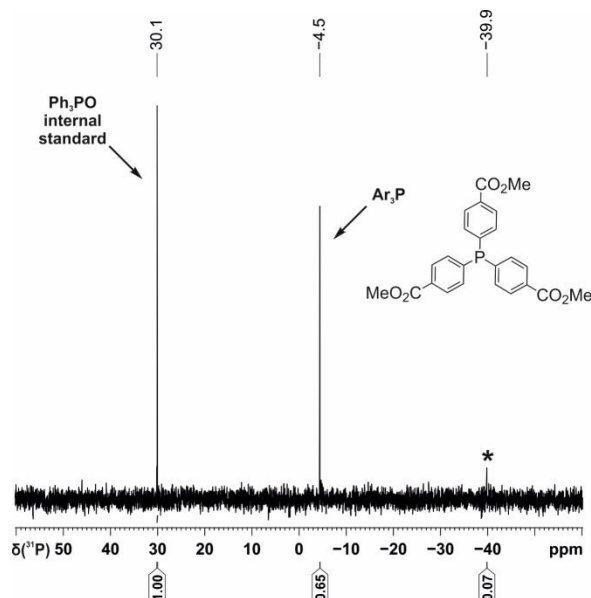


Figure SI 4.13 | Qualitative single scan $^{31}\text{P}\{^1\text{H}\}$ (zgpg) NMR spectrum for the photocatalytic functionalization of P_4 using methyl 4-iodobenzoate. * marks the signal of an unknown by-product.

4.7.4.12 *Tetrakis(3-(trifluoromethyl)phenyl)phosphonium iodide (Table 4.3, Entry 4)*

The general procedure was followed using 3-iodobenzotrifluoride (159 μL , 1.1 mmol), which resulted in 25% conversion to tetrakis(3-(trifluoromethyl)phenyl)phosphonium iodide and 20 % conversion to tris(3-(trifluoromethyl)phenyl)phosphine as judged by quantitative $^{31}\text{P}\{^1\text{H}\}$ (zgpg) NMR spectroscopy.

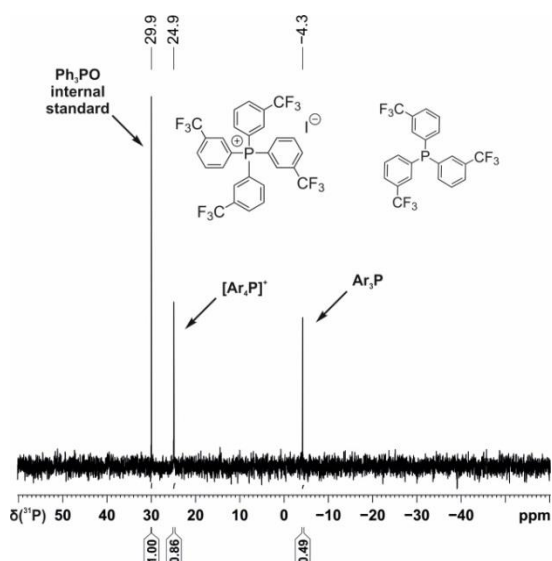


Figure SI 4.14 | Qualitative single scan $^{31}\text{P}\{^1\text{H}\}$ (zgpg) NMR spectrum for the photocatalytic functionalization of P_4 using 3-iodobenzotrifluoride.

4 CATALYTIC TRANSFORMATION OF WHITE PHOSPHORUS

4.7.4.13 *Tris(4-(trifluoromethyl)phenyl)phosphonium iodide (Table 4.3, Entry 7)*

The general procedure was followed using 4-iodobenzotrifluoride (162 μ L, 1.1 mmol), which resulted in 30% conversion to tris(4-(trifluoromethyl)phenyl)phosphine as judged by quantitative $^{31}\text{P}\{^1\text{H}\}$ (zgig) NMR spectroscopy (GC-MS: expected = 466; observed = 466 m/z).

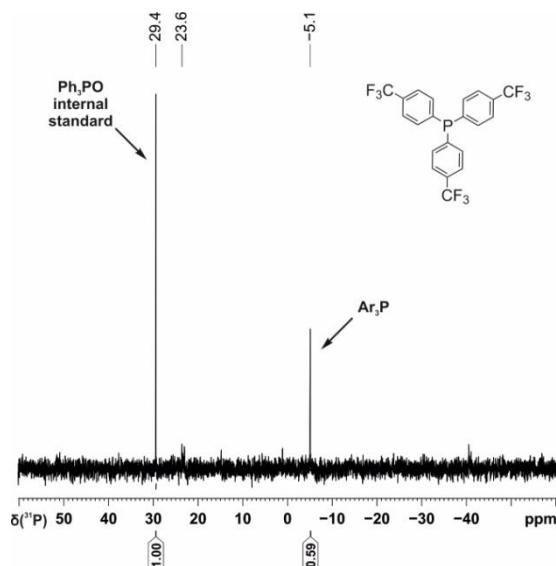


Figure SI 4.15 | Qualitative single scan $^{31}\text{P}\{^1\text{H}\}$ (zgpg) NMR spectrum for the photocatalytic functionalization of P_4 using 4-iodobenzotrifluoride.

4.7.4.14 *Mesityl- and Dimesityl-phosphine (Table 4.3, Entry 9)*

The general procedure was followed with mesityl iodide (2,4,6-trimethyliodobenzene, 271 mg, 1.1 mmol), which resulted in 3% conversion to each of mesitylphosphine and 24% conversion to dimesitylphosphine as judged by quantitative $^{31}\text{P}\{^1\text{H}\}$ (zgig) NMR spectroscopy.

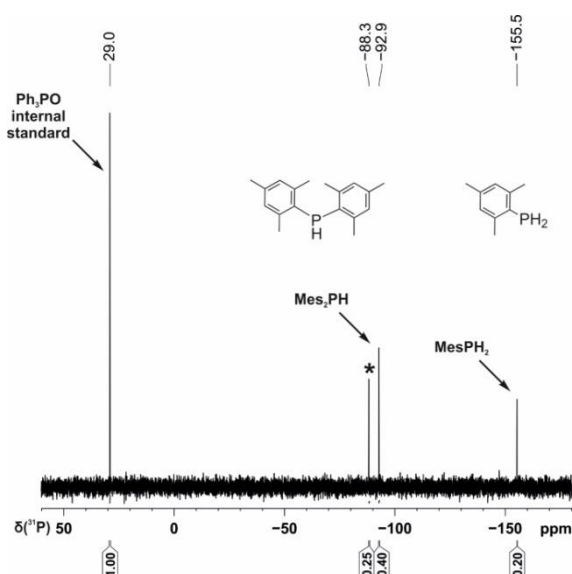


Figure SI 4.16 | Qualitative single scan $^{31}\text{P}\{^1\text{H}\}$ (zgpg) NMR spectrum for the photocatalytic functionalization of P_4 using mesityl iodide. * marks the signal of an unknown by-product.

4 CATALYTIC TRANSFORMATION OF WHITE PHOSPHORUS

4.7.4.15 2,6-dimesitylphenylphosphine (Table 4.3, Entry 10)

The general procedure was modified to use 1.5 mL PhH and 0.5 mL MeCN as solvent, and 2 equiv. 2,6-dimesityliodobenzene based on the phosphorus atom (88.1 mg, 0.2 mmol), which resulted in 12% conversion to (2,6-dimesitylphenyl)phosphine as judged by quantitative ^{31}P NMR (zg) spectroscopy.

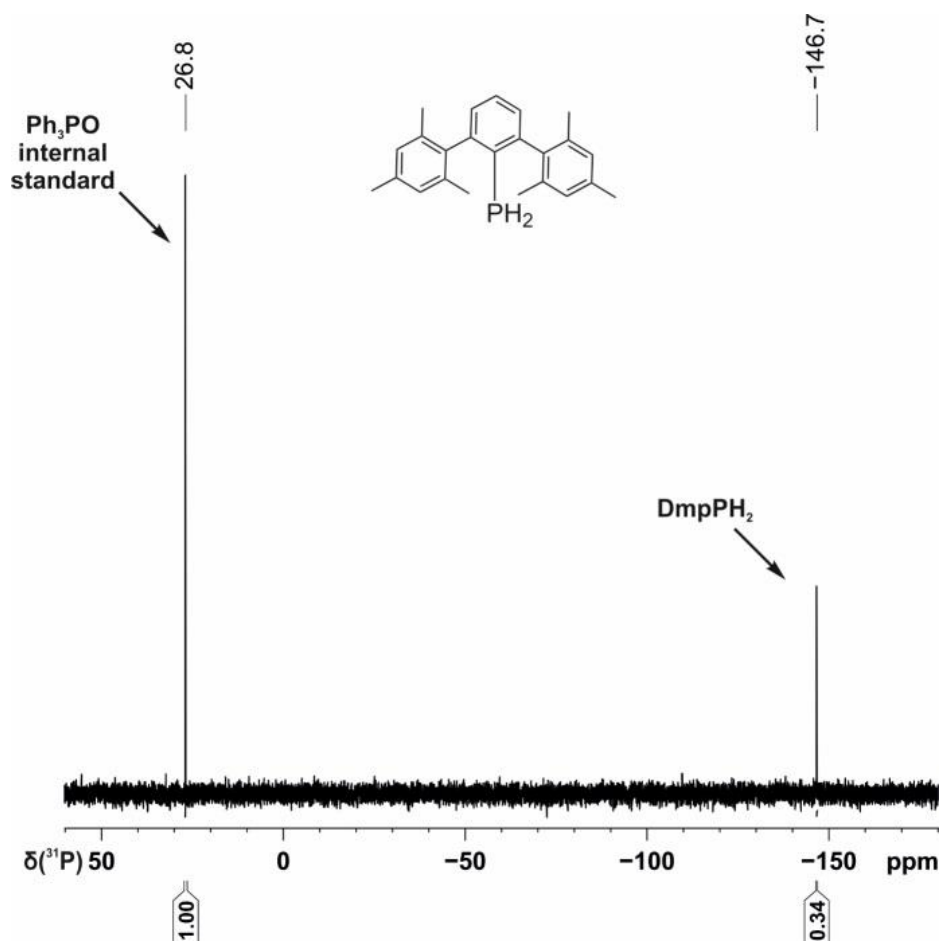


Figure SI 4.17 | Qualitative single scan $^{31}\text{P}\{^1\text{H}\}$ (zgpg) NMR spectrum for the photocatalytic functionalization of P_4 using 2,6-dimesityliodobenzene.

4.7.4.16 *Tris(triphenylstannyl)phosphine* (Table 4.3, Entry 12)

The general procedure was followed with Ph_3SnCl (424 mg, 1.1 mmol), which resulted in 77% conversion to tris(triphenylstannyl)phosphine as judged by quantitative quantitative $^{31}\text{P}\{^1\text{H}\}$ (zgpg) NMR spectroscopy.

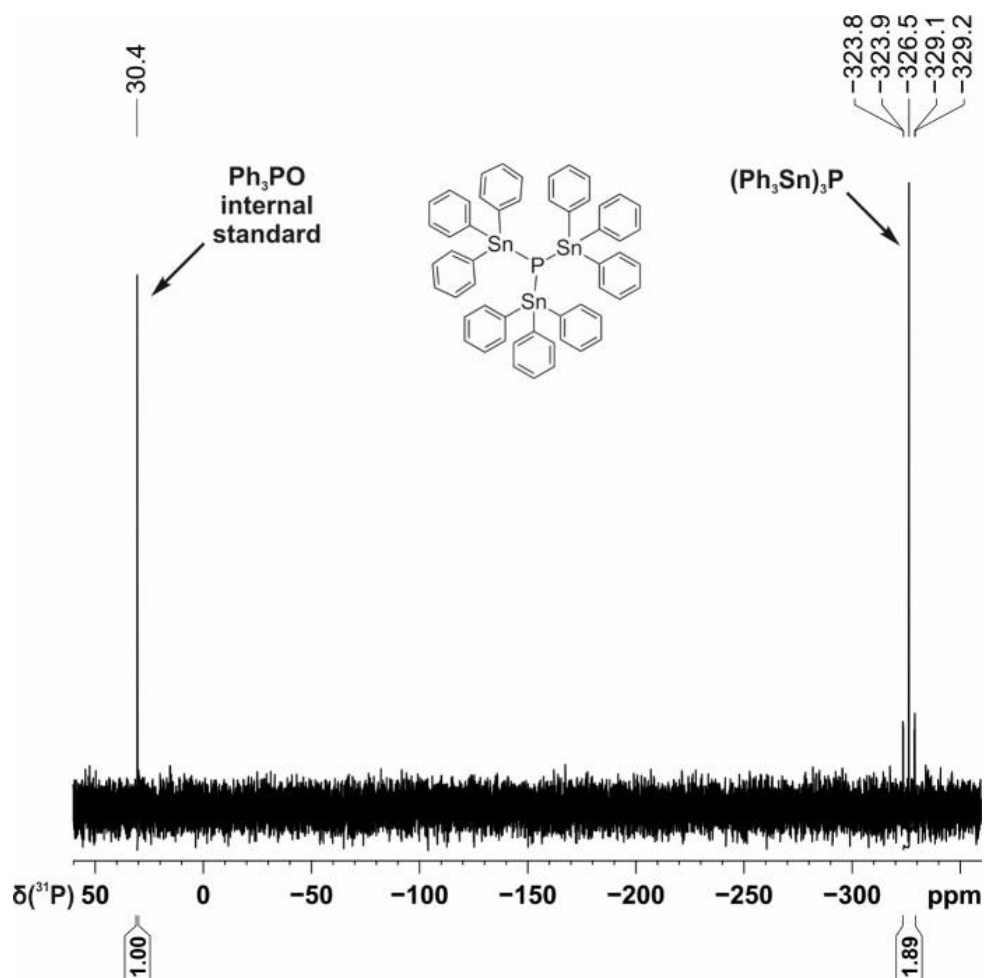


Figure SI 4.18 | Qualitative single scan $^{31}\text{P}\{^1\text{H}\}$ (zgpg) NMR spectrum for the photocatalytic functionalization of P_4 using Ph_3SnCl .

4 CATALYTIC TRANSFORMATION OF WHITE PHOSPHORUS

4.7.5 Reaction on a 1 mmol scale



Figure SI 4.19 | Illustration of the experimental setup used for photocatalytic reactions on a 1 mmol scale.

4.7.5.1 Photocatalytic preparation of tetraphenylphosphonium iodide from P_4 (1 mmol scale, Table 4.2, Entry 1)

In a 50 ml stoppered tube equipped with a stirring bar, iodobenzene (1230 μ L, 11 mmol, 11 equiv. based on the phosphorus atom), Et_3N (2007 μ L, 14.4 mmol, 14.4 equiv.), catalyst $[1]PF_6$ (20.1 mg, 2.2 mol%), and P_4 (30.9 mg, 0.25 mmol, 1 equiv.) were added to 15 mL acetonitrile and 5 mL benzene. The tube was sealed, placed in a water-cooled block to maintain near-ambient temperature (Figure SI 4.19), and irradiated with blue light (7X Osram OSLON SSL80, 455 nm (\pm 15 nm), 20.3 V 1000mA) for 18 h. Subsequent work-up was performed under air. The reaction mixture was added to 1 L of water. The volume of the resulting yellow suspension was reduced to approx. 500 mL using a rotary evaporator at 50 $^{\circ}C$, after which clearer separation of a yellow precipitate could be observed. The solution was filtered (sartorius, filter paper grade 1289) and the volume then further reduced until precipitation of a pale-yellow powder was observed to begin. Crude product was crystallised from the solution at 2 $^{\circ}C$ over the course of two days and isolated by filtration at 0 $^{\circ}C$. Recrystallization from ethanol at -10 $^{\circ}C$ yielded a pale-yellow powder, which was dried under high vacuum (ca. 10^{-5} mbar) for 48 h (160 mg, 34%).

The characterization data of the product are consistent with the data found in the literature.^[2]

1H NMR (400 MHz, $CDCl_3$): 7.94-7.90 (m, 4H), 7.81 (dt, J = 7.8, 3.6 Hz, 8H), 7.67 (dd, J = 12.7, 7.8 Hz, 8H).

$^{13}C\{^1H\}$ NMR (100 MHz, $CDCl_3$): 135.8 (d, J = 3.0 Hz), 134.5 (d, J = 10.3 Hz), 130.9 (d, J = 12.9 Hz), 117.5 (d, J = 89.5 Hz).

$^{31}P\{^1H\}$ NMR (162 MHz, $CDCl_3$): 23.8

4 CATALYTIC TRANSFORMATION OF WHITE PHOSPHORUS

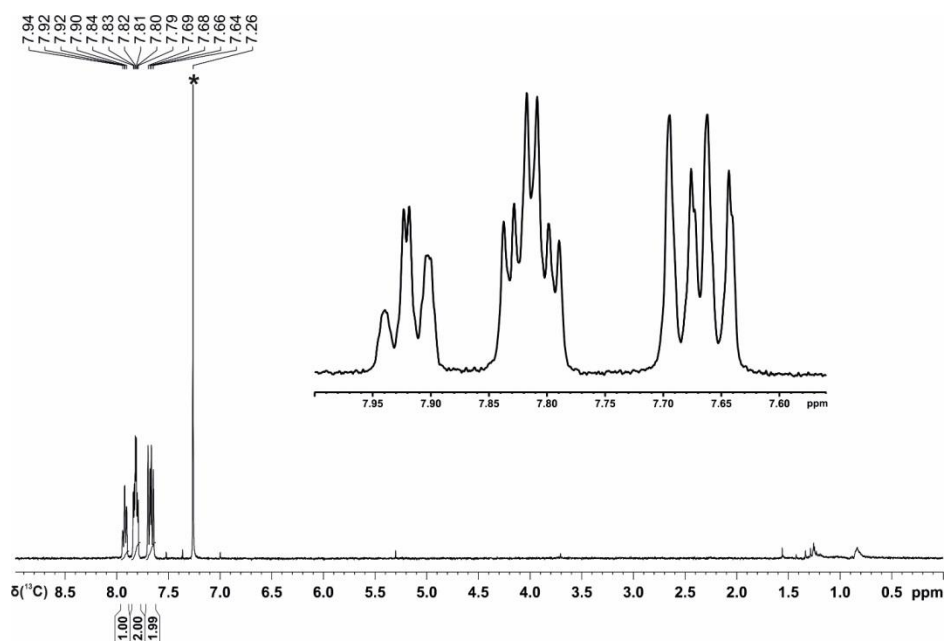


Figure SI 4.20 | ^1H NMR spectrum in CDCl_3 of tetraphenylphosphonium iodide prepared photocatalytically from P_4 on a 1 mmol scale. $^*\text{CDCl}_3$.

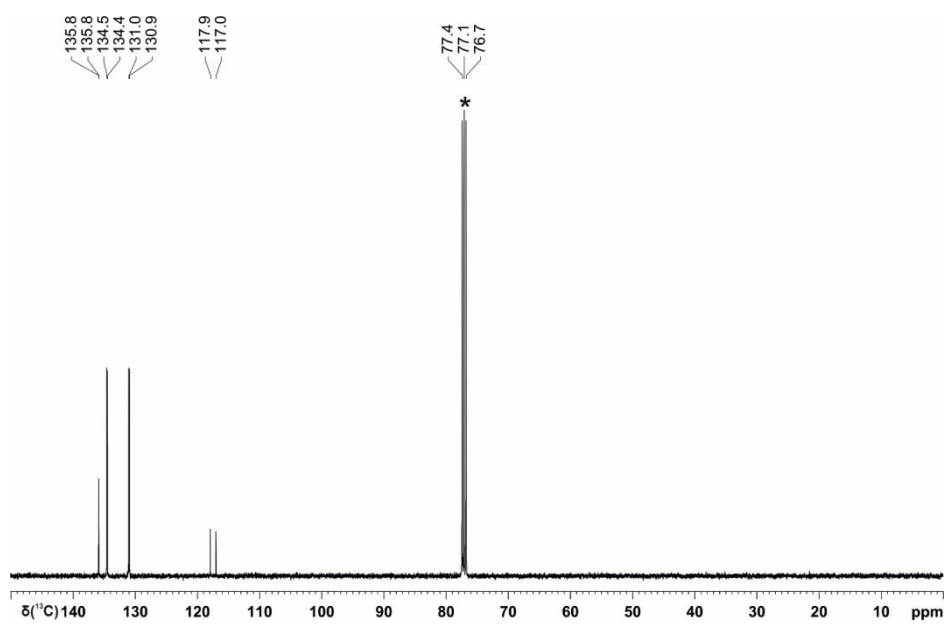


Figure SI 4.21 | $^{13}\text{C}\{^1\text{H}\}$ NMR spectrum in CDCl_3 of tetraphenylphosphonium iodide prepared photocatalytically from P_4 on a 1 mmol scale. $^*\text{CDCl}_3$.

4 CATALYTIC TRANSFORMATION OF WHITE PHOSPHORUS

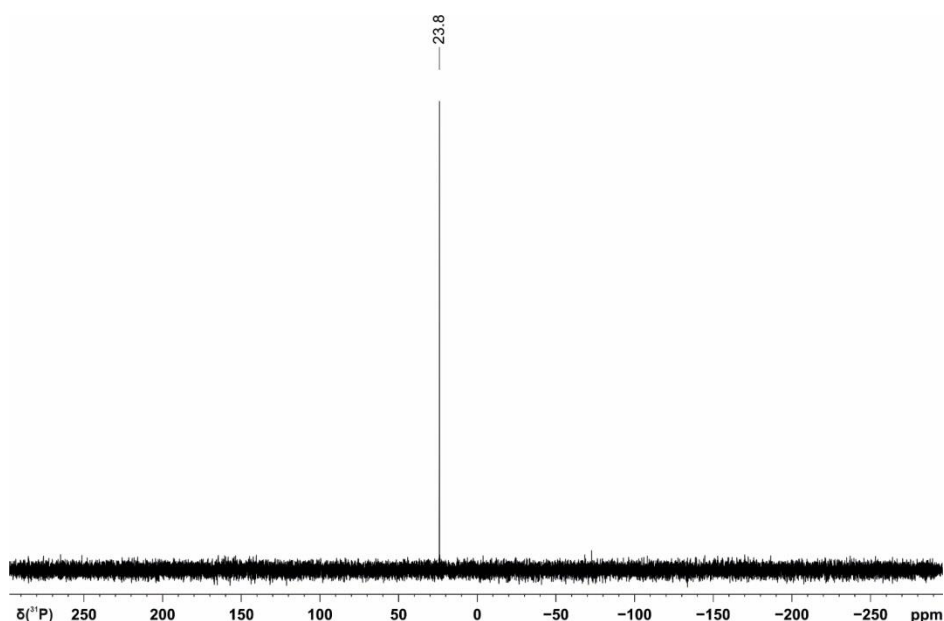


Figure SI 4.22 | $^{31}\text{P}\{^1\text{H}\}$ NMR spectrum in CDCl_3 of tetraphenylphosphonium iodide prepared photocatalytically from P_4 on a 1 mmol scale.

4.7.5.2 Photocatalytic preparation of tetra(*p*-tolyl)phosphonium iodide from P_4 (1 mmol scale, Table 4.2, Entry 2)

In a 50 ml stoppered tube equipped with a stirring bar, 4-iodotoluene (2398 mg, 11 mmol, 11 equiv. based on the phosphorus atom), Et_3N (2007 μL , 14.4 mmol, 14.4 equiv.), catalyst $[\mathbf{1}]\text{PF}_6$ (20.1 mg, 2.2 mol%), and P_4 (30.9 mg, 0.25 mmol, 1 equiv.) were added to 15 mL acetonitrile and 5 mL benzene. The tube was sealed, placed in a water-cooled block to maintain near-ambient temperature (Figure SI 4.19), and irradiated with blue light (7X Osram OSOLON SSL80, 455 nm (± 15 nm), 20.3 V 1000mA) for 30 h. Subsequent work-up was performed under air. The reaction mixture was added to 1 L of water. The volume of the resulting yellow suspension was reduced to approx. 500 mL using a rotary evaporator at 50 $^\circ\text{C}$, after which clearer separation of a yellow precipitate could be observed. The solution was filtered (sartorius, filter paper grade 1289) and the volume then further reduced until precipitation of a white powder was observed to begin. Crude product was crystallised from the solution at 2 $^\circ\text{C}$ over the course of two days and isolated by filtration at 0 $^\circ\text{C}$. Drying of the resulting yellow material at 140 $^\circ\text{C}$ and high vacuum (ca. 10^{-5} mbar) yielded tetra(*p*-tolyl)phosphonium iodide as a spectroscopically clean, off-white powder (216 mg, 41%).

^1H NMR (400 MHz, CDCl_3): 7.56-7.53 (m, 8H), 7.51-7.46 (m, 8H), 2.52 (s, 12H).

$^{13}\text{C}\{^1\text{H}\}$ NMR (100 MHz, CDCl_3): 146.9 (d, $J = 3.0$ Hz), 134.3 (d, $J = 10.7$ Hz), 131.4 (d, $J = 13.3$ Hz), 114.7 (d, $J = 92.5$ Hz), 22.0 (d, $J = 1.4$ Hz).

$^{31}\text{P}\{^1\text{H}\}$ NMR (162 MHz, CDCl_3): 22.8

Elemental analysis: Calculated for $\text{C}_{28}\text{H}_{28}\text{IP}$: C, 64.38; H, 5.40; Found: C, 63.77; H, 5.55; N, 0.20.

4 CATALYTIC TRANSFORMATION OF WHITE PHOSPHORUS

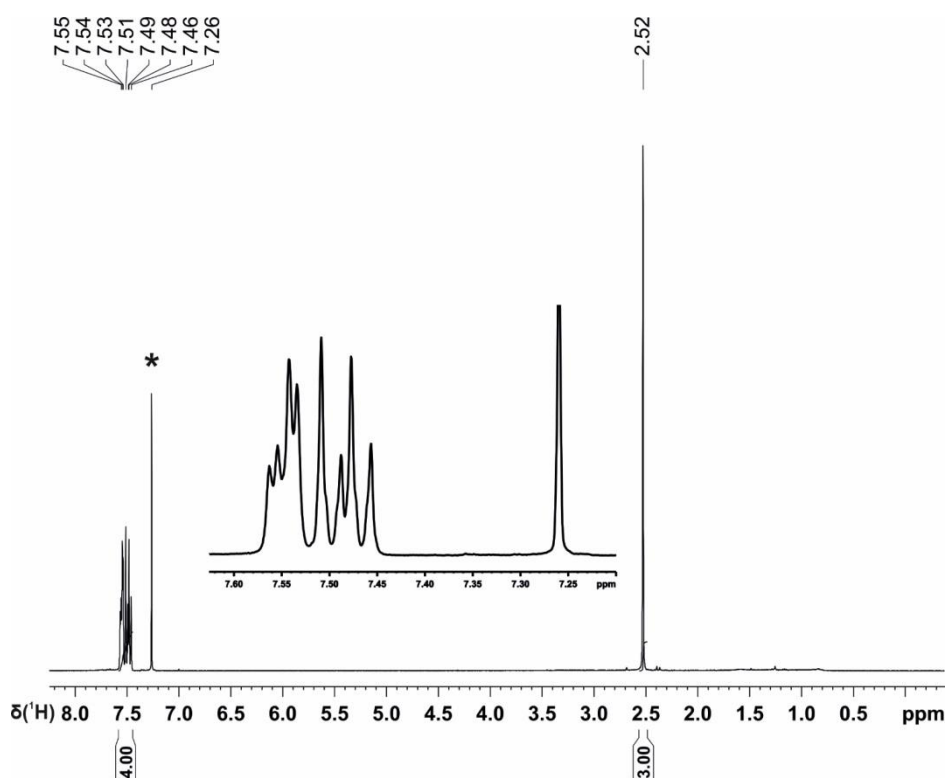


Figure SI 4.23 | ^1H NMR spectrum in CDCl_3 of tetra(*p*-tolyl)phosphonium iodide prepared photocatalytically from P_4 on a 1 mmol scale. * CDCl_3 .

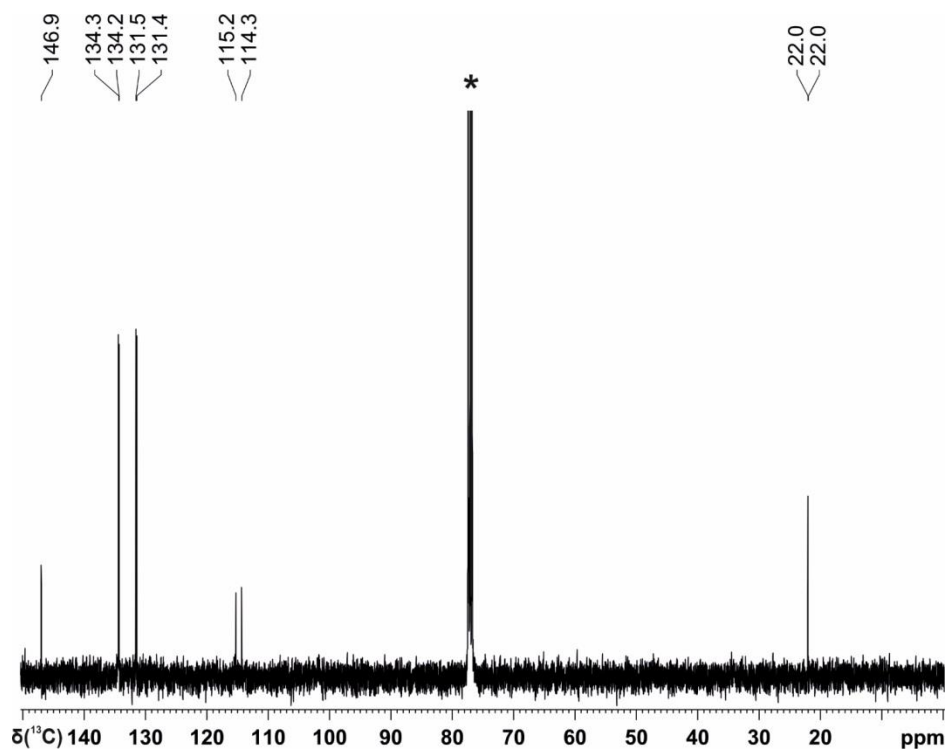


Figure SI 4.24 | $^{13}\text{C}\{^1\text{H}\}$ NMR spectrum in CDCl_3 of tetra(*p*-tolyl)phosphonium iodide prepared photocatalytically from P_4 on a 1 mmol scale. * CDCl_3 .

4 CATALYTIC TRANSFORMATION OF WHITE PHOSPHORUS

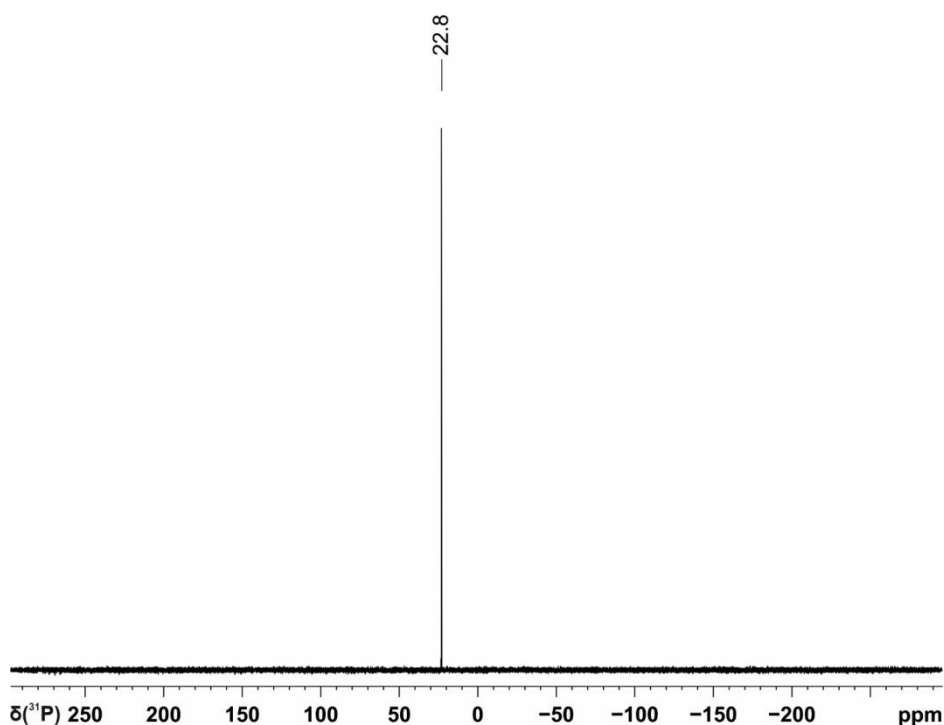


Figure SI 4.25 | $^{31}\text{P}\{^1\text{H}\}$ NMR spectrum in CDCl_3 of tetra(p-tolyl)phosphonium iodide prepared photocatalytically from P_4 on a 1 mmol scale.

4.7.5.3 Photocatalytic preparation of tetrakis(3-methoxyphenyl)phosphonium iodide from P_4 (1 mmol scale, Table 4.2, Entry 3)

In a 50 ml stoppered tube equipped with a stirring bar, 3-iodoanisole (1310 μL , 11 mmol, 11 equiv. based on the phosphorus atom), Et_3N (2007 μL , 14.4 mmol, 14.4 equiv.), catalyst $[\mathbf{1}]\text{PF}_6$ (20.1 mg, 2.2 mol%), and P_4 (30.9 mg, 0.25 mmol, 1 equiv.) were added to 15 mL acetonitrile and 5 mL benzene. The tube was sealed, placed in a water-cooled block to maintain near-ambient temperature (Figure SI 4.19), and irradiated with blue light (7X Osram OSOLON SSL80, 455 nm (± 15 nm), 20.3 V 1000mA) for 24 h. Subsequent work-up was performed under air. The reaction mixture was added to 1.5 L of water. The volume of the resulting yellow suspension was reduced to approx. 500 mL using a rotary evaporator at 50 $^\circ\text{C}$, after which clearer separation of a yellow precipitate could be observed. The solution was filtered (sartorius, filter paper grade 1289) and the solvent was removed *in vacuo*. Drying of the resulting yellow material at 140 $^\circ\text{C}$ and full vacuum (ca. 10^{-3} mbar) yielded tetrakis(3-methoxyphenyl)phosphonium iodide as a spectroscopically-clean off-white powder (350 mg, 60%).

^1H NMR (400 MHz, CDCl_3): 7.75 (dt, $J = 8.1, 4.6$ Hz, 4H), 7.42 (d, $J = 8.5$ Hz, 4H), 7.22-7.15 (m, 4H), 7.01-6.99 (m, 4H), 3.85 (s, 12H).

$^{13}\text{C}\{^1\text{H}\}$ NMR (100 MHz, CDCl_3): 160.6 (d, $J = 16.5$ Hz), 132.5 (d, $J = 15.2$ Hz), 126.4 (d, $J = 9.9$ Hz), 120.6 (d, $J = 2.9$ Hz), 120.4 (d, $J = 11.8$ Hz), 118.4 (d, $J = 89.2$ Hz), 56.2 (s).

4 CATALYTIC TRANSFORMATION OF WHITE PHOSPHORUS

$^{31}\text{P}\{^1\text{H}\}$ NMR (162 MHz, CDCl_3): 24.5

Elemental analysis: Calculated for $\text{C}_{28}\text{H}_{28}\text{IO}_4\text{P}$: C, 57.35; H, 4.81; Found: C, 57.49; H, 4.73, N, 0.00.

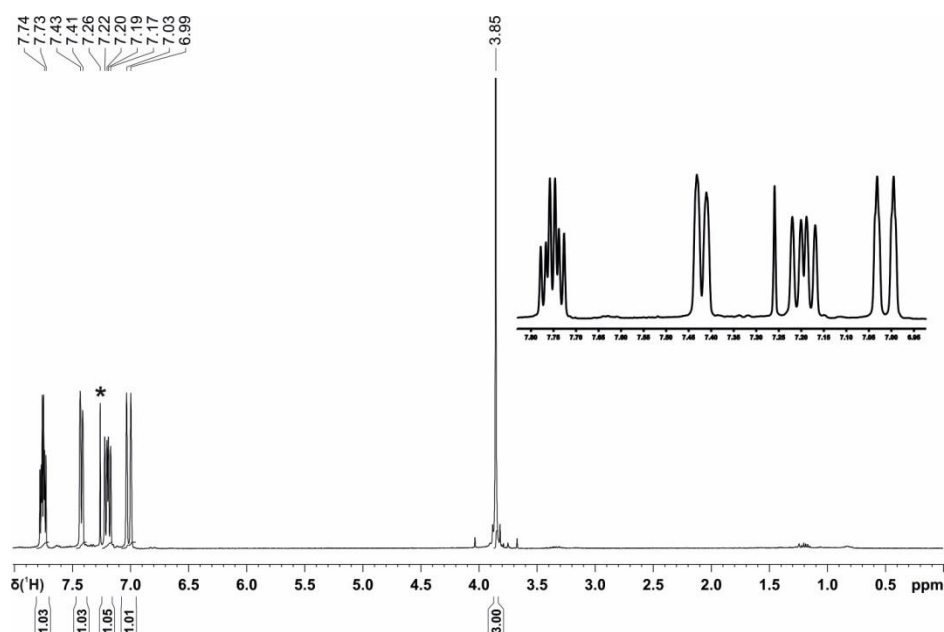


Figure SI 4.26 | ^1H NMR spectrum in CDCl_3 of tetrakis(3-methoxyphenyl)phosphonium iodide prepared photocatalytically from P_4 on a 1 mmol scale. * CDCl_3 .

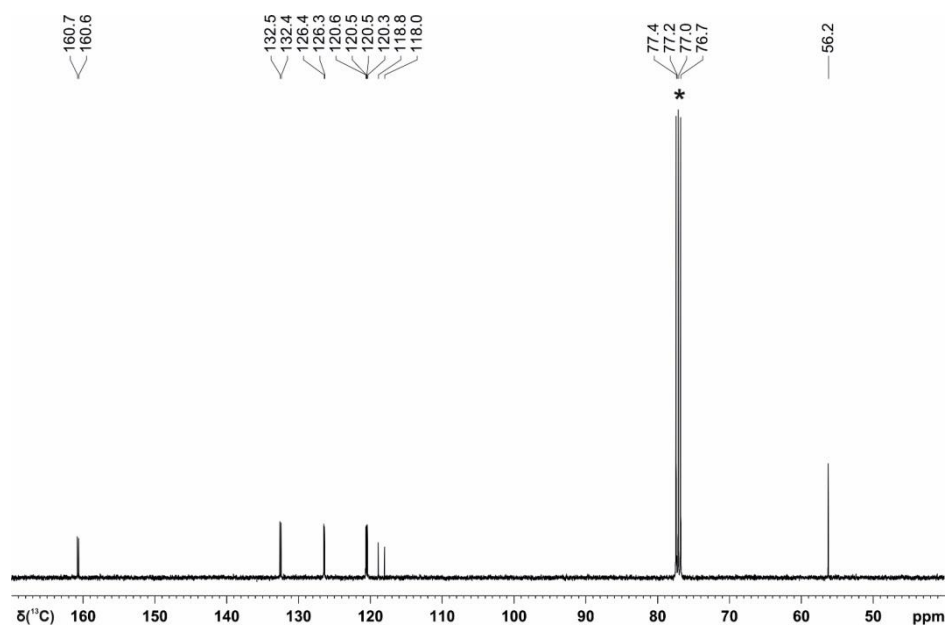


Figure SI 4.27 | $^{13}\text{C}\{^1\text{H}\}$ NMR spectrum in CDCl_3 of tetrakis(3-methoxyphenyl)phosphonium iodide prepared photocatalytically from P_4 on a 1 mmol scale. * CDCl_3 .

4 CATALYTIC TRANSFORMATION OF WHITE PHOSPHORUS

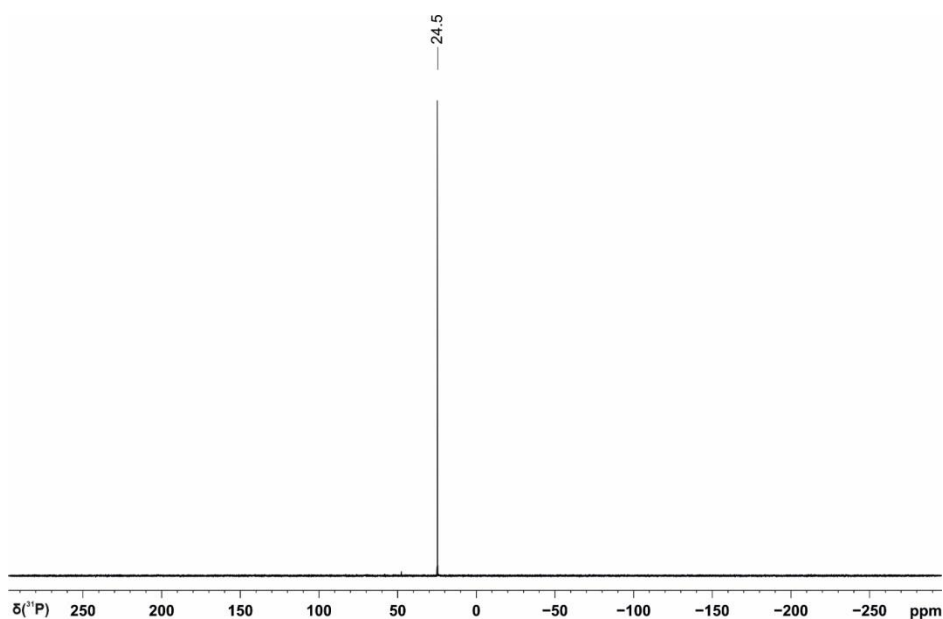


Figure SI 4.28 | $^{31}\text{P}\{^1\text{H}\}$ NMR spectrum in CDCl_3 of tetrakis(3-methoxyphenyl)phosphonium iodide prepared photocatalytically from P_4 on a 1 mmol scale.

4.7.5.4 Photocatalytic preparation of tri(*o*-tolyl)phosphine from P_4 (1 mmol scale, Table 4.2, Entry 4)

In a 50 ml stoppered tube equipped with a stirring bar, 2-iodotoluene (1492 μL , 11 mmol, 11 equiv. based on the phosphorus atom), Et_3N (2007 μL , 14.4 mmol, 14.4 equiv.), catalyst $[\mathbf{1}]\text{PF}_6$ (20.1 mg, 2.2 mol%), and P_4 (30.9 mg, 0.25 mmol, 1 equiv.) were added to 15 mL acetonitrile and 5 mL benzene. The tube was sealed, placed in a water-cooled block to maintain near-ambient temperature (Figure SI 4.19), and irradiated with blue light (7X Osram OSOLON SSL80, 455 nm (± 15 nm), 20.3 V 1000mA) for 18 h. The solvent and other volatiles was evaporated *in vacuo* at 100 $^\circ\text{C}$, and the residue kept under vacuum for 2 h. The resulting yellowish residue was sublimed (*ca.* 3×10^{-2} mbar, 100 $^\circ\text{C}$) twice to obtain tri(*o*-tolyl)phosphine as colorless solid (216 mg, 71%). The characterization data of the product are consistent with the data found in the literature.³

^1H NMR (400 MHz, CDCl_3): 7.28-7.21 (m, 6H), 7.09-7.05 (m, 3H), 6.74-6.71 (m, 3H), 2.39 (s, 9H).

$^{13}\text{C}\{^1\text{H}\}$ NMR (100 MHz, CDCl_3): 142.7 (d, $J = 26.2$ Hz), 134.5 (d, $J = 10.7$ Hz), 133.1, 130.1 (d, $J = 4.8$ Hz), 128.7, 126.2, 21.2 (d, $J = 26.2$ Hz).

$^{31}\text{P}\{^1\text{H}\}$ NMR (162 MHz, CDCl_3): -28.9

4 CATALYTIC TRANSFORMATION OF WHITE PHOSPHORUS

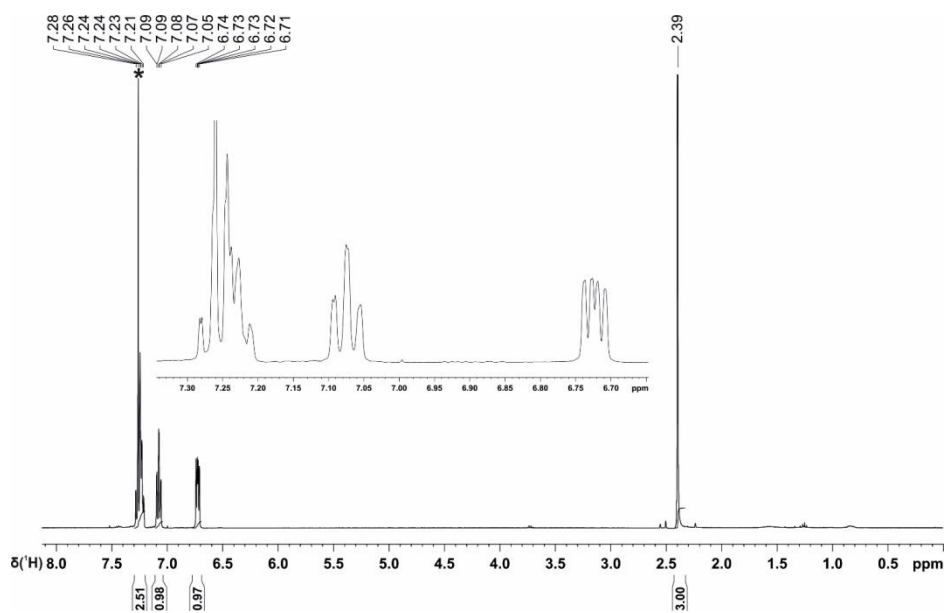


Figure SI 4.29 | ^1H NMR spectrum in CDCl_3 of tri(*o*-tolyl)phosphine prepared photocatalytically from P_4 on a 1 mmol scale. * CDCl_3 .

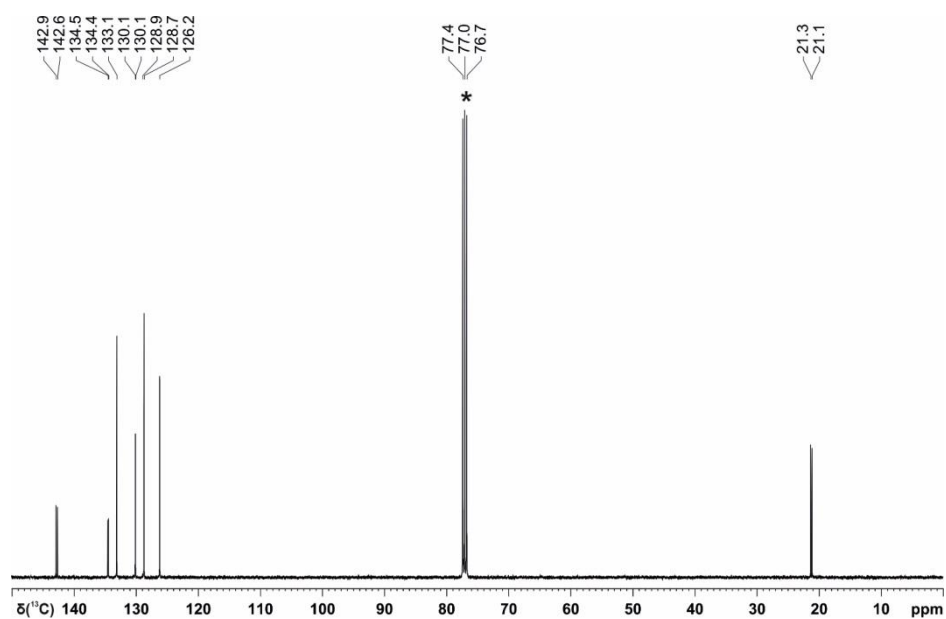


Figure SI 4.30 | $^{13}\text{C}\{^1\text{H}\}$ NMR spectrum in CDCl_3 of tri(*o*-tolyl)phosphine prepared photocatalytically from P_4 on a 1 mmol scale. * CDCl_3 .

4 CATALYTIC TRANSFORMATION OF WHITE PHOSPHORUS

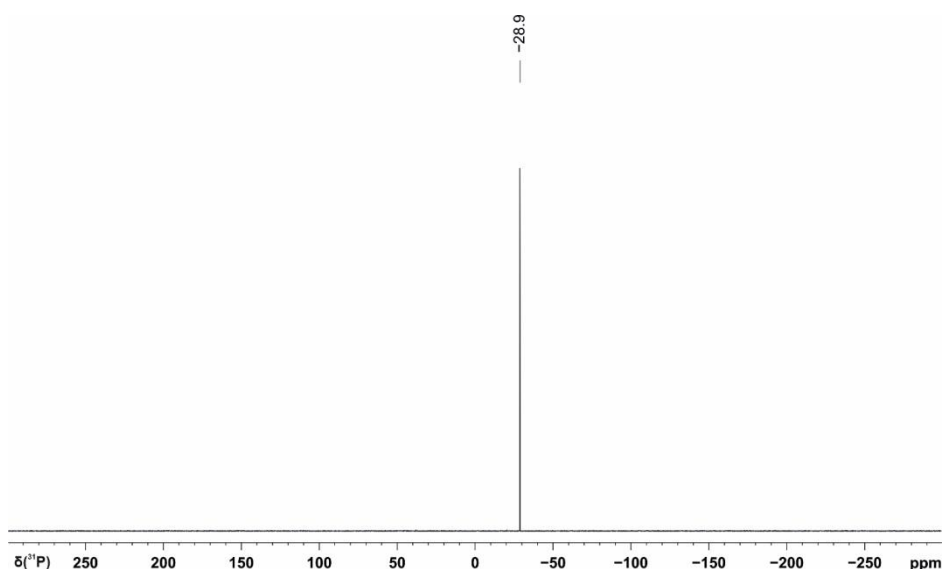


Figure SI 4.31 | $^{31}\text{P}\{^1\text{H}\}$ NMR spectrum in CDCl_3 of tri(*o*-tolyl)phosphine prepared photocatalytically from P_4 on a 1 mmol scale.

4.7.5.5 Photocatalytic preparation of tris(2-methoxyphenyl)phosphine from P_4 (1 mmol scale, Table 4.2, Entry 5)

In a 50 ml stoppered tube equipped with a stirring bar, 2-iodoanisole (1431 μL , 11 mmol, 11 equiv. based on the phosphorus atom), Et_3N (2007 μL , 14.4 mmol, 14.4 equiv.), catalyst $[\text{1}]\text{PF}_6$ (20.1 mg, 2.2 mol%), and P_4 (30.9 mg, 0.25 mmol, 1 equiv.) were added to 15 mL acetonitrile and 5 mL benzene. The tube was sealed, placed in a water-cooled block to maintain near-ambient temperature (Figure SI 4.19), and irradiated with blue light (7X Osram OSRON SSL80, 455 nm (± 15 nm), 20.3 V 1000mA) for 30 h. The solvent and other volatiles was evaporated *in vacuo* at 120 $^\circ\text{C}$, and the residue kept under vacuum for 2h. The target compound crystallized from hot ethanol as pale yellow powder (129 mg, 37%). The characterization data of the product are consistent with the data found in the literature.³

^1H NMR (400 MHz, CDCl_3): 7.36-7.30 (m, 3H), 6.92-6.82 (m, 6H), 6.73-6.68 (m, 3H), 3.74 (s, 9H).

$^{13}\text{C}\{^1\text{H}\}$ NMR (100 MHz, CDCl_3): 161.6 (d, $J = 16.4$ Hz), 133.9, 130.0, 124.4 (d, $J = 11.0$ Hz), 120.9, 110.2 (d, $J = 1.7$ Hz), 55.8

$^{31}\text{P}\{^1\text{H}\}$ NMR (162 MHz, CDCl_3): -38.6

4 CATALYTIC TRANSFORMATION OF WHITE PHOSPHORUS

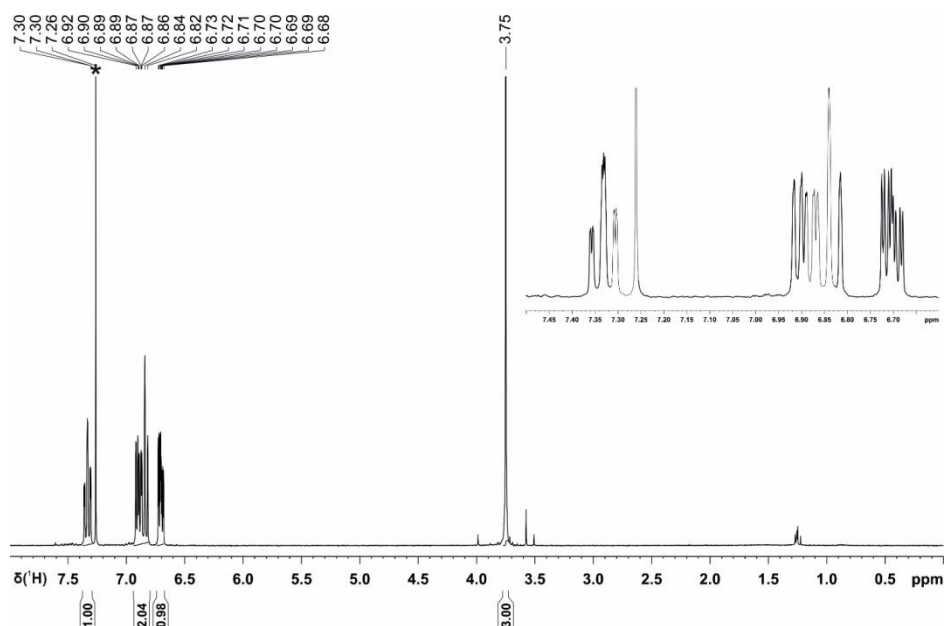


Figure SI 4.32 | ^1H NMR spectrum in CDCl_3 of tris(2-methoxyphenyl)phosphine prepared photocatalytically from P_4 on a 1 mmol scale. $^*\text{CDCl}_3$.

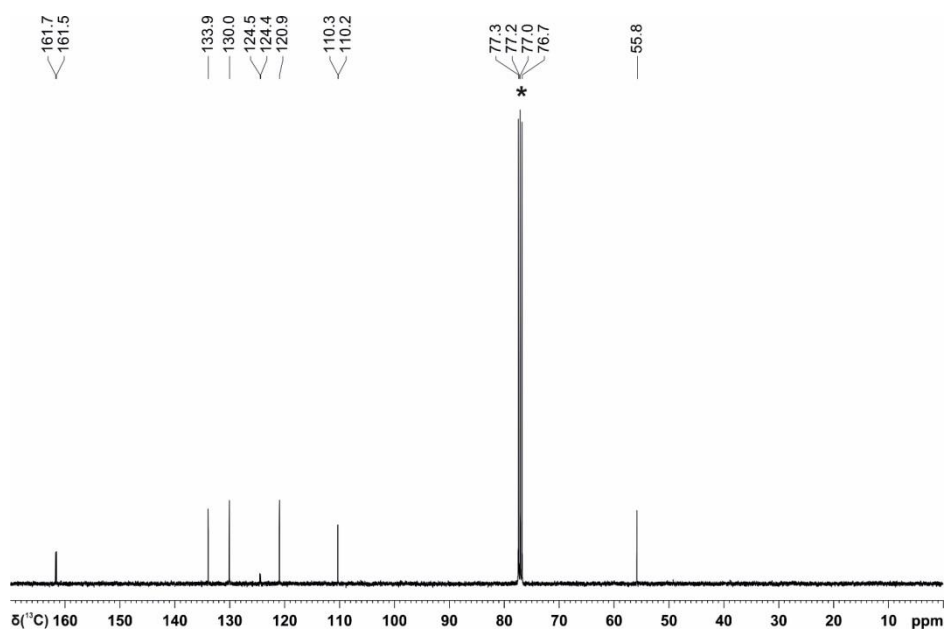


Figure SI 4.33 | $^{13}\text{C}\{^1\text{H}\}$ NMR spectrum in CDCl_3 of tris(2-methoxyphenyl)phosphine prepared photocatalytically from P_4 on a 1 mmol scale. $^*\text{CDCl}_3$.

4 CATALYTIC TRANSFORMATION OF WHITE PHOSPHORUS

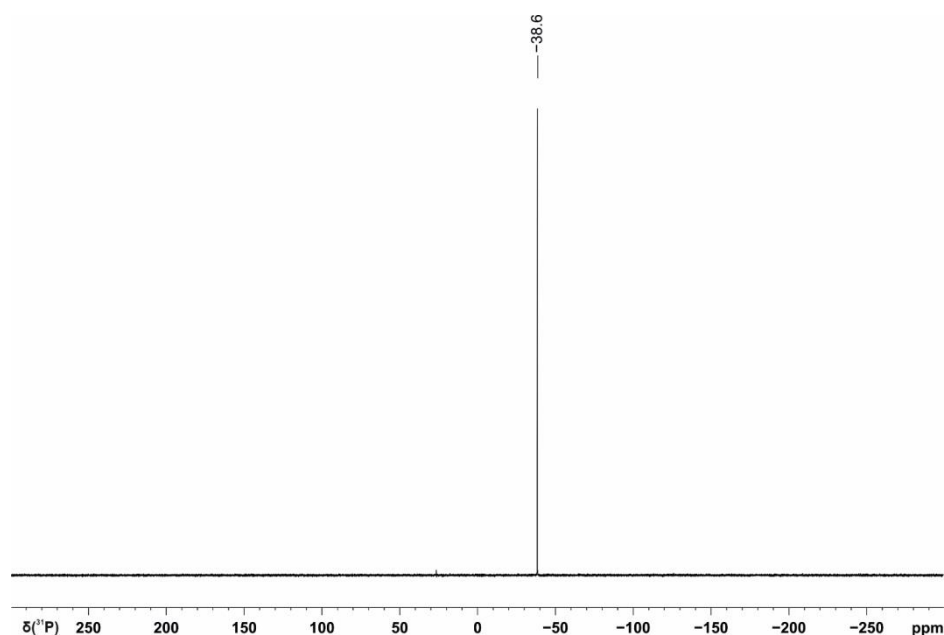


Figure SI 4.34 | $^{31}\text{P}\{^1\text{H}\}$ NMR spectrum in CDCl_3 of tris(2-methoxyphenyl)phosphine prepared photocatalytically from P_4 on a 1 mmol scale.

4.7.5.6 Photocatalytic preparation of tris(2-(methylthio)phenyl)-phosphine from P_4 (1 mmol scale, Table 4.2, Entry 6)

In a 50 ml stoppered tube equipped with a stirring bar, 2-iodothioanisole (1600 μL , 11 mmol, 11 equiv. based on the phosphorus atom), Et_3N (2007 μL , 14.4 mmol, 14.4 equiv.), catalyst $[\mathbf{1}]\text{PF}_6$ (20.1 mg, 2.2 mol%), and P_4 (30.9 mg, 0.25 mmol, 1 equiv.) were added to 15 mL acetonitrile and 5 mL benzene. The tube was sealed, placed in a water-cooled block to maintain near-ambient temperature (Figure SI 4.19), and irradiated with blue light (7X Osram OSLON SSL80, 455 nm (± 15 nm), 20.3 V 1000mA) for 18 h. The solvent and other volatiles was evaporated in vacuo at 120 $^\circ\text{C}$, and the residue kept under vacuum for 2h. The targeted compound precipitated as a white powder (74 mg, 19%) from hot ethanol. The characterization data of the product are consistent with the data found in the literature.^[4]

^1H NMR (400 MHz, CDCl_3): 7.35-7.33 (m, 6H), 7.08-7.03 (m, 3H), 6.75-6.71 (m, 3H), 2.45 (s, 9H).

$^{13}\text{C}\{^1\text{H}\}$ NMR (100 MHz, CDCl_3): 144.2 (d, $J = 29.3$ Hz), 135.6 (d, $J = 9.6$ Hz), 133.6, 129.4, 126.9 (d, $J = 4.3$ Hz), 125.4, 17.4 (d, $J = 9.7$ Hz).

$^{31}\text{P}\{^1\text{H}\}$ NMR (162 MHz, CDCl_3): -30.9

4 CATALYTIC TRANSFORMATION OF WHITE PHOSPHORUS

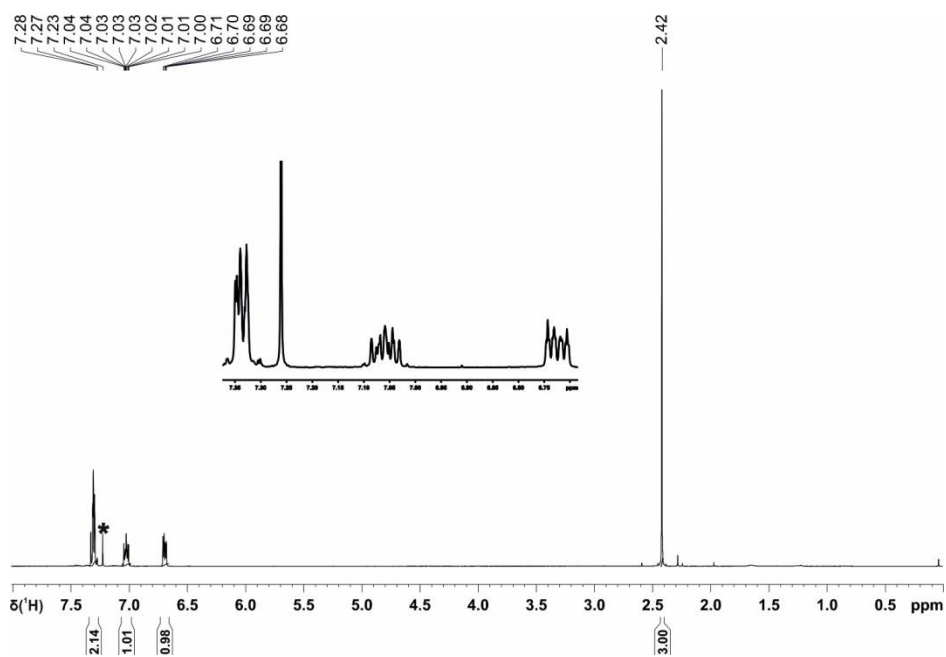


Figure SI 4.35 | ^1H NMR spectrum in CDCl_3 of tris(2-(methylthio)phenyl)phosphine prepared photocatalytically from P_4 on a 1 mmol scale. $^*\text{CDCl}_3$.

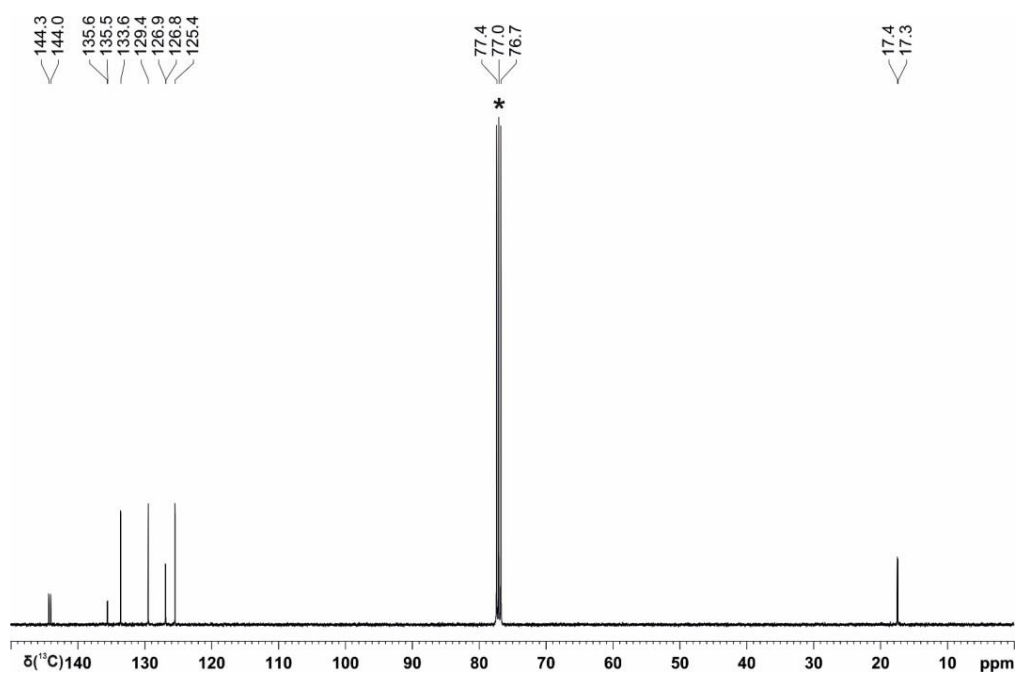


Figure SI 4.36 | $^{13}\text{C}\{^1\text{H}\}$ NMR spectrum in CDCl_3 of tris(2-(methylthio)phenyl)phosphine prepared photocatalytically from P_4 on a 1 mmol scale. $^*\text{CDCl}_3$.

4 CATALYTIC TRANSFORMATION OF WHITE PHOSPHORUS

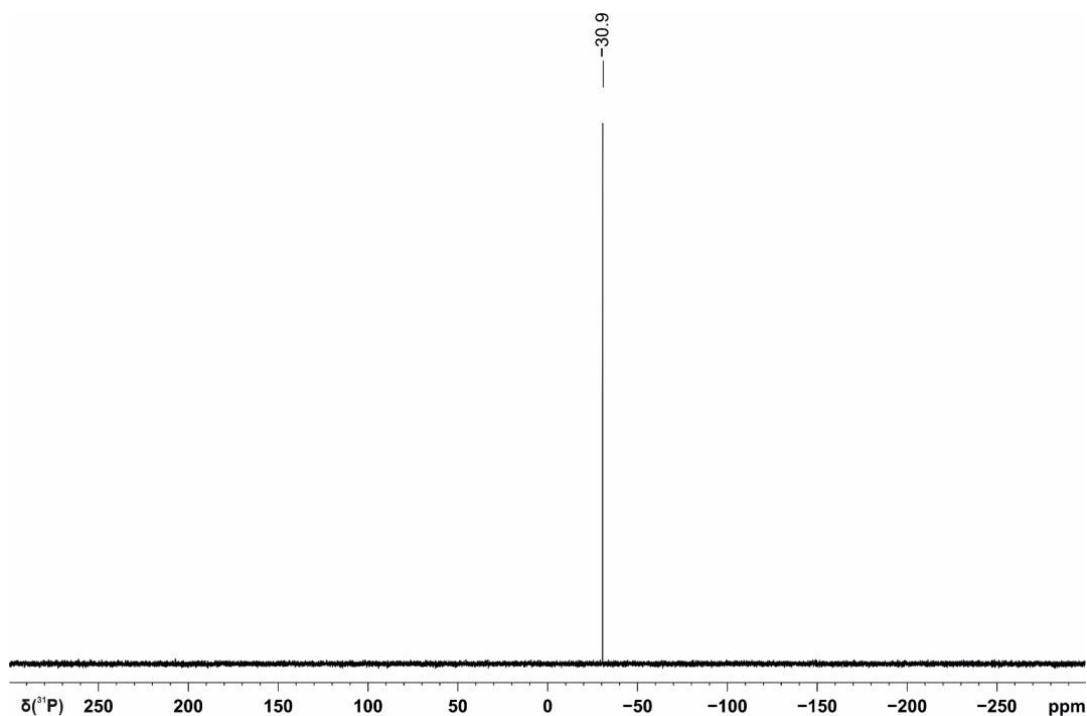


Figure SI 4.37 | $^{31}\text{P}\{^1\text{H}\}$ NMR spectrum in CDCl_3 of tris(2-(methylthio)phenyl)phosphine prepared photocatalytically from P_4 on a 1 mmol scale.

4.7.5.7 Photocatalytic preparation of tris(triphenylstannyl)phosphine from P_4 (1 mmol scale, Table 4.3, Entry 12)

In a 50 ml stoppered tube equipped with a stirring bar, Ph_3SnCl (4.24 g, 11 mmol, 11 equiv. based on the phosphorus atom), Et_3N (2007 μL , 14.4 mmol, 14.4 equiv.), catalyst $[\mathbf{1}]\text{PF}_6$ (20.1 mg, 2.2 mol%), and P_4 (30.9 mg, 0.25 mmol, 1 equiv.) were added to 15 mL acetonitrile and 5 mL benzene. The tube was sealed, placed in a water-cooled block to maintain near-ambient temperature (Figure SI 4.19), and irradiated with blue light (7X Osram OSOLON SSL80, 455 nm (± 15 nm), 20.3 V 1000mA) for 18 h. The solvent was then removed *in vacuo*, and the resulting oily solid triturated with pentane over two days to give an off-white suspension. This suspension was filtered, and the resulting solid washed with further pentane. Extraction into benzene and removal of solvent *in vacuo* yielded another oily solid. The target product was isolated as a spectroscopically-pure white solid by fractional crystallization of this crude material from Et_2O : following precipitation of an initial ^{31}P NMR silent fraction from a saturated solution at -35 $^\circ\text{C}$, three separate crops of the product were obtained from the mother liquor at -80 $^\circ\text{C}$ (155 mg total, 14%).

NMR spectroscopic data are consistent with previous literature reports.^[5]

^1H NMR (400 MHz, benzene- d_6): 7.29-7.17 (m, 18H), 7.10-7.04 (m, 9H), 7.00-6.93 (m, 18H).

$^{13}\text{C}\{^1\text{H}\}$ NMR (100 MHz, benzene- d_6): 140.3 (d, $J = 5.4$ Hz), 137.3 (d, $J = 1.2$ Hz), 128.7, 128.4.

$^{31}\text{P}\{^1\text{H}\}$ NMR (162 MHz, benzene- d_6): -325.1 (d, $J_{119} = 885.5$ Hz, $J_{117} = 847.4$ Hz)

4 CATALYTIC TRANSFORMATION OF WHITE PHOSPHORUS

$^{119}\text{Sn}\{^1\text{H}\}$ NMR (149 MHz, benzene- d_6): -67.6 (d, $J_{119} = 885.5$ Hz)

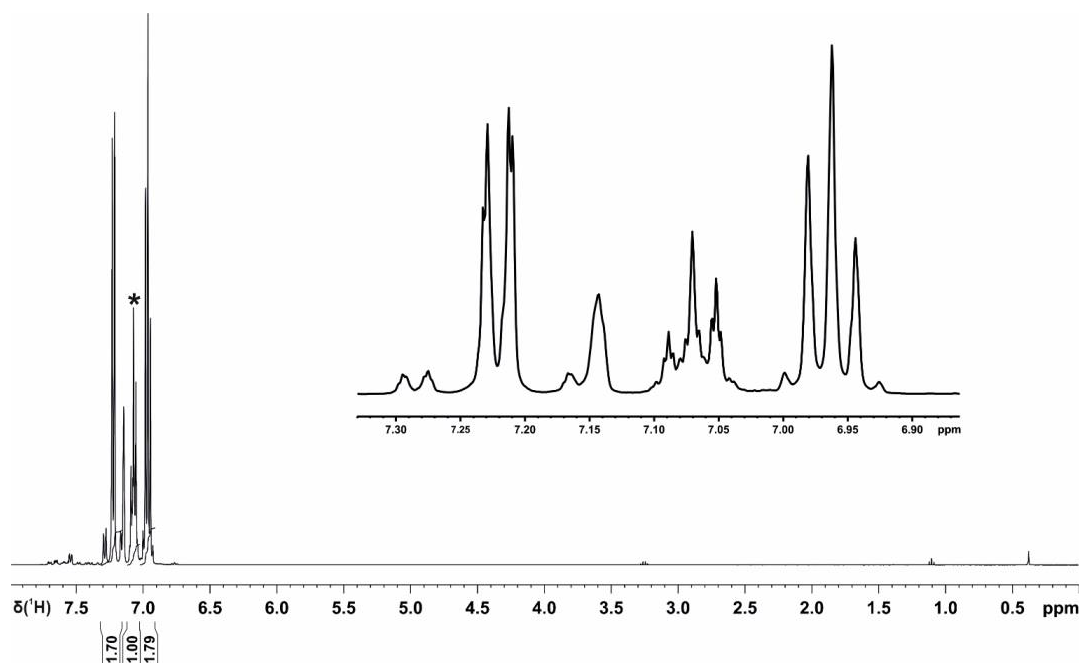


Figure SI 4.38 | ^1H NMR spectrum in C_6D_6 of tris(triphenylstannyl)phosphine prepared photocatalytically from P_4 on a 1 mmol scale. $^*\text{C}_6\text{D}_6$.

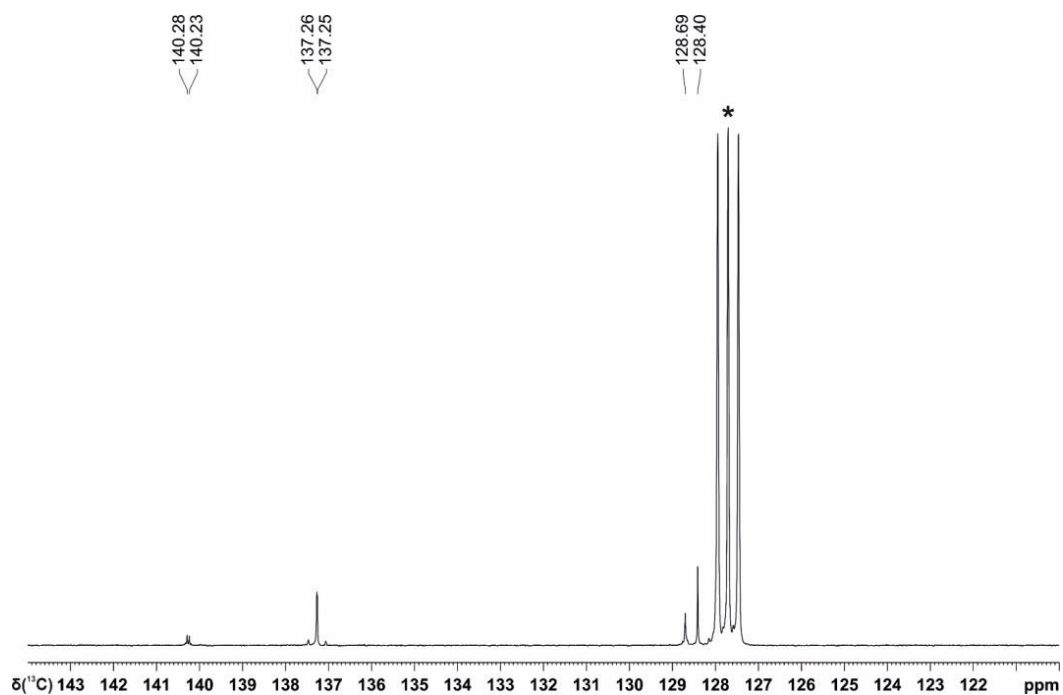


Figure SI 4.39 | $^{13}\text{C}\{^1\text{H}\}$ NMR spectrum in C_6D_6 of tris(triphenylstannyl)phosphine prepared photocatalytically from P_4 on a 1 mmol scale. $^*\text{C}_6\text{D}_6$.

4 CATALYTIC TRANSFORMATION OF WHITE PHOSPHORUS

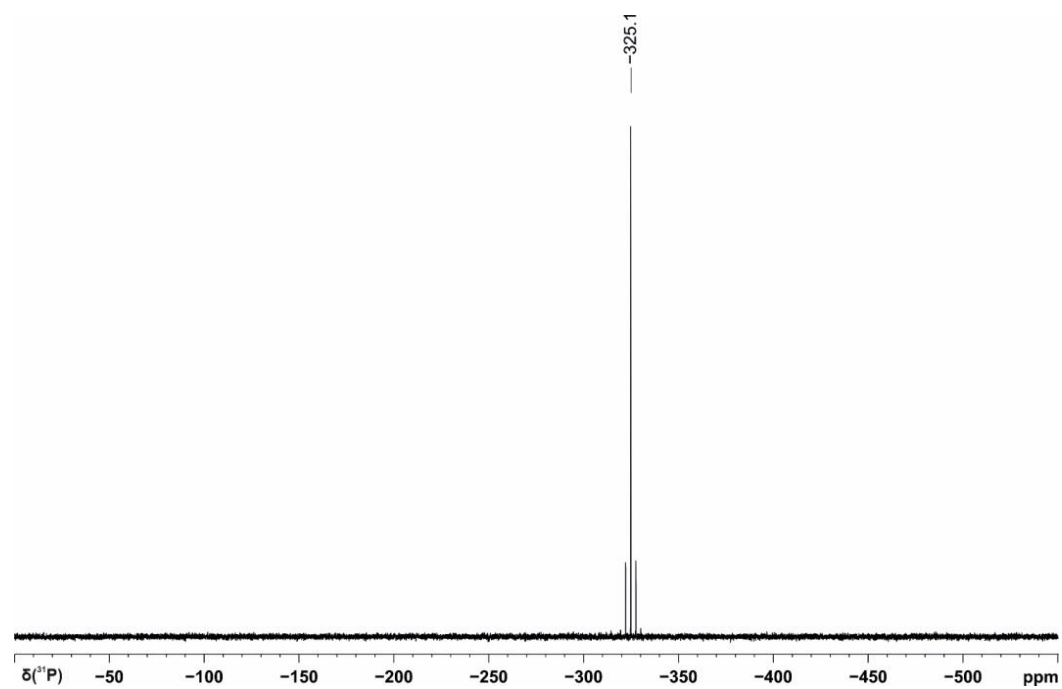


Figure SI 4.40 | ^{31}P NMR spectrum in C_6D_6 of tris(triphenylstannyl)phosphine prepared photocatalytically from P_4 on a 1 mmol scale.

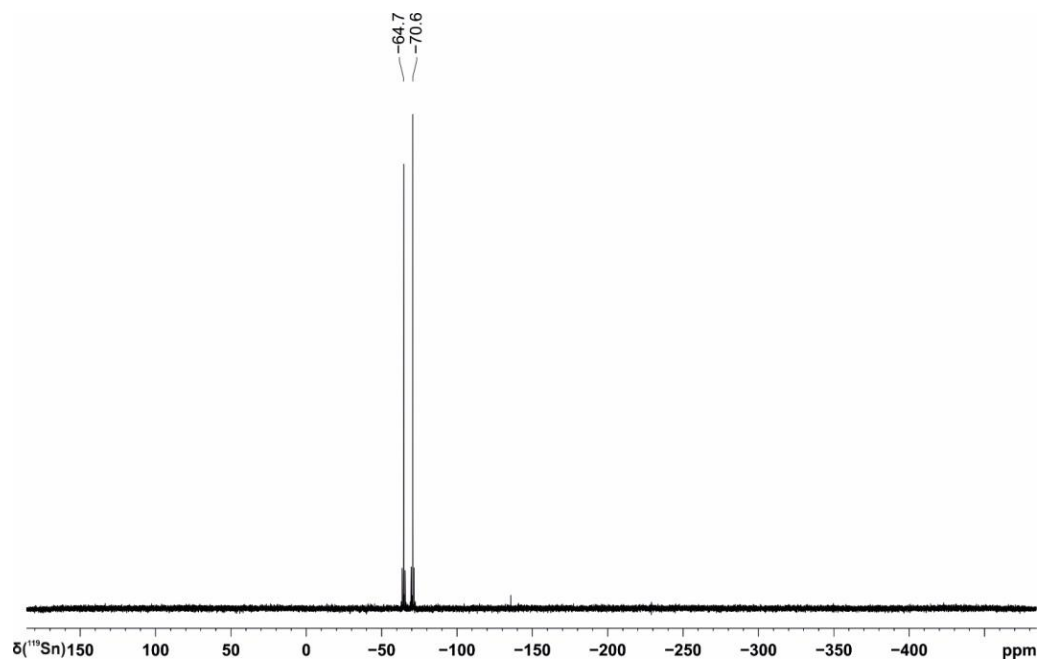


Figure SI 4.41 | $^{119}\text{Sn}\{^1\text{H}\}$ NMR spectrum in C_6D_6 of tris(triphenylstannyl)phosphine prepared photocatalytically from P_4 on a 1 mmol scale.

4.7.6 Cyclic voltammetry studies

Cyclic voltammetry experiments were performed in a single-compartment cell using a CH Instruments CHI600E potentiostat. The cell was equipped with a Pt disc working electrode (2 mm diameter) polished with 0.05 μm Al_2O_3 paste, a Pt wire counter electrode and an Ag/AgNO_3 reference electrode. The supporting electrolyte, $n\text{Bu}_4\text{NPF}_6$, was dried *in vacuo* at 110 $^\circ\text{C}$ for three days prior to use. All redox potentials are reported versus the ferrocene/ferrocenium (Fc/Fc^+) couple. The scan rate is 100 mV s^{-1} unless stated otherwise.

The cyclic voltammogram of $[\mathbf{1}]\text{PF}_6$ recorded in MeCN/PhH (3:1) shows a fully reversible reduction wave at $E_{1/2} = -1.97$ V vs. Fc/Fc^+ (Figure SI 4.42). This value is in excellent agreement with the onset potential of the irreversible reduction wave observed for PhI under the same conditions: $E_{95} = -1.96$ V (Figure SI 4.43; E_{95} is defined as the potential where the current is 95 % lower than at the peak of the wave, i.e. E_{95} occurs when $I = I_{\text{max}} - (0.95 \times \Delta I)$ where $\Delta I = I_{\text{max}} - I_{\text{baseline}}$). This clearly indicates the feasibility of electron transfer to PhI from the reduced catalyst $[\mathbf{1}]$. By comparison, the redox potential for the $[\mathbf{1}]^{*+}/[\mathbf{1}]^{2+}$ couple has been reported to be approximately -1.4 V (in MeCN);^[6] electron transfer to PhI from the photocatalyst excited state is therefore less likely.

The cyclic voltammogram of Et_3N has also been recorded in MeCN/PhH (3:1) and features an irreversible oxidation wave at $E_{95} = +0.24$ V vs. Fc/Fc^+ (Figure SI 4.44).^[8] This is very similar to the potential reported for the $[\mathbf{1}]^{*+}/[\mathbf{1}]$ couple (in MeCN);⁶ accordingly, reduction by Et_3N of the photocatalyst excited state to generate $[\mathbf{1}]$ during the catalytic cycle is expected to be feasible.

Note that attempts to observe a reduction wave for P_4 in MeCN/PhH (3:1) have been unsuccessful.

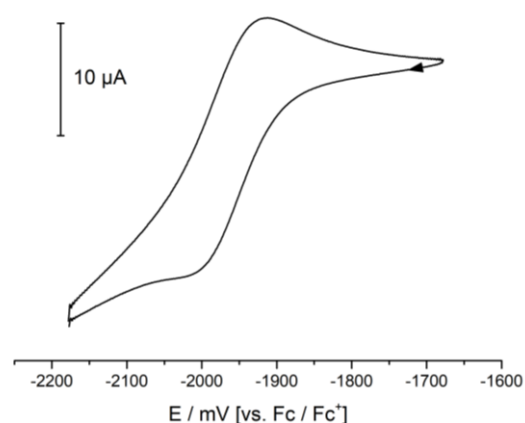


Figure SI 4.42 | Cyclic voltammogram of $[\mathbf{1}]\text{PF}_6$ in MeCN/PhH (3:1) with $n\text{Bu}_4\text{NPF}_6$ supporting electrolyte (0.1 M).

4 CATALYTIC TRANSFORMATION OF WHITE PHOSPHORUS

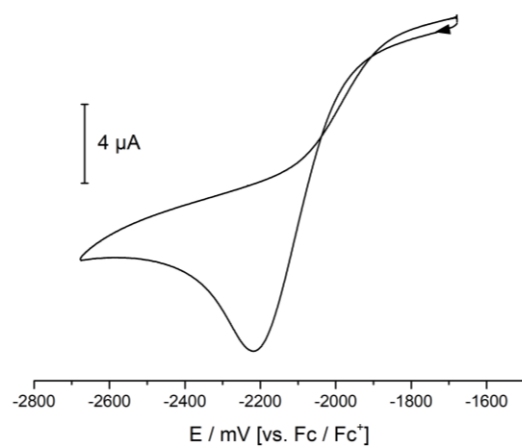


Figure SI 4.43 | Cyclic voltammogram of PhI in MeCN/PhH (3:1) with $n\text{Bu}_4\text{NPF}_6$ supporting electrolyte (0.1 M).

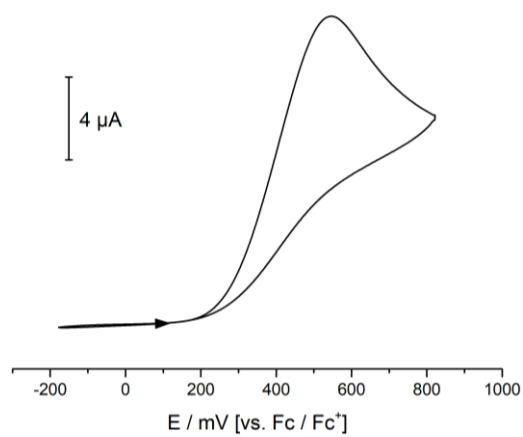


Figure SI 4.44 | Cyclic voltammogram of Et_3N in MeCN/PhH (3:1) with $n\text{Bu}_4\text{NPF}_6$ supporting electrolyte (0.1 M).

4.7.7 Emission quenching experiments

A fluorescence cuvette containing [1]PF₆ (3.9×10^{-6} M) in an MeCN/PhH mixture (3:1) was placed in a fluorescence spectrometer (Fluoromax-4 Spectrofluorometer). The solution was irradiated at 455 nm and the emission spectrum measured (Figure SI 4.45). The maximum emission intensity was obtained at $\lambda_{\text{max}} = 584$ nm (*c.f.* 581 nm, reported in MeCN).^[6] The experiment was then repeated in the presence of potential quenchers (3180 equiv.; Figure SI 4.46-4.51). Significant emission quenching was observed in the presence of Et₃N only (Figure SI 4.47 and 4.52).

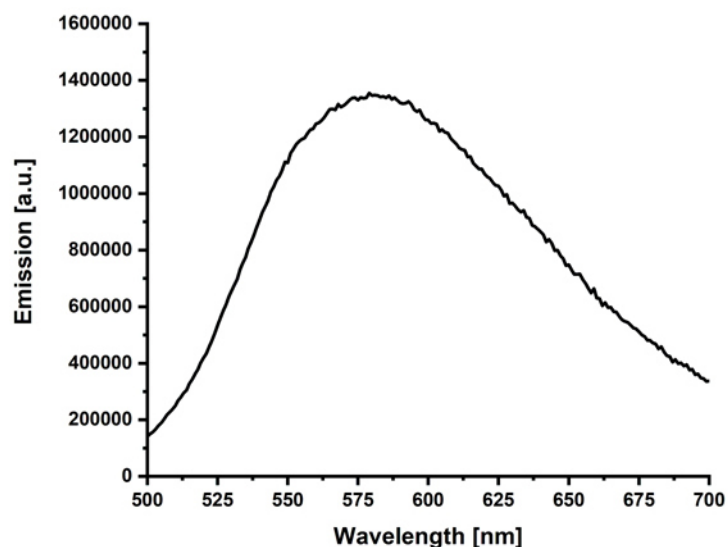


Figure SI 4.45 | Fluorescence emission spectrum for a 3.9×10^{-6} M solution of [1]PF₆ in MeCN/PhH (3:1).

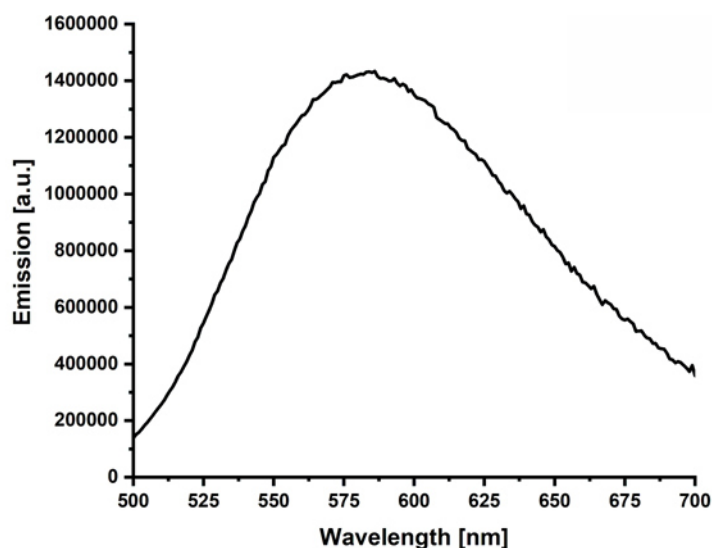


Figure SI 4.46 | Fluorescence emission spectrum for a 3.9×10^{-6} M solution of [1]PF₆ in MeCN/PhH (3:1) in the presence of P₄ (3180 equiv.).

4 CATALYTIC TRANSFORMATION OF WHITE PHOSPHORUS

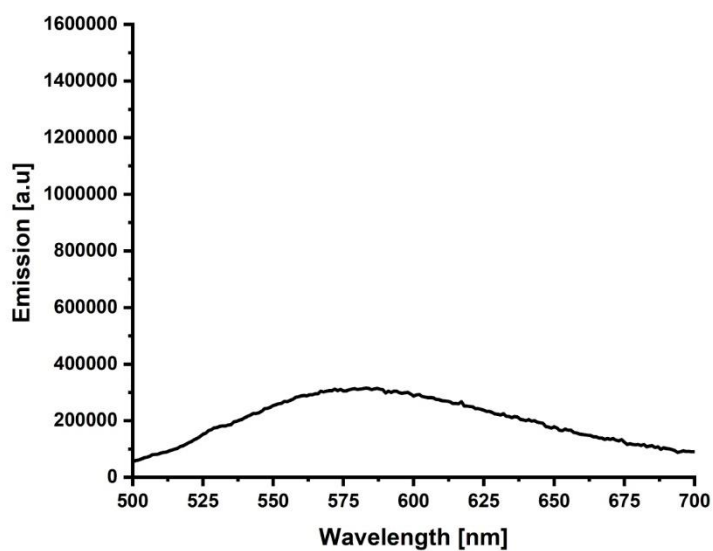


Figure SI 4.47 | Fluorescence emission spectrum for a 3.9×10^{-6} M solution of [1]PF₆ in MeCN/PhH (3:1) in the presence of Et₃N (3180 equiv.).

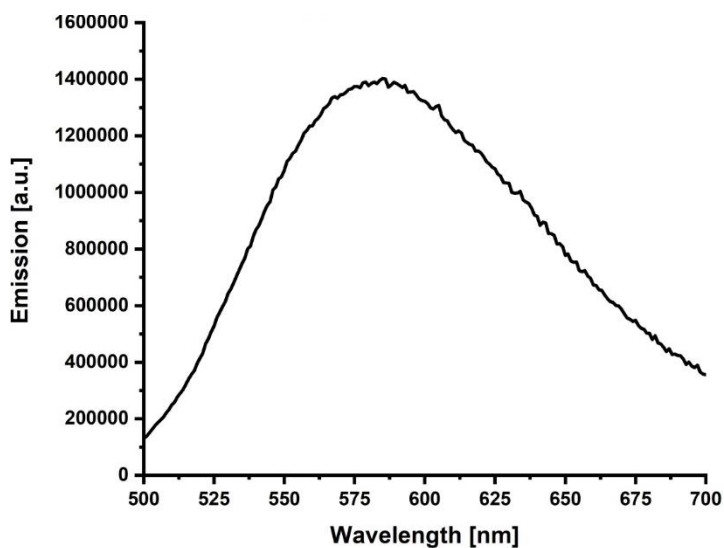


Figure SI 4.48 | Fluorescence emission spectrum for a 3.9×10^{-6} M solution of [1]PF₆ in MeCN/PhH (3:1) in the presence of PhI (3180 equiv.).

4 CATALYTIC TRANSFORMATION OF WHITE PHOSPHORUS

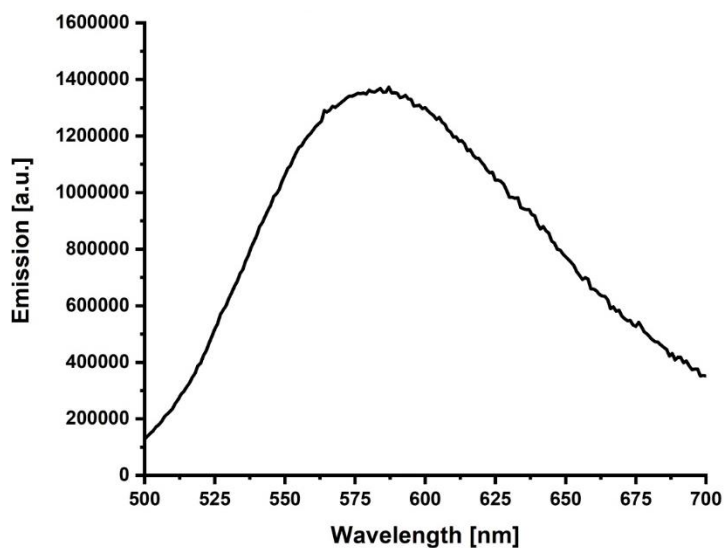


Figure SI 4.49 | Fluorescence emission spectrum for a 3.9×10^{-6} M solution of [1]PF₆ in MeCN/PhH (3:1) in the presence of PhPH₂ (3180 equiv.).

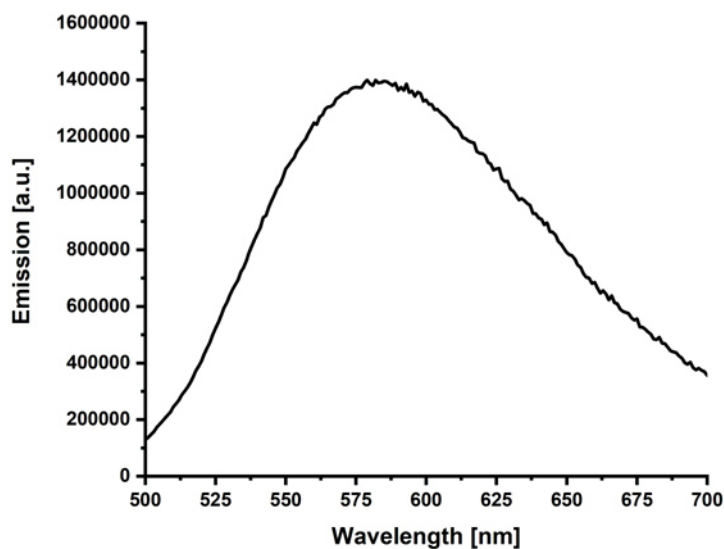


Figure SI 4.50 | Fluorescence emission spectrum for a 3.9×10^{-6} M solution of [1]PF₆ in MeCN/PhH (3:1) in the presence of Ph₂PH (3180 equiv.).

4 CATALYTIC TRANSFORMATION OF WHITE PHOSPHORUS

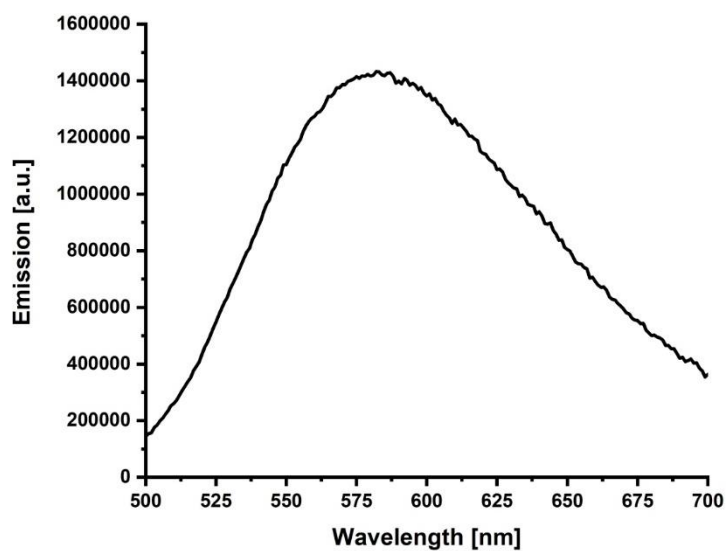


Figure SI 4.51 | Fluorescence emission spectrum for a 3.9×10^{-6} M solution of $[1]PF_6$ in MeCN/PhH (3:1) in the presence of Ph_3P (3180 equiv.).

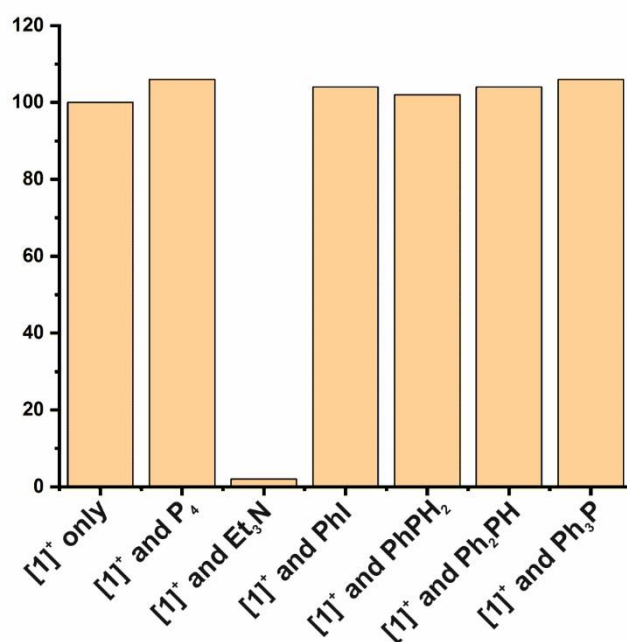
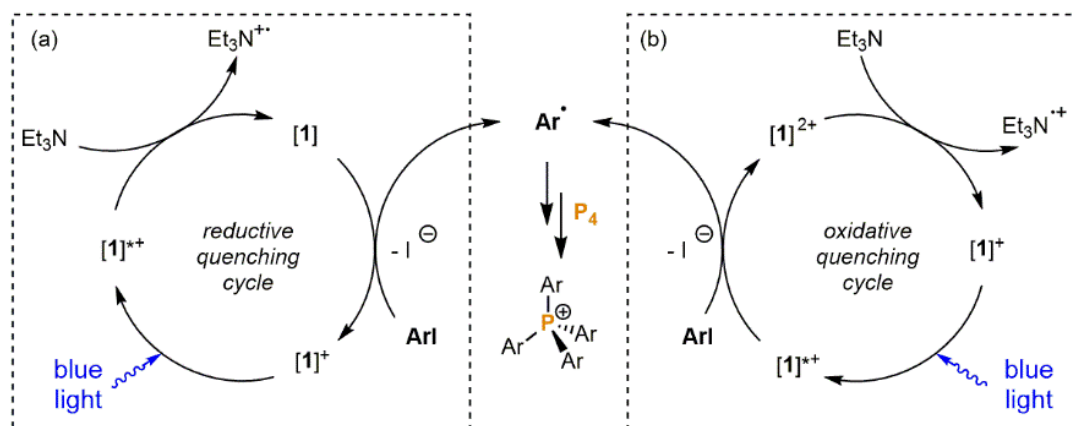


Figure SI 4.52 | Relative emission intensity of $[1]PF_6$ in MeCN/PhH (3:1) at 584 nm in the presence of potential quenchers (3180 equiv.).



Scheme SI 4.1 | Possible catalytic cycles based on a) reductive b) oxidative quenching of the excited state $[1]^*$. Experimental evidence suggests only a) is mechanistically feasible.

4.7.8 UV/VIS spectroscopic studies

A solution containing NEt_3 and $[1]\text{PF}_6$ in MeCN/PhH showed a broad absorption band up to 500 nm in its UV/VIS spectrum. Two new bands ($\lambda_{\text{max}1} = 501 \text{ nm}$, $\lambda_{\text{max}2} = 537 \text{ nm}$) were formed upon irradiation with 455 nm blue light (a new orange/red coloration was also noticeable by eye), which was taken to indicate the formation of reduced $[1]$ (Figure SI 4.53). The initial spectrum was quickly recovered upon addition of excess PhI (neat) or excess P_4 (PhH solution). The $[1]\text{PF}_6$ spectrum was also recovered without PhI after 20 minutes in the absence of blue LED irradiation, which is consistent with re-oxidation by (presumably) the previously-generated $[\text{Et}_3\text{N}]^+$ cation (or decomposition products thereof).

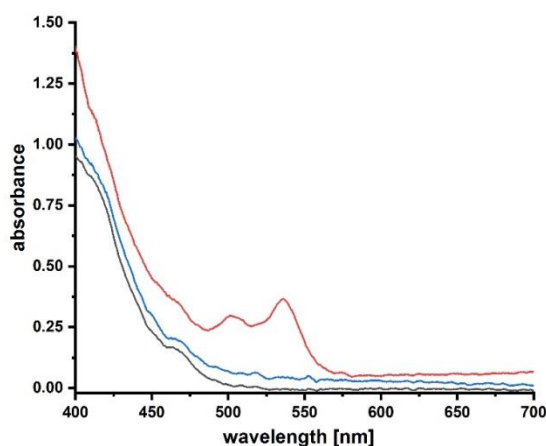


Figure SI 4.53 | UV/VIS spectra of $[1]\text{PF}_6$ and Et_3N (excess) in 3:1 MeCN/PhH : initially (black), following irradiation with 455 nm light (red), following subsequent addition of excess PhI (blue).

To further confirm the formation of reduced $[1]$, $[1]\text{PF}_6$ was treated with a single equivalent of KC_8 in THF (0.01 mmol scale in 0.5 mL THF). UV/VIS spectra of the resulting deep red solution (following separation of solids and dilution with further THF) showed features essentially identical to those previously assigned to $[1]$ in MeCN/PhH (Figure SI 4.54). Again, these disappeared immediately upon addition of PhI, or much more slowly upon addition of P_4 .

4 CATALYTIC TRANSFORMATION OF WHITE PHOSPHORUS

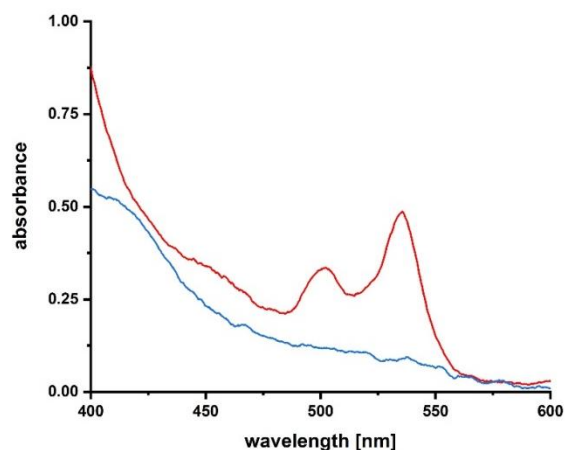


Figure SI 4.54 | UV/VIS spectrum of [1] in THF, prepared *in situ* through treatment of [1]PF₆ with KC₈ (red). After addition of excess PhI (blue).

Finally, changes to the UV/VIS spectrum of [1]PF₆ (1.3 mM in 3:1 MeCN/PhH) were monitored by UV/VIS spectroelectrochemistry using an OTTLE cell.^[7] The stirred solution was exposed to a potential of -2.1 V (versus Fc/Fc⁺) for 80 s, during which time the two previously-observed absorptions attributed to [1] were observed to steadily grow in (Figure SI 4.55a). Subsequently a potential of -0.1 V was applied for 80 s, during which time the initial bands for [1]⁺ was reestablished (Figure SI 4.55b).

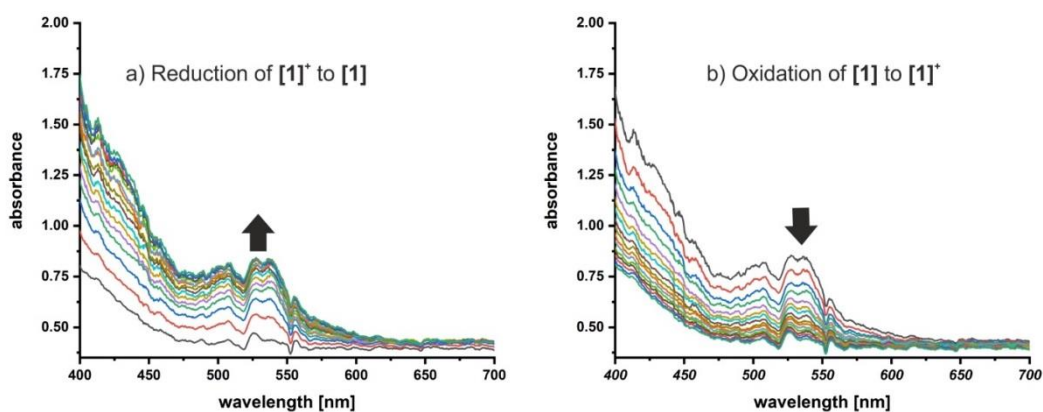


Figure SI 4.55 | UV/VIS spectra showing electrochemical reduction of [1]⁺ to [1] (a), and subsequent reoxidation to [1]⁺ (b).

4.7.9 *In situ* NMR experiments

The apparatus used for *in situ* NMR reaction monitoring with *in situ* illumination has been reported previously.^[8] The insert and the NMR tube were connected with the screw cap of a recently published UVNMR-illumination device to enable measurements under inert conditions.^[9] Two FEP (fluorinated ethylene propylene) coated rubber septa increased the attachment between the insert and the tube. (Figure SI 4.56).

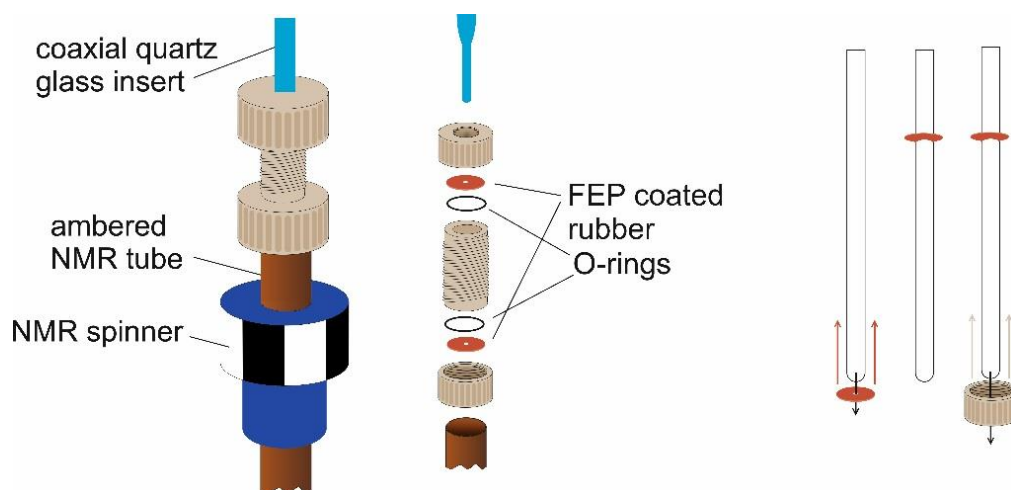


Figure SI 4.56 | Schematic representation showing connection between the ambered NMR tube and illuminating insert used for *in situ* NMR reaction monitoring.

Measurements were conducted on a Bruker Avance III HD 500 MHz with a QXI probe (^1H , ^{13}C , ^{15}N , ^{31}P) or on a Bruker Avance III HD 600 MHz spectrometer with a fluorine selective TBIF probe. A high power Cree XT-E 455 nm LED was employed for sample illumination. All spectra were recorded at 298 K. Spectrum acquisition and processing were managed with Bruker TopSpin 3.2 and TopSpin 4.0.3.

The reaction mixtures were prepared under inert atmosphere (N_2) in an ambered NMR-tube. The *in situ* illumination device was inserted into the tube and fastened with the screw cap. The first NMR-spectra ($t = 0$) were recorded without illumination. The light source was then activated and NMR-measurements for reaction monitoring were simultaneously started. For runs where both nuclei were measured, ^1H and ^{31}P spectra were recorded alternately.

4.7.9.1 Procedure for ^{31}P and ^1H monitoring of the model reaction

The reaction mixture was prepared in accordance with the general procedure for photocatalytic functionalization of P_4 in a 0.1 mmol scale (chapter 4.7.2) using iodobenzene as the substrate, with the exception that a 1:1 mixture of CD_3CN and C_6D_6 was used as solvent (the modified solvent ratio was used to ensure that complete homogeneity was maintained throughout the experiment). A 500 μL aliquot of this reaction mixture was then taken for NMR reaction monitoring.

Measurements were conducted on a Bruker Avance III HD 500 MHz with a QXI probe (^1H , ^{13}C , ^{15}N , ^{31}P). For the ^1H NMR spectra the standard pulse program “zg30” was applied. For ^{31}P NMR reaction monitoring a

4 CATALYTIC TRANSFORMATION OF WHITE PHOSPHORUS

modified “zpgg”-experiment was used, applying a broadband pulse (xyBEBOP) developed and provided by the group of Burkhard Luy. This enabled the recording of a sweep width (SW) of 1000 kHz within a single experiment and allowed for a simultaneous screening of reaction intermediates appearing within the SW of 1000 kHz. A sufficiently high time domain (TD) was adjusted to avoid wiggles in the foothills of the signals. The spectrum in the absence of light and the first two spectra of the reaction monitoring with light were recorded with an NS (number of scans) of 512. For the subsequent spectra, the NS was increased to 1024 to increase the S/N (signal to noise ratio) for small signals. The T_1 relaxation times of the ^{31}P signals were not determined. Hence, only qualitative statements about the sequence of the reaction intermediates and products can be made. After acquisition, a uniformly positive phasing of all signals was not possible. To investigate the presence of real negative signals or artefacts, standard “zpgg30” experiments were recorded of the regions of interest. The spectra resulting from the broadband excitation (xyBEBOP) were processed with magnitude calculation.

4.7.9.2 ^{31}P and ^1H monitoring of photocatalytic PhPH_2 and Ph_2PH arylation reactions

The procedure used for monitoring of the model reaction (chapter 4.7.9.1) was followed, using the appropriate phosphine (PhPH_2 , Ph_2PH ; 0.01 mmol) instead of P_4 .

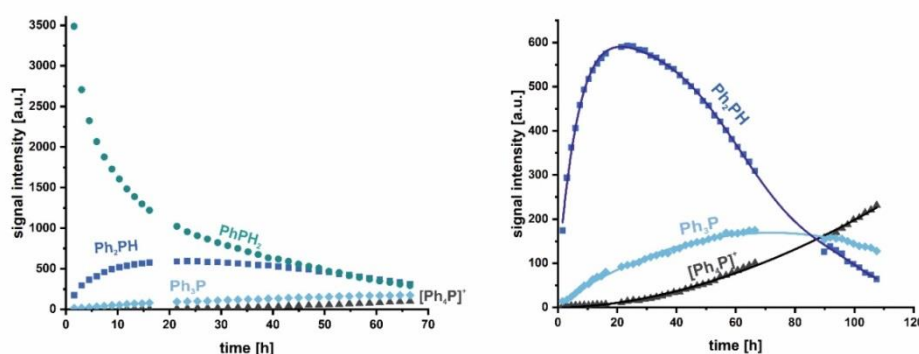


Figure SI 4.57 | *In situ* NMR reaction monitoring of the photocatalytic arylation of PhPH_2 . Left: Consumption of PhPH_2 and formation of Ph_2PH , Ph_3P , and $[\text{Ph}_4\text{P}]^+$. Right: Magnified view showing formation of Ph_2PH , Ph_3P , and $[\text{Ph}_4\text{P}]^+$. Polynomial curve fitting was used to illustrate qualitative trends.

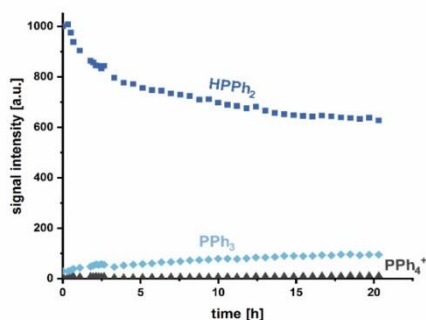


Figure SI 4.58 | *In situ* qualitative NMR monitoring of the photocatalytic arylation of Ph_2PH .

4 CATALYTIC TRANSFORMATION OF WHITE PHOSPHORUS

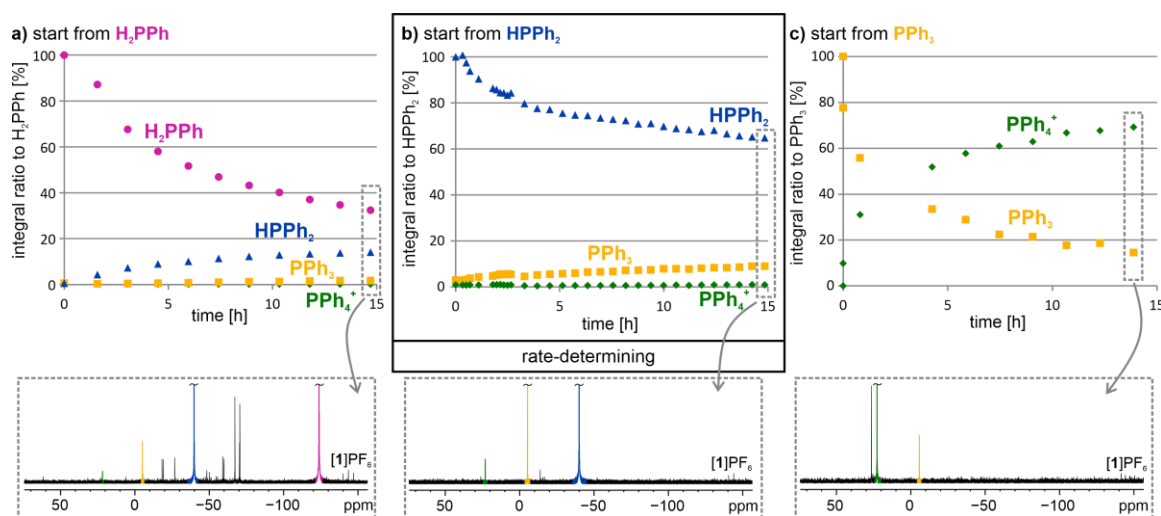


Figure SI 4.59 | Comparison of partial $^{31}\text{P}\{^1\text{H}\}$ -NMR reaction monitorings starting from different intermediates of the $[\text{1}]\text{PF}_6$ catalyzed functionalization of P_4 towards PPh_4^+ . The relative integrals of PPh_4^+ (green) and its precursors H_2PPh (pink), HPPH_2 (blue) and PPh_3 (yellow) over the first 15 hours of $^{31}\text{P}\{^1\text{H}\}$ -NMR reaction monitorings of the respective photocatalytic transformation of H_2PPh (a), HPPH_2 (b) and PPh_3 (c) are displayed. The starting material HPPH_2 (b) shows the slowest decay when applied as starting material, indicating the reaction from HPPH_2 to PPh_3 as rate determining step. The $^{31}\text{P}\{^1\text{H}\}$ -NMR spectra after ~ 15 h of illumination are displayed beneath the respective kinetics. The integral ratios of side products are not included in the kinetics. Reaction conditions: corresponding phosphine (50 mM), PhI (11 eq.), NEt_3 (14.4 eq.) and $[\text{1}]\text{PF}_6$ (2.2 mol%) in $\text{C}_6\text{D}_6/\text{CD}_3\text{CN}$ mixture (1:1), illumination at 455 nm (LED: Cree XT-E @ 1.5 A) at 298 K.

4.7.9.3 ^{31}P and ^1H monitoring of solutions of P_4 and PhI

Solutions were prepared in a 1:1 mixture of CD_3CN and C_6D_6 (2.0 mL total), containing $[\text{1}]\text{PF}_6$ (2.0 mg, 2.2 μmol), Et_3N (200 μL , 1.44 mmol) and either P_4 (3.1 mg, 0.025 mmol) or iodobenzene (11.2 μL , 0.1 mmol) or both. For each solution, a 500 μL sample was taken for NMR monitoring.

Measurements were conducted on a Bruker Avance III HD 600 MHz spectrometer with a fluorine selective TBIF probe. For both ^1H NMR and ^{31}P NMR spectra the standard pulse program “zg30” was applied. Acquisition parameters (except receiver gain) were held constant throughout the three experiments. Important acquisition parameters are as follows:

^1H : TD = 65536, DS = 0, NS = 16, D1 = 2 sec

^{31}P : TD = 32768, DS = 4, NS = 32, D1 = 2 sec

A spectrum in absence of light was recorded resembling the starting point $t = 0$. The light was then activated and the reaction monitored by alternately measuring ^1H and ^{31}P spectra. After the spectra were processed, the signals of the spectra $t > 0$ were referenced to their according signal in the spectrum $t = 0$.

The results of these experiments are summarized in Figure SI 4.59, and are broadly consistent with the mechanism proposed in Scheme SI 4.1 In particular, they provide yet further support for the proposal that

4 CATALYTIC TRANSFORMATION OF WHITE PHOSPHORUS

the reduced state of the photocatalyst [1] (generated through Et₃N reduction of the photoexcited state [1]⁺⁺) can be reoxidised through reaction with PhI (Scheme SI 4.1a). Nevertheless, it must be noted that these results also suggest the feasibility of direct P₄ reduction as a mechanism for regeneration of the ground state catalyst [1]⁺ (Scheme SI 4.1b). At this stage the possibility that this reaction may be mechanistically relevant cannot be conclusively ruled out. However, we note that:

1) Qualitatively, PhI appears to react more rapidly than P₄, and would be expected to react faster still during the catalytic reaction (where its concentration is an order of magnitude higher).

2) P₄ is consumed much more rapidly in the presence of PhI than in the absence, which is consistent with functionalization of P₄ by Ph· radicals generated upon PhI reduction. In contrast, PhI consumption is *slower* in the presence of P₄, which suggests that the species generated upon P₄ reduction cannot react productively with PhI.

As such, we suggest that [1] oxidation by PhI remains a more likely mechanistically-productive step than the analogous oxidation by P₄ (i.e. the cycle shown in Scheme SI 4.1a is proposed to be mechanistically relevant, while that shown in Scheme SI 4.1b may be catalytically unproductive).

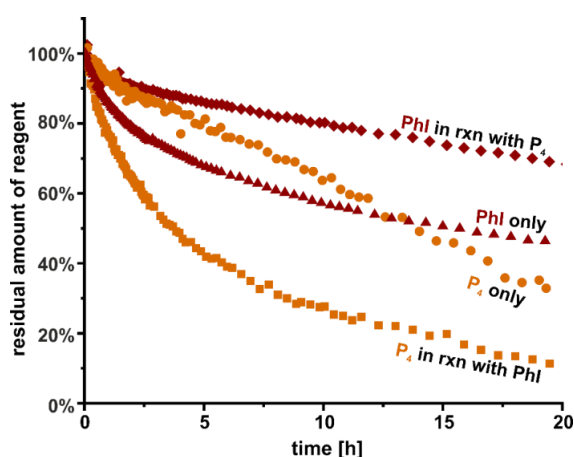
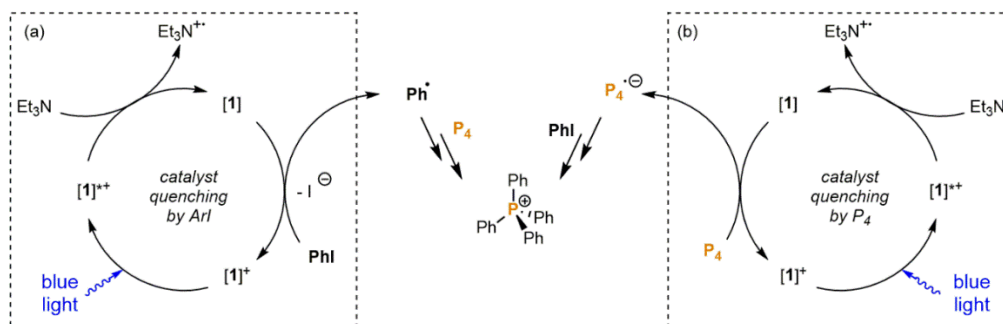


Figure SI 4.60 | Evolution of PhI and P₄ concentrations during *in situ* 455 nm irradiation in the presence of [1]PF₆ and Et₃N. Red traces indicate PhI concentration as measured for solutions of PhI alone (triangles) or as a 1:1 mixture with P₄ (diamonds). Orange traces indicate P₄ concentration as measured for solutions of P₄ alone (circles) and in the presence of PhI (squares).



Scheme SI 4.1 | Possible photoredox cycles involving [1]⁺ regeneration through oxidation of PhI (a) or P₄ (b).

4 CATALYTIC TRANSFORMATION OF WHITE PHOSPHORUS

4.7.9.4 Photo-CIDNP effect

During the *in situ* photocatalytic arylation of PhPH_2 (see chapter 4.7.9.2) a negative signal at 3.23 ppm was observed in the first ^1H NMR spectrum taken after starting to illuminate the mixture with 455 nm light (Figure SI 4.60). This indicates the presence of a photo-CIDNP effect, which arises from the conversion of photogenerated radical species into diamagnetic reaction products.^[10,11] Considering the proposed mechanism (Scheme SI 4.1), in this case this effect may arise from the reaction of the excited photocatalyst $[1]^*$ with Et_3N , generating the reduced catalyst $[1]$ and the radical cation of $\text{Et}_3\text{N}^{\cdot+}$. Due to its chemical shift and multiplicity the negative signal probably belongs to the aliphatic CH_2 -protons of the vinyl-substituted amine $\text{Et}_2\text{NCHCH}_2$ (which formally results from loss of H^\cdot from $\text{Et}_3\text{N}^{\cdot+}$, followed by deprotonation) which was extensively investigated in an earlier CIDNP study as a product of a radical pair involving $\text{NET}_3^{\cdot+}$.^[12]

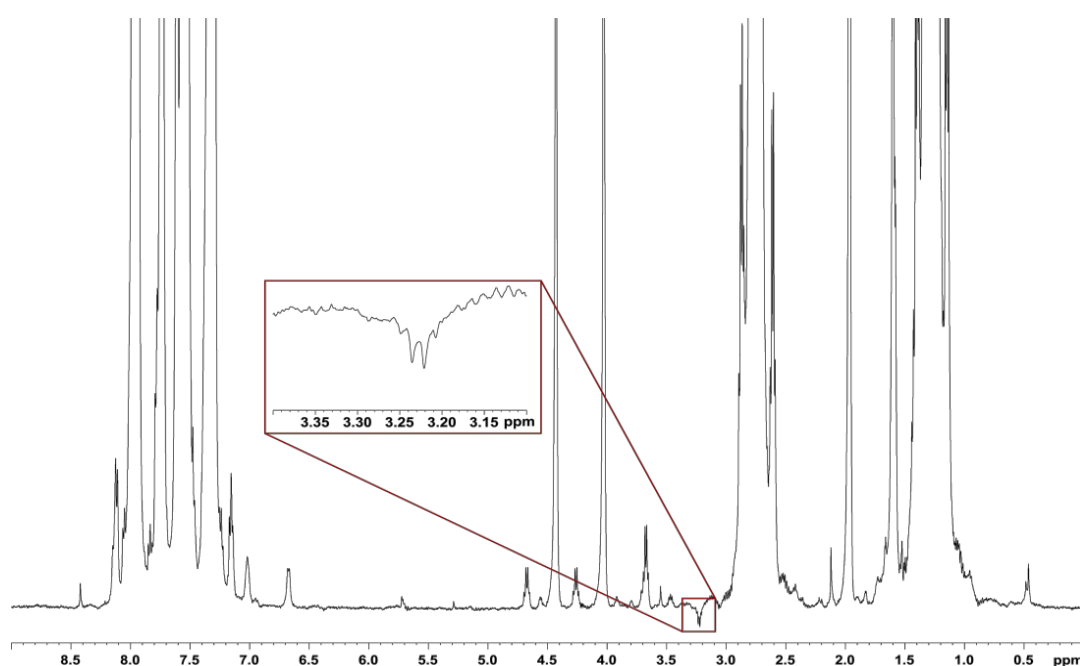
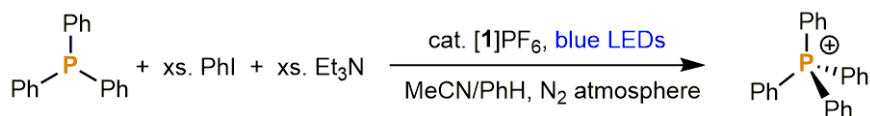


Figure SI 4.61 | Negative ^1H signal observed during *in situ* photocatalytic PhPH_2 arylation due to the photo-CIDNP effect.

4 CATALYTIC TRANSFORMATION OF WHITE PHOSPHORUS

4.7.10 Photocatalytic phenylation of Ph_3P , Ph_2PH and PhPH_2

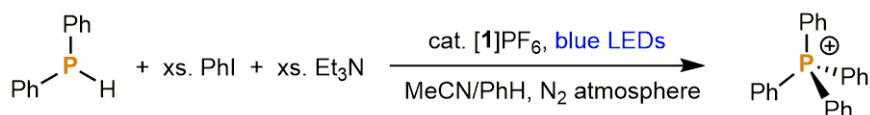
Table SI 4.4. Photocatalytic functionalisation of Ph_3P to $[\text{Ph}_4\text{P}]^+$



Entry	Conditions ^[a]	Conv. to $[\text{Ph}_4\text{P}]^+$ / %	Consumption of Ph_3P / %
1	standard	>99	100
2	no PhI	0	<3
3	no $[\text{1}]\text{PF}_6$	7	15
4	no light	<5	>95
5	no Ph_3P	0	-
6	no Et_3N	4	4

[a] The general procedure for reactions at 0.1 mmol scale (section 4.7.2) was modified by replacing P_4 with Ph_3P (26.3 mg, 0.1 mmol).

Table SI 4.5. Photocatalytic functionalisation of Ph_2PH to $[\text{Ph}_4\text{P}]^+$.

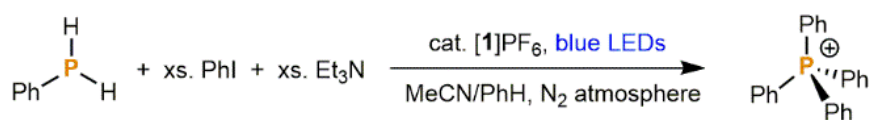


Entry	Conditions ^[a]	Conv. to $[\text{Ph}_4\text{P}]^+$ / %	Consumption of Ph_2PH / %
1	standard	67	100
2	no PhI	0	<3
3	no $[\text{1}]\text{PF}_6$	0	33
4	no light	0	0
5	no Ph_2PH	0	-
6	no Et_3N	_ ^[b]	_ ^[b]

[a] The general procedure for reactions at 0.1 mmol scale (section 4.7.2) was modified by replacing P_4 with Ph_2PH (17.5 μL mg, 0.1 mmol). [b] The standard procedure reproducibly gives a broad resonance for Ph_3PO which precludes accurate integration. Nevertheless, no conversion to $[\text{Ph}_4\text{P}]^+$ was observed.

4 CATALYTIC TRANSFORMATION OF WHITE PHOSPHORUS

Table SI 4.6. Photocatalytic functionalisation of PhPH₂ to [Ph₄P]⁺



Entry	Conditions ^[a]	Conv. to [Ph ₄ P] ⁺ / %	Consumption of PhPH ₂ / %
1	standard	85	100
2	no PhI	0	31
3	no [1]PF ₆	0	44
4	no light	0	19
5	no PhPH ₂	0	-
6	no Et ₃ N	0	73

[a] The general procedure for reactions at 0.1 mmol scale (section 4.7.2) was modified by replacing P₄ with PhPH₂ (11.0 μL mg, 0.1 mmol).

4.7.11 References

- [1] Weitz, I. S. & Rabinovitz, M. The application of C₈K for organic synthesis: reduction of substituted naphthalenes. *J. Chem. Soc. Perkin 1* **0**, 117–120 (1993).
- [2] Marcoux, D., Charrette, A.B. Palladium-Catalyzed Synthesis of Functionalized Tetraarylphosphonium Salts. *J.Org.Chem.* **73**, 590-593 (2008).
- [3] Demchuk, O.M., Jasinski, R., Strelecka, D., Dziuba, K., Kula, K., Chrzanowski, J., Krasowska, D. A clean and simple method for deprotection of phosphines from borane complexes. *Pure Appl. Chem.* **90(1)**, 49-62 (2018).
- [4] Barnes, N. A., Godfrey, S. M., Halton, R. T. A., Mushtaq, I., Pritchard, R. G. The reaction of tertiary phosphines with (Ph₂Se₂)₂—the influence of steric and electronic effects. *Dalton Trans.* **40**, 4795-4804 (2006).
- [5] Cummins, C.C., Huang, C., Miller, T. J., Reintinger, M. W., Stauber, J. M., Tannou, I., Tofan, D., Toubaei, A., Velian, A., Gang, W. The Stannyphosphide Anion Reagent Sodium Bis(triphenylstannyl) Phosphide: Synthesis, Structural Characterization, and Reactions with Indium, Tin, and Gold Electrophiles. *Inorg.Chem.* **53**, 3678-3687 (2014).
- [6] Prier, C. K., Rankic, D. A. & MacMillan, D. W. C. Visible Light Photoredox Catalysis with Transition Metal Complexes: Applications in Organic Synthesis. *Chem. Rev.* **113**, 5322–5363 (2013).

4 CATALYTIC TRANSFORMATION OF WHITE PHOSPHORUS

- [7] Krejčík, M., Daněk, M. & Hartl, F. Simple construction of an infrared optically transparent thin-layer electrochemical cell: Applications to the redox reactions of ferrocene, $\text{Mn}_2(\text{CO})_{10}$ and $\text{Mn}(\text{CO})_3(3,5\text{-di-}t\text{-butyl-catecholate})^-$. *J. Electroanal. Chem. Interfacial Electrochem.* **317**, 179–187 (1991).
- [8] Feldmeier, C., Bartling, H., Riedle, E. & Gschwind, R. M. LED based NMR illumination device for mechanistic studies on photochemical reactions – Versatile and simple, yet surprisingly powerful. *J. Magn. Reson.* **232**, 39–44 (2013).
- [9] Seegerer, A., Nitschke, P. & Gschwind, R. M. Combined In Situ Illumination-NMR-UV/Vis Spectroscopy: A New Mechanistic Tool in Photochemistry. *Angew. Chem. Int. Ed.* **57**, 7493–7497 (2018).
- [10] Goetz, M. Chapter 3 Photo-CIDNP Spectroscopy. in *Annual Reports on NMR Spectroscopy* **66**, 77–147 (Academic Press, 2009).
- [11] Goetz, M. & Sartorius, I. Photo-CIDNP investigation of the deprotonation of aminium cations. *J. Am. Chem. Soc.* **115**, 11123–11133 (1993).
- [12] Goetz, M. & Sartorius, I. CIDNP Determination of the Rate of In-Cage Deprotonation of the Triethylamine Radical Cation. *J. Phys. Chem. A* **107**, 8539–8546 (2003).

4.8 Additional Findings by NMR

Mechanistic elucidation of any kind, be it the understanding of kinetics, intermediates, by- or side-products or the role of reagents, is important for optimizing or controlling a chemical reaction. An established mechanistic understanding may allow adapting the reaction conditions in a way to favor one reaction path over another, leading to maximum yield and minimum amount of side-products (waste). Reaction optimization is not only essential for increasing the yield of the desired product, but also in terms of environmentalism and time and cost savings. NMR offers the possibility for *in situ* reaction monitoring and for structural determination of intermediates and side products, which may not be accessed after workup of the reaction due to e.g. their labile nature. In the following, additional findings obtained by NMR on the photocatalytic functionalization of P₄ or other structural precursors of PPh₄⁺ in presence of iodobenzene and TEA are presented and their significance for the mechanism of the direct photocatalytic transformation of P₄ into tetraarylphosphonium salts is discussed.

Throughout these chapters ³¹P{¹H}-NMR spectra were recorded and used for *in situ* reaction monitoring. In order to obtain a maximum signal enhancement, the ³¹P-NMR spectra were recorded with power-gated ¹H-decoupling. Thereby, decoupling is applied during relaxation delay and acquisition period which achieves signal enhancement due to NOE transfer and collapse of the splitting pattern simplifying the spectrum. Hence, most ³¹P-NMR signals are enhanced to different extents due to the presence of a different number of protons exhibiting disparate J_{HP} coupling constants. This impedes quantitative but not qualitative analyses, e.g. of the sequence and type of intermediates.

4.8.1 Exchanging the metal catalyst by an organocatalyst

Iridium based photocatalysts, such as those based on ruthenium, find extensive use as photoredox catalysts owing to their exceptional photophysical characteristics.^[1] However, since the natural abundance of these noble metals is very limited (~ 1 ppb^[2]), the application of catalysts incorporating Ir or Rh is not only cost-intensive, but also unsustainable and entails environmental problems.^[1] Hence, replacing these metal catalysts by more sustainable and economical alternatives such as organocatalysts is of great interest.^[1] By making the organofunctionalization of P₄ catalytic and direct, an important step towards sustainability and environmental compatibility has already been taken and essential principles of green chemistry^[3] have been followed (e.g. by avoiding hazardous phosphorous chlorides which are intermediates in industrial procedures^[4], or by using catalytic rather than stoichiometric conditions^[5-8]). A further step towards green chemistry is the replacement of the Ir-catalyst, which is based on a depleting feedstock, by an organic photocatalyst. Kirsten Zeitler *et al.* designed a variety of organic photocatalysts which are constructed of commercially available, low-cost cyanobenzenes.^[1] The ground state reduction potential of their photocatalyst 3DPAFIPN (**14**, see Figure AF 4.1) [determined in MeCN; E_{1/2} (PC/PC^{•-}) = - 1.59 V vs SCE^[1] =^[9] -1.97 V vs Fc/Fc⁺] fits perfectly the onset potential of the irreversible reduction wave observed for PhI

4 CATALYTIC TRANSFORMATION OF WHITE PHOSPHORUS

[determined in MeCN/benzene (3:1); $E_{95} = -1.96$ V (E_{95} is defined as the potential where the current is 95 % lower than at the peak of the wave, i.e. E_{95} occurs when $I = I_{\max} - (0.95 \times \Delta I)$ where $\Delta I = I_{\max} - I_{\text{baseline}}$)] (see Figure SI 4.43) indicating a feasible electron transfer to PhI from the reduced photocatalyst $\mathbf{14}^{\cdot-}$. Indeed, when **14** was applied instead of $[\mathbf{1}]\text{PF}_6$ in the photocatalytic functionalization of P_4 with PhI a reduced conversion towards the tetraarylphosphonium salt PPh_4^+I^- was observed by quantitative $^{31}\text{P}\{^1\text{H}\}$ NMR analysis of the reaction mixture ($[\mathbf{1}]\text{PF}_6$: 76 % vs **14**: 60%^[10]).

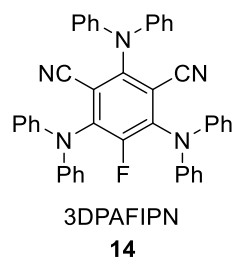


Figure AF 4.1 | Structure of the organocatalyst designed by Zeitler *et al.*^[1]

To investigate the reason behind the reduction in yield, the model reaction ($\text{P}_4 + \text{PhI} + \text{NEt}_3 + \mathbf{14}$ instead of $[\mathbf{1}]\text{PF}_6$ in same equivalents; for concentrations see chapter 4.7.9.1) was followed by ^1H - and $^{31}\text{P}\{^1\text{H}\}$ -NMR under the same reaction conditions (298 K, blue LED: 455 nm). Already in the first ^1H -NMR recorded with illumination, the first difference upon catalyst exchange of $[\mathbf{1}]\text{PF}_6$ by **14** could be noticed. A photo-CIDNP effect, unambiguously identified by the negative signal intensities,^[11] on the NEt_3 derivative **15**^[12] and on other unassigned signals at 9.42 ppm and in between 5.3 ppm and 4.4 ppm was obtained, while in the case of $[\mathbf{1}]\text{PF}_6$ this effect was observed with smaller intensity only on **15** in the partial reaction starting from H_2PPh instead of P_4 (for a comparison see Figure AF 4.2). A photo-CIDNP effect arises from the conversion of photogenerated radical species into diamagnetic reaction products.^[11] In the case of catalysis by $[\mathbf{1}]\text{PF}_6$ we observed this effect on enamine **15**, which formally results from loss of H^\bullet from Et_3N^+ , followed by deprotonation^[12] (**15** was extensively investigated in a CIDNP study as a product of a radical pair involving $\text{NEt}_3^{\cdot+}$ ^[12]). Thereupon, we concluded that this effect may arise from the reaction of the excited photocatalyst $[\mathbf{1}]^{*\cdot}$ with Et_3N , generating the reduced catalyst $[\mathbf{1}]^{\cdot-}$ and the radical cation $\text{Et}_3\text{N}^{\cdot+}$. The appearance of a CIDNP effect on the same species (**15**) by applying another catalyst (**14**) indicates that also in the organocatalyzed reaction this effect arises from the reaction of the excited photocatalyst $\mathbf{14}^{*\cdot}$ with Et_3N , generating the reduced catalyst $\mathbf{14}^{\cdot-}$ and the radical cation $\text{Et}_3\text{N}^{\cdot+}$. The mechanism of the formation of **15** is given in Figure AF 4.2. Within the catalytic cycle of the photocatalytic functionalization of P_4 (see Figure 4.2) TEA functions as sacrificial electron donor and gets oxidized to the radical cation $\text{TEA}^{\cdot+}$. Then, either iminium ion **16** is generated through H^\bullet abstraction (a) or α -amino radical **17** by H^\bullet abstraction (b)^[13]. Due to the strong reducing properties of **17**, it can be oxidized to **16**^[13]. H^\bullet abstraction on **17** (c) can generate enamine **15**^[12], which may also be generated by deprotonation of the iminium ion **16** (d).^[14,15]

4 CATALYTIC TRANSFORMATION OF WHITE PHOSPHORUS

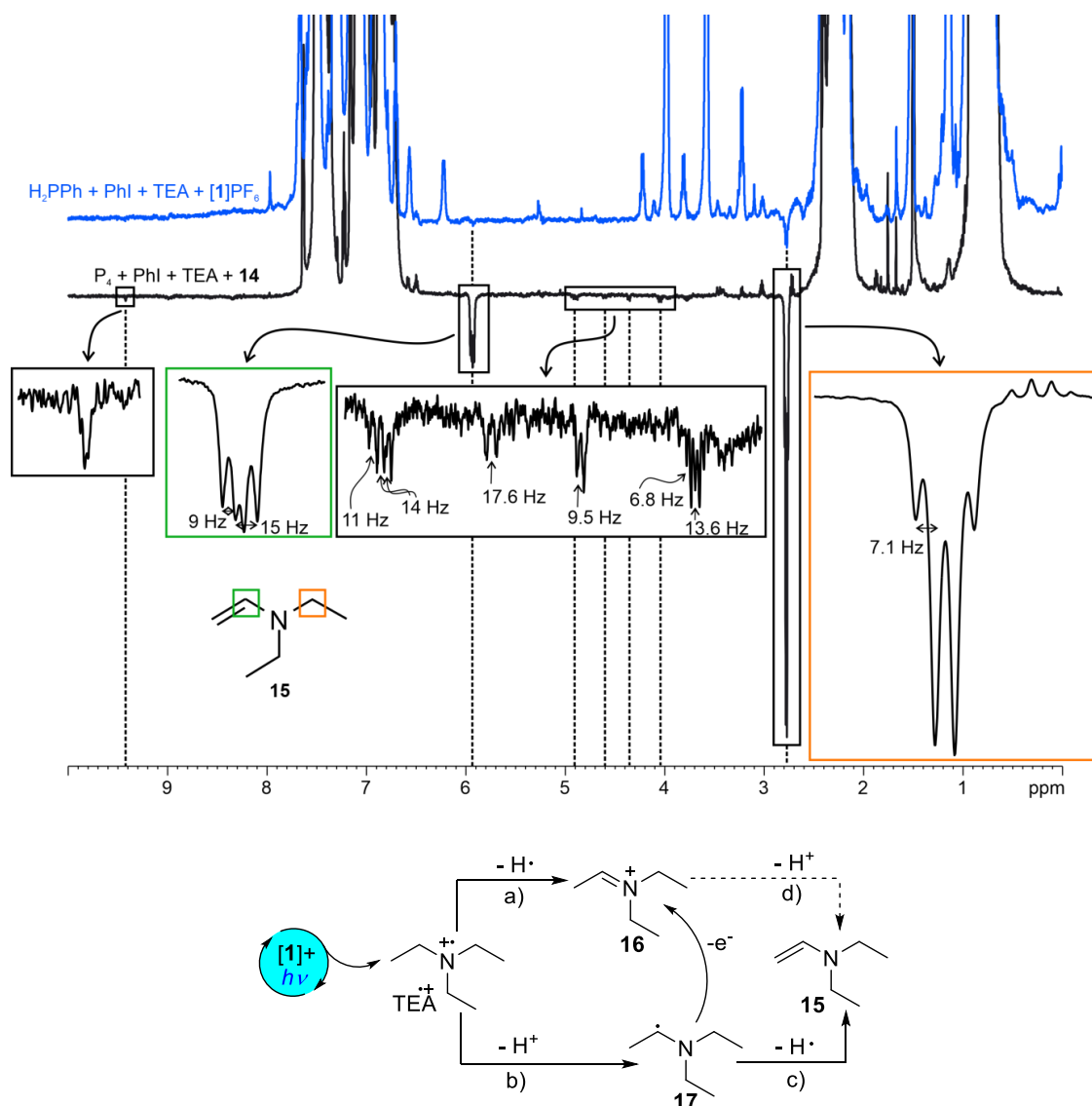


Figure AF 4.2 | Photo-CIDNP effects in $[1]PF_6$ (blue) versus **14** (black) catalyzed reactions. Blue: first 1H -NMR spectrum recorded during illumination of a sample of H_2PPh (50 mM), PhI (11 eq.), NEt_3 (14.4 eq.) and $[1]PF_6$ (2.2 mol%) in C_6D_6/CD_3CN mixture (1:1). A photo-CIDNP effect is evident by the negative 1H -NMR signals at 2.78 ppm (CH_2 of **15**) and at 5.94 ppm (CH of **15**). Black: first 1H -NMR spectrum recorded during illumination (455 nm, LED: Cree XT-E @ 1.5 A) of a sample of P_4 (12.5 mM), PhI (11 eq. referred to one P-atom), NEt_3 (14.4 eq. referred to one P-atom) and **14** (2.2 mol% referred to one P-atom) in C_6D_6/CD_3CN mixture (1:1) at 298 K. A photo-CIDNP effect is evident by the negative 1H -NMR signals at 2.78 ppm (CH_2 of **15**), 5.94 ppm (CH of **15**) and 9.42 ppm and in between 4.4 ppm and 5.3 ppm. Bottom: Mechanism of the formation of **15**.^[12,13]

Because of the low signal intensity of the unknown CIDNP-signals and their sole appearance in the organocatalyzed reaction, their origin was not investigated further.

$^{31}P\{^1H\}$ -NMR reaction monitoring gave further insight into similarities and differences of the organocatalyzed and the iridium catalyzed functionalization of P_4 (for comparison see Figure AF 4.3a-d). Directly after starting the illumination of the organocatalyzed reaction, four new signals (**Int1-Int4**) appeared which were not observed in the functionalization of P_4 catalyzed by $[1]PF_6$ and which were identified to have intermediate character (productive or unproductive) due to their kinetic profile (see Figure AF 4.4 for spectrum and Figure AF 4.3a and c for kinetics). In addition, during the further course of the reaction, several signals appeared

4 CATALYTIC TRANSFORMATION OF WHITE PHOSPHORUS

(Side1-Side5) that are considered to be involved in unproductive pathways (for further information and the discussion of their potential structures see chapter 4.8.6).

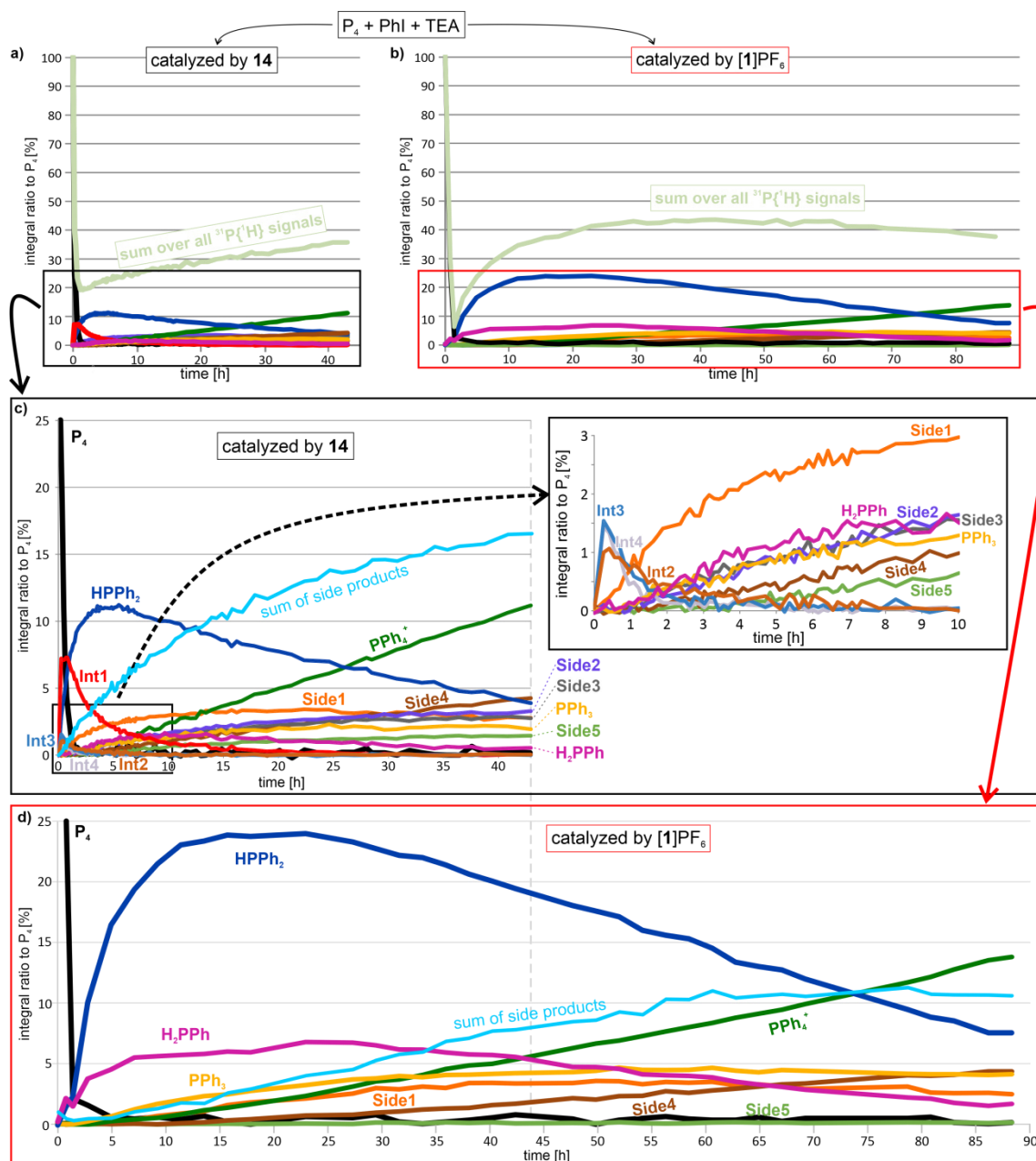


Figure AF 4.3 | ^{31}P -NMR reaction kinetics of the functionalization of P_4 : organocatalyzed (a) versus iridium-catalyzed (b). Both ^{31}P -NMR reaction kinetics were recorded with ^1H decoupling during d1 and acquisition (zgpg) to increase signal-to-noise ratio. Thereby ^{31}P signal intensities of different species are enhanced to different extents (stronger for big ^1H - ^{31}P scalar couplings). For sake of clarity, data points were connected by straight lines. Reaction conditions: a) P_4 (12.5 mM), PhI (11 eq. referred to one P-atom), NEt_3 (14.4 eq. referred to one P-atom) and $[\mathbf{1}]\text{PF}_6$ (2.2 mol% referred to one P-atom) in $\text{C}_6\text{D}_6/\text{CD}_3\text{CN}$ mixture (1:1) at 298 K. b) P_4 (12.5 mM), PhI (11 eq. referred to one P-atom), NEt_3 (14.4 eq. referred to one P-atom) and **14** (2.2 mol% referred to one P-atom) in $\text{C}_6\text{D}_6/\text{CD}_3\text{CN}$ mixture (1:1) at 298 K. Both reaction were illuminated *in situ* at 455 nm (LED: Cree XT-E @ 1.5 A).

4 CATALYTIC TRANSFORMATION OF WHITE PHOSPHORUS

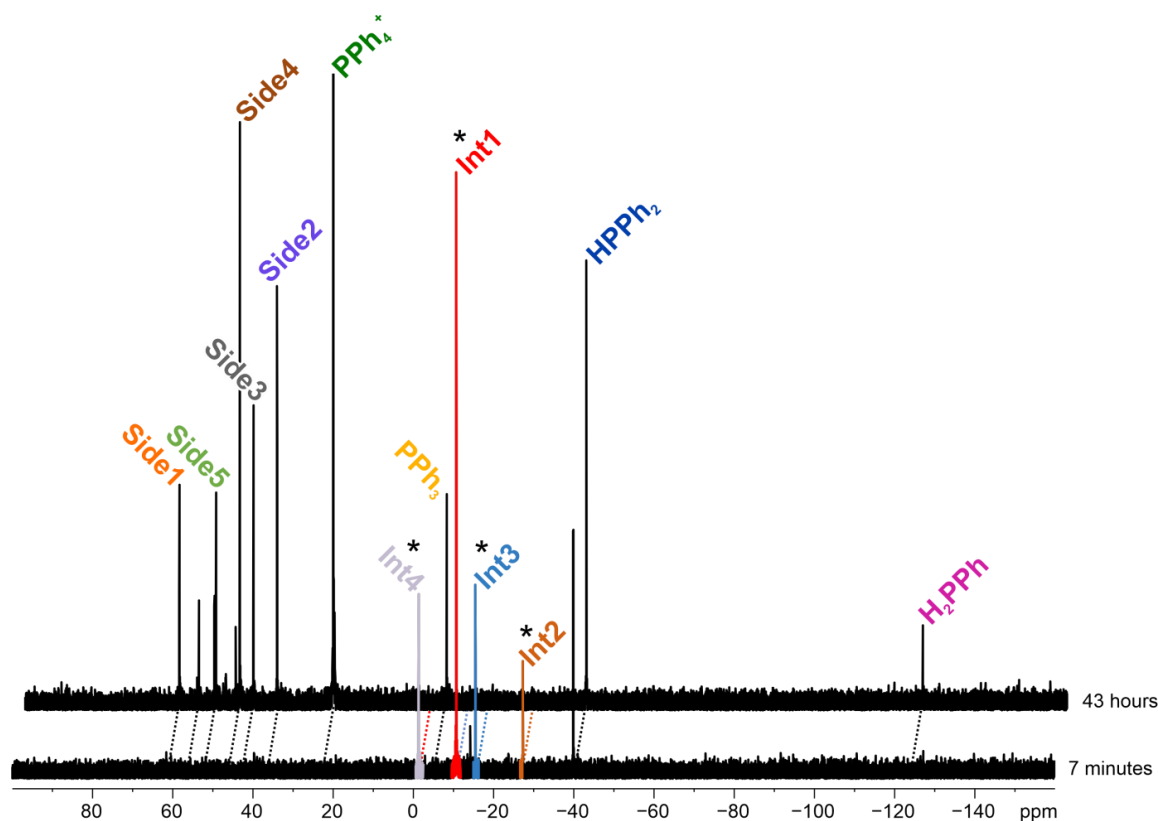


Figure AF 4.4 | Significant signals emerging during *in situ* ^{31}P -NMR reaction monitoring of the organocatalyzed functionalization of P_4 . Bottom: first ^{31}P -NMR spectrum recorded after 7 minutes of illumination. Top: last ^{31}P -NMR spectrum recorded after 43 hours of illumination at 455 nm (LED: Cree XT-E @ 1.5 A). Signals marked with asterisk were never observed in the reaction monitoring of the iridium-catalyzed functionalization of P_4 , H_2PPh , HPPH_2 and PPh_3 . Reaction conditions: P_4 (12.5 mM), PhI (11 eq. referred to one P-atom), NEt_3 (14.4 eq. referred to one P-atom) and **14** (2.2 mol% referred to one P-atom) in $\text{C}_6\text{D}_6/\text{CD}_3\text{CN}$ mixture (1:1) at 298 K.

It has to be mentioned, that many $^{31}\text{P}\{^1\text{H}\}$ -NMR signals increased in intensity when the light source was switched on and decreased again when the illumination was stopped. This increasing decreasing behavior was especially prominent for the signals of **Int1-Int4**, which vanished when the light source was switched off, and for the signal of HPPH_2 . The increase in signal intensity was stronger in the beginning of the reaction illumination and weaker after 19 hours of illumination period (see Figure AF 4.5).

4 CATALYTIC TRANSFORMATION OF WHITE PHOSPHORUS

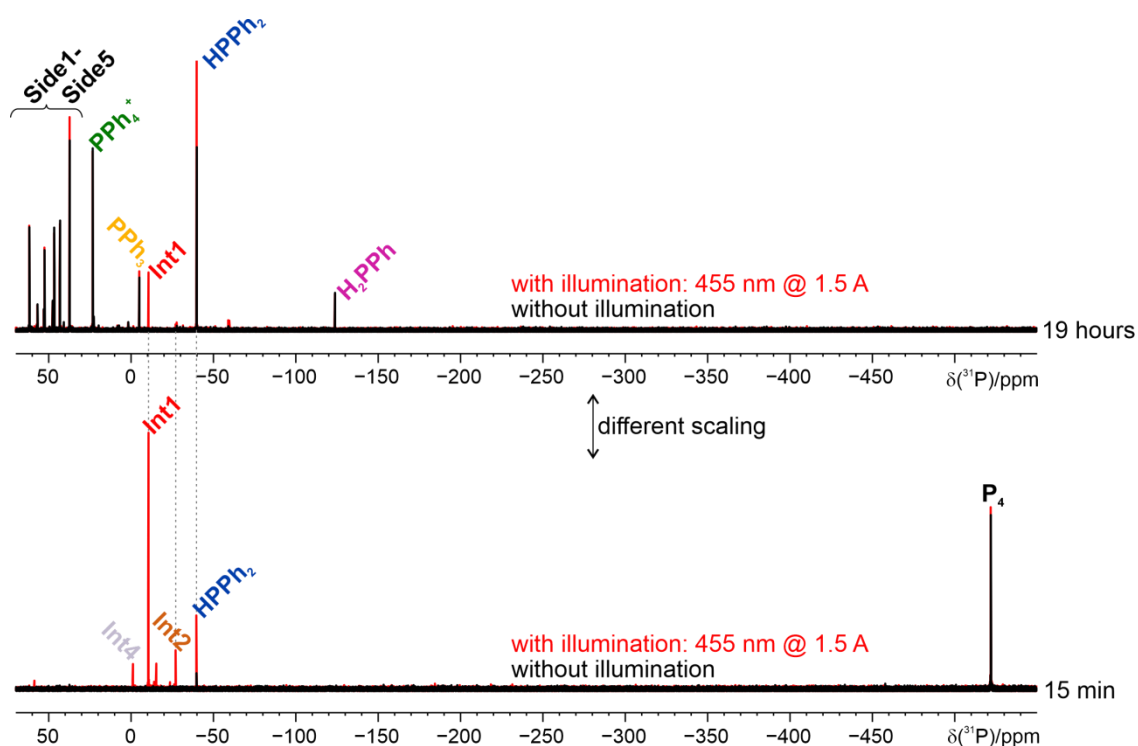


Figure AF 4.5 | $^{31}\text{P}\{^1\text{H}\}$ -NMR spectra recorded during the *in situ* NMR reaction monitoring of the photocatalytic functionalization of P_4 catalyzed by **14**. Spectra in red were recorded during illumination, spectra in black were recorded in the dark upon switching off the illumination source. Bottom and upper spectra were recorded after a total illumination time of 15 min and 19 hours, respectively. Overlapping spectra have the same scaling. Key acquisition parameters: TD = 375k; NS = 128; SW = 625 kHz; AQ = 0.3 s; d1 = 2 s.

The increase of $^{31}\text{P}\{^1\text{H}\}$ -NMR signals upon illumination may arise from positive photo-CIDNP effects, from accumulation of short lived species or from a reduction in relaxation time, e.g. due to the presence of radicals (a small relaxation delay of 2 s was used). Photo-CIDNP effects are generated in the first radical pair of a reaction and can manifest themselves in the diamagnetic products through signal amplification or attenuation, depending on the radical pair mechanism. For the signals of **Int1-Int4** which were not observed in the dark but then in positive intensities upon illumination, it is not clear if this is a result of a real CIDNP effect or of very short lived species that accumulate during illumination and rapidly react further in the dark. Hence, due to a stronger enhancement of the $^{31}\text{P}\{^1\text{H}\}$ -NMR signals of the reaction catalyzed by **14** than for the reaction catalyzed by $[\mathbf{1}]\text{PF}_6$ a quantitative comparison of the intermediate and product ratios of the differently catalyzed reaction is not possible. Yet, since the signals of product and side products were not or only weak enhanced when the light was switched on, the ratio of side products to PPh_4^+ of the differently catalyzed reactions can be compared (compare c) and d) in Figure AF 4.3). This reveals that the organocatalyst **14** leads to higher ratios of side products compared to the Ir-catalyst $[\mathbf{1}]\text{PF}_6$ which is in line with the lower yield of PPh_4^+ obtained in the reaction catalyzed by **14**. Besides, in the reaction catalyzed by organocatalyst **14** the formation the same sequential precursors H_2PPh , HPPH_2 and PPh_3 were observed (compare Figure AF 4.3b and c). Therefore, the application of catalyst **14** in the photocatalytic functionalization of P_4 affords the same intermediates for the productive pathway and it also facilitates the formation of intermediates and products involved in unproductive side reactions.

4 CATALYTIC TRANSFORMATION OF WHITE PHOSPHORUS

In addition, in the beginning of both monitorings of the reactions catalyzed by [1]PF₆ and **14**, a considerable decrease of the sum of all ³¹P{¹H}-NMR signals was observed which then again increased. The decrease of the sum indicates that P₄ is converted to an NMR-undetectable reservoir (either by polymerization or conversion to paramagnetic species or to compounds that precipitate; the polymerization of white phosphorus in presence of light and radicals is known^[16]). This was supported by the observation of a precipitate on the bottom of the NMR-tube after the reaction monitoring. The formation of a precipitate was also observed when the functionalization of P₄ was carried out outside the spectrometer in a stoppered tube under stirring, which then dissolved again as the reaction progressed. The increase of the sums in Figure AF 4.3 indicates that the NMR-undetectable reservoir can constantly supply phosphorus units for further conversion to PPh₄⁺ and side products.

To get ideas about the structures of the intermediates as well as the side-products 2D ¹H-³¹P-HMBC and –HMQC spectra were recorded during the reaction monitoring of the model reaction catalyzed by **14** at lowered temperatures (273 K and 238 K). For **Int3** and **Int4**, no ¹H-³¹P-crosspeaks were observed probably due to signal-to-noise issues. In that case, a comparison of their experimental ³¹P-NMR chemical shifts with literature could provide information about their possible structures. The shift of **Int3** (-15.6 ppm) fits quite well to the literature shift of tetraphenyldiphosphine Ph₄P₂ (-15.4 ppm)^[17]. This signal was also observed in traces in the photocatalytic transformation of P₄ applying the Ir-catalyst [1]PF₆. In addition, Ph₄P₂ was observed as intermediate in transformations of Ph₂PH to unsymmetric phosphines and phosphonium salts catalyzed by **14**.^[10] **Int1** and **Int2** showed cross peaks from their ³¹P signal to protons in the aromatic and olefinic chemical shift regions. In contrast to **Int2**, **Int1** showed further coupling to protons of the aliphatic region. By comparing the ¹H- and ³¹P-NMR chemical shifts with literature (see structures in Figure AF 4.6 and Figure caption), the structures depicted in Figure AF 4.6 may be assigned to **Int1** and **Int2** respectively. It is noticeable that the cross peaks to the other olefinic and aromatic protons are missing, which is probably due to the fact that the HMQC was recorded with an evolution delay optimized for a coupling constant of 8 Hz. Thereby other cross peaks may be reduced in intensity due to the decaying sine dependency of the cross peaks' intensity on the evolution delay. For a more confident assignment of **Int1** and **Int2** additional *in situ* NMR experiments would be required, such as ¹H-¹³C-HSQC (multiplicity-edited) and –HMBC, ¹H-¹H-COSY and –NOESY. Nevertheless, **Int1** clearly shows coupling to the aliphatic ¹H-NMR region. Furthermore, **Int1** as well as **Int2** show couplings to olefinic protons. A transformation of **Int1** and **Int2** into the desired product PPh₄⁺ would require the replacement of the aliphatic and olefinic residues on phosphorus by phenyl. Under the given reaction conditions, this is considered unlikely, wherefore it is assumed that **Int1** and **Int2** are involved in unproductive pathways.

4 CATALYTIC TRANSFORMATION OF WHITE PHOSPHORUS

Extracts of a ^1H - ^{31}P -HMQC recorded at 238 K

τ was adjusted to $J = 8$ Hz

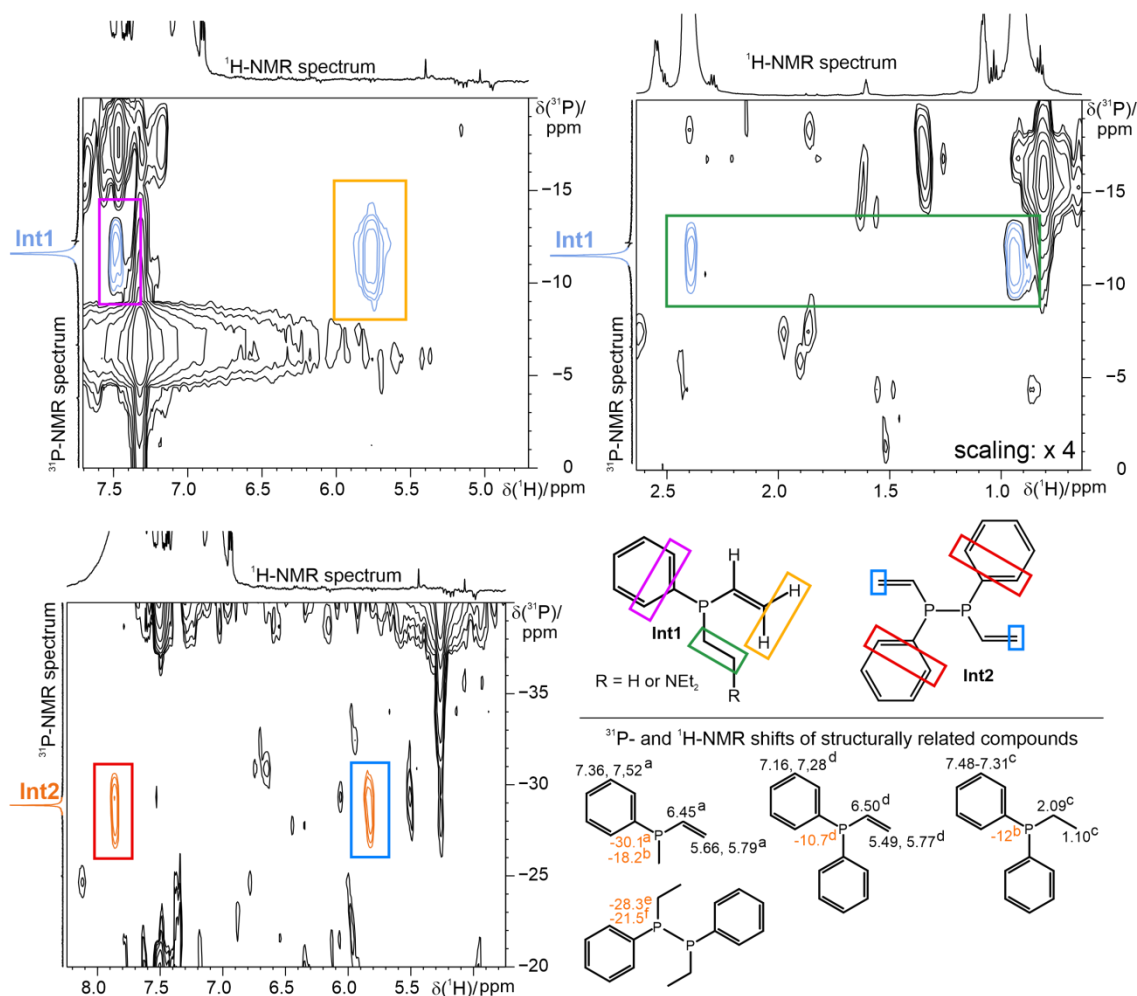


Figure AF 4.6 | Corresponding extracts of a 2D ^1H - ^{31}P -HMQC spectrum (with ^{31}P -decoupling; at 238 K) of **Int1** and **Int2** and tentatively proposed structures. The evolution delay of the HMQCs was adjusted to a coupling constant of 8 Hz. Comparing the ^{31}P -NMR chemical shifts of **Int1** and **Int2** and their corresponding ^1H NMR chemical shifts derived from the HMQC cross peaks with the shifts of similar compounds found in literature, the depicted structures may be proposed. ^{31}P -NMR shifts are highlighted in orange, ^1H -NMR shifts in black. Experimental details: The HMQC was recorded at 238 K during illumination (455 nm; LED: Cree XT-E @ 1.5 A) of a sample containing P_4 (12.5 mM), PhI (11 eq. referred to one P-atom), NEt_3 (14.4 eq. referred to one P-atom) and **14** (2.2 mol% referred to one P-atom) in $\text{C}_6\text{D}_6/\text{CD}_3\text{CN}$ mixture (1:1) after about 4.5 hours of total illumination time. Key acquisition parameters: pulse program: *hmqcpgpf_light+delay* (= modified *hmqcpgpf* sequence with implemented light on/off control)^[18] TD(F2) = 2k; TD(F1) = 64; SW(F2) = 30 ppm; SW(F1) = 200 ppm; DS = 16; NS = 16; CNST2 = 8 Hz. ^a Shifts were taken from literature^[19]. ^b Shifts were taken from literature^[20]. ^c Shifts were taken from literature^[21]. ^d Shifts were taken from literature^[22]. ^e Shifts were taken from literature^[23]. ^f Shifts were taken from literature^[24].

4.8.2 NMR approaches to unveil further intermediates of the productive pathway

Knowing the mechanism of a certain reaction and the intermediates involved therein offers a great potential for reaction optimization. Key parts of the photocatalytic functionalization of P_4 towards arylphosphines and tetraarylphosphonium salts could already be elucidated (see chapter 4.3.3) such as the catalytic cycle and the sequential monophosphoric intermediates H_2PPh , HPPH_2 and PPh_3 . Concerning the reoxidation of the photocatalyst [**1**] (generated through reduction of the photoexcited state [**1**]^{*} by Et_3N ; see Figure 4.2)

4 CATALYTIC TRANSFORMATION OF WHITE PHOSPHORUS

UV/Vis as well as NMR studies showed that this process can occur through reaction with both PhI or P_4 (see Figure AF 4.7 and SI for experimental evidence). Due to a generally faster consumption of PhI compared to P_4 in presence of photocatalyst $[1]PF_6$ and the higher concentration of PhI inside the reaction mixture, we suggested that oxidation of $[1]$ by PhI is a more likely mechanistically productive step than the analogous oxidation by P_4 . To further support this assumption, the detection of (P_n) -radicals or at least indications to their presence would be of particular interest, as this may allow drawing more profound conclusions about the initial radical pathway ($P_4^{\cdot-}$ versus Ph^{\cdot} , see Figure AF 4.7). However, information about multiphosphoric (P_n) intermediates such as P_2 -, P_3 - or P_4 -intermediates, let alone ions or radicals, was sparse (sole P_n -intermediate detected: Ph_4P_2 denoted as **Int3**; see chapter 4.3). Therefore, the model reaction was monitored at lower temperatures with the intention of stabilizing any possible short-lived intermediates and making them accessible for NMR (see chapter 4.8.2.1).

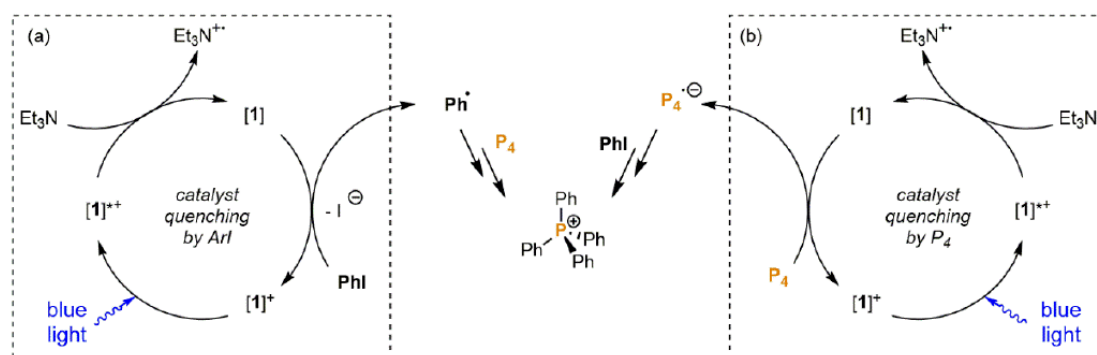


Figure AF 4.7 | Possible photoredox cycles involving $[1]^+$ regeneration through oxidation of PhI (a) or P_4 (b). $[1] = Ir(dtbbpy)(ppy)_2$.

The detection of radicals by NMR is commonly rather challenging owing to their paramagnetic properties causing extreme line broadening of their NMR signals. The thereby associated signal-to-noise problems often impede the direct detection of NMR signals of radicals. Hence, to get an access towards any radicals potentially involved in the photocatalytic functionalization of P_4 , methods of radical trapping by TEMPO and spin traps (PBN and DMPO) were consulted and monitored by NMR (see chapter 4.8.2.2 and 4.8.2.3).

4.8.2.1 Cooling of the reaction mixture & increase of catalyst loading

With the intention of stabilizing any possible short-lived intermediates, the temperature was decreased for the NMR monitoring of the reaction mixtures involving either the Ir-catalyst $[1]PF_6$ or the organocatalyst **14**. For the monitoring of the reaction catalyzed by **14**, the catalyst loading was additionally enlarged (saturated solution) with the intention of increasing the amount of intermediates succeeding the catalytic cycle. Enhanced catalyst loading was not applied to the reaction catalyzed by $[1]PF_6$ because it is quite expensive.

As a first step, the reaction mixture with $[1]PF_6$ was cooled to 273 K and submitted to illumination at 455 nm. Indeed, several new signals (**Int5-Int7** and PH_3) highfield shifted to the signal of $HPPH_2$ were observed in the $^{31}P\{^1H\}$ -NMR spectra (see Figure AF 4.8). No new signals appeared upon further cooling to 253 K and a second illumination period (15 min). In contrast to the signals of **Int1-4** those of **Int5-Int7** and PH_3 did not

4 CATALYTIC TRANSFORMATION OF WHITE PHOSPHORUS

vanish in absence of light. The ^{31}P -NMR signal at -240 ppm was assigned to PH_3 by its characteristic coupling pattern (quartet with $^1J_{\text{HP}} = 189$ Hz, see Figure AF 4.8) and by comparison of its shift with that reported in literature^[25]. Regarding its structure, it may constitute the very first intermediate in the reaction towards PPh_4^+ (see Figure 4.2) which would result in a new intermediate sequence of PH_3 , H_2PPh , HPPH_2 and PPh_3 . However, because of the poor S/N of PH_3 and the complex overall reaction profile of the functionalization of P_4 to PPh_4^+ (due to many side reactions; see Figure AF 4.3), the reaction profile of PH_3 can only be described in very general terms, that PH_3 is initially generated and then consumed over the course of the reaction. Therefore, it cannot be decided whether the functionalization of P_4 proceeds *via* the sequence starting with PH_3 or with H_2PPh or if both pathways occur simultaneously. Latter is considered likely. The general ability of PH_3 to function as an intermediate in the reaction towards PPh_4^+ was further verified by applying it as starting material instead of P_4 , which will be discussed in chapter 4.8.4.

Earlier, the formation of PH_3 was only once observed at 298 K with low S/N in the very beginning of illumination of the model reaction catalyzed by $[\mathbf{1}]\text{PF}_6$. Otherwise, PH_3 was generally observed in higher S/N when the reaction was carried out in absence of iodobenzene.

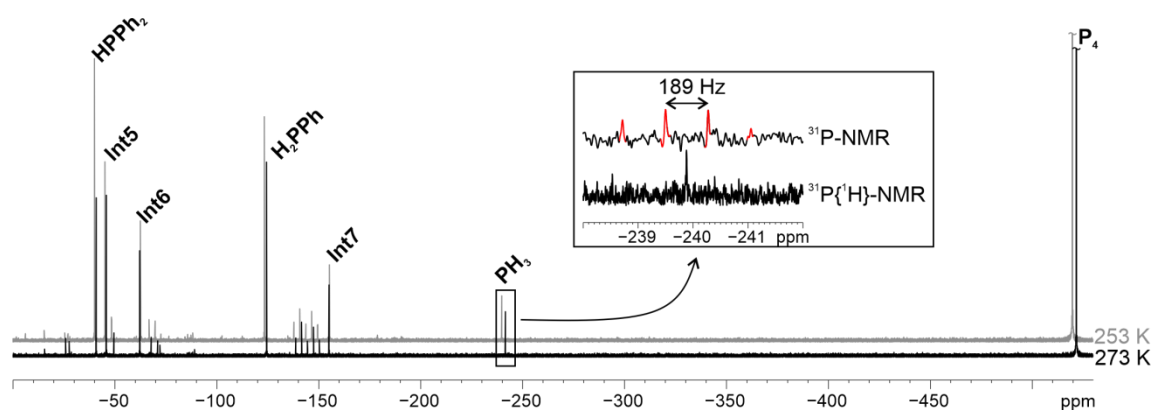


Figure AF 4.8 | $^{31}\text{P}\{^1\text{H}\}$ -NMR spectra of the photocatalytic functionalization of P_4 with $[\mathbf{1}]\text{PF}_6$ at lower temperatures (273 K and 253 K) reveal new signals that were not observed at 298 K. The black spectrum was recorded in absence of light after an illumination period of 30 min at 273 K. The gray spectrum was recorded in absence of light after an additional illumination period of 15 min at 253 K. Framed region: spectral sections were taken from the NMR investigations at 253 K of the sample with saturated amounts of **14**. Reaction conditions for the two bottom spectra (black and gray): P_4 (12.5 mM), PhI (11 eq. referred to one P-atom), NEt_3 (14.4 eq. referred to one P-atom) and $[\mathbf{1}]\text{PF}_6$ (2.2 mol% referred to one P-atom) in $\text{C}_6\text{D}_6/\text{CD}_3\text{CN}$ mixture (1:1). *In situ* illumination was carried out at 455 nm (LED: Cree XT-E @ 1.5 A). b) P_4 (12.5 mM), PhI (11 eq. referred to one P-atom), NEt_3 (14.4 eq. referred to one P-atom) and **14** (saturated amounts) in $\text{C}_6\text{D}_6/\text{CD}_3\text{CN}$ mixture (1:1) at 253 K. *In situ* illumination was carried out at 455 nm (LED: Cree XT-E @ 1.5 A).

Then, another sample containing organocatalyst **14** instead of $[\mathbf{1}]\text{PF}_6$ was also subjected to illumination at lowered temperature (253 K). To eventually increase the amount of initial intermediates (for *in situ* characterization and the potential detection of new signals), the catalyst loading was enlarged by saturating the reaction mixture and removing the unsolved residue through filtration. $^{31}\text{P}\{^1\text{H}\}$ -NMR spectra recorded directly upon illumination displayed identical signals to the low temperature monitoring with $[\mathbf{1}]\text{PF}_6$ and several new signals with a low signal-to-noise ratio (see Figure AF 4.9). Measuring a proton coupled ^{31}P -NMR spectrum gave first hints at the nature of the unknown species. Similar to the familiar intermediates

4 CATALYTIC TRANSFORMATION OF WHITE PHOSPHORUS

H₂PPh and HPPh₂, **Int5-Int8** also exhibit strong proton couplings of around 200 Hz indicating the presence of direct P-H bonds within their structures. More precisely, the structures of **Int5**, **Int6** and **Int8** contain an H-P moiety while **Int7** contains an H₂-P fragment.

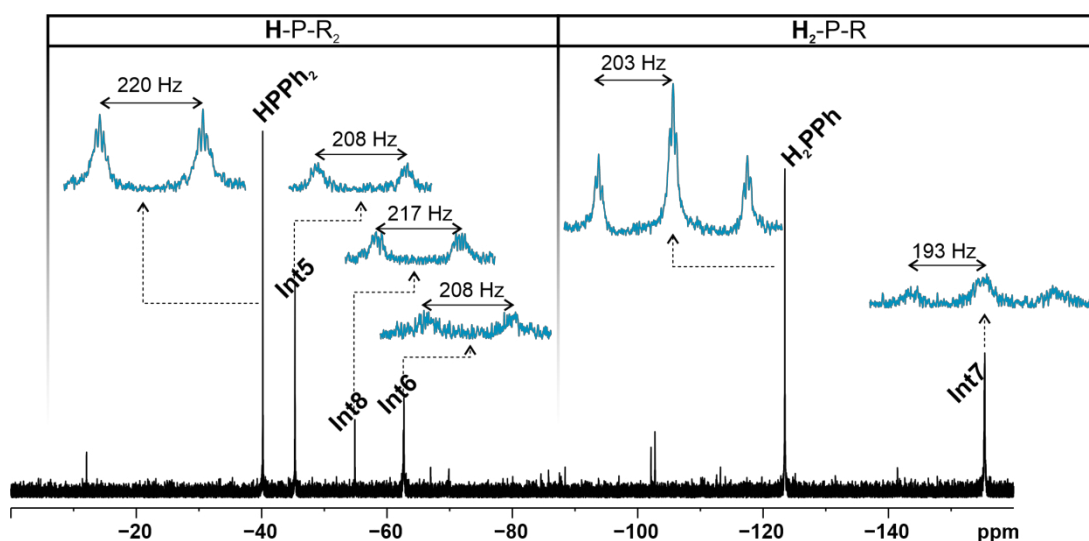


Figure AF 4.9 | ³¹P{¹H}-NMR spectrum of the photocatalytic functionalization of P₄ with saturated amounts of **14** at 253 K reveal new signals which were not observed at 298 K. The black spectrum was recorded under illumination at 455 nm after an illumination time of 5 min at 253 K. Spectral sections in blue are taken from a proton coupled ³¹P-NMR spectrum recorded at 253 K. Reaction conditions: P₄ (12.5 mM), PhI (11 eq. referred to one P-atom), NEt₃ (14.4 eq. referred to one P-atom) and **14** (saturated amounts) in C₆D₆/CD₃CN mixture (1:1) at 253 K. *In situ* illumination was carried out at 455 nm (LED: Cree XT-E @ 1.5 A).

The ³¹P{¹H}-NMR reaction monitoring at 253 K catalyzed by saturated amounts of **14** is displayed in Figure AF 4.10. Prominently, illumination of this reaction mixture yielded higher initial amounts of the intermediates H₂PPh and HPPh₂ in contrast to the reaction with only 2.2 mol% of **14** and at 298 K, as was expected by increasing the catalyst loading (compare Figure AF 4.10a with Figure AF 4.3a and c). Although the reaction was only monitored for a total illumination time of 4.5 hours, for H₂PPh a significantly different intermediate course was observed. Already within the first 6 minutes of illumination, a certain concentration was reached which stayed constant throughout the remaining monitoring, indicating that formation and abreaction of H₂PPh are of the same rate. This shows the complexity of the photocatalytic functionalization of P₄ with TEA and iodobenzene, probably caused by the existence of pathways competing with the productive route.

4 CATALYTIC TRANSFORMATION OF WHITE PHOSPHORUS

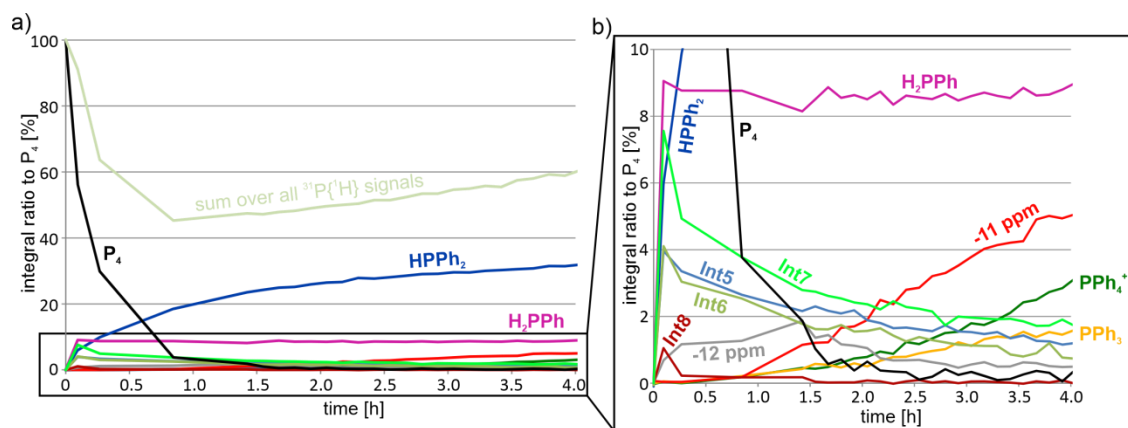


Figure AF 4.10 | $^{31}P\{^1H\}$ -NMR reaction monitoring of the functionalization of P_4 with saturated amounts of organocatalyst **14**. Reaction conditions: P_4 (12.5 mM), PhI (11 eq. referred to one P-atom), NEt_3 (14.4 eq. referred to one P-atom) and **14** (saturated amounts) in C_6D_6/CD_3CN mixture (1:1) at 253 K. *In situ* illumination was carried out at 455 nm (LED: Cree XT-E @ 1.5 A).

Further structural information on **Int5-Int7** was provided by 2D 1H - ^{31}P -HMQC spectra (see Figure AF 4.11) which were recorded without illumination with the intention of preventing further photocatalytic conversion. In contrast to **Int5-Int7**, for **Int8**, unfortunately, no cross peaks were obtained which may be both due to its low lifetime (vanished after total 16 minutes of illumination) and the fact that the HMQC was recorded without illumination (this signal was not observed without illumination, similar to the ^{31}P signals of **Int1-Int4**, see chapter 4.8.1). The ^{31}P -NMR signals of **Int5** and **Int6** exhibited couplings to the aromatic region. As aromatic residue, unsubstituted phenyl would be most obvious as this was also observed in the monophosphoric intermediates H_2PPh , $HPPH_2$, PPh_3 and product PPh_4^+ . Furthermore, **Int5-Int7** all have couplings to the aliphatic 1H -NMR region in common. Within the reaction mixture, TEA is the only reagent containing aliphatic entities and is therefore considered the most likely source of aliphatic residues, either through (partial) self-incorporation or by supplying ethyl-fragments.

4 CATALYTIC TRANSFORMATION OF WHITE PHOSPHORUS

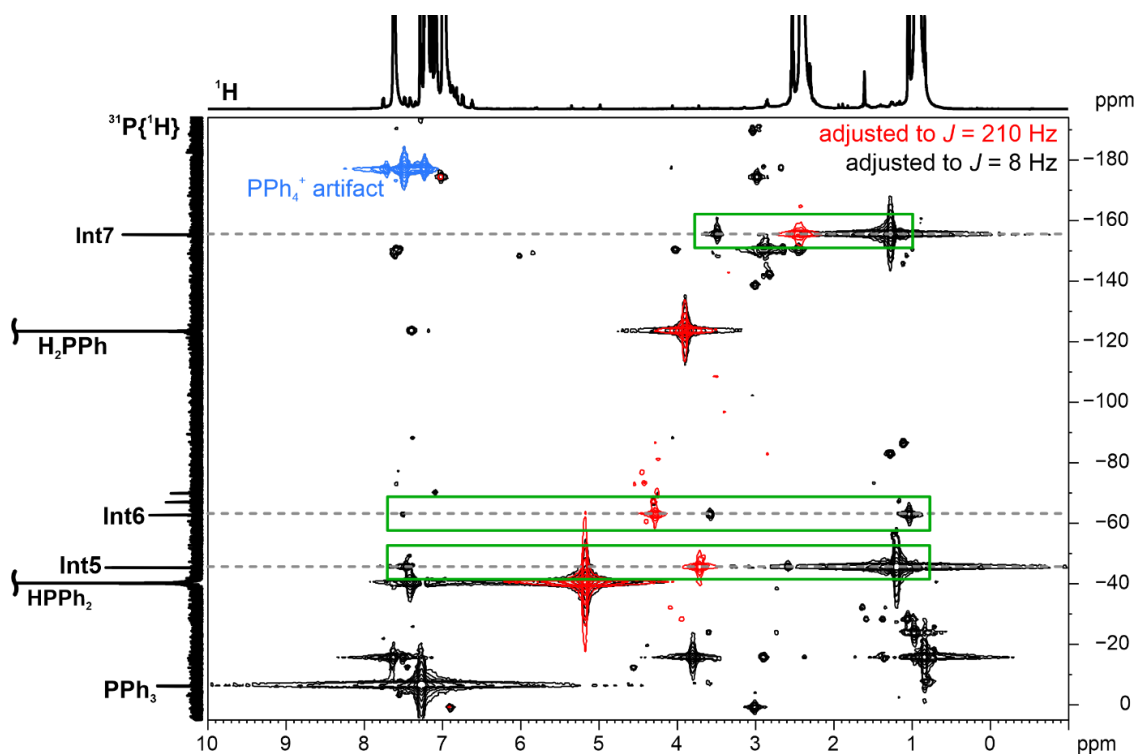


Figure AF 4.11 | Overlapped ^1H - ^{31}P -HMQCs (with ^{31}P -decoupling) with evolution delays adjusted to $J = 210$ Hz (red) and $J = 8$ Hz (black) of the model reaction applying saturated amounts of **14**. ^{31}P - and ^1H -decoupling was used in the respective other dimension. Cross peaks framed in green correlate to the ^{31}P -NMR signals **Int5-Int7**. Cross peaks which don't correlate to any ^{31}P -NMR signal of the external projection either appear due to increased S/N or due to folding/aliasing artifacts such as the cross peaks marked in blue which are aliasing artifacts of PPh_4^+ . Reaction conditions: P_4 (12.5 mM), PhI (11 eq. referred to one P-atom), NEt_3 (14.4 eq. referred to one P-atom) and **14** (saturated amounts) in $\text{C}_6\text{D}_6/\text{CD}_3\text{CN}$ mixture (1:1) at 253 K. *In situ* illumination was carried out at 455 nm (LED: Cree XT-E @ 1.5 A). Key acquisition parameters: pulse program: *hmqcpgpf* with $\text{TD}(\text{F}2) = 2\text{k}$; $\text{TD}(\text{F}1) = 256$; $\text{SW}(\text{F}2) = 30$ ppm; $\text{SW}(\text{F}1) = 200$ ppm; $\text{DS} = 16$; $\text{NS} = 32$ (red spectrum) and 64 (black spectrum); $\text{CNST}2 = 210$ Hz (red spectrum) and 8 Hz (black spectrum).

In the following, possible candidate structures for **Int5-Int7** will be discussed based on comparing experimental ^1H - and ^{31}P -NMR chemical shifts with corresponding shifts reported in literature. The ^1H - and ^{31}P -NMR shifts of **Int5-7** were obtained by 1D spectra and 2D HMQCs and are given related to the suggested structures depicted in Figure AF 4.12. The ^{31}P -NMR shift of **Int5** ($\delta(^{31}\text{P}) = -45.7$ ppm) fits well to that of HPPHt **18** (-43.4 ppm)^[26], however, ^1H -NMR shifts deviate which may be due to considerably different temperatures and solvents (see Figure AF 4.12 a). Other plausible structural candidates would be multiple substituted TEA derivatives such as **19** whose $\delta(^{31}\text{P})$ was estimated based on the shift of $\text{N}(\text{iPr}_2\text{P}(\text{CH}_2)_2)_3$ (**20**) reported in literature, and by comparing ^{31}P -NMR shifts of accordingly substituted phosphines known from literature (see Figure AF 4.12 b). Furthermore, the ^1H -NMR shifts of **20** are in slight better accordance with those of **Int5**. Thus, **19** is considered as more plausible candidate structure for **Int5** than **18**. Overall, **Int5** seems to be a beta substituted TEA-derivative.

4 CATALYTIC TRANSFORMATION OF WHITE PHOSPHORUS

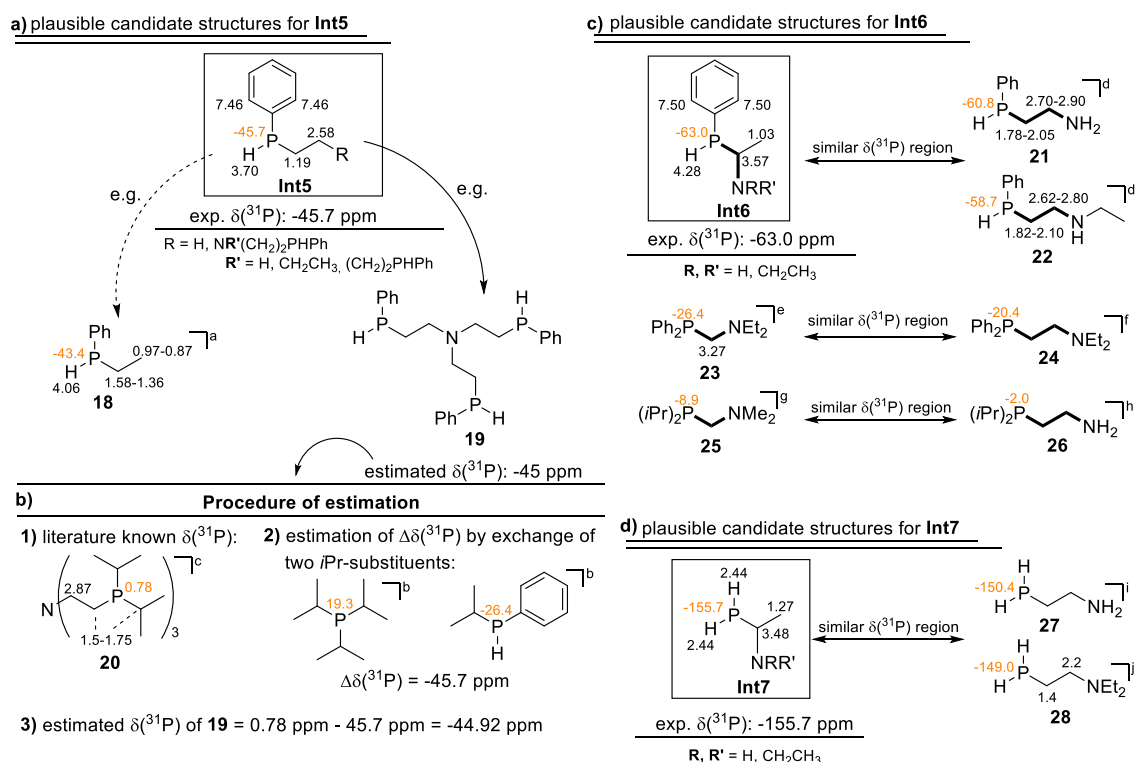


Figure AF 4.12 | Suggestion of plausible candidate structures for **Int5**, **Int6** and **Int7** based on $\delta(^{31}\text{P})$ and $\delta(^1\text{H})$ comparison. Numbers on atoms in black indicate ^1H -NMR chemical shifts in ppm at 253 K. Numbers on atoms in orange indicate ^{31}P -NMR chemical shifts in ppm at 253 K. ^a $\delta(^{31}\text{P})$ and $\delta(^1\text{H})$ were taken from literature^[26]. ^b $\delta(^{31}\text{P})$ were taken from literature^[27]. ^c $\delta(^{31}\text{P})$ and $\delta(^1\text{H})$ were taken from literature^[28]. ^d $\delta(^{31}\text{P})$ and $\delta(^1\text{H})$ were taken from literature^[29]. ^e $\delta(^{31}\text{P})$ was taken from literature^[30]. ^f $\delta(^{31}\text{P})$ was taken from literature^[31]. ^g $\delta(^{31}\text{P})$ was taken from literature^[32]. ^h $\delta(^{31}\text{P})$ was taken from literature^[33]. ⁱ $\delta(^{31}\text{P})$ was taken from literature^[20]. ^j $\delta(^{31}\text{P})$ and $\delta(^1\text{H})$ were taken from literature^[34].

In case of **Int6** ($\delta(^{31}\text{P}) = -63.0$), its ^{31}P -NMR shift fits well to those of $\text{PhHP}-(\text{CH}_2)_2-\text{NH}_2$ (**21**, $\delta(^{31}\text{P}) = -60.8$ ppm)^[20] and $\text{PhHP}-(\text{CH}_2)_2-\text{NHEt}$ (**22**, $\delta(^{31}\text{P}) = -58.7$ ppm)^[20] reported in literature. However, the observed aliphatic ^1H -NMR shift (3.57 ppm) deviates quite much from those of **21**, **22** and that of **Int5** ($\delta(^1\text{H}) = 2.58$ ppm), but is in better accordance with the ^1H -NMR shift of $\text{Ph}_2\text{PCH}_2\text{NEt}_2$ (**23**, $\delta(^1\text{H}) = 3.27$ ppm), see Figure AF 4.12 c). Comparing $-\text{P}-\text{CH}_2-\text{N}-$ species with $-\text{P}-\text{CH}_2\text{CH}_2-\text{N}-$ species it appears that they exhibit ^{31}P -NMR signals in similar shift regions (compare **23** with **24** and **25** with **26**). Thus, the obtained ^1H - and ^{31}P -NMR shifts of **Int6** are in best accordance with the structure of an alpha substituted TEA derivative (see Figure AF 4.12 b).

The ^{31}P -NMR shift of **Int7** ($\delta(^{31}\text{P}) = -155.7$ ppm) fits well to that of $\text{H}_2\text{P}-(\text{CH}_2)_2-\text{NH}_2$ (**27**, $\delta(^{31}\text{P}) = -150.4$ ppm)^[20] and $\text{H}_2\text{P}-(\text{CH}_2)_2-\text{NEt}_2$ (**28**, $\delta(^{31}\text{P}) = -149$ ppm)^[34] reported in literature. However, the ^1H -NMR shift of 3.48 ppm of **Int7** deviates significantly from that of **28** (2.2 ppm)^[34]. Therefore similar to **Int6**, we assumed that **Int7** also constitutes an alpha substituted TEA derivative (see Figure AF 4.12 c).

Reactions of phosphines or corresponding radicals with the TEA derivatives **15**, **16** and **17** are considered likely as possible pathways towards **Int5-7** (see Figure AF 4.13).

4 CATALYTIC TRANSFORMATION OF WHITE PHOSPHORUS

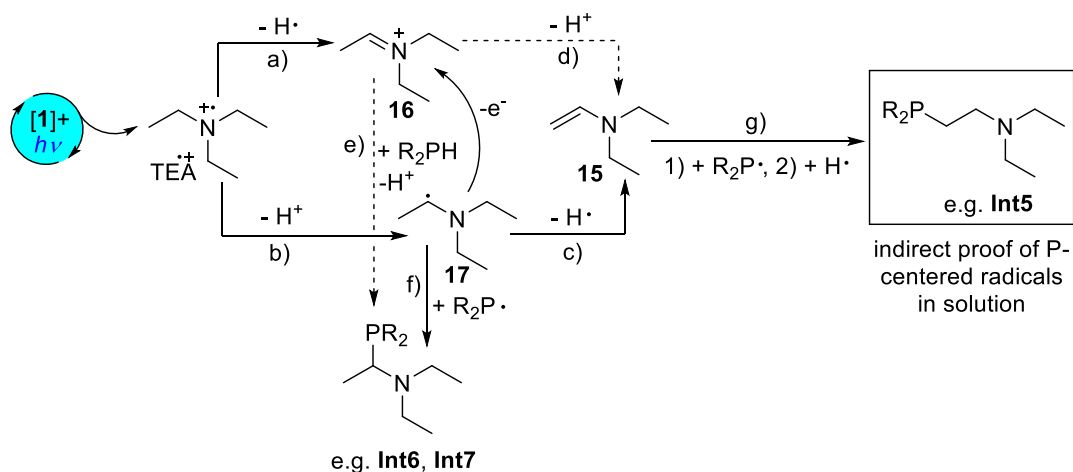


Figure AF 4.13 | Proposed mechanism of the formation of **Int5**, **Int6** and **Int7**.

After TEA is oxidized within the catalytic cycle to the radical cation TEA^{•+}, either iminium ion **16** is generated through H[•] abstraction (a) or α-amino radical **17** by H⁺ abstraction (b)^[13]. Due to the strong reducing properties of **17**, it can be oxidized to **16**^[13]. H[•] abstraction on **17** (c) can generate enamine **15**^[12], which may also be generated by deprotonation (d).^[14,15] **15** was continuously detected in this reaction monitoring over 4.5 hours of total illumination (and in several other monitorings; see Figure AF 4.2) confirming its presence and availability for further transformations. Then, α-substituted TEA derivatives such as **Int6** and **Int7** may be generated *via* the reaction of phosphines with **16** (e) or of phosphorus centered radicals with **17** (f). On the other hand, β-substituted TEA derivatives such as **Int5** may be generated by the addition of phosphorus centered radicals to the β-position of enamine **15** (g) (*via* resonance-stabilized α-N-radicals). In contrast, the non-radical addition of phosphines to **15** is assumed to follow Markovnikov's rule and hence to proceed first *via* β-protonation of **15** providing **16** (reverse reaction of c) which consequently leads to the formation of α-substituted TEA derivatives (e)). Therefore, the detection of β-substituted TEA derivative **Int5** is an indirect proof of the generation of phosphorus centered radicals within the photocatalytic functionalization of P₄.

In order to check for additional ³¹P-NMR signals whose intensity does not reach over the noise due to the limited number of scans (ns) applied per spectrum (in this case: ns = 128 for ³¹P spectra), all ³¹P-spectra (29) recorded during illumination were summed up corresponding to a single spectrum with 3712 scans (see Figure AF 4.14). Indeed, several unknown signals appeared, but whose low S/N-ratio impeded further assignment. Still, this demonstrates that the photocatalytic functionalization of P₄ leads to the formation of several intermediates, which are partially considered as being involved in unproductive pathways, and shows the complexity of this reaction.

4 CATALYTIC TRANSFORMATION OF WHITE PHOSPHORUS

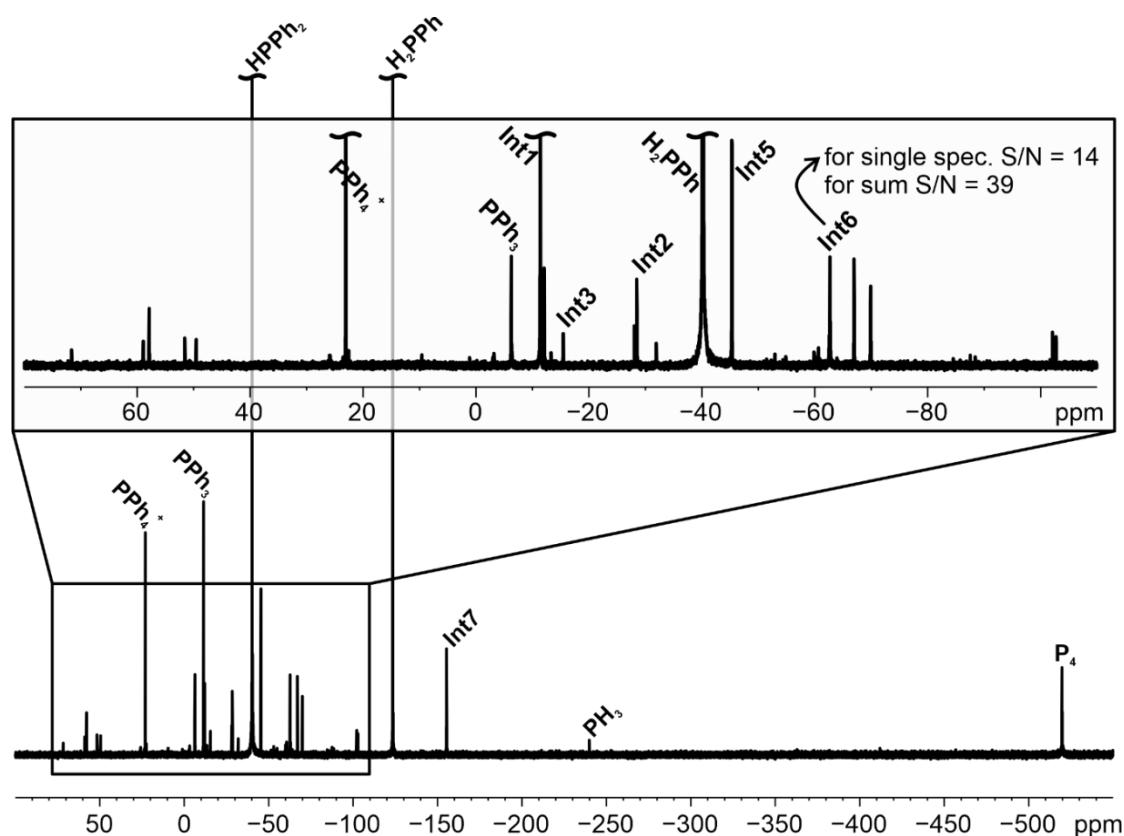


Figure AF 4.14 | Sum over all ^{31}P -spectra (29) recorded during illumination of the reaction mixture with saturated amounts of catalyst **14** at 253 K. It shows that many additional phosphorus species are generated beside the precursors of PPH_4^+ (PH_3 , H_2PPh , HPPH_2 , PPh_3), **Int1-3** and **Int5-7**. Reaction conditions: P_4 (12.5 mM), PhI (11 eq. referred to one P-atom), NEt_3 (14.4 eq. referred to one P-atom) and **14** (saturated amounts) in $\text{C}_6\text{D}_6/\text{CD}_3\text{CN}$ mixture (1:1) at 253 K. *In situ* illumination was carried out at 455 nm (LED: Cree XT-E @ 1.5 A).

To sum up, cooling down of the reaction mixtures indeed revealed another intermediate of the photocatalytic functionalization of P_4 , in particular PH_3 . In another experiment (see chapter 4.8.4) it could be verified that PH_3 can be converted to PPH_4^+ . Thus, in the reaction starting from P_4 , it can act as intermediate entailing a new intermediate sequence of PH_3 , H_2PPh , HPPH_2 and PPh_3 . Besides, three other intermediary signals **Int5-Int7** were detected and found to contain aliphatic residues which are assumed to originate from the reaction of phosphorus species with TEA derivatives. **Int5** was assigned to a β -N-substituted TEA derivative which indirectly verified the presence of phosphorus centered radicals (see Figure AF 4.13 g). These experiments again demonstrated that TEA not only acts as a sacrificial electron donor, but can also interfere in the reaction to PPH_4^+ . Against this background, the photocatalytic functionalization of P_4 still offers potential for improvement: either by finding an alternative sacrificial electron donor to TEA or by trapping the reactive TEA successors to prevent them from interfering with the productive pathway. The role of TEA in this photocatalytic functionalization of P_4 was further investigated by applying fully deuterated TEA (see chapter 4.8.3).

4.8.2.2 Radical Trapping with TEMPO

With the intention of stabilizing any possible short-lived intermediates the radical scavenger TEMPO (2,2,6,6-tetramethylpiperidine-1-oxyl) was added to the reaction mixture prior to illumination. The reaction was then followed by ^1H - and $^{31}\text{P}\{^1\text{H}\}$ -NMR. Already before switching on the light, the shim was considerably worse than in absence of TEMPO due to the paramagnetic properties of the radical TEMPO. Directly after switching on the light, the shim had further worsened. Due to severe signal overlapping and shifting in the ^1H -NMR spectra, the reaction was monitored mainly by $^{31}\text{P}\{^1\text{H}\}$ -NMR.

Still, in the ^1H -NMR spectra it was clearly noticeable that two sets of signals of TEMPO-derivatives emerged during the reaction monitoring. ^1H - and ^{13}C -NMR chemical shift assignments *via* 2D COSY, HSQC and HMBC experiments (see Figure AF 4.15) clearly revealed that one set belongs to TEMPH (deoxygenated and hydrogenated derivative of TEMPO). The other set is tentatively assigned to TEMPOH since both reported ^1H - and ^{13}C -NMR shifts vary considerably from literature to literature^[35–38].

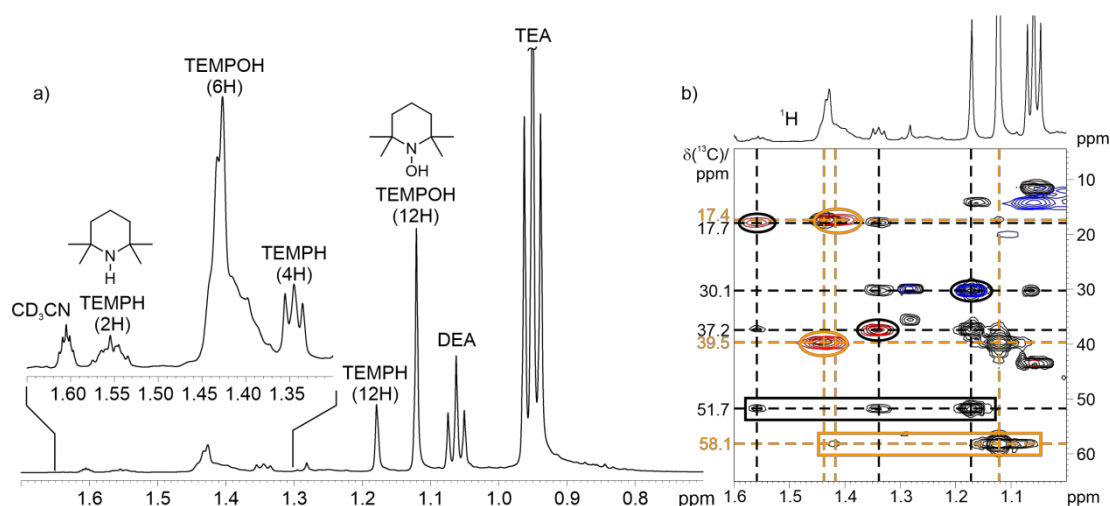


Figure AF 4.15 | Identification of TEMPH and TEMPOH during *in situ* reaction monitoring of the photocatalytic transformation of P_4 in presence of TEMPO. a) ^1H -NMR spectrum recorded after 27 h of illumination. b) Overlaid ^1H - ^{13}C -HMBC (black) and ^1H - ^{13}C -HSQC (red for CH_2 and blue for CH , CH_3) spectra recorded after 23 h of illumination. HSQC cross peaks are framed by circles and quaternary carbons by boxes. Cross peaks of TEMPH are connected by dashed lines in black and those of TEMPOH by dashed lines in orange. Reaction conditions: P_4 (12.5 mM), PhI (11 eq. referred to one P-atom), NEt_3 (14.4 eq. referred to one P-atom), TEMPO (2 eq. referred to one P-atom) and $[\mathbf{1}]\text{PF}_6$ (2.2 mol% referred to one P-atom) in $\text{C}_6\text{D}_6/\text{CD}_3\text{CN}$ mixture (1:1) at 298 K. *In situ* illumination was carried out at 455 nm (LED: Cree XT-E @ 1.5 A).

The corresponding $^{31}\text{P}\{^1\text{H}\}$ -NMR kinetic covering the most prominent ^{31}P -NMR signals is displayed in Figure AF 4.16.

4 CATALYTIC TRANSFORMATION OF WHITE PHOSPHORUS

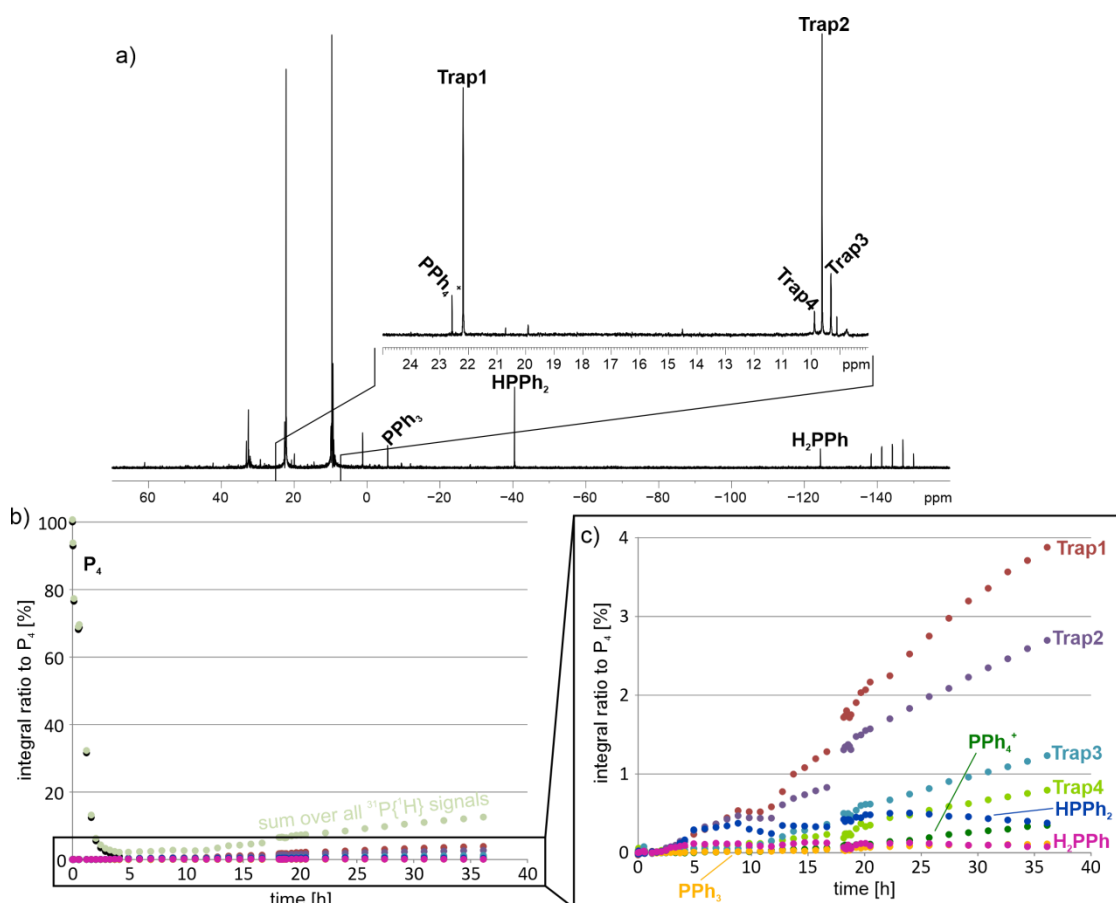


Figure AF 4.16 $^{31}\text{P}\{^1\text{H}\}$ -NMR reaction monitoring of the photocatalytic functionalization of P_4 in presence of TEMPO. a) $^{31}\text{P}\{^1\text{H}\}$ -NMR spectrum recorded in the end of the monitoring. b) Full $^{31}\text{P}\{^1\text{H}\}$ -NMR kinetics displaying the course of the most significant signals. c) Magnified region framed in b). Reaction conditions: P_4 (12.5 mM), PhI (11 eq. referred to one P-atom), NEt_3 (14.4 eq. referred to one P-atom), TEMPO (2 eq. referred to one P-atom) and $[\text{1}]\text{PF}_6$ (2.2 mol% referred to one P-atom) in $\text{C}_6\text{D}_6/\text{CD}_3\text{CN}$ mixture (1:1) at 298 K. *In situ* illumination was carried out at 455 nm (LED: Cree XT-E @ 1.5 A).

The $^{31}\text{P}\{^1\text{H}\}$ -NMR reaction monitoring shows that in presence of TEMPO the formation of PPh_4^+ and its precursors H_2PPh , HPPH_2 and PPh_3 is considerably suppressed (status after 43 h: 21% PPh_4^+ without TEMPO versus 1% PPh_4^+ with TEMPO). Next to PPh_4^+ , several other species (**Trap1-3**) appeared to higher extents which were never observed in absence of TEMPO. After P_4 is nearly completely consumed (after 5h), the amounts of PPh_4^+ and **Trap1-3** increase steadily. This becomes also apparent in the sum over all $^{31}\text{P}\{^1\text{H}\}$ -NMR signals which first decreases and then again increases. Thus, P_4 is probably converted to an NMR-undetectable reservoir (either by polymerization or conversion to paramagnetic species or to compounds that precipitate) which though constantly supplies phosphorus units for further conversion to PPh_4^+ and **Trap1-3** as indicated by their steady increase. The structural characteristics of **Trap1-3** were investigated by ^1H - ^{31}P -HMQCs and will be discussed in the following.

Trap1, **Trap2** and **Trap3** show couplings of their ^{31}P -NMR signals to the aromatic ^1H -NMR region while **Trap1** and **Trap3** show additional cross peaks to the aliphatic ^1H -NMR region. They furthermore exhibit strong ^{31}P - ^1H coupling constants of around 480 to 630 Hz, which are indicative of phosphine oxides ($\text{O}=\text{PH}-\text{R}^1\text{R}^2$)^[39]. For **Trap1**, the aliphatic ^1H -NMR shift was decisive for assigning an ethyl connected TEA-moiety to the phosphorus (see Figure AF 4.17). For **Trap2** and **Trap3**, the ^1H -NMR shift of their directly bound proton

4 CATALYTIC TRANSFORMATION OF WHITE PHOSPHORUS

was decisive for assigning an aminoxy-phosphine oxide to **Trap2** and a phosphinic amide to **Trap3** (see Figure AF 4.17). No further couplings were observed, e.g. due to low signal-to-noise.

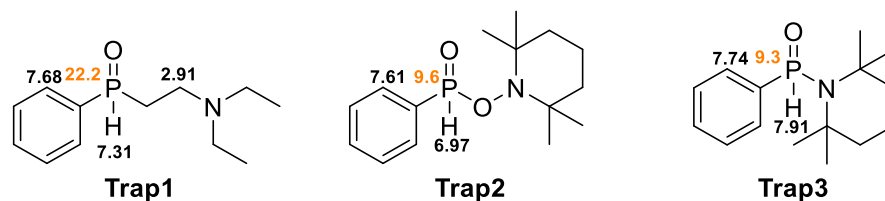


Figure AF 4.17 | Conceivable structures for the detected phosphine oxides **Trap1-3** within the photocatalytic functionalization of P_4 in presence of TEMPO.

Thus, by applying TEMPO, only monophosphorus species could be trapped in significant amounts (indicated by their substitution pattern and singlets in the 1D $^{31}\text{P}\{^1\text{H}\}$ -NMR spectra) which do not give any hints of possible P_2 , P_3 or P_4 precursor. The question arises whether mechanistic information can be extracted from the detected species **Trap1-3**. The oxidation of P_4 or its follow-up phosphines is well known in presence of oxygen^[40] and in some cases of water^[41,42]. However, in our case, deoxygenated and dried solvents were used wherefore oxygen and water can be excluded as main oxygen sources. Thus, TEMPO is considered responsible for the oxidation of P_4 or its follow-up phosphines which fits to the detection of its deoxygenated derivative TEMPH. This concept is known from literature^[43] and may proceed similarly in our case (see Figure AF 4.18). For the mechanism towards **Trap1-3** it is proposed that first, similar to literature, R_2P radicals are trapped by TEMPO (a) which then undergo an N-O bond cleavage (b) generating TEMP (deoxygenated derivative of TEMPO) and an $R_2P=O$ radical.^[43] The $R_2P=O$ radical can either be trapped by TEMPO^[43] resulting in **Trap2**, or recombine with TEMPH^[43] generating phosphinic amide **Trap3**. As in our case also a β -substituted TEA phosphine oxide **Trap1** was detected, we further propose that the $R_2P=O$ radical can be trapped by a TEA derivative **15** (e) (see Figure AF 4.18). Since we observed directly bound protons on phosphorus in all of the three main side-products **Trap1-3**, we suggest that they are generated by a trapping mechanism that involves the monophenyl radical $\text{PhHP}\cdot$ instead of the diphenyl radical $\text{Ph}_2\text{P}\cdot$ described in literature^[43].

Interestingly, in literature the conversion of HPPH_2 with TEMPO happens under mild reaction conditions (-80°C to r.t. in THF) where radicalization of HPPH_2 for subsequent trapping by TEMPO is achieved through H-atom abstraction by TEMPO itself or the *in situ* generated TEMP (see Figure AF 4.18 h).^[43] Thus, the detection of **Trap1-3** shows that radicals are generated, however, it cannot be stated whether the radical generation occurs prior to the formation of the diamagnetic phenylphosphanes due to illumination or afterwards through H-atom abstraction by TEMPO.

4 CATALYTIC TRANSFORMATION OF WHITE PHOSPHORUS

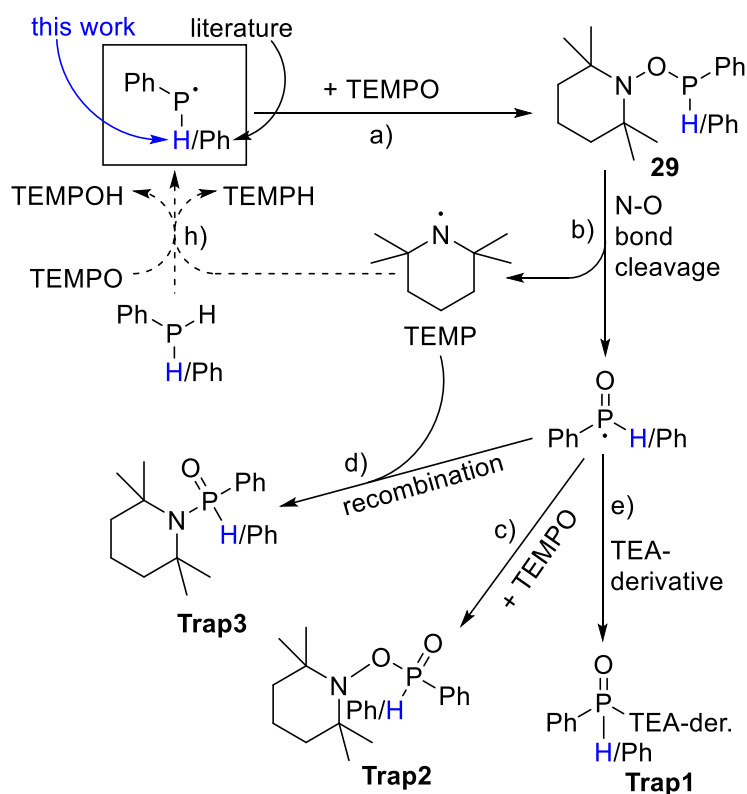


Figure AF 4.18 | Proposed mechanism for radical trapping with TEMPO and the subsequent formation of phosphine oxides.

4.8.2.3 Spin trapping

In order to differently approach the verification of radical intermediates in the photocatalytic functionalization of P_4 , the reaction was monitored by NMR in each presence of the spin traps PBN (*N-tert*-Butyl- α -phenylnitron) and DMPO (5,5-Dimethyl-1-pyrroline *N*-oxide) (see Figure AF 4.19). In contrast to TEMPO, these compounds are diamagnetic and yield paramagnetic spin adducts upon reaction with a radical. Therefore, spin trapping is predominantly used for investigations by EPR spectroscopy. In most cases, paramagnetic species cannot be detected by NMR due to immense signal broadening caused by the unpaired electron. However, diamagnetic follow-up products may allow conclusions about the structure of their radical precursors.

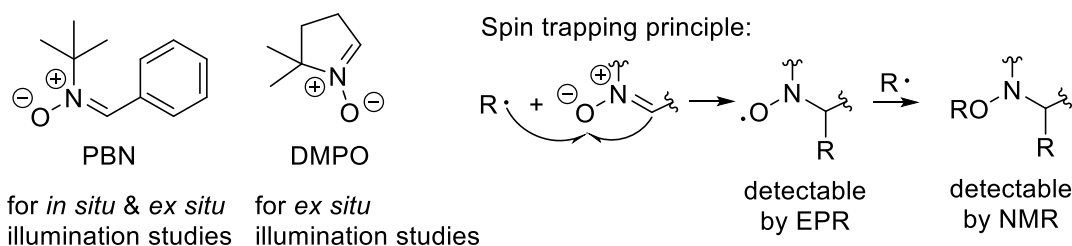


Figure AF 4.19 | Structures of the spin traps used in this work and spin trapping principle. PBN (*N-tert*-Butyl- α -phenylnitron) was used for both *in situ* and *ex situ* studies while DMPO (5,5-Dimethyl-1-pyrroline *N*-oxide) was applied for *ex situ* illumination.

4 CATALYTIC TRANSFORMATION OF WHITE PHOSPHORUS

The herein discussed spin-trapping studies were carried out with *ex situ* and *in situ* illumination of the model reaction catalyzed by [1]PF₆ and applying either PNB or DMPO (2.5 eq. each, based on P-atom). *Ex situ* illumination was carried out in the conventional reaction setup in the glove box using a 1:1 ratio of CD₃CN and C₆D₆ as solvent (samples were prepared analogous to Supplementary Method 1) and samples for NMR investigation were taken after 1 hour and 3 hours of illumination. Samples for *in situ* illumination and reaction monitoring by NMR were prepared according to Supplementary Method 9 applying PNB as spin trap.

All *ex situ* studies showed, that already after 1 hour of illumination, P₄ was completely consumed and a plethora of ³¹P{¹H}-NMR signals was detected in between -30 ppm to +70 ppm. Interestingly, the reaction mixture taken after 1 h of illumination contained less total amount of PPh₄⁺ and corresponding precursors (PH₃, H₂PPh, HPPH₂ and PPh₃) than the mixture taken after 3 h (see Figure AF 4.20).

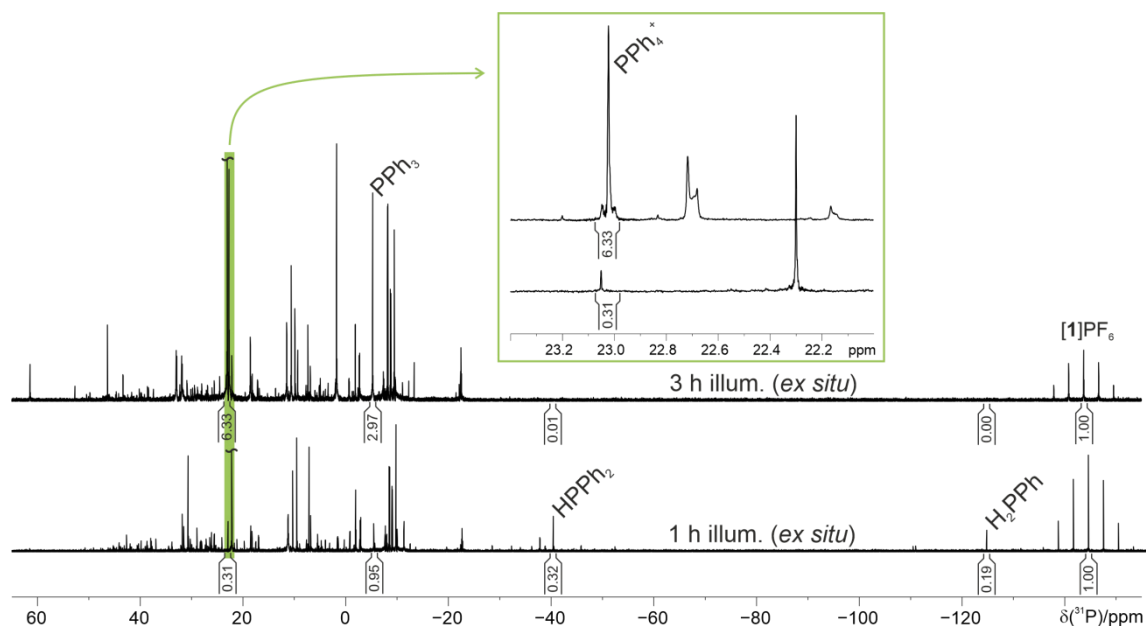


Figure AF 4.20 | ³¹P{¹H}-NMR spectra of samples taken after 1 h and 3 h of the *ex situ* illumination study applying DMPO as spin trap. The signal of P₄ was not detected in both cases indicating a complete consumption or conversion to an NMR-undetectable species. The comparison of the integrals of the ³¹P{¹H}-NMR signals of PPh₄⁺ and its precursors H₂PPh, HPPH₂ and PPh₃ indicates that this reservoir of P₄ still has to provide intermediates for the reaction towards PPh₄⁺ to explain its significant increase in absence of P₄. Reaction conditions: P₄ (12.5 mM), PhI (11 eq. referred to one P-atom), NEt₃ (14.4 eq. referred to one P-atom), DMPO (2.5 eq. referred to one P-atom) and [1]PF₆ (2.2 mol% referred to one P-atom) in C₆D₆/CD₃CN mixture (1:1) at 298 K. *Ex situ* illumination was carried out at 455 nm (LED: Osram OSOLON SSL 80 @ 0.7 A).

Under the assumption, that only the aforementioned precursors are involved in the formation of P₄, this then again hints at an NMR-undetectable reservoir of P₄ or follow-up intermediates (e.g. by polymerization or conversion to paramagnetic species) which probably continuously provide intermediates throughout the reaction towards PPh₄⁺ to explain its increase (see integrals in Figure AF 4.20). This was further suggested by *in situ* ³¹P{¹H}-NMR reaction monitoring which showed that P₄ is consumed within 5 hours, while the subsequent intermediates or products only increase significantly after this time (see Figure AF 4.21 a). Correspondingly, the sum over all ³¹P{¹H}-NMR signals first decreased and then increased again. In contrast

4 CATALYTIC TRANSFORMATION OF WHITE PHOSPHORUS

to the *ex situ* situation, *in situ* illumination yielded less $^{31}\text{P}\{^1\text{H}\}$ -NMR signals probably due to a slower reaction progress owed to less light intensity (illumination fiber versus direct illumination by LED) and non-stirring conditions.

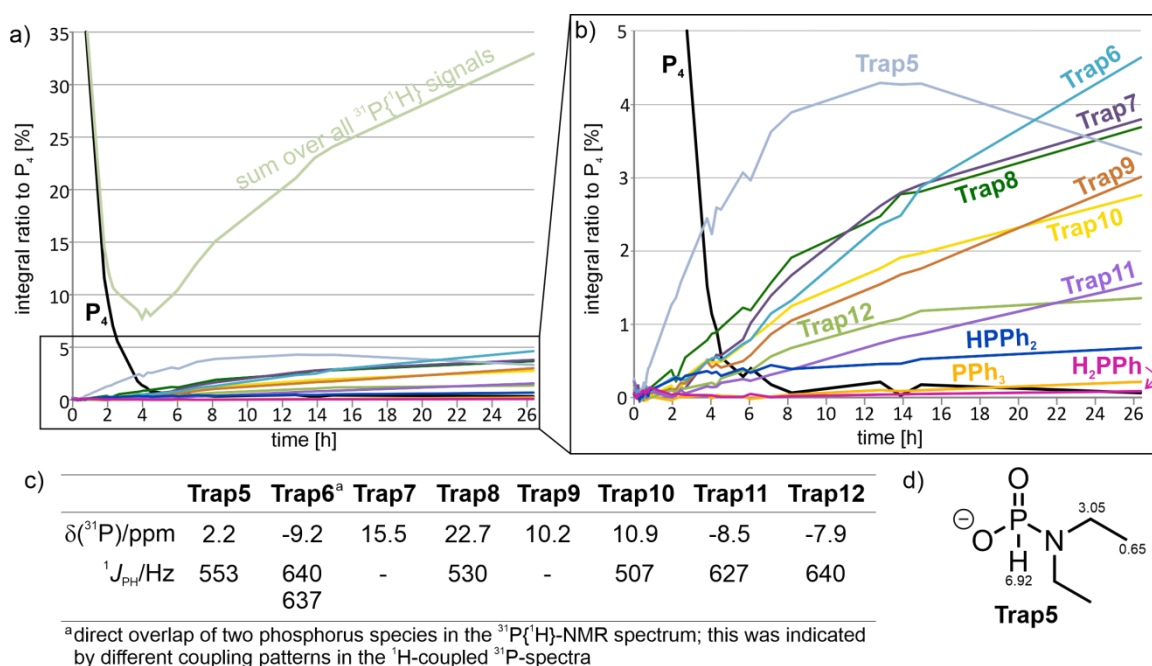


Figure AF 4.21 | $^{31}\text{P}\{^1\text{H}\}$ -NMR reaction monitoring of the photocatalytic functionalization of P_4 in presence of the spin trap PBN. a) Full $^{31}\text{P}\{^1\text{H}\}$ -NMR kinetics displaying the course of the most significant signals. For sake of clarity, data points were connected by straight lines. b) Magnified area framed in a). c) ^{31}P -NMR chemical shifts of Trap5-12 and corresponding $^1J_{\text{HP}}$ coupling constants. d) Plausible structure for **Trap5**. ^1H -NMR shifts are given in Hz. Reaction conditions: P_4 (12.5 mM), PhI (11 eq. referred to one P-atom), NEt_3 (14.4 eq. referred to one P-atom), PBN (2.5 eq. referred to one P-atom) and $[\mathbf{1}]\text{PF}_6$ (2.2 mol% referred to one P-atom) in $\text{C}_6\text{D}_6/\text{CD}_3\text{CN}$ mixture (1:1) at 298 K. *In situ* illumination was carried out at 455 nm (LED: Cree XT-E @ 1.5 A).

In addition, *in situ* reaction monitoring shows that the formation of PPh_4^+ , H_2PPH , HPPH_2 and PPH_3 are suppressed to similar extent as in the trapping study with TEMPO (a small signal of PPh_4^+ only appeared in the last spectrum of the monitoring). Besides, several phosphorus species appeared in more significant quantities (**Trap5-12**, see Figure AF 4.21 b), some of which exhibited large ^1H - ^{31}P - coupling constants (see Figure AF 4.21 c; also detected in *ex situ* study and similar to the investigations with TEMPO) that are indicative of phosphine oxides ($\text{O}=\text{P}-\text{H}-\text{R}^1\text{R}^2$)^[39]. This suggests a transfer of the spin trap bound oxygen onto phosphorus, which was also observed when TEMPO was applied as trapping reagent. Therefore, analogous bond-cleavage and radical combination reactions^[43] are considered likely.

The acquisition of 2D ^1H - ^{31}P -HMBC spectra (see Figure AF 4.22) gave insight into structural characteristics of **Trap5-12** which are summarized in Table AF 4.1. **Trap5** could be assigned to the phosphonamidate displayed in Figure AF 4.21 d due to very good agreement of its shift and coupling pattern ($\delta(^{31}\text{P}) = 2.2$ ppm; $^1J_{\text{HP}} = 553$ Hz) with literature (2.0 ppm, $^1J_{\text{HP}} = 584$)^[44]. The structure of **Trap5** (P_1 -species with $\text{P}=\text{O}$ moiety) and its fast generation compared to **Trap6-12** indicate that trapped phosphorus radicals are rapidly converted to phosphine oxides. Yet, the 2D ^1H - ^{31}P -HMBC spectra recorded during *in situ* (and *ex situ*) reaction monitoring (see Figure AF 4.22) also show that phosphorus radicals were “classically” trapped by

4 CATALYTIC TRANSFORMATION OF WHITE PHOSPHORUS

PBN (via radical addition to the C-N double bond of the spin trap^[45]). This was suggested by ^1H - ^{31}P -cross peaks with doublet splittings ($\sim 7 - 15$ Hz) in the ^1H -NMR region of 3 – 6 ppm (see Figure AF 4.22 frame). Those cross peaks would fit to $^2J_{\text{HP}}$ couplings^[39] of spin adducts of PBN and “classically” trapped PR^1R^2 or $\text{P}(\text{O})\text{R}^1\text{R}^2$ radicals (see Figure AF 4.22 bottom). However, next to trapping of radicals by radical addition, spin traps are also known to react with nucleophiles^[46] (here: H_2PPh , HPPH_2) in a non-radical manner. Thus, the detection of these diamagnetic spin adducts cannot undoubtedly be fully attributed to the trapping of phosphorus centered radicals.

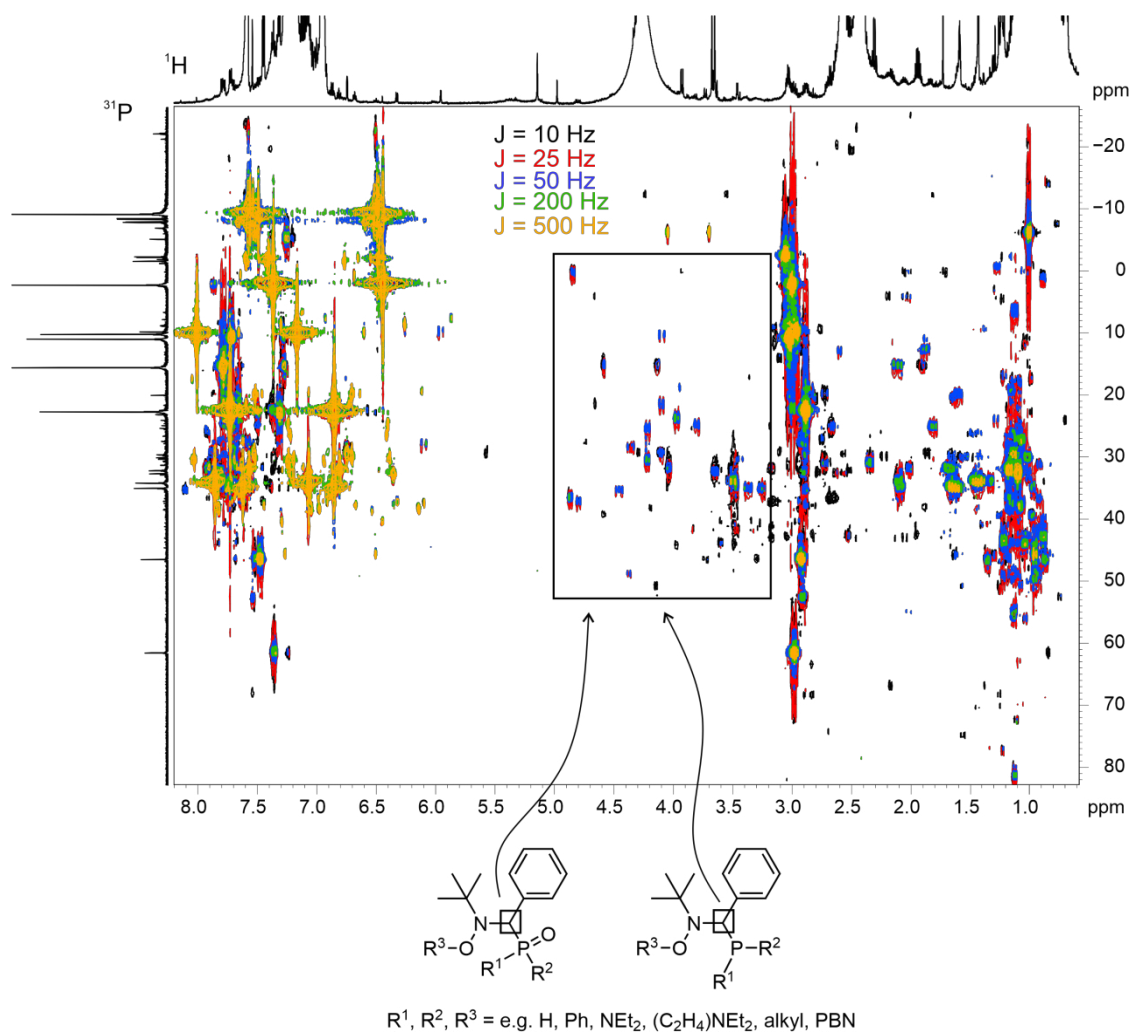
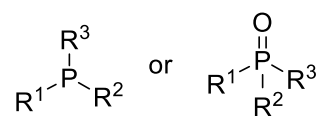


Figure AF 4.22 | Overlap of 2D ^1H - ^{31}P -HMBC spectra with varying evolution delays adjusted to 10 – 500 Hz recorded during *in situ* reaction monitoring applying PBN as spin trap. The frame highlights cross peaks which are assumed to belong to spin adducts of “classically” trapped PR^1R^2 or $\text{P}(\text{O})\text{R}^1\text{R}^2$ radicals through PBN. Reaction conditions: P_4 (12.5 mM), PhI (11 eq. referred to one P-atom), NEt_3 (14.4 eq. referred to one P-atom), PBN (2.5 eq. referred to one P-atom) and $[\mathbf{1}]\text{PF}_6$ (2.2 mol% referred to one P-atom) in $\text{C}_6\text{D}_6/\text{CD}_3\text{CN}$ mixture (1:1) at 298 K. *Ex situ* illumination was carried out at 455 nm (LED: Osram OSRON SSL 80 @ 0.7 A). Key acquisition parameters: pulse program: *hmbcpgpf_bulusp2* with $\text{TD}(\text{F}2) = 4\text{k}$; $\text{TD}(\text{F}1) = 256$; $\text{SW}(\text{F}2) = 12$ ppm; $\text{SW}(\text{F}1) = 300$ ppm; $\text{DS} = 16$; $\text{NS} = 16$; $\text{CNST}13 = \text{see J values in Figure AF 4.22}$.

4 CATALYTIC TRANSFORMATION OF WHITE PHOSPHORUS

Table AF 4.1 | General structural characteristics of Trap5-12 determined by 1D ^{31}P -NMR and 2D- ^1H - ^{31}P -HMBC spectra.



R ¹ /R ² /R ³	Trap5	Trap6 ^a	Trap7	Trap8	Trap9	Trap10	Trap11	Trap12
H	✓	✓	✗	✓	✗	✓	✓	✓
Ph	✗	✗	✓	✓	✓	✓	✗	✗
NEt ₂	✓	✗	✗	✓	✗	✓	✗	✗
aliphatic	✗	✗	✓	✗	✓	✗	✗	✗
P=O	✓	✓	?	✓	?	✓	✓	✓

^a direct overlap of two phosphorus species in the $^{31}\text{P}\{^1\text{H}\}$ -NMR spectrum; this was indicated by different coupling patterns in the ^1H coupled ^{31}P -spectra.

Most notably are the $^{31}\text{P}\{^1\text{H}\}$ -NMR signals of **Trap11** (signal **A**) and **Trap12** (signal **B**) and two other signals at -2.5 ppm (**C**) and -22.5 ppm (**D**), because they showed ^{31}P - ^{31}P couplings (see Figure AF 4.23 a). Two $^{31}\text{P}\{^1\text{H}\}$ doublets (**A**) and (**C**) with $J_{PP} = 23$ Hz were observed as well as a doublet (**B**) and a triplet (**D**) with $J_{PP} = 21$ Hz. The structural affiliation of **A-C** (to **Trap11**) and **B-D** (to **Trap12**) was indicated by the coupling constants and could be further verified by 2D ^{31}P - ^{31}P -COSY experiments (see Figure AF 4.23 b). Phosphorus **B** and **C** further exhibited large ^1H - ^{31}P couplings of 640 Hz and 627 Hz unveiling them as H-P=O unit. By screening literature for compounds having similar ^{31}P -NMR chemical shifts, coupling constants and patterns, phosphorus **B** and **D** could be assigned to a deprotonated anhydride of 2 × phosphonic acid and 1 × phosphoric acid ^[47](**Trap12** in Figure AF 4.23 c). Phosphorus **C** has a similar ^{31}P -NMR shift and coupling pattern as **B** and was therefore also assigned to a deprotonated phosphonic acid moiety. 2D ^1H - ^{31}P -HMBC showed that **A** couples to protons at $\delta(^1\text{H}) = 3.06$ ppm which in turn are coupled to protons at $\delta(^1\text{H}) = 1.06$ ppm (verified *via* 2D ^1H - ^1H -COSY). With regard to the ^{31}P - and ^1H -NMR shifts of **A** and its coupled protons, a diethylphosphoramidate unit is in good agreement with reported ^{31}P - and ^1H -NMR shifts of structurally related compounds^[48,49], which is further supported by the coupling pattern of **A** (doublet of $^2J_{PP}$ + quintet of $^3J_{PH} =$ septet; see Figure AF 4.23 a). Thus, phosphorus **A** and **C** were assigned to the structure of **Trap11** depicted in Figure AF 4.23 d.

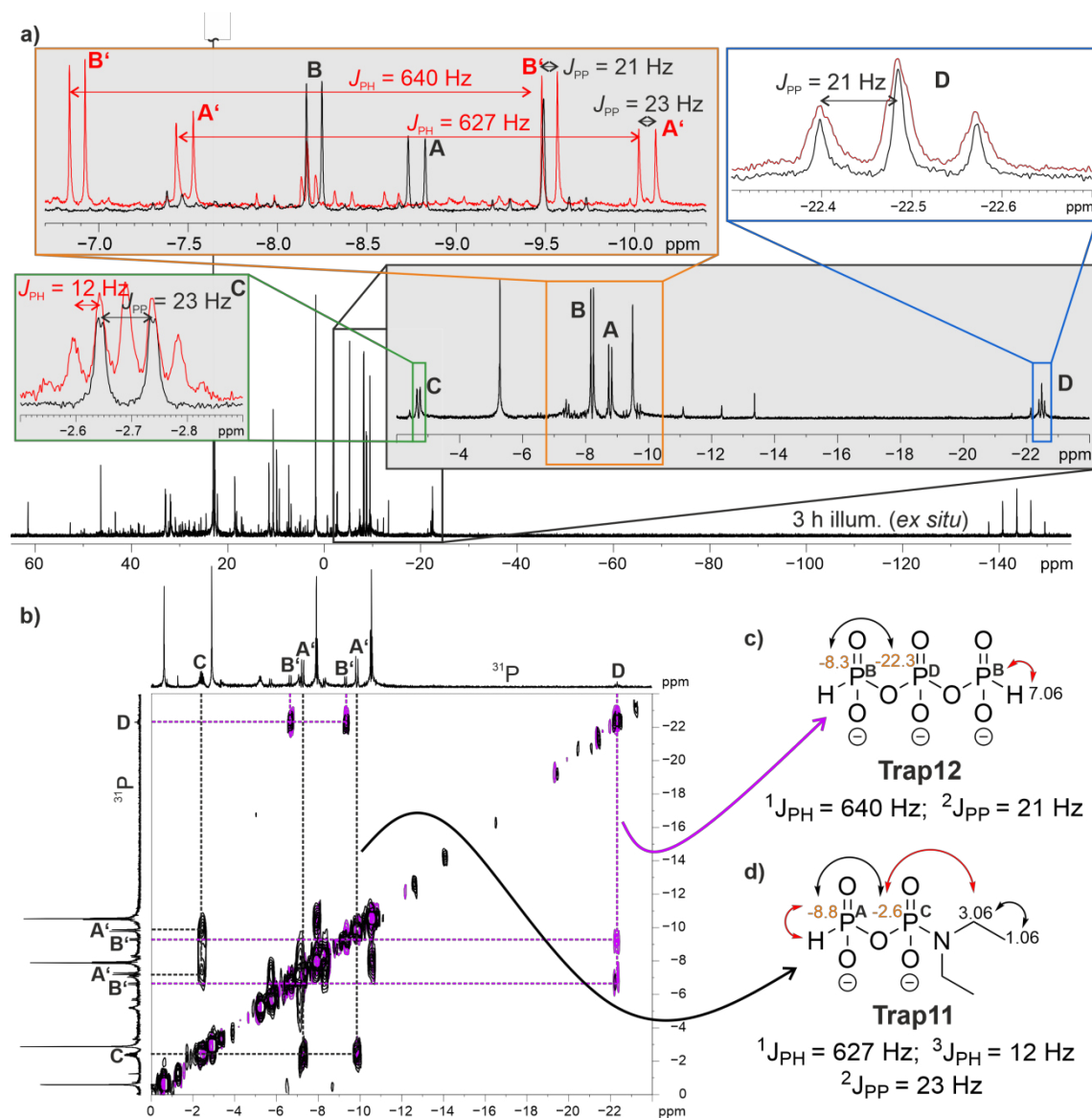


Figure AF 4.23 | Identification of the phosphorus species **Trap11** and **Trap12** which exhibit P-P-couplings. a) Magnified spectral regions of the ^{31}P -signals exhibiting P-P-couplings. Black: $^{31}\text{P}\{^1\text{H}\}$ -NMR spectrum. Red: proton coupled ^{31}P -NMR spectrum. b) Stacked ^{31}P - ^{31}P -COSYs clearly show the affiliation of **A-C** and **B-D**. The black COSY was recorded of a sample containing signals **A** and **C** in higher intensities, while the pink COSY was recorded of a sample containing signals **B** and **D** in higher intensities. c) Structural assignment of **Trap12** which fits well to literature shifts and coupling constants^[47]. d) Proposed structural assignment of **Trap11**. Reaction conditions for a) and ^{31}P - ^{31}P -COSYs in b): P_4 (12.5 mM), PhI (11 eq. referred to one P-atom), NEt_3 (14.4 eq. referred to one P-atom), DMPO (for a) and pink COSY) or PBN (for black COSY) (2.5 eq. referred to one P-atom) and $[\text{1}]\text{PF}_6$ (2.2 mol% referred to one P-atom) in $\text{C}_6\text{D}_6/\text{CD}_3\text{CN}$ mixture (1:1) at 298 K. *Ex situ* illumination was carried out at 455 nm (LED: Osram OSOLON SSL 80 @ 0.7 A). Key acquisition parameters: pulse program: *cosyqf* with TD(F2) = 4k; TD(F1) = 128 (pink COSY) and 256 (black COSY); SW(F2 and F1) = 100 ppm (pink COSY) and 200 ppm (black COSY); DS = 16; NS = 128 (pink COSY) and 416 (black COSY).

Apart from the ^{31}P -NMR signals of **Trap11** and **Trap12** all remaining signals did not show other couplings except to protons wherefore they are assumed to be monophosphoric species.

Concluding the experiments of radical trapping, it can be stated that no species which contain a P-P-bond were trapped in NMR detectable amounts. Over the course of the experiments, it has become increasingly obvious that P_4 is converted into an NMR-undetectable reservoir, which can then provide intermediates for the reaction to PPh_4^+ (recognizable by the initial decrease in the sum over all $^{31}\text{P}\{^1\text{H}\}$ -NMR signals and its

4 CATALYTIC TRANSFORMATION OF WHITE PHOSPHORUS

subsequent increase). In the cases of radical trapping by TEMPO and the spin traps PBN and DMPO, it could be demonstrated that the formation of PPh_4^+ and its sequential precursors is suppressed which indicates that the reaction proceeds *via* radical pathways. The presence of phosphorus-centered radicals was particularly indicated by spin adduct-specific cross peaks of 2D ^1H - ^{31}P -HMBCs. However, in the cases of trapping by TEMPO and spin traps other non-radical pathways may also be responsible for the observed trapped phosphorus species and cannot be excluded.

4.8.3 Investigation of the origin of the intermediate-bound protons by isotopic labeling of TEA

Within the photocatalytic transformation of P_4 to PPh_4^+ , the sequential intermediates PH_3 , HPPH_2 , H_2PPh and PPh_3 were detected. Since the model reaction mixture does not contain a proton donor in the classical sense, the question arises from where the intermediate-bound protons originate. Due to the detection of the TEA derivative **15**, which is generated after reduction of TEA by the catalyst followed by deprotonation, we reasoned that TEA or its successors **27** and **28** (see Figure AF 4.13) may constitute conceivable proton or hydrogen atom sources^[13]. Therefore, fully deuterated TEA was applied in the photocatalytic functionalization of P_4 with the intention of identifying deuterated phosphorus compounds by a change in coupling pattern. While protons have a spin of $\frac{1}{2}$ and therefore cause a doublet splitting in their coupling partners, deuterium has a spin of 1 and engenders a 1:1:1 triplet splitting. The model reaction with TEA- d_{15} and catalyzed by **[1]** PF_6 was thus monitored by ^{31}P - and ^2H -NMR. In fact, proton decoupled ^{31}P -NMR spectra unambiguously revealed the incorporation of deuterium in both phenylphosphine D_2PPh (1:2:3:2:1 quintet) and diphenylphosphine DPPH_2 (1:1:1 triplet; see Figure AF 4.24). Interestingly, also the (partially) protonated phosphines HDPPH and HPPH_2 appeared lowfield shifted to DPPH_2 ($\Delta\delta = 1.37$ ppm) and D_2PPh ($\Delta\delta = 1.18$ ppm). Integration of the diphenylphosphine signals in the proton coupled ^{31}P -NMR spectrum rendered a distribution of 9% HPPH_2 and 91% DPPH_2 . Thus, a higher degree of protonation was observed than the specified isotopic impurity of the purchased deuterated TEA (2% isotopic impurity). However, the breaking of chemical bonds containing lighter isotopes show a faster reaction rate than those of the heavier isotopes, which is known as the kinetic isotope effect.^[50,51] Hence, due to the increased reaction rate of proton compared to deuterium, the protonated intermediates such as HPPH_2 may accumulate faster than the deuterated analogues resulting in increased signal ratios such as for 9% HPPH_2 and 91% DPPH_2 . Another protonation source may be the solvent acetonitrile, since in this experiment, non-deuterated acetonitrile CH_3CN was applied in order to not disturb the acquisition of ^2H -NMR spectra (by reducing receiver gain or overlapping with other signals). The general feasibility of deprotonation (more precisely dedeuteration) of acetonitrile by phosphines under very similar reaction conditions was discovered in another experiment (see chapter 4.8.4).

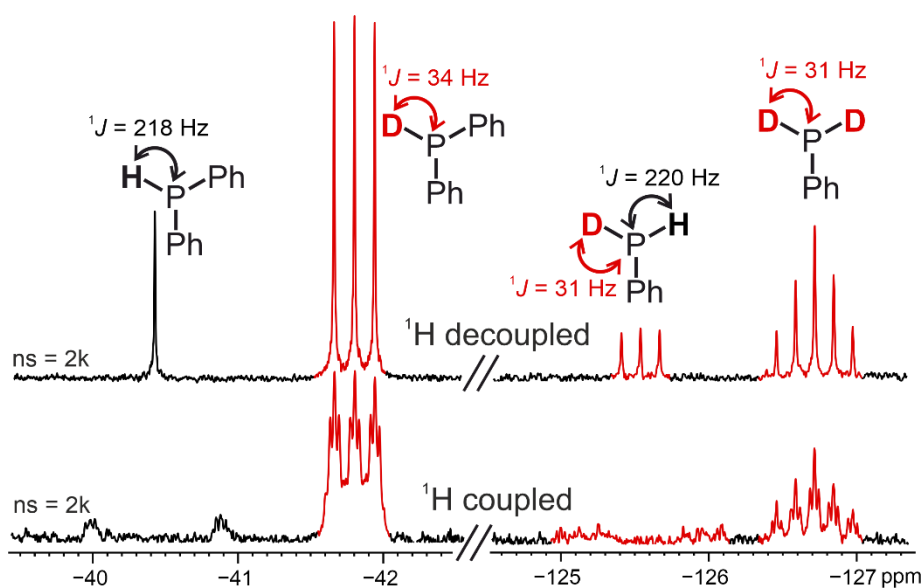


Figure AF 4.24 | ^{31}P -NMR spectrum (bottom) and $^{31}\text{P}\{^1\text{H}\}$ -NMR spectrum (top) of the photocatalytic functionalization of P_4 applying fully deuterated TEA reveal that the protons/deuterium of H_2PPh and HPPH_2 stem from TEA. Reaction conditions: P_4 (12.5 mM), PhI (11 eq. referred to one P-atom), $\text{NEt}_3\text{-d}_{15}$ (14.4 eq. referred to one P-atom) and $[\text{1}]\text{PF}_6$ (2.2 mol% referred to one P-atom) in $\text{C}_6\text{D}_6/\text{CD}_3\text{CN}$ mixture (1:1) at 298 K. *In situ* illumination was carried out at 455 nm (LED: Cree XT-E @ 1.5 A).

^2H -NMR reaction monitoring showed the formation of several deuterated species (see Figure AF 4.24). Especially noticeable was the appearance and shifting of a very broad signal. Analogously, in all ^1H -NMR reaction monitoring applying fully protonated TEA, also a similarly shifted, broad signal appeared. 2D ^1H - ^1H -NOESY spectra of a sample containing protonated TEA revealed crosspeaks between the broad signal and the signals of a $\text{CH}_2\text{-CH}_3$ fragment which are lowfield shifted to the respective signals of TEA. Integration of the respective signals in a 1D ^1H -NMR spectrum yielded a ratio of 2:4:6 for $H_{\text{br}}:\text{CH}_2:\text{CH}_3$, wherefore this species is suggested as protonated diethylamine H_2NEt_2^+ . This was further supported by the isolation and identification of a white precipitate, obtained after workup of the model reaction executed in the laboratory, as diethylammonium salt. ^2H -NMR reaction monitoring further revealed that the amount of TEA consumed is nearly quantitatively converted to D_2NEt_2^+ . This shows that triethylamine decomposes in the course of the reaction, e.g. by abstraction with phosphorus-containing intermediates to form compounds such as **Int1**, **Int2** and **Int5-Int7**. Furthermore, ^2H -NMR spectra revealed that around half as much benzene is produced as D_2NEt_2^+ (the generation of benzene was observed in all of the reaction monitorings, however, quantification was difficult due to signal overlapping). However, it is not possible to distinguish, if benzene is generated *via* H or D abstraction from TEA or from the phosphines (PH_3/PD_3 , $\text{H}_2\text{PPh}/\text{D}_2\text{PPh}$, and $\text{HPPH}_2/\text{DPPH}_2$). This may be verified by applying one of the phosphines such as H_2PPh together with fully deuterated TEA in the photocatalytic formation of PPh_4^+ . Monitoring the reaction by ^1H -, ^2H - and ^{31}P -NMR then might allow to distinguish which species are responsible for the deprotonation of phosphines and which for the dedeuteration of TEA.

4 CATALYTIC TRANSFORMATION OF WHITE PHOSPHORUS

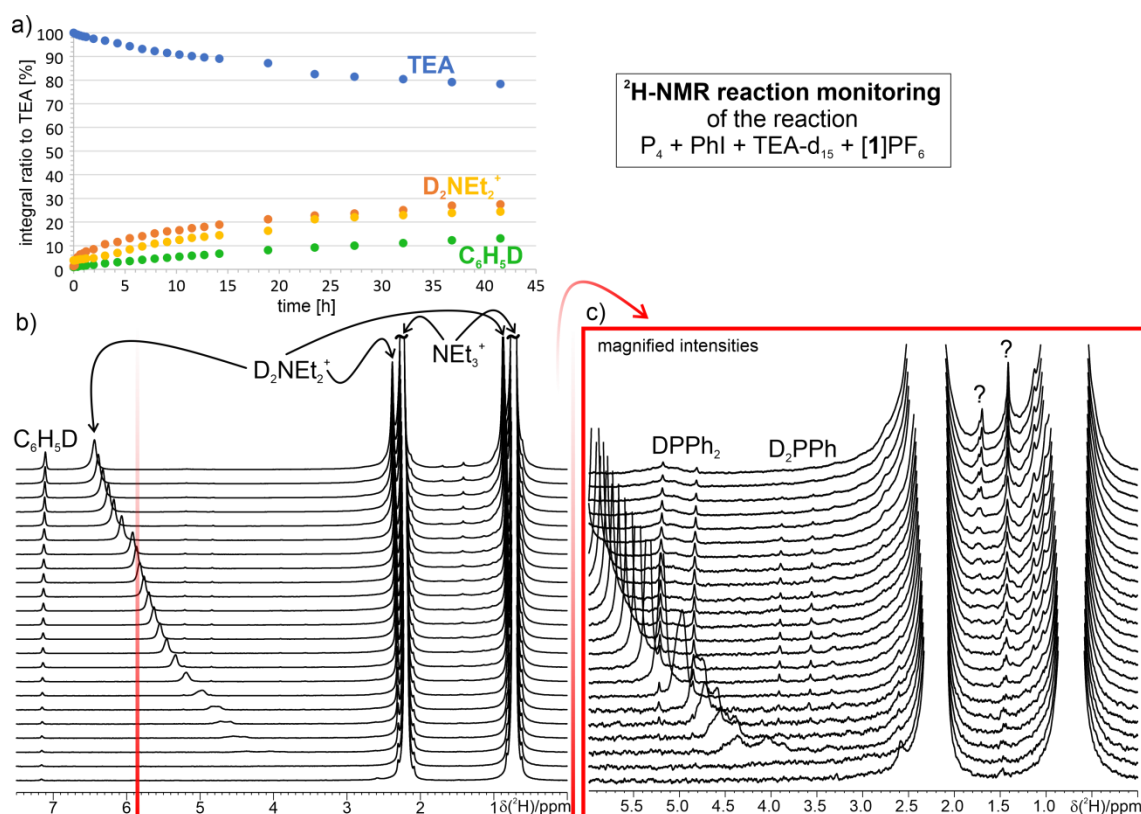


Figure AF 4.25 | ²H-NMR reaction monitoring of the photocatalytic functionalization of P₄ applying fully deuterated TEA. a) ²H-NMR kinetics show that TEA is quantitatively converted to D₂NEt₂⁺ while around half an equivalent of benzene is generated. b) The ²H-NMR spectra were referenced on the CH₃-Signal of TEA and stacked to visualize the formation and shift of a broad signal belonging to D₂NEt₂⁺. Reaction conditions: P₄ (12.5 mM), PhI (11 eq. referred to one P-atom), NEt₃-d₁₅ (14.4 eq. referred to one P-atom) and [1]PF₆ (2.2 mol% referred to one P-atom) in C₆D₆/CD₃CN mixture (1:1) at 298 K. *In situ* illumination was carried out at 455 nm (LED: Cree XT-E @ 1.5 A). Spectra were acquired with the pulse program *zg2h.2*. For the bottom 6 spectra 16 scans were recorded, for the upper 17 spectra 64 scans were recorded. The bottom 6 spectra were accordingly 4 times increased in intensity to match the scaling of the upper 17 spectra.

4.8.4 Verification of PH₃ as sequential precursor

During the cooling down experiments, PH₃ was detected and assumed to be involved in the productive pathway towards PPh₄⁺ of the photocatalytic functionalization of P₄. More precisely, it is suggested to be the first monophosphoric precursor in the sequence of intermediates (PH₃ → H₂PPh → HPPH₂ → PPH₃ → PPh₄⁺). In order to verify this assumption, PH₃ was applied as starting material in the photocatalytic functionalization with [1]PF₆, PhI and TEA. However, due to the difficult handling of PH₃ (= gas at RT), in fact, the easier manageable NaPH₂ (= solid) was used instead of PH₃ with the intention of generating PH₃ *in situ*. NaPH₂ was mixed with PhI, NEt₃ and photocatalyst [1]PF₆ in deuterated acetonitrile. This time, instead of a mixture of benzene and acetonitrile pure acetonitrile turned out to be more beneficial for the reaction from NaPH₂ towards PPh₄⁺. The reaction mixture was then illuminated and followed by *in situ* ³¹P{¹H}-NMR reaction monitoring (see Figure AF 4.26). Interestingly, prior to illumination, several ³¹P-NMR signals of deuterated phosphines were detected (DPPH₂, D₂PPh and PD₃, see Figure AF 4.26 magnified regions), which were never observed in absence of TEA-d₁₅ and a solvent mixture of benzene-d₆/acetonitrile-d₃ (1:1).

4 CATALYTIC TRANSFORMATION OF WHITE PHOSPHORUS

In addition, the signal of the phosphine anion PH_2^- was detected ($\delta(^{31}\text{P}) = -315.3$ ppm is similar to literature: $\delta(^{31}\text{P}) = -303.4$ ppm^[52]). Particularly remarkable is the presence of PD_3 instead of the rather expected monodeuterated phosphine PH_2D and the presence of phenylated phosphines DPPH_2 and D_2PPh without illumination. The detection of PD_3 instead of PH_2D indicates that there exists a reversible deuteration-protonation equilibrium between the strong base PH_2^- ($\text{p}K_b \approx -15$)^[53] and acetonitrile. It is known, that deuterated carboxylic acids and phenols are less acidic than their protonated analogues.^[54] Hence, the deuteration-protonation equilibrium probably settles down at the stage of PD_3 .

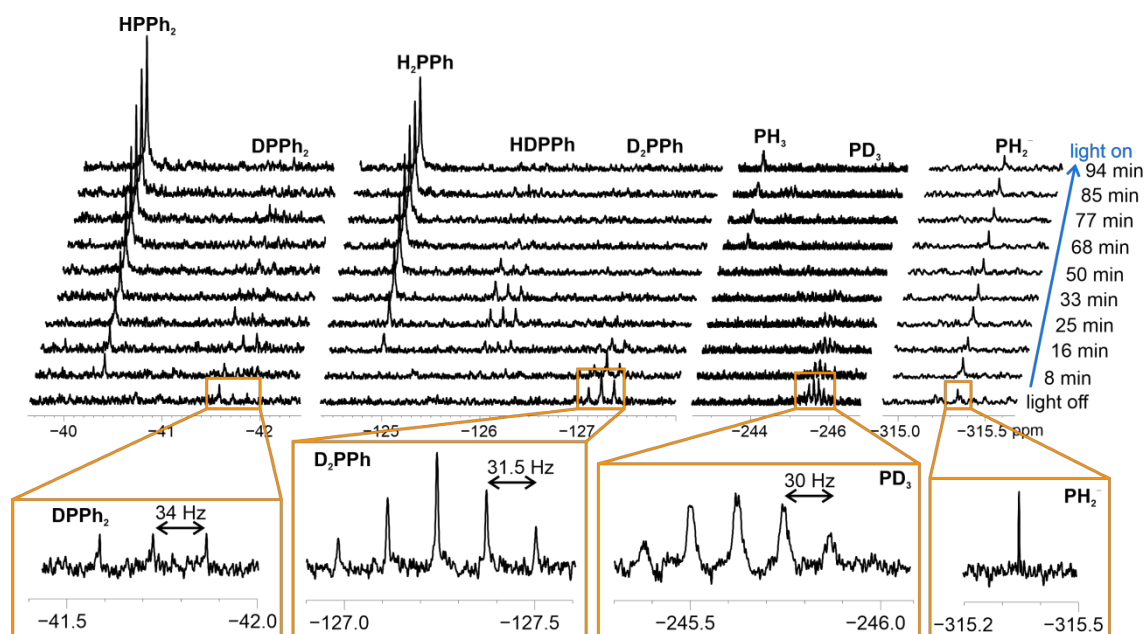


Figure AF 4.26 | $^{31}\text{P}\{^1\text{H}\}$ -NMR reaction monitoring of the functionalization of NaPH_2 catalyzed by $[\mathbf{1}]\text{PF}_6$. The spectra of the monitoring were measured with $n_s = 128$ while the magnified regions were taken from a spectrum measured prior to illumination with $n_s = 512$. Reaction conditions: NaPPh_2 (50 mM), PhI (11 eq.), NEt_3 (14.4 eq.) and $[\mathbf{1}]\text{PF}_6$ (2 mol%) in CD_3CN at 298 K. *In situ* illumination was carried out at 450 nm (LED: Osram Oslon @ 1 A).

Upon illumination at 450 nm, $^{31}\text{P}\{^1\text{H}\}$ -NMR reaction monitoring revealed that the signals of the deuterated species decreased while those of the protonated analogues increased. Under illumination, protonation of the phosphines by TEA apparently overwrites the deuteration by acetonitrile- d_3 . This is most probably due to the fact that within the photocatalytic cycle TEA is oxidized to TEA^+ ($\text{p}K_a \approx 14.7$)^[55] which is considerably more acidic than TEA ($\text{p}K_a \geq 40$)^[55].

Building the sum of all $^{31}\text{P}\{^1\text{H}\}$ -NMR spectra recorded during illumination rendered the spectrum displayed in Figure AF 4.27. It shows that already small amounts of PPh_3 and PPh_4^+ could be detected. Hence, the photocatalytic functionalization of NaPH_2 *via in situ* generation of PH_3 corroborated the assumption of PH_3 being involved in the productive pathway towards PPh_4^+ .

4 CATALYTIC TRANSFORMATION OF WHITE PHOSPHORUS

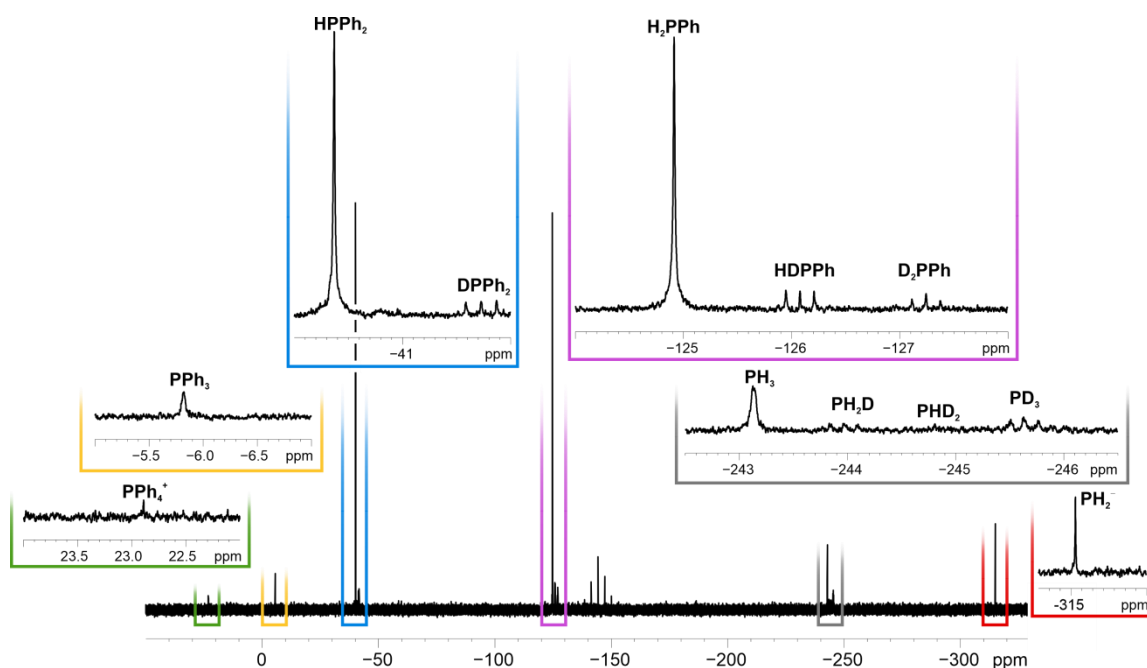


Figure AF 4.27 | Sum over all $^{31}\text{P}\{^1\text{H}\}$ -NMR spectra of the photocatalytic functionalization of NaPH_2 catalyzed by $[\mathbf{1}]\text{PF}_6$ shows all phosphorus species generated at a glance. The sum was calculated from 19 $^{31}\text{P}\{^1\text{H}\}$ -NMR spectra with 128 each, which corresponds to 2432 scans in total. Reaction conditions: NaPH_2 (50 mM), PhI (11 eq.), NEt_3 (14.4 eq.) and $[\mathbf{1}]\text{PF}_6$ (2 mol%) in CD_3CN at 298 K. *In situ* illumination was carried out at 450 nm (LED: Osram Oslon @ 1 A).

In addition, the reaction of NaPH_2 with PhI and TEA was also catalyzed by the organocatalyst **14** and monitored by $^{31}\text{P}\{^1\text{H}\}$ -NMR (see Figure AF 4.28a). Similar to the reaction catalyzed by $[\mathbf{1}]\text{PF}_6$, the intermediates H_2PPh , HPPH_2 and PPh_3 and product PPh_4^+ are generated in sequence. In contrast to the reaction applying P_4 as starting material, negligibly small quantities of side products are generated (see spectrum in Figure AF 4.28b). This may correlate with the concentration of starting material, which in the case of NaPH_2 is kept constantly small (although during sample preparation it seemed that NaPH_2 dissolved completely) (see Figure AF 4.26 and Figure AF 4.28) in contrast to the reactions starting from P_4 or H_2PPh which were applied in higher concentrations led to higher amounts of side products (see Figure AF 4.3 and Supplementary Figure SI 4.57a). Thus, we reasoned that keeping the concentration of starting material low might result in less side product formation. In order to verify this assumption, the conversion of H_2PPh in lower concentration was monitored by NMR (see chapter 4.8.5).

These experiments thus not only verified that PH_3 is involved in the productive pathway towards PPh_4^+ , but also indicated that a further potential for reaction optimization lies in reducing the concentration of the starting material.

4 CATALYTIC TRANSFORMATION OF WHITE PHOSPHORUS

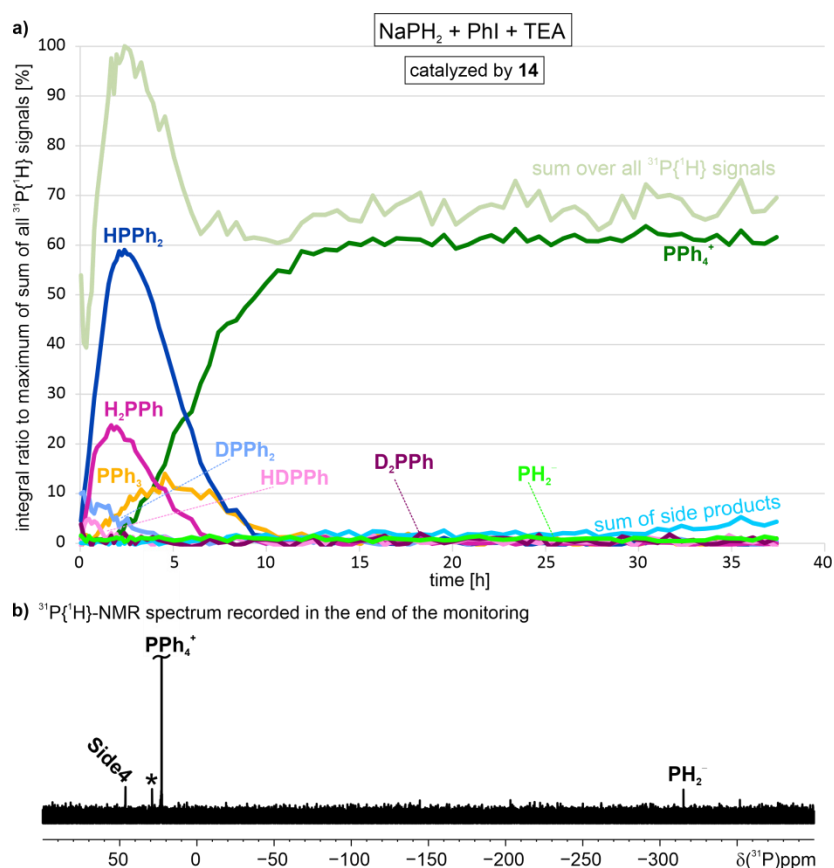


Figure AF 4.28 | ³¹P{¹H}-NMR monitoring of the reaction of NaPH₂ with PhI and TEA catalyzed by **14** in CD₃CN. a) Integrals of the corresponding ³¹P{¹H}-NMR signals were referenced to the maximum of the sum over all ³¹P{¹H}-NMR signals. b) ³¹P{¹H}-NMR spectrum recorded in the end of the reaction monitoring. The unknown ³¹P{¹H}-NMR signal at 29 ppm is labeled with an asterisk. Reaction conditions: NaPH₂ (50 mM), PhI (11 eq.), NEt₃ (14.4 eq.) and **14** (10 mol%) in CD₃CN at 298 K. *In situ* illumination was carried out at 450 nm (LED: Osram Oslon @ 1 A).

4.8.5 Varying the Concentration of Starting Material

The experiments of chapter 4.8.4 indicated that keeping the concentration of starting material and intermediates low may lead to less side product formation and consequently more product. In order to verify this, the photocatalytic functionalization of H₂PPh was chosen as test system since it was observed that it leads to more diverse side products than PPh₃ and HPPH₂ (compare spectra in Supplementary Figure SI 4.57a). Then, H₂PPh was applied in different concentrations (50 mM and 25 mM) for the functionalization with PhI and TEA catalyzed by [1]PF₆, while the concentrations of the other reactants stayed unaltered, and the reactions were monitored by ³¹P{¹H}-NMR under *in situ* illumination for a period of over 40 hours. The first 15 hours of the respective kinetics are displayed in Figure AF 4.29 (the 25 mM reaction was finished after 15 hours and the 50 mM reaction only showed a slight further increase in integral of PPh₄⁺ due to overlap with a shifting ³¹P-NMR signal).

4 CATALYTIC TRANSFORMATION OF WHITE PHOSPHORUS

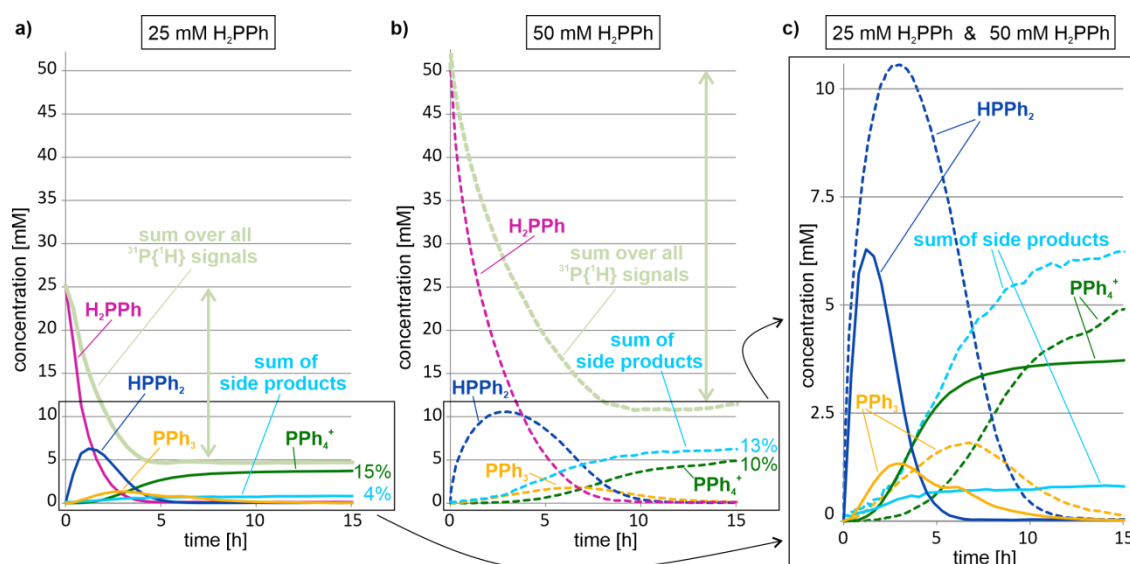


Figure AF 4.29 | $^{31}\text{P}\{^1\text{H}\}$ -NMR reaction monitoring of the photocatalytic functionalization of H_2PPh at different concentration reveals that a lower concentration leads to higher yield and less side product formation. a) $^{31}\text{P}\{^1\text{H}\}$ -NMR kinetics of the reaction of H_2PPh (25 mM) with PhI (22 eq.), TEA (28.8 eq.) and $[\mathbf{1}]\text{PF}_6$ (4 mol%) in acetonitrile- d_3 . b) $^{31}\text{P}\{^1\text{H}\}$ -NMR kinetics of the reaction of H_2PPh (50 mM) with PhI (11 eq.), TEA (14.4 eq.) and $[\mathbf{1}]\text{PF}_6$ (2 mol%) in acetonitrile- d_3 . c) Stacking of both kinetics. *In situ* illumination was carried out at 455 nm (LED: Cree XT-E 1 @ 1.5 A). Key acquisition parameters: TD = 1428570; SW = 980 ppm; NS = 128; d_1 = 2 s. In order to obtain similar S/N ratios for the smaller concentrated reaction, 4 spectra were summed up to generate a single spectrum with total of 512 scans, so each data point in a) is defined by the sum of 4 spectra.

From the ratios of side product formation of the kinetics displayed in Figure AF 4.29 it can be seen that indeed, as expected, a smaller initial concentration (25 mM) of starting material H_2PPh (Figure AF 4.29a) generates considerably less amount of side products (compare Figure AF 4.29a and b). This is in line with the reaction kinetics of the photocatalytic functionalization of NaPH_2 (see Figure AF 4.28). There, NaPH_2 constantly provides small amounts of PH_2^- for the further reaction to PPh_4^+ and only negligibly small quantities of side products were obtained.

It can be further noticed, that for both cases (25 mM and 50 mM of H_2PPh) the sum over all $^{31}\text{P}\{^1\text{H}\}$ -NMR signals decreases and then nearly stays constant from the point when the reaction to PPh_4^+ is finished. The decrease is probably owed to precipitation of *in situ* generated polymers or low soluble compounds, since in the end of both reaction monitorings a solid was observed on the glas-insert of the illumination fiber.

Decreasing the concentration of starting material not only reduced the ratio of side products but also led to a higher yield of PPh_4^+ . This indicates that those side products apparently form the main concurring pathway. In the lab, a constantly low concentration of starting material may be realized by dropping the starting material (kept in an amber syringe to avoid potential degradation by light) to the illuminated reaction vessel.

4.8.6 Identification of Phosphorus Side Products by *In Situ* NMR

Over the course of various *in situ* NMR reaction monitorings of the photocatalytic functionalization of P_4 several side products **Side1-Side8** were detected of which the majority could be structurally characterized by *in situ* 2D NMR experiments. In general, iridium catalyst $[1]PF_6$ yielded less diverse phosphorus side products (mainly **Side1** and **Side4** and only traces of **Side5**, see Figure AF 4.3 and Figure AF 4.30) compared to organocatalyst **14** (mainly **Side1-Side4** and higher ratios of **Side5** and **Side6** compared to $[1]PF_6$, see Figure AF 4.3 and Figure AF 4.30) in the photocatalytic functionalization of P_4 with PhI and TEA. The assignment of the $^{31}P\{^1H\}$ -NMR signals of **Side1-Side8** to their corresponding structures was accomplished by 2D 1H - ^{31}P -HMQC (see Figure AF 4.31) and 1H - 1H -COSY (see Figure AF 4.32) experiments as well as by comparing their 1H -NMR and ^{31}P -NMR shifts with literature values^[56–58]. The double bond configuration of **Side2**, **Side3**, **Side5** and **Side7** was determined based on the 1H - 1H and 1H - ^{31}P -coupling constants derived from 1D 1H -NMR spectra and 2D 1H - 1H -COSY (see Figure AF 4.31). The characterization of these side products again demonstrated that TEA not only acts as a sacrificial electron donor, but also interferes in the reaction to PPh_4^+ .

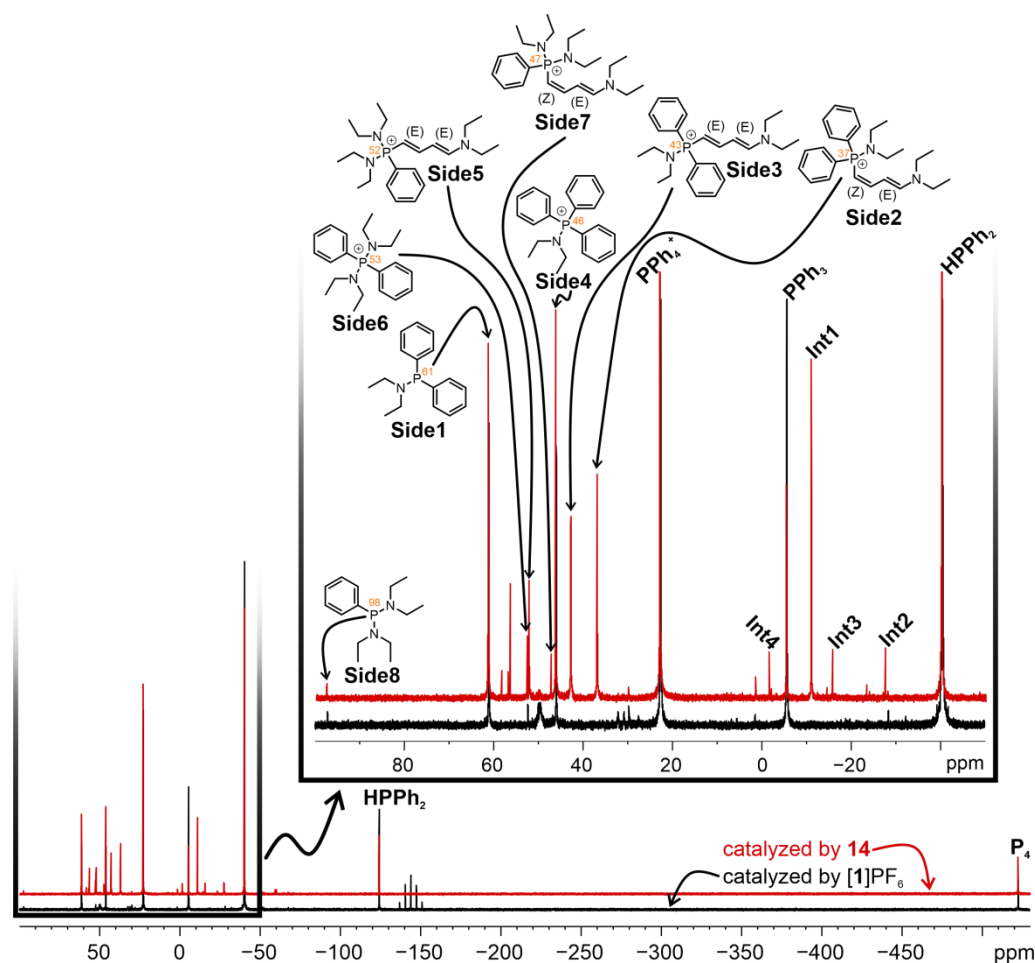


Figure AF 4.30 | Stacking of the sum over all $^{31}P\{^1H\}$ -NMR spectra of the photocatalytic functionalization of P_4 catalyzed by $[1]PF_6$ (black) and **14** (red) gives a comprehensive overview over all phosphorus species generated throughout the reaction monitorings. For reaction conditions and acquisition parameters see Figure AF 4.3.

4 CATALYTIC TRANSFORMATION OF WHITE PHOSPHORUS

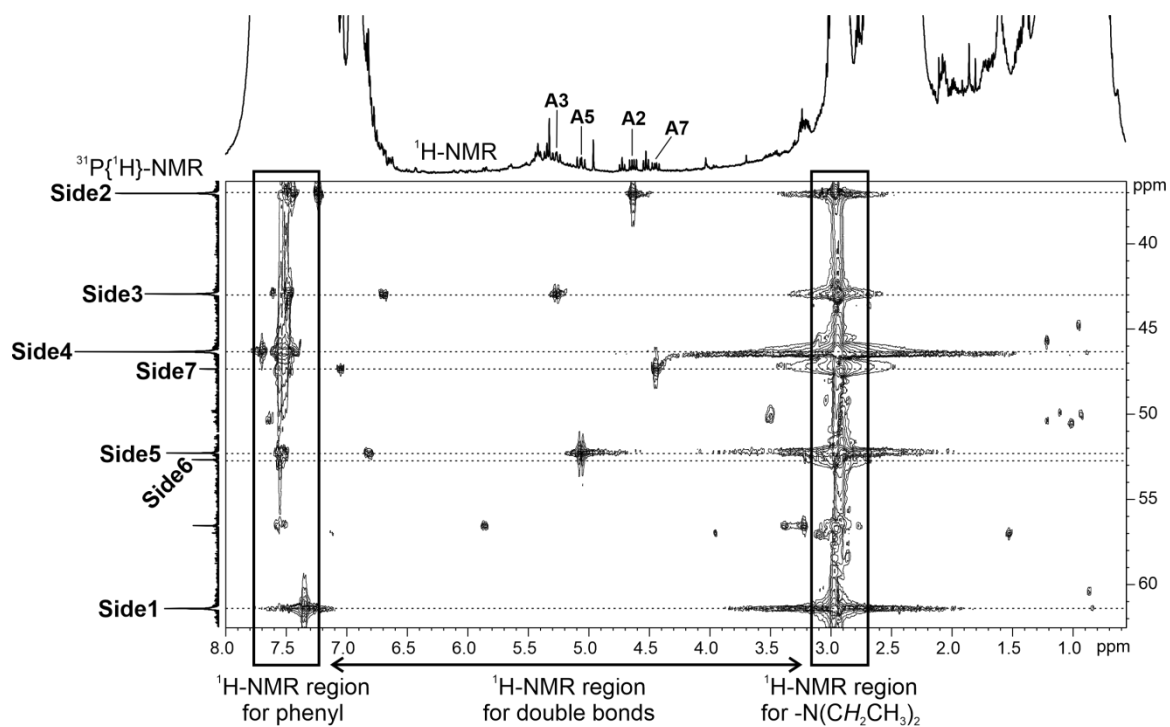


Figure AF 4.31 | 2D ^1H - ^{31}P -HMQC recorded in the end of the photocatalytic functionalization of P_4 catalyzed by **14** at 298 K. The evolution delay was optimized for a coupling constant of 8 Hz. This spectrum shows that the side products all have a diethylamine moiety attached to their phosphorus which indicates that TEA or its successors interfere in the reaction towards PPh_4^+ . For reaction conditions see Figure AF 4.3. *In situ* illumination was carried out at 455 nm (LED: Cree XT-E @ 1.5 A). Key acquisition parameters: pulse program: *hmqcpgpf* with TD(F2) = 4k; TD(F1) = 512; SW(F2) = 14 ppm; SW(F1) = 300 ppm; DS = 16; NS = 20; CNST2 = 8 Hz.

4 CATALYTIC TRANSFORMATION OF WHITE PHOSPHORUS

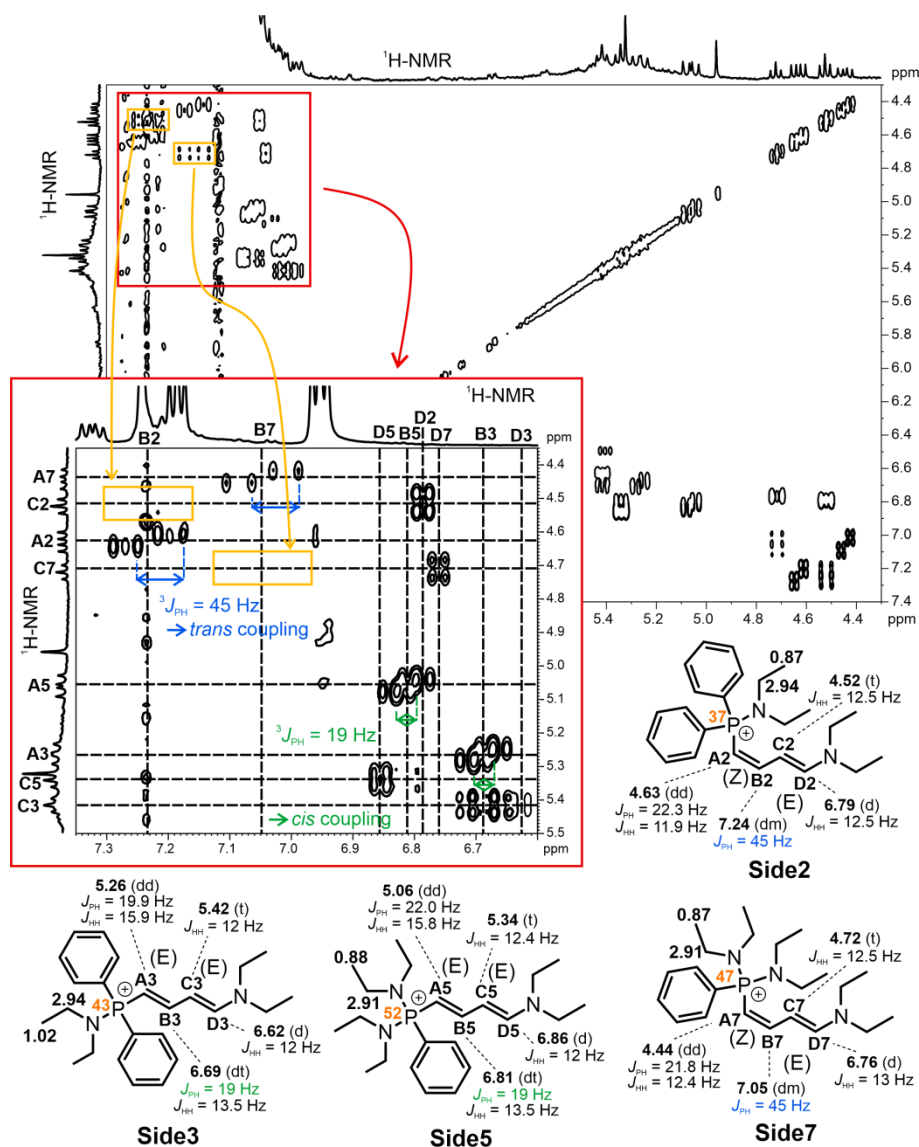


Figure AF 4.32 | Extract of a 2D ^1H - ^1H -COSY spectrum demonstrating the structural assignment of the double bond section of side products **Side2**, **Side3**, **Side5** and **Side7**. ^1H - ^{31}P -coupling constants were read out from the splitting pattern of the ^1H - ^1H -COSY cross peaks as exemplarily demonstrated in the magnified excerpt framed in red. For reaction conditions see Figure AF 4.3. *In situ* illumination was carried out at 455 nm (LED: Cree XT-E @ 1.5 A). Key acquisition parameters: pulse program: *cosygpqf* with TD(F2) = 4k; TD(F1) = 512; SW(F2) = 13 ppm; SW(F1) = 13 ppm; DS = 16; NS = 10; d1 = 2 s.

The structural motif of **Side2**, **Side3**, **Side5** and **Side7** is quite interesting. It resembles very much the motif of a literature known compound **29** (see Figure AF 4.33 a) which can be used to generate valuable λ^5 -phosphinines **31** through electrocyclization via intermediate **30**^[57]. The significant difference between **Side5** and **29** is a methyl group instead of phenyl, which though is crucial for the cyclization to the λ^5 -phosphinine. λ^5 -phosphinines are valuable compounds since they can be used as fluorophores or reduced towards precious λ^3 -phosphinines.^[59,60] Only this year, an OLED (Organic-Light-Emitting Diode) device was developed employing a blue emitting λ^5 -phosphinine.^[61] The photocatalytic functionalization of P_4 by $\text{R-CH}_2\text{-X}$ (X = halide) and TEA might represent a one-pot route towards potential precursors of λ^5 -phosphinines (**32** and **33**, see Figure AF 4.33 b). If synthesizing of **32** and **33** were successful, they then might be converted

4 CATALYTIC TRANSFORMATION OF WHITE PHOSPHORUS

into valuable hetero- and homo- λ^5 -phosphinines **34** and **35** following the procedure described in literature^[57].

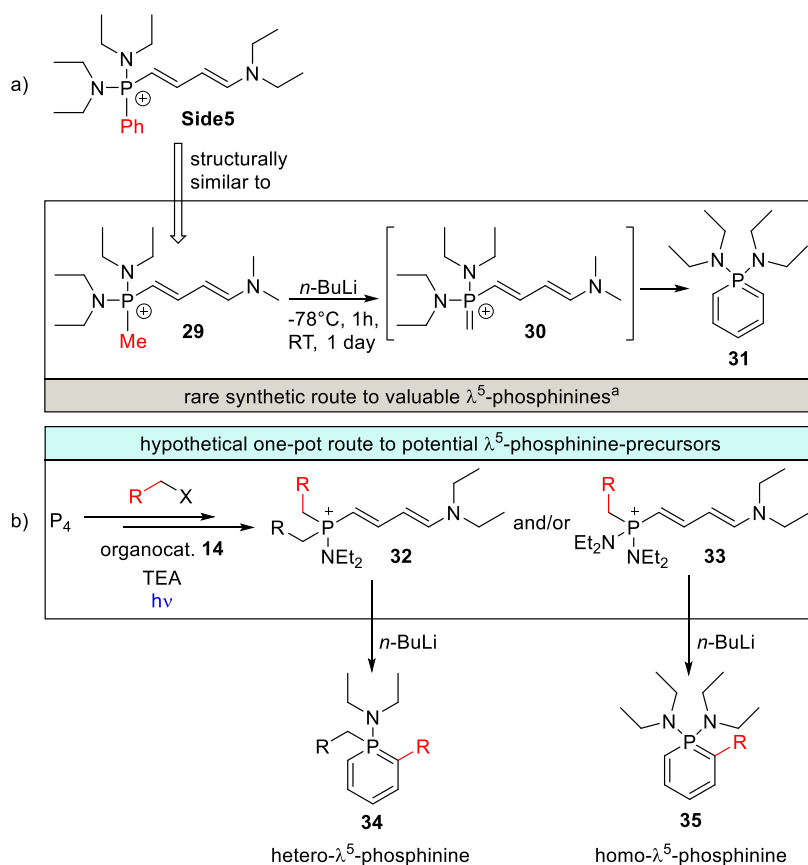


Figure AF 4.33 | The structural similarity of **Side5** to a starting material (**29**) for the synthesis of λ^5 -phosphinines suggests that the photocatalytic conversion of P_4 may possibly yield structurally related starting materials upon reaction with alkyl-halides. a) **Side5** shows a structural similarity to compound **29** which can be converted into valuable λ^5 -phosphinines according to literature a^[57]. b) Hypothetical one-pot route to potential λ^5 -phosphinines **32** and **33** which may further be converted to corresponding λ^5 -phosphinines **34** and **35**.

4.8.7 Conclusion of the Additional Findings

It could be demonstrated, that the iridium catalyst of the photocatalytic functionalization of P_4 can be exchanged by a more sustainable organocatalyst, however, this entails higher ratios of side products. Most notably, by investigating those reactions at low temperatures PH_3 was detected as additional intermediate upstream to PhPH_2 . This was further corroborated by *in situ* NMR reaction monitoring of a solution of NaPH_2 , which upon illumination furnished PH_3 *in situ* and PhPH_2 , Ph_2PH and Ph_3P and Ph_4P^+ in sequence. It was furthermore observed, that the product was only accompanied by negligibly small amounts of side product, which is probably attributable to the constantly small amounts of starting material PH_2^- . Thereupon, *in situ* NMR reaction monitoring of the functionalization of H_2PPh in different concentrations corroborated that a reduction in concentration of starting material led to less side product formation and consequently to higher yield. Despite all efforts (low temperatures, radical trapping or spin trapping) no information about

poly-phosphorus intermediates upstream to PH_3 was obtained. Yet, *in situ* $^{31}\text{P}\{^1\text{H}\}$ -NMR reaction monitoring indicate that P_4 is converted into an NMR-undetectable reservoir that still can provide phosphorus units for further transformation into Ph_4P^+ . ^2H isotopic labeling studies of the functionalization of P_4 in presence of TEA- d_{15} demonstrated the importance of triethylamine beyond its role as sacrificial electron donor, in particular, as proton source for the generation of the sequential intermediates. Apart from the fact that TEA is beneficial for the productive pathway, it was also found that it is detrimental since either TEA or any structural motif thereof is present in most side products. Yet, some side products of the photocatalytic functionalization of P_4 showed a promising structural core that might open up a new synthetic route towards valuable λ^5 -phosphinines.

4.8.8 References

- [1] E. Speckmeier, T. G. Fischer, K. Zeitler, *J. Am. Chem. Soc.* **2018**, *140*, 15353–15365.
- [2] D. R. Lide, in *CRC Handb. Chem. Phys.*, CRC Press, **2003**.
- [3] P. Anastas, N. Eghbali, *Chem. Soc. Rev.* **2010**, *39*, 301–312.
- [4] D. E. C. Corbridge, *Phosphorus 2000. Chemistry, Biochemistry and Technology*, Elsevier, **2000**.
- [5] D. H. R. Barton, J. Zhu, *J. Am. Chem. Soc.* **1993**, *115*, 2071–2072.
- [6] D. H. R. Barton, R. A. Vonder Embse, *Tetrahedron* **1998**, *54*, 12475–12496.
- [7] B. M. Cossairt, C. C. Cummins, *New J. Chem.* **2010**, *34*, 1533–1536.
- [8] S. K. Ghosh, C. C. Cummins, J. A. Gladysz, *Org. Chem. Front.* **2018**, *5*, 3421–3429.
- [9] V. V. Pavlishchuk, A. W. Addison, *Inorganica Chim. Acta* **2000**, *298*, 97–102.
- [10] P. B. Arockiam, U. Lennert, C. Graf, R. Rothfelder, D. J. Scott, T. G. Fischer, K. Zeitler, R. Wolf, *Chem. – A Eur. J.* **2020**, chem.202002646.
- [11] M. Goetz, in *Annu. Reports NMR Spectrosc.*, Academic Press, **2009**, pp. 77–147.
- [12] M. Goetz, I. Sartorius, *J. Phys. Chem. A* **2003**, *107*, 8539–8546.
- [13] J. Hu, J. Wang, T. H. Nguyen, N. Zheng, *Beilstein J. Org. Chem.* **2013**, *9*, 1977–2001.
- [14] M. H. Haindl, J. Hioe, R. M. Gschwind, *J. Am. Chem. Soc.* **2015**, *137*, 12835–12842.
- [15] N. Lokesh, A. Seegerer, J. Hioe, R. M. Gschwind, *J. Am. Chem. Soc.* **2018**, *140*, 1855–1862.
- [16] M. Grayson, *Pure Appl. Chem.* **1964**, *9*, 193–204.
- [17] A. Schmidpeter, G. Burget, *Phosphorus Sulfur Relat. Elem.* **1985**, *22*, 323–335.
- [18] A. Seegerer, P. Nitschke, R. M. Gschwind, *Angew. Chemie Int. Ed.* **2018**, *57*, 7493–7497.
- [19] N. Vinokurov, Novel P-Stereogenic Bidentate Phosphorus Ligands for Asymmetric Catalysis, **2007**.
- [20] J. Tong, S. Liu, S. Zhang, S. Z. Li, *Spectrochim. Acta - Part A Mol. Biomol. Spectrosc.* **2007**, *67*, 837–846.

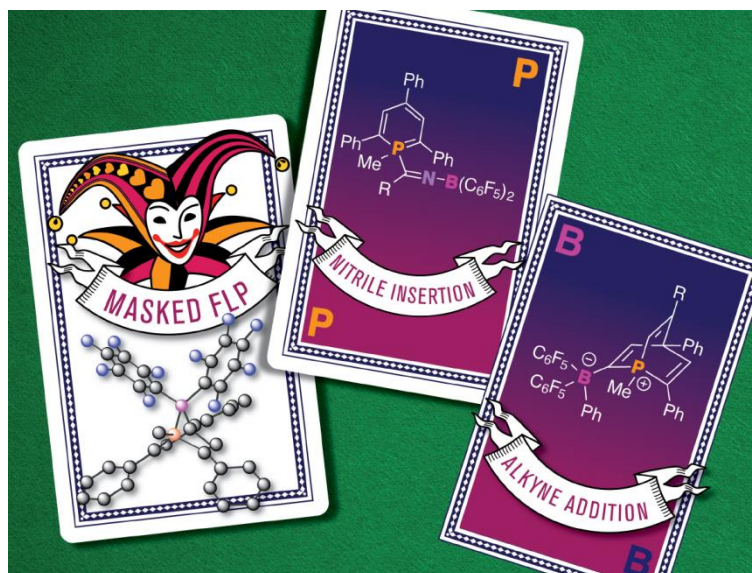
4 CATALYTIC TRANSFORMATION OF WHITE PHOSPHORUS

- [21] A. Bootle-Wilbraham, S. Head, J. Longstaff, P. Wyatt, *Tetrahedron Lett.* **1999**, *40*, 5267–5270.
- [22] C. E. Anderson, D. C. Apperley, A. S. Batsanov, P. W. Dyer, J. A. K. Howard, *J. Chem. Soc. Dalton Trans.* **2006**, 4134–4145.
- [23] SciFinder, “Chemical Abstracts Service: Columbus, OH; Phosphorous-31 NMR Spectrum; Spectrum ID 11P_267.P; CAS RN 3619-93-0,” can be found under <https://scifinder-n.cas.org/searchDetail/substance/5fb55e133ea033033d29dfe8/substanceSpectra> (accessed November 18, 2020), **n.d.**
- [24] SciFinder, “Chemical Abstracts Service: Columbus, OH; Phosphorous-31 NMR Spectrum; Spectrum ID 11P_266.P; CAS RN 3619-93-0;,” can be found under <https://scifinder-n.cas.org/searchDetail/substance/5fb55e133ea033033d29dfe7/substanceSpectra> (accessed November 18, 2020), **n.d.**
- [25] B. Maryasin, H. Zipse, *Phys. Chem. Chem. Phys.* **2011**, *13*, 5150–5158.
- [26] B. J. Anderson, S. C. Reynolds, M. A. Guinoo, Z. Xu, D. S. Glueck, *ACS Catal.* **2016**, *6*.
- [27] R. Bosque, J. Sales, *J. Chem. Inf. Comput. Sci.* **2001**, *41*, 225–232.
- [28] C. E. MacBeth, S. B. Harkins, J. C. Peters, *Can. J. Chem.* **2005**, *83*, 332–340.
- [29] K. R. Basvani, M. K. Kindermann, H. Frauendorf, C. Schulzke, P. G. Jones, J. W. Heinicke, *Polyhedron* **2017**, *130*, 195–204.
- [30] N. Peulecke, M. K. Kindermann, M. Köckerling, J. Heinicke, *Polyhedron* **2012**, *41*, 61–69.
- [31] SciFinder, “Chemical Abstracts Service: Columbus, OH; Phosphorous-31 NMR Spectrum; Spectrum ID 8PNMR5B1_383.P; CAS RN 2359-97-9,” can be found under <https://scifinder-n.cas.org/searchDetail/substance/5fbc85f03ea033033d31b986/substanceSpectra>, **n.d.**
- [32] SciFinder, “Chemical Abstracts Service: Columbus, OH; Phosphorous-31 NMR Spectrum; Spectrum ID CC-01-P_NMR-3321; CAS RN 62474-28-6,” can be found under <https://scifinder-n.cas.org/searchDetail/substance/5fbc86f53ea033033d31ba83/substanceSpectra>, **n.d.**
- [33] W. Jia, X. Chen, R. Guo, C. Sui-Seng, D. Amoroso, A. J. Lough, K. Abdur-Rashid, *J. Chem. Soc. Dalton Trans.* **2009**, 8301–8307.
- [34] D. J. Brauer, J. Fischer, S. Kucken, K. P. Langhans, O. Stelzer, N. Weferling, *Zeitschrift für Naturforsch.* **1994**, *49b*, 1511–1524.
- [35] H. Henry-Riyad, T. T. Tidwell, *Arkivoc* **2008**, *2008*, 113.
- [36] M. Rolff, J. N. Hamann, F. Tuczek, *Angew. Chemie Int. Ed.* **2011**, *50*, 6924–6927.
- [37] S. C. Kin, Z. L. Xin, W. I. Dzik, B. De Bruin, *J. Am. Chem. Soc.* **2008**, *130*, 2051–2061.
- [38] N. A. Giffin, M. Makramalla, A. D. Hendsbee, K. N. Robertson, C. Sherren, C. C. Pye, J. D. Masuda, J. A. C. Clyburne, *Org. Biomol. Chem.* **2011**, *9*, 3672–3680.
- [39] S. Berger, S. Braun, H.-O. Kalinowski, *NMR-Spektroskopie von Nichtmetallen: 31P-NMR-Spektroskopie*, Georg Thieme Verlag, **1993**.
- [40] H. Köhler, A. Michaelis, *Berichte der Dtsch. Chem. Gesellschaft* **1877**, *10*, 807–814.
- [41] E. F. Landvatter, T. B. Rauchfuss, *J. Chem. Soc. - Ser. Chem. Commun.* **1982**, 1170–1171.
- [42] Y. Tanabe, K. Nakajima, Y. Nishibayashi, *Chem. – A Eur. J.* **2018**, *24*, 18618–18622.
- [43] T. Heurich, Z.-W. Qu, S. Nožinović, G. Schnakenburg, H. Matsuoka, S. Grimme, O. Schiemann, R.

4 CATALYTIC TRANSFORMATION OF WHITE PHOSPHORUS

- Streubel, *Chem. - A Eur. J.* **2016**, *22*, 10102–10110.
- [44] J. Szewczyk, J. R. Lloyd, L. D. Quin, *Phosphorus Sulfur Relat. Elem.* **1984**, *21*, 155–160.
- [45] E. G. Janzen, *Free Radic. Res.* **1990**, *9*, 163–167.
- [46] K. Ranguelova, R. P. Mason, *Magn. Reson. Chem.* **2011**, *49*, 152–158.
- [47] N. Yoza, N. Ueda, N. Tokushige, T. Miyajima, Y. Baba, M. Tsuchiko, A. Tateda, *Inorganica Chim. Acta* **1992**, *202*, 237–239.
- [48] B. Punji, J. T. Mague, M. S. Balakrishna, *Inorg. Chem.* **2007**, *46*, 10268–10275.
- [49] M. L. Nielsen, J. V. Pustinger, J. Strobel, *J. Chem. Eng. Data* **1964**, *9*, 167–170.
- [50] À. González-Lafont, J. M. Lluch, *Wiley Interdiscip. Rev. Comput. Mol. Sci.* **2016**, *6*, 584–603.
- [51] K. Karandashev, Z. H. Xu, M. Meuwly, J. Vaníček, J. O. Richardson, *Struct. Dyn.* **2017**, *4*, 61501.
- [52] R. Batchelor, T. Birchall, *J. Am. Chem. Soc.* **1982**, *104*, 674–679.
- [53] D. Möller, in *Fundam. Process.*, De Gruyter, Berlin, Boston, **2019**, pp. 261–460.
- [54] C. L. Perrin, Y. Dong, *J. Am. Chem. Soc.* **2007**, *129*, 4490–4497.
- [55] J. W. Beatty, C. R. J. Stephenson, *Acc. Chem. Res.* **2015**, *48*, 1474–1484.
- [56] H. J. Cristau, A. Chêne, H. Christol, *Synth.* **1980**, *1980*, 551–554.
- [57] Y. V. Svyaschenko, B. B. Barnych, D. M. Volochnyuk, N. V. Shevchuk, A. N. Kostyuk, *J. Org. Chem.* **2011**, *76*, 6125–6133.
- [58] M. L. Movsisyan, *Russ. J. Gen. Chem.* **2011**, *81*, 607–608.
- [59] A. Savateev, Y. Vlasenko, N. Shtil, A. Kostyuk, *Eur. J. Inorg. Chem.* **2016**, *2016*, 628–632.
- [60] N. Hashimoto, R. Umamo, Y. Ochi, K. Shimahara, J. Nakamura, S. Mori, H. Ohta, Y. Watanabe, M. Hayashi, *J. Am. Chem. Soc.* **2018**, *140*, 2046–2049.
- [61] G. Pfeifer, F. Chahdoura, M. Papke, M. Weber, R. Szűcs, B. Geffroy, D. Tondelier, L. Nyulászi, M. Hissler, C. Müller, *Chem. – A Eur. J.* **2020**, *26*, 10534–10543.

5 A PHOSPHININE-DERIVED 1-PHOSPHA-7-BORA-NORBORNADIENE: FRUSTRATED LEWIS PAIR TYPE ACTIVATION OF TRIPLE BONDS



J. Leitl, A. R. Jupp, E. R. M. Habraken, V. Streitferdt, P. Coburger, D. J. Scott, R. M. Gschwind,* C. Müller,* J. C. Slootweg* and R. Wolf*

Chemistry – A European Journal

Chem. Eur.J. **2020**, 26,7788 –7800.

DOI: 10.1002/chem.202000266

V. Streitferdt performed *in situ* NMR monitoring experiments at the 600 MHz spectrometer and was involved in the preparation of the manuscript. J. Leitl performed all reactions and fully characterized compounds **2**, **3a-3e**, **4**, **5a-5c** and **6** by single crystal X-ray analysis, NMR and UV-Vis spectroscopy and elemental analysis. J. Leitl wrote the manuscript with contributions from all authors. A. R. Jupp performed DFT calculations (all mechanisms and NMR shifts) and prepared the manuscript and supporting information. E. R. M. Habraken supplied $(\text{C}_6\text{F}_5)_2\text{BCl}$ and was involved in the initial reaction of **2**. P. Coburger performed DFT calculations for NMR shifts. D. J. Scott was involved in the preparation of the manuscript. R. M. Gschwind, C. Müller, J. C. Slootweg and R. Wolf supervised and directed the project.

Reprinted (adapted) with permission from *Chem. Eur.J.* (via RightsLink). Text and Figures may differ from the original publication. Source of this chapter: <https://doi.org/10.1002/chem.202000266>

5.1 Abstract

Salt metathesis of 2,4,6-triphosfacyclohexadienyl lithium and chlorobis(pentafluorophenyl)borane affords a 1-phospha-7-bora-norbornadiene derivative **2**. The C≡N triple bonds of nitriles insert into the P–B bond of **2** with concomitant C–B bond cleavage, while the C≡C bonds of phenylacetylenes react with **2** to form λ^4 -phosphabarrelenes. Even though **2** must formally be regarded as a classical Lewis adduct, the C≡N and C≡C activation processes observed (and the mild conditions under which they occur) are reminiscent of the reactivity of frustrated Lewis pairs. Indeed, NMR and computational studies give insight into the mechanism of the reactions and reveal the labile nature of the phosphorus-boron bond in **2**, which is also suggested by detailed NMR spectroscopic studies on this compound. Nitrile insertion is thus preceded by ring opening of the bicycle of **2** through P–B bond splitting with a low energy barrier. By contrast, the reaction with alkynes involves formation of a reactive zwitterionic methylphosphininium borate intermediate, which readily undergoes alkyne 1,4-addition.

5.2 Introduction

1-*R*-Phosphacyclohexadienyl anions (**A**, Figure 5.1, also sometimes referred to as λ^4 -phosphinine anions) present a promising, yet underutilized platform for accessing diverse functionalized organophosphorus molecules.^[1] Anions **A** can easily be prepared from organolithium or Grignard reagents and aromatic λ^3, σ^2 -phosphinines and show ambidentate character toward various electrophiles, including transition metal centers. With “soft” alkylating agents, such as CH₃I, an S_N2 reaction with the phosphorus atom lone pair typically results in formation of a 1,1-disubstituted λ^5 -phosphinine (type **B**). On the other hand, with “hard” electrophiles such as acylium ions or protons, alkylation usually occurs at the more electron-rich C4- or C2-positions of the heterocycle (type **C** and **D**, respectively), affording the corresponding 1,2- or 1,4-dihydrophosfacyclohexadienes.^[2]

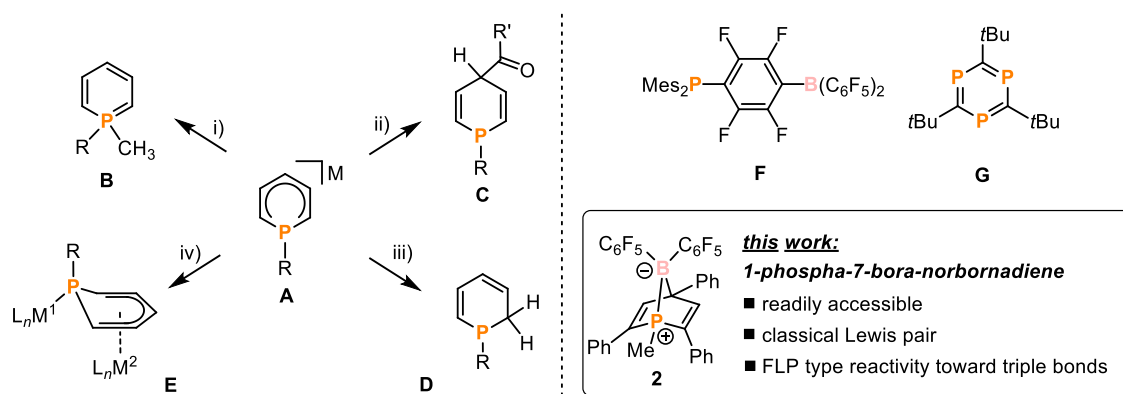


Figure 5.1 | A generic 1-*R*-phosphacyclohexadienyl anion **A** and its reactivity toward various electrophiles; the first reported P/B FLP (**F**); a triphosphabenzene derivative that displays FLP-like reactivity (**G**). Reagents: i) CH₃I, ii) R'COCl, iii) H⁺, iv) M¹L_n = M²L_n = Rh(1,5-cod), cod = cycloocta-1,5-diene; R = aryl or alkyl substituents.

For example, protonation (type **D**) usually proceeds exclusively at the C2-position of the λ^4 -phosphinine anion.^[3] It has been proposed that typically 1,1-products (**B**) are thermodynamically favoured, while 1,2- and

1,4-products (**C** and **D**) arise through kinetically controlled alkylation.^[2b] λ^4 -Phosphinines can also serve as anionic ligands for transition metal complexes. Depending on the nature of the ring-substitution pattern and the metal fragment, either η^1 -, η^2 -, η^5 - or even $\eta^1:\eta^5$ -coordination (type **E**) can be observed.^[4] Some of these coordination compounds have found applications in homogeneous catalysis, such as [(1,5-cod)Rh(η^5 -1-*t*Bu-2,4,5,6-Ph-PC₅H)] for the Rh-catalysed hydroformylation of olefins.^[4b-4e]

As part of our programme to study the chemistry of reactive and catalytically active phosphinine and phosphacyclohexadienyl complexes,^[5] we anticipated that the reaction of λ^4 -phosphinine anions **A** with chloroboranes would lead to neutral, phosphinine-based heterocycles that exhibit both a Lewis basic phosphorus atom moiety and an additional Lewis acidic boryl site.^[5b] Related systems have attracted much attention lately as so-called “frustrated Lewis pairs” (FLPs), which typically consist of trivalent alkyl or aryl phosphine and borane units.^[6] For example, Stephan’s groundbreaking intramolecular FLP Mes₂PC₆F₄B(C₆F₅)₂ (**F**, Figure 5.1) displays unquenched reactivity at the Lewis acidic borane and basic phosphine moieties, allowing it to split dihydrogen reversibly,^[7] and similar systems also react with other small molecules such as CO₂.^[8]

Despite the ubiquity of sp³-hybridised λ^3,σ^3 -phosphorus Lewis bases in FLP chemistry, the use of phosphorus bases in other coordination environments remains essentially unexplored, except for one recent example reported by Stephan and co-workers who showed that 2,4,6-*tert*-butyl-1,3,5-triphosphinine (**G**, Figure 5.1) is able to activate dihydrogen in an FLP type manner.^[9] Herein we describe the synthesis, thorough characterisation and reactivity of a bicyclic 1-phospha-7-boranorbomadiene **2**, which possesses a direct, polar P–B bond. Despite formally being a classical Lewis adduct, compound **2** displays characteristic FLP-like behavior due to the presence of easily thermally-accessible ring-opened isomers, which contain unquenched Lewis acidic and Lewis basic sites. As a result, **2** behaves as a masked FLP and readily activates the strong C≡N and C≡C triple bonds of nitriles and phenylacetylenes, forming unusual nitrile insertion and alkyne addition products.

5.3 Results and Discussion

5.3.1 Synthesis, characterisation and mechanism of formation of 1-phospha-7-boranorbomadiene **2**

Taking the known reactivity of **A** with electrophiles into account (Figure 5.1), it was anticipated that a chloroborane could be used to install a strongly electrophilic boron center onto a phosphacyclohexadienyl scaffold by salt elimination. On this basis, the simple salt Li[1-Me-PC₅H₂Ph₃] (**1**) was chosen as a starting material, which is easily prepared from methyl lithium and 2,4,6-triphenylphosphinine (TPP, Figure 5.1).^[2c] Upon treatment of **1** with (C₆F₅)₂BCl at *T* = –35 °C in *n*-hexane, a colour change from deep pink to orange was observed, with concomitant precipitation of an orange solid. Following filtration, dissolution of the remaining solid in diethyl ether, refiltration (to remove LiCl) and removal of solvent, a new compound **2** was isolated as a bright orange solid in 35% yield.

5 1-PHOSPHA-7-BORA-NORBORNADIENE

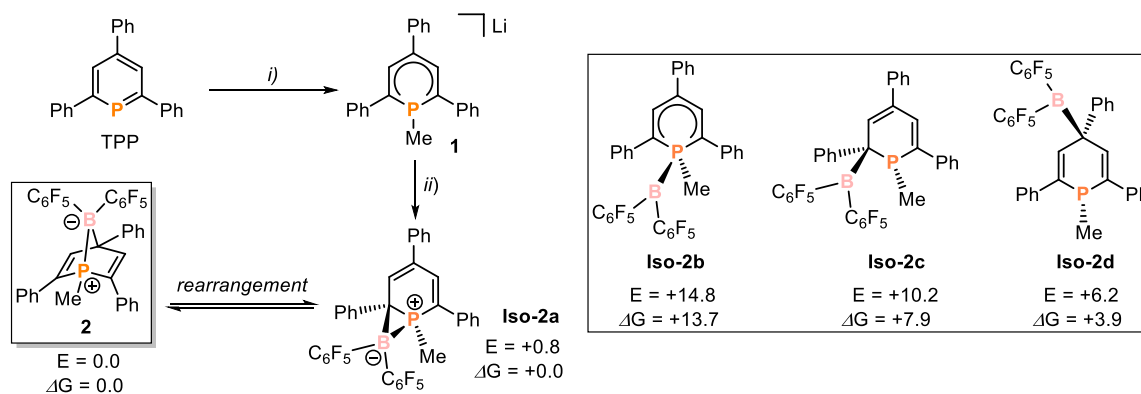


Figure 5.2 | Synthesis of **2** via **1** and **Iso-2a**; reagents and conditions: i) +MeLi (Et₂O, -78 °C), ii) + $(\text{C}_6\text{F}_5)_2\text{BCl}/\text{LiCl}$ (r.t., *n*-hexane). Relative wB97X-D/6-311+G** electronic energies (ΔE in kcal mol⁻¹) and free energies (ΔG in kcal mol⁻¹) for possible isomers of **2** (**Iso-2a** – **Iso-2d**).

Compound **2** was characterized by single crystal X-ray diffraction, NMR and UV-Vis spectroscopy as well as elemental analysis, all of which provided data that are consistent with the molecular structure depicted in Figure 5.2 (*vide infra*). In particular, single crystals of **2**, suitable for X-ray diffraction, were obtained by slow evaporation of the solvent from a solution of **2** in *n*-hexane at room temperature. Crystallographic characterization revealed a hitherto unknown hetero-norbornadiene structure (Figure 5.3), in which the boron atom has adopted a bridging position between the P1 and C4 positions of the phosphorus heterocycle. This unusual structure (c.f. **B** – **D**) can be attributed to the doubly electrophilic nature of the chloroborane, which allows for formation of a second, bridging interaction that is not available to most other main group electrophiles. It is worth noting that hetero-norbornadienes have received significant attention as ligands in homogeneous catalytic reactions, e.g. the hydrogenation and hydroformylation of alkenes as well as Heck reactions.^[10] Furthermore, compound **2** is a rare example of a hetero-norbornadiene based on both phosphorus and boron.^[11] Derivatives with phosphorus and another additional heteroatom in the norbornadiene scaffold are scarce, although Streubel and co-workers have described a 7-aza-1-phospha-norbornadiene and group 13 7-metalla-1,4-diphospha-norbornadienes (mechanistic and reactivity studies of which have unfortunately not been reported).^[12] Also of note are the very mild conditions used for the preparation of **2**, which contrasts with the much more forcing conditions required to prepare many other 1-phosphanorbornadiene derivatives.^[13]

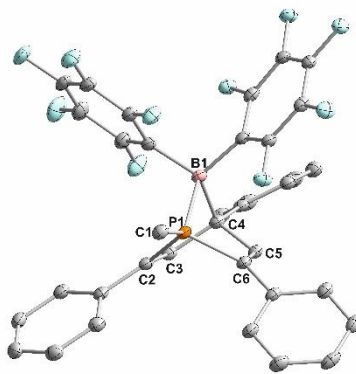


Figure 5.3 | Molecular structure of **2** in the crystal. Displacement ellipsoids are shown at the 40% probability level; H atoms are omitted for clarity; selected bond lengths [Å] and angles [°]: P1–B1 1.9894(19); P1–C1 1.8025(17); B1–C4 1.721(2); P1–C2 1.8146(17); P1–C6 1.8081(17); C2–C3 1.344(3); C6–C5 1.336(2); C1–P1–B1 129.51(8); C2–P1–C6 101.44(8); P1–B1–C4 84.58(10).

While the P1–B1 distance of 1.9894(19) Å in **2** is in the range of phosphorus boron single bonds (sum of covalent radii = 1.96 Å),^[14] the B1–C4 bond is slightly elongated compared both to the sum of the covalent radii (1.721(2) Å vs. 1.60 Å)^[14] and to previously reported 7-bora-norbornadienes (ca. 1.641 Å),^[15] suggesting significant strain in the bicyclic structure.^[16] A similar phenomenon was observed by Braunschweig and co-workers for a heptaphenyl-7-borabicyclohepta-2,5-diene N-heterocyclic carbene adduct (B–C: 1.743 Å), in which the boron atom is also four-coordinate.^[17] Also of note are the C2–C3 and C5–C6 distances within the phosphorus heterocycle, which are characteristic of C=C double bonds (1.344(3) and 1.336(3) Å, respectively).^[18]

The ³¹P{¹H} NMR spectrum of **2** shows a poorly resolved signal at $\delta(\text{ppm}) = +18.6$ at r.t. (see Figures S3 and S79), while the ¹¹B spectrum reveals a resonance at $\delta(\text{ppm}) = +14.1$ consistent with four-coordinate boron (see Figures S5, S82 and S84).

In order to elucidate the pathway for the formation of **2**, variable temperature (VT) ¹¹B and ³¹P{¹H} NMR reaction monitoring was performed, alongside DFT calculations. ¹¹B NMR spectra recorded during the reaction of **1** and (C₆F₅)₂BCl revealed not only the formation of product **2** ($\delta(\text{ppm}) = +13$) but also of an additional species, **Iso-2a**, characterised by a resonance at $\delta(\text{ppm}) = -25$ (Figure SI 5.4). Further information on the reaction was obtained by ³¹P{¹H} NMR monitoring (see Figure 5.4a; see SI for experimental details and Figure SI 5.1 for further spectra) which showed that **1** ($\delta(\text{ppm}) = -72.5$) is fully converted even at low temperature. The signal of product **2** appears within minutes even at 193 K (see Figure 5.4a). However, another intense and broad signal can be observed at $\delta(\text{ppm}) = -102$ (**Iso-2a** in Figure 5.4a), which converts into **2** as the temperature is increased, suggesting an intermediate species. Calculations at the TPSS/IGLO-III CPCM(THF) level of theory showed that the experimental ³¹P shift of -102 ppm and the ¹¹B shift of -25 ppm both fit well to a proposed three-membered B–C–P ring species, and this structure is consequently assigned to **Iso-2a** (see Table 5.1 and Figure 5.2). Calculations also suggested that this structure should be very similar in energy to **2**, and indeed, NMR analysis of even

5 1-PHOSPHA-7-BORA-NORBORNADIENE

authentic samples of crystalline **2** showed the presence of minor amounts of **Iso-2a**, consistent with reversible isomerisation in solution.

Given the known reactivity of λ^4 -phosphinine anions with electrophiles shown in Figure 5.2, other plausible structures **Iso-2b** – **Iso-2d** were also investigated as possible intermediates. DFT calculations at the ω B97X-D/6-311+G** level showed that isomers with a tricoordinate boryl substituent in the 1-, 2- or 4-position are all higher in energy than **2** or **Iso-2a** (see Figure 5.2), and therefore less likely to accumulate during the course of the reaction. This is corroborated by a chemical shift analysis of these structures (Table 5.1), which predicts significantly different NMR shifts for the isomers **Iso-2b** – **Iso-2d** than those observed experimentally. Nevertheless, it should be noted that structure **Iso-2d** in particular is predicted to be thermally accessible at even modest temperatures on the basis of the above calculations.

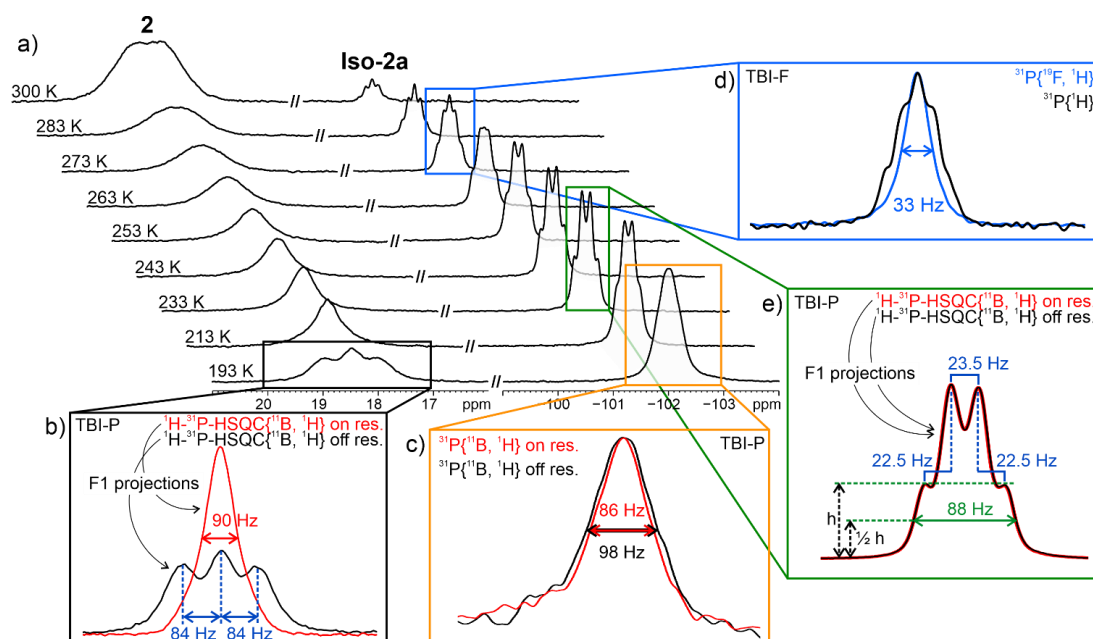


Figure 5.4 | a) $^{31}\text{P}\{^1\text{H}\}$ NMR monitoring (starting from 193 K and warming up to 300 K) of the reaction of **1** with $(\text{C}_6\text{F}_5)_2\text{BCl}$ (see SI for full spectra, Figure SI 5.1). The spectral regions of **2** and **Iso-2a** are displayed with the same expansion and intensity scaling. b) Overlaid F1 (indirect dimension) projections of a ^1H - ^{31}P -HSQC with simultaneous ^{11}B and ^1H decoupling in F1 and ^{31}P decoupling in F2 (direct dimension) acquired in the region of **2** (better signal/noise compared to 1d ^{31}P spectrum, see S81 in SI for pulse program). ^{11}B decoupling was applied on resonance (red) and off resonance (black). The spectra were acquired on a TBI-P probe. c) Overlaid 1d ^{31}P spectra with simultaneous ^{11}B and ^1H decoupling. ^{11}B decoupling was applied on resonance (red) and off resonance (black). The spectra were adjusted to same height for a better comparison of line widths. The spectra were acquired on a TBI-P probe. d) Overlaid 1d ^{31}P spectra with ^1H decoupling only (black) and simultaneous ^{19}F and ^1H decoupling (blue). The spectra were adjusted to same height for a better comparison of line widths (see also S80 in SI). The spectra were acquired on a TBI-F probe. e) Overlaid F1 projections of a ^1H - ^{31}P -HSQC with simultaneous ^{11}B and ^1H decoupling in F1 and ^{31}P decoupling in F2 acquired in the region of **Iso-2a**. The spectra were acquired on a TBI-P probe.

Table 5.1 | Calculated (calcd.) ^{31}P and ^{11}B NMR shifts (ppm) and coupling constants $J_{\text{P-B}}$ (Hz) at the TPSS/IGLO-III CPCM(THF) level of theory. The calculated absolute shieldings of compound **2** served as reference for the other compounds. Experimental (exp.) chemical shifts of **2** and **Iso-2a** are also given.

	2	Iso-2a	Iso-2b	Iso-2c	Iso-2d
$\delta(^{31}\text{P})$	+18 (exp.)	-102 (exp.) -98 (calcd.)	-16	-38	-43
$\delta(^{11}\text{B})$	+14 (exp.)	-25 (exp.) -26 (calcd.)	+32	+66	+47
$J_{\text{P-B}}$	87	6			

5.3.2 Variable temperature NMR characterisation of isomers **2** and **Iso-2a**

During VT NMR monitoring of the formation of **2** it was noted that the $^{31}\text{P}\{^1\text{H}\}$ resonances for both **2** and **Iso-2a** show complex temperature-dependent behaviour. In order to understand these observations (and also further support the structural assignment of **Iso-2a**) an in-depth analysis of the relevant multinuclear VT NMR spectra was carried out.

In the $^{31}\text{P}\{^1\text{H}\}$ NMR spectra, the multiplicities of the $^{31}\text{P}\{^1\text{H}\}$ signals of both **2** and **Iso-2a** change upon warming from 193 K (see Figure 5.4a). Over the entire temperature range examined, the signal of **2** is dominated by scalar couplings to ^{11}B and the quadrupolar relaxation of ^{11}B . This was proven by simultaneously ^{11}B and ^1H decoupled ^{31}P spectra (see $^{31}\text{P}\{^{11}\text{B}, ^1\text{H}\}$ spectrum in Figure 5.4b), which show a clear collapse of the triplet with a coupling constant of $^1J_{\text{PB}} = 84$ Hz at 193 K. Additional $^{31}\text{P}\{^{19}\text{F}, ^1\text{H}\}$ experiments did not change the signal of **2** (Figure SI 5.2), which is reasonable for scalar couplings being significantly smaller than the half line width ($\nu_{1/2} = 90$ Hz). With increasing temperature, the $^{31}\text{P}\{^1\text{H}\}$ signal of **2** becomes first a singlet and then a very broad doublet from 300 K upwards (for a temperature row between 193 K and 333 K of **2**, see Figure SI 5.5). The corresponding ^{11}B signal changes from a very broad singlet to a sharper doublet at 300 K corroborating the large scalar coupling constant between ^{11}B and ^{31}P ($^1J_{\text{PB}} = 90$ Hz, see Figure SI 5.4), which is accompanied by a downfield shift. Similar behaviour was observed in a temperature screening of a solution containing exclusively **2** in which the ^{11}B signal of **2** started out as being relatively sharp at 193 K (see Figure SI 5.6), then first broadened and subsequently narrowed during a steady temperature increase. Again, this went along with a downfield shift (around 1.4 ppm, see Figure SI 5.6). The line broadening associated with a downfield shift is probably related to a coalescence of **2** with another species downfield shifted relative to **2**. Given the relatively low energy predicted for isomer **Iso-2d** (*vide supra*) this is likely to be the relevant species, and these variable temperature measurements therefore further hint at the labile nature of the B–P bond in **2** (a ^{11}B shift of 1.4 ppm for **2** would correspond to the presence of around 4% of **Iso-2d**; see SI for calculation). Within this exchange the P–B bond is broken and re-established, which may alter $^1J_{\text{PB}}$ and could therefore give rise to the observed change in shape of the $^{31}\text{P}\{^1\text{H}\}$ signal of **2** during temperature increase (see Figure 5.4a).

5 1-PHOSPHA-7-BORA-NORBORNADIENE

The $^{31}\text{P}\{^1\text{H}\}$ signal of **Iso-2a** at $\delta(\text{ppm}) = -102$ exhibits a significantly different response upon temperature increase. At 193 K quadrupolar relaxation seems to dominate producing a broad singlet ($\nu_{1/2} = 98$ Hz). During warm-up, this signal becomes sharper (Figure SI 5.1) and develops a quartet splitting which at higher temperatures converts into a quintet (see Figure 5.4a and Figure SI 5.1). ^{31}P NMR with simultaneous ^{19}F and ^1H decoupling revealed that the splitting results from coupling to ^{19}F (see $^{31}\text{P}\{^{19}\text{F}, ^1\text{H}\}$ in Figure 5.4d). The fact that different multiplets are observed at altered temperatures may be attributed to the presence of two chemically-distinct, hindered C_6F_5 rings, each of which may independently suffer from hindered rotation about its B-C bond (of the structures proposed in Figure 5.2 this is only the case for **Iso-2a**). While the ortho (and meta) fluorines of a freely rotating ring would have identical scalar couplings to phosphorus, those in a hindered ring may have different couplings. Thus, similar coupling of ^{31}P to both fluorines of one freely-rotating C_6F_5 ($^5J_{\text{PF}} = 22.5$ Hz) and only one fluorine of a hindered C_6F_5 ($^5J_{\text{PF}} = 23.5$ Hz) would give rise to the observed quartet (see Figure 5.4e). At elevated temperatures, stronger rotation of the fluoroaryls and/or rapid P-B-bond opening and closing presumably results in a similar scalar coupling of ^{31}P to all four ortho fluorines, creating a quintet coupling pattern. $^{31}\text{P}\{^{11}\text{B}, ^1\text{H}\}$ measurements at 193 K showed a small reduction in line width (see Figure 5.4c) while at 233 K no change in line width or multiplet structure was observed (see Figure 5.4e). This implies that at 193 K the ^{31}P signal of **Iso-2a** is dominated by the quadrupolar relaxation effects of ^{11}B . In contrast, at higher temperatures there is an apparently smaller influence of ^{11}B on the line width which is now mainly dominated by coupling to ^{19}F . Calculations at the TPSS/IGLO-III CPCM(THF) level of theory revealed a $^1J_{\text{PB}}$ of 6 Hz for **Iso-2a** (see Table 5.1) which fits well to the observation of a small change in line width at 193 K and no change at 233 K. Verifying the P-B bond in **Iso-2a** via ^{31}P - ^{11}B -HMQC was not successful due to the extremely broad ^{11}B signals associated with very short transverse relaxation times (T_2). A ^1H - ^{31}P -HSQC spectrum revealed the expected break in symmetry of the heterocycle in **Iso-2a** compared to **2** since the protons bound to the P-heterocycle exhibit different shifts and ^1H - ^{31}P coupling constants (Figure SI 5.3). Taken collectively, these NMR observations therefore strongly support the proposed structure of **Iso-2a**.

5.3.3 Reactivity of **2** toward nitriles

Although the solid-state structure of **2** clearly indicated the formation of a classical P/B Lewis acid/base adduct, XRD, DFT and VT NMR analyses all suggested that reversible, thermal P-B bond cleavage could plausibly provide access to a ring-opened isomer **Iso-2d** possessing unquenched acidic and basic sites. It was thus anticipated that FLP-type behaviour might still be observable for compound **2**, in line with both our initial predictions and results reported previously for some other boron-based Lewis adducts.^[19] Indeed, more direct evidence that such reactivity is possible was observed during attempts to dissolve samples of **2** in deuterated acetonitrile for NMR purposes, which led to a clear colour change from orange to deep green. Although activation of other unsaturated C=X bonds by FLPs is very well established, reports of nitrile activation are remarkably scarce, with this having been achieved only for a family of geminal phosphinoboranes reported by Wagner and Sloatweg, which reacted to generate five-membered cyclic structures, and a single, more elaborate enamine/borane system reported by Erker *et al.*^[20] Nevertheless,

addition of acetonitrile to a solution of **2** in diethyl ether at r.t. resulted in an immediate colour change and the $^{31}\text{P}\{^1\text{H}\}$ NMR spectrum of the reaction mixture indicated the selective formation of a single new species **3a** (Figure 5.5), as evidenced by a sharp singlet resonance at $\delta(\text{ppm}) = +0.6$, that is shifted to higher field relative to **2** (Figure S11 in SI).

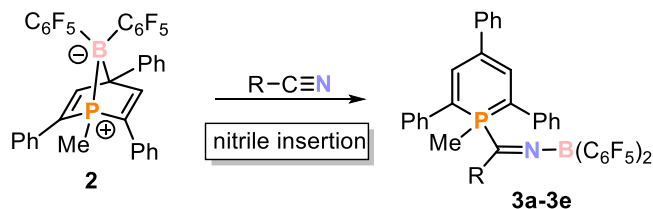


Figure 5.5 | Synthesis of nitrile insertion products **3a-3e** (yields of isolated compounds are given in parentheses in this caption): **3a**: R = Me (33%), **3b**: R = Ph (64%), **3c**: R = 3,5-Br₂C₆H₃ (43%), **3d**: R = CH₂Cl (39%), **3e**: R = Et (41%).

In the proton-coupled ^{31}P NMR spectrum this signal appears as a complex multiplet (Figure S12 in SI). Additionally, the $^{11}\text{B}\{^1\text{H}\}$ NMR spectrum shows a broad signal at $\delta(\text{ppm}) = +21.9$ that is shifted to lower field relative to **2**, which is qualitatively consistent with a change from four- to three-coordinate boron. Single crystals were grown by slow evaporation of an *n*-hexane solution of **3a** at room temperature. Gratifyingly, the crystallographic characterization confirmed activation of the nitrile triple bond, although this was unexpectedly accompanied by cleavage of not just the P–B bond but also the C–B bond of **2** (Figure 5.6) with the nitrile having formally inserted into the former. The resulting BCN moiety is almost linear (C7–N1–B1 172°), and the N1–B1 distance is significantly shortened (1.367(2) Å) compared to common N–B single bonds (1.57 Å),^[14] suggesting some multiple bond character due to donation of electron density from the nitrogen lone pair into the empty p orbital on boron. The nitrile-derived C7–N1 distance is in the range of typical C–N double bonds (1.251(2) Å),^[18] and the P1–C7 separation (1.8822(17) Å) is in the range of single bonds according to the sum of the covalent radii (P–C 1.86 Å).^[14]

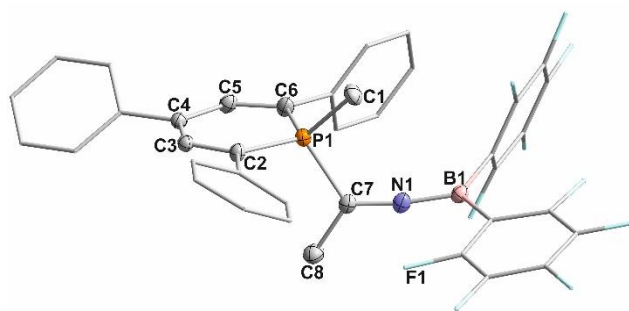


Figure 5.6 | Molecular structure of **3a** in the crystal. Displacement ellipsoids are shown at the 40% probability level; H atoms are omitted for clarity; phenyl and C₆F₅ groups were shown in wireframe for clarity; selected bond lengths [Å] and angles [°]: P1–C1 1.8036(18); P1–C7 1.8822(17); P1–C2 1.7475(16); P1–C6 1.7431(17); C2–C3 1.397(2); C3–C4 1.399(2); C5–C6 1.378(2); C7–N1 1.251(2); N1–B1 1.367(2); C7–C8 1.492(2); C1–P1–C7 102.58(8); P1–C7–N1 120.29(13); C7–N1–B1 172.06(18); C8–C7–N1 124.56(16).

Other substituted nitriles were subsequently employed in similar reactions, yielding compounds **3b-3e** (Figure 5.5) as deep green crystals in moderate yields (33–64 %). The crystallographic characterization of **3b** and **3c** revealed structures similar to that already discussed for **3a**, with essentially linear C–N–B

5 1-PHOSPHA-7-BORA-NORBORNADIENE

arrangements and short B–N distances (for more details, see SI). Multinuclear NMR data of all compounds were also in line with those found for **3a**.

A slightly different outcome was observed using 2-(dimethylamino)acetonitrile (Figure 5.7), which contains an additional pendant donor functionality, as was indicated by an immediate colour change from orange to deep pink (*c.f.* deep green for compounds **3a-3e**) upon addition of the substrate to a solution of **2** in diethyl ether.

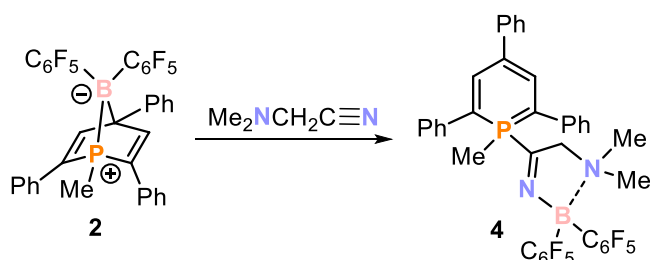


Figure 5.7 | Reaction of **2** with 2-(dimethylamino)acetonitrile.

NMR analysis indicated the clean formation of a new product **4** that features a $^{31}\text{P}\{^1\text{H}\}$ resonance at $\delta(\text{ppm}) = -9.2$, which is shifted to higher field relative to **3a-3e** ($\delta(\text{ppm}) = -1.0$ to $+0.6$). The $^{11}\text{B}\{^1\text{H}\}$ signal (11.5 ppm for **4** vs. *ca.* 22–26 ppm for **3a-3e**) is also shifted to higher field, suggesting a different product structure, which was confirmed by single crystal X-ray diffraction (Figure 5.8). The molecular structure of **4** in the crystal reveals insertion of the nitrile into the P–B bond of **2** analogously to **3a-3e**. However, instead of a linear CNB moiety a five-membered Lewis adduct is formed in which the boron moiety interacts with both available nitrogen atoms. The rather elongated B1–N2 bond (1.7322(16) Å) of **4** is consistent with a dative interaction between B1 and the lone pair of N2. This interaction has a significant influence on the solid-state structure and spectroscopic properties of **4**. The crystallographic characterization further shows that the C–N–B fragment is no longer linear (111.27(10)°) and the B1–N1 bond distance (1.5237(16) Å) is elongated compared to **3a** (1.367(2) Å). The UV-Vis spectrum of **4** shows an additional absorbance at $\lambda = 523$ nm, which explains the apparent colour change from green (for **3a-3e**) to pink.

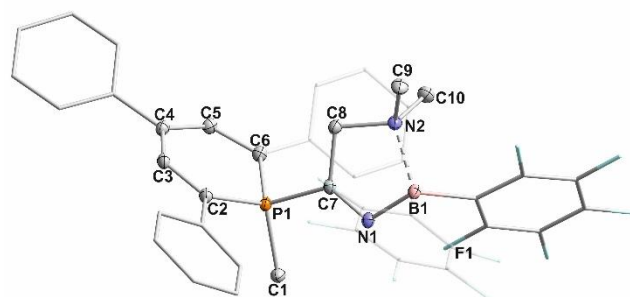


Figure 5.8 | Molecular structure of **4** in the crystal. Displacement ellipsoids are shown at the 40% probability level; H atoms are omitted for clarity; phenyl and C_6F_5 groups were shown in wireframe for clarity; selected bond lengths [Å] and angles [°]: P1–C7 1.8435(12); P1–C2 1.7631(12); P1–C6 1.7612(12); P1–C1 1.8231(12); C2–C3 1.3916(17); C3–C4 1.3985(18); C4–C5 1.4070(17); C5–C6 1.3822(17); C7–C8 1.5084(16); N2–B1 1.7322(16); B1–N1 1.5237(16); N1–C7 1.2578(16); C7–N1–B1 111.27(10); N1–B1–N2 100.38(9); P1–C7–N1 125.34(9); C8–N2–B1 103.

To analyse the reaction course of **2** with nitriles in more detail, DFT calculations were again performed at the ω B97X-D/6-311+G** level of theory (all energy values discussed are ΔG values in kcal·mol⁻¹; see Figure 5.9 and *vide supra*). As already discussed, an initial ring opening of **2** forms isomer **Iso-2d**, which can act as an FLP for the activation of nitriles, modelled here using acetonitrile. This first step is consistent with the chemical exchange between **2** and **Iso-2d** suggested by ¹¹B NMR (Figure SI 5.6 and *vide supra*). Nitrile binding to the boron centre of **Iso-2d** then gives an adduct **Int-A** with almost identical energy. The subsequent rate-determining step involves cyclisation to give the high-energy bridged intermediate **Int-B** (this proceeds over an energy barrier of +21.5 kcal·mol⁻¹, which is slightly higher than expected given the rapid reactivity observed at room temperature, but is nevertheless in satisfactory agreement with the experimental result, given the errors typically associated with the computational methods employed). This compound is highly unstable and rapidly rearranges with cleavage of the B–C bond. Flattening of the six-membered λ^5 -phosphinine-derived ring gives initially **Int-C**, which readily isomerises through P–C bond rotation to the slightly more stable conformer **3a**, as is observed in the solid-state structure.

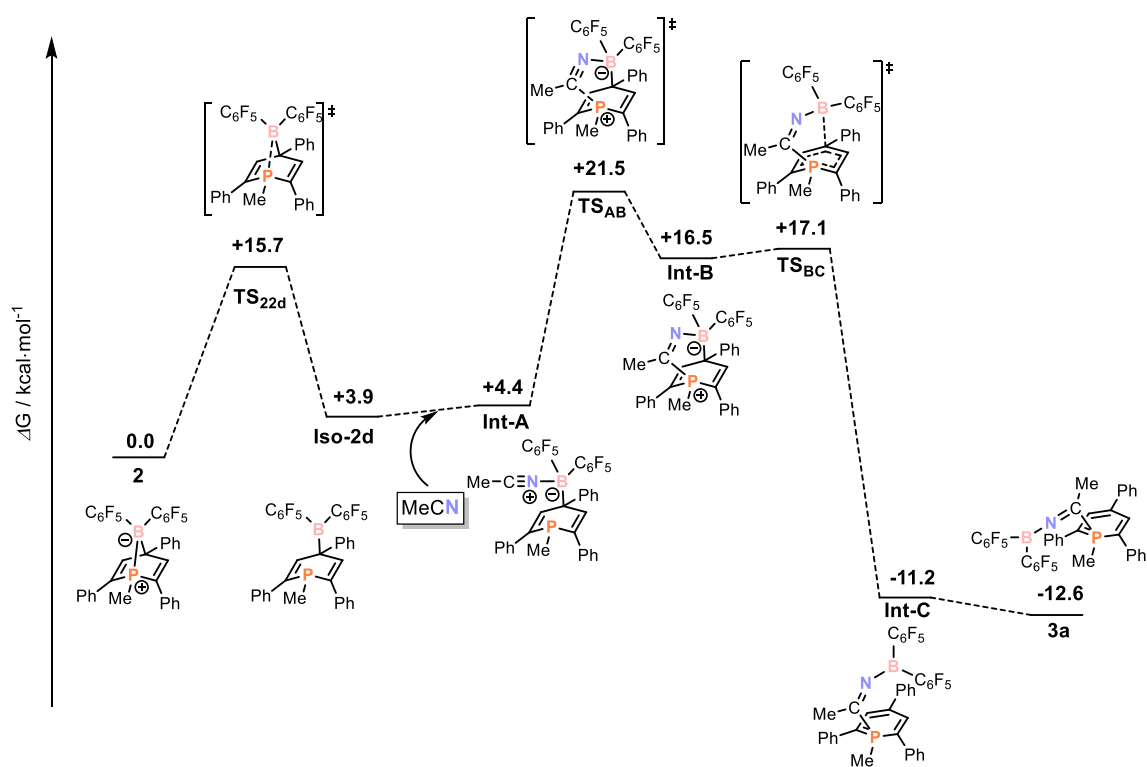


Figure 5.9 | Relative ω B97X-D/6-311+G** energies (calculated free energies ΔG in kcal·mol⁻¹) for the conversion of **2** into **3**.

5.3.4 Reactivity of **2** toward alkynes

Encouraged by the high reactivity of **2** toward the strong, polar triple bond of nitriles, we were motivated to also test the reactivity of **2** toward the similarly strong, but apolar triple bonds of simple alkynes. The combination of **2** with one equivalent of phenylacetylene in benzene did not show any significant reactivity at room temperature. However, when heating this mixture to $T = 60$ °C overnight, the selective formation of a

5 1-PHOSPHA-7-BORA-NORBORNADIENE

new product **5a** was observed (Figure 5.10), indicated by the detection of a single new resonance in the $^{31}\text{P}\{^1\text{H}\}$ NMR spectrum at $\delta(\text{ppm}) = 1.7$ (Figure S53 and Figure S54 in SI). This signal appears within the range observed for the nitrile activation products **3a-3e**, which suggests the formation of a similar tetracoordinate phosphorus environment. In contrast, the $^{11}\text{B}\{^1\text{H}\}$ NMR signal of **5a** is shifted to significantly higher field relative to **3a-3e** (-11.2 ppm for **5a** vs. ca. 22-26 ppm for **3a-3e**), and suggests a tetracoordinate rather than tricoordinate boron moiety (Figure SI55 in SI).

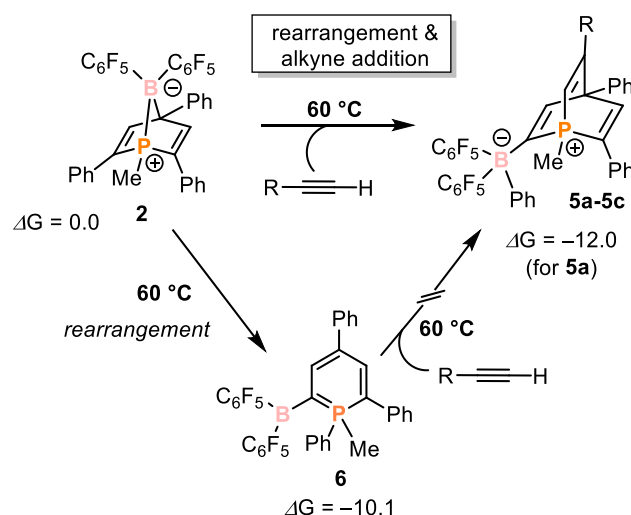


Figure 5.10 | Reaction of **2** with phenylacetylene derivatives, leading to the formation of **5a-5c**, thermal rearrangement of **2** to **6**, and relative $\omega\text{B97X-D/6-311+G}^{**}$ energies (calculated free energies ΔG in $\text{kcal}\cdot\text{mol}^{-1}$); **5a**: R = Ph (61%); **5b**: R = 4- CF_3 - C_6H_4 (62%); **5c**: R = 4-Br- C_6H_4 (72%).

The reactions of **2** with 4-(trifluoromethyl)- and 4-bromophenylacetylene led to analogous results, as the selective formation of the corresponding new compounds **5b** and **5c** was observed, which show very similar heteroatom NMR resonances ($^{31}\text{P}\{^1\text{H}\}$ $\delta(\text{ppm}) = 2.1$ (**5b**), 1.9 (**5c**); $^{11}\text{B}\{^1\text{H}\}$ $\delta(\text{ppm}) = -11.2$ (**5b**), -11.1 (**5c**)). Compounds **5a-5c** could be isolated as light red powders in good yields (up to 72%) by treatment of the crude product with *n*-hexane and thorough drying of the resulting precipitate under vacuum. Single crystals of **5b** and **5c** were grown by slow evaporation of *n*-hexane solutions. The single crystal X-ray structures reveal the formation of a λ^4 -1-phosphabarrelenium moiety, in which the alkyne bridges between P1 and C4 of the phosphinine-derived heterocycle.

As with nitriles, alkyne addition is accompanied by cleavage of both the P-B and C-B bonds of **2**. Remarkably, this is accompanied by migration of the $\text{B}(\text{C}_6\text{F}_5)_2$ moiety *via* formal insertion into the C2-Ph bond of **2**. Due to the modest quality of the structural data of **5c** (Figure S106 and Table S2 in SI), only the structural data of **5b** is discussed in detail here. The P1-C8 bond length (1.783(4) Å) is in the range of common P-C single bonds, while the C4-C7 bond (1.577(5) Å) is in the range of C-C single bonds.^[18] The C2-C3, C5-C6 and C8-C7 distances are typical for C=C double bonds.^[18]

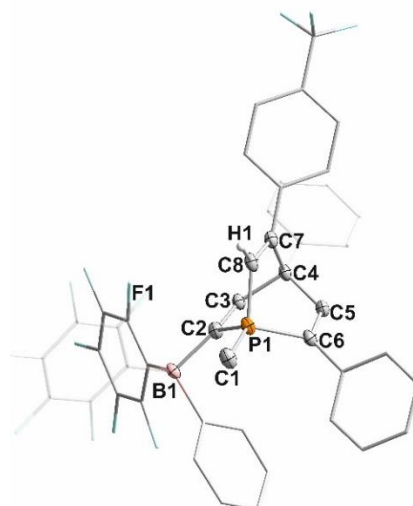


Figure 5.11 | Molecular structure of **5b** in the crystal. Displacement ellipsoids are drawn at the 40% probability level; H atoms are omitted for clarity; phenyl; C₆H₄CF₃ and C₆F₅ groups were shown in wireframe for clarity; a disordered *n*-hexane molecule is omitted for clarity; selected bond lengths [Å] and angles [°]: P1–C8: 1.783(4); C4–C7: 1.577(5); P1–C2: 1.799(4); P1–C6: 1.816(4); P1–C1: 1.781(4); C2–C3: 1.335(5); C3–C4: 1.560(5); C4–C5: 1.541(5); C5–C6: 1.335(5); C7–C8: 1.334(5); C2–B1: 1.636(5); P1–C8–C7: 112.1(3); C8–C7–C4: 116.4(3); C2–P1–C6: 103.36(17); C3–C4–C5: 107.2(3).

The bond lengths and angles of **5b** are consistent with other reported 1-phosphabarrelenes, except for P1–C8, which is slightly shortened (1.783(4) Å vs. average 1.836 Å).^[21] As a corollary, the angle C2–P1–C6 is also widened by roughly 8° compared to other 1-phosphabarrelenes (103.36(17)° vs. average 95.351°). These changes can be attributed to the tetracoordinate nature of the P atom, and were also observed for a selenium-substituted phosphabarrelene.^[21a] Finally, the B1–C2 bond length in **5b** (1.636(5) Å) is consistent with typical B–C single bonds.^[14]

Typically, Diels-Alder type [4+2] cycloaddition of alkynes to neutral phosphinines to form 1-phosphabarrelenes must be performed using highly reactive alkynes or activated alkynes (such as F₃CC≡CCF₃) as dienophiles.^[21,22] That phospho-norbomadiene **2** reacts with simple phenylacetylenes under modest reaction conditions is therefore significant, and is reminiscent of the *cationic* 1-methyl-phosphinium salt [1-Me-2,6-(SiMe₃)₂-3,5-Ph₂-PC₅H][GaCl₄]^[23] that upon reaction with 4-octyne affords a 1-methyl-phosphabarrelenium tetrachlorogallate which was characterized by NMR spectroscopy.

While activation of alkynes is known to occur for other FLP systems, the concomitant B(C₆F₅)₂ migration observed in this case suggests an atypical activation mechanism.^[20a–20b,24] To gain more insight, a solution of **2** was monitored by ³¹P{¹H} NMR spectroscopy at 60 °C in the absence of alkyne, which resulted in the slow formation of a new species observed as a sharp singlet at δ(ppm) = +1.3 ppm (no analogous transformation was observed at r.t.). The chemical shift of this species is quite similar to those of **5a-5c** (δ(ppm) = 1.7–2.0), suggesting a similar environment at P. The structure of this species could not be determined by single crystal X-ray diffraction; however, LIFDI-MS spectrometry, elemental analysis and NMR observations are consistent with the structure **6** depicted in Figure 5.10. In particular, the calculated ³¹P (δ(ppm) = +5 vs. +1.3 observed) and ¹¹B NMR (δ(ppm) = +43 vs. +54 observed) shifts of **6** are in

5 1-PHOSPHA-7-BORA-NORBORNADIENE

agreement with the observed shifts (Table S5 in SI). Additionally, the calculated and observed UV-Vis spectrum of **6** are in reasonable agreement (Figure S104 and S115 in SI).

VT $^{31}\text{P}\{^1\text{H}\}$ NMR monitoring of **2** was also carried out in the presence of an alkyne substrate. When 4-(trifluoromethyl)phenylacetylene was added to **2** at room temperature only a small singlet in the ^{31}P NMR spectrum at $\delta(\text{ppm}) = 1.4$ ppm corresponding to the product **5b** could be observed next to the signals of **2** and **Iso-2a** (Figure SI 5.11). $^{31}\text{P}\{^1\text{H}\}$ NMR monitoring at 60 °C showed that **2** and **Iso-2a** convert quite selectively to the product **5b** (accompanied by generation of only 5% of **6**) within three hours (Figure SI 5.11), with no other observable intermediates. Notably, when the same alkyne was added to compound **6** at room temperature no reaction occurred, even upon heating to 60 °C. Thus, **6** does not appear to be an intermediate during the formation of **5a-5c**, but rather a competitive side-product that forms selectively in the absence of alkyne (Figure 5.10, see Figure S114 in SI, and the discussion in the SI for further details). Based on the structures of products **5** and **6**, it was anticipated that the observed reactivity might be proceeding through the isomeric form of **2**, **Iso-2c** (*vide supra*), in which the $\text{B}(\text{C}_6\text{F}_5)_2$ has migrated fully to the 'ortho' position of the phosphorus heterocycle. This proposal is supported by DFT calculations which show that, following isomerization to this 'open' form, a subsequent 1,2-phenyl migration can occur *via* **TS_{2cD}** ($\Delta G = 25 \text{ kcal}\cdot\text{mol}^{-1}$), which is accessible at elevated temperatures. This results in a zwitterionic methylphosphinium borate species **Int-D**. The alkyne subsequently adds to **Int-D** in a 1,4-manner forming **5a**,^[23] in a step that can formally be considered as a hetero-Diels-Alder reaction. Alternatively, this step can be viewed as another FLP type reaction, in which the conjugated phosphorus heterocycle provides both the Lewis acidic and basic sites (*c.f.* **G**, Figure 5.1) needed to activate the alkyne. In this interpretation it is expected that the aryl-substituted carbon atom from the phenylacetylene derivative should end up bound to the formally Lewis basic fragment of the FLP,^[22b] due to better stabilisation of the positive charge that will accumulate on this carbon atom during the interaction of the alkyne with the Lewis acidic centre. Indeed, an alternative reaction pathway between **Int-D** and phenylacetylene to generate regioisomer **Int-E** was also calculated and it was found that although **Int-E** is thermodynamically slightly favoured over **5a**, the associated transition state **TS_{DE}** is significantly higher in energy than **TS_{D5a}** (+33.3 vs. +26.2 $\text{kcal}\cdot\text{mol}^{-1}$, see Figure 5.12). This implies that the phosphorus centre is the Lewis acidic site in this system, and "para-C4" is the Lewis basic site, which is consistent with the FLP type activation of dihydrogen by 1,3,5-triphosphinine derivatives.^[9] Thus, the phenyl migration that transforms **Iso-2c** into **Int-D** results in an *umpolung* effect, where the phosphorus centre changes in reactivity from nucleophilic (as observed in the activation of nitriles) to electrophilic (as observed in the activation of alkynes).

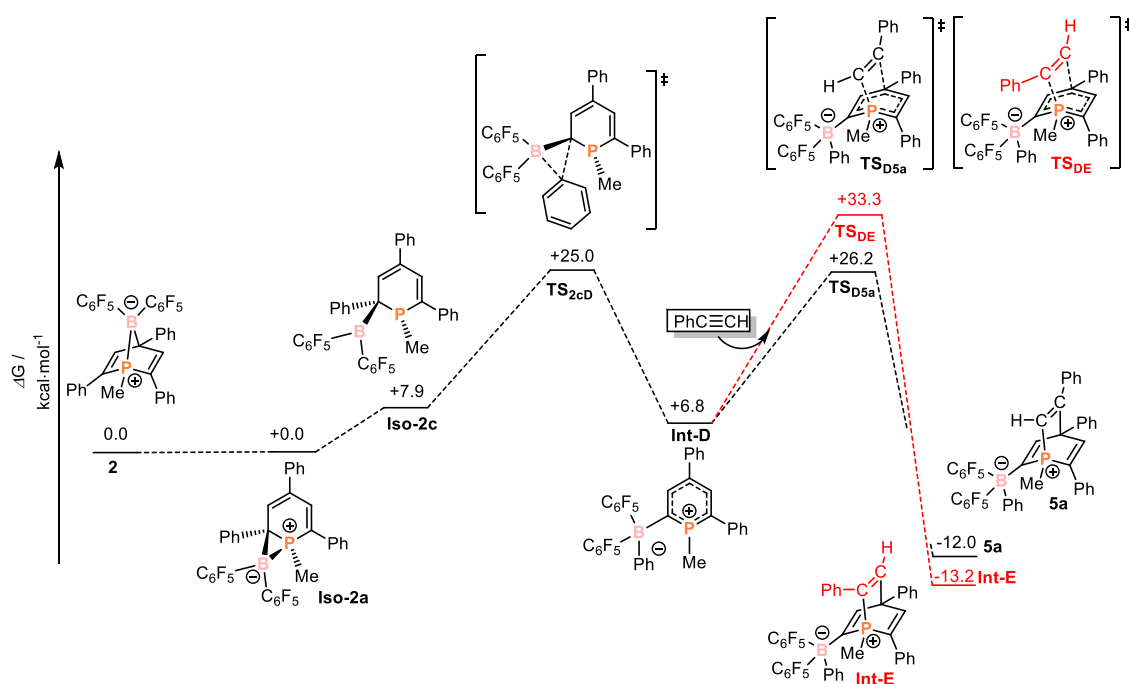


Figure 5.12 | Relative ω B97X-D/6-311+G** energies (calculated free energies ΔG in $\text{kcal}\cdot\text{mol}^{-1}$) for the conversion of **2** into **5a**.

5.4 Conclusion

The unusual compound **2** incorporating a boron atom in a phospho-norbornadiene scaffold is readily accessible by reaction of a λ^4 -phosphinine anion and a chloroborane. Even though **2** is nominally a classical Lewis acid/base adduct it shows FLP type reactivity due to its strained bicyclic structure, readily activating the $\text{C}\equiv\text{N}$ triple bonds of various nitriles. These nitriles formally insert into the P–B bond, with concomitant splitting of the B–C bond, and ultimately connect to the resulting $\text{B}(\text{C}_6\text{F}_5)_2$ moiety in a linear fashion (**3a–3e**) unless an additional donor functionality is also present (as in **4**). DFT calculations revealed that these reactions proceed *via* a low energy ring-opening of the bridging norbornadiene P–B bond. Conversely, reactions of **2** with phenylacetylene derivatives afford phosphabarrelenes **5a–5c** *via* a mechanism that involves initial migration of “ $(\text{C}_6\text{F}_5)_2\text{B}$ ”, through formal insertion into a C–C bond. This work highlights the ability of seemingly classical Lewis pairs to form reactive intermediates by reversible heterolytic element-element bond dissociation, while also illustrating the ability of phosphinine-derived Lewis bases to engage in interesting FLP reactivity that is not easily accessible using more conventional λ^3, σ^3 -phosphines. The application of these principle to the activation of further small molecules is a worthwhile subject for future investigations.

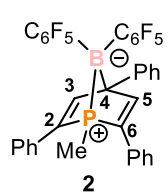
5.5 Experimental Section

All experiments were performed under an atmosphere of dry argon by using standard glovebox techniques. Diethyl ether and *n*-hexane were purified, dried, and degassed with an MBraun SPS800 solvent purification system. NMR spectra were recorded on Bruker Avance 300 MHz and Avance 400 MHz spectrometers at 300 K and a Bruker Avance III HD 600 MHz spectrometer with a fluorine selective TBIF probe at variable temperatures, internally referenced to residual solvent resonances. ^1H and $^{13}\text{C}\{^1\text{H}\}$ spectra were referenced internally to residual solvent resonances, while $^{31}\text{P}\{^1\text{H}\}$ and ^{31}P spectra were referenced externally to 85% H_3PO_4 (aq.). The assignment of ^1H and ^{13}C NMR signals was confirmed by two-dimensional (COSY, HSQC, and HMBC) experiments. For the chemical assignment 2,4,6-triphenylphosphinine will be referred to as TPP. UV/Vis spectra were recorded on a Varian Cary 50 spectrometer. Elemental analyses were determined by the analytical department of Regensburg University. Mass spectra were performed with Jeol AccuTOF GCX LIFDI-MS by the analytical Department of Regensburg University. **1** was synthesized according to a literature procedure and $(\text{C}_6\text{F}_5)_2\text{B-Cl}$ was synthesized by an unpublished procedure.^[2c] Nitriles and alkynes were purchased from Sigma-Aldrich and used as received.

X-ray Crystallography: The single-crystal X-ray diffraction data were recorded on an Agilent Technologies SuperNova and a GV1000, TitanS2 diffractometer with $\text{Cu-K}\alpha$ radiation ($\lambda = 1.54184 \text{ \AA}$). Either semi-empirical multi-scan absorption corrections^[25] or analytical ones^[26] were applied to the data. The structures were solved with SHELXT^[27] and least-square refinements on F^2 were carried out with SHELXL.^[28] The hydrogen atoms were located in idealized positions and refined isotropically with a riding model.

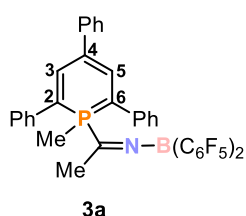
CCDC 1946109 (for **2**), CCDC 1946111 (for **3a**), CCDC 1946112 (for **3b**), CCDC 1946114 (for **3c**), CCDC 1946115 (for **4**), CCDC 1946116 (for **5b**) and CCDC 1946118 (for **5c**), contain the supplementary crystallographic data for this paper. These data can be obtained free of charge from The Cambridge Crystallographic Data Centre.

Synthesis of **2**

 $(\text{C}_6\text{F}_5)_2\text{B-Cl}$ (171 mg, 0.45 mmol, 1 equiv.) was dissolved in *n*-hexane (2 mL), cooled to $-35 \text{ }^\circ\text{C}$ and slowly added to a suspension of **1** (200 mg, 0.45 mmol, 1 equ.) cooled to $-35 \text{ }^\circ\text{C}$ in *n*-hexane (2 mL). An immediate color change from deep pink to orange was observed. The orange suspension was stirred for 15 minutes and the precipitate was separated from the solution. The bright orange solid was extracted into diethyl ether (3 x 2 mL) and the solution was reduced in volume by half. After storage at $-35 \text{ }^\circ\text{C}$, **2** was isolated as a light orange powder. Yield 107 mg, 35%. Elemental analysis calcd. for $\text{C}_{36}\text{H}_{20}\text{BF}_{10}\text{P}$ ($M_w = 684.32 \text{ g}\cdot\text{mol}^{-1}$) C 63.19, H 2.95; found C 63.12, H 3.17. UV-Vis: (*n*-hexane, $\lambda_{\text{max}} / \text{nm}$, $\epsilon_{\text{max}} / \text{L}\cdot\text{mol}^{-1}\cdot\text{cm}^{-1}$): 221 (18278), 229 (15854), 290 (5399). ^1H NMR (400.13 MHz, 300 K, C_6D_6): $\delta = 1.47$ (d, 3H, *Me*, $^2J_{\text{PH}} = 12.5$ Hz), 6.91 (m, 4H, $\text{C}^{2,6}\text{-H}$ of $\text{C}^{2,6}\text{-Ph}$), 7.04 (m, 6H, $\text{C}^{3,4,5}\text{-H}$ of $\text{C}^{2,6}\text{-Ph}$), 7.20 (m, 3H, $\text{C}^{2,4,6}\text{-H}$ of $\text{C}^4\text{-Ph}$), 7.27 (m, 2H, $\text{C}^{3,5}\text{-H}$ of $\text{C}^4\text{-Ph}$), 7.56 (d, 2H, $\text{C}^{3,5}\text{-H}$ of TPP, $^3J_{\text{PH}} = 35$ Hz). $^{13}\text{C}\{^1\text{H}\}$ NMR (100.61 MHz, 300 K, C_6D_6): $\delta = 1.51$ (d, *Me*-TPP,

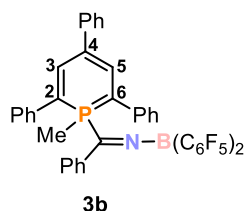
$^1J_{CP} = 25$ Hz), 64.28 (br, C^4 of TPP), 117.02 (br, C^1 of C_6F_5), 126.25 (s, C^4 of C^4-Ph), 127.19 (d, $C^{2,6}$ of $C^{2,6}-Ph$, $^3J_{CP} = 4$ Hz), 127.39 (m, $C^{2,6}$ of C^4-Ph), 128.29 (s, $C^{3,5}$ of $C^{2,6}-Ph$), 129.26 (s, C^4 of $C^{2,6}-Ph$), 134.63 (d, C^1 of $C^{2,6}-Ph$, $^2J_{CP} = 5$ Hz), 137.48 (br d, C_6F_5 , $^1J_{FC} = 250$ Hz), 137.91 (m, $C^{2,6}$ of TPP, $^1J_{CB} = 48$ Hz), 140.12 (br d, C_6F_5 , $^1J_{FC} = 260$ Hz), 143.38 (d, C^1 of C^4-Ph , J_{CF} or $J_{CB} = 14$ Hz), 147.46 (br d, C_6F_5 , $^1J_{FC} = 244$ Hz), 156.62 (d, C^3 and C^5 of TPP, $^2J_{CP} = 17$ Hz). $^{31}P\{^1H\}$ NMR (161.98 MHz, 300 K, C_6D_6): $\delta = 18.7$ (broad unresolved multiplet, the $^1J_{PB}$ could not be exactly determined to the line broadening ca. $^1J_{PB} = 60$ Hz; minor **Iso-2a** is also observed). ^{31}P NMR (161.98 MHz, 300 K, C_6D_6): $\delta = 18.6$ (br m). $^{11}B\{^1H\}$ NMR (128.38 MHz, 300 K, C_6D_6): $\delta = 14.2$ (br s). ^{11}B NMR (128.38 MHz, 300 K, C_6D_6): $\delta = 14.1$ (bs). $^{19}F\{^1H\}$ NMR (376.66 MHz, 300 K, C_6D_6): $\delta = -156.39$ (m, 4F), -163.01 (m, 6F). MS (LIFDI, toluene): m/z (%) = 684.10 M^+ (**2**); 339.12 ([1-Me-P($C_5H_2Ph_3$)]).

Synthesis of 3a-3e



Acetonitrile (μ L, 0.059 mmol, 1 equiv.) was added to a solution of **2** (40 mg, 0.059 mmol, 1 equiv.) in diethylether (1 mL) at room temperature. An immediate color change from orange to deep green was observed. The reaction mixture was stirred for 15 minutes, the solvent was completely removed, and the dark green oily residue was extracted with *n*-pentane (2 x 2 mL). After reducing the solution to half

and storage at room temperature for 1 hour, **3a** could be isolated as dark green needles. Yield: 14 mg (33%). Elemental analysis calcd. for $C_{38}H_{20}BF_{10}NP$ ($M_w = 725.38$ g·mol $^{-1}$) C 62.92, H 3.20, N 1.93; found: C 63.28, H 3.31, N 1.42. UV-Vis: (*n*-hexane, λ_{max} / nm, ϵ_{max} / L·mol $^{-1}$ ·cm $^{-1}$): 224 (41862), 253 (33000), 320sh (11060). 1H NMR (400.13 MHz, 300 K, C_6D_6): $\delta = 1.74$ (d, 3H, $^2J_{PH} = 13$ Hz, *Me*-TPP), 2.09 (d, 3H, $^3J_{PH} = 8$ Hz, *Me*CN), 6.94 – 7.13 (m, 11H, $H_{aromatic}$), 7.27 (m, 2H, $H_{aromatic}$), 7.41 (m, 2H, $H_{aromatic}$), 7.63 (s, 1H, $H_{aromatic}$), 7.70 (s, 1H, $H_{aromatic}$). $^{13}C\{^1H\}$ NMR (100.61 MHz, 300 K, C_6D_6): $\delta = 9.00$ (d, *Me*-TPP, $^1J_{CP} = 69$ Hz), 24.43 (d, *Me*CN, $^2J_{CP} = 29$ Hz), 82.00, 114.39, 124.50, 125.74, 126.97, 128.59, 128.68, 137.30, 139.36, 140.15, 142.75, 147.50, 156.87; 12 $^{13}C\{^1H\}$ NMR signals are missing. $^{31}P\{^1H\}$ NMR (161.98 MHz, 300 K, C_6D_6): $\delta = 0.6$ (s). ^{31}P NMR (161.98 MHz, 300 K, C_6D_6): $\delta = 0.6$ (m). $^{11}B\{^1H\}$ NMR (128.38 MHz, 300 K, C_6D_6): $\delta = 21.92$ (br). ^{11}B NMR (128.38 MHz, 300 K, C_6D_6): $\delta = 21.4$ (br s). $^{19}F\{^1H\}$ NMR (376.66 MHz, 300 K, C_6D_6): $\delta = -131.81$ (m, 4F), -151.07 (m, 2 F), -161.51 (m, 4F).

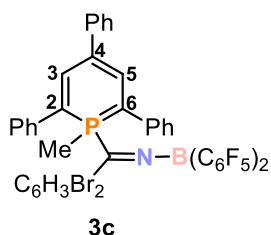


Benzonitrile (7.5 μ L, 0.073 mmol, 1 equiv.) was added to a solution of **2** (50 mg, 0.073 mmol, 1 equiv.) in diethyl ether (1 mL) at room temperature. An immediate color change from orange to deep green was observed. The reaction mixture was stirred for 15 minutes, the solvent was completely removed, and the dark green oily residue was extracted with *n*-pentane (3 x 2 mL). After reducing the solution to half

and storage at -35 °C for 1 hour, **3b** could be isolated as dark green needles. Yield: 37 mg (64%). Elemental analysis calcd. for $C_{43}H_{25}BF_{10}NP$ ($M_w = 787.45$ g·mol $^{-1}$) C 65.59, H 3.20, N 1.78; found: C 65.33, H 3.34, N 1.80. UV-Vis: (*n*-hexane, λ_{max} / nm, ϵ_{max} / L·mol $^{-1}$ ·cm $^{-1}$): 259 (12766), 320sh (3979). 1H NMR (400.13 MHz, 300 K, C_6D_6): $\delta = 2.00$ (d, 3H, $^2J_{PH} = 13$ Hz, *Me*-TPP), 6.89 – 7.11 (m, 15H, $H_{aromatic}$), 7.26 (m,

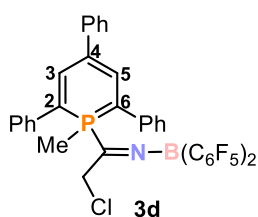
5 1-PHOSPHA-7-BORA-NORBORNADIENE

2H, H_{aromatic}), 7.38 (m, 2H, H_{aromatic}), 7.50 (s, 1H, H_{aromatic}), 7.59 (s, 1H, H_{aromatic}), 7.94 (d, 1H, H_{aromatic}). $^{13}\text{C}\{^1\text{H}\}$ NMR (100.61 MHz, 300 K, C_6D_6): δ = 12.10 (d, Me-TPP , $^1J_{\text{CP}} = 77$ Hz), 85.55, 108.11, 115.10, 124.89, 125.10, 126.37, 128.82, 128.99, 129.44, 129.69, 131.95, 132.39, 132.65, 132.96, 137.65, 139.69, 140.16, 140.29, 147.96, 151.26; 21 $^{13}\text{C}\{^1\text{H}\}$ NMR signals are missing. $^{31}\text{P}\{^1\text{H}\}$ NMR (161.98 MHz, 300 K, C_6D_6): δ = -0.1 (s). ^{31}P NMR (161.98 MHz, 300 K, C_6D_6): δ = -0.1 (m). $^{11}\text{B}\{^1\text{H}\}$ NMR (128.38 MHz, 300 K, C_6D_6): δ = 23.02 (bs). ^{11}B NMR (128.38 MHz, 300 K, C_6D_6): δ = 23.18 (br s). $^{19}\text{F}\{^1\text{H}\}$ NMR (376.66 MHz, 300 K, C_6D_6): δ = -131.26 (m, 4F), -151.01 (m, 2 F), -161.19 (m, 4F).



3,5-Dibromobenzonitrile (19 mg, 0.073 mmol, 1 equiv.) was added to a solution of **2** (50 mg, 0.073 mmol, 1 equiv.) in diethyl ether (1 mL) at room temperature. An immediate color change from orange to deep green was observed. The reaction mixture was stirred for 15 minutes, the solvent was completely removed, and the dark green oily residue was extracted with *n*-hexane (2 mL).

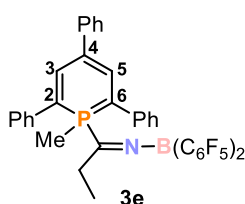
After reducing the solution to half and storage at room temperature, **3c** could be isolated as dark green crystals. Yield: 30 mg (43%). Elemental analysis calcd. for $\text{C}_{43}\text{H}_{23}\text{BBr}_2\text{F}_{10}\text{NP}$ ($M_w = 945.24 \text{ g}\cdot\text{mol}^{-1}$) C 54.64, H 2.45, N 1.48; found: C 53.99, H 2.58, N 1.39. UV-Vis: (*n*-hexane, λ_{max} / nm, ϵ_{max} / $\text{L}\cdot\text{mol}^{-1}\cdot\text{cm}^{-1}$): 260 (14990), 310sh (7040), 432 (2230). ^1H NMR (400.13 MHz, 300 K, C_6D_6): δ = 2.12 (d, 3H, $^2J_{\text{PH}} = 13$ Hz, Me-TPP), 7.08 – 7.13 (m, 2H, H_{aromatic}), 7.15 (s, 4H, H_{aromatic}), 7.31 – 7.34 (m, 3H, H_{aromatic}), 7.45 – 7.50 (m, 3H, H_{aromatic}), 7.68 (m, 2H, H_{aromatic}), 7.73 (s, 1H, H_{aromatic}), 7.81 (s, 1H, H_{aromatic}), 8.19 (s, 1H, H_{aromatic}). $^{13}\text{C}\{^1\text{H}\}$ NMR (100.61 MHz, 300 K, C_6D_6): δ = 11.54 (d, Me-TPP , $^1J_{\text{CP}} = 77$ Hz), 84.93, 115.74, 124.15, 124.89, 125.33, 126.28, 128.56, 128.61, 130.93, 137.26, 137.94, 138.94, 142.24, 140.14, 147.52, 148.24; 25 $^{13}\text{C}\{^1\text{H}\}$ NMR signals are missing. $^{31}\text{P}\{^1\text{H}\}$ NMR (161.98 MHz, 300 K, C_6D_6): δ = 0.6 (s). ^{31}P NMR (161.98 MHz, 300 K, C_6D_6): δ = 0.6 (m). $^{11}\text{B}\{^1\text{H}\}$ NMR (128.38 MHz, 300 K, C_6D_6): δ = 23.3 (br s). ^{11}B NMR (128.38 MHz, 300 K, C_6D_6): δ = 23.6 (br s). $^{19}\text{F}\{^1\text{H}\}$ NMR (376.66 MHz, 300 K, C_6D_6): δ = -131.29 (m, 4F), -150.18 (m, 2F), -160.82 (m, 4F).



2-Chloroacetonitrile (4.6 μL , 0.073 mmol, 1 equiv.) was added to a solution of **2** (50 mg, 0.073 mmol, 1 equiv.) in diethylether (1 mL) at room temperature. An immediate color change from orange to deep green was observed. The reaction mixture was stirred for 15 minutes, the solvent was completely removed, and the dark green oily residue was extracted with *n*-hexane (3 x 2 mL).

After reducing the solution to half and storage at room temperature, **3d** could be isolated as dark green solid. Yield: 22 mg (39%). Elemental analysis calcd. for $\text{C}_{38}\text{H}_{22}\text{BClF}_{10}\text{NP}$ ($M_w = 759.82 \text{ g}\cdot\text{mol}^{-1}$) C 60.07, H 2.92, N 1.84; found: C 60.46, H 3.27, N 1.23. UV-Vis: (*n*-hexane, λ_{max} / nm, ϵ_{max} / $\text{L}\cdot\text{mol}^{-1}\cdot\text{cm}^{-1}$): 248 (22550), 307 (13470), 416 (6130). ^1H NMR (400.13 MHz, 300 K, C_6D_6): δ = 1.78 (d, 3H, $^2J_{\text{PH}} = 13$ Hz, Me-TPP), 4.25 (s, CH_2CN), 6.97 – 7.13 (m, 11H, H_{aromatic}), 7.28 (m, 2H, H_{aromatic}), 7.36 (m, 2H, H_{aromatic}), 7.55 (s, 1H, H_{aromatic}), 7.63 (s, 1H, H_{aromatic}). $^{13}\text{C}\{^1\text{H}\}$ NMR (100.61 MHz, 300 K, C_6D_6): δ = 10.05 (d, Me-TPP , $^1J_{\text{CP}} = 70$ Hz), 45.78 (d, CH_2Cl , $^2J_{\text{CP}} = 42$ Hz), 81.91, 114.97, 124.63, 124.75, 126.08, 126.91, 128.73, 137.19, 138.76, 139.86, 140.13, 147.80, 153.86; 23 $^{13}\text{C}\{^1\text{H}\}$ NMR signals are missing. $^{31}\text{P}\{^1\text{H}\}$ NMR (161.98 MHz, 300 K, C_6D_6): δ = -1.0 (s).

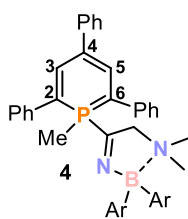
^{31}P NMR (161.98 MHz, 300 K, C_6D_6): $\delta = -1.0$ (m). $^{11}\text{B}\{^1\text{H}\}$ NMR (128.38 MHz, 300 K, C_6D_6): $\delta = 25.8$ (br s). ^{11}B NMR (128.38 MHz, 300 K, C_6D_6): $\delta = 25.8$ (br s). $^{19}\text{F}\{^1\text{H}\}$ NMR (376.66 MHz, 300 K, C_6D_6): $\delta = -131.13$ (m, 4F), -150.22 (m, 2 F), -161.29 (m, 4F).



Propionitrile (5.1 μL , 0.073 mmol, 1 equiv.) was added to a solution of **2** (50 mg, 0.073 mmol, 1 equiv.) in diethylether (1 mL) at room temperature. An immediate colour change from orange to deep green was observed. The reaction mixture was stirred for 15 minutes, the solvent was completely removed, and the dark green oily residue was extracted with *n*-hexane (2 mL). After reducing the solution to half

and storage at room temperature, **3e** was isolated as dark green crystals. Yield: 22 mg (41%). Elemental analysis calcd. for $\text{C}_{39}\text{H}_{25}\text{BF}_{10}\text{NP}$ ($M_w = 739.40 \text{ g}\cdot\text{mol}^{-1}$) C 63.35, H 3.41, N 1.89; found: C 62.43, H 3.41, N 1.39. UV-Vis: (*n*-hexane, λ_{max} / nm, ϵ_{max} / $\text{L}\cdot\text{mol}^{-1}\cdot\text{cm}^{-1}$): 259 (12766), 320sh (3979). ^1H NMR (400.13 MHz, 300 K, C_6D_6): $\delta = 0.93$ (t, 3H, CH_2CH_3 , $^3J_{\text{HH}} = 7$ Hz), 1.89 (d, 3H, $^2J_{\text{PH}} = 13$ Hz, *Me*-TPP), 2.65 (dq, 2H, CH_2CH_3 , $^3J_{\text{HH}} = 7$ Hz, $^3J_{\text{PH}} = 2.7$ Hz), 7.06 – 7.23 (m, 11H, H_{aromatic}), 7.38 (m, 2H, H_{aromatic}), 7.53 (m, 2H, H_{aromatic}), 7.76 (s, 1H, H_{aromatic}), 7.84 (s, 1H, H_{aromatic}). $^{13}\text{C}\{^1\text{H}\}$ NMR (100.61 MHz, 300 K, C_6D_6): $\delta = 7.95$ (d, CH_2CH_3 , $^3J_{\text{CP}} = 5$ Hz), 8.84 (d, *Me*-TPP, $^1J_{\text{CP}} = 69$ Hz), 29.56 (d, CH_2CH_3 , $^2J_{\text{CH}} = 27$ Hz), 82.22, 107.9, 114.22, 124.45, 124.48, 125.78, 126.99, 128.59, 128.69, 137.24, 139.35, 139.94, 142.00, 142.76, 147.55, 161.49; 20 $^{13}\text{C}\{^1\text{H}\}$ NMR signals are missing. $^{31}\text{P}\{^1\text{H}\}$ NMR (161.98 MHz, 300 K, C_6D_6): $\delta = 0.1$ (s). ^{31}P NMR (161.98 MHz, 300 K, C_6D_6): $\delta = 0.1$ (m). $^{11}\text{B}\{^1\text{H}\}$ NMR (128.38 MHz, 300 K, C_6D_6): $\delta = 23.2$ (br s). ^{11}B NMR (128.38 MHz, 300 K, C_6D_6): $\delta = 23.2$ (br s). $^{19}\text{F}\{^1\text{H}\}$ NMR (376.66 MHz, 300 K, C_6D_6): $\delta = -131.71$ (m, 4F), -151.15 (m, 2 F), -161.43 (m, 4F).

Synthesis of 4



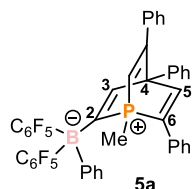
2-(dimethylamino)acetone (7.1 μL , 0.073 mmol, 1 equiv.) was added to a solution of **2** (50 mg, 0.073 mmol, 1 equiv.) in diethylether (1 mL) at room temperature. An immediate color change from orange to deep pink was observed. The reaction mixture was stirred for 15 minutes, while a suspension with a pink solid was formed. The solution was decanted and the pink solid was washed with *n*-hexane (2 x 2 mL). **4** was

isolated as a pink crystalline powder after drying under vacuum. Yield: 28 mg (50%). Elemental analysis calcd. for $\text{C}_{40}\text{H}_{28}\text{BF}_{10}\text{N}_2\text{P}$ ($M_w = 768.45 \text{ g}\cdot\text{mol}^{-1}$) C 62.52, H 3.67, N 3.65; found: C 62.41, H 3.60, N 3.49. UV-Vis: (diethyl ether, λ_{max} / nm, ϵ_{max} / $\text{L}\cdot\text{mol}^{-1}\cdot\text{cm}^{-1}$): 260sh (17060), 316 (17420), 411 (4100), 523 (6644). ^1H NMR (400.13 MHz, 300 K, C_6D_6): $\delta = 1.39$ (s, 6H, $\text{Me}_2\text{NCH}_2\text{CN}$), 2.05 (d, 3H, $^2J_{\text{PH}} = 13$ Hz, *Me*-TPP), 3.43 (s, 2H, $\text{Me}_2\text{NCH}_2\text{CN}$), 6.97 – 7.00 (m, 2H, H_{aromatic}), 7.13 (m, 1H, H_{aromatic}), 7.17 (m, 4H, H_{aromatic}), 7.34 – 7.39 (m, 6H, H_{aromatic}), 7.67 (m, 2H, H_{aromatic}), 7.96 (s, 1H, H_{aromatic}), 8.03 (s, 1H, H_{aromatic}). $^{13}\text{C}\{^1\text{H}\}$ NMR (100.61 MHz, 300 K, C_6D_6): $\delta = 12.68$ (d, *Me*-TPP, $^1J_{\text{CP}} = 60$ Hz), 48.80 (s, CH_3 of NMe_2), 73.10 (br d, $\text{Me}_2\text{NCH}_2\text{CN}$, $^2J_{\text{CP}} = 40$ Hz), 82.08, 113.76, 124.25, 124.43, 124.98, 125.61, 128.59, 128.81, 137.40, 137.47, 140.38, 143.45, 147.95, 165.69; 23 $^{13}\text{C}\{^1\text{H}\}$ NMR signals are missing. $^{31}\text{P}\{^1\text{H}\}$ NMR (161.98 MHz, 300 K, C_6D_6): $\delta = -9.2$ (s). ^{31}P NMR (161.98 MHz, 300 K, C_6D_6): $\delta = -9.2$ (m). $^{11}\text{B}\{^1\text{H}\}$ NMR (128.38 MHz,

5 1-PHOSPHA-7-BORA-NORBORNADIENE

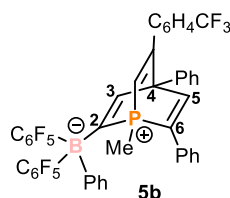
300 K, C₆D₆): $\delta = 11.5$ (br s). ¹¹B NMR (128.38 MHz, 300 K, C₆D₆): $\delta = 11.3$ (br s). ¹⁹F{¹H} NMR (376.66 MHz, 300 K, C₆D₆): $\delta = -128.79$ (m, 4F), -154.91 (m, 2F), -162.45 (m, 4F).

Synthesis of 5a–5c



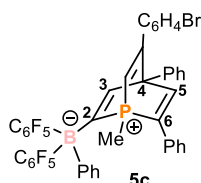
Phenylacetylene (16 μ L, 0.146 mmol, 1 equiv.) was added to a solution of **2** (100 mg, 0.146 mmol, 1 equiv.) in benzene (2 mL), the mixture was warmed up to 60 °C overnight. A colour change from orange to deep red was observed. After cooling down to room temperature, the solvent was completely removed. The remaining oily residue

was triturated with *n*-hexane (2 mL). After drying under vacuum, **5a** was isolated as a light red powder. Yield: 70 mg (61%). Elemental analysis calcd. for C₄₄H₂₆BF₁₀P (Mw = 786.46 g·mol⁻¹) C 67.20, H 3.33; found: C 66.52, H 3.51. UV-Vis: (diethyl ether, λ_{\max} / nm, ϵ_{\max} / L·mol⁻¹·cm⁻¹): 451 (414). ¹H NMR (400.13 MHz, 300 K, C₆D₆): $\delta = 1.20$ (d, 3H, ²J_{PH} = 15 Hz, *Me*-TPP), 6.05 (d, 1H, ²J_{PH} = 22 Hz, *HCCPh*), 6.36 (m, 2H, *H_{aromatic}*), 6.58 (m, 2H, *H_{aromatic}*), 6.76–6.87 (m, 5H, *H_{aromatic}*), 7.02–7.18 (m, 7H, *H_{aromatic}*), 7.36 (m, 2H, *H_{aromatic}*), 7.58 (s, 1H, *H_{aromatic}*), 7.65 (s, 1H, *H_{aromatic}*). ¹³C{¹H} NMR (100.61 MHz, 300 K, C₆D₆): $\delta = -0.33$ (d, *Me*-TPP, ¹J_{CP} = 52 Hz), 66.35 (d, *HCCPh*, ²J_{CP} = 45 Hz), 120.78 (d, *HCCPh*, ¹J_{CP} = 67 Hz), 125.09, 127.20, 128.14, 128.53, 128.70, 128.76, 128.96, 132.05, 134.99, 136.90, 139.46, 148.25, 150.38; 28 ¹³C{¹H} NMR signals are missing. ³¹P{¹H} NMR (161.98 MHz, 300 K, C₆D₆): $\delta = 1.70$ (s). ³¹P NMR (161.98 MHz, 300 K, C₆D₆): $\delta = 1.67$ (s). ¹¹B{¹H} NMR (128.38 MHz, 300 K, C₆D₆): $\delta = -11.16$ (s). ¹¹B NMR (128.38 MHz, 300 K, C₆D₆): $\delta = -11.18$ (s). ¹⁹F{¹H} NMR (376.66 MHz, 300 K, C₆D₆): $\delta = -128.18$ (m, 4F), -159.44 (m, 2F), -164.02 (m, 4F).



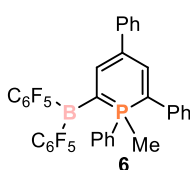
4-(Trifluoromethyl)phenylacetylene (24 μ L, 0.146 mmol, 1 equiv.) was added to a solution of **2** (100 mg, 0.146 mmol, 1 equiv.) in benzene (2 mL), the mixture was warmed up to 60 °C overnight. A colour change from orange to deep red was observed. After cooling down to room temperature, the solvent was completely removed. The remaining oily residue was triturated with *n*-hexane (2 mL). After

drying under vacuum, **5b** was isolated as a light red powder. Yield: 77 mg (62%). Elemental analysis calcd. for C₄₅H₂₅BF₁₃P (Mw = 854.46 g·mol⁻¹) C 63.26, H 2.95; found: C 63.58, H 3.30. UV-Vis: (diethyl ether, λ_{\max} / nm, ϵ_{\max} / L·mol⁻¹·cm⁻¹): 467 (431). ¹H NMR (400.13 MHz, 300 K, C₆D₆): $\delta = 1.19$ (s, 3H, *Me*-TPP), 6.00 (d, 1H, ²J_{PH} = 23 Hz, *HCCC6H4CF3*), 6.35 (m, 2H, *H_{aromatic}*), 6.46 (m, 2H, *H_{aromatic}*), 6.74–6.82 (m, 3H, *H_{aromatic}*), 6.98–7.17 (m, 9H, *H_{aromatic}*), 7.33 (m, 2H, *H_{aromatic}*), 7.50 (s, 1H, *H_{aromatic}*), 7.58 (s, 1H, *H_{aromatic}*). ¹³C{¹H} NMR (100.61 MHz, 300 K, C₆D₆): $\delta = -0.33$ (d, *Me*-TPP, ¹J_{CP} = 52 Hz), 66.01, 122.37, 124.51, 125.19, 125.40, 128.49, 128.69, 128.84, 129.15, 129.92, 130.25, 131.77, 135.00, 138.79, 140.34, 141.25, 148.27, 150.00, 171.76; 25 ¹³C{¹H} NMR signals are missing. ³¹P{¹H} NMR (161.98 MHz, 300 K, C₆D₆): $\delta = 2.07$ (s). ³¹P NMR (161.98 MHz, 300 K, C₆D₆): $\delta = 2.07$ (s). ¹¹B{¹H} NMR (128.38 MHz, 300 K, C₆D₆): $\delta = -11.16$ (s). ¹¹B NMR (128.38 MHz, 300 K, C₆D₆): $\delta = -11.17$ (s). ¹⁹F{¹H} NMR (376.66 MHz, 300 K, C₆D₆): $\delta = -62.68$ (s, 3F, *CF3*), -128.39 (m, 2F, C₆F₅), -159.12 (m, 2F, C₆F₅), -163.94 (m, 4F, C₆F₅).



4-Bromophenylacetylene (26 mg, 0.146 mmol, 1 equiv.) was added to a solution of **2** (100 mg, 0.146 mmol, 1 equiv.) in benzene (2 mL), the mixture was warmed up to 60 °C overnight. A color change from orange to deep red was observed. After cooling down to room temperature, the solvent was completely removed. The remaining oily residue was triturated with *n*-hexane (2 mL). After drying under vacuum, **5c** was isolated as a light red powder. Yield: 91 mg (72%). Elemental analysis calcd. for $C_{44}H_{25}BBrF_{10}P$ ($M_w = 865.36 \text{ g}\cdot\text{mol}^{-1}$) C 61.07, H 2.91; found: C 64.45, H 3.42. UV-Vis: (diethyl ether, $\lambda_{\text{max}} / \text{nm}$, $\epsilon_{\text{max}} / \text{L}\cdot\text{mol}^{-1}\cdot\text{cm}^{-1}$): 470 (500). ^1H NMR (400.13 MHz, 300 K, C_6D_6): $\delta = 1.19$ (s, 3H, *Me*-TPP), 5.98 (d, 1H, $^2J_{\text{PH}} = 23 \text{ Hz}$, *HCCC* $_6\text{H}_4\text{Br}$), 6.27 (m, 2H, H_{aromatic}), 6.34 (m, 2H, H_{aromatic}), 6.77–6.82 (m, 3H, H_{aromatic}), 6.95 (m, 3H, H_{aromatic}), 7.00–7.08 (m, 6H, H_{aromatic}), 7.33 (m, 2H, H_{aromatic}), 7.51 (s, 1H, H_{aromatic}), 7.58 (s, 1H, H_{aromatic}). $^{13}\text{C}\{^1\text{H}\}$ NMR (100.61 MHz, 300 K, C_6D_6): $\delta = -0.31$ (d, *Me*-TPP, $^1J_{\text{CP}} = 53 \text{ Hz}$), 66.03, 121.26, 122.75, 125.15, 128.59, 128.69, 128.80, 129.07, 130.86, 131.46, 131.87, 133.38, 135.00, 135.58, 135.71, 139.05, 148.36, 150.00, 172.24; 24 $^{13}\text{C}\{^1\text{H}\}$ NMR signals are missing. $^{31}\text{P}\{^1\text{H}\}$ NMR (161.98 MHz, 300 K, C_6D_6): $\delta = 1.92$ (s). ^{31}P NMR (161.98 MHz, 300 K, C_6D_6): $\delta = 1.94$ (s). $^{11}\text{B}\{^1\text{H}\}$ NMR (128.38 MHz, 300 K, C_6D_6): $\delta = -11.15$ (s). ^{11}B NMR (128.38 MHz, 300 K, C_6D_6): $\delta = -11.16$ (s). $^{19}\text{F}\{^1\text{H}\}$ NMR (376.66 MHz, 300 K, C_6D_6): $\delta = -128.09$ (m, 2F), -159.25 (m, 2F), -164.01 (m, 4F).

Synthesis of 6



2 (50 mg, 0.073 mmol) was dissolved in benzene (0.5 mL) and heated to 60 °C over two days. The solvent of the deep red reaction mixture was completely evaporated, and the remaining red oily residue was extracted with *n*-hexane (2 x 2 mL). After slow evaporation at room temperature and recrystallization from *n*-hexane, **6** could be isolated as deep red crystalline solid. Yield 18 mg, 36%. Elemental analysis calcd. for $C_{36}H_{20}BF_{10}P$ ($M_w = 684.32 \text{ g}\cdot\text{mol}^{-1}$) C 63.19, H 2.95; found C 63.54, H 3.17. UV-Vis: (diethyl ether, $\lambda_{\text{max}} / \text{nm}$, $\epsilon_{\text{max}} / \text{L}\cdot\text{mol}^{-1}\cdot\text{cm}^{-1}$): 270 (22251), 490 (9017). ^1H NMR (400.13 MHz, 300 K, C_6D_6): $\delta = 1.65$ (d, 3H, $^2J_{\text{PH}} = 14 \text{ Hz}$), 6.96 (m, 9H, H_{aromatic}), 7.11 (m, 2H, H_{aromatic}), 7.33 (m, 2H, H_{aromatic}), 7.54 (m, 3H, H_{aromatic}), 8.04 (bd, 1H, H_{aromatic}). $^{13}\text{C}\{^1\text{H}\}$ NMR (100.61 MHz, 300 K, C_6D_6): $\delta = 125.37$, 125.72, 126.84, 126.88, 128.73, 128.88, 128.94, 137.72, 137.74, 142.25, 146.42, 146.49, 146.60; 23 $^{13}\text{C}\{^1\text{H}\}$ NMR signals are missing. $^{31}\text{P}\{^1\text{H}\}$ NMR (161.98 MHz, 300 K, C_6D_6): $\delta = 1.7$ (s). ^{31}P NMR (161.98 MHz, 300 K, C_6D_6): $\delta = 1.8$. $^{11}\text{B}\{^1\text{H}\}$ NMR (128.38 MHz, 300 K, C_6D_6): $\delta = 54.2$ (br s). ^{11}B NMR (128.38 MHz, 300 K, C_6D_6): $\delta = 54.4$ (br s). $^{19}\text{F}\{^1\text{H}\}$ NMR (376.66 MHz, 300 K, C_6D_6): $\delta = -129.3$ (m), -130.3 (s), -133 (m), -144.7 (m), -154.8 (m), -159.5 (s), -160.8 (s), -161.9 (s), -162.7 (s). MS (LIFDI, toluene): m/z (%) = 684.14 M^+ (**6**).

5.6 Acknowledgements

Funding by the Deutsche Forschungsgemeinschaft (WO1496/9 1 and MU1657/5-1) is gratefully acknowledged. JCS and DJS acknowledge the Alexander von Humboldt Foundation for Humboldt Research Fellowships. ARJ is grateful for the support of a Veni grant from the Netherlands Organisation for Scientific Research (NWO).

5.7 References

- [1] a) G. Märkl, *Angew. Chem.* **1966**, *78*, 907–908. b) A. Moores, L. Ricard, P. Le Floch, N. Mézailles, *Organometallics* **2003**, *22*, 1960–1966. c) A. J. Ashe, *Acc. Chem. Res.* **1978**, *11*, 153–157. d) A. J. Ashe, T. W. Smith, *Tetrahedron Lett.* **1977**, *18*, 407–410.
- [2] a) G. Märkl, A. Merz, *Tetrahedron Lett.* **1968**, *9*, 3611–3614. b) G. Märkl, A. Merz, *Tetrahedron Lett.* **1971**, *12*, 1215–1218. c) G. Märkl, F. Lieb, A. Merz, *Angew. Chem. Int. Ed. Engl.* **1967**, *6*, 87–88.
- [3] a) G. Märkl, C. Martin, W. Weber, *Tetrahedron Lett.* **1981**, *22*, 1207–1210. b) M. Bruce, G. Meissner, M. Weber, J. Wiecko, C. Müller, *Eur. J. Inorg. Chem.* **2014**, *2014*, 1719–1726.
- [4] a) A. Moores, N. Mézailles, L. Ricard, Y. Jean, P. le Floch, *Organometallics* **2004**, *23*, 2870–2875. b) A. Moores, N. Mézailles, L. Ricard, P. Le Floch, *Organometallics* **2005**, *24*, 508–513. c) M. Dochnahl, M. Doux, E. Faillard, L. Ricard, P. L. Floch, *Eur. J. Inorg. Chem.* **2005**, *2005*, 125–134. d) M. Bruce, *Doctoral Thesis*, Freie Universität Berlin, Berlin, **2016**. e) M. Doux, N. Mézailles, M. Melaimi, L. Ricard, P. Le Floch, *Chem. Commun.* **2002**, 1566–1567.
- [5] a) B. Rezaei Rad, U. Chakraborty, B. Mühldorf, J. A. W. Sklorz, M. Bodensteiner, C. Müller, R. Wolf, *Organometallics* **2015**, *34*, 622–635. b) C. M. Hoidn, R. Wolf, *Dalton Trans.* **2016**, *45*, 8875–8884. c) C. M. Hoidn, J. Leitl, C. G. P. Ziegler, I. G. Shenderovich, R. Wolf, *Eur. J. Inorg. Chem.* **2019**, *2019*, 1567–1574.
- [6] D. W. Stephan, *J. Am. Chem. Soc.* **2015**, *137*, 10018–10032.
- [7] G. C. Welch, R. R. San Juan, J. D. Masuda, D. W. Stephan, *Science* **2006**, *314*, 1124–1126.
- [8] a) R. Liu, X. Liu, K. Ouyang, Q. Yan, *ACS Macro Lett.* **2019**, *8*, 200–204. b) C. M. Mömning, E. Otten, G. Kehr, R. Fröhlich, S. Grimme, D. W. Stephan, G. Erker, *Angew. Chem. Int. Ed.* **2009**, *48*, 6643–6646.
- [9] L. E. Longobardi, C. A. Russell, M. Green, N. S. Townsend, K. Wang, A. J. Holmes, S. B. Duckett, J. E. McGrady, D. W. Stephan, *J. Am. Chem. Soc.* **2014**, *136*, 13453–13457.
- [10] a) D. Neibecker, R. Réau, *Angew. Chem. Int. Ed. Engl.* **1989**, *28*, 500–501. b) M. Siutkowski, F. Mercier, L. Ricard, F. Mathey, *Organometallics* **2006**, *25*, 2585–2589.
- [11] a) J. H. Barnard, S. Yruegas, S. A. Couchman, D. J. D. Wilson, J. L. Dutton, C. D. Martin, *Organometallics* **2016**, *35*, 929–931. b) S. Dong, L. Wang, T. Wang, C. G. Daniliuc, M. Brinkkötter, H. Eckert, G. Kehr, G. Erker, *Dalton Trans.* **2018**, *47*, 4449–4454.

- [12] a) U. Rohde, F. Ruthe, P. G. Jones, R. Streubel, *Angew. Chem. Int. Ed.* **1999**, *38*, 215–217. b) A. Koner, B. M. Gabidullin, Z. Kelemen, L. Nyulászi, G. I. Nikonov, R. Streubel, *Dalton Trans.* **2019**, *48*, 8248–8253.
- [13] F. Mathey, *Chem. Rev.* **1988**, *88*, 429–453.
- [14] P. Pyykkö, M. Atsumi, *Chem. – Eur. J.* **2009**, *15*, 186–197.
- [15] a) F. Ge, G. Kehr, C. G. Daniliuc, G. Erker, *Organometallics* **2015**, *34*, 229–235. b) C. Fan, W. E. Piers, M. Parvez, R. McDonald, *Organometallics* **2010**, *29*, 5132–5139. c) F. Ge, G. Kehr, C. G. Daniliuc, G. Erker, *J. Am. Chem. Soc.* **2014**, *136*, 68–71.
- [16] a) C. P. Sindlinger, F. S. W. Aicher, H. Schubert, L. Wesemann, *Angew. Chem. Int. Ed.* **2017**, *56*, 2198–2202. b) J. Schneider, C. P. Sindlinger, S. M. Freitag, H. Schubert, L. Wesemann, *Angew. Chem.* **2017**, *129*, 339–343.
- [17] H. Braunschweig, J. Maier, K. Radacki, J. Wahler, *Organometallics* **2013**, *32*, 6353–6359.
- [18] P. Pyykkö, M. Atsumi, *Chem. – Eur. J.* **2009**, *15*, 12770–12779.
- [19] a) L. J. Hounjet, C. Bannwarth, C. N. Garon, C. B. Caputo, S. Grimme, D. W. Stephan, *Angew. Chem. Int. Ed.* **2013**, *52*, 7492–7495. b) R. Dobrovetsky, K. Takeuchi, D. W. Stephan, *Chem. Commun.* **2015**, *51*, 2396–2398. c) L. Wu, S. S. Chitnis, H. Jiao, V. T. Annibale, I. Manners, *J. Am. Chem. Soc.* **2017**, *139*, 16780–16790. d) R. Dobrovetsky, D. W. Stephan, *J. Am. Chem. Soc.* **2013**, *135*, 4974–4977. e) D. J. Scott, M. J. Fuchter, A. E. Ashley, *Angew. Chem. Int. Ed.* **2014**, *53*, 10218–10222.
- [20] a) K. Samigullin, I. Georg, M. Bolte, H.-W. Lerner, M. Wagner, *Chem. – Eur. J.* **2016**, *22*, 3478–3484. b) E. R. M. Habraken, L. C. Mens, M. Nieger, M. Lutz, A. W. Ehlers, J. C. Slootweg, *Dalton Trans.* **2017**, *46*, 12284–12292. c) J. Möricke, B. Wibbeling, C. G. Daniliuc, G. Kehr, G. Erker, *Philos. Trans. R. Soc. Math. Phys. Eng. Sci.* **2017**, *375*, 20170015.
- [21] a) M. Rigo, J. a. W. Sklorz, N. Hatje, F. Noack, M. Weber, J. Wiecko, C. Müller, *Dalton Trans.* **2016**, *45*, 2218–2226. b) B. Breit, E. Fuchs, *Chem. Commun.* **2004**, *0*, 694–695. c) M. Blug, C. Guibert, X.-F. Le Goff, N. Mézailles, P. Le Floch, *Chem Commun* **2008**, 201–203.
- [22] a) G. Märkl, F. Lieb, C. Martin, *Tetrahedron Lett.* **1971**, *12*, 1249–1252. b) E. Fuchs, M. Keller, B. Breit, *Chem. – Eur. J.* **2006**, *12*, 6930–6939. c) M. Rigo, E. R. M. Habraken, K. Bhattacharyya, M. Weber, A. W. Ehlers, N. Mézailles, J. C. Slootweg, C. Müller, *Chem. – Eur. J.* **2019**, *25*, 8769–8779.
- [23] A. Moores, L. Ricard, P. L. Floch, *Angew. Chem. Int. Ed.* **2003**, *42*, 4940–4944.

5 1-PHOSPHA-7-BORA-NORBORNADIENE

- [24] a) K. Chernichenko, Á. Madarász, I. Pápai, M. Nieger, M. Leskelä, T. Repo, *Nat. Chem.* **2013**, *5*, 718–723. b) C. Jiang, O. Blacque, H. Berke, *Organometallics* **2010**, *29*, 125–133. c) M. A. Dureen, C. C. Brown, D. W. Stephan, *Organometallics* **2010**, *29*, 6594–6607. d) R. L. Melen, L. C. Wilkins, B. M. Kariuki, H. Wadepl, L. H. Gade, A. S. K. Hashmi, D. W. Stephan, M. M. Hansmann, *Organometallics* **2015**, *34*, 4127–4137. e) V. Fasano, L. D. Curless, J. E. Radcliffe, M. J. Ingleson, *Angew. Chem. Int. Ed.* **2017**, *56*, 9202–9206. f) C. Chen, R. Fröhlich, G. Kehr, G. Erker, *Chem. Commun.* **2010**, *46*, 3580–3582. g) J. Li, C. G. Daniliuc, G. Kehr, G. Erker, *Chem. Commun.* **2018**, *54*, 6344–6347. h) M. A. Dureen, D. W. Stephan, *J. Am. Chem. Soc.* **2009**, *131*, 8396–8397. i) T. Wang, X. Jentgens, C. G. Daniliuc, G. Kehr, G. Erker, *ChemCatChem* **2017**, *9*, 651–658.
- [25] a) SCALE3ABS, CrysAlisPro, Agilent Technologies Inc., Oxford, GB, **2012**. b) G. M. Sheldrick, SADABS, Bruker AXS, Madison, USA, **2007**.
- [26] R. C. Clark, J. S. Reid, *Acta Crystallogr. Sect. A* **1995**, *51*, 887–897.
- [27] G. M. Sheldrick, *Acta Crystallogr. Sect. C Struct. Chem.* **2015**, *71*, 3–8.
- [28] G. M. Sheldrick, *Acta Crystallogr. A* **2008**, *64*, 112–122.

5.8 Supporting Information

The full supporting information of **Chapter 5** can be found on the supplied CD-ROM and on <https://chemistry-europe.onlinelibrary.wiley.com/doi/abs/10.1002/chem.202000266>. The supporting information contains: Experimental procedures and data, NMR and UV/Vis spectra, X-ray crystallography details and results of quantum chemical calculations including Cartesian coordinates of all optimized structures.

5.8.1 Variable temperature NMR monitoring – formation of **2**

For the $^{31}\text{P}\{^1\text{H}\}$ and $^{11}\text{B}\{^1\text{H}\}$ NMR monitoring, **1** (30 mg, 0.067 mmol, 1 equiv.) and $(\text{C}_6\text{F}_5)_2\text{BCl}$ (25 mg, 0.067 mmol, 1 equiv.) were dissolved in toluene- d_8 (0.5 mL) and loaded in a J. Young NMR tube. The sample was immediately cooled to 193 K and quickly loaded into the NMR device. $^{31}\text{P}\{^1\text{H}\}$ and $^{11}\text{B}\{^1\text{H}\}$ NMR spectra were recorded from 193 K to 300 K in a 30 minutes interval.

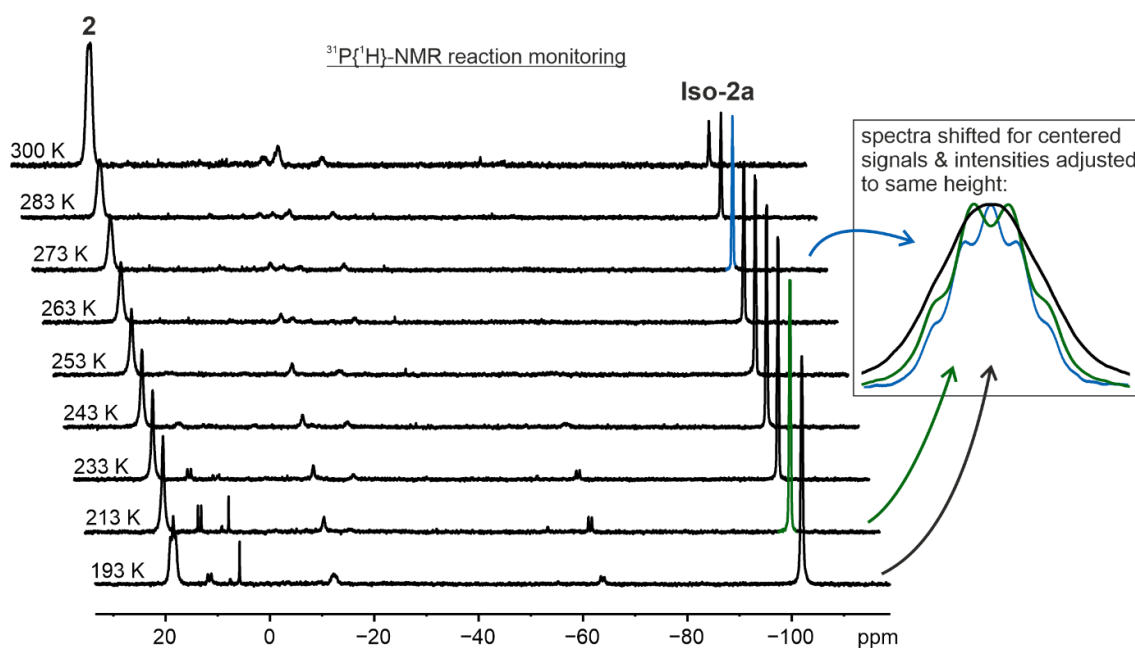


Figure SI 5.1 | $^{31}\text{P}\{^1\text{H}\}$ NMR temperature monitoring of the reaction of **1** with $(\text{C}_6\text{F}_5)_2\text{BCl}$ (161.98 MHz, toluene- d_8 , 256 scans recorded) starting from 193 K and warming up to 300 K. Formation of **2** at ca. $\delta = +18$ ppm and formation of **Iso-2a** at ca. $\delta = -101$ ppm. The spectra of 193 K, 213 K and 273 K were selected and overlaid separately in a way that the signals of **Iso-2a** are centered and adjusted in height to show that the overall signal width decreases with increasing temperature.

The shape of the ^{31}P signals of **2** and **Iso-2a** change upon temperature increase. At a temperature of 273 K, several ^1H and ^{19}F decoupling experiments were performed to investigate the line widths and the origin of the signal splitting (see Figure SI 5.1). For compound **2** no change in line width was observed upon ^1H and/or ^{19}F decoupling. This indicates a strong line broadening caused by the direct interaction with the quadrupolar isotopes ^{10}B and ^{11}B . Compound **Iso-2a** showed a quintet like splitting of its ^{31}P signal when ^1H

5 1-PHOSPHA-7-BORA-NORBORNADIENE

decoupling was applied. Further ^{19}F decoupling parallel to ^1H decoupling led to an increase in signal intensity and a decrease in line width.

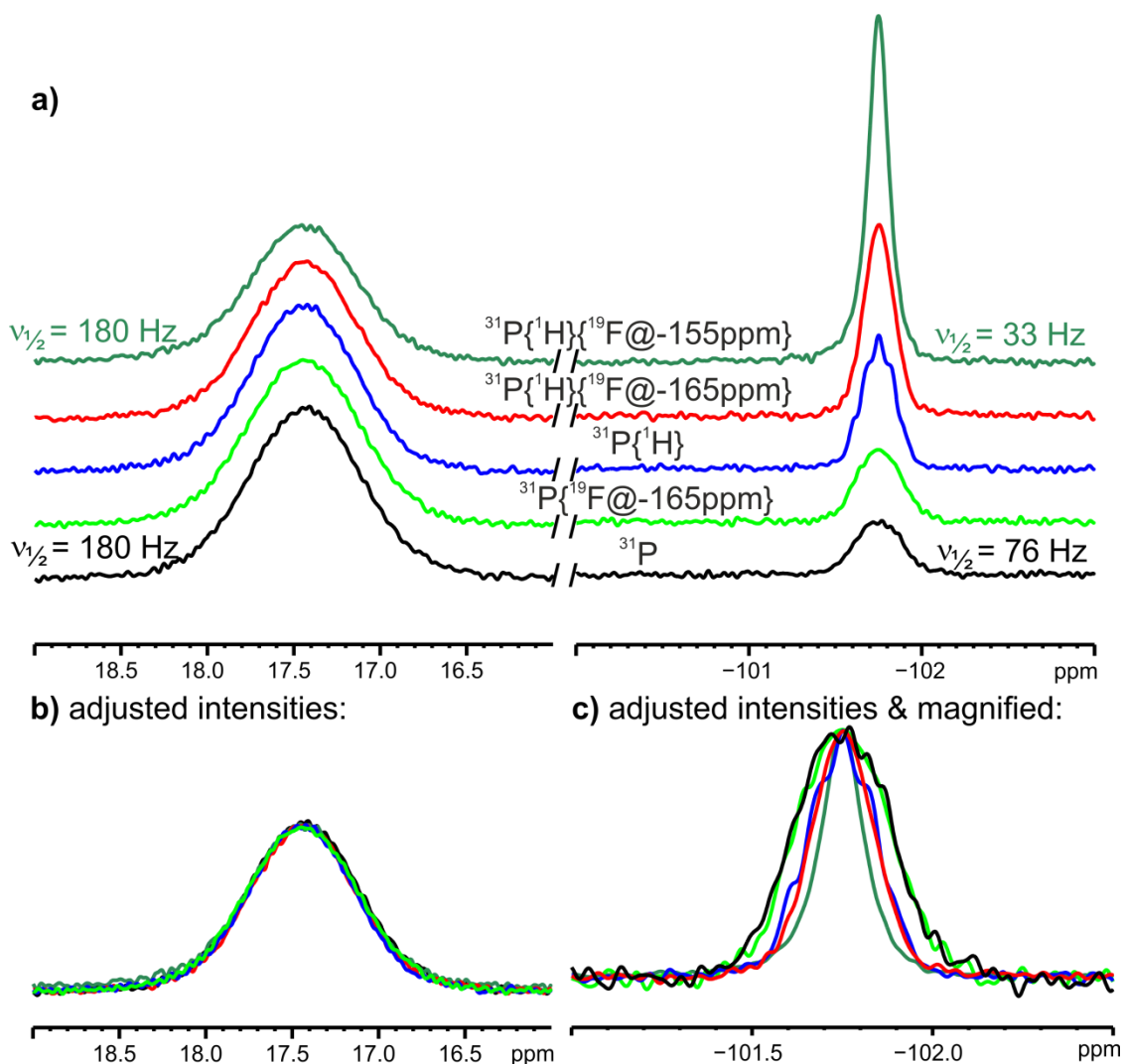


Figure SI 5.2 | ^{31}P NMR decoupling experiments (zgigf2igf3) of the reaction of **1** with $(\text{C}_6\text{F}_5)_2\text{BCl}$ (242.87 MHz, TBI-F, 273 K, toluene- d_8): no decoupling (black), ^{19}F decoupling at -165 ppm (light green), ^1H decoupling (blue), simultaneous ^1H and ^{19}F decoupling at a fluorine frequency of -165 ppm (red) and simultaneous ^1H and ^{19}F decoupling at a fluorine frequency of -155 ppm (dark green). Waltz16 was used for ^1H and ^{19}F decoupling and 512 scans were recorded for each spectrum. A) stacked spectra, no intensity adjustment; b) overlaid spectra of the ^{31}P signal of compound **2**; the intensities were adjusted to the same height to show that the line width doesn't change upon decoupling; c) overlaid spectra of the ^{31}P signal of compound **Iso-2a**; the intensities were adjusted to the same height to show that the line width decreases upon decoupling.

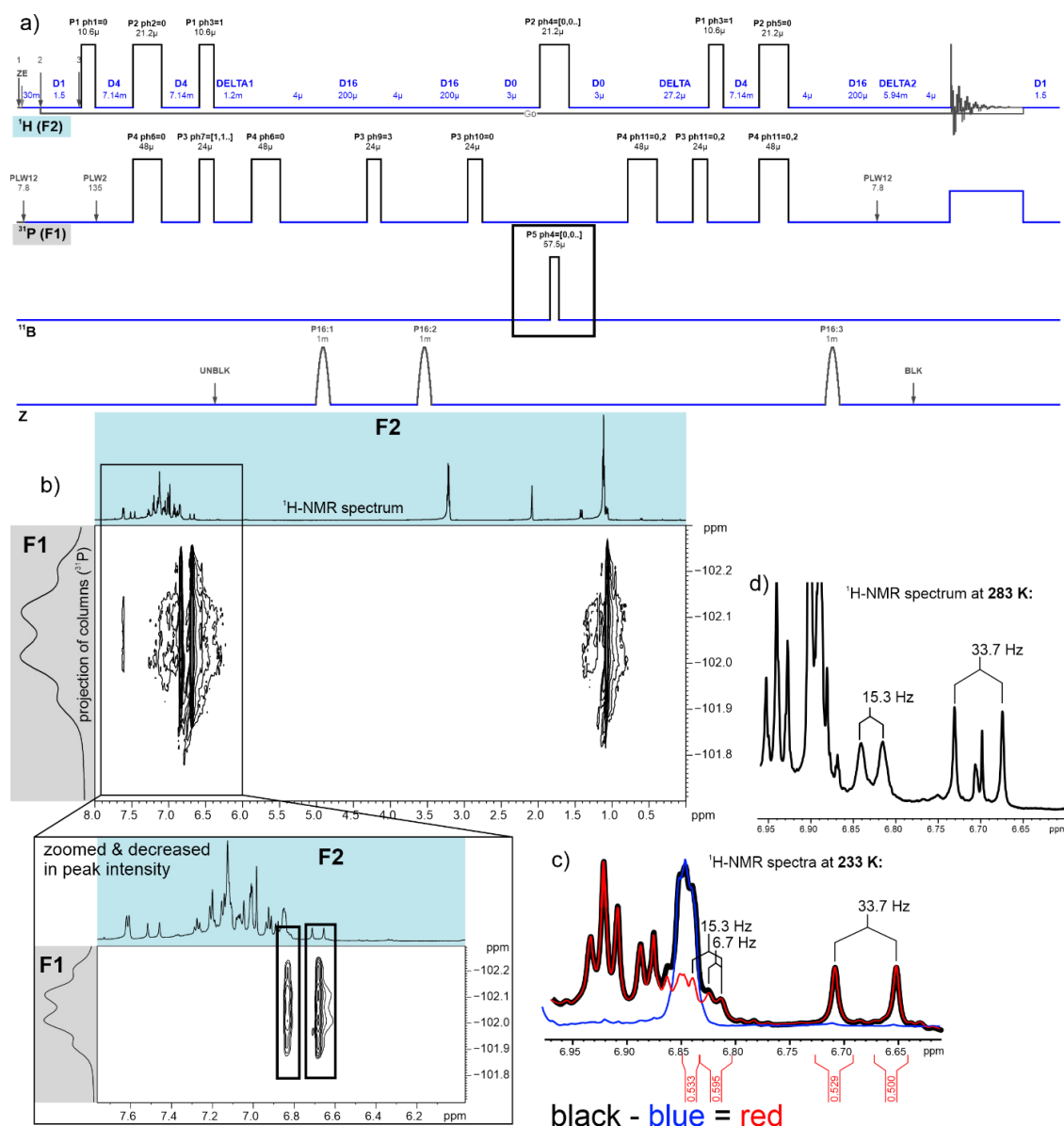


Figure SI 5.3 | a) Pulse program of ^1H - ^{31}P -HSQC (^{11}B & ^1H in F1 (indirect dimension); ^{31}P in F2 (direct dimension)) based on a standard HSQC (hsqcgpph) with an additional third channel (^{11}B) containing a 180° hard pulse (framed) to enable ^{11}B decoupling in the F1 dimension (^{31}P). b) ^1H - ^{31}P -HSQC (^{11}B & ^1H in F1; ^{31}P in F2) during the reaction of **1** with $(\text{C}_6\text{F}_5)_2\text{BCl}$ (600 MHz spectrometer, toluene- d_8 , $\text{cnst}2=35$ Hz) at 233 K. A stronger coupling of 33.7 Hz is observed to a proton at 6.68 ppm and a smaller coupling of 15.3 Hz to the proton at 6.83 ppm. c) Overlaid ^1H -NMR spectra of the reaction of **1** with $(\text{C}_6\text{F}_5)_2\text{BCl}$ (600.03 MHz, toluene- d_8) at 233 K (black), compound **2** in toluene- d_8 at 233 K (blue) and their difference (red). For the difference, the blue spectrum was shifted and adjusted in intensity so that the big signals at 6.85 ppm overlap as good as possible. The proton at 6.68 ppm shows next to the coupling of 15.3 Hz to ^{31}P another coupling of 6.7 Hz which disappears during temperature increase (see d) at 283 K). This coupling could be a $^6J_{\text{HF}}$ coupling being only observable at low temperature probably due to matching geometry between the coupling partners which may be disturbed upon temperature increase.

5 1-PHOSPHA-7-BORA-NORBORNADIENE

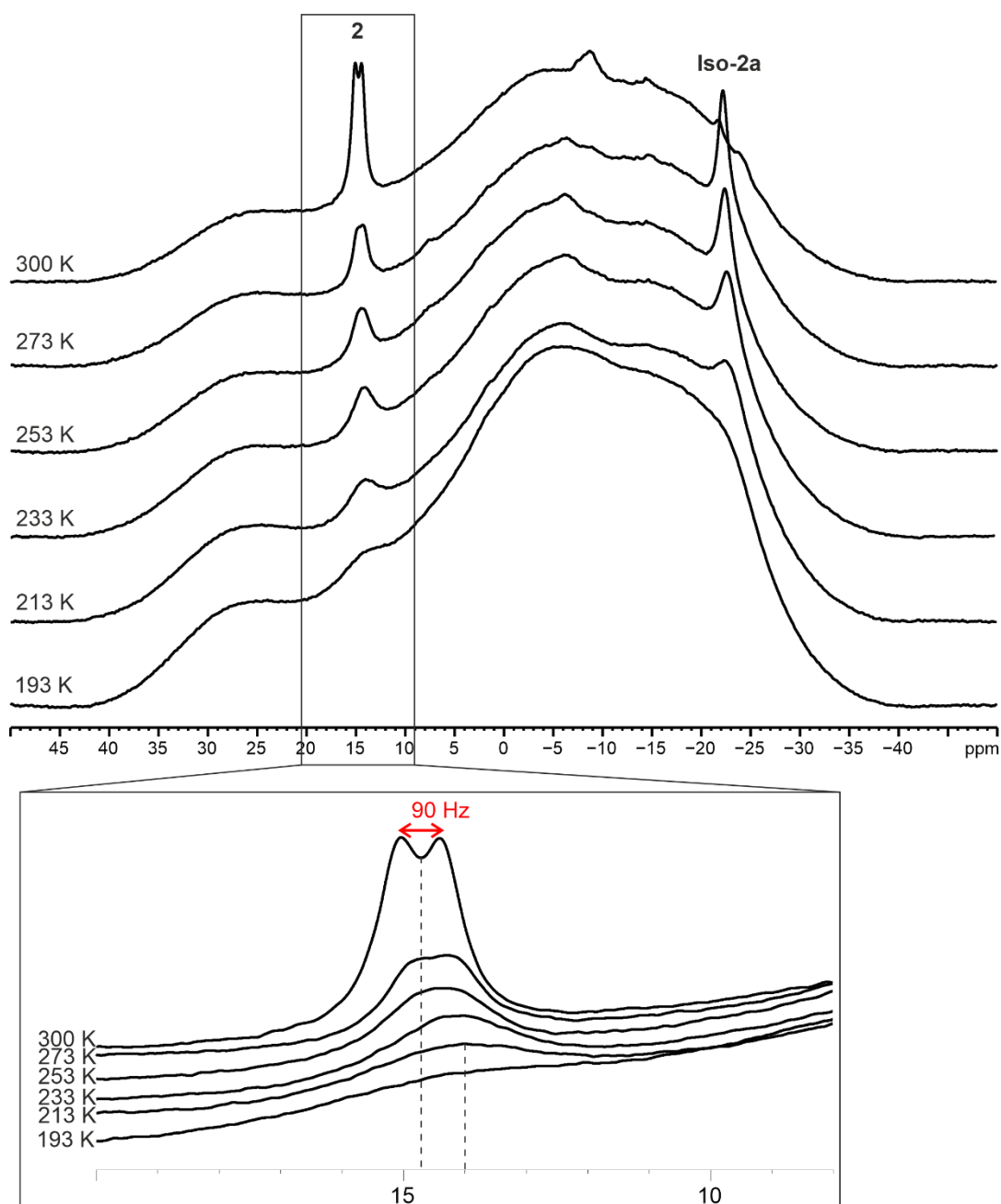


Figure SI 5.4 | $^{11}\text{B} \{^1\text{H}\}$ VT NMR monitoring of the reaction of **1** with $(\text{C}_6\text{F}_5)_2\text{BCl}$ (128.38 MHz, 193 K to 300 K, toluene- d_8). The $^{11}\text{B} \{^1\text{H}\}$ NMR signal of **2** arises as a doublet at $\delta = +14.7$ ppm with a coupling constant of $^1J_{\text{PB}} = 90$ Hz probably to phosphorus at 300 K, indicating a small shift of the signal belonging to **2**. ^{11}B spectra were processed with WDW = EM and LB = 100 Hz and baseline corrected to remove the extremely broad overlapping peak of the NMR-tube.

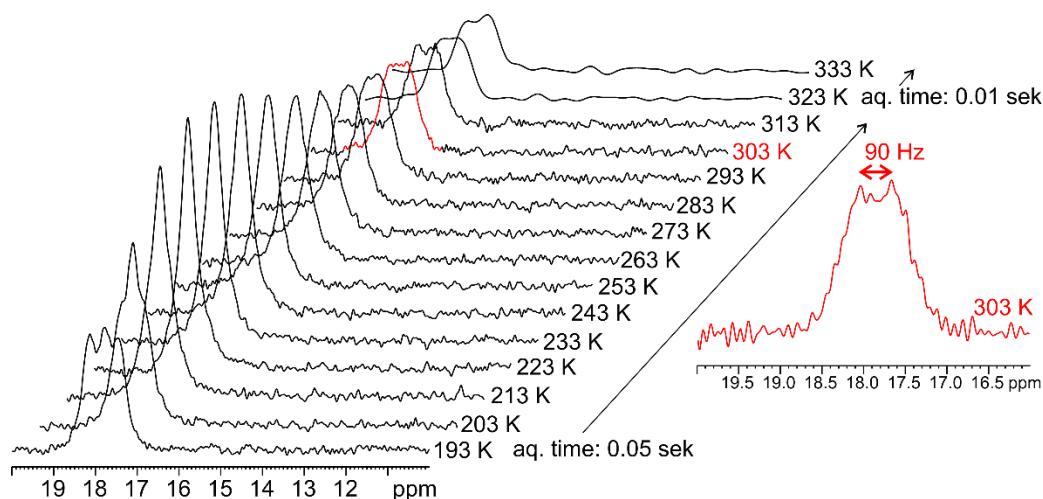
5.8.2 Variable temperature NMR monitoring of **2**

Figure SI 5.5 | $^{31}\text{P}\{^1\text{H}\}$ NMR monitoring (242.87 MHz, toluene- d_8 , 16 scans recorded) of **2** at different temperatures. Spectra were processed with an exponential function (EM), a linebroadening factor (LB) of 10 Hz. The red, zoomed spectrum was recorded at 303 K with 128 scans and processed with a gauss function (GM), LB = -10, GB = 0.6 and shows a big coupling constant of 90 Hz probably to boron (see Figure SI 5.4 for $^{11}\text{B}\{^1\text{H}\}$ spectrum at 300K with a similar coupling of 90 Hz).

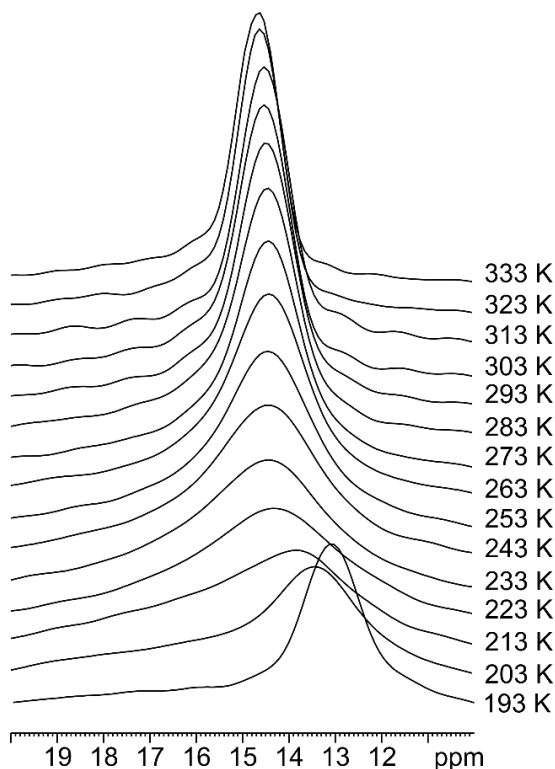


Figure SI 5.6 | ^{11}B NMR monitoring (192.51 MHz, toluene- d_8) of **2** at different temperatures. Spectra were processed with an exponential function (EM), a line broadening factor (LB) of 10 Hz. An acquisition time of 0.006 seconds was adjusted, which is probably the reason why there is no splitting of the ^{11}B signal at 303K in this case. Upon temperature increase the signal first broadens and then narrows again, both accompanied by a downfield shift. A total downfield shift of around 1.4 ppm was observed between 193 K and 303 K. Under the assumption, that this is the result of a chemical exchange with **Iso-2d** (calculated shift of 48 ppm, see chapter S5), around 4% of **Iso-2d** would cause a downfield shift of 1.4 ppm of **2** ($(1 - x) \times 13.13 \text{ ppm (2 @ 193K)} + x \times 48 \text{ ppm (Iso-2d)} = 14.54 \text{ ppm (2 @ 303K)}$; $\rightarrow x = 4\%$).

5 1-PHOSPHA-7-BORA-NORBORNADIENE

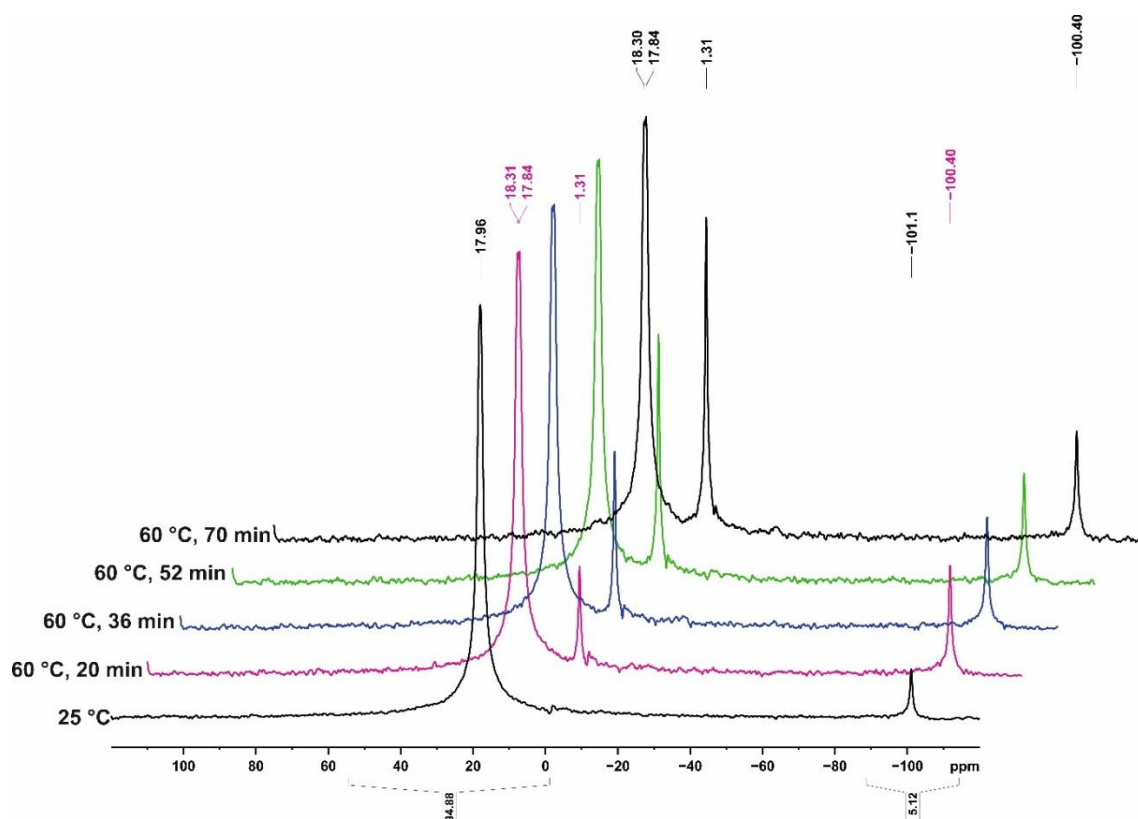


Figure SI 5.7 | $^{31}\text{P}\{^1\text{H}\}$ NMR monitoring (242.87 MHz, 333 K, C_6D_6) of **2** at 60 °C. Spectra were processed with an exponential function (EM), a line broadening factor (LB) of 100 Hz and magnitude calculation (mc).

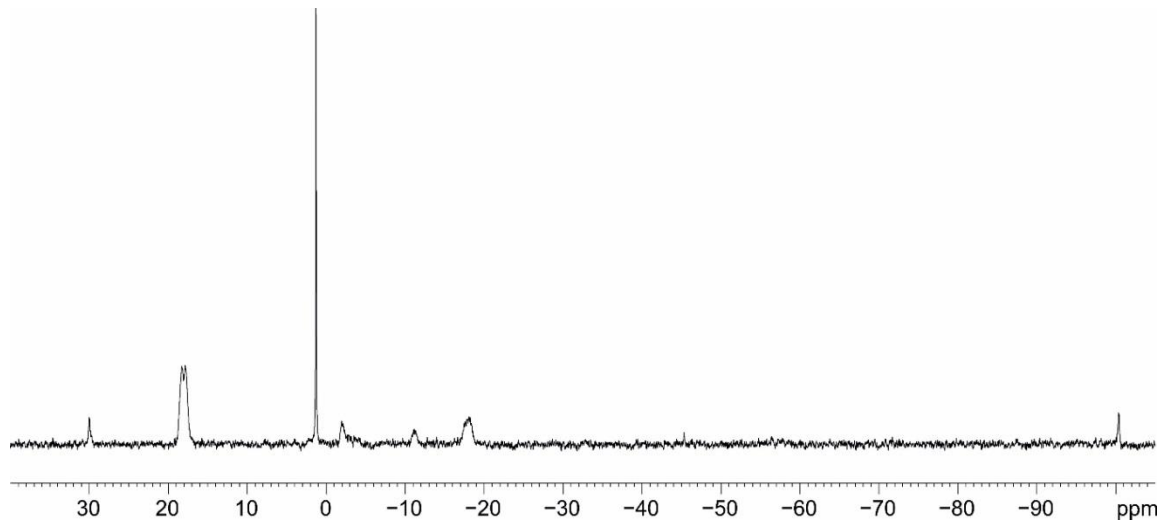


Figure SI 5.8 | $^{31}\text{P}\{^1\text{H}\}$ NMR monitoring (242.87 MHz, 333 K, C_6D_6) of **2** at 60 °C after 21 h. It is noteworthy that additional species can be observed upon heating for longer time.

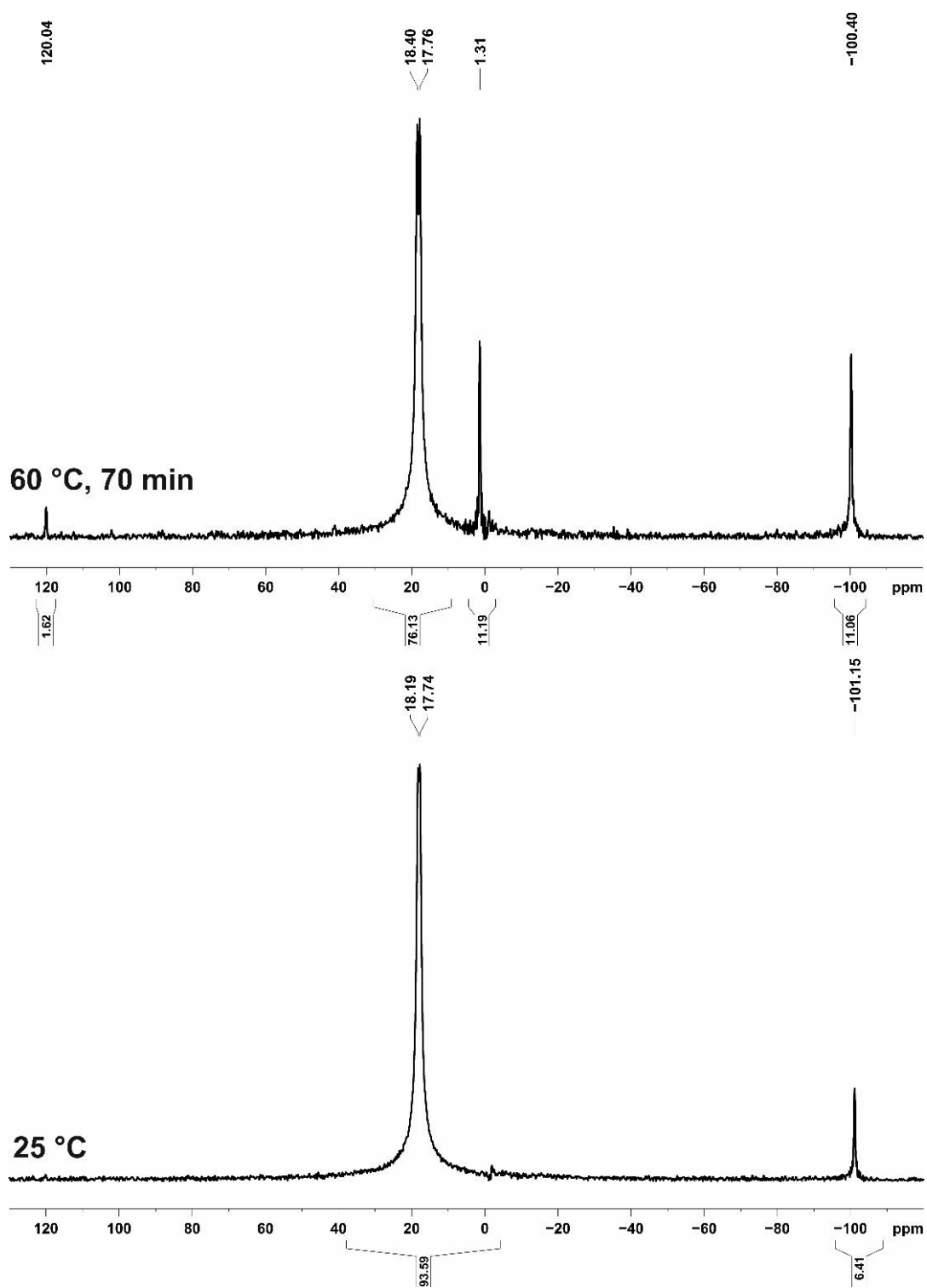


Figure SI 5.9 | $^{31}\text{P}\{^1\text{H}\}$ NMR spectrum (242.87 MHz, 300 K (bottom) and 333 K (top), C_6D_6) of **2** for comparison.

5 1-PHOSPHA-7-BORA-NORBORNADIENE

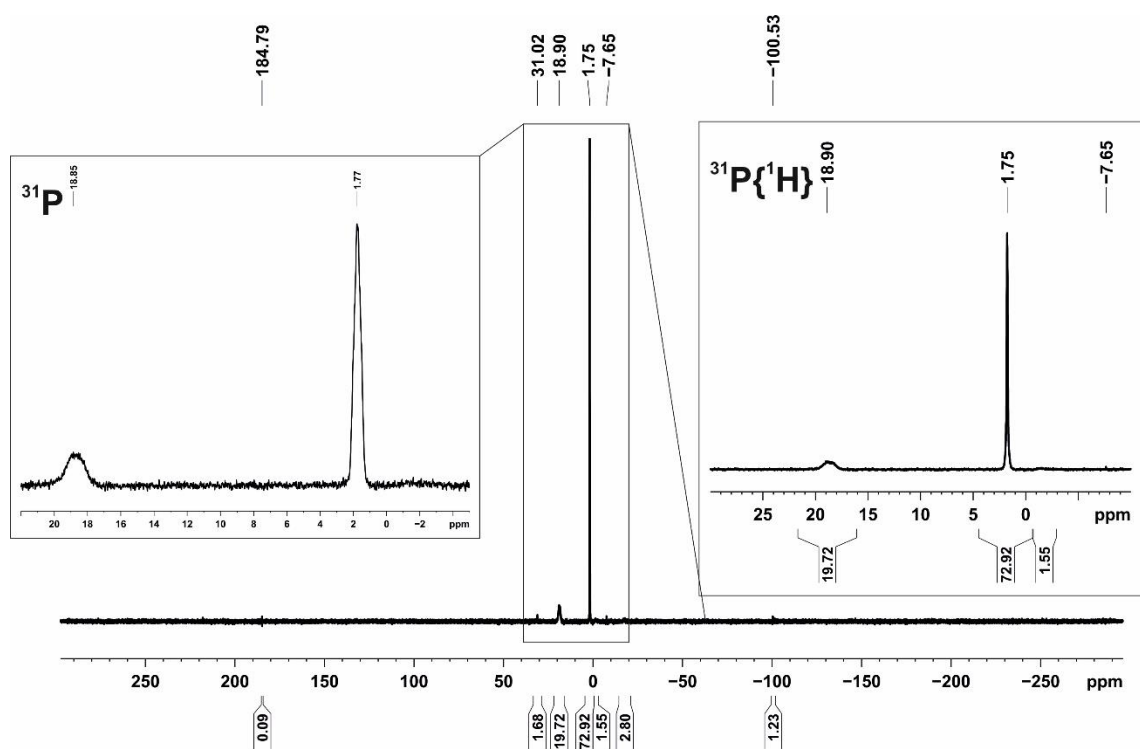


Figure SI 5.10 | $^{31}\text{P}\{^1\text{H}\}$ NMR spectrum (161.98 MHz, 300 K, C_6D_6) of **2** after heating to 60 °C overnight; the spectrum was recorded at room temperature.

5.8.3 Variable temperature NMR monitoring – formation of 5c

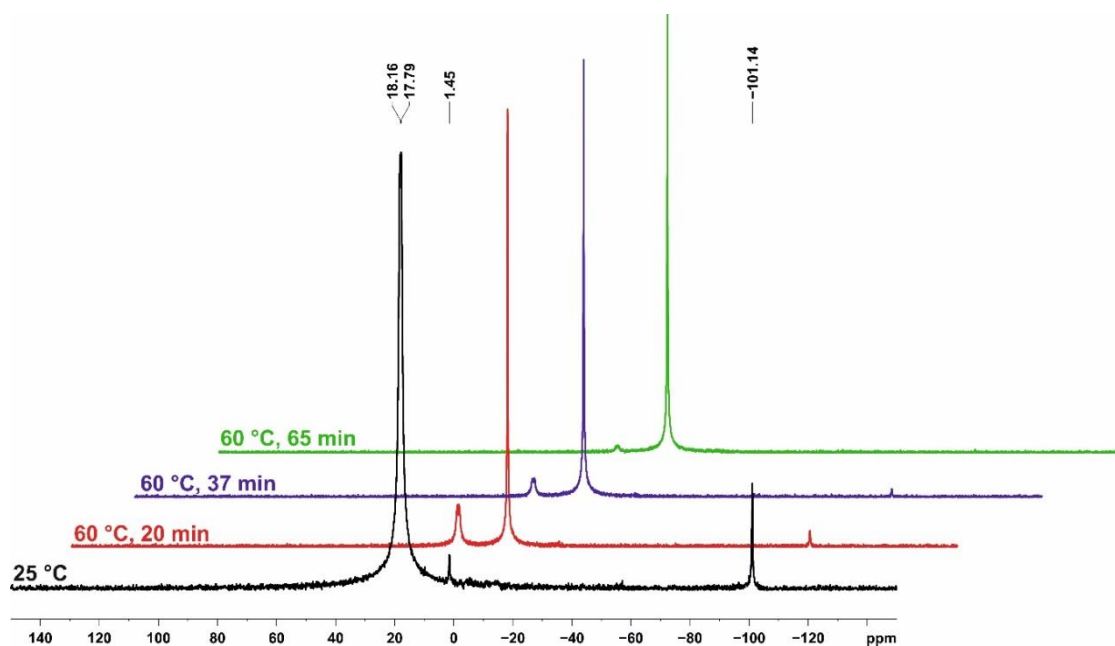


Figure SI 5.11 | $^{31}\text{P}\{^1\text{H}\}$ VT NMR monitoring (242.87 MHz, 300 K and 333 K, C_6D_6 (0.5 mL)) of the reaction of **2** (50 mg, 0.073 mmol, 1 equiv.) with 4-(trifluoromethyl)phenylacetylene (24 μL , 0.073 mmol, 1 equiv.).

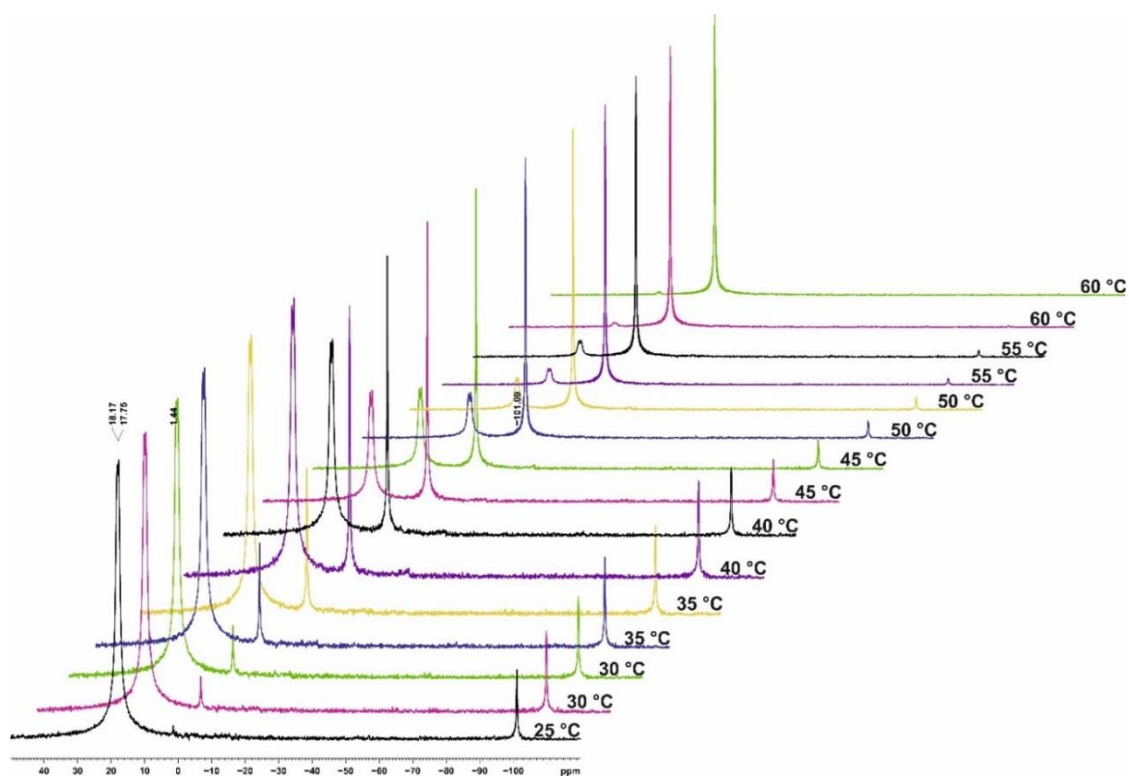


Figure SI 5.12 | $^{31}\text{P}\{^1\text{H}\}$ VT NMR monitoring (242.87 MHz, 300 K to 333 K, C_6D_6 (0.5 mL)) of the reaction of **2** (50 mg, 0.073 mmol, 1 equiv.) with 4-(trifluoromethyl)phenylacetylene (24 μL , 0.073 mmol, 1 equiv.) in 5 °C steps (the reaction was kept at the certain temperature for 30 min each).

5 1-PHOSPHA-7-BORA-NORBORNADIENE

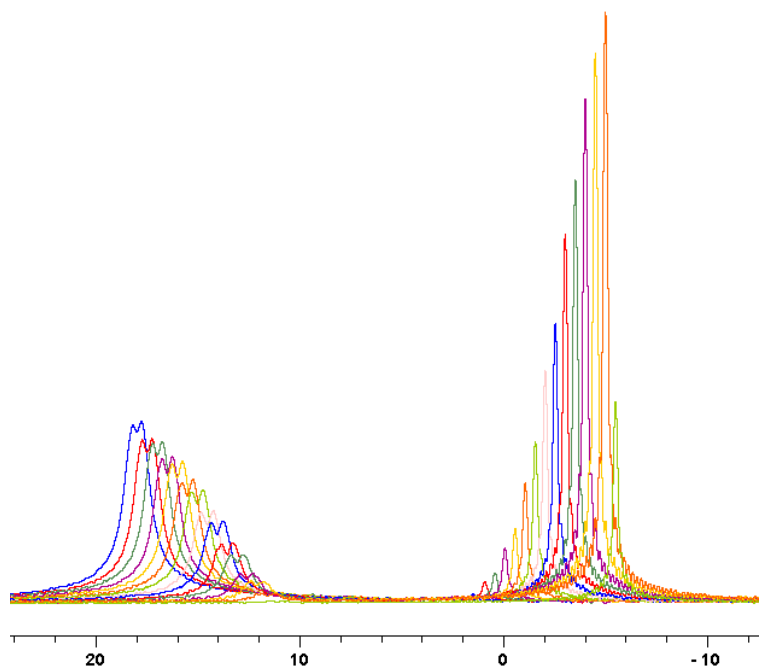


Figure SI 5.13 | $^{31}\text{P}\{^1\text{H}\}$ VT NMR monitoring (242.87 MHz, 300 K to 333 K, C_6D_6 (0.5 L)) of the reaction of **2** (50 mg, 0.073 mmol, 1 equiv.) with 4-(trifluoromethyl)phenylacetylene (24 μL , 0.073 mmol, 1 equiv.) with 5 $^\circ\text{C}$ steps (reaction was kept 30 minutes at the certain temperature); decrease of starting material **2** (left) and increase of product **5b** (right). Spectra are overlaid with a horizontal offset and no vertical offset.

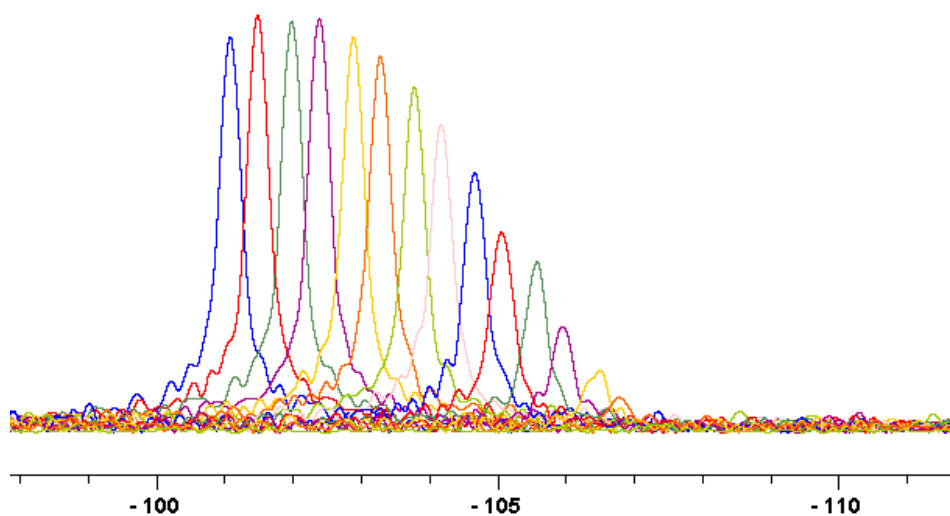


Figure SI 5.14 | $^{31}\text{P}\{^1\text{H}\}$ VT NMR monitoring (242.87 MHz, 300 K to 333 K, C_6D_6 (0.5 mL)) of the reaction of **2** (50 mg, 0.073 mmol, 1 equiv.) with 4-(trifluoromethyl)phenylacetylene (24 μL , 0.073 mmol, 1 equiv.) with 5 $^\circ\text{C}$ steps (reaction was kept 30 minutes at the certain temperature); decrease of compound **Iso-2a**. Spectra are overlaid with a horizontal offset and no vertical offset.

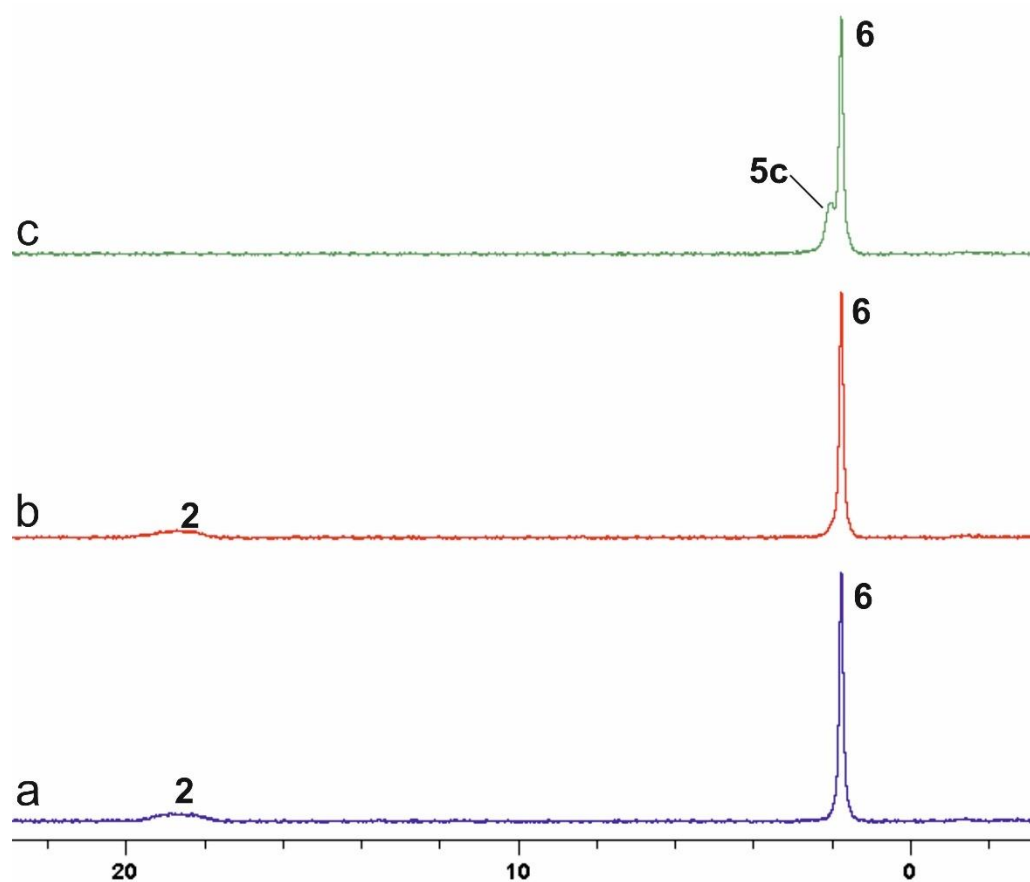
5.8.4 Reaction of **6** with 4-(trifluoromethyl)phenylacetylene

Figure SI 5.15 | $^{31}\text{P}\{^1\text{H}\}$ NMR monitoring (161.98 MHz, 300 K, C_6D_6 (0.5 mL)) of the reaction of **6** with 4-(trifluoromethyl)phenylacetylene. a) **2** (50 mg, 0.073 mmol, 1 equiv.) was heated to 60 °C overnight to form **6**; b) 4-(trifluoromethyl)phenylacetylene (24 μL , 0.073 mmol, 1 equiv.) was added to the reaction mixture of a) at room temperature – no reaction observed; c) the mixture of b) was heated to 60 °C – reaction of **2** with alkyne leading to the formation of **5c**; no change for **6** observable.

6 FACILE C=O BOND SPLITTING OF CARBON DIOXIDE INDUCED BY METAL-LIGAND COOPERATIVITY IN A PHOSPHININE IRON(0) COMPLEX



Julia Leitl, Michael Marquardt, Peter Coburger, Daniel J. Scott, **Verena Streitferdt**, Ruth M. Gschwind,
Christian Müller* and Robert Wolf*

Angewandte Chemie International Edition

Angew. Chem. Int. Ed. **2019**, *58*, 15407–15411.

DOI: 10.1002/anie.201909240

V. Streitferdt performed NMR monitoring experiments at the 600 MHz spectrometer. J. Leitl performed all reactions and fully characterized compounds **1- σ** , **1- π** , **2**, **3- σ** and **3- π** by single crystal X-ray analysis, NMR and UV/Vis spectroscopy and elemental analysis. J. Leitl prepared the manuscript and supporting information with assistance by D. J. Scott. M. Marquardt supplied ligand L and proof-read the manuscript. P. Coburger performed all DFT calculations. I. Shenderovich performed the ^{31}P CP-MAS NMR spectroscopic measurement. C. Müller and R. Wolf supervised and directed the project.

Reprinted (adapted) with permission from *Angew. Chem. Int. Ed.* (via RightsLink). Text and Figures may differ from the original publication. Source of this chapter: <https://doi.org/10.1002/anie.201909240>

6.1 Abstract

New iron complexes $[\text{Cp}^*\text{FeL}]^-$ (**1- σ** and **1- π** , $\text{Cp}^* = \text{C}_5\text{Me}_5$) containing the chelating phosphinine ligand 2-(2'-pyridyl)-4,6-diphenylphosphinine (**L**) have been prepared, and found to undergo facile reaction with CO_2 under ambient conditions. The outcome of this reaction depends on the coordination mode of the versatile ligand **L**. Interaction of CO_2 with the isomer **1- π** , in which **L** binds to Fe through the phosphinine moiety in an η^5 fashion, leads to the formation of **3- π** , in which CO_2 has undergone electrophilic addition to the phosphinine group. In contrast, interaction with **1- σ** – in which **L** acts as a σ -chelating [P,N] ligand – leads to product **3- σ** in which one C=O bond has been completely broken. Such CO_2 cleavage reactions are extremely rare for late 3d metals, and this represents the first such example mediated by a single Fe centre.

6.2 Introduction

The transformation of carbon dioxide into novel and useful chemicals remains one of the most important research challenges of modern chemistry. Consumption of CO_2 as a C_1 building block is highly attractive both due to its relative abundance, and as a method to mitigate long-established concerns about its role as an atmospheric greenhouse gas.^[1] One potential method is the transformation of CO_2 into carbon monoxide, CO, which is a common feedstock for large-scale industrial processes (e.g Fischer-Tropsch alkane synthesis).^[2] This has led to great interest in the identification and study of well-defined molecular systems capable of directly cleaving the C=O bond in CO_2 . Such transformations are highly challenging due to the high strength of the C=O bond (bond enthalpy 532 kJ mol^{-1}).^[3] Nevertheless, these reactions have become relatively established for highly-reducing, low-valent early 3d metals^[4] and a number of examples based on precious^[5] and f-block metals^[6] have also been reported. In comparison, the use of earth-abundant late 3d metals remains surprisingly underexplored, particularly given the role that such metals play in biological CO_2 reduction to CO, mediated by Ni,Fe CO dehydrogenase.^[7]

Currently, only a handful of examples of CO_2 cleavage based on 3d metals are known (Figure 6.1).^[8] In 2005, Sadighi *et al.* reported abstraction of an oxygen atom from CO_2 by NHC copper boryl complexes, resulting in formal O atom insertion into the Cu—B bond to give compound **A**.^[9] Subsequently, in 2007, Peters and co-workers reported the formation of a dinuclear Fe(II) complex **B** containing bridging CO and O^{2-} ligands, which was prepared by reaction of CO_2 with an Fe(I) precursor (similar results were also published by Holland *et al* shortly thereafter).^[4d,10] Recently, the group of Milstein has described a more complex CO_2 activation sequence mediated by a nickel pincer complex, involving the cleavage of a ligand C—P bond as well as one CO_2 C=O bond to give the products **C** and **D**.^[11]

6 C=O BOND SPLITTING BY A PHOSPHININE IRON(0) COMPLEX

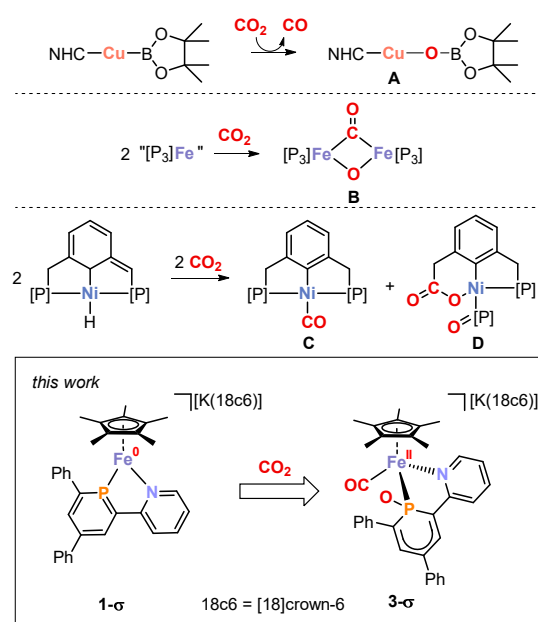


Figure 6.1 | C=O cleavage in CO₂ mediated by well-defined late 3d metal complexes. NHC = *N*-heterocyclic carbene. [P₃] = PhB(CH₂P(CH₂Cy)₂)₃. [P] = P'Pr₂.

The complexes **A-D** all form through some manner of cooperative CO₂ activation. In each case, the small molecule substrate is cleaved as a result of combined interaction with either more than one metal centre (**B**, **C/D**), or with both a metal centre and a 'non-innocent' ligand (**A**, **C/D**). On this basis, we reasoned that the use of other ligands capable of metal-ligand cooperation (MLC)^[12] should allow us to expand the range of structural motifs available for mediating challenging CO₂ cleavage reactions at late 3d metals.

In this context, we have recently become interested in the use of phosphinines (sometimes referred to as phosphabenzenes) as ligands in late 3d metal transition metal chemistry.^[13] Previous work has shown that these compounds exhibit a rich coordination chemistry, and are capable of displaying diverse coordination modes.^[13,14] Furthermore, we have previously shown that Cp*Fe complexes of the simple phosphinine TPP (TPP = 2,4,6-triphenylphosphinine) show considerable non-innocent behaviour, with the TPP ligand capable of displaying either nucleophilic or electrophilic character towards external reagents.^[15] We anticipated that the coordination chemistry (and, hence, onward reactivity) of these complexes might be further diversified through incorporation of the phosphinine moiety into a chelating ligand scaffold. We therefore decided to target the synthesis of an analogue of our previously-reported complex [K([18]crown-6)][Cp*Fe(η⁴-TPP)],^[16] in which TPP is replaced by the known ligand 2-(2'-pyridyl)-4,6-diphenylphosphinine (**L**).^[17]

6.3 Results and Discussion

Pursuing an analogous method to that previously used to prepare [K([18]crown-6)][Cp*Fe(η⁴-TPP)], treatment of [K([18]crown-6)][Cp*Fe(η⁴-C₁₀H₈)] with **L** at -35 °C in dimethoxyethane (DME) gave a deep purple reaction mixture after warming to room temperature and stirring overnight. Dark purple crystals of a new product **1** were obtained in good yield (68%) by layering this reaction mixture with *n*-hexane and subsequent filtration (Figure 6.2, top). X-ray analysis of these crystals confirmed the expected formulation of

6 C=O BOND SPLITTING BY A PHOSPHININE IRON(0) COMPLEX

1 as $[K([18\text{crown-6})][\text{Cp}^*\text{FeL}]$ (**1- σ**), in which the ligand **L** has displaced naphthalene from the anionic Cp^*Fe moiety (Figure 6.3). The crystal structure reveals that, in contrast to the η^4 -TPP binding mode in $[K([18\text{crown-6})][\text{Cp}^*\text{Fe}(\eta^4\text{-TPP})]$, the phosphinine ligand acts as a sigma-coordinated [P,N] chelate in $[K([18\text{crown-6})][\text{Cp}^*\text{FeL}]$, with the Cp^* and **L** ligands coordinating the iron centre in a trigonal planar fashion. The Fe1–P1 (2.0811(4) Å) and Fe1–N1 (1.9428(12) Å) bonds in **1- σ** are shorter than typical single bonds of known [P,N] chelate transition metal complexes (mean distance M–P: 2.293 Å; mean distance M–N: 2.156 Å), consistent with a measure of π -backbonding from the electron-rich metal to **L**.^[18]

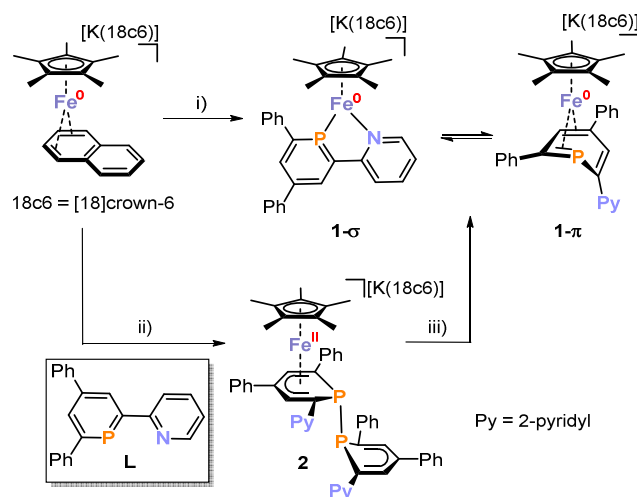


Figure 6.2 | Reaction of $[K([18\text{crown-6})][\text{Cp}^*\text{Fe}(\text{C}_{10}\text{H}_8)]$ with 2-(2'-pyridyl)-4,6-diphenylphosphinine (**L**) forming **1- σ** and **1- π** ; i) **L**, DME, $-35\text{ }^\circ\text{C}$ to room temperature, -naphthalene; ii) 1 equiv. $[K([18\text{crown-6})][\text{Cp}^*\text{Fe}(\text{C}_{10}\text{H}_8)]$, 2 equiv. **L**, toluene/THF $-35\text{ }^\circ\text{C}$ to room temperature; iii) 1 equiv. $[K([18\text{crown-6})][\text{Cp}^*\text{Fe}(\text{C}_{10}\text{H}_8)]$, THF.

Further structural assignment of **1- σ** in the solid state is supported by ^{31}P CP MAS NMR spectroscopy, which indicates the presence of a single species with $\delta_{\text{iso}} = 121.1$ ppm. This chemical shift is in the range expected for this coordination mode of **L**.^[19] In contrast, solution phase $^{31}\text{P}\{^1\text{H}\}$ NMR analysis of crystalline **1** dissolved in suitable solvents^[20] shows two distinct resonances. For example, in THF- d_8 a sharp singlet at 130.7 ppm (which splits into a triplet with $^3J_{\text{P-H}} = 13$ Hz in the coupled ^{31}P NMR spectrum) is assigned to **1- σ** , but is accompanied by a second, very broad resonance ($\tau_{1/2} = 1000$ Hz) at -46.2 ppm. Attempts to selectively crystallise the species corresponding to this resonance have been unsuccessful, with XRD and ^{31}P CP MAS measurements consistently showing the presence of only **1- σ** in the solid state. Nevertheless, the broadness and chemical shift of this signal are very similar to those observed previously for the complex $[K([18\text{crown-6})][\text{Cp}^*\text{Fe}(\eta^4\text{-TPP})]$. In this compound the TPP ligand is rapidly equilibrating between different η^4 π -coordination modes.^[16] We therefore assign this signal to an isomeric structure of **1** (**1- π**) where the ligand **L** coordinates in an η^4 fashion as shown in Figure 6.2, and which exists in equilibrium with **1- σ** in solution. This conclusion is supported by DFT calculations. A minimum energy structure corresponding to **1- π** is only 0.9 kcal mol^{-1} higher in energy than the optimized structure for **1- σ** (which reproduces well the structure observed by crystallography; for full details, see the SI). Furthermore, conversion of **1- π** to **1- σ** is calculated to proceed with a barrier of $27.0\text{ kcal mol}^{-1}$. This is consistent with an equilibrium at room

6 C=O BOND SPLITTING BY A PHOSPHININE IRON(0) COMPLEX

temperature. $^{31}\text{P}\{^1\text{H}\}$ NMR integration indicates an approximately 2:1 ratio of $1-\sigma$ to $1-\pi$ at room temperature, and that this ratio does not change significantly at lower temperature ($-30\text{ }^\circ\text{C}$; at elevated temperatures other reactivity is observed, see SI).

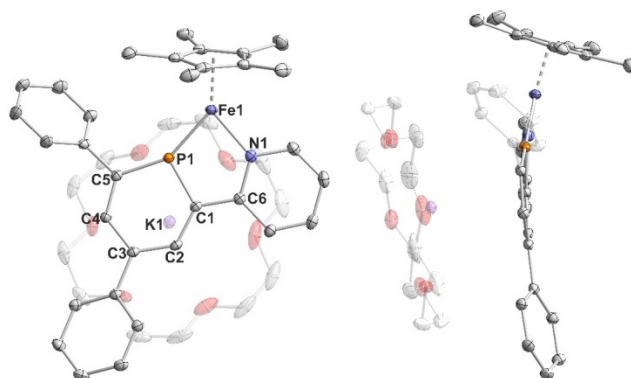


Figure 6.3 | Solid state molecular structure of $1-\sigma$ (left); ellipsoids are drawn at the 40% probability level; H atoms are omitted and the K[18]crown-6 cation is transparent for clarity; selected bond lengths [Å] and bond angles [$^\circ$]: Fe1–P1: 2.0811(4), Fe1–N1: 1.9428(12), P1–C1: 1.7733(13), C1–C2: 1.3953(19), C2–C3: 1.3947(18), C3–C4: 1.4343(18), C4–C5: 1.3756(18), C5–P1: 1.7757(13), P1–Fe1–N1: 82.32(4), Fe1–P1–C1: 107.62(4), Fe1–N1–C6: 124.18(9), Cp*–Fe1–N1: 135.513(8), P1–Fe1–Cp*: 140.545(9). Side view of solid state molecular structure of $1-\sigma$ (right); for clarity, one additional phenyl group is also transparent.

In the hope of gaining more insight into the formation of both isomers of **1**, the reaction of $[\text{K}([\text{18}]\text{crown-6})][\text{Cp}^*\text{Fe}(\text{C}_{10}\text{H}_8)]$ with **L** was monitored by $^{31}\text{P}\{^1\text{H}\}$ NMR spectroscopy at 273 K. The initial spectrum showed immediate, full consumption of ligand **L**, and formation of two major new groups of resonances at ca. -25 and -42 ppm.^[21] Only after approximately 30 minutes did signals attributable to $1-\sigma$ and $1-\pi$ become readily discernible, growing in steadily over the course of several hours with concomitant loss of the intermediate resonances.

Close inspection of the observed multiplets suggested that they could be assigned to a pair of AB spin systems with very similar chemical shifts and coupling constants. Notably, the chemical shifts at approximately -42 ppm are almost identical to those of the P–P bonded dimeric species $[\text{Cp}^*\text{Fe}(\eta^5\text{-TPP})_2]$.^[16] Indeed, when the reaction between **L** and $[\text{K}([\text{18}]\text{crown-6})][\text{Cp}^*\text{Fe}(\text{C}_{10}\text{H}_8)]$ was repeated with a 2:1 molar ratio, these resonances were seen to form selectively. Only upon addition of a further equivalent of $[\text{K}([\text{18}]\text{crown-6})][\text{Cp}^*\text{Fe}(\text{C}_{10}\text{H}_8)]$ were the isomers of **1** observed (Figure 6.2, bottom). Conversely, addition of 1 eq. **L** to an isolated sample of **1** regenerates the intermediate resonances. It was therefore proposed that these resonances might correspond to two isomers of the P–P dimer $[\text{K}([\text{18}]\text{crown-6})][\text{Cp}^*\text{Fe}(\eta^5\text{-L-L})]$, **2**, which differ only in the relative orientations of the **L** pyridyl groups. This assignment was confirmed by X-ray analysis of single crystals grown by slow diffusion of *n*-hexane into a DME solution of **2**, which resolved to show the expected L_2 dimer. One half of the molecule is coordinated in an η^5 fashion to a Cp^*Fe moiety (Figure 6.4).^[22] The P1–P2 bond is longer than typical P–P single bonds (2.3149(14) vs. 2.04 Å)^[23], suggesting a relatively weak interaction that is consistent with facile cleavage upon addition of a second equivalent of $[\text{K}([\text{18}]\text{crown-6})][\text{Cp}^*\text{Fe}(\eta^4\text{-C}_{10}\text{H}_8)]$.

6 C=O BOND SPLITTING BY A PHOSPHININE IRON(0) COMPLEX

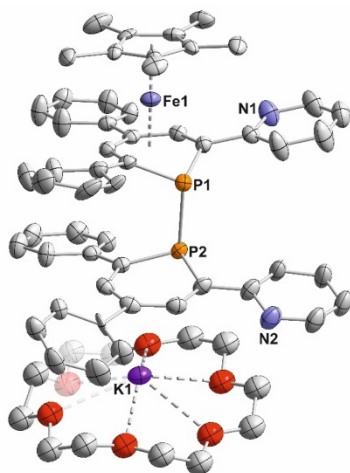


Figure 6.4 | Solid state molecular structure of **2**; ellipsoids are drawn at the 40% probability level; H atoms are omitted for clarity; selected bond lengths [Å] and bond angles [°]: P1–P2: 2.3149(14), P1–C1: 1.821(4), P1–C5: 1.805(4), C1–C2: 1.416(5), C2–C3: 1.422(6), C3–C4: 1.420(5), C4–C5: 1.411(5), P2–C6: 1.822(4), P2–C10: 1.816(4), C6–C7: 1.382(6), C7–C8: 1.408(7), C8–C9: 1.404(6), C9–C10: 1.378(6), C1–P1–C5: 92.99(17), C6–P2–C10: 99.58(19), fold angle C1–P1–C5: 32.64, fold angle C6–P2–C10: 14.79.

Complex **2** likely arises through rapid addition of initially-formed **1** to a second equivalent of **L**. When **L** is consumed, further coordination of “Cp*Fe⁻” leads to formation of free **1**. Transiently-formed **1** is believed to act as a nucleophile in this reaction, with the second equivalent of **L** behaving as a formal electrophile. This is consistent with previous observations of nucleophilic character for the P atom in [K([18]crown-6)][Cp*Fe(η^4 -TPP)],^[32] as well as with DFT calculations, which suggest that the phosphinine moiety not directly bound to Fe is best described as an anionic phosphahexacyclodiényl fragment (see SI). These calculations also indicate that formation of **2** from **1- π** and **L** is favourable by 23.5 kcal mol⁻¹, and proceeds over a low energy barrier of 7.5 kcal mol⁻¹.

Encouraged by the evidence of both coordinative flexibility and non-innocent reactivity already displayed by the phosphinine ligand **L** simply during the synthesis of compound **1**, we were encouraged to investigate the reactivity of this complex towards CO₂. Thus, a THF solution of **1- σ** and **1- π** was charged with CO₂ (1 atm) at room temperature (Figure 6.5). Gratifyingly, an immediate colour change from deep purple to deep green was observed, and ³¹P{¹H} NMR spectroscopy indicated the formation of two major new species, identified by signals at 97.0 and 116.0 ppm, with the former splitting into a triplet in the proton-coupled ³¹P NMR spectrum (³J_{P-H} = 13 Hz). The species corresponding to these two resonances could be separated from each other (and from more minor reaction side-products) by fractional crystallisation, and the identity of both was established by single crystal X-ray diffraction studies (Figure 6.6).

6 C=O BOND SPLITTING BY A PHOSPHININE IRON(0) COMPLEX

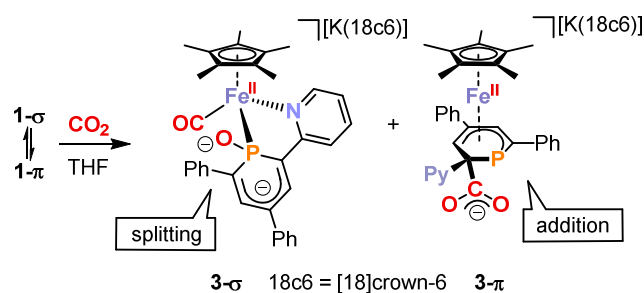


Figure 6.5 | Reaction of **1- σ** and **1- π** with CO₂ (1 atm) in THF at room temperature.

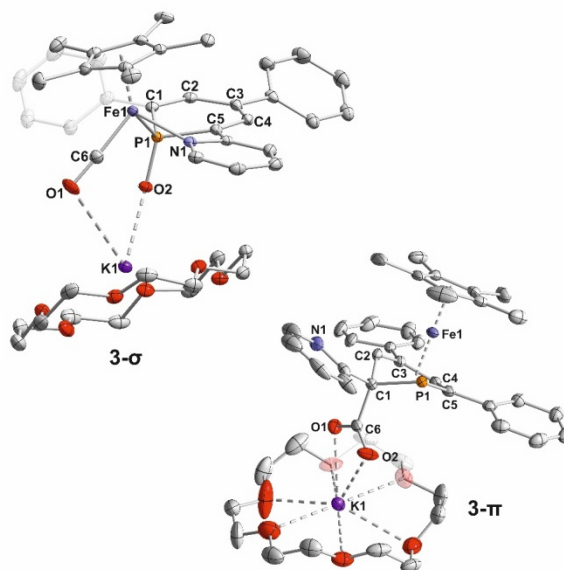


Figure 6.6 | Solid state molecular structures of **3- σ** and **3- π** ; ellipsoids are drawn at the 40% probability level; H atoms are omitted for clarity; selected bond lengths [Å] and bond angles [°] of **3- σ** : Fe1–P1: 2.2434(4), Fe1–N1: 2.0060(14), Fe1–C6: 1.7272(18), C6–O1: 1.170(2), P1–O2: 1.5272(12), P1–C1: 1.8043(17), C1–C2: 1.371(2), C2–C3: 1.431(2), C3–C4: 1.394(2), C4–C5: 1.389(2), P1–C5: 1.7936(16), K1–O1: 3.3043(16), K2–O2: 2.558(17), O1–C6–Fe1= 177.49(17), C6–Fe1–P1= 88.41(6), Fe1–P1–O2= 114.45(5), C6–Fe1–N1: 98.78(7); for **3- π** : C6–O1: 1.236(5), C6–O2: 1.229(5), P1–C1: 1.865(4), C1–C2: 1.497(7), C2–C3: 1.443(7), C3–C4: 1.421(5), C4–C5: 1.421(5), P1–C5: 1.768(4), C1–C6: 1.575(5), K1–O1: 2.723(3), K1–O2: 3.050(4), O1–C6–O2= 127.3(4), P1–C1–C2= 97.5(3), C1–P1–C5= 98.36(19).

Thus, the $^{31}\text{P}\{^1\text{H}\}$ resonance at 116.0 ppm can be assigned to the new compound **3- π** , in which an intact CO₂ moiety has attached to the phosphinine carbon 'ipso' to the pyridyl group.^[24] The resulting carboxylate-substituted phosphacyclohexadienyl ligand coordinates to Fe in an η^5 fashion, and the carboxylate itself interacts in a κ^2 manner with the potassium countercation. It is noteworthy that no reaction is observed between CO₂ and the free ligand **L** under analogous conditions. Thus, while no direct interaction between the carboxylate and the Fe centre is present in the solid-state structure, an electron-rich metal is nevertheless necessary for the reaction to proceed, presumably to increase the nucleophilicity of the phosphinine through π -back-donation.

A more dramatic outcome is revealed by the second major reaction product, **3- σ** . In this case, the molecular structure in the crystal clearly shows full cleavage of one C=O bond in the CO₂ substrate, with coordination of the resulting CO molecule to the Fe centre, and of the remaining O atom to the ligand P atom.

6 C=O BOND SPLITTING BY A PHOSPHININE IRON(0) COMPLEX

Nonetheless, the coordination mode of the ligand **L** remains unchanged from **1- σ** , which may be attributed to the electronic flexibility of the phosphinine moiety. In contrast to Milstein's product **D** (as well as an Ir-based system described recently by Langer, Hamza and Papai), O atom transfer to P does not require cleavage of any bonds in the ligand backbone.^[5e,11] Again, this can be attributed to the use of an unsaturated phosphinine moiety in place of a more conventional phosphine donor. This reaction represents the first example of full CO₂ C=O cleavage mediated by a single well-defined Fe centre.

Intuitively, the structures observed for **3- σ** and **3- π** appear to suggest that they are formed through the reaction of CO₂ with isomers **1- σ** and **1- π** of **1**, respectively. This conclusion is further supported by ³¹P{¹H} spectra of the crude product mixture, which indicate the formation of **3- σ** and **3- π** in the same 2:1 ratio observed for the equilibrium between **1- σ** and **1- π** . To provide more conclusive evidence, DFT studies were performed to establish the mechanisms of formation of both **3- σ** and **3- π** (for full details, see the SI). As expected, interaction of CO₂ with **1- σ** was calculated to lead to formation of **3- σ** , with only a very small energy barrier of 3.5 kcal mol⁻¹. Interaction with **1- π** was calculated to lead to **3- π** over a similarly small barrier (5.5 kcal mol⁻¹). Notably, both barriers are significantly lower than the barrier to isomerisation between **1- σ** and **1- π** (*vide supra*).

6.4 Conclusion

In summary, we have prepared a new anionic Fe complex **1** incorporating a chelating phosphinine ligand. **1** exists in solution as a pair of isomers in which the phosphinine adopts distinct coordination modes at the metal. Both isomers react with CO₂: for the π -coordinated isomer **1- π** addition of CO₂ to a carbon atom of the phosphinine moiety is observed, while full cleavage of one C=O bond occurs in the σ -coordinated isomer **1- σ** to give an Fe-coordinated CO moiety and P-bound O atom. This is the first reported example of C=O cleavage of a CO₂ molecule mediated by a single Fe centre, and clearly demonstrates the potential of coordinatively- and electronically-flexible phosphinine ligands to help mediate challenging bond activation reactions. Research into the further applications of such complexes, as well as the derivatisation of CO₂ cleavage product **3- σ** , are currently underway in our laboratories.

6.5 Acknowledgements

We thank Dr. Ilya G. Shenderovich for the CP MAS NMR measurement and Dr. Stefanie Gartner for crystallographic advice. Funding by the Deutsche Forschungsgemeinschaft (MU1657/5-1 and WO1496/9-1) and the Alexander von Humboldt foundation (postdoctoral fellowship to D.J.S.) is gratefully acknowledged.

6.6 References

- [1] a) E. V. Kondratenko, G. Mul, J. Baltrusaitis, G. O. Larrazabal, J. Perez-Ramerez, *Energy Environ. Sci.* **2013**, *6*, 3112–3135. b) Q. Liu, L. Wu, R. Jackstell, M. Beller, *Nat. Commun.* **2015**, *6*, 5933. c) C. Maeda, Y. Miyazaki, T. Ema, *Catal. Sci. Technol.* **2014**, *4*, 1482–1497. d) D. M. D'Alessandro, B. Smit, J. R. Long, *Angew. Chem. Int. Ed.* **2010**, *49*, 6058–6082.

6 C=O BOND SPLITTING BY A PHOSPHININE IRON(0) COMPLEX

- [2] H. H. Storch, in *Adv. Catal.* (Eds.: W.G. Frankenburg, V.I. Komarewsky, E.K. Rideal), Academic Press, **1948**, pp. 115–156.
- [3] Data Taken from CRC Handbook of Chemistry and Physics, 73rd Ed.; Lide, D. R., Ed.; CRC Press Inc.: Boca Raton, 1992-1993., **n.d.**
- [4] a) G. Fachinetti, C. Floriani, A. Chiesi-Villa, C. Guastini, *J. Am. Chem. Soc.* **1979**, *101*, 1767–1775. b) J. C. Bryan, S. J. Geib, A. L. Rheingold, J. M. Mayer, *J. Am. Chem. Soc.* **1987**, *109*, 2826–2828. c) L. J. Procopio, P. J. Carroll, D. H. Berry, *Organometallics* **1993**, *12*, 3087–3093. d) C. T. Saouma, C. C. Lu, M. W. Day, J. C. Peters, *Chem. Sci.* **2013**, *4*, 4042–4051.
- [5] a) S. I. Källäne, T. Braun, M. Teltewskoi, B. Braun, R. Herrmann, R. Laubenstein, *Chem. Commun.* **2015**, *51*, 14613–14616. b) M. Feller, U. Gellrich, A. Anaby, Y. Diskin-Posner, D. Milstein, *J. Am. Chem. Soc.* **2016**, *138*, 6445–6454. c) M. A. McLoughlin, N. L. Keder, W. T. A. Harrison, R. J. Flesher, H. A. Mayer, W. C. Kaska, *Inorg. Chem.* **1999**, *38*, 3223–3227. d) W. C. Kaska, S. Nemeš, Ata. Shirazi, Suzan. Potuznik, *Organometallics* **1988**, *7*, 13–15. e) J. Langer, A. Hamza, I. Pápai, *Angew. Chem. Int. Ed.* **2018**, *57*, 2455–2458.
- [6] a) N. Tsoureas, L. Castro, A. F. R. Kilpatrick, F. G. N. Cloke, L. Maron, *Chem. Sci.* **2014**, *5*, 3777–3788. b) O. P. Lam, K. Meyer, *Polyhedron* **2012**, *32*, 1–9. c) I. Castro-Rodriguez, K. Meyer, *J. Am. Chem. Soc.* **2005**, *127*, 11242–11243.
- [7] a) S. W. Ragsdale, M. Kumar, *Chem. Rev.* **1996**, *96*, 2515–2540. b) D. J. Evans, *Coord. Chem. Rev.* **2005**, *249*, 1582–1595.
- [8] a) C. Bianchini, A. Meli, *J. Am. Chem. Soc.* **1984**, *106*, 2698–2699. b) D. Sahoo, C. Yoo, Y. Lee, *J. Am. Chem. Soc.* **2018**, *140*, 2179–2185. c) C. Yoo, Y.-E. Kim, Y. Lee, *Acc. Chem. Res.* **2018**, *51*, 1144–1152.
- [9] D. S. Laitar, P. Müller, J. P. Sadighi, *J. Am. Chem. Soc.* **2005**, *127*, 17196–17197.
- [10] a) C. C. Lu, C. T. Saouma, M. W. Day, J. C. Peters, *J. Am. Chem. Soc.* **2007**, *129*, 4–5. b) A. R. Sadique, W. W. Brennessel, P. L. Holland, *Inorg. Chem.* **2008**, *47*, 784–786.
- [11] D. Oren, Y. Diskin-Posner, L. Avram, M. Feller, D. Milstein, *Organometallics* **2018**, *37*, 2217–2221.
- [12] J. R. Khusnutdinova, D. Milstein, *Angew. Chem. Int. Ed.* **2015**, *54*, 12236–12273.
- [13] N. Mézailles, P. L. Floch, *Curr. Org. Chem.* **2006**, *10*, 3–25.
- [14] a) P. L. Floch, *Coord. Chem. Rev.* **2006**, *250*, 627–681. b) C. Müller, L. E. E. Broeckx, I. de Krom, J. J. M. Weemers, *Eur. J. Inorg. Chem.* **2013**, 187–202.

6 C=O BOND SPLITTING BY A PHOSPHININE IRON(0) COMPLEX

- [15] a) C. M. Hoidn, R. Wolf, *Dalton Trans.* **2016**, 45, 8875–8884. b) C. M. Hoidn, J. Leidl, C. G. P. Ziegler, I. G. Shenderovich, R. Wolf, *Eur. J. Inorg. Chem.* **2019**, 1567–1574.
- [16] B. Rezaei Rad, U. Chakraborty, B. Mühldorf, J. A. W. Sklorz, M. Bodensteiner, C. Müller, R. Wolf, *Organometallics* **2015**, 34, 622–635.
- [17] C. Müller, D. Wasserberg, J. J. M. Weemers, E. A. Pidko, S. Hoffmann, M. Lutz, A. L. Spek, S. C. J. Meskers, R. A. J. Janssen, R. A. van Santen, D. Vogt, *Chem. Eur. J.* **2007**, 13, 4548–4559.
- [18] a) A. Campos-Carrasco, L. E. E. Broeckx, J. J. M. Weemers, E. A. Pidko, M. Lutz, A. M. Masdeu-Bultó, D. Vogt, C. Müller, *Chem. Eur. J.* **2011**, 17, 2510–2517. b) A. C. Carrasco, E. A. Pidko, A. M. Masdeu-Bultó, M. Lutz, A. L. Spek, D. Vogt, C. Müller, *New J. Chem.* **2010**, 34, 1547–1550. c) I. de Krom, E. A. Pidko, M. Lutz, C. Müller, *Chem. Eur. J.* **2013**, 19, 7523–7531.
- [19] C. Müller, J. A. W. Sklorz, I. de Krom, A. Loibl, M. Habicht, M. Bruce, G. Pfeifer, J. Wiecko, *Chem. Lett.* **2014**, 43, 1390–1404.
- [20] **1** shows poor solubility in *n*-hexane, Et₂O and PhMe, but dissolves well in more polar solvents such as THF and DME.
- [21] Additional significant resonances are also observed at ca. 38 ppm to 46 ppm. The corresponding species could not be identified.
- [22] The pyridyl nitrogens are hard to assign with confidence (and may plausibly be disordered over several positions), but have been located at the positions that give the lowest final R1 value.
- [23] P. Pykkö, M. Atsumi, *Chem. Eur. J.* **2009**, 15, 186–197.
- [24] Addition of a range of electrophiles to the analogous positions in TPP has been reported previously for [K([18]Crown-6)][Cp*Fe(TPP)], see ref. [15a].

6.7 Supporting Information

The supporting information of **Chapter 6** can be found on the supplied CD-ROM and on <https://doi.org/10.1002/anie.201909240>. The supporting information contains: Experimental procedures and data, NMR, UV/Vis and IR spectra, X-ray crystallography details and results of quantum chemical calculations including Cartesian coordinates of all optimized structures.

6.7.1 Variable Temperature NMR

NMR spectra were recorded on Bruker Avance 300 and Avance 400 spectrometers at 300 K and a Bruker Avance III HD 600 MHz spectrometer with a fluorine selective TBIF probe at 273 K. ^1H and $^{13}\text{C}\{^1\text{H}\}$ spectra were referenced internally to residual solvent resonances, while $^{31}\text{P}\{^1\text{H}\}$ and ^{31}P spectra were referenced externally to 85% $\text{H}_3\text{PO}_4(\text{aq.})$. The assignment of ^1H and ^{13}C NMR signals was confirmed by two-dimensional (COSY, HSQC, and HMBC) experiments.

6.7.1.1 Variable temperature $^{31}\text{P}\{^1\text{H}\}$ NMR spectra of compounds 1- σ and 1- π

$[\text{K}([\text{18}]\text{crown-6})][\text{Cp}^*\text{Fe}(\text{C}_{10}\text{H}_8)]$ (38 mg, 0.061 mmol) and **L** (20 mg, 0.061 mmol) were dissolved in $[\text{D}_8]\text{THF}$ (0.5 mL) at room temperature. $^{31}\text{P}\{^1\text{H}\}$ NMR spectra were recorded at 300 K, 243 K and 333 K.

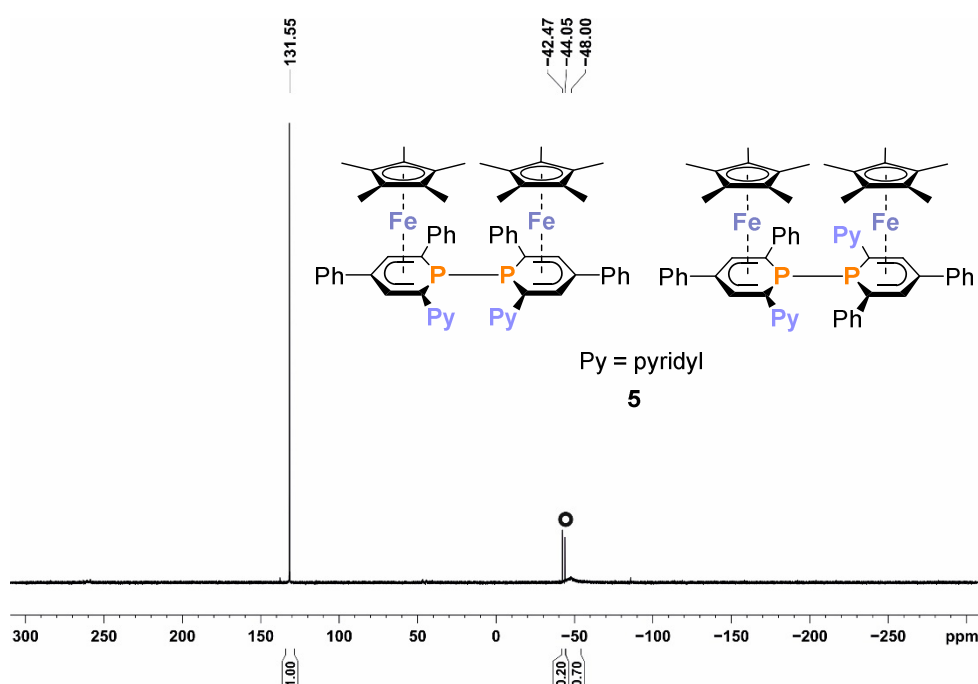


Figure SI 6.1 | $^{31}\text{P}\{^1\text{H}\}$ NMR spectrum (161.98 MHz, $[\text{D}_8]\text{THF}$) at 300 K ($^{\circ}$ = phosphininone iron dimers **5**).^[8]

6 C=O BOND SPLITTING BY A PHOSPHININE IRON(0) COMPLEX

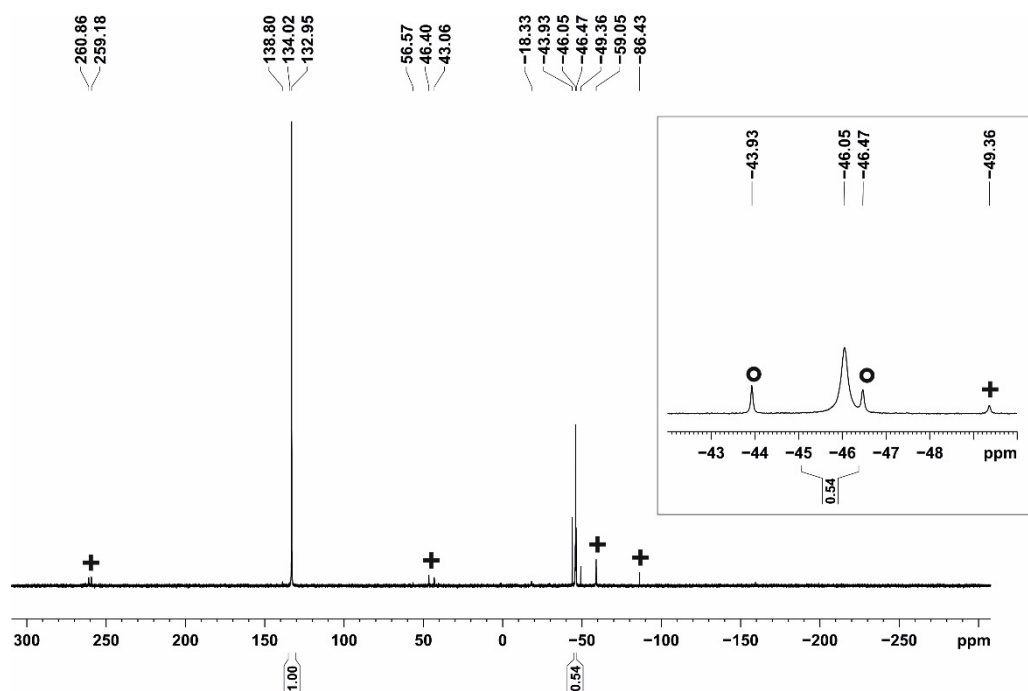


Figure SI 6.2 | $^{31}\text{P}\{^1\text{H}\}$ NMR spectrum (161.98 MHz, $[\text{D}_8]$ THF) at 243 K ($^\circ$ = phosphinine iron dimers **5**, + = unidentified impurities).

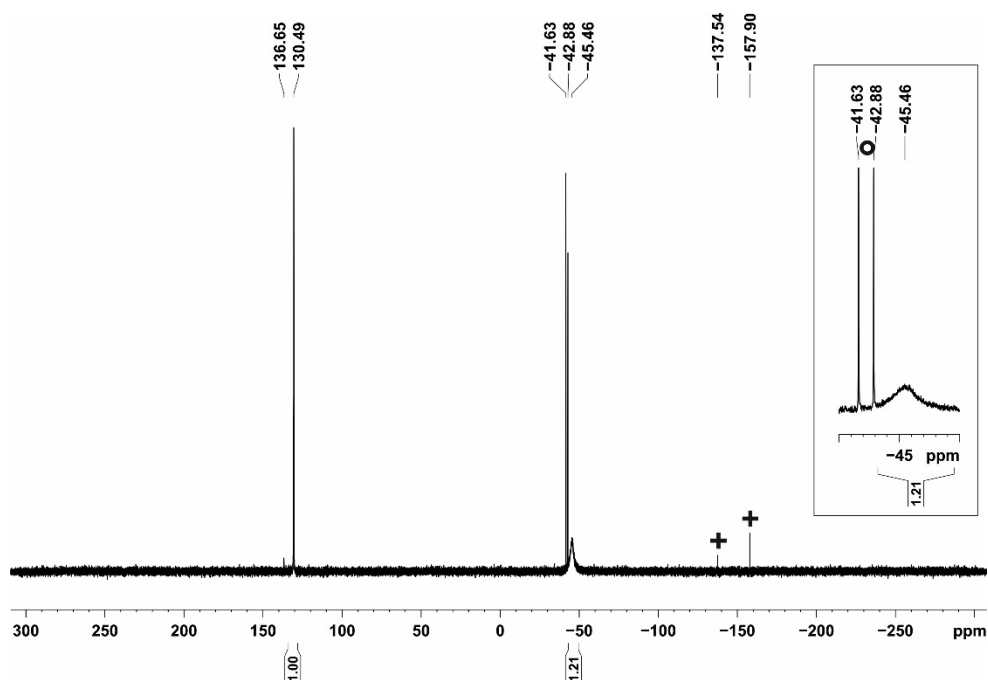


Figure SI 6.3 | $^{31}\text{P}\{^1\text{H}\}$ NMR spectrum (161.98 MHz, $[\text{D}_8]$ THF) at 333 K ($^\circ$ = phosphinine iron dimers **5**, + = hydrophosphinine iron complexes **endo-4** and **exo-4**).

6 C=O BOND SPLITTING BY A PHOSPHININE IRON(0) COMPLEX

6.7.1.2 $^{31}\text{P}\{^1\text{H}\}$ NMR monitoring of the formation of $1-\sigma$ and $1-\pi$ at 273 K

[K([18]crown-6)][Cp*Fe(C₁₀H₈)] (38 mg, 0.061 mmol) and L (20 mg, 0.061 mmol) were dissolved in [D₈]THF (0.8 mL) cooled to -35 °C inside an NMR tube fitted with a screw cap. $^{31}\text{P}\{^1\text{H}\}$ NMR spectra were immediately recorded at a controlled temperature of 273 K, and recorded periodically while being maintained at the same temperature.

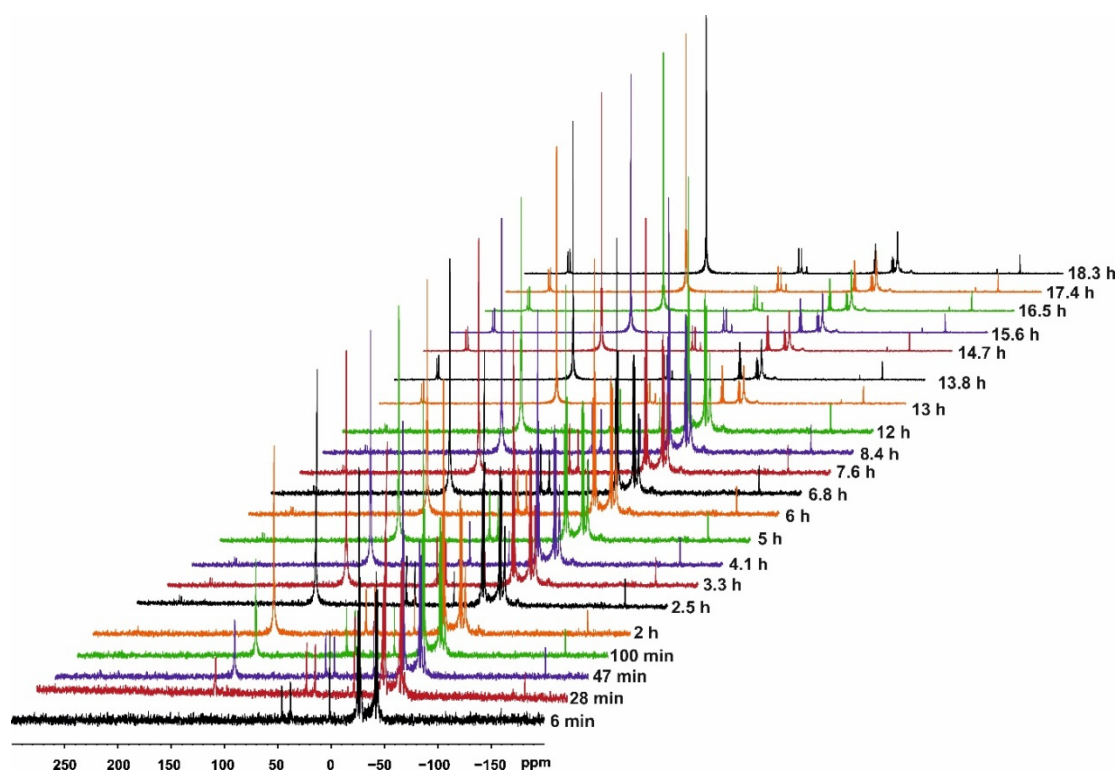


Figure SI 6.4 | $^{31}\text{P}\{^1\text{H}\}$ NMR monitoring (242.87 MHz, [D₈]THF) of the reaction between [K([18]crown-6)][Cp*Fe(C₁₀H₈)] and L at 273 K; range of 300 ppm $\geq \delta \geq$ -200 ppm.

6 C=O BOND SPLITTING BY A PHOSPHININE IRON(0) COMPLEX

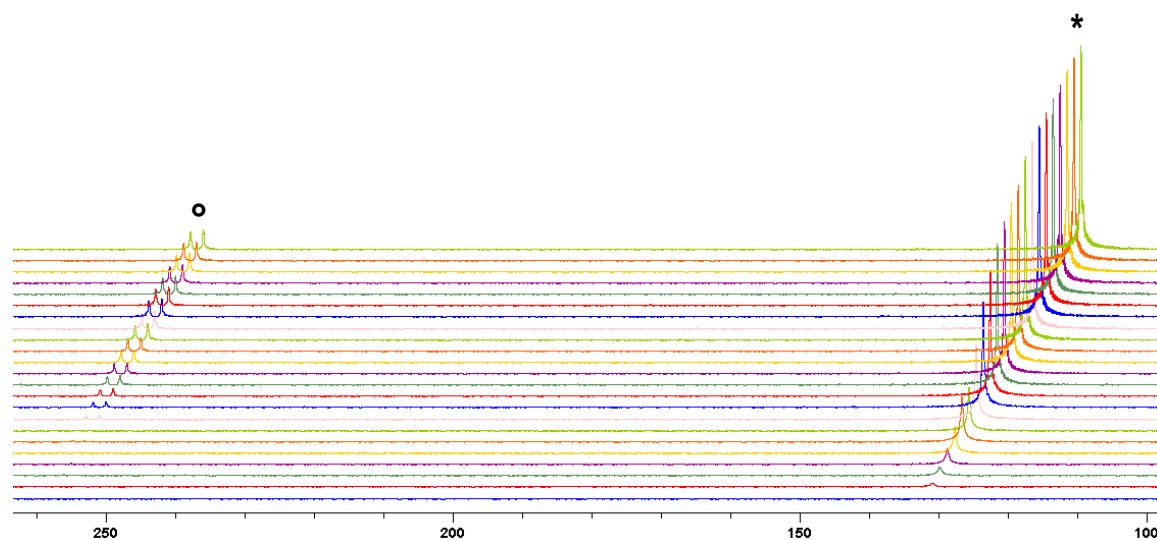


Figure SI 6.5 | $^{31}\text{P}\{^1\text{H}\}$ NMR monitoring (242.87 MHz, $[\text{D}_8]\text{THF}$) of the reaction between $[\text{K}([\text{18}]\text{crown-6})][\text{Cp}^*\text{Fe}(\text{C}_{10}\text{H}_8)]$ and **L** at 273 K; range of $260 \text{ ppm} \geq \delta \geq 130 \text{ ppm}$. * = **1- σ** , $^\circ$ = unknown species.

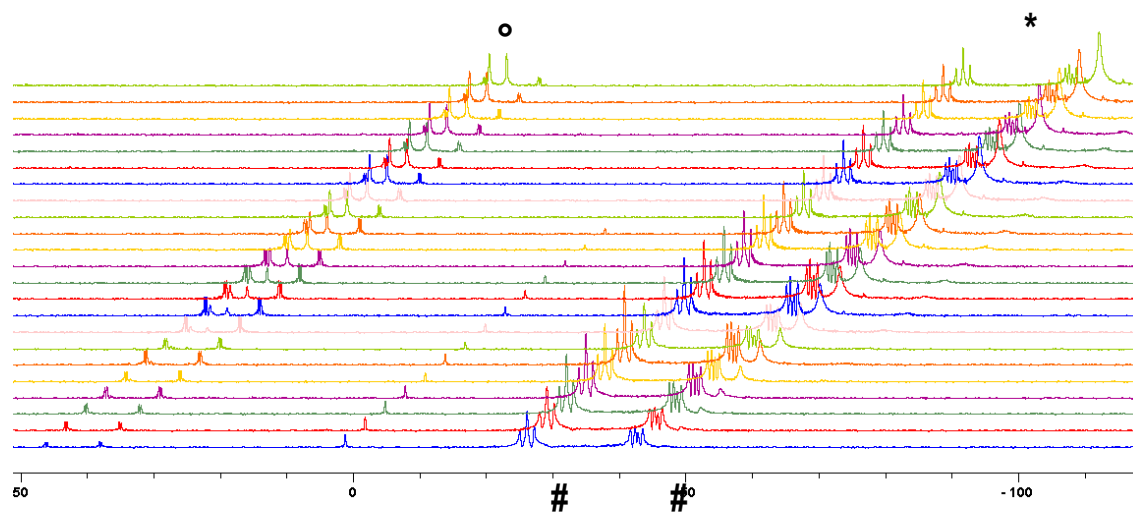


Figure SI 6.6 | $^{31}\text{P}\{^1\text{H}\}$ NMR monitoring (242.87 MHz, $[\text{D}_8]\text{THF}$) of the reaction between $[\text{K}([\text{18}]\text{crown-6})][\text{Cp}^*\text{Fe}(\text{C}_{10}\text{H}_8)]$ and **L** at 273 K; range of $50 \text{ ppm} \geq \delta \geq -50 \text{ ppm}$. * = **1- π** , $^\circ$ = unknown species, # = **2**.

6 C=O BOND SPLITTING BY A PHOSPHININE IRON(0) COMPLEX

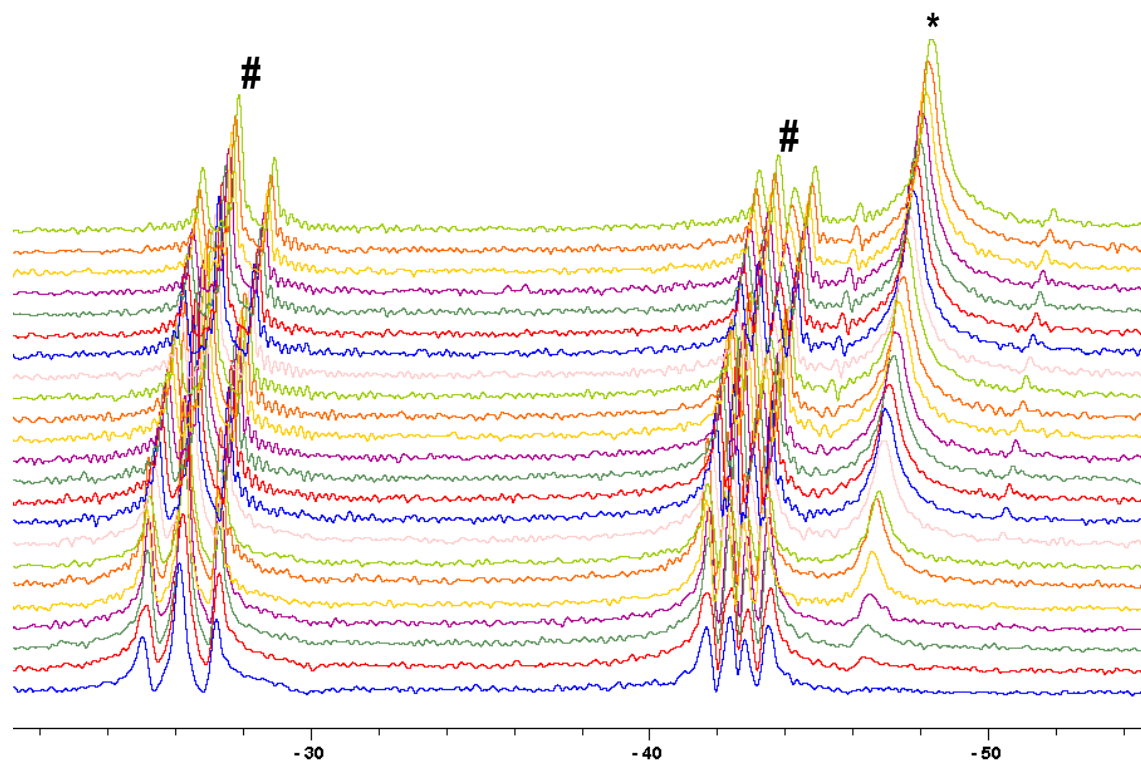


Figure SI 6.7 | $^{31}\text{P}\{^1\text{H}\}$ NMR monitoring (242.87 MHz, $[\text{D}_8]\text{THF}$) of the reaction between $[\text{K}([\text{18}\text{crown-6})][\text{Cp}^*\text{Fe}(\text{C}_{10}\text{H}_8)]$ and **L** at 273 K; range of $-20 \text{ ppm} \geq \delta \geq -50 \text{ ppm}$. * = $1-\pi$, # = 2 .

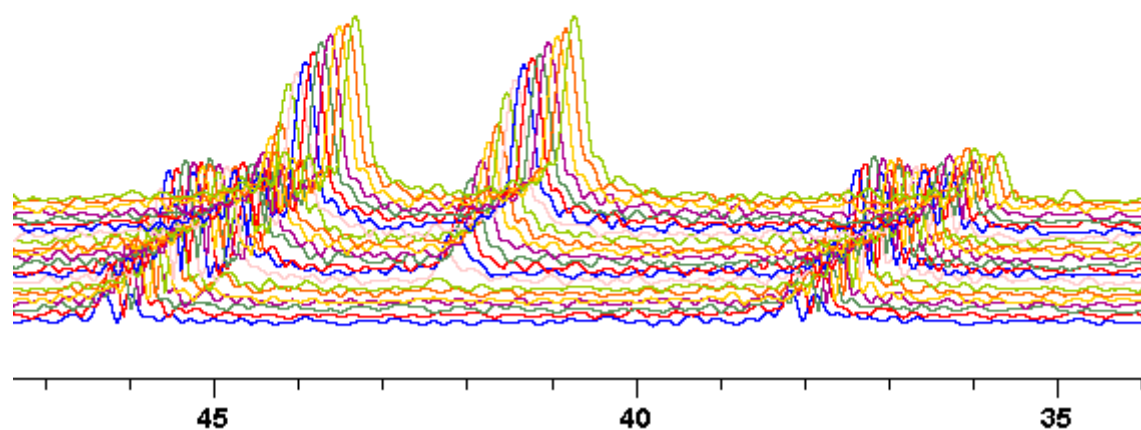
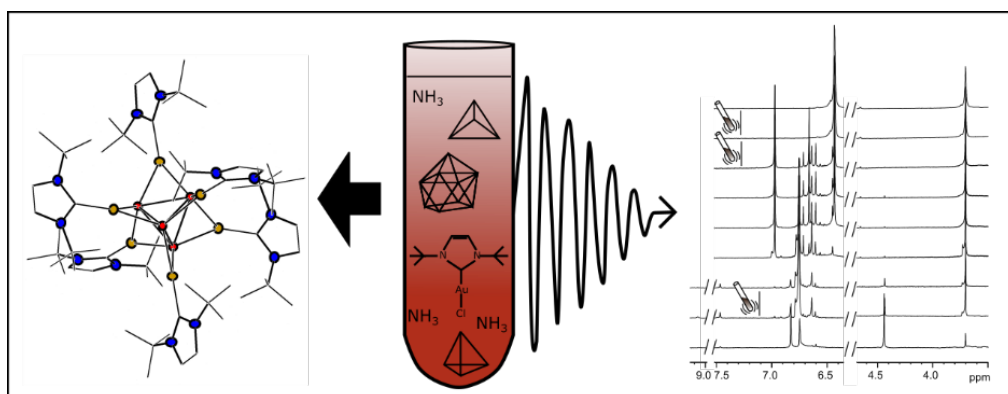


Figure SI 6.8 | $^{31}\text{P}\{^1\text{H}\}$ NMR monitoring (242.87 MHz, $[\text{D}_8]\text{THF}$) of the reaction between $[\text{K}([\text{18}\text{crown-6})][\text{Cp}^*\text{Fe}(\text{C}_{10}\text{H}_8)]$ and **L** at 273 K; range of $50 \text{ ppm} \geq \delta \geq 35 \text{ ppm}$; unknown species.

7 ON THE REACTIVITY OF $\text{NHC}^{\text{tBu}}\text{AuCl}$ TOWARDS $\text{Rb}_6\text{Cs}_6\text{Si}_{17}$: THE FIRST GOLD - SILICON CLUSTER $[(\text{NHC}^{\text{tBu}}\text{Au})_6(\text{H}^2\text{-Si}_4)]\text{Cl}_2 \cdot 7 \text{NH}_3$ AND AN IMIDE CAPPED GOLD TRIANGLE $(\text{NHC}^{\text{tBu}}\text{Au})_3\text{NHCl}$



Susanne M. Tiefenthaler,[†] Verena Streitferdt,[†] Josef Baumann, Stefanie Gärtner, Ruth M. Gschwind and Nikolaus Korber*

Zeitschrift für anorganische und allgemeine Chemie

Z. Anorg. Allg. Chem. **2020**, 646, 1595–1602.

DOI: 10.1002/zaac.202000275

[†] Both authors contributed equally to the publication

S. M. Tiefenthaler and V. Streitferdt both prepared the manuscript with input from all authors. V. Streitferdt did all NMR measurements and prepared corresponding Figures and sections in the SI. S. M. Tiefenthaler prepared all samples for NMR measurements and did all crystallization studies. J. Baumann performed theoretical calculations. Stefanie Gärtner contributed with data evaluation and discussions. R. M. Gschwind and N. Korber supervised and directed the project.

Reprinted (adapted) with permission from *Chem. Eur.J.* (via RightsLink). Text and Figures may differ from the original publication.
Source of this chapter: <https://doi.org/10.1002/zaac.202000275>

7.1 Abstract

Crystals of the two new compounds $(\text{NHC}^{\text{tBu}}\text{Au})_3\text{NHCl}$ and $[(\text{NHC}^{\text{tBu}}\text{Au})_6(\eta^2\text{-Si}_4)]\text{Cl}_2 \cdot 7 \text{NH}_3$ could be isolated from the reaction of $\text{Rb}_6\text{Cs}_6\text{Si}_{17}$ with $\text{NHC}^{\text{tBu}}\text{AuCl}$ in the presence of [2.2.2]-cryptand in liquid ammonia. Both compounds were characterized by single crystal X-ray diffraction and crystallize trigonally without any alkali metals or chelating ligands. Additionally, the crystal of $[(\text{NHC}^{\text{tBu}}\text{Au})_6(\eta^2\text{-Si}_4)]\text{Cl}_2 \cdot 7 \text{NH}_3$ was further interpreted by means of ELF and NBO calculations. In the case of $(\text{NHC}^{\text{tBu}}\text{Au})_3\text{NHCl}$, NMR experiments provided an exceptional insight into the reaction processes in solution and allowed for the detection of sequential precursors. In the class of capped gold triangles $(\text{NHC}^{\text{tBu}}\text{Au})_3\text{NHCl}$ impresses with its unique characteristics of being capped by an imide and bound to *N*-heterocyclic carbenes as ligands instead of the ubiquitously employed phosphines. The gold capped silicon tetrahedron $[(\text{NHC}^{\text{tBu}}\text{Au})_6(\eta^2\text{-Si}_4)]\text{Cl}_2 \cdot 7 \text{NH}_3$ represents the first known silicide-gold compound, as well as the first known functionalized Zintl anion, crystallized with a cationic central moiety.

7.2 Introduction

Gold is known to form intraelemental bonds, especially when in the oxidation state +1. This effect is commonly referred to as aurophilicity, since gold is the prime example of this interaction, even though it occurs in other late closed shell transition metals as well.^[1] A well-known type of gold(I) phosphine complexes are gold triangles, often capped with a nitrogen atom, which is usually connected to an organic or metalorganic group.^[2, 3] Over the past few years, *N*-heterocyclic carbenes (NHC) gained interest as ligands in organometallic chemistry. Among NHC-transition metal complexes, those containing Au(I) have proven great applicability in the fields of luminescence, medicinal chemistry and homogenous catalysis.^[4] NHC-Au(I) complexes find also use in coordination to homoatomic polyanions of main group metals, also termed Zintl anions, which provide versatile reaction possibilities.^[5] While homoatomic polyanions of germanium, tin and lead exhibit a rich coordination chemistry with transition metal complexes, only four examples of transition metal functionalized silicon clusters are known so far, starting with the publication of $[\text{Si}_9\text{ZnPh}]^{3-}$ by Sevov in 2006.^[6] Since then, two additional compounds containing a functionalized $[\text{Si}_9]^{x-}$ moiety have been reported ($[(\text{Ni}(\text{CO})_2)_2(\mu\text{-Si}_9)]^{8-}$ and $[\text{NHC}^{\text{Dipp}}\text{Cu}(\eta^4\text{-Si}_9)]^{3-}$),^[7, 8] as well as the mesitylcopper adduct $[(\text{MesCu})_2\text{Si}_4]^{4-}$.^[9] The latter represents the only known case of a tetrasilicide transition metal complex. Here, face capping of the tetrahedral anion by a 3d metal seems to be the most favorable coordination setting. Five compounds of functionalized Zintl ions containing gold – germanium bonds are known ($[\text{Au}_3\text{Ge}_{18}]^{5-}$, $[\text{Au}_3\text{Ge}_{45}]^{9-}$, $[(\eta^3\text{-Ge}\{\text{Si}(\text{SiMe}_3)_3\})\text{Au}(\text{NHC}^{\text{Dipp}})]$, $[\text{Au}[\text{Ge}_9(\text{Si}(i\text{Bu})_3)_3]_2]^-$ and $[\text{AuGe}_{18}\{\text{Si}(\text{SiMe}_3)_3\}_6]^-$),^[10] whereas literature only provides one example each for tin ($[\text{NHC}^{\text{Dipp}}\text{Au}(\eta^4\text{-Sn}_9)]^{3-}$) and lead ($[\text{Au}@\text{Pb}_{12}]^{3-}$).^[11] Gold silicon compounds are promising materials, particularly on the nanoparticle scale.^[12]

Despite the growing use of silicon Zintl ions, studies of Zintl ions in solution in general have only emerged in the last decade. NMR would be a suitable and non-destructive examination method, amongst others because of its applicability to a variety of different heteronuclei. However, NMR studies are particularly

challenging due to the complex preparation of the samples as well as the low solubility of the initial (silicon) Zintl phases entailing resolution problems. Despite great efforts, many solvation and reaction processes remain still unknown. Nevertheless, in recent years we were able to detect novel silicides, naked,^[13] as well as protonated,^[14, 15] in solutions of ammonia by means of multinuclear NMR spectroscopy and to show unexpected protonation and dynamic behavior. Reactions using complexes with a transition metal bound to aryl groups and, more recently, to NHCs have proven successful in the functionalization of silicide clusters, however, reactivity as well as structural studies in solution are still rare. In the case of gold functionalized silicides, no crystal structures are known, let alone studies in solution. By the herein investigated reactivity of silicide anions derived by dissolution of a phase with the nominal composition $\text{Rb}_6\text{Cs}_6\text{Si}_{17}$ towards the complex $\text{NHC}^{\text{tBu}}\text{AuCl}$, we were able to fill these gaps. Crystals of the compounds $(\text{NHC}^{\text{tBu}}\text{Au})_3\text{NHCl}$, consisting of an imide capped NHC functionalized gold triangle, and $[(\text{NHC}^{\text{tBu}}\text{Au})_6(\eta^2\text{-Si}_4)]\text{Cl}_2 \cdot 7 \text{NH}_3$, the first gold functionalized silicide, were obtained. Thereby we could open up the field of NHC functionalized and imide capped gold triangles, as well as of gold functionalized silicides.

7.3 Results and Discussion

7.3.1 Crystallographic Investigations

Crystals with the compositions $(\text{NHC}^{\text{tBu}}\text{Au})_3\text{NHCl}$ (**1**) and $[(\text{NHC}^{\text{tBu}}\text{Au})_6(\eta^2\text{-Si}_4)]\text{Cl}_2 \cdot 7 \text{NH}_3$ (**2**) were isolated from a liquid ammonia solution of $\text{Rb}_6\text{Cs}_6\text{Si}_{17}$, $\text{NHC}^{\text{tBu}}\text{AuCl}$ and [2.2.2]-cryptand, with **1** being the main product. The crystallographic data obtained by single crystal X-ray diffractometry is listed in Table 7.1. The molecular unit of **1** consists of an imide capped triangle of gold atoms, each bound to an NHC^{tBu} fragment (Figure 7.1). Chloride and imide generate a charge of -3 which is compensated by a threefold positively charged $(\text{NHC-Au})_3$ moiety. This corresponds well to the assumption of an oxidation number of $+1$ for each gold atom.^[2, 3]

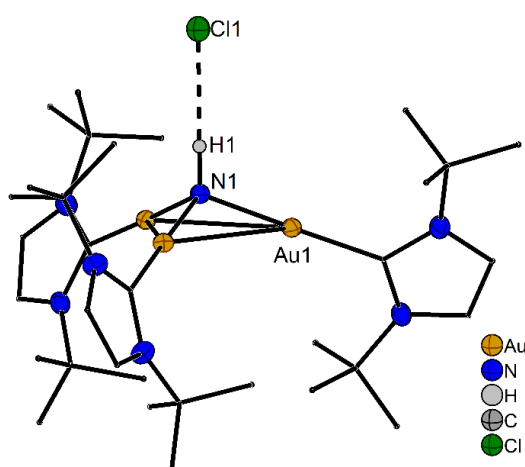


Figure 7.1 | Formular unit of **1**; hydrogen atoms are omitted and carbon atoms displayed as wires/sticks for added visibility; thermal displacement ellipsoids are drawn with 50 % probability.

While the gold atom and the NHC^{tBu} fragment are situated on a general position, the imide and chloride ion occupy the special position 3a of space group $R\bar{3}$. The nitrogen atom is elevated above the plane of the gold

7 ON THE REACTIVITY OF $\text{NHC}^{\text{tBu}}\text{AuCl}$ TOWARDS $\text{RB}_6\text{CS}_6\text{SI}_{17}$

triangle and the bond length between nitrogen and gold (2.026(3) Å) is slightly shorter than in known structures.^[2] The gold-gold distance is in the range of aurophilic bonds with a length of 3.2598(3) Å.^[1] The chloride is surrounded by 13 hydrogen bonds in total, with bond distances ranging from 2.424 to 3.858 Å. To summarize, we were able to isolate crystals of the first example of an NHC functionalized gold(I) triangle capped by an imide. As it is known, that the $[\text{NHC}^{\text{tBu}}\text{Au}]^+$ is isolobal to H^+ , compound **1** can be considered a heavy derivative of ammonium chloride.

The central moiety in the compound $[(\text{NHC}^{\text{tBu}}\text{Au})_6(\eta^2\text{-Si}_4)]\text{Cl}_2 \cdot 7 \text{NH}_3$ (**2**) is a silicon tetrahedron with a $\text{NHC}^{\text{tBu}}\text{Au}$ fragment capping each edge (Figure 7.2). A 50:50 disorder is present in the structure, giving the silicon center the appearance of a cube. This cube is comprised of two interlocked tetrahedra, each present in the structure with 50 % occupation. This 50% disorder is even present in $P1$, therefore the description in $P\bar{3}1c$ is correct. The two symmetrically independent Si-Si bond lengths are slightly elongated with 2.530(3) Å and 2.537(4) Å, in comparison to the bonds in the naked $[\text{Si}_4]^{4-}$ with lengths between 2.4032 Å and 2.4329 Å.^[16] The phenomenon of the elongation of a capped edge is also known from the cluster $[\text{HSi}_4]^{3-}$, recently reported by us^[14], from $[(\mu_2\text{-H})(\eta^2\text{-Ge}_4)\text{ZnPh}_2]^{3-}$ reported by Fässler *et al.*^[17], as well as $(\text{tBu}_3\text{Si})_4\text{Si}_4$.^[18] The Si-Au bond lengths range from 2.4020(3) Å to 2.412(2) Å and are therefore in between the length of a silicon-nickel (2.3 Å)^[7] and a silicon-copper bond (2.43 Å).^[8, 9] Incidentally, this distance is the exact sum of the single bond radii calculated by Pyykkö, accounting for experimental uncertainty.^[19]

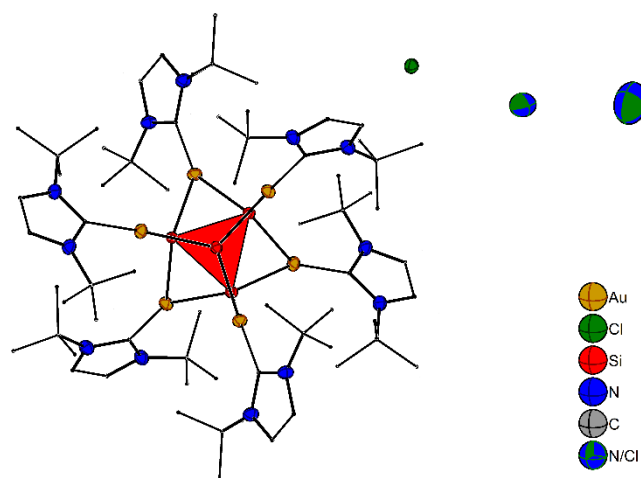


Figure 7.2 | Formular unit of **2**; Hydrogen atoms are omitted and carbon atoms are displayed as wires/sticks for added visibility; thermal displacement ellipsoids are drawn with 50 % probability.

Since the oxidation state of gold in $\text{NHC}^{\text{tBu}}\text{AuCl}$ is +1, as well as in the fragments in compound **1**, we assume a charge of +1 for each $\text{NHC}^{\text{tBu}}\text{Au}$ fragment in compound **2**. This assumption leads us to assign a total charge of +2 to the central moiety $[(\text{NHC}^{\text{tBu}}\text{Au})_6(\eta^2\text{-Si}_4)]$ (**2A**), as the involved $[\text{Si}_4]$ cluster retains its fourfold negative charge. In addition to the gold-silicon moiety, only three other crystallographically independent positions are present. Of these positions, only one can unequivocally be determined to be a chlorine atom (Cl1). We presume a charge of -1 for this atom, assigning it to be a chloride ion which results in a charge balance of +1. The remaining two atoms are on the special positions $12i$ and $4f$ respectively,

leading to eight symmetry-generated positions. For these remaining eight positions, mixed occupied sites involving ammonia and chloride were realized resulting in an overall single negative charge (see SI). Together with Cl1 the twofold positive charge is balanced. This model is also strongly supported by the observed thermal stability of the crystal, as the cell could still be determined after several minutes at room temperature, despite the known extreme thermal instability of ammoniates due to the evaporation of ammonia. This might be an indication for additional strong interactions between Cl and NH_3 , keeping the ammonia in the crystal, due to strong ion dipole interactions.

Similar to compound **1**, the central moiety can be seen as a heavier derivative of an unknown $[\text{Si}_4\text{H}_6]^{2+}$, considering the isolobal analogy between $[\text{NHC}^{\text{tBu}}\text{Au}]^+$ and a proton. Interestingly though, calculations predicted an open structure for $[\text{Si}_4\text{H}_6]^{2+}$, and not, as it is the case in **2a**, a tetrahedron.^[20]

7.3.2 Theoretical calculations

Since the charge of the gold-silicon moiety could not be determined unequivocally based on the crystallographic data, calculations were performed to clarify the charge situation. Due to the high number of atoms and the amount of electrons from the gold atoms, the *tert*-butyl groups were replaced by methyl groups. In order to confirm the charge of +2, geometry optimizations (BP86/def2-TZVPP, CPCM = ammonia) were carried out assigning different charges +2, 0 and -4 to the cluster (see SI). The optimized geometries show a tetrahedral Si_4 moiety only in the case of the twofold positively charged compound. The exact calculated values for bond lengths and angles are listed in Table SI 7.1.

Table 7.1 | Crystallographic data and details of the structure determinations of $(\text{NHC}^{\text{tBu}}\text{Au})_3\text{NHCl}$ (**1**) and $[(\text{NHC}^{\text{tBu}}\text{Au})_6(\eta^2\text{-Si}_4)]\text{Cl}_2 \cdot 7\text{NH}_3$ (**2**).

Chemical Formula	$(\text{NHC}^{\text{tBu}}\text{Au})_3\text{NHCl}$	$[(\text{NHC}^{\text{tBu}}\text{Au})_6(\eta^2\text{-Si}_4)]\text{Cl}_2 \cdot 7\text{NH}_3$
CSD No.*	1954886	1957884
Composition	$\text{C}_{33}\text{H}_{61}\text{Au}_3\text{ClN}_7$	$\text{C}_{66}\text{H}_{120}\text{Au}_6\text{Cl}_{1.97}\text{N}_{19.02}\text{Si}_4$
M [g·mol ⁻¹]	1182.24	2544.27
Crystal System	trigonal	trigonal
Space group	<i>R</i> 3	<i>P</i> 31 <i>c</i>
a [Å]	16.2851(3)	14.1243(3)
b [Å]	16.2851(3)	14.1243(3)
c [Å]	12.9883(3)	26.6537(5)
α [°]	90	90
β [°]	90	90
γ [°]	120	120
V [Å ³]	2983.07(13)	4604.9(2)
Z	3	2
F(000) (e)	1686.0	2426.0
ρ _{calc} [g·cm ⁻³]	1.974	1.835
μ [mm ⁻¹]	11.136	9.676
2θ-range for data collection [°]	6.908 to 52.756	6.53 to 61.162
Reflections collected/independent	3753 / 2311	25958 / 4454
Data / restraints / parameters	2311 / 1 / 139	4454 / 0 / 161
Goodness-of-fit on F ²	1.035	1.050
Final R indices [I > 2σ(I)]	R ₁ = 0.0148, wR ₂ = 0.0353	R ₁ = 0.0318, wR ₂ = 0.0478
R indices (all data)	R ₁ = 0.0148, wR ₂ = 0.0353	R ₁ = 0.0571, wR ₂ = 0.0532
R _{int}	0.014	0.0552
Δρ _{max} , Δρ _{min} [e·Å ⁻³]	0.67 / -0.45	0.66 / -0.55
Flack parameter	-0.005(10)	

*Further details of the crystal structure investigations may be obtained from FIZ Karlsruhe, 76344 Eggenstein-Leopoldshafen, Germany (Fax: (+49)7247-808-666; E-mail: crysdata@fiz-karlsruhe.de, on quoting the deposition numbers.

7 ON THE REACTIVITY OF $\text{NHC}^{\text{tBu}}\text{AuCl}$ TOWARDS $\text{RB}_6\text{Cs}_6\text{Si}_{17}$

A study of the isosurface from ELF (Electron Localization Function) calculation on $[\text{Si}_4(\text{Au}^{\text{Me}}\text{NHC})_6]^{2+}$ shows a tetrasynaptic basin in the center of the Si tetrahedron (Figure 7.3). With a population of 1.57 electrons, it can be interpreted as a four-center bond. Furthermore, there are no attractors between two silicon atoms but between each silicon atom and its three neighboring gold atoms. These basins are populated with 0.8 electrons each.

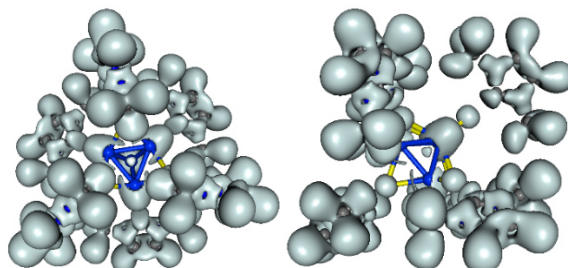


Figure 7.3 | ELF isosurface of $[(\text{NHC}^{\text{tBu}}\text{Au})_6(\eta^2\text{-Si}_4)]^{2+}$ with $\eta = 0.67$; blue atoms represent silicon, yellow bonds lead to gold atoms.

Calculating the NPA of the cluster atoms with BP86/def2-TZVPP level of theory results in a negative charge of -0.53 at the Si atoms and a positive charge of +0.39 at every Au atom. The Au-C bonds are nearly fully occupied with 1.94062 electrons. Looking at the hybridization, one can notice the quite low contribution of d-orbitals in the Si lone pairs ($\text{sp}^{0.27\text{d}^{0.01}}$), Si-Si- bonds ($\text{sp}^{12.8\text{d}^{0.27}}$) and Au-C bonds (Au: $\text{sd}^{0.08}$, C: $\text{sp}^{1.6\text{d}^{0.01}}$). The Au-NHC fragments and the Si_4 tetrahedron are treated separately by NBO. Studying the second order perturbation, however, shows a substantial stabilization energy due to electron delocalization from the Si-Si bond to the antibonding Au-C bond. This corresponds to the side-on coordination of the tetrahedron to the adjacent Au-NHC fragments (see Table 7.1/SI).

In the case of germanium, recently the compound $[(\mu_2\text{-H})(\eta^2\text{-Ge}_4)\text{ZnPh}_2]^{3-}$ has been reported by Fässler *et al.*, in which functionalization, as well as protonation occurs edge-on.^[17] For silicon, so far no compound with a transition metal ligand capping the edge of a tetrahedron has been published. However, in 2018 a structure for protonated P_4 was published, showing the edge-on protonation of the compound, which is electronically comparable to $[\text{Si}_4]^{4-}$, according to the pseudo-electron concept.^[21]

In conclusion, the crystallographic studies, as well as the calculations suggest the charge of **2A** as twofold positive. Compound **2** is unique in three ways, as it not only represents the first gold-functionalized silicide but also the first silicon Zintl cluster the edges of which are capped by transition metal ligands. Moreover, it represents the first known example of a cationic moiety crystallized from ammonia which contains a functionalized Zintl ion.

7.3.3 NMR Studies

In recent years, we were able to discover fascinating new silicides (Si_4^{4-} , HSi_9^{3-} , HSi_4^{3-} and Si_5^{2-}) in solutions of $\text{K}_6\text{Rb}_6\text{Si}_{17}$ in liquid ammonia by means of NMR spectroscopy. Hence, we were curious which species would arise in a solution of $\text{K}_6\text{Rb}_6\text{Si}_{17}$ in presence of the gold complex $\text{NHC}^{\text{tBu}}\text{AuCl}$. To increase solubility for NMR spectroscopic investigation in liquid ammonia, $\text{K}_6\text{Rb}_6\text{Si}_{17}$ instead of $\text{Cs}_6\text{Rb}_6\text{Si}_{17}$ was applied and [2.2.2]-cryptand was added.^[22] In the following, based on the NMR spectroscopic examination of three samples (i-iii), first possible structures of the species detected in solution are discussed and a potential reaction mechanism to **1** is presented. Thereupon follows the analysis of a ^1H -NMR reaction monitoring and finally the presence of silicides in solution is examined. We started our investigations with a sample of silicide, gold complex and cryptand in a 1:1:1.5 ratio (sample i). One hour after preparation of the colorless mixture, the reaction was followed by ^1H -NMR at 233 K (see Figure 7.4). The ^1H -NMR monitoring revealed the formation of various species containing the ligand NHC^{tBu} . Due to the structure of the ligand and the resulting complexes, exclusively chemical shifts can be used for the assignment of the species. Yet, 2D ^1H - ^{13}C -HSQC, -HMQC and -HMBC, ^1H - ^{15}N -HSQC, ^1H - ^1H -NOESY, ^1H -DOSY together with 1D ^1H signal monitoring and integration enabled the assignment of the majority of the signals, even though being almost exclusively singlets (see Figure 7.4 left). Carbenic carbons, denoted as C^2 , exhibit distinctly different ^{13}C -NMR shifts depending especially on the type of their substituent. For C^2 connected to Au(I) chemical shifts between 156 ppm and 200 ppm are reported,^[23-26] while C^2 of the free NHC^{tBu} carbene appears at a higher ^{13}C -NMR shift of around 213 ppm.^[26, 27] The C^2 shift of the corresponding $\text{NHC}^{\text{tBu}}\text{H}^+\text{Cl}^-$ salt is reported at 135.5 ppm,^[27] whereas shifts of dihydro NHC species such as $\text{NHC}^{\text{tBu}}\text{H}_2$ and $(\text{NHC}^{\text{tBu}})_2\text{H}_2$ are reported at much lower values, i.e. between 63 and 91 ppm.^[28, 29] Consequently, the chemical shift of the carbenic carbon C^2 was a key factor for the following assignments. In case of $\text{L}^1\text{-Au(I)-L}^2$ complexes, the connectivity between those ligands was indicated either *via* signal monitoring and integration or *via* ^1H - ^1H -NOESY. A sample with a slightly different ratio of $\text{K}_6\text{Rb}_6\text{Si}_{17}$ to $\text{NHC}^{\text{tBu}}\text{AuCl}$ and [2.2.2]-cryptand (1:2:2; sample ii) was found to react considerably slower than sample i (1:1:1.5 ratio) while generating mainly the same NHC species (see SI for exemplary spectrum) allowing for in-depth NMR investigations at 233 K and lower temperatures down to 203 K.

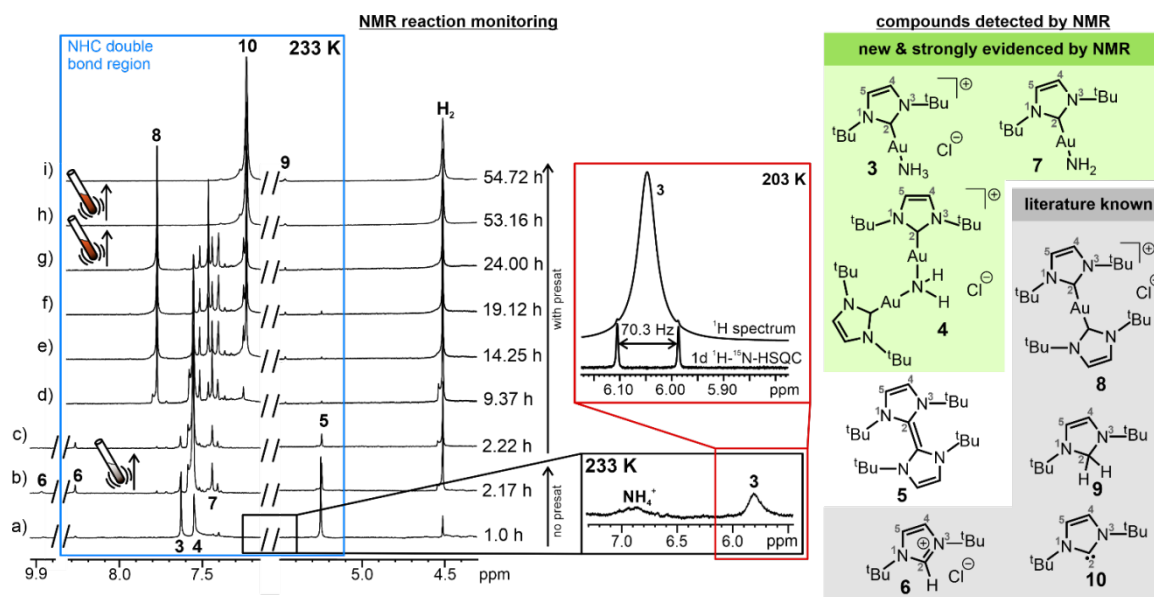


Figure 7.4 | Left: ^1H -NMR reaction monitoring of a mixture of $\text{K}_6\text{Rb}_6\text{Si}_{17}$ (1 eq.), $\text{NHC}^{\text{tBu}}\text{AuCl}$ (1 eq.) and [2.2.2]-cryptand (1.5 eq.) in liquid ammonia at 233 K reveals several reaction intermediates and their sequence. For spectra a) and b) solvent saturation was switched off to enable the detection of intermediates which exchange with NH_3 such as **3** and NH_4^+ ; for spectra c) – i) solvent saturation was switched on to increase sensitivity for the detection of small intermediates such as **9**. NMR tubes with lines of motion indicate shaking of the NMR tube. (In the light of past experience, the presence of Zintl ions in solution was usually associated with a coloration of the solution. Hence, by shaking the colorless sample from time to time, we hoped for dissolution of Zintl ions.) Middle bottom: spectral zoom of a) of the not displayed region. Middle top: stacked spectra (standard ^1H -NMR spectrum and 1D ^1H - ^{15}N -HSQC) of the ^1H -NMR region of NH_3 of **3** in sample iii at 203 K. Right: Compounds detected throughout the NMR-spectroscopic investigation of samples i-iii. Structures, strongly evidenced by NMR, are highlighted by boxes. The structure of signal **5** can only be tentatively assigned since spectroscopical evidence was limited.

7.3.4 Structural Assignment

The majority of the signals emerging during the ^1H -NMR reaction monitoring displayed in Figure 7.4 were assigned by a combined investigation of the samples i and ii as well as a sample consisting solely of $\text{NHC}^{\text{tBu}}\text{AuCl}$ in liquid ammonia (sample iii).

Of particular note is the detection and assignment of the complexes $\text{NHC}^{\text{tBu}}\text{-Au(I)-NH}_3^+\text{Cl}^-$ (**3**) and $[(\text{NHC}^{\text{tBu}}\text{-Au(I)})_2\text{-NH}_2]^+\text{Cl}^-$ (**4**) (see Figure 7.4), both of which were yet unknown to literature. Only for **3** a similar copper complex $\text{NHC}^{\text{Dipp}}\text{Cu-NH}_3^+\text{BF}_4^-$ has been reported,^[30] which may support the structural assignment of **3**. For **4**, there exists a hydroxyl analogue $[\text{NHCAu-OH-AuNHC}][\text{BF}_4]$ which is used as catalyst in organic chemistry.^[31] Key chemical shifts such as the ^{13}C -NMR shifts of C^2 (166 ppm for **3** and 168 ppm for **4**) were used to identify the coordination of NHC to Au(I). The existence of NH_3 and NH_2 moieties in **3** and **4** were elucidated by ^1H - ^{15}N -HSQC experiments and integration (see Figure 7.4 bottom right and SI). The associated ^1H -NMR signals of H^4 and H^5 at double bond (see Figure 7.4) followed the intensity pattern of NH_3 in **3** and NH_2 in **4**. In the case of complex **4**, this relation was confirmed by an NOE crosspeak. Furthermore, ^1H -DOSY (diffusion ordered spectroscopy) experiments revealed a larger hydrodynamic radius of **4** compared to **3** supporting their structures (see SI for more information on DOSY). Considering the structures of **3**, **4** and **1** (see Figure 7.1 and Figure 7.4), **3** might be the structural precursor of **4** and **4** might

be the precursor of **1**. The other signals could be assigned to structures **6**, **8**, **9** and **10** (see Figure 7.4) with the help of the existing literature.^[23, 27, 28, 32] A crystal structure for compound **8** could be determined from a separate reaction containing tin (for details, see SI). The structure belonging to the signal at 5.25 ppm could only be guessed as NHC^{tBu} -dimer (**5**) based on the assumption of an existing Wanzlick equilibrium between the NHC and its dimer^[33] and upon comparison of its $^1\text{H-NMR}$ shift with literature values (see SI for more information).^[34] For **7** (see Figure 7.4) $^1\text{H-}^1\text{H-EXSY}$ and $^1\text{H-DOSY}$ experiments evinced that this compound is in chemical exchange with **3** and of similar size. From a chemical point of view and with regard to an assumed exchange *via* protonation/deprotonation, we considered $\text{NHC}^{\text{tBu}}\text{-Au-NH}_2$ (**7**) as an appropriate exchange partner (for EXSY studies see discussion below and Figure 7.6; for further information see SI).

7.3.5 Proposed Mechanism towards the Formation of **1**

The $^1\text{H-NMR}$ signals of the starting material $\text{NHC}^{\text{tBu}}\text{-AuCl}$ (H^4 , H^5 at 7.12 ppm^[24]) have never been observed even in freshly prepared samples. Instead of $\text{NHC}^{\text{tBu}}\text{-AuCl}$, **3** and **4** were detected in all samples. This indicates a fast ligand exchange from Cl^- to NH_3 on gold due to the enormous excess of NH_3 (see Figure 7.5a), which provides the first precursor **3** in the formation of crystal **1**. As the next step, we propose a chemical equilibrium between **3** and **7** as indicated by proton exchange in EXSY experiments (Figure 7.5b). The detected intermediates provide several pathways for the abstracted protons. NH_4^+ (see Figure 7.4 middle and discussion below) and the generation of **6** hint at trapping by the solvent NH_3 or by the NHC^{tBu} carbene **10**. H_2 and **9** indicate the transformation of protons into hydrides (H^-) *via* oxidation of silicides (for the presence of silicides see discussion below, for the discussion of a trapping by Au-species see SI). Next, complex **4** can be formed from **3** *via* a ligand exchange of NH_3 by **7** (c). For the further reaction pathway towards **1**, no additional intermediates could be detected. However, a repetition of the discussed reaction scheme directly leads to the formation of **1**. Formal abstraction of HCl from **4** leads to **11**. Next again complex **1** can be formed from **3** *via* a ligand exchange of NH_3 by **11**(e).^[35] Therefore, we assume the proposed reaction mechanism in Figure 7.5 to be highly probable.

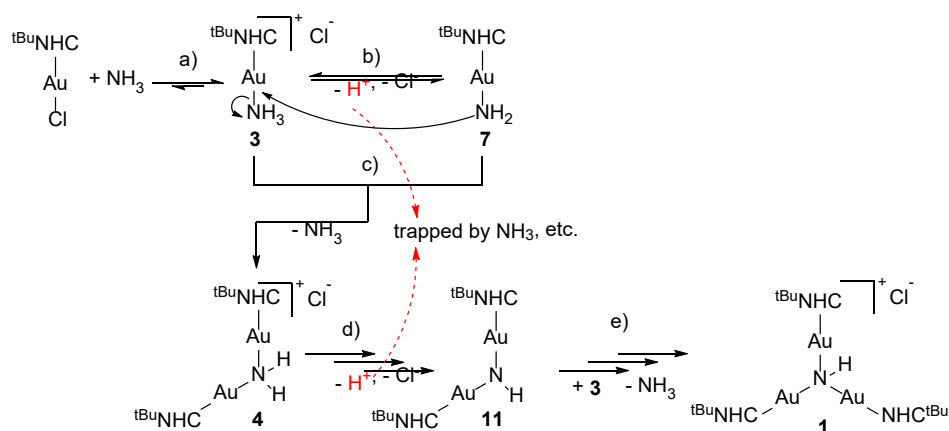


Figure 7.5 | Proposed mechanism for the formation of crystal **1** in solution.

Next, the reaction monitoring was analyzed in light of the proposed mechanism. Due to the limited solubility of most of the intermediates (see Figure SI 7.28 for evidence), only the sequence of the intermediates can

be interpreted. Indeed, in accordance with our mechanism, after one hour, a remarkable decrease of complex **3** was observed while the signals of **4** and **7** increased (see Figure 7.4b). Furthermore, after about 9 hours, the precursor **3** and the $\text{NHC}^{\text{tBu}}\text{H}^+\text{Cl}^-$ salt **6** disappeared and a significant signal of $\text{NHC}^{\text{tBu}}\text{-Au-NHC}^{\text{tBu}}\text{-Cl}^-$ **8** emerged confirming the principle possibility of ligand exchange NH_3 versus NHC^{tBu} .

Without silicides the reaction stops at **3** as main species accompanied by small amounts of **4**, **6** and **8** (even up to one year at 193 K). This shows that the presence of silicides seems to be important for the reaction progress, most probably due to their potential to transform protons for further interactions. This deviates from other previous reports, in which ammonia can easily be fully aminated^[36]. E.g. for R_3P ligands instead of NHCs on gold (I) the full auration can be obtained under suitable reaction conditions.^[37]

Beyond the proposed mechanism, some additional observations are interesting. About 14 hours after sample preparation, the signal of free carbene **10** appeared (see Figure 7.4e). One day after preparation (Figure 7.4g), the NMR tube was shaken causing the supernatant to turn orange typical for dissolved silicides. In addition, the signals of the $\text{NHC}^{\text{tBu}}\text{-Au}$ -species vanished and only the free carbene remained (see Figure 7.4i). Via ^{29}Si -NMR we could observe that the shaking really dissolved significant amounts of silicides (see below and Figure SI 7.32) which seem to change drastically the solubility of the gold complexes.

7.3.6 Chemical Exchange and ^{29}Si Studies

Next saturation transfer and EXSY experiments were used to gain insight into the chemical equilibria in solution. **3** exchanges with **7**, NH_3 and **6**. Furthermore, NH_3 exchanges with NH_4^+ and **6**.^[40] The exchange between **3** and **7** (see Figure 7.6a) corroborates the second step in the proposed mechanism (see Figure 7.5b). The exchange of **3** with NH_3 (see Figure 7.6b) supports both the feasibility of ligand exchange on Au and the structure of **3**. At first glance the detected chemical exchange between NH_3 and **6** (Figure 7.6d) seems to be unlikely, however we assume a multistep exchange over NH_4^+ (Figure 7.6c, e; the direct exchange between ammonium and **6** is below the detection limit). This is in line with the detected exchange between **6** and **3** (see Figure 7.6f), which is one step further in the multistep exchange between **6** and NH_3 (see SI for an in-depth investigation).

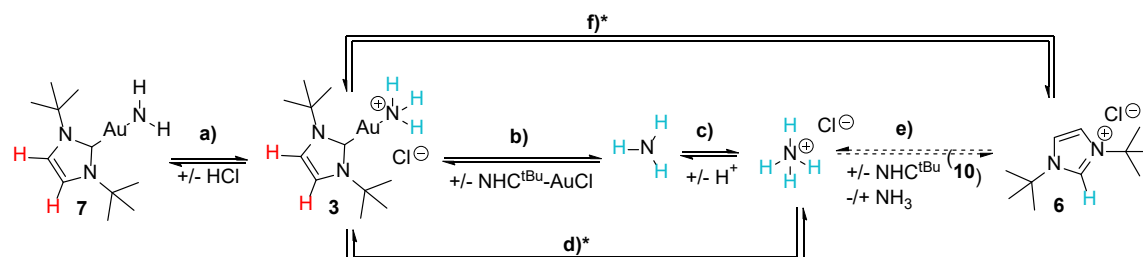


Figure 7.6 | Observed chemical exchange matrix from EXSY cross peaks. The exchange between ammonia and **3**, as well as between **3** and **7** corroborate parts of the proposed reaction mechanism. Asterisks indicate EXSY crosspeaks, which are assumed to be multistep exchange peaks. The exchange e) is below the detection limit most due to the low signal intensities of **6** and ammonium.

Finally, ^{29}Si -NMR experiments were used to gain insight into the silicide species present during this reaction. For the sample shown in Figure 7.4, only after 24 h and shaking of the sample silicides could be detected (without shaking also after 24 h no silicides can be observed). Then, the well-known degradation product H_3Si^- ,^[13, 41] as well as the literature known protonated silicide $[\text{HSi}_9]^{3-}$ were detected (see Figure SI 7.30-32 for spectra).^[15] Besides, 1D ^{29}Si spectra showed a couple of broad signals in the range between -300 and -360 ppm without coupling pattern, which could not be assigned (see Figure SI 7.32a in SI). Nonetheless also below NMR detectability the silicides seem to play a key role since the reaction progress stops mainly at **3** without silicides present.

Overall, our combined NMR investigations of three samples (i-iii) allowed for the detection of the sequential structural precursors **3** and **4** of crystal **1** in solution. Furthermore, an exchange matrix and a plausible mechanism for the formation of crystal **1** could be postulated upon experimental evidence obtained by NMR.

7.4 Conclusion

Single crystal X-ray diffractometry of two different crystals obtained from a reaction of $\text{Rb}_6\text{Cs}_6\text{Si}_{17}$ with $\text{NHC}^{\text{tBu}}\text{AuCl}$ in presence of [2.2.2]-cryptand in liquid ammonia revealed two new structures: $(\text{NHC}^{\text{tBu}}\text{Au})_3\text{NHCl}$ (**1**) and $[(\text{NHC}^{\text{tBu}}\text{Au})_6(\eta^2\text{-Si}_4)]\text{Cl}_2 \cdot 7 \text{NH}_3$ (**2**). The compound $(\text{NHC}^{\text{tBu}}\text{Au})_3\text{NHCl}$ (**1**) represents a first in its class of complex, as, while the motif of a nitrogen capped gold triangle is quite well known, no species with an imide has ever been reported. Furthermore, instead of NHC fragments being bound to the gold atoms, generally a phosphine ligand is in place. In case of **2**, crystal structure determination and calculations suggested a silicon tetrahedron capped with six $\text{NHC}^{\text{tBu}}\text{Au}$ fragments on the edges with a total charge of +2. In addition to being only the fifth reported metal functionalized silicide, **2** represents the first gold-functionalized silicide and also the first silicon cluster with edge-capping by transition metal ligands. Furthermore, it is the first reported crystal structure with a cationic central moiety, comprised of a functionalized silicon cluster.

^1H -NMR reaction monitoring of samples containing $\text{K}_6\text{Rb}_6\text{Si}_{17}$, $\text{NHC}^{\text{tBu}}\text{-Au-Cl}$ and [2.2.2]-cryptand in liquid ammonia together with various 2D NMR experiments allowed for the detection and characterization *inter alia* of $\text{NHC}^{\text{tBu}}\text{Au-NH}_3^+$ (**3**) and $(\text{NHC}^{\text{tBu}}\text{Au})_2\text{-NH}_2^+$ (**4**), two potential precursors in the formation of crystal **1**. Moreover, we could demonstrate that ammonia is not an innocent solvent, since it is involved in Brønsted acid-base equilibria with NHC-carbenes and in association-dissociation equilibria with NHC-Au-complexes considerably influencing the product outcome. Furthermore, based on our NMR studies, we could postulate a mechanism towards the formation of crystal **1** and understand the quantity distribution of crystals **1** and **2**.

7.5 Experimental Section

All operations were carried out under argon atmosphere, either in a glovebox or with the help of Schlenk techniques. Liquid ammonia was dried and stored over sodium and cooled with a dry ice/ethanol mixture. The alkali metals were synthesized by reaction of the respective chloride with calcium and subsequently purified by distillation.

Synthesis of $\text{Rb}_6\text{Cs}_6\text{Si}_{17}$: The phase was synthesized by solid-state reaction techniques. Elemental rubidium (717.1 mg, 8.39 mmol), caesium (1115.2 mg, 8.39 mmol) and silicon (667.7 mg, 23.77 mmol) were put into a tantalum ampoule that was subsequently welded shut and jacketed in a fused silica ampoule. The ampoule was heated to 1223 K at a rate of 25 K/h, held at that temperature for two hours and consequently cooled to room temperature at 20 K·h⁻¹. The brittle, black reaction product was isolated and stored in an argon filled glovebox and characterized by powder X-ray diffraction and Raman spectroscopy.

Synthesis of $\text{K}_6\text{Rb}_6^{29}\text{Si}_{17}$ (100 % enriched): The phase was synthesized by solid-state reaction techniques. Elemental potassium (119.1 mg, 3.05 mmol), rubidium (260.3 mg, 3.05 mmol) and enriched silicon (250.0 mg, 8.63 mmol) were put into a tantalum ampoule that was subsequently welded shut and jacketed in a fused silica ampoule. The ampoule was heated to 973 K at a rate of 25 K/h, held at that temperature for 24 hours and consequently cooled to room temperature at 20 K·h⁻¹. The brittle, black reaction product was isolated and stored in an argon filled glovebox and characterized by powder X-ray diffraction and Raman spectroscopy. $\text{K}_6\text{Rb}_6^{29}\text{Si}_{17}$ (10 mg, 0.01 mmol), $\text{NHC}^{\text{tBu}}\text{AuCl}$ (4.6 mg, 0.01 mmol or 9.2 mg, 0.02 mmol) and [2.2.2]-cryptand (4.6 mg, 0.015 mmol or 6.1 mg, 0.02 mmol) were weighed into heated heavy wall precision NMR sample tubes (Pyrex) under an argon atmosphere. Subsequent condensation of ammonia lead to an initially colorless solution, after which the NMR tube was sealed shut by melting under an ammonia atmosphere. The sample was stored at 193 K until examination by NMR spectroscopy.

Synthesis of $(\text{NHC}^{\text{tBu}}\text{Au})_3\text{NHCl}$ and $[(\text{NHC}^{\text{tBu}}\text{Au})_6(\eta^2\text{-Si}_4)]\text{Cl}_2 \cdot 7 \text{NH}_3$: $\text{Rb}_6\text{Cs}_6\text{Si}_{17}$ (150 mg, 0.08 mmol) and $\text{NHC}^{\text{tBu}}\text{AuCl}$ (34.6 mg, 0.08 mmol) with [2.2.2]-cryptand (47.4 mg, 0.13 mmol) as a chelating agent were weighed into a heated Schlenk tube under argon atmosphere and subsequently approximately 5 mL of ammonia were condensed onto the reactants. After six weeks of storage at 233 K, yellow crystals of **1** could be isolated from the slightly reddish solution as the main product, as well as one orange-red crystal of **2**, and characterized by single-crystal X-ray diffraction.

X-ray Crystal Structure Determination: Perfluorether oil was cooled in a stream of liquid nitrogen and crystals were transferred from the cooled reaction vessel into the oil under argon counter current. Suitable crystals were scooped up on MiTeGen holders and transferred onto the diffractometer in liquid nitrogen. Both crystals were measured on a diffractometer SuperNova by the company Agilent, equipped with a molybdenum micro focus tube. Data reductions were performed using the software CrysAlisPro 39.37b.^[42] The software Olex2-1.2-alpha,^[43] as well as the programs ShelXS and ShelXT were used for structure solution,^[44] ShelXL for the refinement.^[45] For visualization Diamond 4 was employed.^[46]

Further details of the crystal structure investigations may be obtained from the FIZ Karlsruhe, 76344 Eggenstein-Leopoldshafen, Germany (Fax: (+49)7247-808-666; E-Mail: crysdata@fiz-karlsruhe.de, [http://www.fiz-karlsruhe.de/request for deposited data.html](http://www.fiz-karlsruhe.de/request%20for%20deposited%20data.html)) on quoting the depository numbers CSD-1954886.

NMR Studies

NMR spectra were recorded on a Bruker Avance III HD 600 MHz spectrometer equipped with a fluorine selective TBIF probe and a Bruker Avance NEO 600 MHz spectrometer equipped with a double resonance broad band probe (BBO). ^1H , ^{13}C and ^{29}Si NMR spectra were referenced externally to TMS (tetramethylsilane). In case the ^{29}Si signal of the HSi_9^{3-} was detected, the spectra were calibrated on the literature known chemical shift of HSi_9^{3-} (-358.5 ppm). ^{15}N NMR spectra were referenced externally to NH_3 . The temperature (233K) for measurements at Bruker Avance NEO were controlled by a Bruker BVTE 3000 temperature unit. The temperatures (203K-233K) for measurements at Bruker Avance III HD were controlled by a Bruker BVTE 3900 temperature unit. Data was processed with the Bruker software TOPSPIN 3.2 and TOPSPIN 4.0.7. For spectra and assignments see SI.

Computational Details

DFT calculations were performed using the software package ORCA 4.0,^[47] which also has an interface for the NBO 6 program.^[48] ELF calculations were performed with MultiWFN,^[49] obtained attractors were evaluated with Avogadro,^[50] and 3D isosurface pictures were created with Molekel.^[51]

7.6 Acknowledgements

We gratefully acknowledge financial support from the German Science Foundation (DFG) (KO 1857/10–1, and GS 13/5–1).

7.7 References

- [1] H. Schmidbaur, A. Schier, *Chem. Soc. Rev.* **2008**, 37, 1931-1951; H. Schmidbaur, A. Schier, *Chem. Soc. Rev.* **2012**, 41, 370-412.
- [2] K. Angermaier, H. Schmidbaur, *J. Chem. Soc., Dalton Trans.* **1995**, 559-564; J. M. López-de-Luzuriaga, A. Sladek, A. Schier, H. Schmidbaur, *Inorg. Chem.* **1997**, 36, 966-968; U. M. Tripathi, W. Scherer, A. Schier, H. Schmidbaur, *Inorg. Chem.* **1998**, 37, 174-175.
- [3] V. Ramamoorthy, P. R. Sharp, *Inorg. Chem.* **1990**, 29, 3336-3339; V. Ramamoorthy, Z. Wu, Y. Yi, P. R. Sharp, *J. Am. Chem. Soc.* **1992**, 114, 1526-1527; X. He, Y. Wang, H. Jiang, L. Zhao, *J. Am. Chem. Soc.* **2016**, 138, 5634-5643.
- [4] D. Marchione, L. Belpassi, G. Bistoni, A. Macchioni, F. Tarantelli, D. Zuccaccia, *Organometallics* **2014**, 33, 4200-4208.
- [5] S. Scharfe, F. Kraus, S. Stegmaier, A. Schier, T. F. Fässler, *Angew. Chem. Int. Ed.* **2011**, 50, 3630-3670; S. C. Sevov, J. M. Goicoechea, *Organometallics* **2006**, 25; J. M. Goicoechea, S. C. Sevov, *J. Am. Chem. Soc.* **2006**, 128, 4155-4161.

- [6] J. M. Goicoechea, S. C. Sevov, *Organometallics* **2006**, *25*, 4530-4536.
- [7] S. Joseph, M. Hamberger, F. Mutzbauer, O. Hartl, M. Meier, N. Korber, *Angew. Chem. Int. Ed.* **2009**, *48*, 8770-8772.
- [8] F. S. Geitner, T. F. Fässler, *Chem. Commun.* **2017**, *53*, 12974-12977.
- [9] M. Waibel, F. Kraus, S. Scharfe, B. Wahl, T. F. Fässler, *Angew. Chem. Int. Ed.* **2010**, *49*, 6611-6615.
- [10] A. Spiekermann, S. D. Hoffmann, T. F. Fässler, I. Krossing, U. Preiss, *Angew. Chem. Int. Ed.* **2007**, *46*, 5310-5313; A. Spiekermann, S. D. Hoffmann, F. Kraus, T. F. Fässler, *Angew. Chem. Int. Ed.* **2007**, *46*, 1638-1640; F. S. Geitner, T. F. Fässler, *Eur. J. Inorg. Chem.* **2016**, 2688-2691; L. J. Schiegerl, F. S. Geitner, C. Fischer, W. Klein, T. F. Fässler, *Z. anorg. allg. Chem.* **2016**, *642*, 1419-1426; C. Schenk, A. Schnepf, *Angew. Chem. Int. Ed.* **2007**, *46*, 5314-5316.
- [11] F. S. Geitner, W. Klein, T. F. Fässler, *Dalton Trans.* **2017**, *46*, 5796-5800; L.-J. Li, F.-X. Pan, F.-Y. Li, Z.-F. Chen, Z.-M. Sun, *Inorg. Chem. Front.* **2017**, *4*, 1393-1396.
- [12] S. Mohapatra, Y. K. Mishra, D. K. Avasthi, D. Kabiraj, J. Ghatak, S. Varma, *Appl. Phys. Lett.* **2008**, *92*, 103105; H. Zhang, Y. Zhu, L. Qu, H. Wu, H. Kong, Z. Yang, D. Chen, E. Mäkilä, J. Salonen, H. A. Santos, M. Hai, D. A. Weitz, *Nano Lett.* **2018**, *18*, 1448-1453; S. Kutrovskaia, S. Arakelian, A. Kucherik, A. Osipov, A. Evlyukhin, A. V. Kavokin, *Sci. Rep.* **2017**, *7*, 10284.
- [13] M. Neumeier, F. Fendt, S. Gaertner, C. Koch, T. Gaertner, N. Korber, R. M. Gschwind, *Angew. Chem., Int. Ed.* **2013**, *52*, 4483-4486.
- [14] F. Hastreiter, C. Lorenz, J. Hioe, S. Gärtner, N. Lokesh, N. Korber, R. Gschwind, *Angew. Chem.* **2019**, *131*, 3165-3169.
- [15] C. Lorenz, F. Hastreiter, J. Hioe, N. Lokesh, S. Gärtner, N. Korber, R. M. Gschwind, *Angew. Chem. Int. Ed.* **2018**, *57*, 12956-12960.
- [16] C. Lorenz, S. Gartner, N. Korber, *Z. Anorg. Allg. Chem.* **2017**, *643*, 141-145.
- [17] T. Henneberger, W. Klein, J. V. Dums, T. F. Fässler, *Chem. Commun.* **2018**, *54*, 12381-12384.
- [18] N. Wiberg, C. M. M. Finger, K. Polborn, *Angew. Chem. Int. Ed.* **1993**, *32*, 1054-1056.
- [19] P. Pykkö, *J. Phys. Chem. A* **2015**, *119*, 2326-2337.
- [20] T. Müller, in *Organosilicon Chemistry IV: From Molecules to Materials, Vol. 1* (Eds.: N. Auner, J. Weis), Wiley-Vch, **2000**, pp. 110-117.
- [21] A. Wiesner, S. Steinhauer, H. Beckers, C. Müller, S. Riedel, *Chem. Sci.* **2018**, *9*, 7169-7173.

- [22] J. D. Corbett, D. G. Adolphson, D. J. Merryman, P. A. Edwards, F. J. Armatis, *J. Am. Chem. Soc.* **1975**, *97*, 6267-6268.
- [23] M. V. Baker, P. J. Barnard, S. J. Berners-Price, S. K. Brayshaw, J. L. Hickey, B. W. Skelton, A. H. White, *Dalton Trans.* **2006**, 3708-3715.
- [24] A. Collado, A. Gomez-Suarez, A. R. Martin, A. M. Z. Slawin, S. P. Nolan, *Chem. Commun.* **2013**, 5541-5543.
- [25] M. Alcarazo, T. Stork, A. Anakuthil, W. Thiel, A. Fürstner, *Angew. Chem. Int. Ed.* **2010**, *49*, 2542-2546; M. V. Baker, P. J. Barnard, S. K. Brayshaw, J. L. Hickey, B. W. Skelton, A. H. White, *Dalton Trans.* **2005**, 37-43.
- [26] S. Patil, A. Deally, F. Hackenberg, L. Kaps, H. Müller-Bunz, R. Schobert, M. Tacke, *Helv. Chim. Acta* **2011**, *94*, 1551-1562.
- [27] E. C. Hurst, K. Wilson, I. J. S. Fairlamb, V. Chechik, *New J. Chem.* **2009**, *33*, 1837-1840.
- [28] J. W. Runyon, O. Steinhof, H. V. Rasika Dias, J. C. Calabrese, W. J. Marshall, A. J. Arduengo III, *Aust. J. Chem.* **2011**, *64*, 1165-1172.
- [29] I. A. Shkrob, *J. Phys. Chem. B* **2010**, *114*, 368-375.
- [30] H. Ibrahim, R. Guillot, F. Cisnetti, A. Gautier, *Chem. Commun.* **2014**, *50*, 7154-7156.
- [31] R. S. Ramon, S. Gaillard, A. Poater, L. Cavallo, A. M. Z. Slawin, S. P. Nolan, *Chem. Eur. J.* **2011**, *17*, 1238-1246.
- [32] N. M. Scott, R. Dorta, E. D. Stevens, A. Correa, L. Cavallo, S. P. Nolan, *J. Am. Chem. Soc.* **2005**, *127*, 3516-3526.
- [33] H.-W. Wanzlick, E. Schikora, *Chem. Ber.* **1961**, *94*, 2389-2393; H.-W. Wanzlick, E. Schikora, *Angew. Chem.* **1960**, *72*, 494-494.
- [34] P. I. Jolly, S. Zhou, D. W. Thomson, J. Garnier, J. A. Parkinson, T. Tuttle, J. A. Murphy, *Chem. Sci.* **2012**, *3*, 1675-1679.
- [35] H^{4,5} of **11** may be assigned to one of the signals around **7** which we assume to belong to NHC^{tBu} species with a chemical environment similar to **7** which would be the case for **11**.
- [36] A. N. Nesmeyanov, E. G. Peralova, Y. T. Struchkov, M. Y. Antipin, K. I. Grandberg, V. P. Dyadhenko, *J. Organomet. Chem.* **1980**, *201*, 343-349.
- [37] A. Bauer, F. Gabbai, A. Schier, H. Schmidbaur, *Philos. T. R. Soc. A* **1996**, *354*, 381-394.

7 ON THE REACTIVITY OF $\text{NHC}^{\text{TBU}}\text{AuCl}$ TOWARDS $\text{Rb}_6\text{Cs}_6\text{Si}_{17}$

- [38] A. J. Bellamy, W. S. J., P. Golding, *Propellants Explos. Pyrotech.* **2002**, 27, 59-61.
- [39] R. A. J. Ogg, *J. chem. Phys.* **1954**, 22, 560-561.
- [40] NH_4^+ was detected in sample **ii** at 203 K evidenced by a characteristic triplet^[38] at 7.02 ppm; $J = 51.5$ Hz; ^{14}N : spin=1; similar pattern for ^1H -NMR signal of dry ammonia]^[39].
- [41] H. Bürger, R. Eujen, H. C. Marsmann, *Z. Naturforsch. B* **1947**, 29, 149-152.
- [42] Agilent Technologies, Santa Clara, CA, USA, **2017**.
- [43] O. V. Dolomanov, L. J. Bourhis, R. J. Gildea, J. A. K. Howard, H. Puschmann, *J. Appl. Cryst.* **2009**, 42, 339-341.
- [44] G. M. Sheldrick, *Acta Cryst. A* **2008**, 64, 112-122; G. M. Sheldrick, *Acta Cryst. A* **2015**, 71, 3-8.
- [45] G. M. Sheldrick, *Acta Crystallogr. Sect C* **2015**, 71, 3-8.
- [46] K. Brandenburg, **2018**; K. Brandenburg, *Vol. Version 3.2k*, Crystal Impact GbR, Bonn, Germany, **2014**.
- [47] F. Neese, *Wiley Interdiscip. Rev. Comp. Mol. Sci.* **2017**, 8, e1327; F. Neese, *Wiley Interdiscip. Rev. Comput. Mol. Sci.* **2012**, 2, 73-78.
- [48] E. D. Glendening, C. R. Landis, F. Weinhold, *J. Comput. Chem.* **2013**, 34, 1429-1437.
- [49] T. Lu, F. Chen, *J. Comput. Chem.* **2012**, 33, 580-592.
- [50] M. D. Hanwell, D. E. Curtis, D. C. Lonie, T. Vandermeersch, E. Zurek, G. R. Hutchison, *J. Cheminformatics* **2012**, 4.
- [51] U. Varetto, **2009**.

7.8 Supporting Information

7.8.1 X-ray analysis

7.8.1.1 $(\text{NHC}^{\text{tBu}}\text{Au})_3\text{NHCl}$

As can be seen from Figure SI 7.1, compound **1** is stacked along the crystallographic c-axis in the unit cell. The asymmetric unit (Figure SI 7.2) consists of one gold atom, a NHC^{tBu} moiety, as well as the nitrogen, hydrogen and chloride atoms located on the threefold rotation axis.

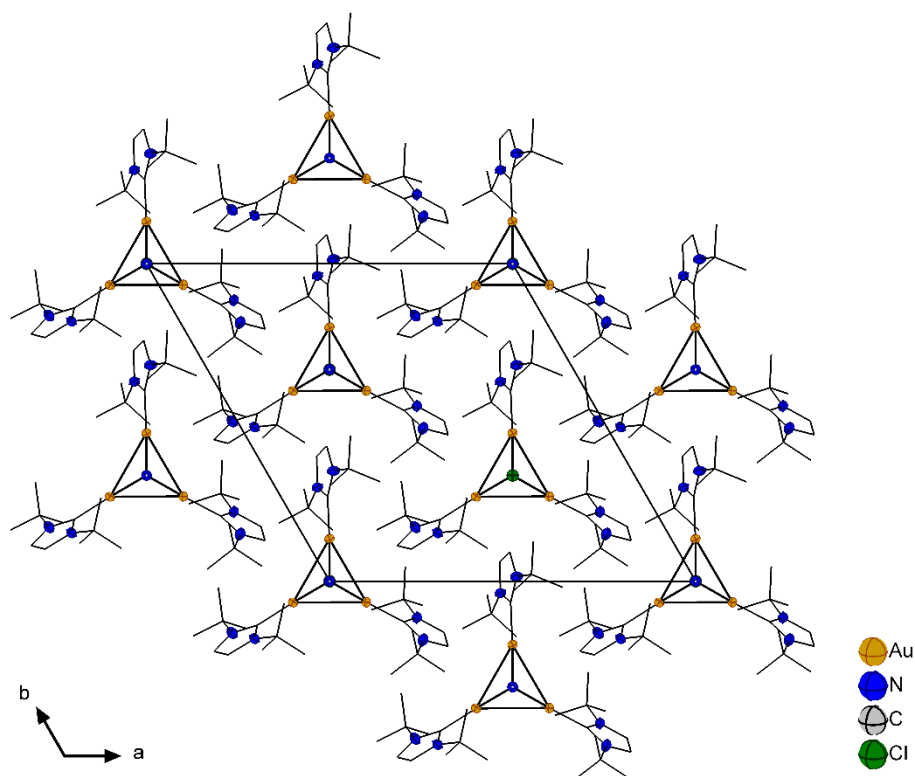


Figure SI 7.1 | View of the unit cell of compound **1** along the crystallographic c-axis.

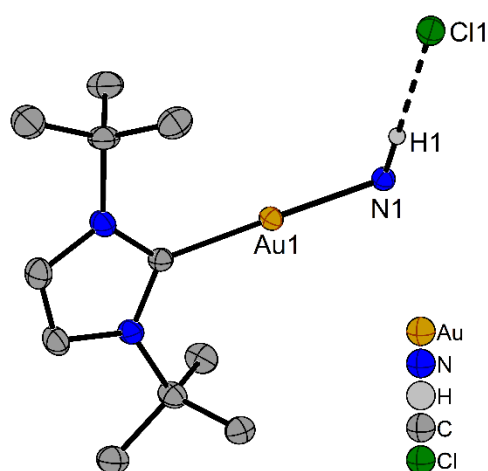


Figure SI 7.2 | Asymmetrical unit of **1**; Hydrogen atoms are omitted for added visibility; thermal displacement ellipsoids are drawn with 50 % probability.

7 ON THE REACTIVITY OF $\text{NHC}^{\text{tBu}}\text{AuCl}$ TOWARDS $\text{R}_6\text{Cs}_6\text{Si}_{17}$

7.8.1.2 $[(\text{NHC}^{\text{tBu}}\text{Au})_6(\eta^2\text{-Si}_4)]\text{Cl}_2 \cdot 7 \text{NH}_3$

Additional views of compound **2** are provided for a better understanding of the complex. Views of the cell along the c-axis (Figure SI 7.3) and b-axis (Figure SI 7.4), as well as the cube made up of the two interlocked Si_4 tetrahedra are displayed (Figure SI 7.5).

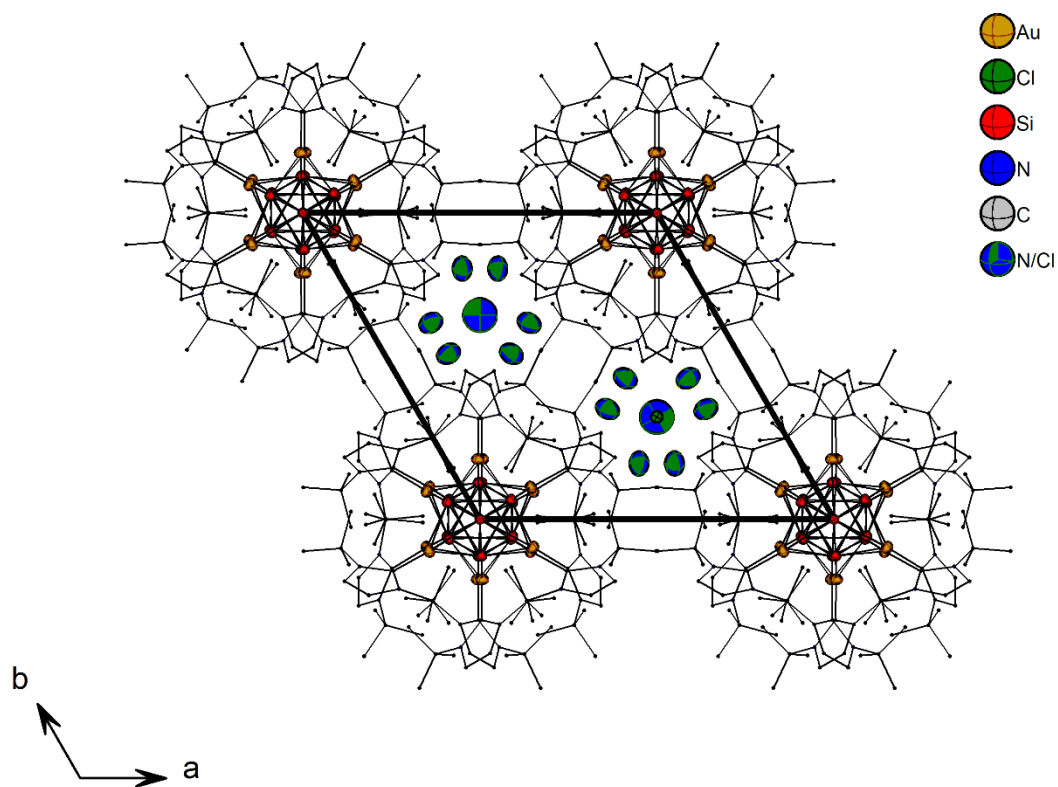


Figure SI 7.3 | View of the unit cell of compound **2** along the c-axis.

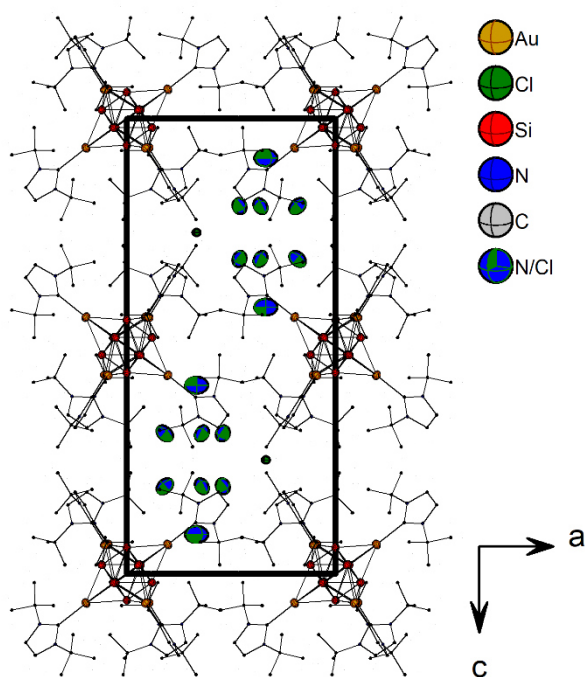
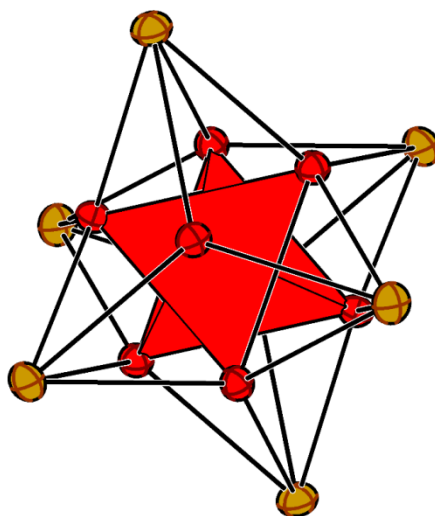
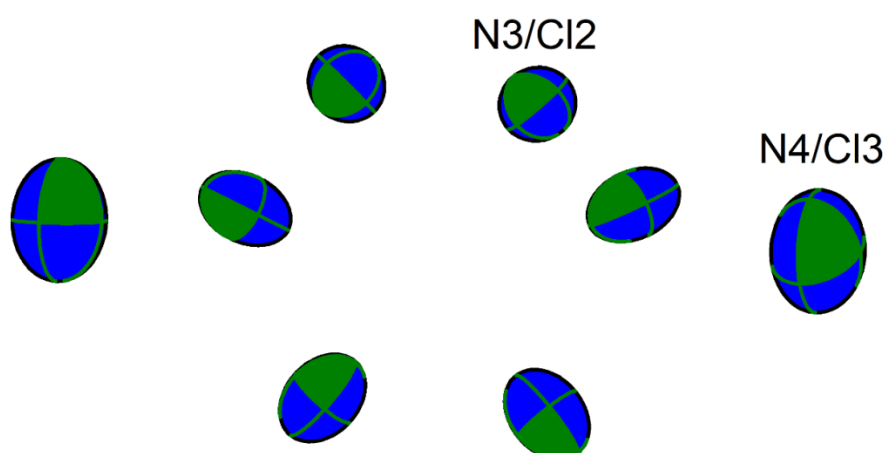


Figure SI 7.4 | View of the unit cell of compound **2** along the crystallographic b-axis.**Figure SI 7.5** | Central moiety of **1a** depicted with both disordered and interwoven Si_4 tetrahedra and the six capping gold atoms.**Figure SI 7.6** | Positions of the atoms N3/Cl2 and N4/Cl3 around the inversion center.**Table SI 7.1** | Wyckoff positions and occupation of the shared positions N3/Cl2 and N4/Cl3.

Atom	Wyckoff position	amount of NH_3	amount of Cl
N3/Cl2	$12i$	0.852	0.148
N4/Cl3	$4f$	0.958	0.042

As position N4/Cl3 is duplicated via the inversion center, the amount of Cl for this position has to be doubled ($0.042 \cdot 2 = 0.084$), whereas the amount of Cl for position N3/Cl2 has to be multiplied by six, as the position is generated sixfold by the threefold axis, as well as the inversion center ($0.148 \cdot 6 = 0.888$). Combining the two resulting values for amounts of Cl, it becomes apparent, that the positions N3/Cl2 and N4/Cl3 combined add up to roughly one complete chloride ($0.084 + 0.888 = 97.2$) (Table SI 7.1, Figure SI 7.6)

7 ON THE REACTIVITY OF $\text{NHC}^{\text{tBu}}\text{AuCl}$ TOWARDS $\text{Rb}_6\text{Cs}_6\text{Si}_{17}$

A second option for the occupation of the shared Cl/N position is possible, as the free refinement of cesium at these positions gives a value of approximately one cesium atom. This would put the total charge in the structure at zero, as the negative charge from the chloride cancels out the cation. Hence, this would mean a charge of +0.66 for each gold atom, in order to counteract the fourfold negative charge of the $[\text{Si}_4]^{4-}$ unit. Due to this consideration, we see this solution as rather improbable. However, we still performed calculations to check up on the possibility.

As gold is usually present in structures in the oxidation states -1 , 0 , $+1$ and $+3$, we considered all options, but were quick to discard -1 and $+3$, as there is no evidence of 10 cation or 14 anion sites respectively in the crystal structure. Apart from an oxidation state of $+1$ at each gold atom, the only other plausible charge to be contemplated was no charge at the gold atoms, effectively putting the oxidation state at zero. However, contrasting this proposal is the absence of the needed four cation sites to make the whole compound neutral. Still, calculations were performed, assuming a charge of -4 for the moiety **2A**.

7.8.1.3 $[(\text{NHC}^{\text{tBu}})_2\text{Au}]\text{Cl} \cdot 7 \text{NH}_3$

A crystal with the composition $[(\text{NHC}^{\text{tBu}})_2\text{Au}]\text{Cl} \cdot 7 \text{NH}_3$ was isolated from the dark orange solution of Rb_4Sn_4 (30.0 mg, 0.04 mmol), $\text{NHC}^{\text{tBu}}\text{AuCl}$ (91.0 mg, 0.22 mmol) and [2.2.2]-cryptand (20.7 mg, 0.06 mmol) in ammonia, after 9 months of storage at 233 K. The molecular unit is comprised of a gold atom with two NHC^{tBu} -ligands attached (Figure SI 7.8). To balance the positive charge from the Au(I), one chlorine per formula unit is present in the structure, as well as seven ammonia molecules (Figure SI 7.7). The crystallographic data and structure determination details are listed in Table SI 7.2.

Table SI 7.2 | Crystallographic data and details of the structure determination of $[(\text{NHC}^{\text{tBu}})_2\text{Au}]\text{Cl} \cdot 7 \text{NH}_3$.

Chemical Formula	$(\text{NHC}^{\text{tBu}})_2\text{Au}$
CSD No.	2017991
Composition	$\text{C}_{66}\text{H}_{120}\text{Au}_3\text{Cl}_3\text{N}_{19}$
M [$\text{g} \cdot \text{mol}^{-1}$]	1877.05
Crystal System	orthorhombic
Space group	$P2_12_12_1$
a [Å]	9.35290(10)
b [Å]	26.6862(4)
c [Å]	33.0101(4)
α [°]	90
β [°]	90
γ [°]	90
V [Å ³]	8239.10(18)
Z	4
F(000) (e)	3748.0
ρ_{calc} [$\text{g} \cdot \text{cm}^{-3}$]	1.513
μ [mm^{-1}]	5.473
2 θ -range for data collection [°]	5.804 to 55.754
Reflections collected/independent	109940 / 19625
Data / restraints / parameters	19625 / 0 / 857
Goodness-of-fit on F^2	1.070
Final R indices [$I > 2\sigma(I)$]	$R_1 = 0.0306$, $wR_2 = 0.0550$
R indices (all data)	$R_1 = 0.0363$, $wR_2 = 0.0565$
R_{int}	0.0623
$\Delta\rho_{\text{max}}$, $\Delta\rho_{\text{min}}$ [$\text{e} \cdot \text{Å}^{-3}$]	0.73 / -0.61
Flack parameter	$-0.016(3)$

7 ON THE REACTIVITY OF $\text{NHC}^{\text{tBu}}\text{AuCl}$ TOWARDS $\text{Rb}_6\text{Cs}_6\text{Si}_{17}$

The Au-C distances are in the range of known Au-C bonds with lengths between 2.018(7) Å and 2.038(7) Å. As is known from previous publications, the compound is almost linear at the C-Au-C axis, with angles ranging from 174.4(2)° to 178.0(2)°. The NHC-moieties are approximately perpendicular to one another, as the torsion angles lie in between 87.562° and 98.020°.[1]

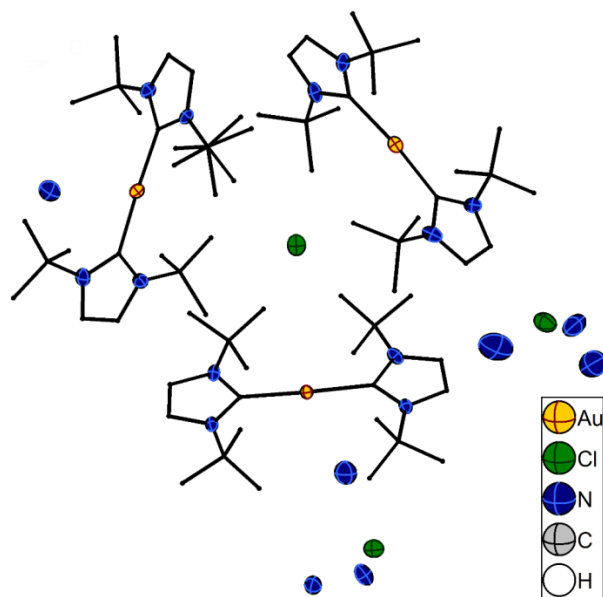


Figure SI 7.7 | Asymmetric moiety of the compound $[(\text{NHC}^{\text{tBu}})_2\text{Au}]\text{Cl} \cdot 7 \text{NH}_3$. Ellipsoids are shown at 50 % probability.

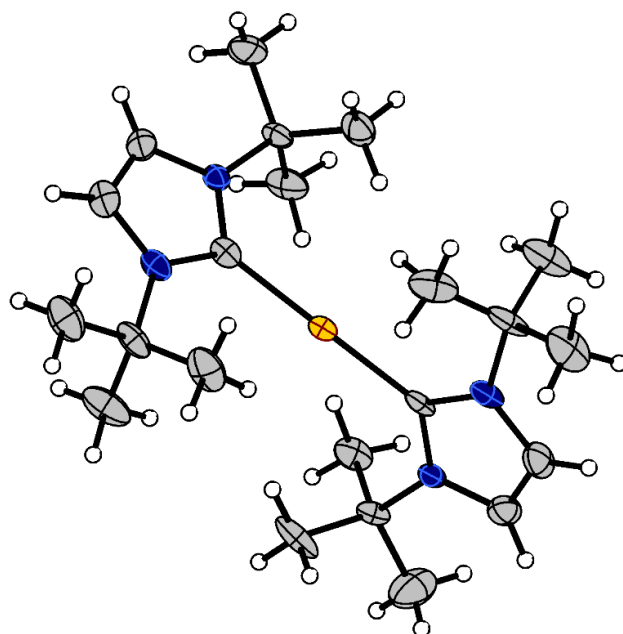


Figure SI 7.8 | $[(\text{NHC}^{\text{tBu}})_2\text{Au}]^+$ moiety. Ellipsoids are shown at 50 % probability.

7.8.2 Theoretical calculations

7.8.2.1 *ELF*

In the charge neutral case, one Si-Si distance is decreased, whereas the opposing Si-Si distance widens resulting in a formal Si_4^{6-} butterfly. Assuming a charge of -4 for the cluster results in an elongation of the Si-Si distances of one triangle face, resulting in a formal Si_4^{10-} trigonal pyramid. The exact calculated bond distances are listed in Table SI 7.3.

Table SI 7.3 | Experimental and calculated values for the distances and angles in $[(\text{NHC}^{\text{tBu}}\text{Au})_6(\eta^2\text{-Si}_4)]$ with assumed charges of +2, 0 and -4.

charge	exp.	+2	0	-4
Au-C	2.069(4)	2.08	2.06 – 2.09	2.05
Au-Si	2.4040(3)- 2.418(2)	2.45	2.42 – 2.50	2.44 – 2.46, 2.41, 2.54
Si-Si	2.530(3), 2.537(4)	2.56	2.49, 2.62, 2.83	2.63, 2.79
Si-Si- Si	59.90(5)- 60.19(11)	60.0	56.7, 61.4-61.8, 57.1-57.4	58.059.9-60.1, 64.1
Si-Au- Si	63.32(9)- 63.51(10)	62.9	70.9, 64.1-64.4, 60.5	64.2, 69.4
Si-Au- C	145.74(14)- 150.79(12)	148.3- 148.8	150.5, 149.0, 137.4-140.8, 154.6-158.0, 144.4-144.6	131.1-133.7, 162.0-164.7, 141.5- 142.8, 148.0-149.1

7.8.2.2 *NBO*

Hybridization:

BD(1) (Si-Si): 7.1% s, 91.0% p, 1.9% d (sp^{12.75}d^{0.27})

LP(1) (Si): 78.61% s, 20.86% p, 0.48% d (sp^{0.27}d^{0.01})

BD(1) (Au-C): Au: 92.3% s, 7.4% d (Anteil: 23.6%) (sd^{0.08})

C: 38.4% s, 61.6% p (Anteil: 76.4%) (sp^{1.6})

The calculated values for the donor – acceptor delocalization are listed in Table SI 7.4, while the visualization of the bonds and lone pairs in the central moiety is provided in Figure SI 7.9.

7 ON THE REACTIVITY OF $\text{NHC}^{\text{tBu}}\text{AuCl}$ TOWARDS $\text{Rb}_6\text{Cs}_6\text{Si}_{17}$

Table SI 7.4 | Donor – acceptor delocalization (2nd order perturbation)

→ Au1-C4	Si2	Si13	Si44	Si55
Si2	21.39	7.78	139.89	8.52
Si13		--	8.71	3.50
Si44			21.51	7.72
Si55				--

→ Au12-C15	Si2	Si13	Si44	Si55
Si2	21.51	139.68	8.48	7.87
Si13		21.35	7.74	8.55
Si44			--	3.48
Si55				--

→ Au23-C25	Si2	Si13	Si44	Si55
Si2	--	3.48	8.70	7.75
Si13		--	7.59	8.50
Si44			21.36	139.65
Si55				21.41

→ Au33-C35	Si2	Si13	Si44	Si55
Si2	21.41	8.43	7.91	139.48
Si13		--	3.47	7.82
Si44			--	8.40
Si55				21.24

→ Au43-C46	Si2	Si13	Si44	Si55
Si2	--	8.43	7.80	3.45
Si13		21.38	139.69	7.85
Si44			21.43	8.50
Si55				--

→ Au54-C57	Si2	Si13	Si44	Si55
Si2	--	7.70	3.52	8.51
Si13		21.52	8.72	139.98
Si44			--	7.83
Si55				21.45

7 ON THE REACTIVITY OF $\text{NHC}^{\text{tBu}}\text{AuCl}$ TOWARDS $\text{Rb}_6\text{Cs}_6\text{Si}_{17}$

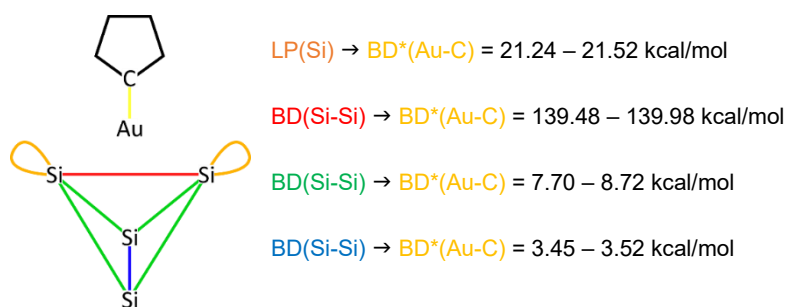


Figure SI 7.9 | Color coordinated scheme of the bonds and lone pairs in the central moiety of **2A**.

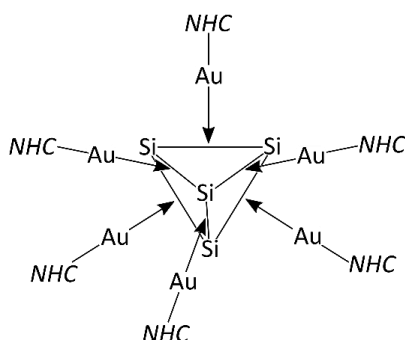


Figure SI 7.10 | Lewis structure of the cation **2a**.

The cluster's Lewis structure can be explained by calculating NBOs out of the electron density (Figure SI 7.10). The lone pairs of the Si atoms and the Si-Si bonds have an occupation of 1.74171 and 1.66709 electrons, respectively. Visualizations of the electron pairs n_{Si} , as well as the donor-acceptor interactions, according to the NBO calculations, are depicted in Figures SI 7.9 and SI 7.10.

Since the Au-C bond is a polar bond, the contributions of the atoms are not equal, but bigger from the Carbon atom with 76.4 %. Charges at the silicon and gold atoms were calculated using NPA and Loewdin methods, the obtained values are listed in Table SI 7.5.

Table SI 7.5 | Charges at the silicon and gold atoms, according to NPA and Loewdin calculations.

	NPA	Loewdin
Si2	-0.526	-0.228
Si13	-0.526	-0.228
Si44	-0.526	-0.228
Si55	-0.526	-0.228
Au1	0.390	0.183
Au12	0.390	0.183
Au23	0.390	0.183
Au33	0.390	0.183
Au43	0.390	0.183
Au54	0.390	0.183

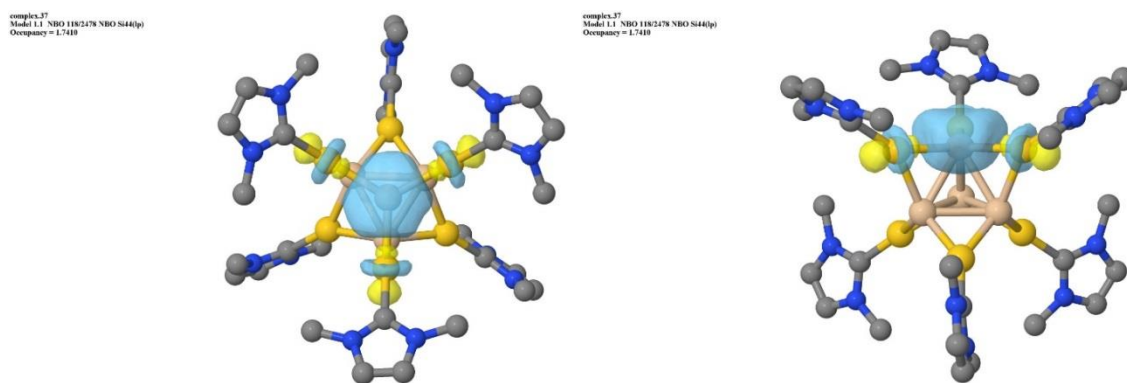


Figure SI 7.11. Depiction of the electron pair n_{Si} ; left: bird's eye view, right: side view of the central moiety.

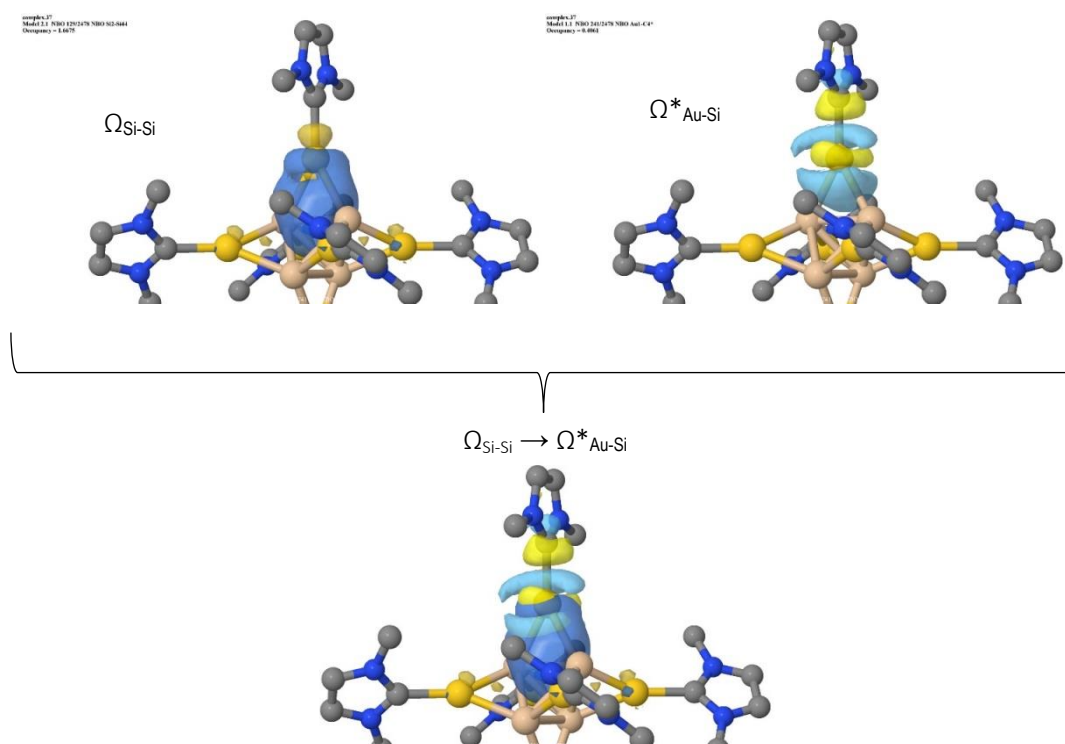


Figure SI 7.12 | Depiction of the donor-acceptor interactions according to the NBO calculations. Upper left: $\Omega_{\text{Si-Si}}$, lower left: $\Omega^*_{\text{Au-C}}$, right: $\Omega_{\text{Si-Si}} \rightarrow \Omega^*_{\text{Au-C}}$.

7.8.3 NMR-Spectroscopy

7.8.3.1 Diffusion ordered spectroscopy (DOSY)

The ^1H -diffusion measurements were performed with the convection suppressing DSTE (double stimulated echo) pulse sequence, developed by Müller and Jerschow in a pseudo 2D mode.^[2] The diffusion coefficients of the analytes were internally referenced to that of $\text{NHC}^{\text{tBu}}\text{-HCl}$.

A set of 120 dummy scans/256 scans, respectively, were used with a relaxation delay of 3 s. Square shapes were used for the gradient and a linear gradient ramp with 20 increments between 5 % and 95 % of the maximum gradient strength ($g(0)=5.34$ G/mm) were applied. An effective diffusion time (D_{eff}) of 45 ms was

7 ON THE REACTIVITY OF NHC^{tBu}AuCl TOWARDS RB₆Cs₆SI₁₇

applied. For each compound in the sample, the gradient pulses were adjusted in order to obtain optimized diffusion times Δ and gradient lengths δ according to following correlation:

$$\Delta [ms] = D_{eff} + \frac{\delta}{3}; P_{16}[ms] = \frac{\delta}{2}$$

The NMR spectra were processed with the Bruker program TopSpin 3.2 and the diffusion coefficients were determined according Müller and Jerschow.^[2] Since the DOSY measurement was carried out without locking (NH₃ as solvent), the sample was exposed to a small magnetic field drift, which caused the signals to shift over the period of the measurement. Hence, the measurement could not be evaluated with the T1/T2 software incorporated in topspin by default. All of the FIDs of the indirect dimension were processed and integrated separately. The thereby received experimental integration values (of the protons located at the double bond of the NHC moiety) were then manually evaluated in Excel using the following equation by Müller and Jerschow:^[2]

$$\ln \frac{I}{I(0)} = -D \times \gamma_{1H}^2 \times g^2 \times \delta^2 \times D_{eff}$$

Further, the experimental translational self-diffusion coefficients D of the molecules in solution were determined according to the Stejskal-Tanner equation.^[3] To get an estimate about the molecular size, the obtained diffusion coefficients were reciprocally referenced (see following equation) to the coefficient of NHC^{tBu}-HCl by using the Stokes-Einstein equation.

$$r = \frac{k_B \times T}{6\pi \times \eta \times D}; \quad \frac{r_i}{r_{ref}} = \frac{\frac{1}{D_i}}{\frac{1}{D_{ref}}} = \frac{1}{(D_i/D_{ref})}$$

With the hydrodynamic radius (r), Boltzmann constant (k_B), temperature (T), dynamic viscosity (η) and diffusion coefficient (D). The compound of interest is marked with i , while the reference is marked with ref . The results are displayed in Table SI 7.6 in increasing size ratio.

Table SI 7.6 | Diffusion coefficients and their reciprocal referencing to the diffusion coefficient of NHC^{tBu}-HCl. The compounds are listed in increasing size.

compound number	structure	diffusion coefficient D [m ² /s]	reciprocal referencing of D_i (species) to D_{ref} (NHC ^{tBu} -HCl)
6	[NHC ^{tBu} H]Cl	1.70 x 10 ⁻⁹	1.00
7	NHC ^{tBu} AuNH ₂	1.49 x 10 ⁻⁹	1.14
3	[NHC ^{tBu} AuNH ₃]Cl	1.47 x 10 ⁻⁹	1.15
8	[(NHC ^{tBu}) ₂ Au]Cl	1.28 x 10 ⁻⁹	1.33
4	[(NHC ^{tBu} Au) ₂ NH ₂]Cl	1.19 x 10 ⁻⁹	1.43

The size ratios fit well to the proposed structures, considering that they are mostly salts and that the hydrodynamic radii not only include the compounds but probably also a considerable amount of ammonia.

7.8.3.2 Characterizations/Assignment

General aspects

The assignment of the signals detected during reaction monitoring, discussed in the manuscript, to intermediates and products was performed by interpretation of 2D ^1H - ^{13}C -HSQC, -HMQC and -HMBC, ^1H - ^{15}N -HSQC, ^1H - ^1H -NOESY, ^1H -DOSY of three samples and integration of the respective 1D ^1H -NMR spectra.

Experimental condition of the three samples:

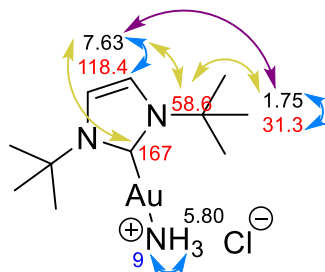
- i) $\text{K}_6\text{Rb}_6\text{Si}_{17} + \text{NHC}^{\text{tBu}}\text{AuCl} + [2.2.2]\text{-cryptand (1:1:1.5)}$ in liq. NH_3
- ii) $\text{K}_6\text{Rb}_6\text{Si}_{17} + \text{NHC}^{\text{tBu}}\text{AuCl} + [2.2.2]\text{-cryptand (1:2:2)}$ in liq. NH_3
- iii) $\text{K}_6\text{Rb}_6\text{Si}_{17}$ in liq. NH_3 .

In the following, ^1H NMR chemical shifts are displayed in black, ^{13}C chemical shifts in red and ^{15}N chemical shifts in blue. Homo- and heteronuclear correlations detected in 2D spectra are indicated by arrows: purple for ^1H - ^1H -NOE contacts, blue for ^1H - ^{13}C or ^{15}N -HSQC cross peaks and yellow for ^1H - ^{13}C -HMBC correlations. For reasons of clarity, the atoms of the NHC core are numbered and indicated as atom^{number} (e.g. $\text{H}^{4,5}$, C^2 , etc.), while compounds are given as bold numbers.

A different ratio of $\text{K}_6\text{Rb}_6\text{Si}_{17}$ to ligand and crypt (1:2:2) led to a slightly different course of the reaction. Besides the signals of the already assigned NHC-species **3**, **4**, **6**, **7**, **8** and **9**, close to the signals of the hydrogenated carbene **9** ($\text{NHC}^{\text{tBu}}\text{-H}_2$), small signals at 5.34 ppm and 4.03 ppm of another NHC-species (**12**) appeared in the 1:2:2 reaction mixture. For assignment see below.

[NHC^{tBu}AuNH₃]Cl (3**)**

The formation of **3** was observed in all samples (i-iii). Signals were integrated at 203K and without solvent saturation to avoid intensity loss of the broad signal at 5.80 ppm upon chemical exchange with NH_3 .



^1H NMR (600 MHz, liq. NH_3 , 233 K): $\delta/\text{ppm} = 7.63$ (2H, s), 5.80 (3H, br s), 1.75 (18 H, s). ^{13}C NMR (600 MHz, liq. NH_3 , 233 K): $\delta/\text{ppm} = 167$, 118.4, 58.6, 31.3. ^{15}N NMR (600 MHz, liq. NH_3 , 203 K): $\delta/\text{ppm} = 9$.

7 ON THE REACTIVITY OF $\text{NHC}^{\text{tBu}}\text{AuCl}$ TOWARDS $\text{Rb}_6\text{Cs}_6\text{Si}_{17}$

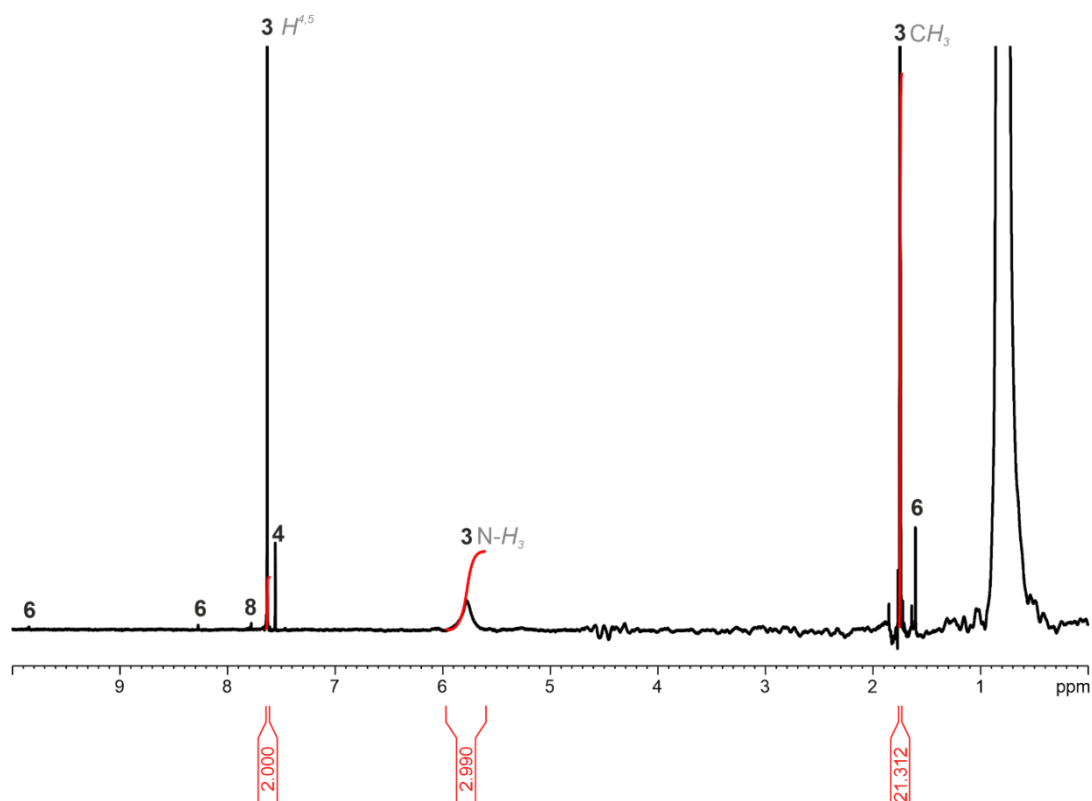


Figure SI 7.13 | ^1H -NMR spectrum (600.03 MHz) of sample iii at 233K. The signals of **3** are integrated. The *tert*-butyl signals of **3**, **4**, and **8** are overlapping.

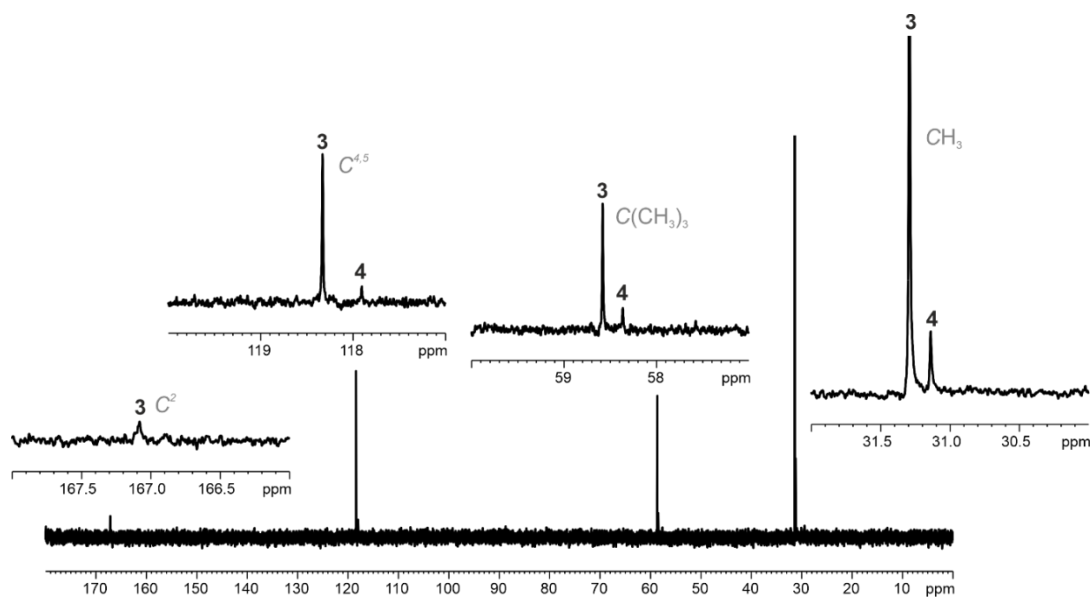


Figure SI 7.14 | $^{13}\text{C}\{^1\text{H}\}$ -NMR spectrum (150.88 MHz) of sample iii at 233K. The signal of C^2 of **4** is missing in the 1D spectrum due to the low concentration of **4**, but it could be assigned *via* ^1H - ^{13}C -HMBC.

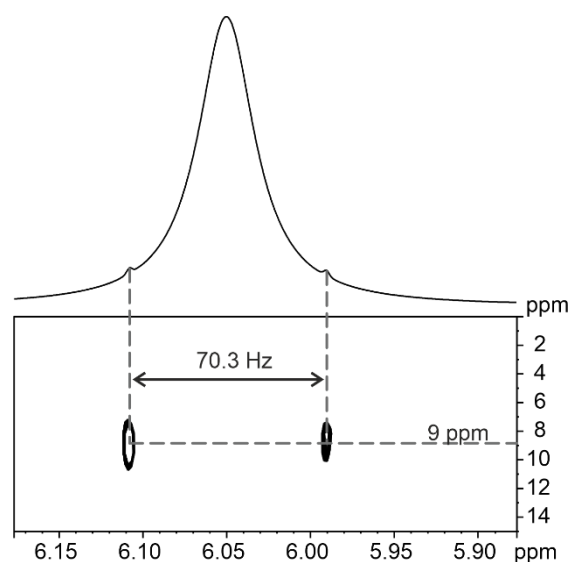
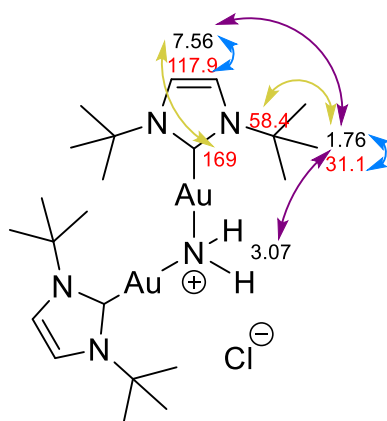


Figure SI 7.15 | $^1\text{H}^{15}\text{N}$ -HSQC spectrum of sample iii at 203K. The shows a crosspeak between the NH_3 signal of **3** and a nitrogen at around 9 ppm. (The corresponding ^1H NMR shift is 5.80 ppm at 233K)

$[(\text{NHC}^{\text{tBu}}\text{Au})_2\text{NH}_2]\text{Cl}$ (**4**)

The formation of this species was observed in all samples (i-iii). Signals were integrated at 203K and with solvent saturation to avoid signal overlap with baseline wiggles caused by the intense solvent signal NH_3 . In the ^1H - ^1H -EXSY, no exchange between the NH protons and ammonia was observed, allowing for signal integration in solvent saturated spectra.



^1H NMR (600 MHz, liq. NH_3 , 233 K): δ/ppm = 7.56 (4H, s), 3.07 (2H, br s), 1.76 (36 H, s). ^{13}C NMR (600 MHz, liq. NH_3 , 233 K): δ/ppm = 169, 117.9, 58.4, 31.1.

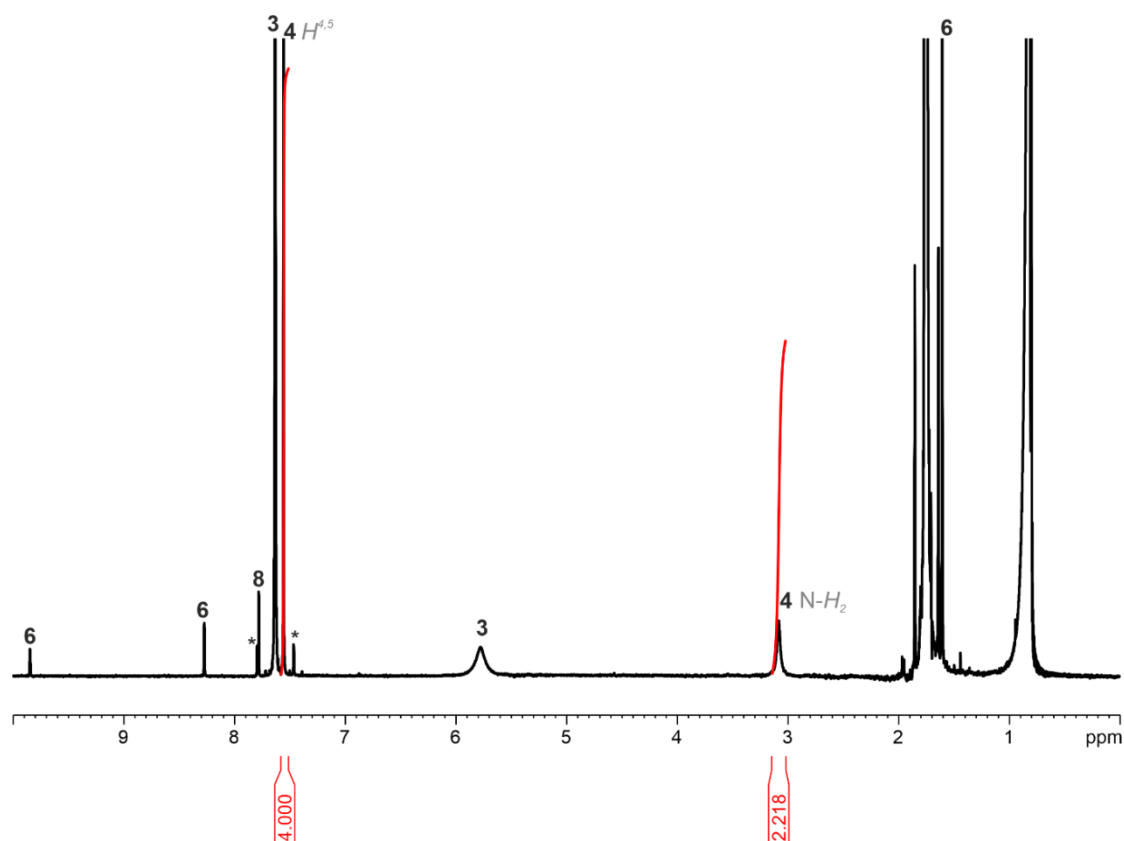


Figure SI 7.16 | ^1H -NMR spectrum (600.03 MHz) with solvent saturation of sample **iii** at 233K. The signals of **4** are integrated. The *tert*-butyl signals of **3**, **4**, and **8** are overlapping.

For a 1D ^{13}C -NMR spectrum see Figure SI 7.14.

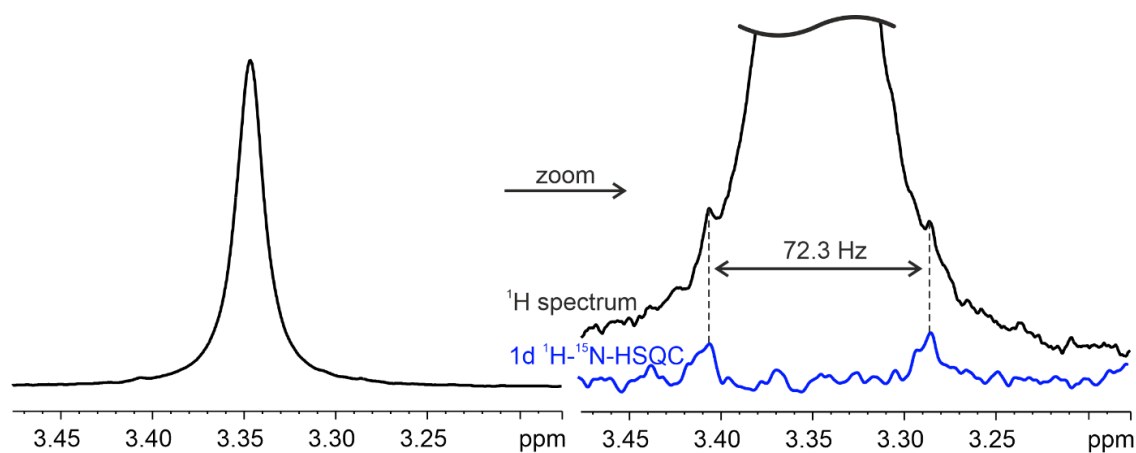
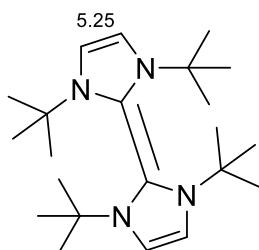


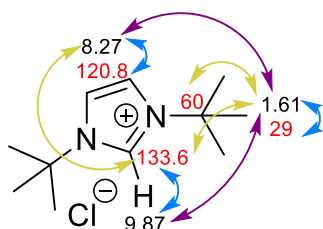
Figure SI 7.17 | Left: ^1H -NMR signal of NH_2 of **4** in sample **iii** at 203K. Right: Zoom of the signal on the left and overlap with the corresponding 1D ^1H - ^{15}N -HSQC NMR signal at 203K. No crosspeak was obtained in the 2D version, which is why the ^{15}N chemical shift could not be determined. (The corresponding ^1H NMR shift is 3.07 ppm at 233K)

(NHC^{tBu})₂ (5)

This compound is tentatively assigned to the signal at 5.25 ppm (see manuscript) based on comparison of its shift with literature, as no further information on this signal was available. The chemical shift of the signal at 5.25 ppm fits quite well to the literature value of $\text{H}^{4,5}$ of an NHC^{Me} -dimer (5.45 ppm), which was reported to be generated in liquid ammonia in presence of the reducing agent sodium hydride roughly resembling the reducing conditions of silicides in liquid ammonia.^[4] Here instead of methyl *t*-butyl is bound to the NHC, which should have a similar effect on the chemical shift of $\text{H}^{4,5}$ though. Hence, the signal at 5.25 ppm may belong to the NHC^{tBu} -dimer (5).

[NHC^{tBu}H]Cl (6)

The formation of this species was observed in all samples (i-iii). A chemical assignment can also be found in literature.^[5]



^1H NMR (600 MHz, liq. NH_3 , 233 K): δ/ppm = 9.87 (1H, t, 4J = 1.7 Hz), 8.27 (2H, d, 4J = 1.7 Hz), 1.61 (18 H, s). ^{13}C NMR (600 MHz, liq. NH_3 , 233 K): δ/ppm = 133.6, 120.8, 60, 29.

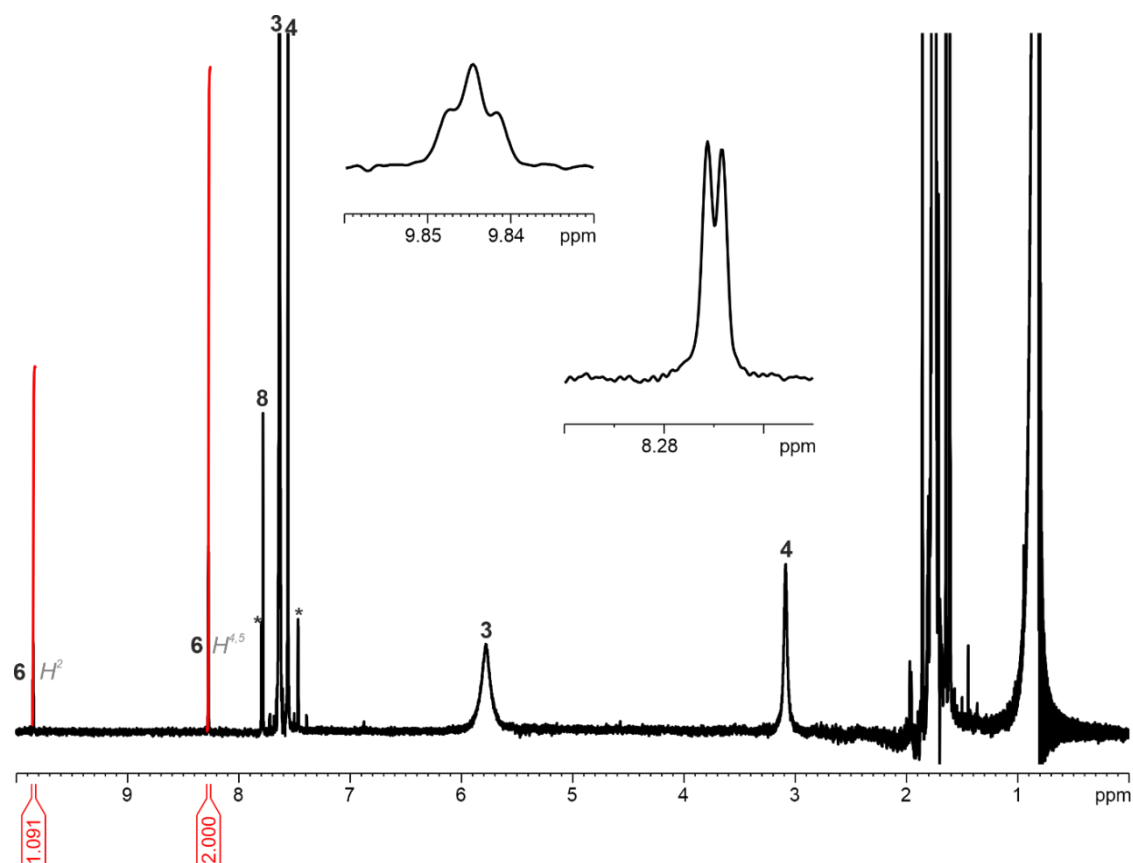
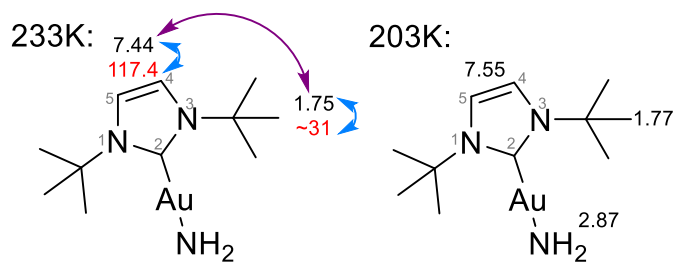


Figure SI 7.18 | ^1H -NMR spectrum (600.03 MHz) with solvent saturation of sample **iii** at 233K. The signals of **6** are integrated. The *tert*-butyl signal of **6** is disturbed by wiggles of the very intense signal of **3**.

$\text{NHC}^{\text{tBu}}\text{AuNH}_2$ (**7**)



Due to the low signal to noise, the carbenic and the quaternary carbon could not be assigned.

^1H NMR (600 MHz, liq. NH_3 , 233 K): δ/ppm = 7.44 (2H, s), 1.75 (18 H, s). ^1H NMR (600 MHz, liq. NH_3 , 203 K): δ/ppm = 7.28 (2H, s), 1.51 (18 H, s).

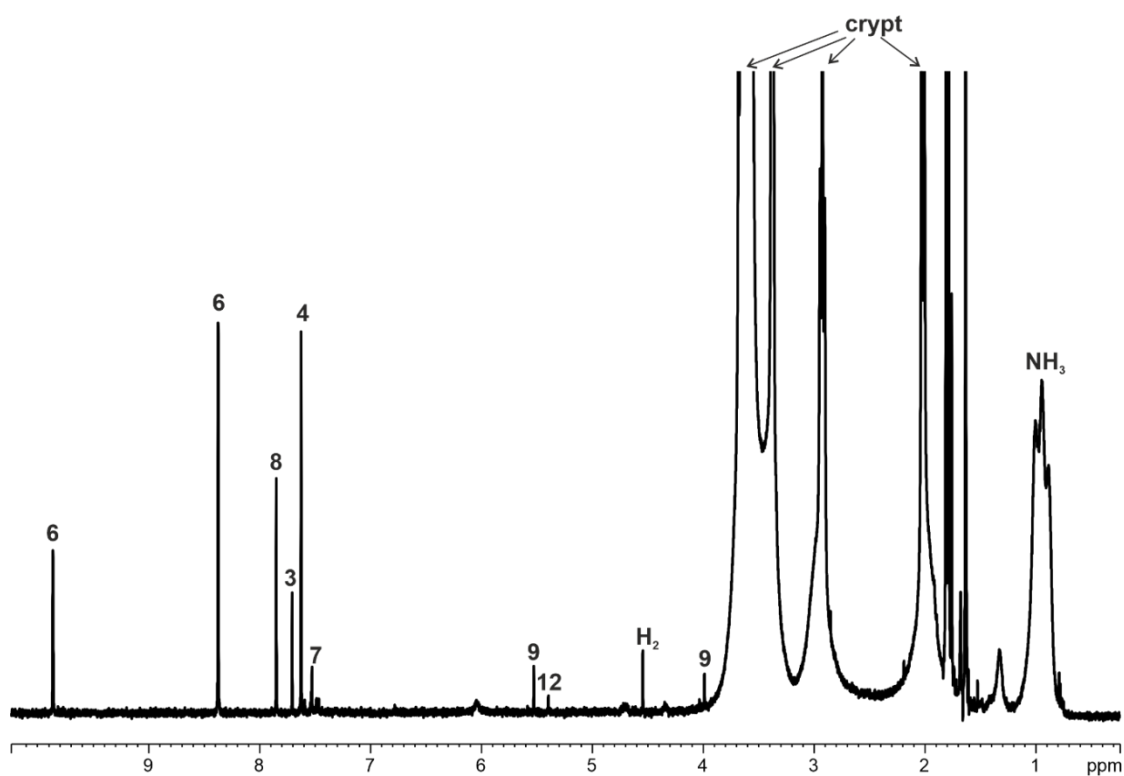


Figure SI 7.19 | ^1H -NMR spectrum (600.03 MHz) with solvent saturation of sample ii at 203K.

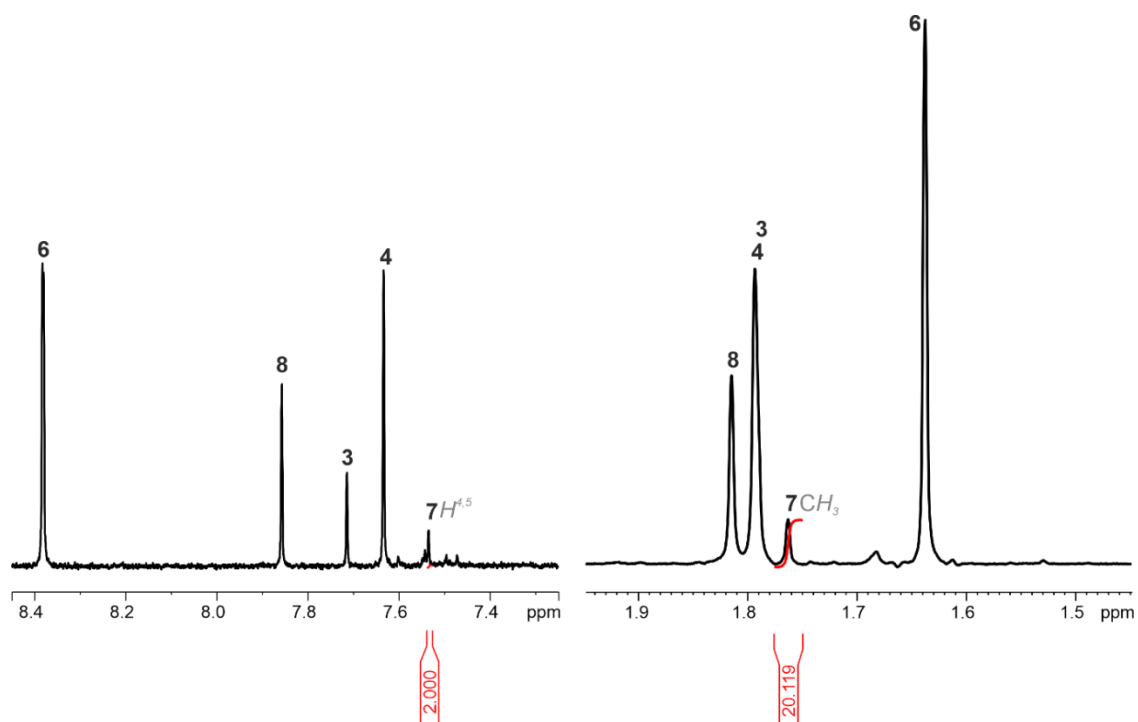


Figure SI 7.20 | Regions of a ^1H -NMR spectrum of Figure SI 7.19 (600.03 MHz; with solvent saturation; sample ii at 203K). The baseline in the *tert*-butyl region (right) was manually corrected. The signals belonging to 7 are integrated.

A chemical exchange between 7 and 3 was observed at 233K (see Figure SI 7.21).

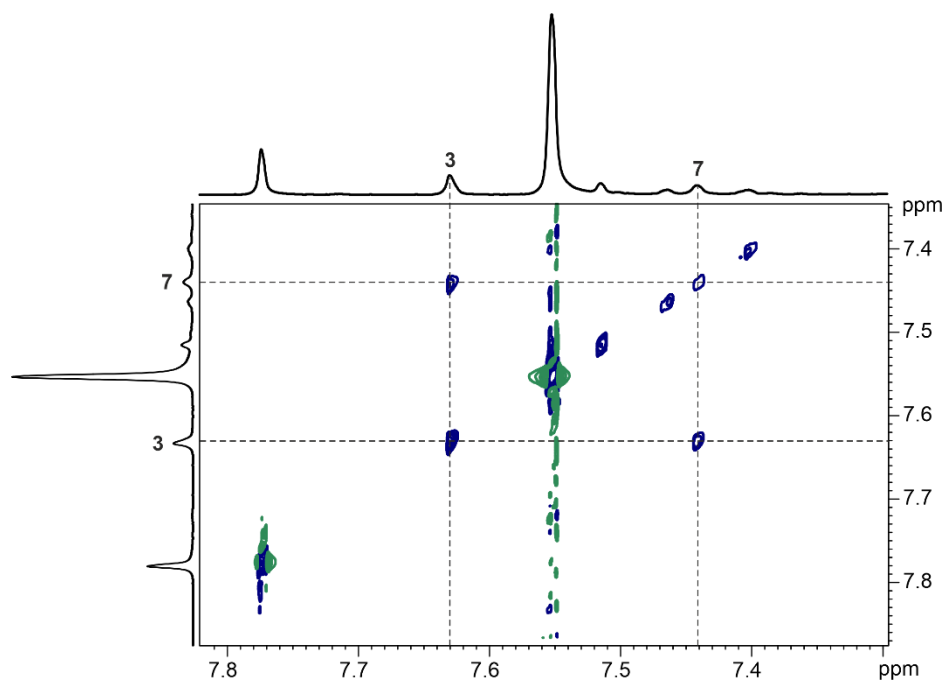
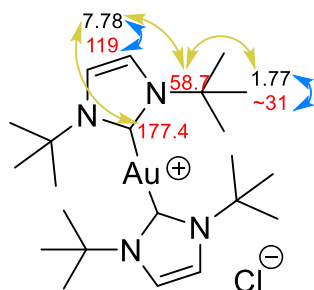


Figure SI 7.21 | Extract of a ^1H - ^1H -EXSY spectrum of sample ii at 233K showing a chemical exchange between 3 and 7.

$[(\text{NHC}^{\text{tBu}})_2\text{Au}]\text{Cl}$ (8)

The formation of this species was observed in all samples (i-iii). A chemical assignment can also be found in literature.^[1]



^1H NMR (600 MHz, liq. NH_3 , 233 K): δ/ppm = 7.78 (4H, s), 1.77 (36 H, s). ^{13}C NMR (600 MHz, liq. NH_3 , 233 K): δ/ppm = 177.4, 119, 58.7, 31.

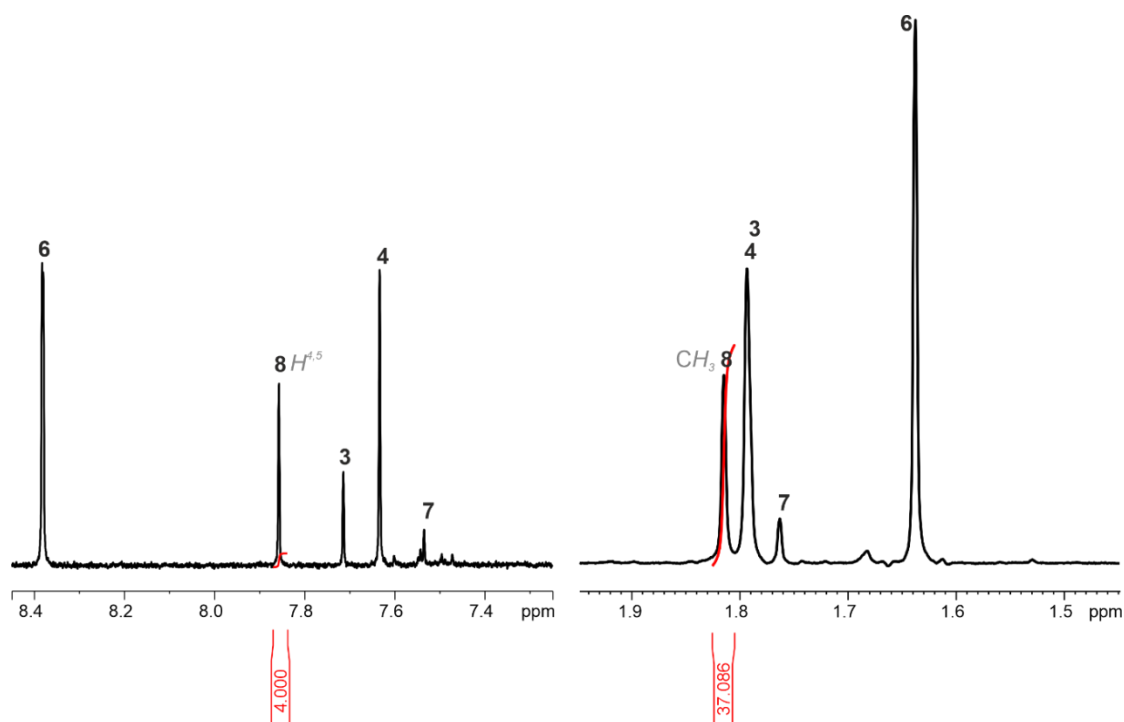
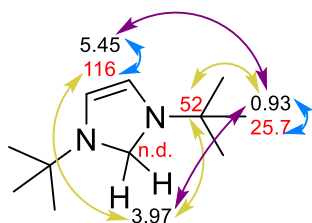


Figure SI 7.22 | Regions of a ^1H -NMR spectrum of Figure SI 7.19 (600.03 MHz; with solvent saturation; sample ii at 203K). The baseline in the *tert*-butyl region (right) was manually corrected. The signals belonging to **8** are integrated.

$\text{NHC}^{\text{tBu}}\text{H}_2$ (**9**)

The formation of this species was only observed in samples i and ii. A chemical assignment can also be found in literature.^[6]



^1H NMR (600 MHz, liq. NH_3 , 233 K): δ/ppm = 5.45 (2H, s), 3.97 (2H, s), 0.93 (18 H, s). ^{13}C NMR (600 MHz, liq. NH_3 , 233 K): δ/ppm = 116, 52, 25.7. The ^{13}C chemical shift of carbon C^2 could not be assigned due to low signal-to-noise ratio.

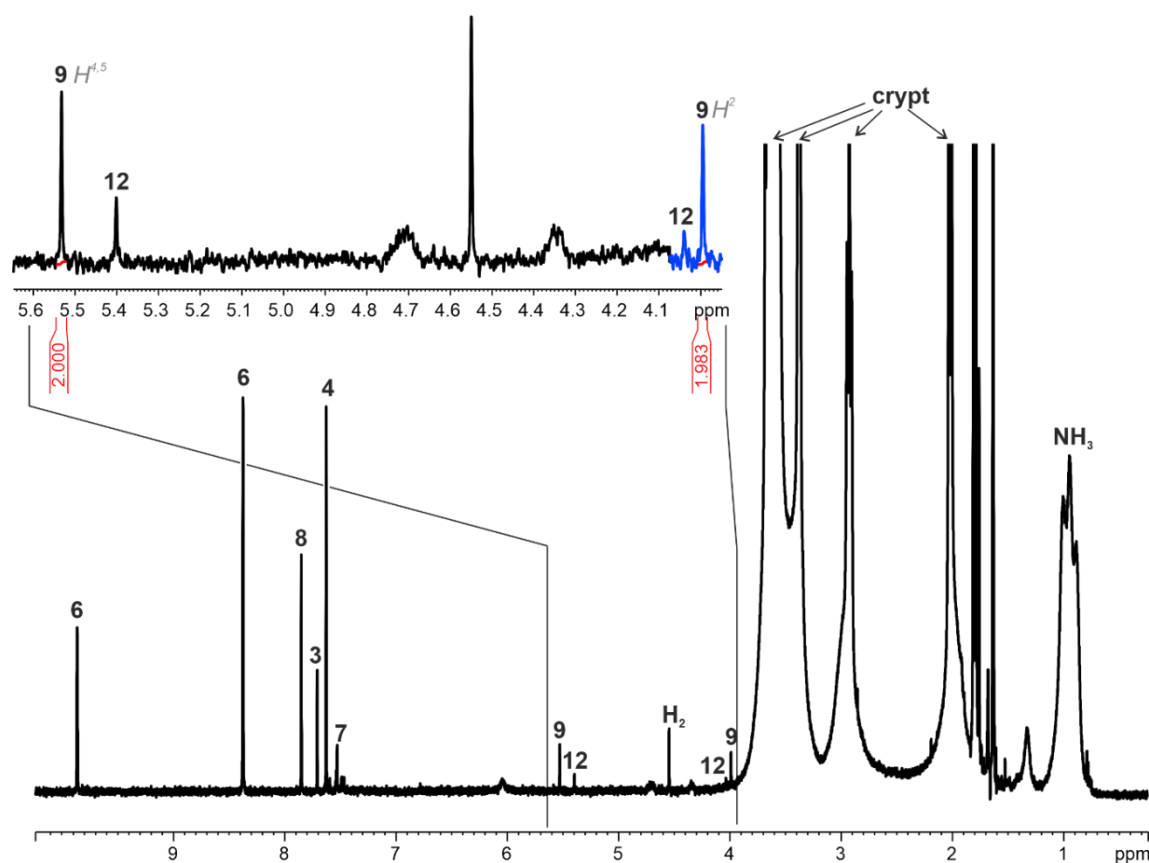
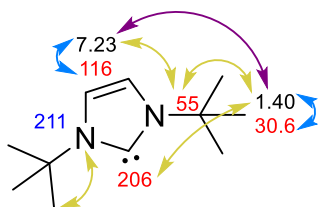


Figure SI 7.23 | ^1H -NMR spectrum (600.03 MHz) with solvent saturation of sample **ii** at 203K. The region of $\text{H}^{4,5}$ and H^2 of **9** and **12** is zoomed in and the baseline of the region marked in blue was manually corrected for integration. The signals of **9** are integrated.

NHC^{tBu} (**10**)

A chemical assignment can also be found in literature.^[5, 7] The chemical shift of the the carbenic carbon, in contrast to the other carbons, differs quite much from the values found in literature (213.4 ppm in THF-d_8 ^[7] and 213.2 ppm in benzene- d_6 ^[5]). Therefore, a sample of NHC^{tBu} -carbene in liquid ammonia was prepared and subsequently measured. 1D (see Figure SI 7.24) as well as 2D experiments verified that the signals belonging to **10** are those of the free carbene.



^1H NMR (600 MHz, liq. NH_3 , 233 K): $\delta/\text{ppm} = 7.23$ (2H, s), 1.40 (18 H, s). ^{13}C NMR (600 MHz, liq. NH_3 , 233 K): $\delta/\text{ppm} = 206, 116, 55, 30.6$.

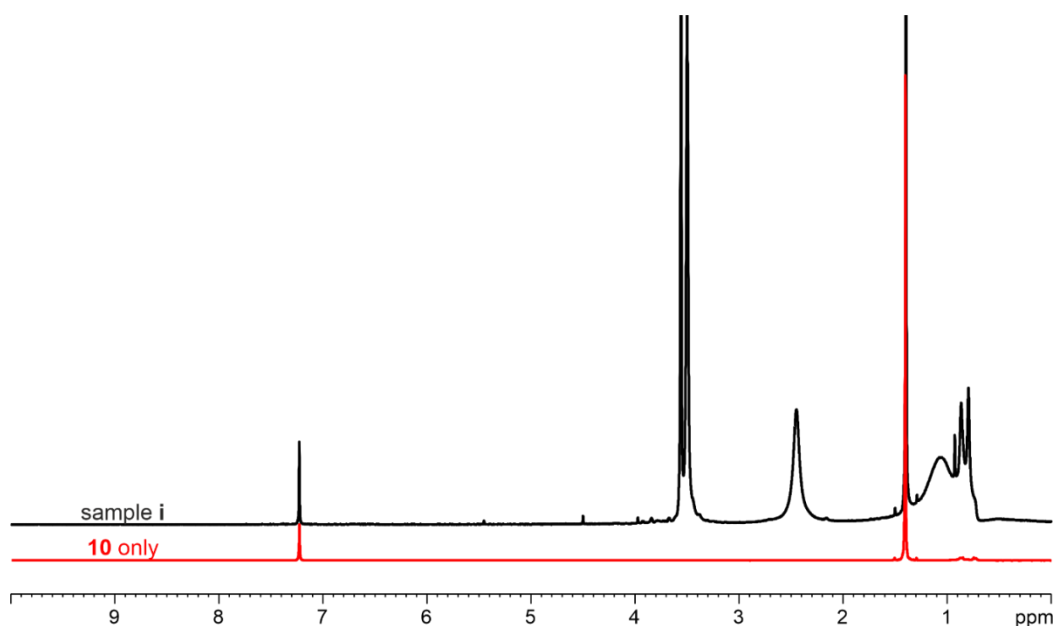
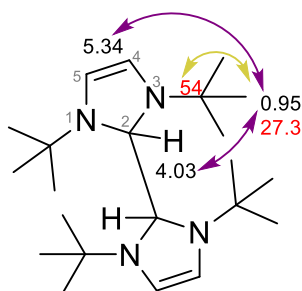


Figure SI 7.24 | Stacked ^1H -NMR spectra (600.03 MHz; 233K; with solvent saturation) of sample **i** after completion of the reaction monitoring (black) and a sample of carbene **10** in liquid ammonia (red).

$(\text{NHC}^{\text{tBu}}\text{H})_2$ (**12**)

The signals of $\text{H}^{4,5}$ and H^2 were very small. Hence, not all of the corresponding ^{13}C signals could be detected by ^1H - ^{13}C -HSQC or -HMBC. For **12** the corresponding proton assignment by NOESY as well as the partial carbon assignment by ^1H - ^{13}C -HSQC and- HMBC suggested a compound with a chemical environment similar to **9**. The integral ratio (see Figure SI 7.25) of the signals mentioned suggests the hydrogenated form of the NHC^{tBu} -dimer (**5**) as a conceivable structure of **12**, which appears plausible with regard to the shifts of similar hydrogenated NHC -dimers reported in literature.^[8]



^1H NMR (600 MHz, liq. NH_3 , 233 K): δ/ppm = 5.34 (4H, s), 4.03 (2H, s), 0.95 (36 H, s). ^{13}C NMR (600 MHz, liq. NH_3 , 233 K): δ/ppm = 54, 27.3. The ^{13}C chemical shift of the carbons of the double bond and NCHN could not be assigned.

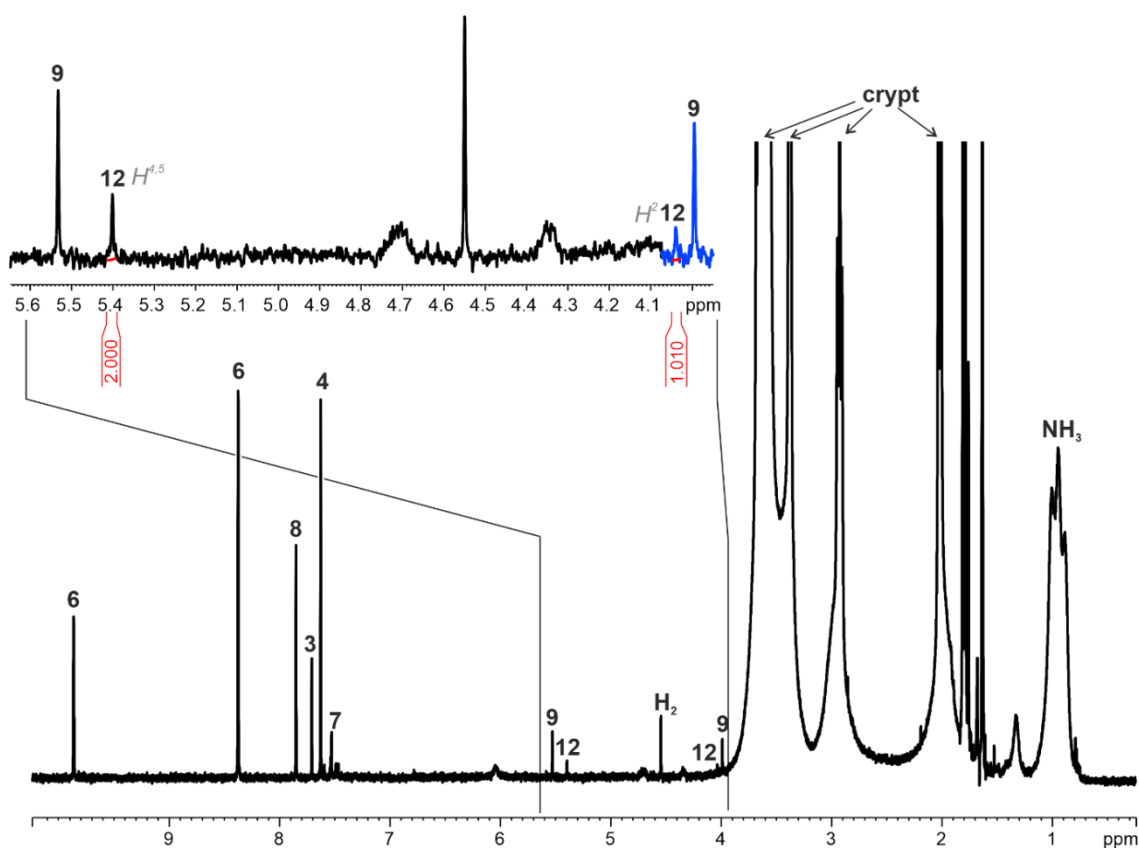


Figure SI 7.25 | $^1\text{H-NMR}$ spectrum (600.03 MHz) with solvent saturation of sample **ii** at 203K. The region of $H^{4,5}$ and H^2 of **9** and **12** is zoomed in and the baseline of the region marked in blue was manually corrected for integration. The signals of **12** are integrated.

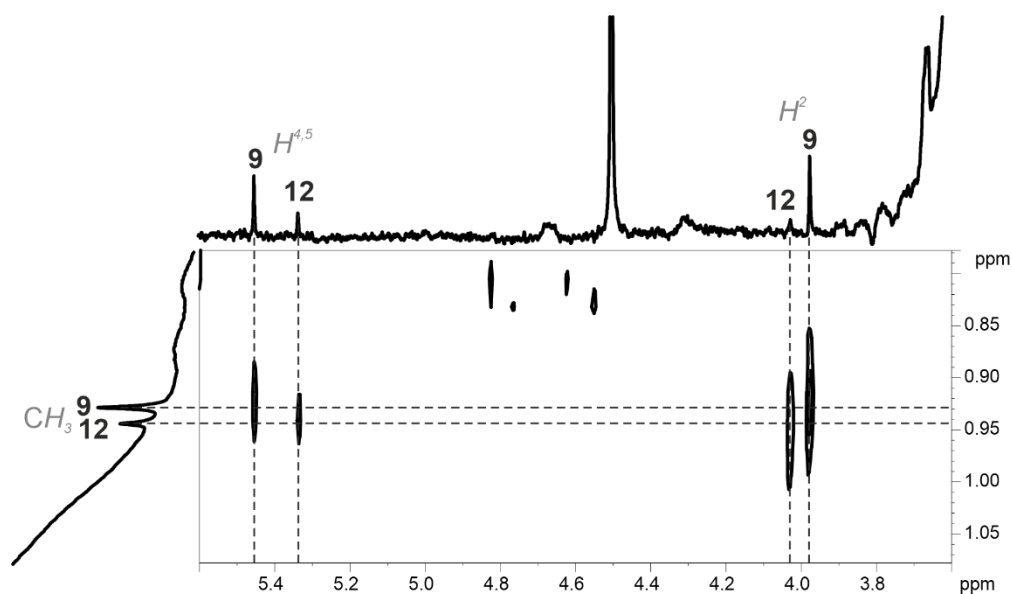


Figure SI 7.26 | Extract of a $^1\text{H-}^1\text{H-NOESY}$ of sample **ii** recorded at 233K. The phase of the displayed crosspeaks is of different phase as the diagonal peaks (not displayed), identifying them as NOE crosspeaks.

7.8.3.3 Proton Trapping

Cooling the silicide free sample **iii** down to 203 K revealed a broad signal at 5.71 ppm (see ? Figure SI 7.27), which is in chemical exchange with ammonia (this signal disappears upon saturation of ammonia). In literature, the NH_2^- signal as a counter ion to Au(III) complexes appears at around 5.8 ppm.^[9] However, in our case in sample **iii**, we exclude the presence of NH_2^- considering the presence of protons according to the proposed mechanism (see manuscript). In contrast, we assume that this signal may belong to protons in a trapped version.

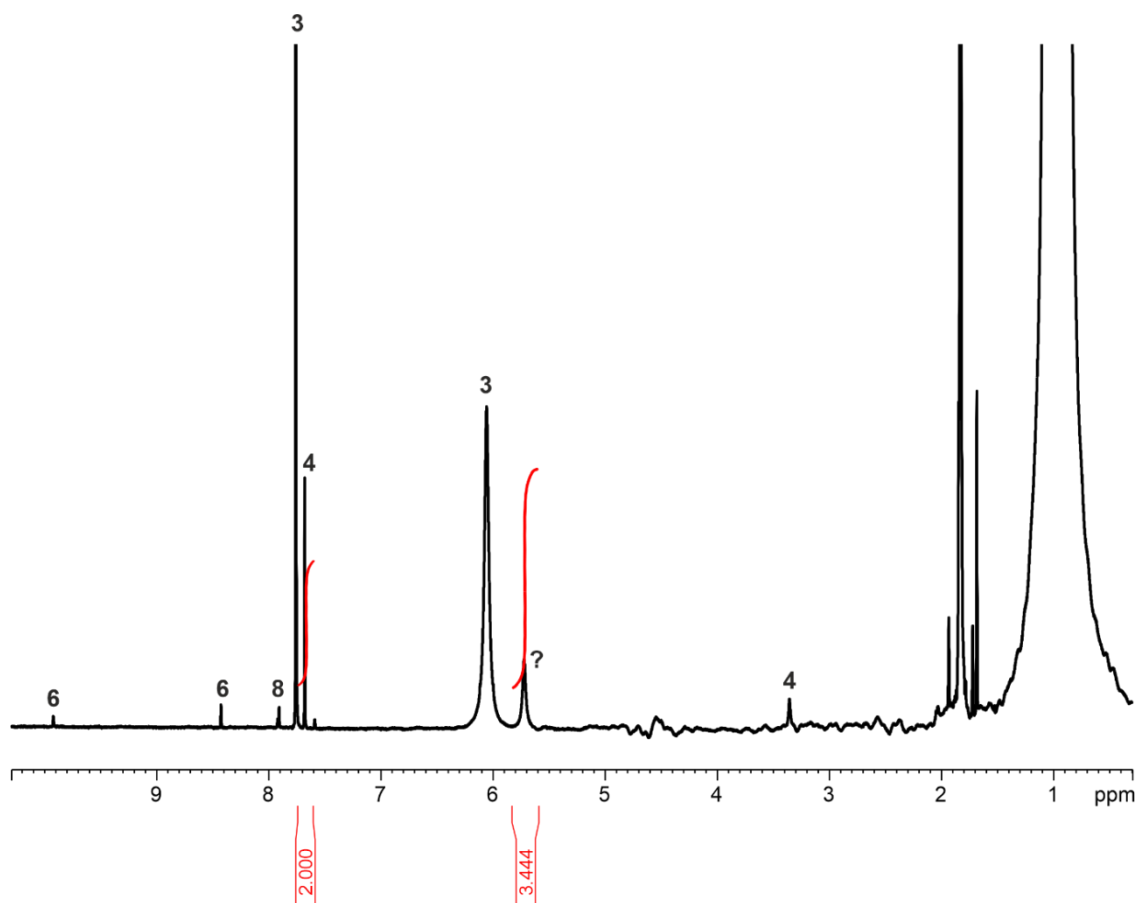


Figure SI 7.27 | ^1H -NMR spectrum (600.03 MHz) of sample **iii** recorded at 203K. A new broad signal at 5.71 ppm appeared.

Complexes including NHC^{tBu} -ligands were excluded as possible structural candidate for the proton labeled ?, since no NHC^{tBu} -signals were found correlating in intensity or appearance with the signal ? at 5.71 ppm. Furthermore, ? is assumed to be not directly connected to nitrogen since in the 1D ^1H - ^{15}N -HSQC no corresponding peak at 5.71 ppm was present and correlations to signals with by far lower intensities e.g. of **4** could be detected. This observation plus the significant deviation in chemical shift (NH_4Cl at 7.1 ppm^[10] vs. 5.71 ppm) would exclude NH_4Cl as a possible structure of ? (a fast proton exchange between NH_4Cl and another unknown species, highfield shifted to NH_4Cl , cannot be totally excluded but seems to be unlikely since other protonation equilibria result in slow exchanges. Nevertheless, the disappearance of signal ? upon saturation of ammonia indicates that ? is certainly involved in proton exchange equilibria with ammonia). Considering that the proton ? is not incorporated in a complex with NHC^{tBu} -ligands and is part of

an exchange equilibrium with ammonia, a tentative assignment for the unknown species could be HAu(I)Cl_2 . Some chemical shifts of HAu(III)L_3 compounds are known in literature and their $^1\text{H-NMR}$ shift of $H\text{-Au}$ (hydridic in literature) appears in a chemical shift range from 6.33 ppm for $H\text{-Au-tridentate-L}$, -0.8 ppm up to 0.1 ppm for $[\text{H}_2\text{-Au-bidentate-L}]\text{Li}^+$ and 1.2 ppm up to 3.25 ppm for $[\text{HX-Au-bidentate-L}]\text{Li}^+$.^[9] Per molecule of **4**, one equivalent HCl is expected to dissociate from **3** resulting in a 2/1 ratio of $\text{H}^{4,5}$ of **4** and ? of HAuCl_2 . The detected ratio of 2/3.4 and thus the solved amount of **4** (see Figure SI 7.27) are too small. However, the solubility of **4** in ammonia is close to precipitation, which was shown for sample **ii** (see Figure SI 7.28). For sample **iii** no effect of shaking was observed.

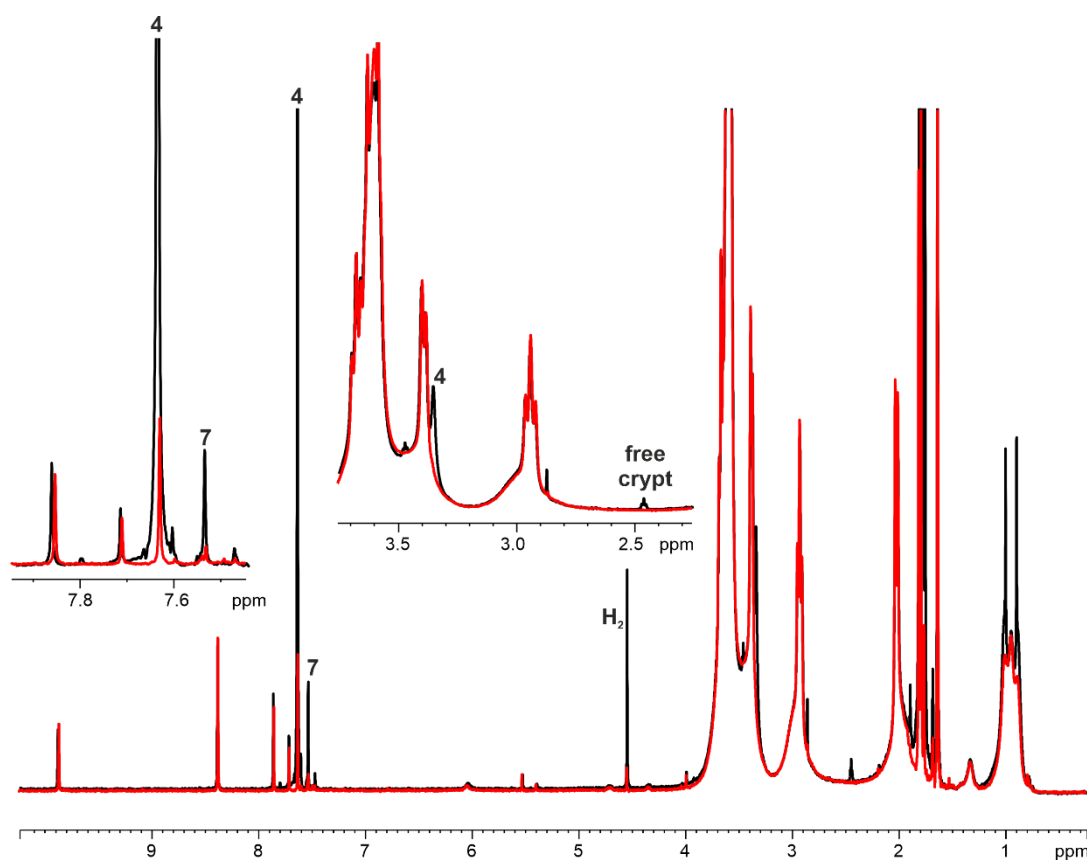


Figure SI 7.28 | Overlap of $^1\text{H-NMR}$ spectra (600.03 MHz) with solvent saturation of sample **ii** recorded at 203K. Red: before shaking the NMR tube. Black: after shaking the tube. After shaking the tube, the amount of **4**, **7**, H_2 and free cryptand in solution increased, while all other signal intensities remained nearly constant.

In depth NMR investigation of the 1:2:2 sample (ii)

For a spectrum of this sample at 203 K see Figure SI 7.23 or SI25.

By investigating the slower reaction of sample **ii** at 203 K a characteristic triplet ($J = 51.5$ Hz) was observed at 7.02 ppm which, due to its chemical shift and splitting pattern, matches ammonium.^[10] Upon temperature increase, the signal of NH_4^+ broadens and decreases accompanied by a small highfield shift of around 0.1

ppm (see Figure 29a). Concurrently, the signal at 6.05 ppm (NH_3 signal of **3**) experiences a stronger highfield shift of around 0.3 ppm with no significant decrease in intensity (see Figure SI 7.29 a).

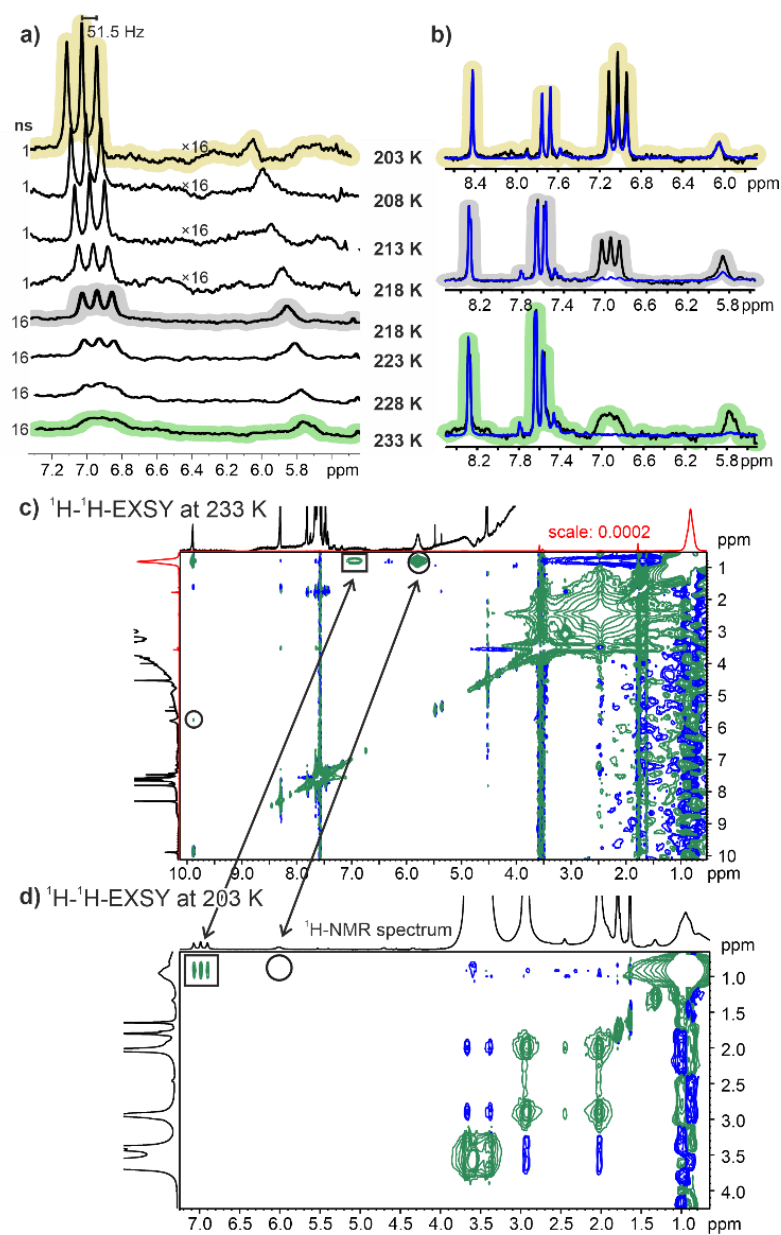


Figure SI 7.29 | a) Stacked ^1H NMR spectra of a mixture of $\text{K}_6\text{Rb}_6\text{Si}_{17}$ (1 eq.), $\text{NHC}^{\text{tBu}}\text{AuCl}$ (2 eq.) and [2.2.2]-cryptand (2 eq.) in liquid ammonia recorded at different temperatures. b) Overlapping of spectra without solvent saturation (black) and with solvent saturation (blue) of selected temperatures. c) ^1H - ^1H -EXSY at 233K. d) ^1H - ^1H -EXSY at 203K.

Saturating the NH_3 frequency at different temperatures (see SI29 b) led, in the case of ammonium, to a reduction in signal intensity at all temperatures examined. In the case of the signal at 6.05 ppm, however, the intensity only decreased at temperatures above 203 K. These saturation transfers suggest that NH_4^+ and ammonia are in faster chemical exchange over the entire temperature range (203K-233K) while the amide signal at 6.05 ppm starts to exchange with NH_3 in an NMR detectable velocity only at temperatures above 203 K. This was further supported by ^1H 2D exchange spectroscopy (EXSY) which showed exchange peaks between NH_3 and both NH_4^+ and amide at 233K (Figure SI 7.29 c), whereas at 203K only the crosspeak

between NH_3 and NH_4 remained (Figure SI 7.29 d). With ascending temperature, both exchange rates increase due to higher intensity loss upon saturation of NH_3 (see Figure SI 7.29 b). Furthermore, we also observed an exchange between the acidic proton of **6** ($\text{NHC}^{\text{tBu}}\text{-HCl}$) and both NH_3 and **3** ($\text{NHC}^{\text{tBu}}\text{-Au-NH}_3^+$) (see Figure SI 7.29 c). The EXSY spectrum also shows an exchange between the protons bound to the double bond of the NHC moiety of **3** and **7** as was already mentioned above. A schematic proton exchange at 233 K is given in Scheme 2 in the manuscript. Since the EXSY shows crosspeaks between the ^1H signals on the carbenic part of **3** and **6**, while for their double bond bound protons it does not, this crosspeak may be a result of NOE maintenance during the full exchange series from **3** over ammonia to **6**. We suspect that the exchange between ammonia and **3** takes place *via* coordination and dissociation of the NHC from gold.

Besides, in a solution of $\text{NHC}^{\text{tBu}}\text{AuCl}$ in NH_3 in absence of $\text{K}_6\text{Rb}_6\text{Si}_{17}$, no ammonium was formed. Additionally, in our previous studies of $\text{K}_6\text{Rb}_6\text{Si}_{17}$ dissolved in ammonia in presence or absence of cryptand, the signal for NH_4^+ has never been observed.

7.8.3.4 Silicon Species

It has to be mentioned, that no protonated silicide signals were directly detected during the reaction monitoring discussed in the manuscript within sample i, which however does not exclude their presence in small amounts below the detection limit of NMR. Only after the $\text{NHC}^{\text{tBu}}\text{-Au}$ -species disappeared from solution, signals of the protonated silicide HSi_9^{3-} (see Figure SI 7.30) and the degradation product H_3Si^- (see Figure SI 7.31) could be detected.^[11, 12]

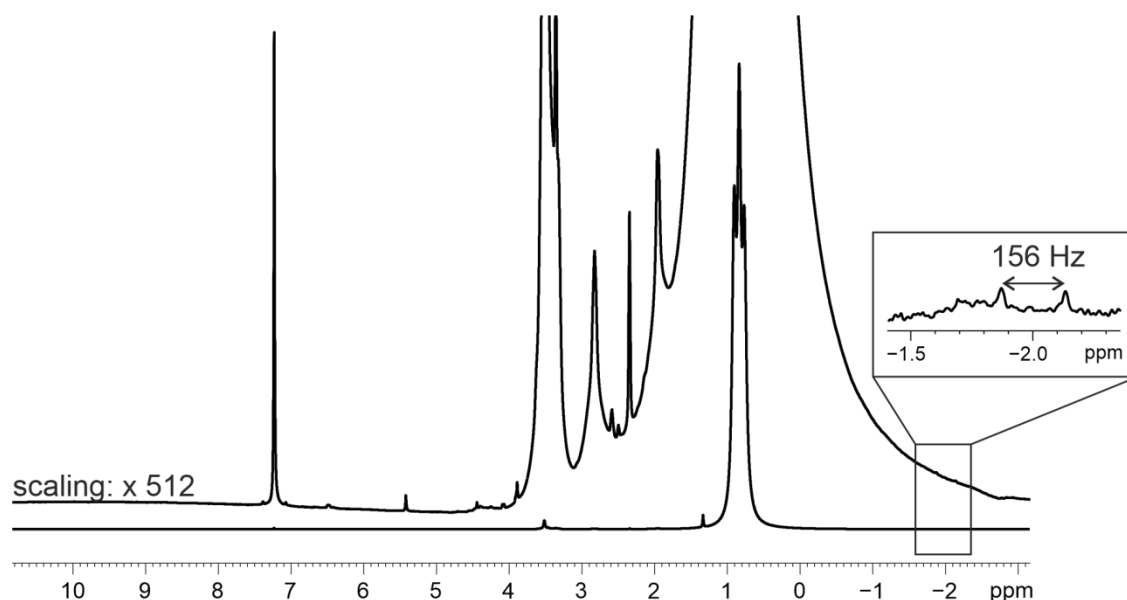


Figure SI 7.30 | ^1H NMR spectrum of sample i after the reaction monitoring at 203K. The baseline of the zoomed region was manually corrected. The zoomed region displays the proton signal of HSi_9^{3-} . The corresponding ^{29}Si -NMR signal of the Si_9 moiety can be seen in Figure SI 7.32 at -358.5 ppm.^[11]

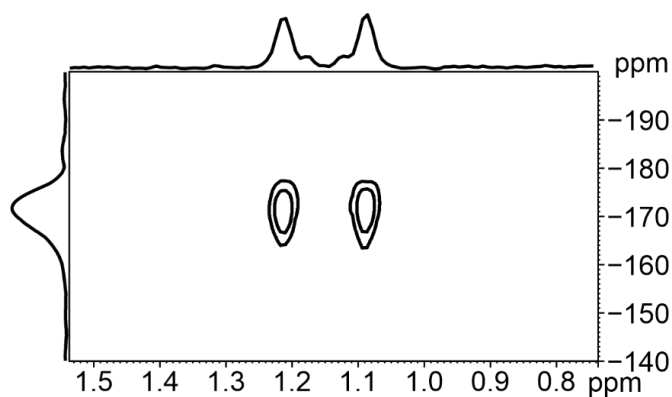


Figure SI 7.31. Extract of a $^1\text{H}^{29}\text{Si}$ -HMBC spectrum of sample i after the reaction monitoring at 233K showing the crosspeak for H_3Si^- .^[12]

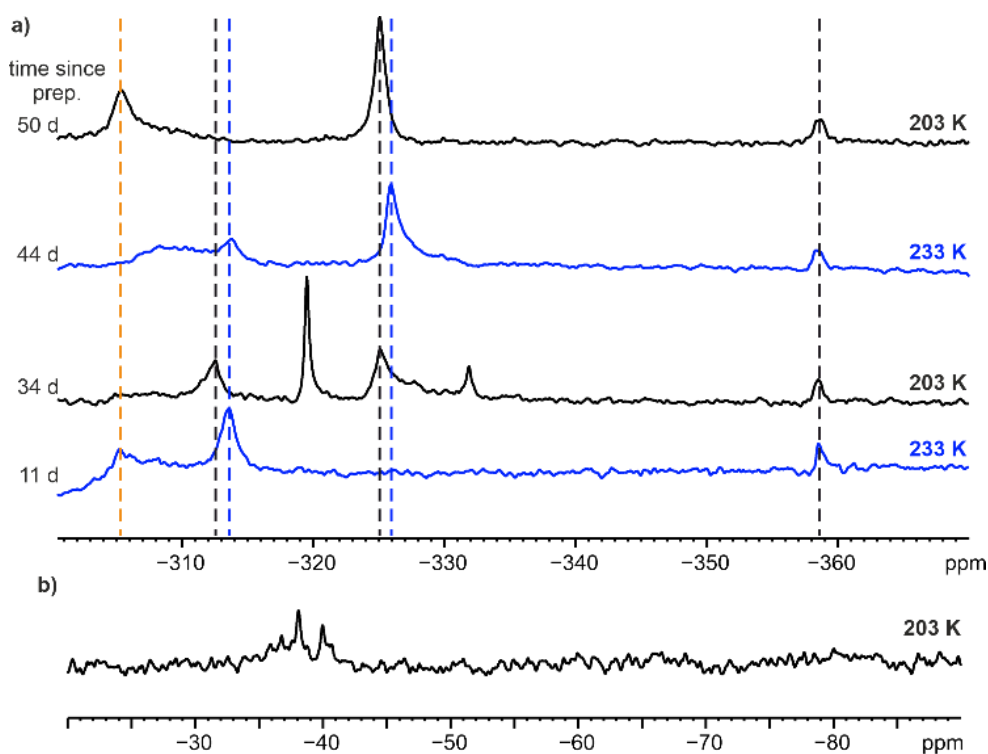


Figure SI 7.32 | a) Stacked ^{29}Si -NMR spectra (119.21 MHz) of sample i after reaction monitoring at different temperatures (black: 203K; blue 233K) sorted by increasing time interval between preparation and measurement. Several peaks could be detected in a chemical shift region, which is common for signals of silicides. b) ^{29}Si -NMR spectrum (119.21 MHz) of the slower reacting sample ii at 203 K. No other ^{29}Si -NMR signals were detected in the 1D spectrum.

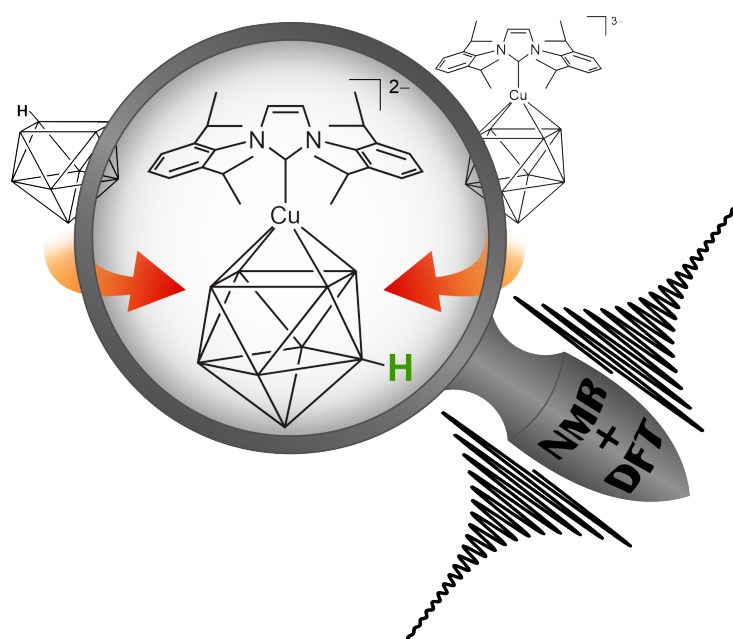
7.8.4 References

- [1] M. V. Baker, P. J. Barnard, S. J. Berners-Price, S. K. Brayshaw, J. L. Hickey, B. W. Skelton, A. H. White, *Dalton Trans.* **2006**, 3708-3715.
- [2] A. Jerschow, N. Müller, *J. Mag. Res.* **1997**, 125, 372-375.

7 ON THE REACTIVITY OF $\text{NHC}^{\text{tBu}}\text{AuCl}$ TOWARDS $\text{Rb}_6\text{Cs}_6\text{Si}_{17}$

- [3] C. S. Johnson Jr., *Prog. Nucl. Mag. Res. Sp.* **1999**, *34*, 203-256; W. S. Price, *Concept Magn. Reson. A* **1998**, *10*, 197-237; E. O. Stejskal, J. E. Tanner, *J. Chem. Phys.* **1965**, *42*, 288.
- [4] P. I. Jolly, S. Zhou, D. W. Thomson, J. Garnier, J. A. Parkinson, T. Tuttle, J. A. Murphy, *Chem. Sci.* **2012**, *3*, 1675-1679.
- [5] N. Bridonneau, L. Hippolyte, D. Mercier, D. Portehault, M. Desage-El Murr, P. Marcus, L. Fensterbank, C. Chaneac, F. Ribot, *Dalton Trans.* **2018**, *47*, 6850-6859.
- [6] J. W. Runyon, O. Steinhof, H. V. Rasika Dias, J. C. Calabrese, W. J. Marshall, A. J. Arduengo III, *Aust. J. Chem.* **2011**, *64*, 1165-1172.
- [7] J. Raynaud, N. Liu, M. Fevre, Y. Gnanou, D. Taton, *Polym. Chem.* **2011**, *2*, 1706-1712.
- [8] I. A. Shkrob, *J. Phys. Chem. B* **2010**, *114*, 368-375.
- [9] L. Rocchigiani, J. Fernandez-Cestau, I. Chambrier, P. Hrobarik, M. Bochmann, *J. Am. Chem. Soc.* **2018**, *140*, 8287-8302.
- [10] A. J. Bellamy, W. S. J., P. Golding, *Propellants Explos. Pyrotech.* **2002**, *27*, 59-61.
- [11] C. Lorenz, F. Hastreiter, J. Hioe, N. Lokesh, S. Gärtner, N. Korber, R. M. Gschwind, *Angew. Chem. Int. Ed.* **2018**, *57*, 12956-12960.
- [12] H. Bürger, R. Eujen, H. C. Marsmann, *Z. Naturforsch. B* **1947**, *29*, 149-152.

8 NMR-DETECTION OF AN ELUSIVE PROTONATED AND COINAGE METALIZED SILICIDE [NHC^{DIPP}Cu(η⁴-Si₉)H]²⁻ IN SOLUTION



Verena Streitferdt,[†] Susanne M. Tiefenthaler,[†] Ilya G. Shenderovich, Stefanie Gärtner, Nikolaus Korber*
and Ruth M. Gschwind*

To be submitted.

[†] Both authors contributed equally to the publication.

V. Streitferdt prepared the manuscript and all Figures with input from all authors. V. Streitferdt did all NMR measurements and prepared corresponding Figures and sections in the SI. S. M. Tiefenthaler prepared all samples for NMR measurements and did all crystallization studies. I. G. Shenderovich performed the theoretical calculations. S. Gärtner contributed with data evaluation and discussions. N. Korber and R. M. Gschwind supervised and directed the project.

8.1 Abstract

An elusive, two-fold functionalized silicon cluster $[\text{NHC}^{\text{DIPP}}\text{Cu}(\eta^4\text{-Si}_9\text{H})]^{2-}$ was detected and characterized in liquid ammonia by NMR spectroscopy. $^1\text{H-NMR}$ line-widths revealed that $[\text{NHC}^{\text{DIPP}}\text{Cu}(\eta^4\text{-Si}_9\text{H})]^{2-}$ is more rigid than the non-complexed silicide $[\text{HSi}_9]^{3-}$. Key NMR results were corroborated by theoretical calculations. $[\text{NHC}^{\text{DIPP}}\text{Cu}(\eta^4\text{-Si}_9\text{H})]^{2-}$ represents the first protonated and coinage metallized group 14 *Zintl* cluster.

8.2 Introduction

Silicon holds an important role in our daily lives, as the use of Si-based technology is now, more than ever, ubiquitous. The semiconducting property of silicides renders them as useful material for nanoelectronics. Over the last years, the polyanionic clusters (*Zintl* ions) of silicides have garnered interest in the field of mesostructured extended solids, new crystalline modifications and nanoparticles,^[1] since they constitute preformed, soluble building blocks. Especially functionalized silicon-building blocks have proven to be successful, as their functionalization enabled to control the size of nanoparticles.^[2] However, not just functionalized, but also protonated silicon materials are of interest, as, for example, recently a possible way towards new solar cell was found, starting from hydrogen doted amorphous silicon.^[3] *Zintl* ions are usually functionalized by silylation or transition metal complexes.^[4] While the heavier homologues Ge, Sn and Pb were found to have an extensive complexation chemistry, such as $[\text{Pt}@\text{Sn}_9\text{Pt}(\text{PPh}_3)]^{2-}$,^[5] $[\text{Pb}_9\text{W}(\text{CO})_3]^{4-}$,^[6] or $\{(\text{Ge}_9)_2[\eta^6\text{-Ge}(\text{PdPPh}_3)_3]\}^{4-}$,^[7] transition metal (TM) functionalized silicides are still rare. So far, only five compounds are known which contain a silicon *Zintl* ion acting as the ligand for a metal complex. Beside the reported complexes $[\text{Si}_9\text{ZnPh}]^{3-}$ by Sevov *et al.*^[8] and $[(\text{MesCu})_2\text{Si}_4]^{4-}$ and $[\text{NHC}^{\text{DIPP}}\text{Cu}(\eta^4\text{-Si}_9)]^{3-}$ (the latter was experimentally characterized by crystal structure, ESI-MS and $^1\text{H-NMR}$) by Fässler *et al.*,^[9,10] we were able to synthesize and characterize $\{[\text{Ni}(\text{CO})_2]_2(\mu\text{-Si}_9)_2\}^{8-}$ and more recently $[(\text{NHC}^{\text{tBu}}\text{Au})_6(\eta^2\text{-Si}_4)]^{2+}$.^[11,12]

Zintl ions and their functionalized analogues are mainly characterized *via* single crystal X-ray diffraction. However Rudolph *et al.* already demonstrated that especially solution NMR can provide valuable information about structures, solution-equilibria or dynamics. They used ^{119}Sn NMR to prove experimentally the fluctuation of the nonastannide^[13] Sn_9^{4-} that had already been postulated by Corbett *et al.* the year before.^[14] Subsequently, more and more results were obtained *via* ^{119}Sn and ^{207}Pb NMR,^[15] as well as more recently *via* ^{29}Si NMR.^[16] The groups of Eichhorn^[17] and Schrobilgen^[6] were the first to report on NMR signals stemming from a TM functionalized stannide, when they both discovered the three distinct resonances of the compound $\text{M}(\text{CO})_3\text{Sn}_9$ ($\text{M} = \text{Cr}, \text{Mo}, \text{W}$) in the ^{119}Sn NMR. Since then a number of *Zintl* ions other than silicides with exo-bound metal complexes have been detected and reported on.^[15] In addition, Eichhorn *et al.* were able to obtain the first NMR signals of some endohedral *Zintl* cages $[\text{M}@\text{Pb}_{12}]^{2-}$ ($\text{M} = \text{Pt}, \text{Pd}, \text{Ni}$),^[18] which was followed by reports on NMR signals of clusters such as $[\text{Pd}_2@\text{Sn}_{18}]^{4-}$ by Wang *et al.*^[19] or $[\text{Cu}@\text{Sn}_9]^{3-}$ by Fässler *et al.* ^[20]

Compared to the rich chemistry of *Zintl* ions of tin and lead, little is known about silicides, especially about their structures in solution *via* NMR studies. There are many reasons for this, e.g. the difficulties in synthesizing, handling and preparing the silicide samples as well as the low solubility in ammonia combined with the low natural abundance of the NMR active ^{29}Si . These factors, together with the long relaxation time of ^{29}Si , lead to low signal to noise ratios, making the recording and evaluation of spectra difficult and time consuming.

Recently, reports of the protonated silicon *Zintl* ions $[\text{HSi}_9]^{3-}$, $[\text{H}_2\text{Si}_9]^{2-}$ and $[\text{HSi}_4]^{3-}$ in solution have been published,^[21–23] relying on NMR studies, as well as on crystal structures. Our study on $[\text{HSi}_9]^{3-}$ revealed a fluxional behavior of the Si-H and more unexpectedly of the Si-Si bonding.^[21] Shortly after that, we reported on our findings of the cluster $[\text{HSi}_4]^{3-}$ which demonstrated the importance of charge delocalization upon protonation of silicides.^[23]

Simultaneously protonated and TM functionalized *Zintl* clusters are rare and mainly known for the heavier homologues Ge and Sn ($[(\mu_2\text{-H})(\eta^2\text{-Ge}_4)\text{ZnPh}_2]^{3-}$ or $[\text{M}@\text{Sn}_9\text{H}]^{3-}$ with $\text{M} = \text{Pt}, \text{Pd}, \text{Ni}$).^[24,25] In contrast, for silicides such a protonated and TM functionalized complex is still elusive in crystals and in solution. So far, only in the gas phase ESI-MS indicated the existence of a $\{[(\text{NHC}^{\text{Dipp}}\text{Cu})_n(\text{Si}_9)]^{(4-n)-} + (3-n)\text{H}^+\}$ with $n = 1, 2$.^[22]

To fill this gap, we here report the first detection of a protonated and TM functionalized silicon cluster $[\text{NHC}^{\text{Dipp}}\text{Cu}(\eta^4\text{-Si}_9\text{H})]^{2-}$ in solution which is further supported by crystallographic and computational analyses. To the best of our knowledge, this also represents the first case of a protonated coinage metallized group 14 *Zintl* cluster in solution.

8.3 Results and Discussion

For the NMR studies, samples of $\text{K}_6\text{Rb}_6\text{Si}_{17}$ (fully ^{29}Si enriched) in presence of $\text{NHC}^{\text{Dipp}}\text{CuCl}$ (2 eq.) and [2.2.2]cryptand (2 eq.) in liquid ammonia were prepared. The dissolution and transformation process of NHC^{Dipp} -containing species was followed by ^1H -NMR (see ^1H -NMR region of $H^{a,b,c}$ in Figure 8.1a). After 28 days highly resolved multiplets of a major (marked in blue in Figure 8.1a) and some minor NHC^{Dipp} -containing species were observed. The major set of NHC^{Dipp} -characteristic ^1H -NMR signals fits well with the previously reported^[10] ^1H -NMR shifts of the non-protonated $[\text{NHC}^{\text{Dipp}}\text{Cu}(\eta^4\text{-Si}_9)]^{3-}$ (for spectra and further information see SI). In addition, two doublets were observed at chemical shifts typical for protonated silicides $\delta(^1\text{H})$ at 233 K = -1.88 ppm ($J = 156$ Hz) and -2.04 ppm ($J = 193$ Hz). The doublet at $\delta(^1\text{H}) = -1.88$ ppm represents the recently reported^[21] elusive silicide cluster $[\text{HSi}_9]^{3-}$ (for 2D ^1H - ^{29}Si -HMQC spectra see SI).^[26]

The doublet at $\delta(^1\text{H}) = -2.04$ ppm has neither been observed in any of our previous NMR investigations of *Zintl* phases nor, to the best of our knowledge, has it been reported in literature so far. Its negative ^1H -NMR chemical shift is indicative for an attachment to a silicide. Furthermore, the doublet splitting pattern indicates that the silicide is protonated at a vertex and the large coupling constant of 193 Hz implies that only one

proton is attached (compare with $[\text{HSi}_9]^{3-}$ at $\delta(^1\text{H}) = -2.85$ ppm with $^1J_{\text{HSi}} = 156$ Hz,^[21] $[\mu\text{-HSi}_4]^{3-}$ at $\delta(^1\text{H}) = -10.62$ ppm with $^1J_{\text{HSi}} = 12$ Hz,^[23] and $[\text{H}_2\text{Si}_9]^{2-}$ at $\delta(^1\text{H}) = -0.71$ ppm with $^1J_{\text{HSi}} = 19.7$ Hz,^[22]). In addition, one set of NHC^{Dipp} signals was detected (marked in green in Figure 8.1a), whose integrals directly correlate with that of the doublet at $\delta(^1\text{H}) = -2.04$ ppm over time (see SI for spectra). This together with the integral ratios of $\text{NHC}^{\text{Dipp}} : \text{H-Si} = 1 : 1$ unveils that the green signals in Figure 8.1a correspond to a mono-protonated silicide attached to one $\text{NHC}^{\text{Dipp}}\text{Cu}$ unit. Indeed, the CH_3 protons of the green ligand set exhibit considerable shift inequality (for spectra see SI) similar to the CH_3 protons^[10] of $[\text{NHC}^{\text{Dipp}}\text{Cu}(\eta^4\text{-Si}_9)]^{3-}$ which is commonly observed for $\text{NHC}^{\text{Dipp}}\text{-Cu}$ moieties connected to *Zintl* ions^[27–29].

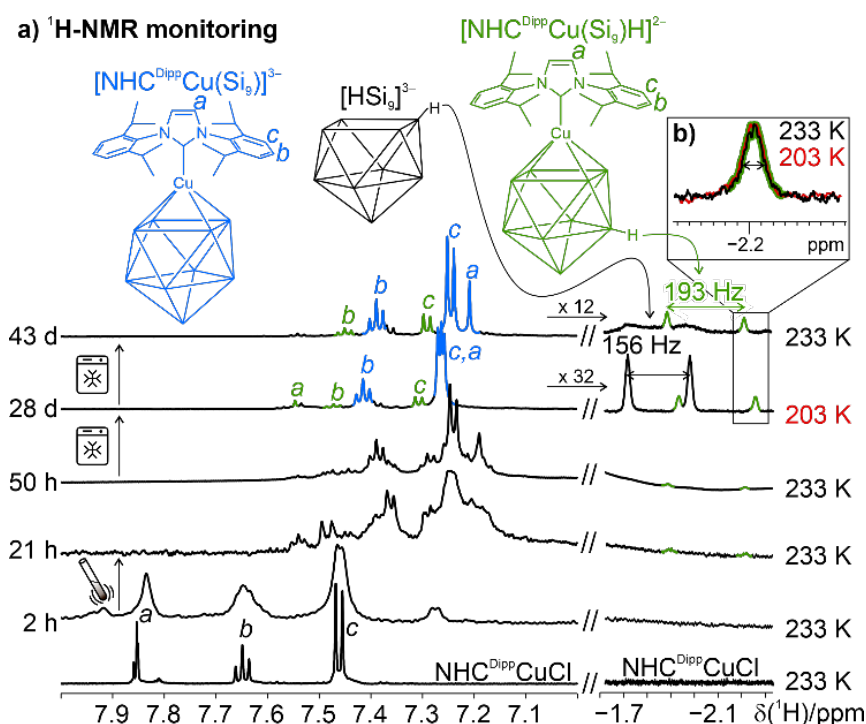


Figure 8.1 | ^1H -NMR monitoring (a) of the solvation and transformation processes of NHC^{Dipp} -containing species in solution of a sample of $\text{K}_6\text{Rb}_6\text{Si}_{17}$ (fully ^{29}Si enriched) with $\text{NHC}^{\text{Dipp}}\text{CuCl}$ (2 eq.) and [2.2.2]cryptand (2 eq.) in liquid ammonia. Bottom: ^1H -NMR spectrum of a sample of $\text{NHC}^{\text{Dipp}}\text{CuCl}$ in liquid ammonia. All other spectra were obtained by measuring the sample containing $\text{K}_6\text{Rb}_6\text{Si}_{17}$, $\text{NHC}^{\text{Dipp}}\text{CuCl}$ and [2.2.2]cryptand. The time between preparation and NMR measurement is shown on the left. The temperature during NMR measurements is shown on the right. In between 2 h and 21 h after sample preparation, the NMR tube was shaken to facilitate the dissolution of silicides. After around 50 h of NMR measurements at 233 K, the sample was stored in the freezer at 193 K in between the NMR measurements. The spectra were calibrated on the chemical shift of H_2 (4.61 ppm) and their regions are displayed in individual scaling. For the better resolved spectra (28 d and 43 d) the scaling factor of the H-Si ^1H -NMR region is given ($\times 32$ and $\times 12$ respectively). The spectra in the magnified region (b) are shifted to enable direct signal overlap and the intensities are scaled to the same peak height.

Next the silicide clusters were addressed. In the ^1H and ^{29}Si spectra (see Figure 8.1 and SI) mainly Si_9 -clusters were detected and scalar couplings, chemical shifts and reduced flexibilities (see below) of the new metallized complex hint at a protonated Si_9 -cluster $[\text{NHC}^{\text{Dipp}}\text{Cu}(\eta^4\text{-Si}_9\text{H})]^{2-}$ (see green structure in Figure 8.1a). The low intensity of the new Si-H signals did not allow for a direct detection. However, 2D ^1H - ^{29}Si -HMQC spectra and 1D $^1\text{H}\{^{29}\text{Si}\}$ -NMR spectra with selective silicon decoupling (see Figure 8.2 and SI) unveiled that a silicon signal at $\delta(^{29}\text{Si}) = -135$ ppm causes the doublet splitting. Upon temperature increase the line width of this H-Si proton remained unaltered (see Figure 8.1b magnified and stacked regions) in

8 PROTONATED AND METALIZED SILICIDE $[\text{NHC}^{\text{Dipp}}\text{Cu}(\eta^4\text{-Si}_9\text{H})]^{2-}$

contrast to that of $[\text{HSi}_9]^{3-}$, in which H-hopping^[21] leads to a line broadening. This reduced flexibility of $[\text{NHC}^{\text{Dipp}}\text{Cu}(\eta^4\text{-Si}_9\text{H})]^{2-}$ is in line with observations of Eichhorn *et al.*^[17] and Schrobilgen *et al.*^[6] that the cluster flexibility for *Zintl* complexes $(\text{E}_9\text{M}(\text{CO})_3)$ with $\text{E} = \text{Sn}, \text{Pb}$; $\text{M} = \text{Cr}, \text{Mo}, \text{W}$) decreases upon metallization.

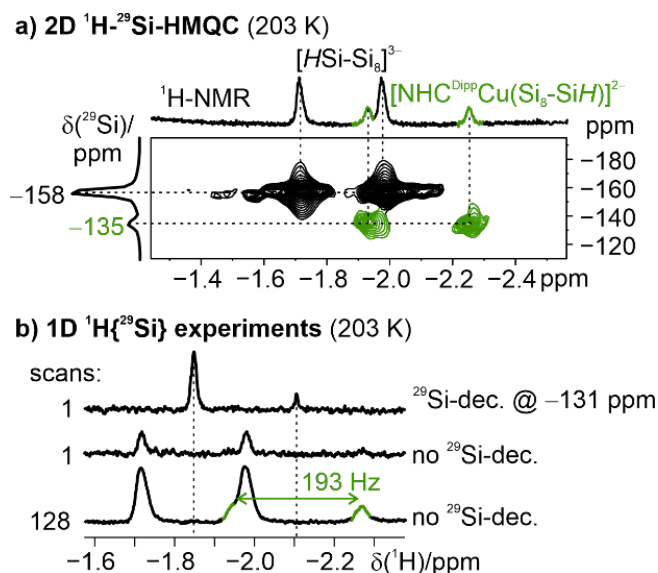


Figure 8.2 | 2D ^1H - ^{29}Si -HMQC spectra and 1D $^1\text{H}\{^{29}\text{Si}\}$ -NMR spectra unveil the attachment of the proton assigned to $[\text{NHC}^{\text{Dipp}}\text{Cu}(\eta^4\text{-Si}_9\text{H})]^{2-}$ to a silicon signal at $\delta(^{29}\text{Si}) = -135$ ppm. a) Slice of a 2D ^1H - ^{29}Si -HMQC spectrum recorded 31 days after sample preparation at 203 K. b) $^1\text{H}\{^{29}\text{Si}\}$ -NMR decoupling experiments recorded 44 days after sample preparation at 203 K revealed that the splitting of 193 Hz of the signal at $\delta(^1\text{H}) = -2.1$ ppm is caused by coupling to the silicon signal at $\delta(^{29}\text{Si}) = -135$ ppm. For more information on a) and b) see SI.

It is worth mentioning that in ^{29}Si -NMR spectra recorded at 233 K, two intense and unequally broadened signals were observed at -276 ppm ($\nu_{1/2} \approx 220$ Hz) and -290 ppm ($\nu_{1/2} \approx 440$ Hz) close by the typical ^{29}Si -NMR shift range of Si_9 -cluster.^[21,22] Relative ^{29}Si - and ^1H -NMR integral ratios to the signals of $[\text{HSi}_9]^{3-}$ (see SI) suggested that the ^{29}Si -NMR signals belong to $[\text{NHC}^{\text{Dipp}}\text{Cu}(\eta^4\text{-Si}_9)]^{3-}$ (literature^[10] reports experimental ^1H -NMR data but not ^{29}Si -NMR data for this complex). In our case, full ^{29}Si -labelling allowed for the detection of the elusive ^{29}Si -NMR signals. The coordination of copper to the Si_9 -cluster is in line with the observation of differently pronounced line broadening that probably results from distance-dependent interactions with the quadrupolar nature of ^{63}Cu and ^{65}Cu . The less broadened ^{29}Si -NMR signal (-276 ppm) is assigned to the middle Si_4 -unit of $[\text{NHC}^{\text{Dipp}}\text{Cu}(\eta^4\text{-Si}_9)]^{3-}$ and the more broadened ^{29}Si -NMR signal (-290 ppm) to the Cu-coordinated Si_4 -unit. Theoretical calculations revealed that the experimental shifts are in good agreement with the ^{29}Si shifts calculated for $[\text{NHC}^{\text{Dipp}}\text{Cu}(\eta^4\text{-Si}_9)]^{3-}$ (data not shown). The observation of two distinct ^{29}Si -NMR shifts for the Si_4 planes of $[\text{NHC}^{\text{Dipp}}\text{Cu}(\eta^4\text{-Si}_9)]^{3-}$ suggests that the Si-Si scrambling is reduced compared to $[\text{HSi}_9]^{3-}$ and $[\text{H}_2\text{Si}_9]^{2-}$,^[21,22] which in addition corroborates the observed reduced flexibility of $[\text{NHC}^{\text{Dipp}}\text{Cu}(\eta^4\text{-Si}_9\text{H})]^{2-}$ compared to $[\text{HSi}_9]^{3-}$ (see above).

A comprehensive overview of ^{29}Si NMR shifts of silicon *Zintl* anions in solution reported in literature is provided in the end of this chapter in Figure 8.4.

8 PROTONATED AND METALIZED SILICIDE $[\text{NHC}^{\text{Dipp}}\text{Cu}(\eta^4\text{-Si}_9\text{H})]^{2-}$

Next, calculations using the solvation model based on density (SMD^[30]) were performed to check for structural energetic minima and to validate the experimental NMR data. For two complex structures **A** and **B** energetic minima were found for protons located at vertices (see Figure 8.3).

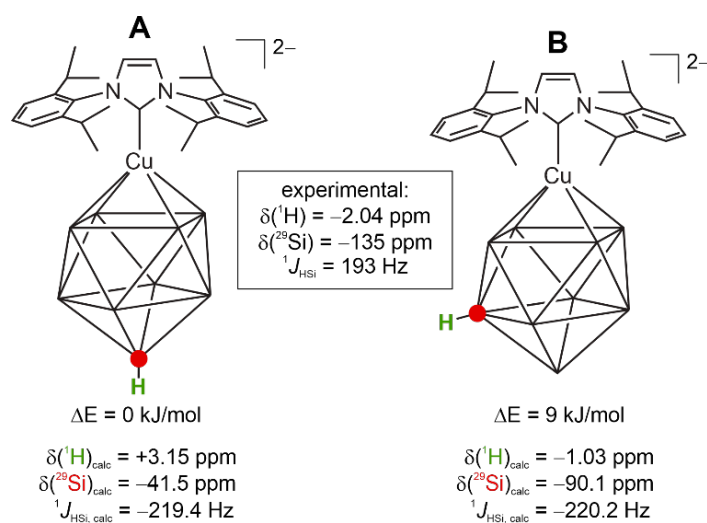


Figure 8.3 | Calculated lowest energetic complex structures **A** and **B** of $[\text{NHC}^{\text{Dipp}}\text{Cu}(\eta^4\text{-Si}_9\text{H})]^{2-}$. Complex **A** is energetically slightly favoured over **B** while calculated ^1H - and ^{29}Si -NMR chemical shifts are in better accordance with complex **B**.

A corresponding complex with a bridging proton was found to be very energetically disfavoured (see SI). Complex **A** is energetically slightly favoured over **B** by 9 kJ/mol, while calculated ^1H - and ^{29}Si -NMR chemical shifts are in better accordance with complex **B**. Calculations rendered similar $^1J_{\text{HSi}}$ coupling constants (~ 220 Hz) for **A** and **B** in equivalent magnitude as the experimental value (193 Hz). Analogous to the experimental case, the calculated absolute value of $^1J_{\text{HSi}}$ of **A** and **B** is larger than that of $[\text{HSi}_9]^{3-}$ ($^1J_{\text{HSi, calc.}} = 189$ Hz)^[21] indicating a stronger H-Si bond which corroborates that $[\text{NHC}^{\text{Dipp}}\text{Cu}(\eta^4\text{-Si}_9\text{H})]^{2-}$ is less flexible. These calculations don't consider the presence of cations in solution, which may acidify ammonia. This is known for metal ammoniates such as $[\text{Pt}(\text{NH}_3)_6]^{4+}$ ^[31] or $[\text{L}_3\text{Mo}(\text{NH}_3)]^+\text{X}^-$ (its N-H bond weakening ability is mainly attributed to the overall cationic charge and its formal oxidation state of Mo(II))^[32] and may occur similarly for copper ammoniates (for an indication of the presence of copper ammoniates in solution see SI). NMR chemical shifts and J coupling constants depend measurably on noncovalent interactions.^[33,34] Therefore, the observed deviation between the calculated and measured values are not surprising and cannot be overcome using a higher level of theory. The solvation of **A** and **B** can be different as well. Therefore, a difference of 9 kJ/mol cannot be taken as evidence that **A** is the most plausible structure for $[\text{NHC}^{\text{Dipp}}\text{Cu}(\eta^4\text{-Si}_9\text{H})]^{2-}$ in solution. In contrast, we consider **B** as such a structure due to better agreement with chemical shifts and HMQC results.

For the crystallization study, a solution of a phase with the nominal composition $\text{K}_6\text{Rb}_6\text{Si}_{17}$ (150 mg, 0.12 mmol), $\text{NHC}^{\text{Dipp}}\text{CuCl}$ (59.7 mg, 0.12 mmol) and [2.2.2]-cryptand (69.2 mg, 0.18 mmol) in liquid ammonia was prepared. After three months of storage at 233 K, yellow crystals of $(\text{K}[2.2.2]\text{-crypt})_2\text{K}_{0.48}\text{Rb}_{3.52}[\text{NHC}^{\text{Dipp}}\text{Cu}(\eta^4\text{-Si}_9)]_2 \cdot 15.2 \text{NH}_3$ **1** were isolated. While the central moiety $[\text{NHC}^{\text{Dipp}}\text{Cu}(\eta^4\text{-$

8 PROTONATED AND METALIZED SILICIDE $[\text{NHC}^{\text{Dipp}}\text{Cu}(\eta^4\text{-Si}_9)\text{H}]^{2-}$

$\text{Si}_9\text{H}]^{3-}$ is known from the structure $\text{A}_3[\text{A}[2.2.2]\text{-crypt}]_3[\text{NHC}^{\text{Dipp}}\text{Cu}(\eta^4\text{-Si}_9)]_2 \cdot 26 \text{NH}_3$ ($\text{A} = \text{K}, \text{K/Rb}, \text{Rb}$) published by Fässler *et al.* in 2017, the cationic counterpart is different. In addition to the two complexated potassium atoms in the [2.2.2]-crypt, four cation positions are present in the structure. The central moiety of the compound consists of a chain of $[\text{NHC}^{\text{Dipp}}\text{Cu}(\eta^4\text{-Si}_9)]^{3-}$ cages connected *via* rubidium atoms along the crystallographic *b*-axis. Two of these chains are further connected *via* two alkali metal positions along the crystallographic *a*-axis, leading to double strands along *b* (for Figures and further details, see SI). The formation of these double strands is in contrast to the single strands observed in $\text{A}_3[\text{A}[2.2.2]\text{-crypt}]_3[\text{NHC}^{\text{Dipp}}\text{Cu}(\eta^4\text{-Si}_9)]_2 \cdot 26 \text{NH}_3$ ($\text{A} = \text{K}, \text{K/Rb}, \text{Rb}$). All distances are in similar ranges as the distances reported for the compound $\text{A}_3[\text{A}[2.2.2]\text{-crypt}]_3[\text{NHC}^{\text{Dipp}}\text{Cu}(\eta^4\text{-Si}_9)]_2 \cdot 26 \text{NH}_3$, with the Cu-Si distances between 2.4174(14) and 2.4786(13) Å and the Si-Si distances between 2.4038(18) and 2.653(2) Å. Further details of the crystal structure investigation can be obtained from the FIZ Karlsruhe by quoting the depository number CSD-2043546.

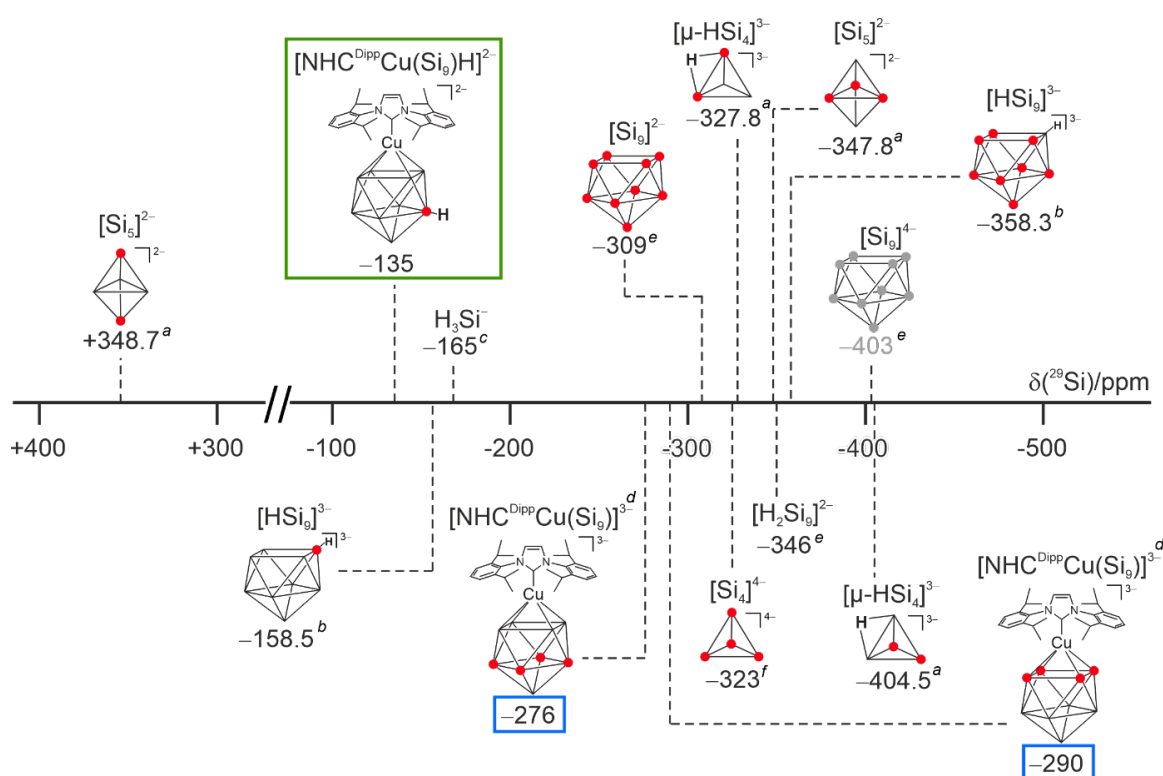


Figure 8.4 | Comprehensive overview of the ^{29}Si -NMR chemical shift range of silicon *Zintl* ions in solution. ^{29}Si -NMR are given for the highlighted silicon atoms. Red indicates experimental shifts, gray calculated shifts. The structure highlighted in green ($[\text{NHC}^{\text{Dipp}}\text{Cu}(\eta^4\text{-Si}_9)\text{H}]^{2-}$) was detected and investigated in this study by NMR and theoretical calculations. The hitherto unknown ^{29}Si -NMR signals of $[\text{NHC}^{\text{Dipp}}\text{Cu}(\eta^4\text{-Si}_9)]^{3-}$ with the shifts highlighted in blue could be detected in this work. Shifts taken from literature: $a^{[23]}$, $b^{[21]}$, $c^{[35]}$, $e^{[22]}$, $f^{[16]}$. Literature $d^{[10]}$ provides experimental characterization of $[\text{NHC}^{\text{Dipp}}\text{Cu}(\eta^4\text{-Si}_9)]^{3-}$ by crystal structure, ESI-MS and ^1H -NMR but not by ^{29}Si -NMR.

8.4 Conclusion

In summary, for the first time characteristic signals of a two-fold functionalized silicon cluster could be detected in solution by NMR spectroscopy. Their assignment to $[\text{NHC}^{\text{DIPP}}\text{Cu}(\eta^4\text{-Si}_9\text{H})]^{2-}$ was supported *via* NMR by signal monitoring, integration and 2D experiments and *via* theoretical calculations. In addition, NMR revealed that the metallized complex $[\text{NHC}^{\text{DIPP}}\text{Cu}(\eta^4\text{-Si}_9\text{H})]^{2-}$ is more rigid than the non-complexed silicide $[\text{HSi}_9]^{3-}$. Besides, the elusive ^{29}Si NMR signals of $[\text{NHC}^{\text{DIPP}}\text{Cu}(\eta^4\text{-Si}_9)]^{3-}$ were detected in solution and corroborated by theoretical calculations. Crystals of $(\text{K}[2.2.2]\text{-crypt})_2\text{K}_{0.48}\text{Rb}_{3.52}[\text{NHC}^{\text{DIPP}}\text{Cu}(\eta^4\text{-Si}_9)]_2$, including the non-protonated $\text{NHC}^{\text{DIPP}}\text{Cu}(\eta^4\text{-Si}_9)$ fragment, prove its availability in solution. To our knowledge the detection of $[\text{NHC}^{\text{DIPP}}\text{Cu}(\eta^4\text{-Si}_9\text{H})]^{2-}$ represents the first case of a protonated coinage metallized group 14 *Zintl* cluster in solution so far.

8.5 Acknowledgements

We gratefully acknowledge financial support from the German Science Foundation (DFG) (KO 1857/10–1, and GS 13/5–1). Furthermore, we thank Prof. Dr. Burkhard Luy for providing us unpublished xy-BEBOP pulses covering excitation windows of 500 and 1000 kHz respectively.

8.6 References

- [1] M. Beekman, S. Kauzlarich, L. Doherty, G. Nolas, *Materials (Basel)*. **2019**, *12*, 1139.
- [2] M. H. Nayfeh, L. Mitas, in *Nanosilicon*, **2008**, pp. 1–78.
- [3] A. Seyhan, T. Altan, O. C. Ecer, R. Zan, in *J. Phys. Conf. Ser.*, Institute Of Physics Publishing, **2017**, p. 12024.
- [4] F. S. Geitner, T. F. Fässler, *Inorg. Chem.* **2020**, *59*, 15218–15227.
- [5] B. Kesanli, J. Fettinger, D. R. Gardner, B. Eichhorn, *J. Am. Chem. Soc.* **2002**, *124*, 4779–4786.
- [6] J. Campbell, H. P. A. Mercier, H. Franke, D. P. Santry, D. A. Dixon, G. J. Schrobilgen, *Inorg. Chem.* **2002**, *41*, 86–107.
- [7] H. L. Xu, N. V. Tkachenko, Z. C. Wang, W. X. Chen, L. Qiao, A. Muñoz-Castro, A. I. Boldyrev, Z. M. Sun, *Nat. Commun.* **2020**, *11*, 1–8.
- [8] J. M. Goicoechea, S. C. Sevov, *Organometallics* **2006**, *25*, 4530–4536.
- [9] M. Waibel, F. Kraus, S. Scharfe, B. Wahl, T. F. Fässler, *Angew. Chemie* **2010**, *122*, 6761–6765.
- [10] F. S. Geitner, T. F. Fässler, *Chem. Commun.* **2017**, *53*, 12974–12977.
- [11] S. Joseph, M. Hamberger, F. Mutzbauer, O. Härtl, M. Meier, N. Korber, *Angew. Chemie Int. Ed.* **2009**, *48*, 8770–8772.

- [12] S. M. Tiefenthaler, V. Streitferdt, J. Baumann, S. Gaertner, R. M. Gschwind, N. Korber, *Zeitschrift für Anorg. und Allg. Chemie* **2020**, 646, 1595–1602.
- [13] W. L. Wilson, R. W. Rudolph, L. L. Lohr, R. C. Taylor, P. Pyykkö, *Inorg. Chem.* **1986**, 25, 1535–1541.
- [14] J. D. Corbett, P. A. Edwards, *J. Am. Chem. Soc.* **1977**, 99, 3313–3317.
- [15] B. Eichhorn, S. Kocak, in *Zintl Ions. Struct. Bond.*, Springer, Berlin, Heidelberg, **2011**, pp. 59–89.
- [16] M. Neumeier, F. Fendt, S. Gärtner, C. Koch, T. Gärtner, N. Korber, R. M. Gschwind, *Angew. Chemie Int. Ed.* **2013**, 52, 4483–4486.
- [17] B. Kesanli, J. Fettingner, B. Eichhorn, *Chem. - A Eur. J.* **2001**, 7, 5277–5285.
- [18] E. N. Esenturk, J. Fettingner, B. Eichhorn, *J. Am. Chem. Soc.* **2006**, 128, 9178–9186.
- [19] Z. M. Sun, H. Xiao, J. Li, L. S. Wang, *J. Am. Chem. Soc.* **2007**, 129, 9560–9561.
- [20] S. Scharfe, T. F. Fässler, S. Stegmaier, S. D. Hoffmann, K. Ruhland, *Chem. - A Eur. J.* **2008**, 14, 4479–4483.
- [21] C. Lorenz, F. Hastreiter, J. Hioe, N. Lokesh, S. Gärtner, N. Korber, R. M. Gschwind, *Angew. Chemie Int. Ed.* **2018**, 57, 12956–12960.
- [22] L. J. Schiegerl, A. J. Karttunen, J. Tillmann, S. Geier, G. Raudaschl-Sieber, M. Waibel, T. F. Fässler, *Angew. Chemie Int. Ed.* **2018**, 57, 12950–12955.
- [23] F. Hastreiter, C. Lorenz, J. Hioe, S. Gärtner, N. Lokesh, N. Korber, R. M. Gschwind, *Angew. Chemie Int. Ed.* **2019**, 58, 3133–3137.
- [24] T. Henneberger, W. Klein, J. V. Dums, T. F. Fässler, *Chem. Commun.* **2018**, 54, 12381–12384.
- [25] B. Kesanli, J. E. Halsig, P. Zavalij, J. C. Fettingner, Y. F. Lam, B. W. Eichhorn, *J. Am. Chem. Soc.* **2007**, 129, 4567–4574.
- [26] *In Addition, Small $^1\text{H-NMR}$ Signals of $[\mu\text{-HSi}_4]^{3-}$ and a Broad Peak at -7.4 Ppm Were Detected. Due to the Very Weak S/N Ratio This Signal Could Not Be Further Investigated. However, since It Is Located Close to the Region of the Protonated Silicide $[\mu\text{-HSi}_4]^{3-}$, n.d.*
- [27] F. S. Geitner, M. A. Giebel, A. Pöthig, T. F. Fässler, *Molecules* **2017**, 22, 1204.
- [28] L. J. Schiegerl, F. S. Geitner, C. Fischer, W. Klein, T. F. Fässler, *Zeitschrift für Anorg. und Allg. Chemie* **2016**, 642, 1419–1426.
- [29] F. S. Geitner, T. F. Fässler, *Eur. J. Inorg. Chem.* **2016**, 2016, 2688–2691.

8 PROTONATED AND METALIZED SILICIDE $[\text{NHC}^{\text{DIPP}}\text{Cu}(\eta^4\text{-Si}_9\text{H})]^{2-}$

- [30] A. V. Marenich, C. J. Cramer, D. G. Truhlar, *J. Phys. Chem. B* **2009**, *113*, 6378–6396.
- [31] B. Klein, L. Heck, *Zeitschrift für Anorg. und Allg. Chemie* **1975**, *416*, 269–284.
- [32] M. J. Bezdek, S. Guo, P. J. Chirik, *Science (80-.)*. **2016**, *354*, 730–733.
- [33] I. G. Shenderovich, G. S. Denisov, *J. Chem. Phys.* **2019**, *150*, 204505.
- [34] I. G. Shenderovich, *J. Chem. Phys.* **2018**, *148*, 124313.
- [35] H. Bürger, R. Eujen, H. C. Marsmann, *Zeitschrift für Naturforsch. - Sect. B J. Chem. Sci.* **1974**, *29*, 149–152.

8.7 Supporting Information

8.7.1 Experimental Details

All operations were carried out under argon atmosphere, either in a glovebox or with the help of Schlenk techniques. Liquid ammonia was dried and stored over sodium and cooled with a dry ice/ethanol mixture. The alkali metals were synthesized by reaction of the respective chloride with calcium and subsequent purification by distillation.

Synthesis of $\text{K}_6\text{Rb}_6^{29}\text{Si}_{17}$ (99.2 % enriched) and $\text{K}_6\text{Rb}_6\text{Si}_{17}$: The compound was synthesised via solid-state reaction techniques. Elemental potassium (119.1 mg, 3.05 mmol), rubidium (260.3 mg, 3.05 mmol) and enriched silicon (250.0 mg, 8.63 mmol) were put into a tantalum ampoule that was subsequently welded shut and jacketed in a fused silica ampoule. The ampoule was heated to 973 K at a rate of 25 K/h, held at that temperature for 24 hours and consequently cooled to room temperature at 20 K/h. The brittle, black reaction product was isolated and stored in an argon filled glovebox and characterized by powder X-ray diffraction and Raman spectroscopy. The same procedure was used in the preparation of $\text{K}_6\text{Rb}_6\text{Si}_{17}$ with non-enriched silicon (974.5 mg, 34.70 mmol), potassium (478.8 mg, 12.25 mmol) and rubidium (1046.7 mg, 12.25 mmol) being used and the temperature profile was altered to hold at 1223 K for 2 hours.

Synthesis of $(\text{K}[\text{2.2.2}]\text{-crypt})_2\text{K}_{0.48}\text{Rb}_{3.52}[\text{NHC}^{\text{DIPP}}\text{Cu}(\eta^4\text{-Si}_9)]_2 \cdot 15.2 \text{ NH}_3$ (1): $\text{K}_6\text{Rb}_6\text{Si}_{17}$ (150 mg, 0.12 mmol), $\text{NHC}^{\text{DIPP}}\text{CuCl}$ (59.7 mg, 0.12 mmol) and [2.2.2]-cryptand (69.2 mg, 0.18 mmol) were weighted into a heated Schlenk tube, after which approximately 10 mL of pre-dried ammonia were condensed onto the reactants. The orange-red solution was stored at 193 K for 3 months, before orange crystals of **1** were isolated and characterized via single crystal X-ray diffraction.

X-ray Crystal Structure Determination: Perfluorether oil was cooled in a stream of liquid nitrogen and crystals were transferred from the cooled reaction vessel into the oil under argon counter current. A suitable specimen of the very air- and temperature sensitive crystals was scooped up on a MiTeGen holder and transferred onto the diffractometer in liquid nitrogen. The crystal was measured on a diffractometer SuperNova by the company Agilent, equipped with a molybdenum micro focus tube. Data reduction was performed using the software CrysAlisPro 41.83a.^[1] The software Olex2-1.3-alpha,^[2] as well as the program ShelXT were used for structure solution,^[3] ShelXL for the refinement.^[4] For visualization Diamond 4 was employed.^[5]

Further details of the crystal structures may be obtained from the ICSD at FIZ Karlsruhe (<http://www.fiz-karlsruhe.de/request>) on quoting the depository number CSD-2043546.

Sample preparation for NMR studies: $\text{K}_6\text{Rb}_6^{29}\text{Si}_{17}$ (12.5 mg, 0.01 mmol), $\text{NHC}^{\text{DIPP}}\text{CuCl}$ (9.8 mg, 0.02 mmol) and [2.2.2]-cryptand (7.6 mg, 0.02 mmol) were weighed into heated heavy wall precision NMR

sample tubes (Pyrex) under an argon atmosphere. Subsequent condensation of ammonia lead to an initially colourless solution, after which the NMR tube was sealed shut by melting under an ammonia atmosphere. The sample was stored at 193 K until examined by NMR.

8.7.2 NMR Spectroscopy

8.7.2.1 *General Information*

NMR spectra were recorded on a Bruker Avance III HD 600 MHz spectrometer equipped with a fluorine selective TBIF probe and a Bruker Avance NEO 600 MHz spectrometer equipped with a double resonance broad band probe (BBO). ^1H and ^{29}Si NMR spectra were referenced externally to TMS (tetramethylsilane). In case the ^{29}Si signal of the HSi_9^{3-} was detected, the spectra were calibrated on the literature known chemical shift of HSi_9^{3-} (-358.5 ppm). The temperatures 203 K and 233 K were controlled by Bruker BVTE units. Data was processed with the Bruker software TOPSPIN 3.2 and TOPSPIN 4.0.7.

8.7.2.2 *Structural Investigations*

1D ^1H -NMR spectra with solvent saturation used for structural assignment and integration are displayed in Figure SI 8.1. The signal of the solvent (NH_3) is close to the CH_3 signals of the NHC^{DIPP} species. Upon solvent saturation (NH_3), signals close to the solvent signal such as the highfield shifted CH_3 signals of the NHC^{DIPP} species also get partially saturated which results in a reduction of signal and consequently integration value. At 233 K this effect was smaller than at 203 K. Furthermore, at 203 K, the protons of each CH_2 group of [2.2.2]crypt become chemically inequivalent and cause signal overlap with the CH protons of the isopropyl groups of the NHC^{DIPP} species. In contrast, at 233 K, each CH_2 group of crypt exhibits chemically equivalent protons which causes considerably less signal overlap with the CH protons of the isopropyl groups of the NHC^{DIPP} species wherefore these protons were integrated at 233 K. The signal integration in Figure SI 8.1 indicates a coherence of the signals marked in green and those marked in blue, respectively. The respective signal coherences were further corroborated by corresponding concomitant decreases in signal intensities (see Figure SI 8.1) after a storage period at 193 K of 85 days and by 2D ^1H - ^1H -NOESY and -COSY experiments which (see Figure SI 8.1 c).

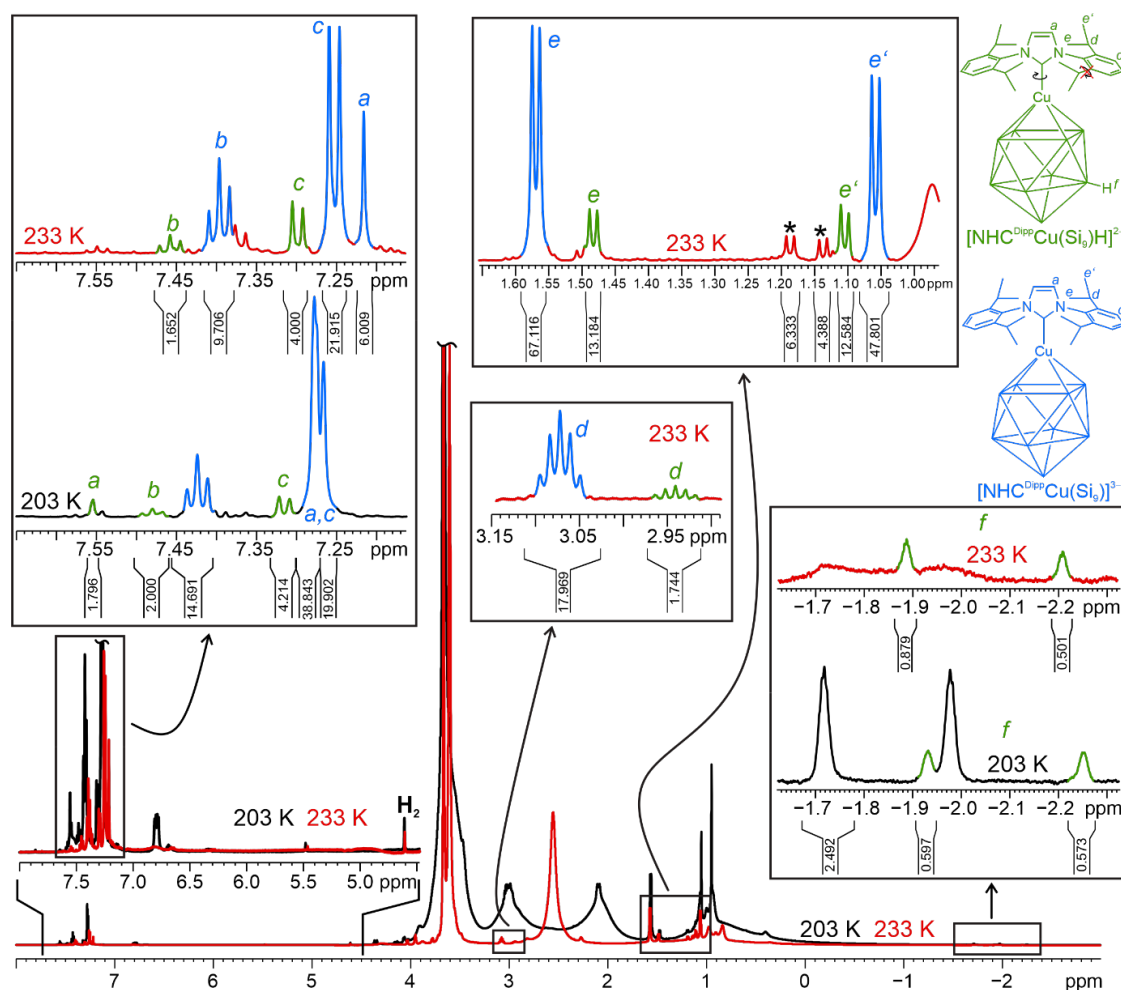


Figure SI 8.1 | Magnified and integrated spectral regions of the $^1\text{H-NMR}$ signals of $[\text{NHC}^{\text{Dipp}}\text{Cu}(\eta^4\text{-Si}_9)]^{3-}$ (literature^[6]) and $[\text{NHC}^{\text{Dipp}}\text{Cu}(\eta^4\text{-Si}_9)\text{H}]^{2-}$ taken from $^1\text{H-NMR}$ spectra with solvent saturation (zgpppr) recorded at 203 K (black) and 233 K (red). The baseline was manually corrected for all magnified regions. The integration value of signal *d* of $[\text{NHC}^{\text{Dipp}}\text{Cu}(\eta^4\text{-Si}_9)\text{H}]^{2-}$ is too low (1.74 versus 4) which is probably owed to its low S/N and consequently big integration error upon baseline correction. The signals marked with asterisks probably belong to an NHC^{Dipp} -moiety which is not coordinated to a silicide. The spectra were referenced to the chemical shift of H_2 (4.61 ppm). All spectra were recorded of the sample discussed in the manuscript ($\text{K}_6\text{Rb}_6\text{Si}_{17}$ (fully ^{29}Si enriched) (1 eq.) + $\text{NHC}^{\text{Dipp}}\text{CuCl}$ (2 eq.) + [2.2.2]cryptand (2 eq.) in liquid ammonia).

8 PROTONATED AND METALIZED SILICIDE $[\text{NHC}^{\text{DIPP}}\text{Cu}(\eta^4\text{-Si}_9\text{H})]^{2-}$

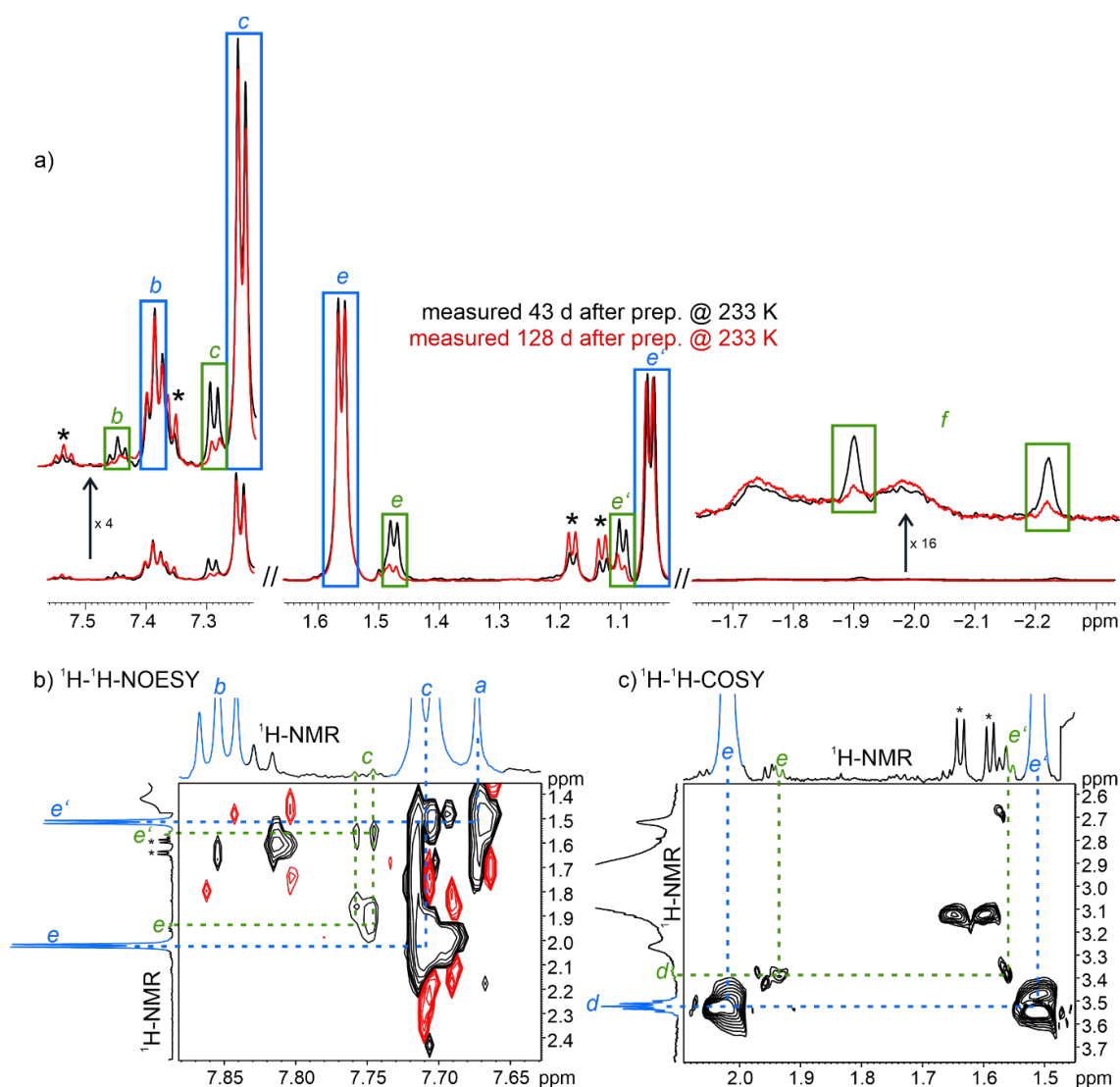


Figure SI 8.2 | a) The stacking of $^1\text{H-NMR}$ regions of spectra recorded 43 days (black) and 128 days (red) after sample preparation at 233 K shows a concomitant decrease of the signals marked in green and suggests a structural coherence which was corroborated by integration (see Figure SI 8.1). The spectra were recorded with solvent saturation (zgpgpr), processed with $\text{LB} = 3 \text{ Hz}$ and the baseline of the displayed regions was corrected manually. The spectra were scaled to same intensity of the signals of [2.2.2]crypt. 2D $^1\text{H-}^1\text{H-NOESY}$ (b) and 2D $^1\text{H-}^1\text{H-COSY}$ experiments (c) further corroborated the structural coherence between peaks c, d, e and e' of $[\text{NHC}^{\text{DIPP}}\text{Cu}(\eta^4\text{-Si}_9\text{H})]^{2-}$. The baseline of the external projections was manually corrected. All spectra were recorded of the sample discussed in the manuscript ($\text{K}_6\text{Rb}_6\text{Si}_{17}$ (fully ^{29}Si enriched) (1 eq.) + $\text{NHC}^{\text{DIPP}}\text{CuCl}$ (2 eq.) + [2.2.2]cryptand (2 eq.) in liquid ammonia).

A 2D $^1\text{H-}^{29}\text{Si-HMQC}$ spectrum (see Figure SI 8.3a) revealed that the proton at -2.1 ppm is attached to a silicon atom at -135 ppm . Then, 1D $^1\text{H}\{^{29}\text{Si}\}$ decoupling experiments at 203 K were performed (see Figure SI 8.3b). WALTZ-16 was used as decoupling sequence which has a decoupling bandwidth of $\pm 2 \text{ kHz}^{[7]}$ ($= \pm 17 \text{ ppm}$ at a 600 MHz spectrometer). When comparing the ^{29}Si decoupling efficiency for the $^1\text{H-NMR}$ signal of $[\text{HSi}_9]^{3-}$ of the upper both spectra in Figure SI 8.3b it becomes clear that when the ^{29}Si frequency of Si-H (-158 ppm for $[\text{HSi}_9]^{3-}$) lies within the bandwidth of WALTZ-16 (^{29}Si dec. @ -168 ppm), the decoupling yields a sharper signal in higher intensity. This is similar for the proton of $[\text{NHC}^{\text{DIPP}}\text{Cu}(\eta^4\text{-Si}_9\text{H})]^{2-}$ whose

8 PROTONATED AND METALIZED SILICIDE $[\text{NHC}^{\text{DIPP}}\text{Cu}(\eta^4\text{-Si}_9\text{H})]^{2-}$

signal intensity upon ^{29}Si decoupling is slightly higher when the ^{29}Si frequency of Si-H of $[\text{NHC}^{\text{DIPP}}\text{Cu}(\eta^4\text{-Si}_9\text{H})]^{2-}$ (-135 ppm) lies within the bandwidth of WALTZ-16 (^{29}Si dec. @ -131 ppm).

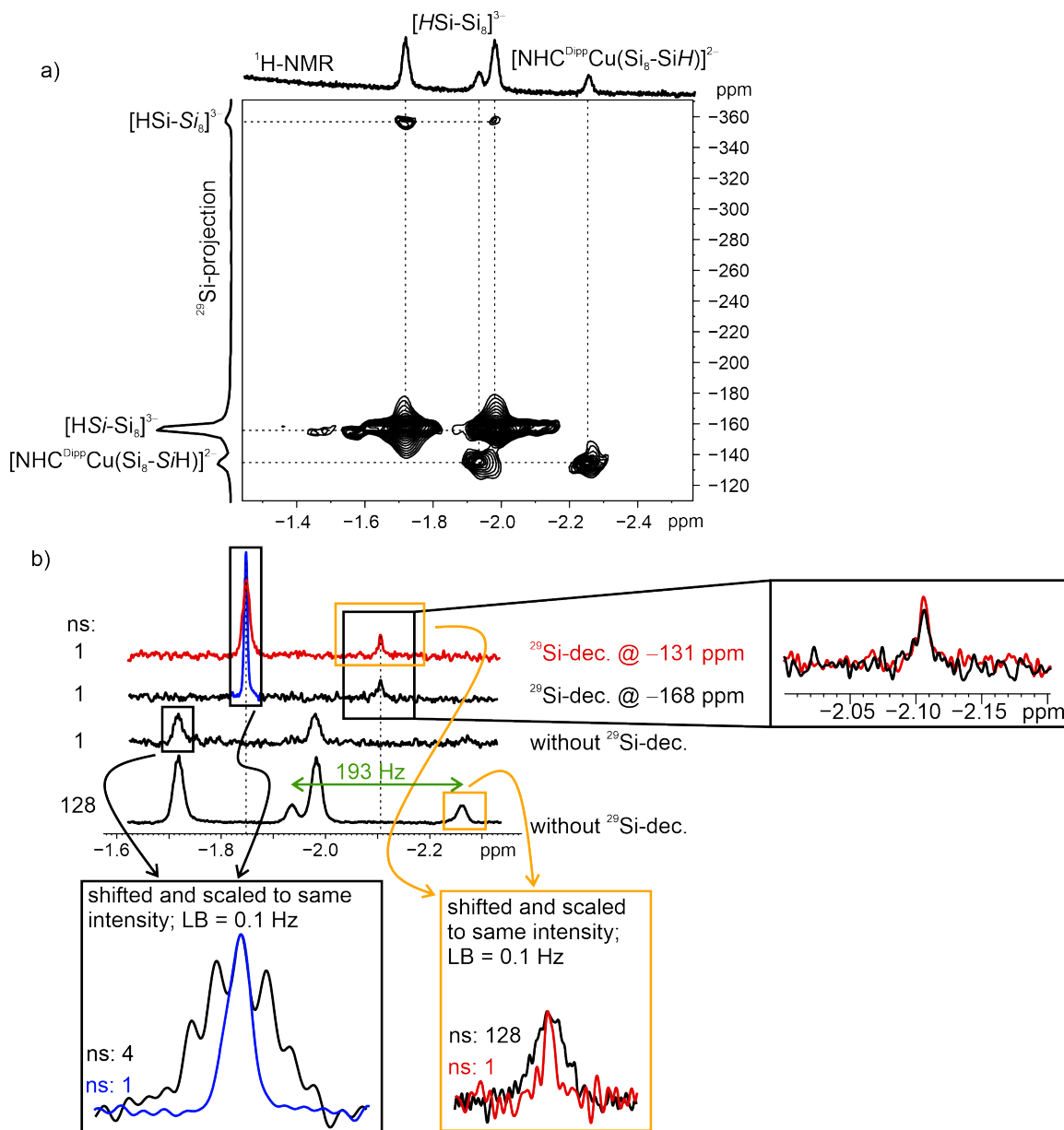


Figure SI 8.3 | a) Extract of a ^1H - ^{29}Si -HMQC recorded at 203 K displaying the characteristic cross peaks of the $[\text{HSi}_9]^{3-}$ and the cross peak of the new ^1H -NMR signal at 2.1 ppm to a silicon at $\delta(^{29}\text{Si}) = -135$ ppm. The evolution delay τ was optimized for a coupling constant of 60 Hz. b) $^1\text{H}\{^{29}\text{Si}\}$ -NMR decoupling experiments at 203 K revealed that the splitting of 193 Hz of the signal at $\delta(^1\text{H}) = -2.1$ ppm is caused by coupling to the silicon signal at $\delta(^{29}\text{Si}) = -135$ ppm. WALTZ-16 was used as decoupling sequence which has a decoupling bandwidth of ± 2 kHz^[7] ($= \pm 17$ ppm at 600 MHz spectrometer). The baseline of the bottom spectrum was corrected manually. All spectra were recorded of the sample discussed in the manuscript ($\text{K}_6\text{Rb}_6\text{Si}_{17}$ (fully ^{29}Si enriched) (1 eq.) + $\text{NHC}^{\text{DIPP}}\text{CuCl}$ (2 eq.) + $[\text{2.2.2}]$ cryptand (2 eq.) in liquid ammonia).

Interestingly, selective ^{29}Si decoupling at -168 ppm did not only lead to a collapse of the doublet of the ^1H -NMR signal of $[\text{HSi}_9]^{3-}$ caused by $^1J_{\text{HSi}}$ coupling to the directly bound silicon (see Figure SI 8.3b bottom left magnified and stacked spectra), but also to the collapse of the splitting pattern caused by the scalar

coupling to the scrambling Si_8 unit ($\delta(^{29}\text{Si}) = -358$ ppm). This means that both scalar couplings of the proton to the directly bound silicon and the Si_8 unit were decoupled which implies, that either proton hopping or Si-Si-scrambling occurred during the decoupling sequence (a decoupling of the splitting pattern to the Si_8 unit upon hitting the frequency by the decoupler pulses is excluded, since the frequency lies far off resonance). In case of the $^1\text{H-NMR}$ signal of $[\text{NHC}^{\text{Dipp}}\text{Cu}(\eta^4\text{-Si}_9\text{H})]^{2-}$ statements about the effect of selective $^1J_{\text{H-Si}}$ -decoupling on long range H-Si scalar couplings cannot be made due to the bad S/N of the signal (see Figure SI 8.3b bottom left magnified and stacked spectra). Nevertheless, the selective $^1\text{H}\{^{29}\text{Si}\}$ decoupling experiments represent an easy, highly sensitive NMR method for investigating cluster dynamics that fall in the time window of the decoupling sequence.

8.7.2.3 Long-Range H-Si Cross Peak Investigations and Signal-to-Noise Analysis

In order to check for long-range $^1\text{H-}^{29}\text{Si}$ couplings of the proton of $[\text{NHC}^{\text{Dipp}}\text{Cu}(\eta^4\text{-Si}_9\text{H})]^{2-}$ at $\delta(^1\text{H}) = -2.04$ ppm, 2D $^1\text{H-}^{29}\text{Si}$ -HMQC experiments were recorded (see Figure SI 8.4a and b) with broadband excitation in the ^{29}Si dimension (for further info see chapter 2) with an evolution delay (τ) adjusted to coupling constants in the range of $^2J_{\text{H-Si}}$ and $^3J_{\text{H-Si}}$ (see also calculated $J_{\text{H-Si}}$ of $[\text{HSi}_9]^{3-}$ in literature^[8]). The HMQCs did not show cross peaks of $[\text{NHC}^{\text{Dipp}}\text{Cu}(\eta^4\text{-Si}_9\text{H})]^{2-}$ but those of $[\text{HSi}_9]^{3-}$, the degradation product^[9] H_3Si^- and an unknown species marked with ?. Then, a signal-to-noise (S/N) analysis was performed to calculate theoretical S/N ratios for expected cross peaks of $[\text{NHC}^{\text{Dipp}}\text{Cu}(\eta^4\text{-Si}_9\text{H})]^{2-}$. The ratio of $[\text{NHC}^{\text{Dipp}}\text{Cu}(\eta^4\text{-Si}_9\text{H})]^{2-}$ to $[\text{HSi}_9]^{3-}$ can be extracted from the $^1\text{H-NMR}$ spectrum (see Figure SI 8.4c). This together with the S/N ratio of the experimentally obtained long-range H-Si coupling to the Si_8 unit of $[\text{HSi}_9]^{3-}$ allow for an estimation of the S/N ratios of the long-range H-Si cross peaks of $[\text{NHC}^{\text{Dipp}}\text{Cu}(\eta^4\text{-Si}_9\text{H})]^{2-}$. For the S/N analysis, it was assumed that $^2J(\text{H-Si})$ and $^3J(\text{H-Si})$ coupling constants of $[\text{NHC}^{\text{Dipp}}\text{Cu}(\eta^4\text{-Si}_9\text{H})]^{2-}$ are similar to $J(\text{H-Si}_8)$ of $[\text{HSi}_9]^{3-}$. The S/N for the long-range H-Si cross peaks of the eight silicon atoms in $[\text{NHC}^{\text{Dipp}}\text{Cu}(\eta^4\text{-Si}_9\text{H})]^{2-}$ was estimated for both HMQC spectra in Figure SI 8.4a and b with the equation depicted in Figure SI 8.4d. Then, three cases were examined that address different flexibility and constitution of $[\text{NHC}^{\text{Dipp}}\text{Cu}(\eta^4\text{-Si}_9\text{H})]^{2-}$ and therefore render different groups of chemically equivalent silicon atoms (see Figure SI 8.4e; chemically equivalent silicon atoms are highlighted in the same color). The following statements can only be made under the assumption that ^{63}Cu does not cause any line broadening:

In case 1 (dynamic Si_8 moiety of $[\text{NHC}^{\text{Dipp}}\text{Cu}(\eta^4\text{-Si}_9\text{H})]^{2-}$) the calculated S/N for both HMQCs suggests that a corresponding cross peak should probably have been detected in both HMQCs due to sufficient S/N (see table in Figure SI 8.4d and compare with other cross peaks in Figure SI 8.4a and b whose S/N is lower but which could still be detected). Therefore, a fluctuating Si_8 unit^[8] of $[\text{NHC}^{\text{Dipp}}\text{Cu}(\eta^4\text{-Si}_9\text{H})]^{2-}$ similar to that of $[\text{HSi}_9]^{3-}$ is excluded.

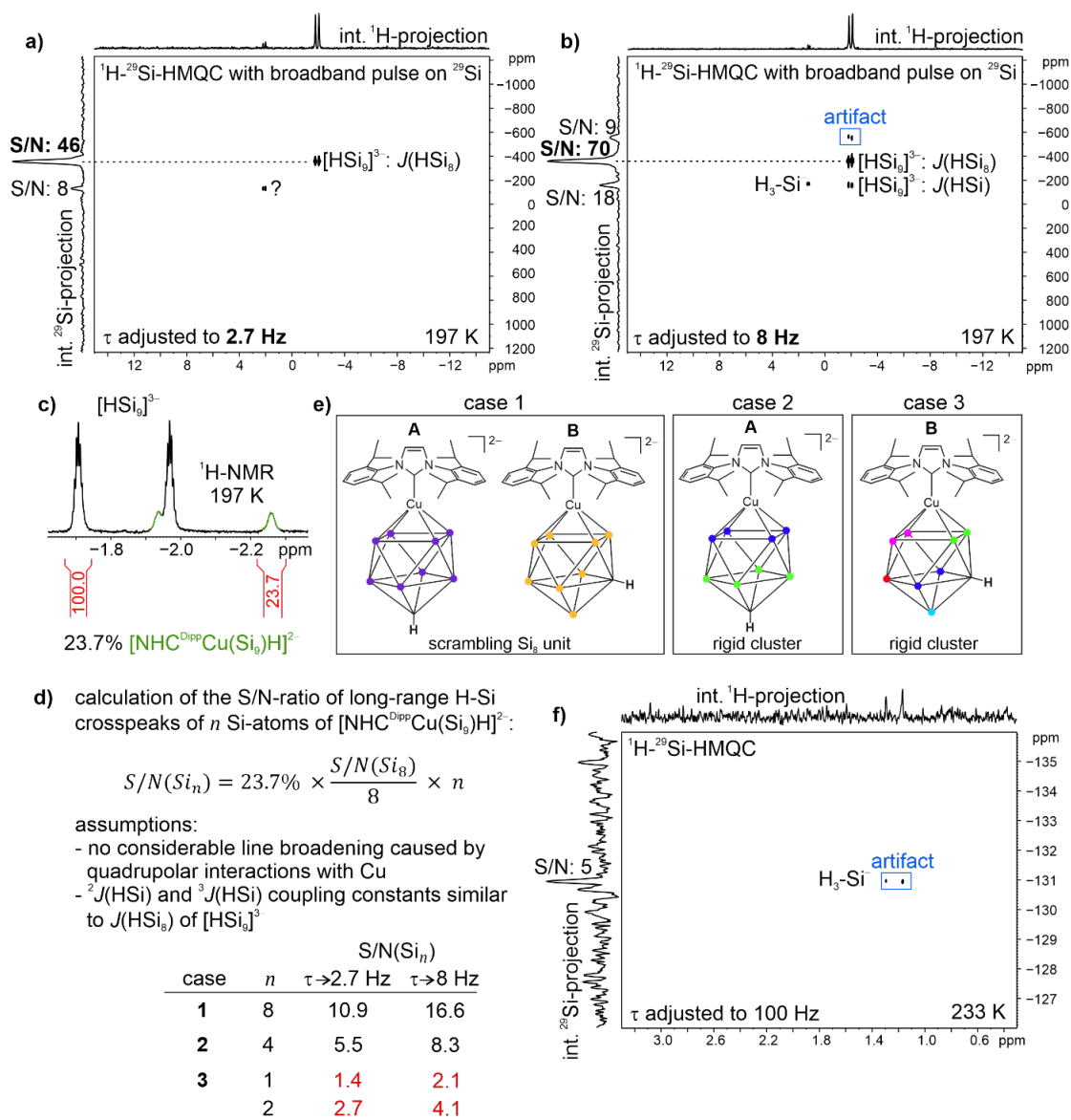


Figure SI 8.4 | Procedure of the S/N ratio estimation of long-range H-Si cross peaks of $[\text{NHC}^{\text{Dipp}}\text{Cu}(\eta^4\text{-Si}_9\text{H})]^{2-}$ for the HMQCs in a) and b). a) and b) ^1H - ^{29}Si -HMQC spectra with broadband excitation in the ^{29}Si dimension (for further info see chapter 2) with an evolution delay (τ) adjusted to a coupling constants of 2.7 Hz and 8 Hz respectively. The spectra were recorded 33 days after sample preparation at 197 K. The internal projections are displayed on top and on the left of the HMQCs. S/N ratios were determined in the extracted ^{29}Si -projections. c) ^1H -NMR spectrum recorded 33 days after sample preparation at 197 K. d) Calculation of the theoretical S/N ratio of the long-range H-Si cross peaks of $[\text{NHC}^{\text{Dipp}}\text{Cu}(\eta^4\text{-Si}_9\text{H})]^{2-}$ for the HMQCs in a) and b). e) Investigated cases that address different flexibility and constitution of $[\text{NHC}^{\text{Dipp}}\text{Cu}(\eta^4\text{-Si}_9\text{H})]^{2-}$ and therefore render different groups of chemically equivalent silicon atoms (highlighted in the same color). f) A ^1H - ^{29}Si -HMQC spectra recorded 43 days after sample preparation at 233 K shows a folding or aliasing artifact of H_3Si^- . Such artifacts appear at frequencies which differ from the real frequency that is located outside of the spectral window (here $\delta(^{29}\text{Si})$ of $\text{H}_3\text{Si}^- = -168$ ppm)^[9]. Independent of the fact that the cross peak is an artifact, it shows that with a S/N ratio of five, it can still be detected. All spectra were recorded of the sample discussed in the manuscript ($\text{K}_6\text{Rb}_6\text{Si}_{17}$ (fully ^{29}Si enriched) (1 eq.) + $\text{NHC}^{\text{Dipp}}\text{CuCl}$ (2 eq.) + [2.2.2]cryptand (2 eq.) in liquid ammonia). For the HMQC spectra in a) and b) the pulse program *hmqcgpqfbulusp2* was used (see chapter 2).

8 PROTONATED AND METALIZED SILICIDE $[\text{NHC}^{\text{Dipp}}\text{Cu}(\eta^4\text{-Si}_9\text{H})]^{2-}$

In case 2 (rigid silicide protonated at the cap silicon opposite $\text{NHC}^{\text{Dipp}}\text{Cu}$) two cross peaks to four chemically equivalent silicon atoms of each square plane would be expected. The S/N analysis revealed that the cross peaks should probably have been detected (see table in Figure SI 8.4d and compare with the low S/N ratio of five of a cross peak being a folding or aliasing artifact of H_3Si^-). Therefore, protonation at the cap silicon is excluded as well.

In contrast, case 3 (protonation at the middle square plane) renders six chemically non-equivalent silicon positions in “groups” of one or two silicon atoms. In this case, the S/N analysis rendered S/N ratios of the corresponding six cross peaks that are probably beyond the detection limit (see table in Figure SI 8.4d). Therefore, HMQC results are in best accordance with an $\text{NHC}^{\text{Dipp}}\text{Cu-Si}_9$ cluster protonated at the middle square plane under the assumption that ^{63}Cu does not cause any line broadening.

However, considering that in $[\text{NHC}^{\text{Dipp}}\text{Cu}(\eta^4\text{-Si}_9\text{H})]^{2-}$ ^{63}Cu may cause similar line broadening as for the ^{29}Si signals of $[\text{NHC}^{\text{Dipp}}\text{Cu}(\eta^4\text{-Si}_9)]^{3-}$ (see manuscript), this would decrease the S/N ratios estimated in Figure SI 8.4d and thus would impede to distinguish between the discussed structures in Figure SI 8.4e only based on the HMQC results. Yet, experimental ^1H - and ^{29}Si -shifts are in better accordance with corresponding shifts of case 3 (cluster B in Figure SI 8.4e, see also manuscript and below) obtained by theoretical calculations.

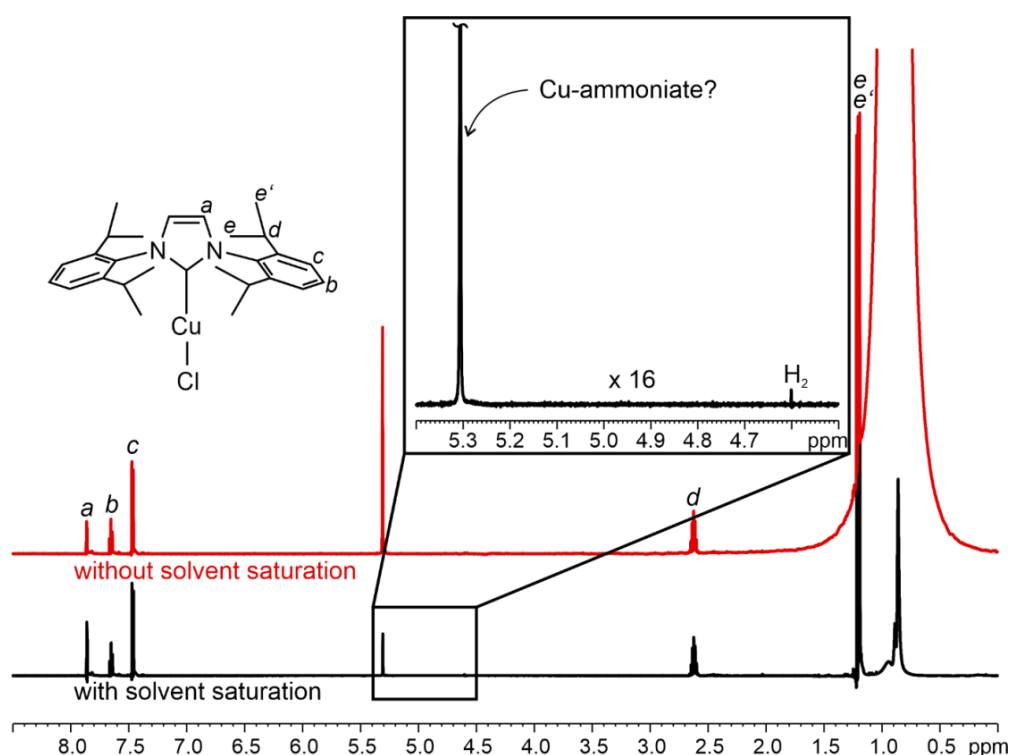


Figure SI 8.5 | Stacking of ^1H -NMR spectra of a sample of saturated amounts of $\text{NHC}^{\text{Dipp}}\text{CuCl}$ in NH_3 recorded with (bottom) and without (top) solvent saturation (zgpgpr). The spectra were scaled to similar signal intensities of peaks *b*, *c* and *d*. The spectra show that solvent saturation leads to a significant decrease of the signal at 5.3 ppm which indicates that this signal is in chemical exchange with the solvent NH_3 . Thus, this signal may belong to a Cu-ammoniate. The detection of H_2 in absence of Silicide further supports the presence of Cu-ammoniates since it is known that other ammoniates can acidify NH_3 which can lead to the formation of H_2 .

8 PROTONATED AND METALIZED SILICIDE $[\text{NHC}^{\text{DIPP}}\text{Cu}(\eta^4\text{-Si}_9\text{H})]^{2-}$

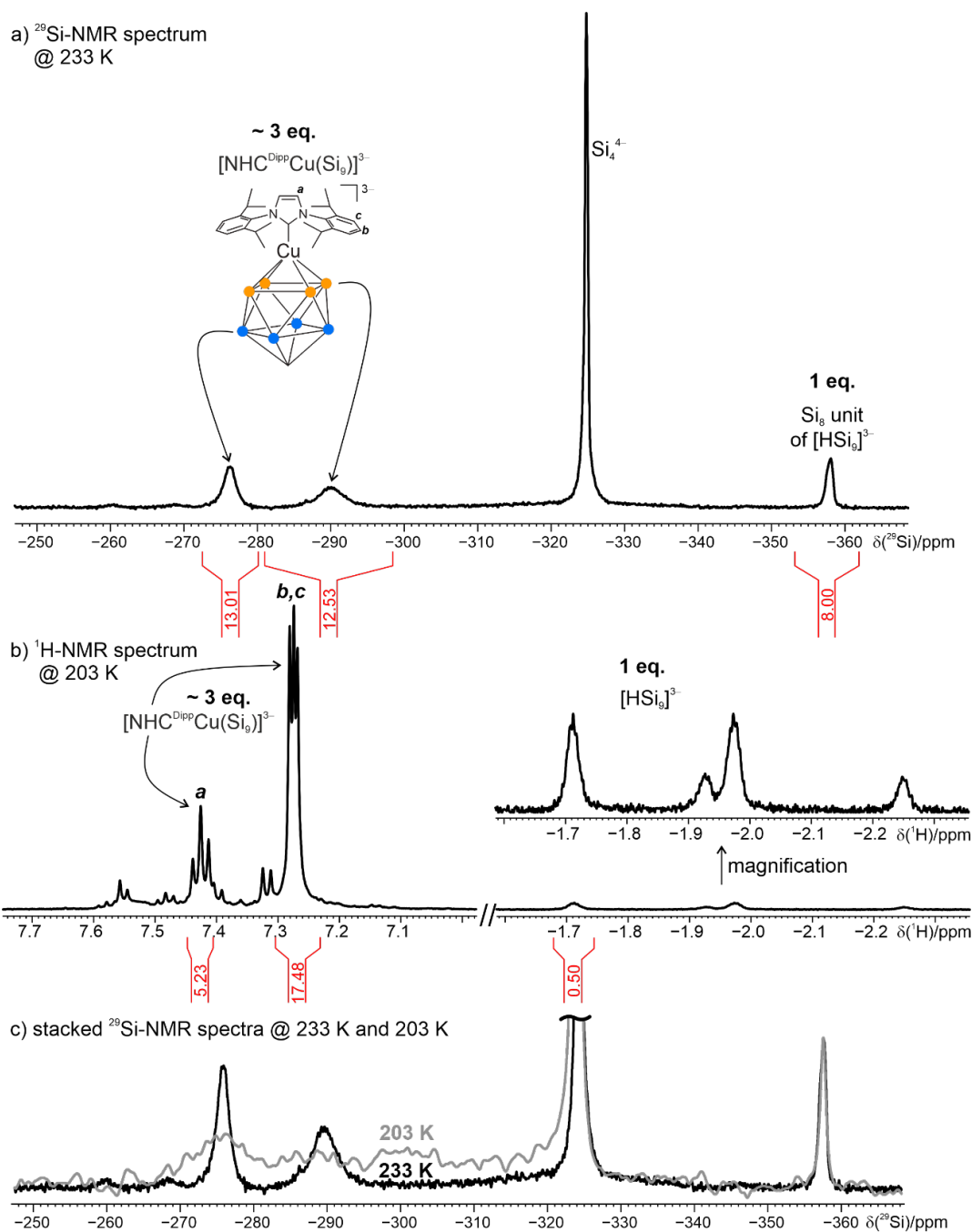


Figure SI 8.6 | A ^{29}Si -NMR spectrum recorded at 233 K (a) revealed two significant new signals at -276 ppm and -290 ppm. The integral ratios from the ^{29}Si -NMR spectrum were found to be in reasonable agreement with corresponding integral ratios taken from a ^1H -NMR spectrum recorded at 203 K (b). Therefore, the signals at -276 ppm and -290 ppm were assigned to $[\text{NHC}^{\text{DIPP}}\text{Cu}(\eta^4\text{-Si}_9)]^{3-}$. A comparison of the ^{29}Si -NMR spectrum recorded at 233 K with one recorded at 203 K (gray in c) revealed that the signals broaden considerably, which may be due to interactions with temperature dependent quadrupolar relaxation mechanisms^[12] of ^{63}Cu and ^{65}Cu . While the ^{29}Si -NMR signals of $[\text{NHC}^{\text{DIPP}}\text{Cu}(\eta^4\text{-Si}_9)]^{3-}$ broaden upon temperature decrease, the ^1H -NMR signal of $[\text{HSi}_9]^{3-}$ significantly broadens upon temperature increase (see Figure SI 8.1). The grey spectra in c) was processed with a line broadening of 100 Hz and was scaled to same signal intensity of the ^{29}Si -NMR signal of $[\text{HSi}_9]^{3-}$ of the black spectrum (same spectrum as in a) but magnified).

8.7.3 X-ray Crystallography

K[2.2.2]crypt) ₂ K _{0.47} Rb _{3.53} [NHC ^{DIPP} Cu(η ⁴ -Si ₉)] ₂ · 15 NH ₃	
CCDC number	2043546
Empirical Formula	C ₉₀ H _{189.3} Cu ₂ K _{2.47} Rb _{3.53} O ₁₂ N _{23.3} Si ₁₈
Formula weight/g·mol ⁻¹	2819.46
Temperature/K	123.00(12)
Crystal System	Monoclinic
Space Group	<i>P</i> 2 ₁ / <i>c</i>
<i>a</i> /Å	23.8295(5)
<i>b</i> /Å	18.7385(3)
<i>c</i> /Å	33.3833(10)
<i>α</i> /°	90
<i>β</i> /°	110.410(3)
<i>γ</i> /°	90
Volume/Å ³	13970.7(6)
<i>Z</i>	4
ρ_{calc} g·cm ⁻³	1.340
μ /mm ⁻¹	1.806
<i>F</i> (000) (e)	5901.0
Crystal size/mm ³	0.308 x 0.129 x 0.064
Radiation	MoK α (λ = 0.71073 Å)
2 θ range for data collection/°	6.752 to 56.564
Index ranges	-31 ≤ <i>h</i> ≤ 30, -24 ≤ <i>k</i> ≤ 24, -14 ≤ <i>l</i> ≤ 44
Reflexions collected	57833
Independent reflections	34479 [<i>R</i> _{int} = 0.0530, <i>R</i> _{sigma} = 0.1044]
Data/restraints/parameters	34479/829/1745
Goodness-of-fit	1.050
Final <i>R</i> indexes [<i>I</i> > 2 σ (<i>I</i>)]	<i>R</i> ₁ = 0.0660, <i>wR</i> ₂ = 0.1173
Final <i>R</i> indexes [all data]	<i>R</i> ₁ = 0.1300, <i>wR</i> ₂ = 0.1399
Largest diff peak/hole /e·Å ⁻³	0.81/-0.74

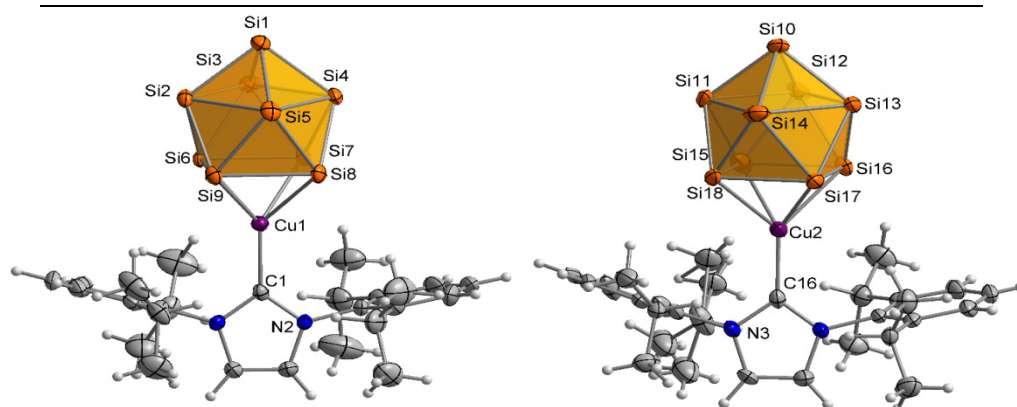


Figure SI 8.7 | The two crystallographically independent $[\text{NHC}^{\text{DIPP}}\text{Cu}(\eta^4\text{-Si}_9)]^{3-}$ moieties in compound 1. Thermal displacement ellipsoids are drawn with 50% probability.

8 PROTONATED AND METALIZED SILICIDE $[\text{NHC}^{\text{DIPP}}\text{Cu}(\eta^4\text{-Si}_9)\text{H}]^{2-}$

The motif of $[\text{NHC}^{\text{DIPP}}\text{Cu}(\eta^4\text{-Si}_9)]$ is known from the structure of $\text{A}_3[\text{A}@[2.2.2]\text{-crypt}]_3[\text{NHC}^{\text{DIPP}}\text{Cu}(\eta^4\text{-Si}_9)_2]$ published by Fässler et al.^[6]

All observed distances in the structure are in the range of previously reported Si-Si, as well as Cu-Si bonds.

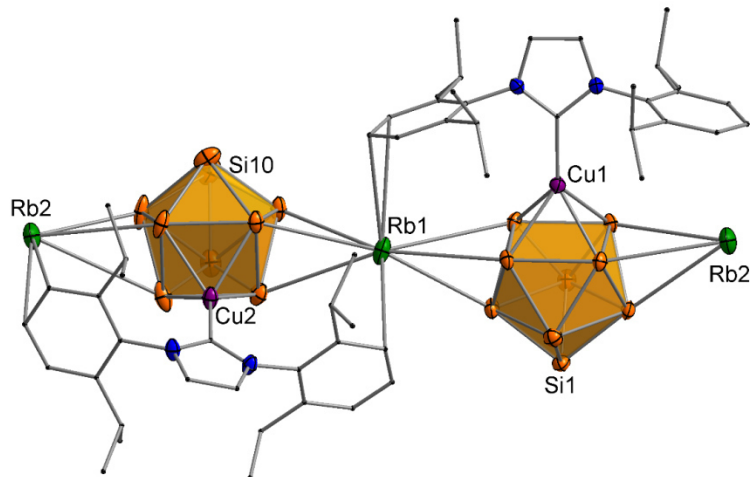


Figure SI 8.8 | Strand of $[\text{NHC}^{\text{DIPP}}\text{Cu}(\eta^4\text{-Si}_9)]^{3-}$, connected through rubidium atoms along the crystallographic b-axis. Hydrogen atoms are omitted and carbon atoms displayed as wires/sticks for added visibility; thermal displacement ellipsoids are drawn with 50% probability.

As can be seen in Figure SI 8.9, the nonasilicide clusters are connected along the crystallographic b-axis via rubidium atoms and along the crystallographic a-axis via one mixed occupied alkali metal position and one further rubidium atom.

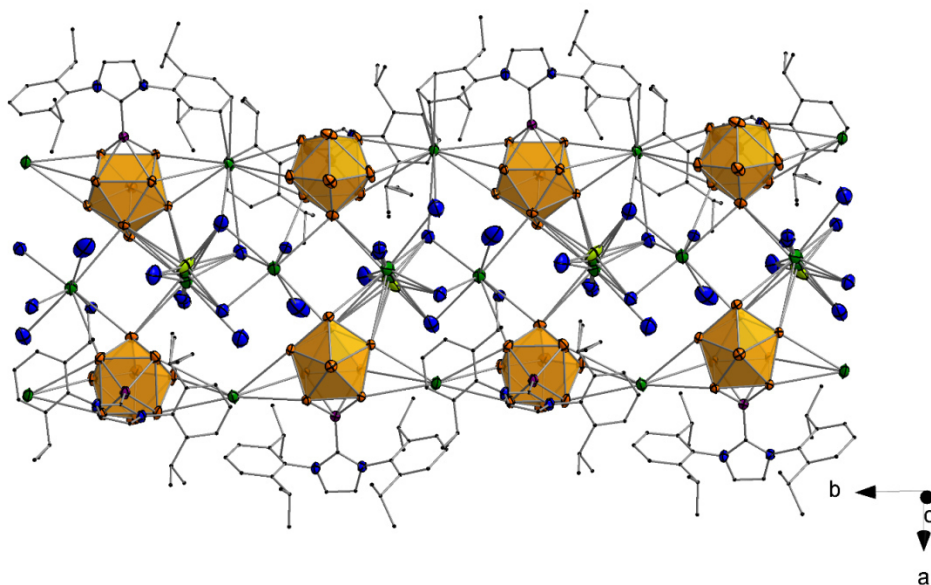


Figure SI 8.9 | Connection of the strands of 1 via mixed alkali metal positions along the crystallographic a-axis. Hydrogen atoms are omitted and carbon atoms displayed as wires/sticks for added visibility; thermal displacement ellipsoids are drawn with 50% probability.

8.7.4 Computational Details

All geometries were optimized at the $\omega\text{b97xd/def2tzvp}^{[13,14]}$ level of theory in the continuum of NH_3 (SMD) at 200 K ($\text{eps} = 22.63$; $\text{epsinf} = 1.76$; $\text{Rsolv} = 1.7$; $\text{HbondAcidity} = 0.14$; $\text{HbondBasicity} = 0.62$; $\text{SurfaceTensionAtInterface} = 29.00$; $\text{CarbonAromaticity} = 0.0$; $\text{ElectronegativeHalogenicity} = 0.0$). The dielectric constant was increased to 22.63 to adapt the low temperature measurement. Single point energies were obtained at the MP2/def2qzvpp level of theory on top the optimized geometry.^[15] NMR shift and coupling calculations were performed at TPSSH/pcSseg-4 .^[16] The ^1H and ^{29}Si chemical shifts of $[\text{NHC}^{\text{DIPP}}\text{Cu}(\eta^4\text{-Si}_9\text{H})]^{2-}$ were referenced to that of $[\text{HSi}_9]^{3-}$.

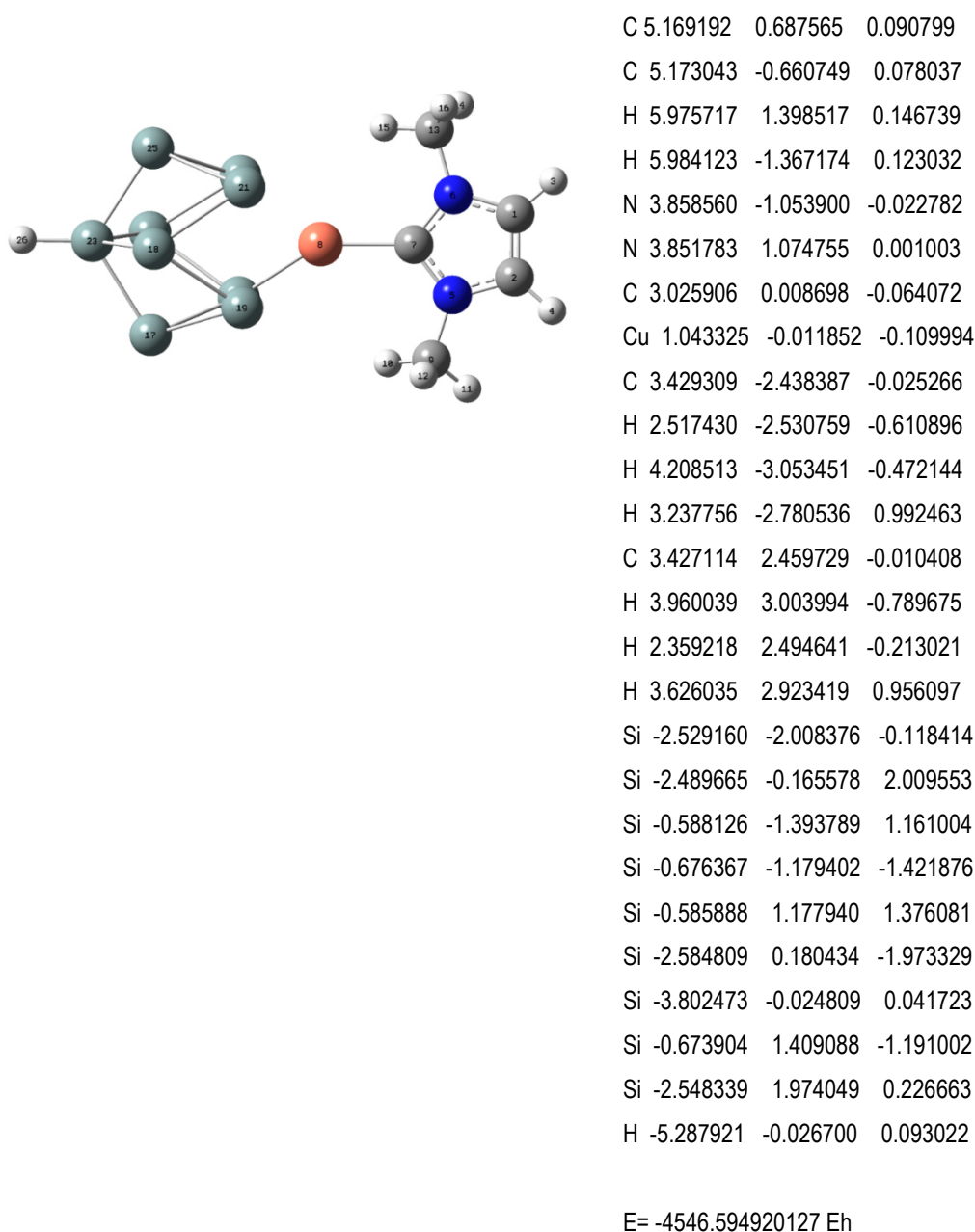
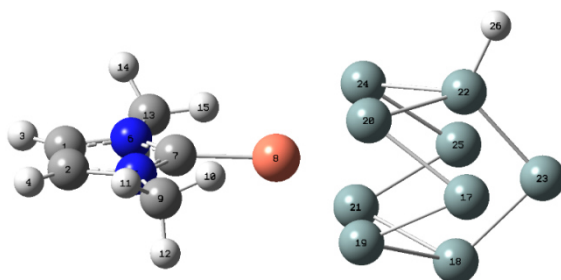


Figure SI 8.10 | The molecular structure and the Cartesian coordinates of complex A optimized at the $\omega\text{b97xd/def2tzvp}$ level of theory in the continuum of NH_3 (SMD) at 200 K. The MP2 energy calculated MP2/def2qzvpp level of theory on top the optimized geometry in Hartrees.

8 PROTONATED AND METALIZED SILICIDE $[\text{NHC}^{\text{DIPP}}\text{Cu}(\eta^4\text{-Si}_9\text{H})]^{2-}$

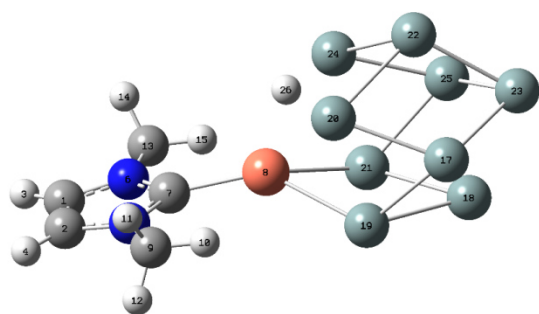


C	-5.212901	0.658276	-0.088919
C	-5.217495	-0.689601	-0.111931
H	-6.019673	1.370782	-0.115362
H	-6.029715	-1.394680	-0.159450
N	-3.900653	-1.085471	-0.057645
N	-3.893833	1.043025	-0.018375
C	-3.066862	-0.024608	-0.000506
Cu	-1.079071	-0.027596	0.043053
C	-3.484608	-2.473447	-0.045300
H	-2.397916	-2.510013	-0.071399
H	-3.841900	-2.964741	0.859919
H	-3.884072	-2.988972	-0.918359
C	-3.468133	2.427618	0.004695
H	-3.995145	2.963364	0.793663
H	-2.398749	2.460451	0.199262
H	-3.673721	2.902256	-0.955136
Si	2.643285	-1.891926	0.100797
Si	2.605060	-0.061370	-1.851631
Si	0.663363	-1.366974	-1.149930
Si	0.632468	-1.281338	1.363303
Si	0.618055	1.238583	-1.283003
Si	2.532909	0.115620	1.605437
Si	4.201596	0.052544	-0.068183
Si	0.592829	1.417263	1.222502
Si	2.582233	1.954278	-0.104968
H	3.071584	0.195337	2.989924

E= -4546.591303063 Eh

Figure SI 8.11 | The molecular structure and the Cartesian coordinates of complex B optimized at the ω b97xd/def2tzvp level of theory in the continuum of NH_3 (SMD) at 200 K. The MP2 energy calculated MP2/def2qzvp level of theory on top the optimized geometry in Hartrees.

8 PROTONATED AND METALIZED SILICIDE $[\text{NHC}^{\text{DIPP}}\text{Cu}(\eta^4\text{-Si}_9\text{H})]^{2-}$



C	5.297992	-0.024295	-0.568060
C	5.199969	-0.080714	0.776170
H	6.157588	-0.004757	-1.215828
H	5.958178	-0.120447	1.539264
N	3.856736	-0.080599	1.070520
N	4.010251	0.008453	-1.051161
C	3.106667	-0.025687	-0.050605
Cu	1.138245	-0.001341	-0.193913
C	3.314256	-0.132907	2.415410
H	4.138263	-0.170747	3.124745
H	2.712979	0.753282	2.614040
H	2.696576	-1.021537	2.538402
C	3.686565	0.071873	-2.462291
H	2.604615	0.086468	-2.570608
H	4.104927	0.977253	-2.901637
H	4.088609	-0.800134	-2.977769
Si	-2.648549	1.845178	0.034956
Si	-2.615998	0.103581	-1.840085
Si	-0.643166	1.350941	-1.200692
Si	-0.679632	1.389088	1.350323
Si	-0.666932	-1.229837	-1.311169
Si	-2.553237	-0.058617	1.938280
Si	-4.199712	0.032087	0.170660
Si	-0.705904	-1.484777	1.227380
Si	-2.681880	-1.790915	-0.120307
H	0.242340	-0.064234	1.471303

E= -4546.554073001 Eh

Figure SI 8.12 | The molecular structure and the Cartesian coordinates of the complex with a bridging proton optimized at the ω b97xd/def2tzvp level of theory in the continuum of NH_3 (SMD) at 200 K. The MP2 energy calculated MP2/def2qzvpp level of theory on top the optimized geometry in Hartrees.

8.7.5 References

- [1] Agilent, *CrysAlisPRO*, Agilent Technologies Ltd, Yarnton, Oxfordshire, England, **2014**.
- [2] O. V. Dolomanov, L. J. Bourhis, R. J. Gildea, J. A. K. Howard, H. Puschmann, *J. Appl. Crystallogr.* **2009**, *42*, 339–341.
- [3] G. M. Sheldrick, *Acta Crystallogr. Sect. A Found. Crystallogr.* **2015**, *71*, 3–8.
- [4] G. M. Sheldrick, *Acta Crystallogr. Sect. C Struct. Chem.* **2015**, *71*, 3–8.
- [5] K. Brandenburg, *Diamond Version 4.6.1*, Crystal Impact GbR, Bonn, Germany, **2019**.
- [6] F. S. Geitner, T. F. Fässler, *Chem. Commun.* **2017**, *53*, 12974–12977.
- [7] A. J. Shaka, J. Keeler, T. Frenkiel, R. Freeman, *J. Magn. Reson.* **1983**, *52*, 335–338.
- [8] C. Lorenz, F. Hastreiter, J. Hioe, N. Lokesh, S. Gärtner, N. Korber, R. M. Gschwind, *Angew. Chemie Int. Ed.* **2018**, *57*, 12956–12960.
- [9] H. Bürger, R. Eujen, H. C. Marsmann, *Zeitschrift für Naturforsch. - Sect. B J. Chem. Sci.* **1974**, *29*, 149–152.
- [10] A. M. Torres, W. S. Price, *Common Problems and Artifacts Encountered in Solution-State NMR Experiments. Concepts Magn Reson Part A*, **2017**.
- [11] T. E. Skinner, T. O. Reiss, B. Luy, N. Khaneja, S. J. Glaser, *J. Magn. Reson.* **2003**, *163*, 8–15.
- [12] P. Kroneck, J. Kodweiß, O. Lutz, A. Nolle, D. Zepf, *Zeitschrift für Naturforsch. - Sect. A J. Phys. Sci.* **1982**, *37*, 186–190.
- [13] J. Da Chai, M. Head-Gordon, *Phys. Chem. Chem. Phys.* **2008**, *10*, 6615–6620.
- [14] F. Weigend, R. Ahlrichs, *Phys. Chem. Chem. Phys.* **2005**, *7*, 3297–3305.
- [15] C. Riplinger, B. Sandhoefer, A. Hansen, F. Neese, *J. Chem. Phys.* **2013**, *139*, 134101.
- [16] F. Jensen, *J. Chem. Theory Comput.* **2015**, *11*, 132–138.

9 CONCLUSION

Over the last decades, NMR spectroscopy has established itself as an extremely valuable analytical tool that has become an integral part of chemical research. Due to the continuous improvements of NMR, it can provide solutions to increasingly specific problems throughout most diverse research areas. It is therefore no wonder that NMR could also pave its way as indispensable technique in the fields of medicine, pharmacy and biology. Especially valued as a non-destructive and quantitative method that requires no major sample preparation procedures, NMR can enrich all fields of research with detailed information about molecular structures on an atomic basis and dynamic processes in natural environments or under real reaction conditions. Furthermore, NMR offers the possibility to obtain time-resolved information about reactions by *in situ* monitoring and thus is helping to understand underlying mechanisms and processes. This thesis demonstrated the versatility of NMR as a powerful analytical method in the various fields of organo- and photocatalysis, organometallic and inorganic chemistry. Therein, this thesis presented the detection and structural characterization of elusive reaction intermediates as well as the elucidation of reaction mechanisms and chemical processes in solution alongside the development of profound substrate scopes and synthetic procedures.

One of the main tasks in this work was the acquisition of ^{31}P - and ^{29}Si -NMR spectra covering signals that appear over the entire chemical shift range of the respective nuclei within a single scan. Therefore, special techniques were required that on the one hand provide a uniform broadband excitation in presence of ^1H -decoupling to enable 1D $^{31}\text{P}\{^1\text{H}\}$ -NMR reaction monitoring of the photocatalytic functionalization of P_4 ($\delta(^{31}\text{P}) = -522$ ppm; side-products/-intermediates: $\delta(^{31}\text{P})$ up to +100 ppm). On the other hand, uniform broadband excitation in the F1 domain of 2D ^1H - ^{29}Si -HMQC and -HMBC spectra was desired to facilitate cross peak screening of protonated silicon cages in solution in absence of folding or aliasing artifacts of peaks located outside a confined spectral window, restricted in its size by the general application of hard pulses. The xyBEBOP, which was developed and kindly provided to us by Prof. Dr. Burkhard Luy, was the broadband pulse of choice since it features the rare property of being relatively short (0.5 ms or 1 ms) while covering extremely large frequency ranges (500 kHz and 1000 kHz, respectively). The compatibility of this broadband pulse in combination with decoupling sequences could be demonstrated by comparing the performance of the new sequence containing the xyBEBOP pulse (*bulu_zgpg*) with the standard sequence (*zgpg*) applying a hard pulse. It was found that the *bulu_zgpg* sequence furnished $^{31}\text{P}\{^1\text{H}\}$ -NMR signals with intensities, multiplet collapse and line widths identical to those obtained by hard pulse excitation, however, with the great benefit that full 90° excitation is achieved even when the xyBEBOP is applied far off resonance in contrast to hard pulses. For the objective of broadband excitation in the F1 domain of 2D ^1H - ^{29}Si -HMQC and -HMBC spectra, the xyBEBOP pulse was implemented in the 2D sequences *hmqcgpqf* and *hmbcgpndqf*. The testing was performed on the new HMQC sequence *hmqcgpqfbulusp2* which revealed that this sequence reduces the cross peaks' intensity by 9% compared to the standard sequence containing hard pulses, probably due to stronger relaxation losses. Yet, the testing also showcased the clear benefits of the

9 CONCLUSION

hmqcgpqfbulusp2 experiment, that are uniform excitation in F1, also when the transmitter frequency is set far off resonance, and preventing aliasing artifacts. The successful implementation of the xyBEBOP in 1D experiments with ^1H -decoupling and in the F1 dimension of 2D experiments laid the groundwork for numerous $^{31}\text{P}\{^1\text{H}\}$ -NMR reaction monitorings and 2D ^1H - ^{29}Si -HMQC and -HMBC spectra that extensively promoted the research behind many results presented in this thesis.

In chapter three, a comprehensive mechanistic proposal of a combined organocatalytic route to conjugated enynes and cyclic nitronates could be proposed, which was achieved by means of *in situ* NMR and isotopic labeling in combination with theoretical calculations. This reaction that starts from nitroalkene dimers was found to be base initiated and to proceed *via* a central linking intermediate common to both pathways of enynes and nitronates. Its unusual structure containing a cyclic isoxazolidine-2,5-diol core was verified by 2D NMR experiments, ^{15}N labelling studies and theoretical calculations. After this common intermediate, the pathways are proposed to separate into the formation of enynes accomplished by an unusual buildup of the triple bond out of a single bond *via* a combination of oxidation, dehydration and retro-1,3-dipolar cycloaddition and into the pathway of nitronates by a change in heteroatom connectivity through intramolecular rearrangements over open chain intermediates. The proposed mechanism was corroborated experimentally by screening various reaction conditions and by the detection of the byproducts H_2O , N_2 and CO_2 of which latter two were obtained from the reaction of isotopically enriched starting material. It was furthermore identified, that the product outcome can effectively be controlled by adjusting the pH. While only moderate to good yields (< 57%) were obtained for conjugated enynes, due to omnipresent polymerization pathways, for cyclic nitronates high yields up to 84% could be achieved. Nevertheless, with the help of various NMR experiments mechanistic and selectivity issues were solved that provide a basis for further improvements of this extremely valuable, combined metal-free route to conjugated enynes and cyclic nitronates.

Chapter four focused on the development of the first photocatalytic functionalization of P_4 towards precious triarylphosphines and tetraarylphosphonium salts *via* the direct formation of P-C bonds. After thorough screening of reactants and reaction conditions, good yields were obtained in the reaction of a solution of P_4 , PhI and Et_3N (as a reductive quencher of the excited-state photocatalyst) catalyzed by an iridium-catalyst under blue-light irradiation (455 nm) which laid the basis for establishing a profound synthetic scope. The application of differently substituted aryl iodides demonstrated that electron withdrawing and bulky substituents disfavor the formation of quaternary phosphonium salts. By performing UV/Vis experiments in combination with a plethora of different *in situ* NMR methods, key mechanistic steps of this complex functionalization of P_4 could be identified and an elaborate mechanism could be proposed. First, the photocatalyst is excited by blue light and then gets reduced by TEA within the first radical pair of the reaction which was corroborated by UV/Vis quenching experiments and CIDNP effects detected by NMR. Both analytical techniques could demonstrate that the reduced catalyst can then either be oxidized by PhI or P_4 whereas PhI is considered to mainly account to the productive pathway, due to application in a vast excess. The aryl radicals thus generated then sequentially functionalize P_4 , producing in sequence PhPH_2 ,

Ph₂PH, Ph₃P and finally Ph₄P⁺ which was verified by *in situ* ³¹P{¹H}-NMR reaction monitoring of the reactions applying either P₄ or the sequential intermediates PhPH₂, Ph₂PH and Ph₃P as starting material. NMR investigations performed at low temperatures indicated PH₃ as further intermediate upstream to PhPH₂. This could be confirmed by *in situ* NMR reaction monitoring of a solution of NaPH₂, which upon illumination unexpectedly provided constantly small amounts of PH₂⁻ and led to the clean formation of PH₃, PhPH₂, Ph₂PH and Ph₃P and Ph₄P⁺ with negligibly small side product formation. *In situ* NMR reaction monitoring of the functionalization of H₂PPh corroborated that a reduction in concentration of starting material led to less side product formation and consequently to higher yield. Despite all efforts (low temperatures, radical trapping or spin trapping) to obtain any information about poly-phosphorus intermediates upstream to PH₃, this was not successful. Yet, from *in situ* ³¹P{¹H}-NMR reaction monitoring it could be perceived that P₄ is converted into an NMR-undetectable reservoir which though can supply phosphorus units for further conversion to Ph₄P⁺. ²H isotopic labeling studies demonstrated the importance of triethylamine (TEA) beyond its role as sacrificial electron donor, in particular, as proton source for the generation of the sequential intermediates. It was found that TEA is not only beneficial for the productive pathway, but at the same time also detrimental since it is responsible for the generation of main side products. Yet, some side products of the photocatalytic functionalization of P₄ showed a promising structural core that might open up a new synthetic route towards phosphinines. In summary, the first direct catalytic organo-functionalization of P₄ was described and key mechanistic steps could be elucidated that provide starting points for further reaction optimizations or development of new synthetic strategies.

Chapter five presented the organometallic synthesis and detailed characterization of an unprecedented 1-phospha-7-norbornadiene exhibiting a direct and polar P-B-bond and discussed its reactivity towards triple bonds. This 1-phospha-7-norbornadiene could be obtained by a reaction of the λ⁴-phosphinine salt Li[1-Me-PC₅H₂Ph₃] with (C₆F₅)₂BCl and its structure was fully characterized by NMR and UV/Vis spectroscopy, single crystal X-ray diffraction and elemental analysis. Upon results obtained by NMR and DFT calculations a comprehensive mechanism for the formation of this 1-phospha-7-norbornadiene could be postulated. *In situ* ³¹P{¹H}-NMR and ¹¹B{¹H}-NMR reaction monitoring at variable temperatures revealed the generation of an unusual bicyclic intermediate performing the P-B bond, whose proposed structure was supported by DFT calculations. The unusual splitting patterns of the ³¹P-NMR signals of both 1-phospha-7-norbornadiene and its intermediate could be elucidated by exceptional modern, multinuclear 1D and inverse 2D NMR experiments (³¹P{¹⁹F, ¹H}-NMR and ¹H-³¹P{¹¹B, ¹H}-HSQCs) with specially adapted pulse programs exploiting the full potential of two different triple resonance probes (TBI-P: ¹H, ³¹P and tunable BB channel; TBI-F: ¹H, ¹⁹F and tunable BB channel). Although the 1-phospha-7-norbornadiene represents a classical Lewis acid-base adduct, its reactivity rather resembled that of a frustrated Lewis pair since it was found to react readily with triple bonds of both polar nitriles and apolar phenylacetylenes generating exceptional insertion and addition products. The corresponding underlying mechanisms of the nitrile insertion into the P-B bond with concomitant B-C bond splitting and of the alkyne addition accompanied by cleavage of both the P-B and C-B bonds were postulated upon results obtained by ³¹P{¹H}-NMR and ¹¹B{¹H}-NMR at variable

9 CONCLUSION

temperatures and DFT calculations. This work showcased the ability of seemingly classical Lewis pairs to form reactive intermediates by reversible heterolytic element-element bond dissociation. Therein, by using modern NMR experiments, product- and key intermediate structures were identified and the labile nature of the P-B bond of 1-phospha-7-norbornadiene was demonstrated which lays the foundation for its high reactivity.

In chapter six, the synthesis and application of a new iron complex $[K([18]\text{crown } 6)][\text{Cp}^*\text{FeL}]$ incorporating a chelating phosphinine ligand (**L**) was reported. While crystal structure analysis of this complex showed that **L** coordinates in a chelating σ -fashion to the iron center, solution phase $^{31}\text{P}\{^1\text{H}\}$ NMR analysis of the crystal and *in situ* $^{31}\text{P}\{^1\text{H}\}$ NMR monitoring of the formation of this complex demonstrated the presence of another isomeric structure where the ligand **L** coordinates in an η^4 fashion to the iron center. They further indicated an isomeric equilibrium in solution that was supported by DFT calculations. Treating these isomers with CO_2 was found to yield different reactivities depending on the coordination mode of the attached phosphinine ligand. While the iron complex with an η^4 -coordinated ligand **L** resulted in addition of CO_2 to a carbon atom of the phosphinine moiety, the iron complex with the σ -coordinated ligand **L** was found to be able to fully cleave one C=O bond to give an Fe-coordinated CO moiety and P-bound O atom. This work presents the first reported example of C=O cleavage of a CO_2 molecule mediated by a single Fe center, and demonstrates the potential of coordinatively- and electronically-flexible phosphinine ligands to help mediate challenging bond activation reactions.

In chapter seven and eight, the application of liquid NMR could prove itself as a valuable analysis tool in the field of inorganic chemistry. By performing low temperature NMR experiments rare insights were gained in solution processes of silicon *Zintl* phases, which were fully enriched in ^{29}Si , in presence of transition metal complexes in liquid ammonia. Chapter seven presents the study on the crystals $[(\text{NHC}^{\text{tBu}}\text{Au})_6(\eta^2\text{-Si}_4)]\text{Cl}_2 \cdot 7 \text{NH}_3$, the first gold-functionalized silicide, and $(\text{NHC}^{\text{tBu}}\text{Au})_3\text{NHCl}$, an imide capped gold triangle. These crystals were obtained from a reaction of $\text{Rb}_6\text{Cs}_6\text{Si}_{17}$ with $\text{NHC}^{\text{tBu}}\text{AuCl}$ in presence of [2.2.2]-cryptand in liquid ammonia and characterized by single crystal X-ray diffractometry and theoretical calculations. This reaction mixture was found to yield a plethora of ^1H -NMR singlets accountable to various NHC-containing species. The structural assignment of these low concentrated compounds could be achieved by *inter alia* by ^1H - ^1H -DOSY and time-consuming ^1H - ^{13}C - and ^1H - ^{15}N 2D NMR experiments. Thereby, two sequential precursors were detected and characterized that are potentially involved in the formation of the $(\text{NHC}^{\text{tBu}}\text{Au})_3\text{NHCl}$ crystal. Thus, this study provides an exceptional insight in the mechanism of crystal formation in solution. We could furthermore demonstrate that ammonia is involved in Brønsted acid-base equilibria with NHC-carbenes and in association-dissociation equilibria with NHC-Au-complexes considerably influencing the product outcome. Chapter eight provided a thorough solution NMR study on the first two-fold hetero-functionalized silicon cluster $[\text{NHC}^{\text{Dipp}}\text{Cu}(\eta^4\text{-Si}_9)\text{H}]^{2-}$. This complex was obtained in a mixture of $\text{K}_6\text{Rb}_6\text{Si}_{17}$ in presence of $\text{NHC}^{\text{Dipp}}\text{CuCl}$ and [2.2.2]cryptand in liquid ammonia. ^1H -NMR monitoring revealed the formation of a doublet which due to its negative shift, coupling constant and pattern was assigned to a mono-protonated silicide, protonated at its vertex. By integration, a corresponding set of

NHC^{Dipp} signals was detected revealing the attachment of one $\text{NHC}^{\text{Dipp}}\text{Cu}$ unit to the protonated silicide. The connectivity of this new proton signal to a silicide was demonstrated by 2D ^1H - ^{29}Si -HMQC spectra and 1D $^1\text{H}\{^{29}\text{Si}\}$ -NMR spectra with selective silicon decoupling. The latter turned out to be an easy, highly sensitive NMR method for investigating cluster dynamics that fall in the time window of the decoupling sequence. Experimental NMR data were corroborated by theoretical calculations. NMR data furthermore revealed that the metallized complex $[\text{NHC}^{\text{Dipp}}\text{Cu}(\eta^4\text{-Si}_9)\text{H}]^{2-}$ is more rigid than the uncomplexed silicide $[\text{HSi}_9]^{3-}$. To our knowledge the detection of $[\text{NHC}^{\text{Dipp}}\text{Cu}(\eta^4\text{-Si}_9)\text{H}]^{2-}$ represents the first case of a protonated coinage metallized group 14 Zintl cluster in solution so far. The results of the work presented in chapters seven and eight extended the field of functionalized silicon clusters by two new examples $[(\text{NHC}^{\text{tBu}}\text{Au})_6(\eta^2\text{-Si}_4)]\text{Cl}_2 \cdot 7 \text{NH}_3$ and $[\text{NHC}^{\text{Dipp}}\text{Cu}(\eta^4\text{-Si}_9)\text{H}]^{2-}$.

In summary, this work presented exceptional novel synthetic procedures and provided insights into elusive processes in solution in the various fields of organo- and photocatalysis, organometallic and inorganic chemistry. This thesis furthermore showcased the versatility of NMR in the most diverse fields of chemistry: from the elucidation of reaction mechanisms by *in situ* detection and characterization of key intermediates, through the detection of equilibria and dynamic processes, over to exposing elusive solution processes. The constant improvements and adaptations of NMR methods render NMR spectroscopy as more and more universal analytical technique for solving most diverse tasks and show that the potential of NMR is still far from being exhausted.

10 GLOSSARY

1D	one dimensional
2D	two dimensional
ABSTRUSE	adjustable, broadband, sech/tanh-rotation uniform selective excitation
aq	acquisition time
BEBOP	broadband excitation by optimized pulses
cat	catalyst
CHORUS	chirped ordered pulses for ultra-broadband spectroscopy
conv.	conversion
COSY	correlation spectroscopy
CV	cyclic voltammetry
d1	relaxation delay
DABCO	1,4-diazabicyclo[2.2.2]octane
DBU	1,8-diazabicyclo(5.4.0)undec-7-ene
DCM	dichloromethane
DEA	diethylamine
DEE	diethylether
DFT	density-functional theory
Dipp	2,6-diisopropylphenyl
DME	dimethoxyethane
DMF	dimethylformamide
Dmp	2,6-dimesitylphenyl
DMSO	dimethylsulfoxide
DOSY	diffusion ordered spectroscopy
DPP	diphenylprolinol
DSTE	double stimulated echo
EA	ethylacetate
EDTA	Ethylenediamine tetraacetic acid
ee	enantiomeric excess
EI	electron ionization
ELF	electron localization function
EPR	electron paramagnetic resonance
ESI	electrospray ionization
EXSY	exchange spectroscopy
F1, F2	frequency axis
FEP	fluorinated ethylene propylene

10 GLOSSARY

FID	free induction decay
FIDRES	FID resolution
FLP	frustrated Lewis pair
GC	gas chromatography
GC-FID	gas chromatography with flame ionization detector
GC-MS	gas chromatography–mass spectrometry
gd	gated decoupling
HD	high-definition
HMBC	heteronuclear multiple bond correlation
HMQC	heteronuclear multiple-quantum correlation
HPLC	high-performance liquid chromatography
HRMS	High-resolution mass spectra
HS	hyperbolic secant
HSQC	heteronuclear single quantum coherence
Hz	hertz
ig	inverse-gated decoupling
INEPT	insensitive nuclei enhancement by polarization transfer
IR	infrared
kHz	kilo hertz
LED	light-emitting diode
LIFDI	liquid injection field desorption ionisation
MAS	magic angle spinning
Mes	mesityl
MHz	mega hertz
NBO	natural bond orbital
NHC	n-heterocyclic carbene
NMR	nuclear magnetic resonance
NOE	nuclear overhauser effect
NOESY	nuclear Overhauser enhancement Spectroscopy
NS	number of scans
ω_1 p	transmitter frequency offset
OLED	organic light-emitting diode
OMS	octamethylcyclotetrasiloxane
PE	petroleum ether
pg	power-gated decoupling
photo-CIDNP	photochemically induced dynamic nuclear polarization
ppm	parts per million

rf	radio frequency
RT	room temperature
S/N	signal to noise
SI	supporting information
SPOAL	phase alignment
SW	spectral width
TBD	triazabicyclodecene
TD	time domain
TEA	triethylamine
TFAA	trifluoroacetic anhydride
TLC	thin-layer chromatography
TM	transition metal
TMS	tetramethylsilane
TPP	2,4,6-triphenylphosphinine
TPPI	time proportional phase incrementation
UHD	ultra-high definition
UV	ultraviolet
Vis	visible
VT	variable temperature
XRD	X-ray diffraction
xs.	excess

CURRICULUM VITAE

Personal Information

Name: Verena Streitferdt
Date of birth: 18.08.1992
Address: Kelheimwinzerstraße 74
93309, Kelheim
Phone: +49 1577 7274990
E-Mail: verena.streitferdt@ur.de

Experience

01/2017 – present PhD student, group of Prof. Dr. Ruth Gschwind, Institute of Organic Chemistry, University of Regensburg

Activities:

- Adaption and implementation of NMR experiments, implementation of heteronuclei and exchange of NMR probes.
- Application of modern NMR techniques in the various fields of chemistry for mechanistic and structural of elusive intermediates and processes in solution.

Education

10/2014 – 09/2016 M. Sc. Chemistry, University of Regensburg, Grade: 1.0

Master Thesis: "Reaction Optimization of the Organocatalytic Formation of Conjugated Enynes and Cyclic Nitronates", Grade: 1.0

10/2011 – 09/2014 B.Sc. Chemistry, University of Regensburg, Grade: 2.5

Bachelor Thesis "Neue Strukturen zur Inhibition des MIA Proteins", Grade: 1.0

Languages

German (native), English (business fluent), French (elementary), Rumanian (beginner), Spanish (beginner)

Publications:

V. Streitferdt, M.H. Haindl, J. Hioe, F. Morana, P. Renzi, F. von Rekowski, A. Zimmermann, M. Nardi, K. Zeitler, R.M. Gschwind, *European Journal of Organic Chemistry* **2019**, 2019, 328-337

Unprecedented Mechanism of an Organocatalytic Route to Conjugated Enynes with a Junction to Cyclic Nitronates

DOI: [10.1002/ejoc.201801153](https://doi.org/10.1002/ejoc.201801153)

U. Lennert, P. Arockiam, V. Streitferdt, D.J. Scott, C. Rödl, R.M. Gschwind, R. Wolf, *Nature Catalysis* **2019**, 2, 1101-1106

Direct catalytic transformation of white phosphorus into arylphosphines and phosphonium salts

DOI: [10.1038/s41929-019-0378-4](https://doi.org/10.1038/s41929-019-0378-4)

J. Leidl, M. Marquardt, P. Coburger, D.J. Scott, V. Streitferdt, R.M. Gschwind, C. Müller, R. Wolf, *Angewandte Chemie International Edition* **2019**, 58, 15407-15411

Facile C=O Bond Splitting of Carbon Dioxide Induced by Metal-Ligand Cooperativity in a Phosphinine Iron(0) Complex

DOI: [10.1002/anie.201909240](https://doi.org/10.1002/anie.201909240)

S.M. Tiefenthaler, V. Streitferdt, J. Baumann, S. Gaertner, R.M. Gschwind, N. Korber, *Zeitschrift für anorganische und allgemeine Chemie* **2020**, 646, 1595-1602

On the Reactivity of NHC t Bu AuCl towards Rb₆Cs₆Si₁₇: The First Gold-Silicon Cluster [(NHC t Bu Au)₆(η²-Si₄)Cl₂·7NH₃] and an Imide Capped Gold Triangle (NHC t Bu Au)₃NHCl

DOI: [10.1002/zaac.202000275](https://doi.org/10.1002/zaac.202000275)

J. Leidl, A.R. Jupp, E.R.M. Habraken, V. Streitferdt, P. Coburger, D.J. Scott, R.M. Gschwind, C. Müller, J.C. Slootweg, R. Wolf, *Chemistry – A European Journal* **2020-02-13**, 26, 7788-7800

A Phosphinine-derived 1-Phospha-7-bora-norbornadiene: Frustrated Lewis Pair Type Activation of Triple Bonds

DOI: [10.1002/chem.202000266](https://doi.org/10.1002/chem.202000266)

Award

Chemical Communications Poster Prize award for the work of “Unusual Approaches towards NMR Investigations of Group 14 Zintl Ions in Solution” at the 16th International Conference on the Coordination and Organometallic Chemistry of Germanium, Tin and Lead (ICCOG-GTL-16) in Saitama, Japan, in 2019

DANKSAGUNG

Meinen ersten und besonderen Dank möchte ich meiner Doktormutter Frau Prof. Dr. Ruth M. Gschwind widmen. Ich durfte seit Beginn meiner Masterarbeit an ihrem Arbeitskreis viele spannende Themen bearbeiten und mit ihr zusammen viele interessante, belebende und positive Diskussionen erleben. Dies hat mich in meiner Arbeit bestärkt und positiv geprägt.

Ein weiterer großer Dank geht an den Zweitgutachter Herrn Prof. Dr. Werner Kremer, nicht nur für die Übernahme des Zweitgutachters, sondern auch für die vielen Hilfestellungen beim Messen in der Biophysik.

Außerdem möchte ich mich herzlich bei Herrn Prof. Dr. Nikolaus Korber bedanken für die Übernahme der Rolle des Dritprüfers und für die tolle Kooperation im Bereich der *Zintl* Ionen. Auch dem Vorsitzenden des Prüfungsausschusses, Herrn Apl. Prof. Dr. Rainer Müller, gebührt bester Dank.

Auch ein großes Dankeschön an Herrn Prof. Dr. Remco Sprangers, dem ich sehr viel Messzeit in der Biophysik und dementsprechend viele Ergebnisse zu verdanken habe.

Ganz besonders möchte ich mich auch bei meinen Kooperationspartner*innen bedanken. Danke an Susanne Tiefenthaler, Stefanie Gärtner und Corinna Lorenz vom AK Korber für die schöne Zusammenarbeit im Bereich der *Zintl* Ionen und die vielen tollen Diskussionen. Vielen Dank an Ulrich Lennert vom AK Wolf für die großartige und immer lustige Kooperation auf dem Gebiet der Organofunktionalisierung von weißem Phosphor. Herzlichen Dank an Julia Leitl vom AK Wolf, du warst mir über die gesamte Studienzeit nicht nur eine sehr gute Freundin sondern während der Promotion auch eine tolle Kooperationspartnerin. In diesem Zuge auch einen großen Dank an Herrn Prof. Dr. Robert Wolf für die Ermöglichung der Kooperationen.

Ganz herzlichen Dank auch an alle bestehenden und ehemaligen Kolleg*innen am Arbeitskreis Gschwind. Hervorzuheben ist an dieser Stelle meine sehr gute Freundin Nele Berg, mit der ich viele schöne Erinnerungen teile. Von den täglichen Kaffees bis hin zu Konferenzbesuchen und den schönen gemeinsamen Urlauben. Ganz besonders muss ich mich bei Philipp Nitschke bedanken, der mir bei allen NMR-Problemen stets mit Rat und Tat zur Seite stand. Vielen Dank auch an Kerstin Rothermel, für die schöne gemeinsame Zeit am und außerhalb des Arbeitskreises. Weiterhin bedanke ich mich bei Willibald Stockerl, Johannes Gramüller, Dr. Michael Haindl, Dr. Julian Greindl, Dr. Florian Hastreiter, Dr. Andreas Seegerer, Dr. Hanna Bartling, Dr. Johnny Hioe, Dr. Matej Žabka, Lavakumar Naviri, Philipp Dullinger, Dr. Maxime Melikian, Dr. Lokesh Nanjundappa und Dr. Nils Sorgenfrei. Vielen Dank auch an meine Forschungspraktikanten Johannes Wilhelm, Maximilian Franta und Franz Westermair. Letzteren beiden und Anton Abramov wünsche ich außerdem eine schöne weitere Zeit am AK Gschwind und viele tolle Forschungsergebnisse.

Des Weiteren möchte ich mich bei meinen ehemaligen Kommiliton*innen für die tolle Studienzeit und die guten Freundschaften bedanken die daraus entstanden sind. Vielen Dank an Marlene Bödl, Veronika Sötz, Katja Steck, Claudia Kirschner, Daniel Schneider und Sebastian Sandl.

Auch meinen Freundinnen aus der Schulzeit in Ingolstadt danke ich sehr herzlich. Sie hatten in den vergangenen Jahren stets ein offenes Ohr und erhielten die Freundschaft über die ganze Welt verteilt noch lange über die Schulzeit hinaus aufrecht.

Die größte Unterstützung jedoch erhielt ich von meiner Familie. Besonders von meinen Eltern Wiltrud und Siegfried, die sich immer so liebevoll und mit außerordentlicher Hingabe um mich kümmerten und kümmern. Ihr steht schon immer hinter mir und werdet es auch sicher zukünftig tun. Vielen lieben Dank auch an meinen Freund Maximilian, der in der Zeit der Doktorarbeit besonders hinter mir stand und mich tagtäglich über die Maße unterstützte.

Eidesstattliche Erklärung

- (1) Ich erkläre hiermit an Eides statt, dass ich die vorliegende Arbeit ohne unzulässige Hilfe Dritter und ohne Benutzung anderer als der angegebenen Hilfsmittel angefertigt habe; die aus anderen Quellen direkt oder indirekt übernommenen Daten und Konzepte sind unter Angabe des Literaturzitats gekennzeichnet.
- (2) Bei der Auswahl und Auswertung folgenden Materials haben mir die zu Beginn des jeweiligen Kapitels aufgeführten Personen in der jeweils beschriebenen Weise unentgeltlich geholfen.
- (3) Weitere Personen waren an der inhaltlich-materiellen Herstellung der vorliegenden Arbeit nicht beteiligt. Insbesondere habe ich hierfür nicht die entgeltliche Hilfe eines Promotionsberaters oder anderer Personen in Anspruch genommen. Niemand hat von mir weder unmittelbar noch mittelbar geldwerte Leistungen für Arbeiten erhalten, die im Zusammenhang mit dem Inhalt der vorgelegten Dissertation stehen.
- (4) Die Arbeit wurde bisher weder im In- noch im Ausland in gleicher oder ähnlicher Form einer anderen Prüfungsbehörde vorgelegt.

Regensburg, den _____

Verena Streitferdt